

DTIC FILE COPY

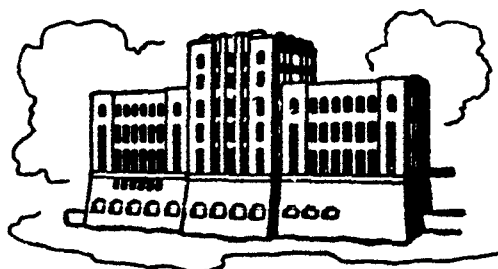
④

SHIP STERN AND WAKE FLOWS:
SOLUTIONS OF THE
FULLY-ELLIPTIC REYNOLDS-AVERAGED
NAVIER-STOKES EQUATIONS AND
COMPARISONS WITH EXPERIMENTS

by
V. C. Pate¹, H.C. Chen and S. Ju

Sponsored by
Office of Naval Research
Accelerated Research Initiative (Special Focus) Program in
Ship Hydrodynamics

Contract N00014-83-K-0136
Work Unit No. 432b-002
and
Contract N00014-88-K-0001



DTIC
ELECTED
AUG 31 1988
S E D

IIHR Report No. 323

Iowa Institute of Hydraulic Research
The University of Iowa
Iowa City, Iowa 52242-1585

April 1988

Approved for Public Release; Distribution Unlimited

88 8 30 065

Ship Stern and Wake Flows:
Solutions of the Fully-Elliptic Reynolds-Averaged
Navier-Stokes Equations and Comparisons with Experiments

by

V.C. Patel, H.C. Chen and S. Ju

Sponsored by
Office of Naval Research
Accelerated Research Initiative (Special Focus) Program in
Ship Hydrodynamics

Contract N00014-83-K-0136
Work Unit No. 432b-002
and
Contract N00014-88-K-0001

IIHR Report No. 323

Iowa Institute of Hydraulic Research
The University of Iowa
Iowa City, Iowa 52242-1585

April 1988

Approved for Public Release; Distribution Unlimited

Unclassified

SECURITY CLASSIFICATION OF THIS PAGE (When Data Entered)

REPORT DOCUMENTATION PAGE		READ INSTRUCTIONS BEFORE COMPLETING FORM
1. REPORT NUMBER IIHR Report No. 323	2. GOVT ACCESSION NO.	3. RECIPIENT'S CATALOG NUMBER
4. TITLE (and Subtitle) Ship Stern and Wake Flows: Solutions of the Fully-Elliptic Reynolds-Averaged Navier-Stokes Equations and Comparisons with Experiments		5. TYPE OF REPORT & PERIOD COVERED November 1982 - April 1988 Technical Report
7. AUTHOR(s) V.C. Patel, H.C. Chen, and S. Ju		6. PERFORMING ORG. REPORT NUMBER IIHR Report No. 323 8. CONTRACT OR GRANT NUMBER(s) N00014-83-K-0136 N00014-88-K-0001
9. PERFORMING ORGANIZATION NAME AND ADDRESS Iowa Institute of Hydraulic Research The University of Iowa Iowa City, Iowa 52242-1585		10. PROGRAM ELEMENT, PROJECT, TASK AREA & WORK UNIT NUMBERS 432b-002
11. CONTROLLING OFFICE NAME AND ADDRESS Office of Naval Research 800 N Quincy St Arlington, VA 22217		12. REPORT DATE April 1988 13. NUMBER OF PAGES 271
14. MONITORING AGENCY NAME & ADDRESS (if different from Controlling Office) Office of Naval Research 536 S Clark St Chicago, Illinois 60605		15. SECURITY CLASS. (of this report) Unclassified 16a. DECLASSIFICATION/DOWNGRADING SCHEDULE
16. DISTRIBUTION STATEMENT (of this Report) Approved for public release; distribution unlimited		
17. DISTRIBUTION STATEMENT (of the abstract entered in Block 20, if different from Report)		
18. SUPPLEMENTARY NOTES		
19. KEY WORDS (Continue on reverse side if necessary and identify by block number) Reynolds-Averaged Navier-Stokes Equations; Turbulence Models; Body-Fitted Coordinates; Ship Stern Flows; Ship Wake; Computational Fluid Dynamics → (jhd) ←		
20. ABSTRACT (Continue on reverse side if necessary and identify by block number) The numerical method developed by Chen and Patel (IIHR Report No. 285, April 1985) for the solution of the partially-parabolic Reynolds-averaged Navier-Stokes equations has been generalized to solve the fully-elliptic equations. This method is applied to calculate the flow over the stern and in the wake of several ship forms for which extensive data are available. The report also provides an overview of the present status of experiments and computational capabilities for such flows. <i>Key words:</i>		

Table of Contents

	<u>Page</u>
ABSTRACT.....	iii
ACKNOWLEDGEMENTS.....	iii
NOMENCLATURE.....	iv
I. INTRODUCTION.....	1
II. SHIP STERN AND WAKE FLOW.....	2
II.1 Developments in Theory.....	2
II.2 A Guide to Experiments.....	4
II.3 Scope of the Present Work.....	6
III. CALCULATION STRATEGY AND METHOD.....	8
III.1 Equations and Coordinates.....	8
(a) Body-Fitted Coordinates.....	14
(b) Reynolds Equations in Transformed Coordinates.....	17
III.2 Numerical Procedures.....	21
(a) Grid Generation.....	22
(b) Finite-Analytic Discretization for the Transformed Coordinates.....	28
(c) Solution of the Continuity Equation: Velocity-Pressure Coupling.....	33
(d) Boundary Conditions.....	39
(e) The Overall Solution Algorithm.....	46
IV. SOME NUMERICAL ASPECTS OF THE METHOD.....	48
IV.1 Convergence.....	48
IV.2 Grid Dependence.....	49
IV.3 Solution Domain.....	51
IV.4 Computing Times.....	52
V. TEST CASES AND COMPARISONS WITH EXPERIMENTS.....	52
V.1 Wigley Parabolic Hull.....	58
(a) Available Experimental Information.....	58
(b) Body Shape and Numerical Grid.....	58
(c) Description of Results and Comparisons with Experiments.....	59
(d) Summary.....	65
V.2 SSPA Cargo Liner.....	66
(a) Hull Geometry and Available Experimental Information.....	66
(b) Numerical Grid.....	67
(c) Description of Results and Comparisons with Experiments.....	67
(d) Summary.....	71

V.3	HSVA Tanker.....	72
	(a) Hull Geometry and Available Experimental Information.....	72
	(b) Numerical Grid.....	72
	(c) Description of Results and Comparisons with Experiments.....	73
	(d) Discussion.....	77
V.4	SR107 Ore Carrier.....	77
	(a) Hull Geometry and Experimental Information.....	77
	(b) Numerical Grid.....	77
	(c) Description of Results and Comparisons with Experiments.....	78
	(d) Discussion.....	80
V.5	Series 60, $C_b = 0.60$	80
	(a) Hull Geometry and Experimental Information.....	80
	(b) Numerical Grid.....	81
	(c) Description of Results and Comparisons with Experiments.....	82
	(d) Discussion.....	83
VI.	SUMMARY AND CONCLUSIONS.....	83
REFERENCES.....	86	
FIGURES.....	91	

ABSTRACT

The numerical method developed by Chen and Patel (IIHR Report No. 285, April 1985) for the solution of the partially-parabolic Reynolds-averaged Navier-Stokes equations has been generalized to solve the fully-elliptic equations. This method is applied to calculate the flow over the stern and in the wake of several ship forms for which extensive data are available. The report also provides an overview of the present status of experiments and computational capabilities for such flows.

ACKNOWLEDGEMENTS

The research described herein was sponsored by the Office of Naval Research, Accelerated Research Initiative (Special Focus) Program in Ship Hydrodynamics, under Contract N00014-83-K-0136, and under Contract N00014-88-K-0001. The authors appreciate the support and encouragement of ONR Program Managers, Dr. C.M. Lee, Mr. J. Fein, and Dr. E.P. Rood during the course of this research.

The Graduate College of The University of Iowa provided a large share of the computer funds utilized in the initial development of the numerical method. Its application to ship hulls, which are reported here, were greatly facilitated by the allocation of time on the CRAY XMP-24 supercomputer of the Naval Research Laboratory, and on the CRAY XMP-48 machine of the National Center for Supercomputing Applications at Urbana-Champaign.

The extensive comparisons between the calculations and experimental data were made possible by the timely cooperation of the experimenters. In this regard, the authors are particularly grateful to Professor L. Larsson of SSPA and Chalmers University, Goteborg, Dr. L. Lofdahl of Chalmers University, Goteborg, Dr. J. Kux of IfS, Hamburg, Dr. C. Collatz of HSVA, Hamburg, and Professor I. Tanaka and Drs. T. Suzuki and Y. Toda of Osaka University, Osaka, for providing us with tabulated data.

Accession For	
NTIS GRA&I	<input checked="" type="checkbox"/>
DTIC TAB	<input type="checkbox"/>
Unannounced	<input type="checkbox"/>
Justification	
By	
Distribution/	
Availability Codes	
Dist	Avail and/or Special
A-1	



NOMENCLATURE

Alphabetical

A	grid-attraction amplitude function defined in equation (41)
A,B,C,R	convection coefficients in the linearized convective-transport equation (45)
a,b,c	(1) modified grid-control functions defined by equation (36) (2) constants in analytical solution of the one-dimensional equations (49) and (51)
A_ϕ, B_ϕ, C_ϕ	convection coefficients in the linearized convective-transport equation for $\phi (=U, V, W, k, \epsilon)$
a_p, a_d , etc.	finite-analytic coefficients for pressure and pressure-correction equations
b_ϕ, c_ϕ, d_ϕ	constants in transport equations (16) for $\phi (=U, V, W, k, \epsilon)$
b_0	two-dimensional grid-control function defined by equation (40)
b_C	three-dimensional grid correction function defined by equation (41)
b_i^j	geometric coefficients as defined in equation (27)
C	dimensionless crossflow velocity, normalized by U_0
c	grid-adjustment factor defined in equation (41)
c_b	block coefficient
c_{nb}	finite analytic coefficients for transport equations (nb = NE, NW, SE, SW, EC, WC, NC, SC)
c_d, c_n, c_e	finite-analytic coefficients for pressure and pressure-correction equations
c_f	$\tau_w / \frac{1}{2} \rho U_0^2$, friction coefficient ($= 2 U_\tau^2$)
c_p	$= 2 p$, pressure coefficient normalized by $\frac{1}{2} \rho U_0^2$

C_p, C_U, C_D	finite analytic coefficients for transport equations at central, upstream and downstream nodes
$C_\mu, C_{\epsilon 1}, C_{\epsilon 2}$	turbulence-model constants
d	constant defined in (41)
D_1	partial mass source term defined in equation (60a)
\hat{D}	source function in pressure equation (61)
D^*	mass source term in pressure-correction equation (65)
d_d, d_n, etc	finite-analytic coefficients for pressure and pressure-correction equations
E_2	series summation term in equation (52)
f^i	grid-control functions in equations (19) and (20)
G	turbulence generation term in equation (9) and (26f)
g	(1) geometric coefficient in equation (29) (2) source function in linearized transport equations (50) and (52)
g_{ij}	metric tensor in general curvilinear coordinates
g^{ij}	conjugate metric tensor in general curvilinear coordinates
h	grid size in equation (46)
h_i	metric coefficients or scale factors in orthogonal coordinates
x^i	
J	Jacobian
k	(1) dimensionless turbulent kinetic-energy, normalized by U_0^2 (2) grid size in equation (46)
L	length scale (body length)
l	grid size in equation (46)
N	distance normal to the body cross-section
N^*	$U_0 N / \nu$

\mathbf{n}^i	unit vectors normal to the coordinate lines
p	dimensionless pressure, normalized by ρU_0^2
\mathbf{p}^*	guessed (imperfect) pressure field
p'	$p - p^*$, pressure-correction
\mathbf{q}	dimensionless total velocity vector, normalized by U_0
\mathbf{q}^*	projection of the velocity vector on the body surface
q	magnitude of \mathbf{q}
q^ξ, q^η, q^ζ	dimensionless component velocities along ξ, η, ζ directions, respectively
\bar{R}	radius
r	\bar{R}/L , dimensionless radius
\mathbf{r}	position vector
r_s, r_{max}	dimensionless radius of the body surface and outer boundaries
Re	$U_0 L / \nu$, Reynolds number
R_ϕ	$1/Re + v_t / \sigma_\phi$, as in equation (10)
S_ϕ, s_ϕ	source functions for transport quantities $\phi (\equiv U, V, W, k, \epsilon)$
t	dimensionless time, normalized by L/U_0
U, V, W	dimensionless velocity components, normalized by U_0
U^*, V^*, W^*	velocities obtained from guessed pressure field p^*
$\tilde{U}, \tilde{V}, \tilde{W}$	pseudovelocities in equation (57)
$\hat{U}, \hat{V}, \hat{W}$	modified pseudovelocities in equation (59)
U_0	constant free-stream (reference) velocity
U_c	wake centerline velocity normalized by U_0
\mathbf{u}	velocity vector
U_τ	$(\tau_w / \rho U_0^2)^{1/2}$, normalized friction (wall shear) velocity
$\overline{uu}, \overline{uv}$, etc.	dimensionless Reynolds stresses, normalized by U_0^2
U_δ	velocity at the edge of boundary layer

X, Y, Z	Cartesian coordinates
$x, y, z; X, Y, Z$	dimensionless Cartesian coordinates
x^i	dimensionless orthogonal coordinates ($i=1,2,3$)
x, r, θ	dimensionless cylindrical-polar coordinates
y^+	$ReU_\tau y$, dimensionless distance normal to the wall
y^*	dimensionless distance from the hull surface in the y -direction

Greek

α	angle between \tilde{z}_n and \tilde{y}^n
α_ϕ^i	coefficients in transport equation (22) for $\phi (=U, V, W, k, \epsilon)$ and $i=1,2,3$
β	angle between \tilde{q}^* and ξ -direction on the body surface
γ	angle between $\tilde{\xi}$ and $\tilde{\zeta}$
δ	boundary-layer thickness
ϵ	rate of turbulent energy dissipation, normalized by U_0^3/L
κ	von Karman constant
λ_m	eigenvalues
ν	kinematic viscosity
ν_t	turbulent eddy-viscosity, normalized by $U_0 L$
ξ, η, ζ	transformed (general curvilinear) coordinates
ξ^i	general curvilinear coordinates ($i=1,2,3$)
ξ^*, η^*, ζ^*	transformed coordinates in linearized convective transport equations (45)
π	$= 3.141592653589793$
σ_ϕ	turbulence model constants for $\phi (=U, V, W, k, \epsilon)$
ϕ	(1) transport quantities (U, V, W, k, ϵ) (2) y or z in equation (42)

Superscripts

d,e, etc. downstream, east, etc., control surfaces

n,n-1 n^{th} and $(n-1)^{\text{th}}$ time step

I. INTRODUCTION

This report is concerned with the three-dimensional shear flow over the stern and in the wake of a ship. A review of the general features of such flows was provided by Patel (1982). On the basis of available experimental evidence it was observed that these flows could not be adequately described by boundary-layer theory or simple extensions of it, and recourse had to the so-called partially-parabolic (or parabolized) Navier-Stokes equations. The need for further experiments to provide the details required for the development and verification of solution procedures was also identified. Over the past few years, much effort has been devoted at many organizations to the development of solution procedures appropriate for the complex geometries of ship hulls, and additional experiments have been conducted on a number of different ship and ship-like models to establish a data base.

In the research at The University of Iowa, a method for the solution of the partially-parabolic equations was first developed and applied to a variety of trailing-edge and wake flows, including the flow over axisymmetric bodies and ship-like three-dimensional bodies. This method was described in detail by Chen and Patel (1985a) and its applications have been reported in several publications [Chen and Patel (1984; 1985a,b), Patel and Chen (1986a)]. During the course of this development it became clear that the numerical algorithms and physical models incorporated into the method could be employed equally well in the solution of the complete, fully-elliptic, Reynolds-averaged Navier-Stokes equations without incurring a significant penalty in computing times or storage. Although, as noted in Patel (1982), the partially-parabolic approximations are quite appropriate for most ship stern flows, the greater range of applicability of the fully-elliptic formulation was considered very attractive. For this reason, the partially-parabolic method of Chen and Patel (1985a) has been generalized to a fully-elliptic mode. The changes which are required in the original formulation are described here. This more general method is then applied to calculate the flow over several ship forms for which experimental data are available.

In what follows, we shall first put the present work in perspective by reviewing the different approaches which are being adopted to develop calculation procedures for ship stern flows. The status of the experimental informa-

tion is then reviewed to identify suitable test cases for the assessment of calculation methods. This is followed by a description of the fully-elliptic method, and its evaluation by application to the selected test cases. Detailed comparisons are made between the experiments and calculations with respect to the hull pressure distribution, the mean velocity field, and, when available, the turbulence parameters. It is shown that the numerical method is capable of handling all the geometrical and physical features of the flow. Some improvements are, however, necessary in the modelling of the turbulence, particularly in the near-wall and near-wake regions.

II. SHIP STERN AND WAKE FLOW

II.1 DEVELOPMENTS IN THEORY

An accurate prediction of the flow at the stern is of great practical interest in the determination of ship resistance, in the design of propellers and appendages, and in the determination of the ensuing wake. The failure of conventional boundary-layer calculation methods, of the type which have been used with considerable success on aerodynamic configurations, to predict the thickening of the viscous flow over the stern was demonstrated quite dramatically by the results presented at the SSPA-ITTC Workshop [Larsson (1981)]. Figure 1, adapted from that reference, shows the contours of the axial component of velocity at a transverse section close to the stern of two double models tested in wind tunnels. There are many reasons for the observed disagreement among the calculations with different methods and experiments. Among these are: failure of the boundary-layer approximations, inadequacies of the empirical inputs to effect closure of the equations, and, of course, inaccuracies in the numerical schemes.

As noted in the recent Report of the Resistance and Flow Committee of the 18th ITTC [referred to here as ITTC (1987)], methods for the calculation of stern flows have evolved in two general directions. One of these involves generalization and extension of the thin boundary-layer methods, of both integral and differential types, to include such factors as changes in coordinate metrics normal to the surface, normal variation of pressure, and interaction between the viscous and inviscid flow regions. The development of these so-called higher-order integral methods for thick boundary layers has

been pursued by Nagamatsu (1985), Soejima (1985), and Toda et al. (1985), among others. These methods involve numerous approximations with respect to the terms which are retained in the equations, velocity-profile assumptions, friction formulas, and auxiliary closure equations. Similar attempts to generalize differential thin boundary-layer methods have been made by Soejima (1983) and Lee (1985) but they have not reached the level of development of the simpler integral methods due to the difficulties of coupling such calculations with the external inviscid flow to obtain matched and converged solutions.

The alternative approach to the calculation of stern flows involves numerical solutions of the complete Reynolds-averaged Navier-Stokes equations, or the somewhat less general partially-parabolic equations, in domains which, in principle, encompass the viscous as well as the inviscid flow. Initial development of such methods was restricted to two-dimensional and axisymmetric shapes, but applications to three-dimensional problems are now beginning to be made. Patel and Chen (1986a) presented a review of these, and other methods of the type discussed above, for the simpler case of axisymmetric flow over the tail and in the wake of bodies of revolution. They concluded that the numerical complexities of the traditional iterative approach to viscous-inviscid interactions is fast approaching those of the global, large-domain methods which involve fewer assumptions. However, comparative study of interactive and noninteractive procedures for the solution of the partially-parabolic viscous-flow equations made by Stern et al. (1986) suggests that both approaches lead to satisfactory results with comparable computing effort.

Although experience with global numerical methods in three-dimensional flows, in general, and for ship hulls, in particular, is still quite limited, different approaches are being followed to develop such methods. This is evidenced by the recent work of Broberg and Larsson (1984), Chen and Patel (1984, 1985a,b), Hoekstra and Raven (1985a,b), Huang and Zhou (1985), Ito and Mori (1985), Janson and Larsson (1985), Kodama (1985,1987), Raven and Hoekstra (1985), Tzabiras (1984, 1985), and Stern et al. (1986). These methods are at various stages of development and differ quite substantially from one another in many important respects. The principal differences stem from: (a) coordinates used and methods employed to construct them; (b) approximations introduced in the Reynolds-averaged Navier-Stokes equations, leading to the so-

called thin-layer equations, or the partially-parabolic equations; (c) the turbulence model employed, ranging from algebraic eddy-viscosity to multi-equation models, and the treatment of the boundary conditions; (d) formulas used to discretize the differential equations and the numerical methods used to solve them; (e) in the size of the solution domain and coupling with the inviscid flow, if any; and (f) in the manner in which the solution is initiated, e.g. using inviscid solution, starting with a boundary-layer solution, marching in time from rest, etc. A detailed discussion of these differences is well beyond the scope of this report. However, we shall address some of them in subsequent sections as we describe the particular procedures adopted in the present development.

Most of the methods mentioned above have been developed and applied thus far to the case of double models. Thus, the free surface is considered to be flat and treated as a plane of symmetry. Extension of these methods to treat the effects of the free surface have not yet received much attention largely because the difficulties are even greater than those encountered within the framework of thin boundary-layer theory [see Stern (1985, 1986)]. Such extensions may evolve along two different directions. In one, a viscous-flow method may be combined with an inviscid-flow method in an interactive mode to take advantage of the well developed techniques of classical ship-wave theory. The alternative approach, which does not separate the viscous and wave effects, would require the satisfaction of the proper boundary conditions at the free surface which is itself determined as a part of the solution. This latter approach has been pursued by, among others, Miyata et al. (1984, 1985, 1986) and Hino (1987). In both cases, however, much further work is needed to realistically and accurately account for the boundary layer and turbulent flow effects.

II.2 A GUIDE TO EXPERIMENTS

Measurements in ship boundary layers and in ship wakes have been made over many years. The review of Patel (1980) for the Stanford Conference on Complex Turbulent Flows, which emphasized turbulence modeling, indicated that none of the data available could be regarded as complete enough for the validation of stern and wake flow calculation methods because the measurements were restricted to the mean flow. Among the most detailed mean-flow measure-

ments on ship hulls were those of Larsson (1974) on the SSPA 720 Liner and Hoffman (1976) on the HSVA Tanker. Both experiments were conducted with double models in wind tunnels. These two data sets were in fact used as test cases in the 1980 SSPA-ITTC Workshop on ship boundary layers (Larsson, 1981), the results of which were mentioned above in connection with Figure 1. These experiments continue to be among the most detailed available to date, and their value has been greatly increased by the subsequent turbulence measurements of Lofdahl (1982) [see also Lofdahl and Larsson (1984)] on the SSPA Liner, and the extensive wake measurements of Wieghardt and Kux (1980) and Wieghardt (1982, 1983), and turbulence measurements of Knaack (1984) and Knaack, Kux and Wieghardt (1985) in the wake of the HSVA tanker. The data on these two hull forms, therefore, are detailed enough to test several critical aspects of ship stern and wake flow calculation methods.

The Cooperative Experimental Program of the ITTC Resistance and Flow Committee provided an impetus to the establishment of a comprehensive data base on the flow around ship hulls against which emerging theoretical methods could be tested. While the focus of this program was on quantities of principal concern in tankery, it also led to some detail measurements in the viscous flow. The present status of the program is reviewed in ITTC (1987). Of the four hulls which were initially selected for the program, which included the HSVA Tanker mentioned above, measurements in the boundary layers and wakes of two have been reported to date. These are the Wigley parabolic form and the Series 60, $C_B = 0.60$ form. In spite of the concerted international effort over a period of years, not all of the available data are suitable as test cases for numerical methods of the type described in the previous section. As pointed out in ITTC (1987), many experiments were confined to a few stations over the stern and in the very near wake and, therefore, it is difficult to establish proper initial and boundary conditions for them. Some involve large scatter and uncertainty due to blockage and model attitude. Also, quite different measurement locations and coordinates have been employed by different experimenters even for tests on the same hull form. While this precludes direct comparisons among data sets from different experiments and test facilities, some of the data sets are sufficiently well documented for use in testing the capabilities of calculation methods to predict certain important aspects of the flow.

In addition to the measurements on the Wigley and Series 60 hulls made under the auspices of the ITTC program, data have been obtained in the stern flow of other ship hulls and ship-like forms. Fukuda and Fujii (1985) have reported measurements on three hulls, including a Series 60, $C_B=0.8$ form and an elongated model derived from it by adding a parallel middle body to study scale effects, by Hotta and Hatano (1985) on a tanker model, and by Hinatsu and Takeshi (1985) on two other hulls. Of these, the first were conducted on double models in a wind tunnel, the second used a free-surface model in a water channel, and the last was performed in a towing tank. Only the first two included turbulence measurements. Among the experiments on ship-like bodies are those of Huang et al. (1983) on two models of elliptic cross section with the same sectional area distributions as that of one of the axisymmetric bodies which were tested earlier.

Although the foregoing summary of experiments gives the impression that there is now a substantial body of experimental information on stern flows over a variety of shapes, in reality the available data are not sufficiently complete or extensive enough to be used as comprehensive test cases for calculation methods. In fact, this deficiency is not restricted to ship flows. It is shared by practically all measurements in three-dimensional flows because such measurements are time consuming and expensive, and the experimental techniques themselves are not well developed. Also, the experiments are rarely conducted for the purpose of validating all aspects of any particular calculation method. The choice of test cases for this purpose is, therefore, a difficult one. We shall address this issue in a later section.

II.3 SCOPE OF THE PRESENT WORK

The purpose of this report is two-fold: (a) to describe the generalization of the partially-parabolic method of Chen and Patel (1985a) to a fully-elliptic capability, and (b) to assess the performance of the method by comparisons between calculations and experiments. The first aspect is relatively straightforward because the partially-parabolic method was described in considerable detail in the above reference, and the changes in the numerical structure of the method are not extensive. In the interest of completeness, however, the essential parts of the method are reviewed. The method is described in the next section (Section III).

The second task is more formidable for several reasons. First, it is important to identify the most critical and the most successful aspects of the overall method by evaluating, to the extent possible, the performance of each of the many components of the method. This involves the selection of simple test cases in which a particular feature of the method can be evaluated. Fortunately, the present method has been subjected to such tests and the results have been reported in the literature. For example, the performance of the $k-\epsilon$ turbulence model, together with the two-point wall functions approach, features which are retained in the present method, has been examined in the previous applications of the partially-parabolic method, and the capability of the elliptic numerical scheme to handle separation and reattachment in axisymmetric laminar and turbulent flows was demonstrated by Patel and Chen (1986b) and Chen and Patel (1987b, 1988), respectively. Secondly, it is necessary to evaluate the complete methodology by comparisons with experimental data on a wide variety of realistic ship forms. Here, the previous experience is somewhat limited. The partially-parabolic method was first compared with data on the relatively simple ship-like bodies of elliptic cross section in Chen and Patel (1984, 1985a) and with experiments on the Wigley and SSPA hulls in Chen and Patel (1985b). Although satisfactory agreement was observed in all cases, some difficulties were noted, particularly in the last reference, with regard to grid refinement and turbulence modeling. That reference also pointed out yet another, and equally important difficulty of carrying out detailed comparisons between calculations and experiment. This relates to the different coordinates employed in the two, and the loss of accuracy resulting from the required interpolation. While these difficulties cannot be readily resolved, they emphasize the need to make comparisons with a number of data sets, collected in different ways and on different models, to provide a more complete account of the capabilities of the numerical method. Special attention is therefore paid in the present work to examine the available data summarized in the previous section to identify potential test cases. The rational for selecting five hull forms, namely the Wigley parabolic ship, the SSPA 720 Cargo Liner, the HSVA Tanker, the SR107 Ore Carrier, and the Series 60, $C_b = 0.6$ form, will be discussed along with the corresponding calculations and comparisons with data in Section IV.

III. CALCULATION STRATEGY AND METHOD

III.1. EQUATIONS AND COORDINATES

For three-dimensional flows involving complex geometries, it is desirable to employ body-fitted coordinate systems so that the flow in the wall layer can be accurately resolved with a reasonable number of grid points. Once such a coordinate system is selected for a given geometry, there remains the task of formulating the equations of motion in that system. Two different approaches can be adopted for this purpose. One of these uses what may be termed "partial transformations", in which only the independent coordinate variables are transformed, leaving the dependent variables (i.e. velocity components) in a preselected coordinate system in the physical domain. This approach, which has been used by Chen and Patel (1985a,b), among others, has the advantages that the resulting equations are relatively simple and the results can be readily interpreted. Since the velocity vectors, in general, do not align with the coordinate directions, this approach may lead to increased numerical diffusion when the angles between the velocity components and coordinate surfaces become large. The alternative is to transform the equations completely, including the independent as well as the dependent variables. This approach has been used by, among others, Richmond et al. (1986), Stern et al. (1986), and Ogawa and Ishiguro (1987). The use of contravariant velocity components in such a complete transformation allows a much more accurate resolution of the boundary-layer flow near a solid surface. However, the fully-transformed equations involve many geometric coefficients and their higher-order derivatives. This not only leads to increased computer storage requirements but also can adversely affect the solution of the flow equations if the coefficients are not evaluated accurately. In many practical applications, it is not necessary to use the complete transformations if the basic coordinate systems are chosen carefully so as to avoid large skew angles between velocity components and the faces of the computational cell.

In the present study, which is concerned with external flows past ship forms, the restrictions associated with the partial transformations can be easily alleviated by choosing cylindrical polar coordinates as the basic coordinate system in the physical plane. A detailed description of such partial transformations and the corresponding equations was given in Chen and

Patel (1985a). For the sake of completeness, we shall briefly describe these in the following.

Consider the equations of motion in cylindrical coordinates (x, r, θ) for unsteady, three-dimensional, incompressible flow. The exact Reynolds-averaged equations of continuity and momentum of the mean flow, in dimensionless form, are,

$$\frac{\partial U}{\partial x} + \frac{1}{r} \frac{\partial}{\partial r} (rV) + \frac{1}{r} \frac{\partial W}{\partial \theta} = 0 \quad (1)$$

$$\begin{aligned} \frac{\partial U}{\partial t} + U \frac{\partial U}{\partial x} + V \frac{\partial U}{\partial r} + \frac{W}{r} \frac{\partial U}{\partial \theta} + \frac{\partial}{\partial x} (p + \bar{u}u) + \frac{\partial}{\partial r} (\bar{u}v) \\ + \frac{1}{r} \frac{\partial}{\partial \theta} (\bar{u}w) + \frac{\bar{u}v}{r} - \frac{1}{Re} \nabla^2 U = 0 \end{aligned} \quad (2)$$

$$\begin{aligned} \frac{\partial V}{\partial t} + U \frac{\partial V}{\partial x} + V \frac{\partial V}{\partial r} + \frac{W}{r} \frac{\partial V}{\partial \theta} - \frac{W^2}{r} + \frac{\partial}{\partial x} (\bar{u}v) + \frac{\partial}{\partial r} (p + \bar{v}v) \\ + \frac{1}{r} \frac{\partial}{\partial \theta} (\bar{v}w) + \frac{\bar{v}v}{r} - \frac{\bar{w}w}{r} - \frac{1}{Re} (\nabla^2 V - \frac{2}{r^2} \frac{\partial W}{\partial \theta} - \frac{V}{r^2}) = 0 \end{aligned} \quad (3)$$

$$\begin{aligned} \frac{\partial W}{\partial t} + U \frac{\partial W}{\partial x} + V \frac{\partial W}{\partial r} + \frac{W}{r} \frac{\partial W}{\partial \theta} + \frac{WV}{r} + \frac{\partial}{\partial x} (\bar{u}w) + \frac{\partial}{\partial r} (\bar{v}w) \\ + \frac{1}{r} \frac{\partial}{\partial \theta} (p + \bar{w}w) + 2 \frac{\bar{v}w}{r} - \frac{1}{Re} (\nabla^2 W + \frac{2}{r^2} \frac{\partial V}{\partial \theta} - \frac{W}{r^2}) = 0 \end{aligned} \quad (4)$$

$$\text{with } \nabla^2 = \frac{\partial^2}{\partial x^2} + \frac{\partial^2}{\partial r^2} + \frac{1}{r} \frac{\partial}{\partial r} + \frac{1}{r^2} \frac{\partial^2}{\partial \theta^2}$$

where $x = \frac{X}{L}$, $r = \frac{R}{L}$, θ are the dimensionless coordinates normalized by a characteristic length L , and t is the time normalized by L/U_0 . U , V , W are, respectively, the longitudinal, radial and circumferential components of mean velocity normalized by the characteristic velocity U_0 . p is the pressure

normalized by ρU_0^2 . $Re = U_0 L / \nu$ is the Reynolds number defined in terms of U_0 , L and molecular kinematic viscosity ν . The barred quantities $\bar{u}u$, $\bar{u}v$, etc., are the Reynolds stresses, normalized by U_0^2 .

In the present study, the two-equation $k-\epsilon$ turbulence model is used to model the Reynolds stresses. Each stress is related to the corresponding mean rate of strain by an isotropic eddy viscosity ν_t as follows:

$$\begin{aligned}
 - \bar{u}v &= \nu_t \left(\frac{\partial U}{\partial r} + \frac{\partial V}{\partial x} \right) \\
 - \bar{u}w &= \nu_t \left(\frac{\partial W}{\partial x} + \frac{1}{r} \frac{\partial U}{\partial \theta} \right) \\
 - \bar{v}w &= \nu_t \left(\frac{1}{r} \frac{\partial V}{\partial \theta} + \frac{\partial W}{\partial r} - \frac{W}{r} \right) \\
 - \bar{u}u &= \nu_t \left(2 \frac{\partial U}{\partial x} \right) - \frac{2}{3} k \\
 - \bar{v}v &= \nu_t \left(2 \frac{\partial V}{\partial r} \right) - \frac{2}{3} k \\
 - \bar{w}w &= \nu_t \left(\frac{2}{r} \frac{\partial W}{\partial \theta} + 2 \frac{W}{r} \right) - \frac{2}{3} k
 \end{aligned} \tag{5}$$

The eddy viscosity is related to the dimensionless turbulent kinetic energy k , and its rate of dissipation ϵ , by

$$\nu_t = c_\mu \frac{k^2}{\epsilon} \tag{6}$$

where c_μ is a constant, and k and ϵ are governed by the convective transport equations

$$\begin{aligned}
 \frac{\partial k}{\partial t} + U \frac{\partial k}{\partial x} + V \frac{\partial k}{\partial r} + W \frac{\partial k}{\partial \theta} &= \frac{\partial}{\partial x} \left(\frac{1}{R_k} \frac{\partial k}{\partial x} \right) \\
 &+ \frac{1}{r} \frac{\partial}{\partial r} \left(\frac{1}{R_k} r \frac{\partial k}{\partial r} \right) + \frac{1}{r^2} \frac{\partial}{\partial \theta} \left(\frac{1}{R_k} \frac{\partial k}{\partial \theta} \right) + G - \epsilon \\
 \frac{\partial \epsilon}{\partial t} + U \frac{\partial \epsilon}{\partial x} + V \frac{\partial \epsilon}{\partial r} + W \frac{\partial \epsilon}{\partial \theta} &= \frac{\partial}{\partial x} \left(\frac{1}{R_\epsilon} \frac{\partial \epsilon}{\partial x} \right)
 \end{aligned} \tag{7}$$

$$\begin{aligned}
& + \frac{1}{r} \frac{\partial}{\partial r} \left(\frac{1}{R_\epsilon} r \frac{\partial \epsilon}{\partial r} \right) + \frac{1}{r^2} \frac{\partial}{\partial \theta} \left(\frac{1}{R_\epsilon} \frac{\partial \epsilon}{\partial \theta} \right) \\
& + C_{\epsilon 1} \frac{\epsilon}{k} G - C_{\epsilon 2} \frac{\epsilon^2}{k}
\end{aligned} \tag{8}$$

where G is the turbulence generation term:

$$\begin{aligned}
G = v_t \{ & 2 \left[\left(\frac{\partial U}{\partial x} \right)^2 + \left(\frac{\partial V}{\partial r} \right)^2 + \left(\frac{1}{r} \frac{\partial W}{\partial \theta} + \frac{V}{r} \right)^2 \right] + \left(\frac{1}{r} \frac{\partial U}{\partial \theta} + \frac{\partial W}{\partial x} \right)^2 \\
& + \left(\frac{\partial V}{\partial x} + \frac{\partial U}{\partial r} \right)^2 + \left(\frac{1}{r} \frac{\partial V}{\partial \theta} + \frac{\partial W}{\partial r} - \frac{W}{r} \right)^2 \}
\end{aligned} \tag{9}$$

The effective Reynolds number, R_ϕ , is defined as

$$\frac{1}{R_\phi} = \frac{1}{Re} + \frac{v_t}{\sigma_\phi} \tag{10}$$

Where $\phi \equiv (U, V, W, k, \epsilon)$. The constants in these equations were taken as $C_\mu = 0.09$, $C_{\epsilon 1} = 1.44$, $C_{\epsilon 2} = 1.92$, $\sigma_U = \sigma_V = \sigma_W = \sigma_k = 1.0$, $\sigma_\epsilon = 1.3$. We note again that v_t , k , and ϵ are all made dimensionless by the characteristic velocity and length scales, U_0 and L , respectively.

Using equations (5, 6 and 10), the momentum equations (2) through (4) and the turbulence-model equations (7) and (8) can be written

$$\begin{aligned}
& \frac{\partial U}{\partial t} + (U - 2 \frac{\partial v_t}{\partial x}) \frac{\partial U}{\partial x} + (V - \frac{\partial v_t}{\partial r}) \frac{\partial U}{\partial r} + (W - \frac{1}{r} \frac{\partial v_t}{\partial \theta}) \frac{1}{r} \frac{\partial U}{\partial \theta} \\
& + \frac{\partial p}{\partial x} + \frac{2}{3} \frac{\partial k}{\partial x} - \frac{\partial v_t}{\partial r} \frac{\partial V}{\partial x} - \frac{1}{r} \frac{\partial v_t}{\partial \theta} \frac{\partial W}{\partial x} - \frac{1}{R_U} \nabla^2 U = 0 \\
& \frac{\partial V}{\partial t} + (U - \frac{\partial v_t}{\partial x}) \frac{\partial V}{\partial x} + (V - 2 \frac{\partial v_t}{\partial r}) \frac{\partial V}{\partial r} + (W - \frac{1}{r} \frac{\partial v_t}{\partial \theta}) \frac{1}{r} \frac{\partial V}{\partial \theta} \\
& + \frac{\partial p}{\partial r} + \frac{2}{3} \frac{\partial k}{\partial r} - \frac{\partial v_t}{\partial x} \frac{\partial U}{\partial r} - \frac{1}{r} \frac{\partial v_t}{\partial \theta} \left(\frac{\partial W}{\partial r} - \frac{W}{r} \right) - \frac{W^2}{r}
\end{aligned} \tag{11}$$

$$-\frac{1}{R_V} (\nabla^2 V - \frac{2}{r^2} \frac{\partial W}{\partial \theta} - \frac{V}{r^2}) = 0 \quad (12)$$

$$\begin{aligned} \frac{\partial W}{\partial t} + (U - \frac{\partial v_t}{\partial x}) \frac{\partial W}{\partial x} + (V - \frac{\partial v_t}{\partial r}) \frac{\partial W}{\partial r} + (W - \frac{2}{r} \frac{\partial v_t}{\partial \theta}) \frac{1}{r} \frac{\partial W}{\partial \theta} \\ + \frac{1}{r} \frac{\partial p}{\partial \theta} + \frac{WV}{r} + \frac{2}{3} \frac{1}{r} \frac{\partial k}{\partial \theta} - \frac{\partial v_t}{\partial x} \left(\frac{1}{r} \frac{\partial U}{\partial \theta} \right) - \frac{\partial v_t}{\partial r} \left(\frac{1}{r} \frac{\partial V}{\partial \theta} - \frac{W}{r} \right) \\ - \frac{1}{r} \frac{\partial v_t}{\partial \theta} \left(\frac{2V}{r} \right) - \frac{1}{R_W} (V^2 W + \frac{2}{r^2} \frac{\partial V}{\partial \theta} - \frac{W}{r^2}) = 0 \end{aligned} \quad (13)$$

$$\begin{aligned} \frac{\partial k}{\partial t} + (U - \frac{1}{\sigma} \frac{\partial v_t}{\partial x}) \frac{\partial k}{\partial x} + (V - \frac{1}{\sigma} \frac{\partial v_t}{\partial r}) \frac{\partial k}{\partial r} + (W - \frac{1}{\sigma} \frac{\partial v_t}{\partial \theta}) \frac{1}{r} \frac{\partial k}{\partial \theta} \\ - \frac{1}{R_k} \nabla^2 k - G + \epsilon = 0 \end{aligned} \quad (14)$$

$$\begin{aligned} \frac{\partial \epsilon}{\partial t} + (U - \frac{1}{\sigma} \frac{\partial v_t}{\partial x}) \frac{\partial \epsilon}{\partial x} + (V - \frac{1}{\sigma} \frac{\partial v_t}{\partial r}) \frac{\partial \epsilon}{\partial r} + (W - \frac{1}{\sigma} \frac{\partial v_t}{\partial \theta}) \frac{1}{r} \frac{\partial \epsilon}{\partial \theta} \\ - \frac{1}{R_\epsilon} \nabla^2 \epsilon - C_{\epsilon 1} \frac{\epsilon}{k} G + C_{\epsilon 2} \frac{\epsilon^2}{k} = 0 \end{aligned} \quad (15)$$

It is convenient to rewrite these transport equations (11) through (15) in the following general form

$$\begin{aligned} \nabla^2 \phi = R_\phi [(U - b_\phi v_{t,x}) \phi_x + (V - c_\phi v_{t,r}) \phi_r + \\ (W - d_\phi \frac{1}{r} v_{t,\theta}) (\frac{1}{r} \phi_\theta) + \phi_t] + s_\phi \end{aligned} \quad (16)$$

where ϕ again represents any one of the convective transport quantities: U , V , W , k or ϵ , and the subscripts x, r, θ denote derivatives. The corresponding coefficients b_ϕ , c_ϕ and d_ϕ are

$$\begin{aligned}
b_U &= 2, & c_U &= 1, & d_U &= 1 \\
b_V &= 1, & c_V &= 2, & d_V &= 1 \\
b_W &= 1, & c_W &= 1, & d_W &= 2 \\
b_k &= \frac{1}{\sigma_k}, & c_k &= \frac{1}{\sigma_k}, & d_k &= \frac{1}{\sigma_k}, \\
b_\epsilon &= \frac{1}{\sigma_\epsilon}, & c_\epsilon &= \frac{1}{\sigma_\epsilon}, & d_\epsilon &= \frac{1}{\sigma_\epsilon},
\end{aligned} \tag{17}$$

and the source functions s_ϕ for U, V, W, k and ϵ are, respectively,

$$s_U = R_U [p_x + \frac{2}{3} k_x - v_{t,r} v_x - (\frac{1}{r} v_{t,\theta}) w_x] \tag{18a}$$

$$\begin{aligned}
s_V = R_V [p_r + \frac{2}{3} k_r - v_{t,x} u_r - (\frac{1}{r} v_{t,\theta}) (w_r - \frac{w}{r}) - \frac{w^2}{r}] \\
+ \frac{2}{r^2} w_\theta + \frac{v}{r^2}
\end{aligned} \tag{18b}$$

$$\begin{aligned}
s_W = R_W [\frac{1}{r} p_\theta + \frac{2}{3} \frac{1}{r} k_\theta + \frac{wv}{r} - v_{t,x} (\frac{1}{r} u_\theta) - v_{t,r} (\frac{1}{r} v_\theta - \frac{w}{r}) \\
- (\frac{1}{r} v_{t,\theta}) (\frac{2v}{r})] - \frac{2}{r^2} v_\theta + \frac{w}{r^2}
\end{aligned} \tag{18c}$$

$$s_k = - R_k (G - \epsilon) \tag{18d}$$

$$s_\epsilon = - R_\epsilon (C_{\epsilon 1} \frac{\epsilon}{k} G - C_{\epsilon 2} \frac{\epsilon^2}{k}) \tag{18e}$$

Equations (11) through (15) are coupled, nonlinear, partial differential equations and, together with the continuity equation (1), are sufficient, in principle, to solve for the six unknowns p, U, V, W, k and ϵ when proper initial and boundary conditions are specified.

(a) Body-Fitted Coordinates

Three-dimensional geometries, such as ship hulls are usually quite complex and cannot be conveniently described by simple orthogonal coordinate systems. It is, therefore, desirable to introduce analytic or numerical coordinate transformations which simplify the computational domain in the transformed plane and facilitate applications of the boundary conditions. In the present study, we shall use a numerically-generated, body-fitted coordinate system, since it offers the advantages of generality and flexibility and, most importantly, transforms the computational domain into a simple rectangular region with equal grid spacing.

In the numerical grid-generation technique, we seek a coordinate system for the numerical analysis of the flow in the domain D shown in Figure 2. This domain is bounded by an arbitrary hull surface S , the ship centerplane C , the free surface or water plane W , the upstream and downstream sections A and B , respectively, and an external boundary Σ . Section A may be located at a hull section where the boundary layer is thin to avoid calculation of the flow over the bow or it may be placed far ahead of the ship if the bow is to be included. The downstream boundary B may be placed at a section in the far wake. The choice of the external boundary Σ is also arbitrary. It could be far away from the hull or it could coincide with the walls of a towing tank or wind tunnel. The basic idea of a boundary-conforming curvilinear system is to find a transformation such that the boundary surfaces of the physical domain D in cylindrical or in any other basic orthogonal coordinate system, say (x^1, x^2, x^3) , are transformed into boundaries of a simple rectangular domain in the computational space (ξ, η, ζ) shown in Figure 3.

With the values of the curvilinear coordinates specified on the boundaries of D , it remains to generate the values of these coordinates in the interior of D . This is a boundary-value problem in the physical field with the curvilinear coordinates (ξ, η, ζ) as dependent variables and the orthogonal coordinates (x^1, x^2, x^3) as the independent variables, with boundary conditions specified on the curved boundaries. Thus, a system of elliptic partial differential equations can be used to generate the coordinates since the field solution of such a system is determined entirely by the boundary conditions.

However, the elliptic system must be chosen such that it precludes the occurrence of extrema in the interior of the domain and assures a one-to-one mapping between the physical and transformed planes.

For the general three-dimensional but simply-connected domain of interest here, a set of Poisson equations of the form

$$\begin{aligned}\nabla^2 \xi^1 &= f^1(\xi, \eta, \zeta) \\ \nabla^2 \eta &= f^2(\xi, \eta, \zeta) \\ \nabla^2 \zeta &= f^3(\xi, \eta, \zeta)\end{aligned}\tag{19}$$

or simply

$$\nabla^2 \xi^i = f^i, \quad i = 1, 2, 3\tag{20}$$

with $\xi^1 = \xi$, $\xi^2 = \eta$, $\xi^3 = \zeta$

may be taken as the coordinate generating system. Here, ∇^2 is the Laplacian operator in orthogonal coordinates x^i . The nonhomogeneous source functions f^i may be assigned appropriate values to yield the desired concentration of coordinate surfaces. The choice of these functions for specific applications will be discussed later in Section III.2(a). Equation (20) is subject to either Dirichlet or Neumann boundary conditions on the boundary surfaces, which are surfaces of constant ξ^i .

Since it is desirable to perform all numerical computations in the transformed (ξ, η, ζ) plane with equal grid spacing, i.e., $\Delta\xi = \Delta\eta = \Delta\zeta = 1$, equation (20) is cumbersome to use. It is more convenient to invert it and solve for the orthogonal coordinates. In other words, the dependent and independent variables are interchanged so that the orthogonal coordinates (x^1, x^2, x^3) in the physical plane become the dependent variables, with the curvilinear coordinates (ξ, η, ζ) as the independent variables. The boundary-value problem in the transformed field then involves generating the values of the orthogonal coordinates $x^i = x^i(\xi, \eta, \zeta)$ in the interior from the specified boundary values of x^i on the rectangular boundary surfaces of the transformed field. Since the boundaries in the transformed plane are all rectangu-

lar (constant ξ , η , or ζ plane), these computations are carried out on a cubic grid regardless of the shape of the physical boundaries.

In obtaining the inverse transformation of equation (20), several general relations between the physical (x^1, x^2, x^3) and the transformed (ξ, η, ζ) coordinates are required. The basic expressions may be found in many reference books, for example Aris (1971) and Lass (1975), although some of the relations are not explicitly given. A summary of some important relations are given in Appendix I of Chen and Patel (1985a) with specific reference to the transformation between an orthogonal coordinate system (x^1, x^2, x^3) and general coordinates $(\xi^1, \xi^2, \xi^3) = (\xi, \eta, \zeta)$. The latter are not necessarily orthogonal. With these transformation formulae, equations (20) become:

$$\begin{aligned}\nabla^2 x^1 &= \frac{1}{h_1 h_2 h_3} \frac{\partial}{\partial x^1} \left(\frac{h_2 h_3}{h_1} \right) \\ \nabla^2 x^2 &= \frac{1}{h_1 h_2 h_3} \frac{\partial}{\partial x^2} \left(\frac{h_1 h_3}{h_2} \right) \\ \nabla^2 x^3 &= \frac{1}{h_1 h_2 h_3} \frac{\partial}{\partial x^3} \left(\frac{h_1 h_2}{h_3} \right)\end{aligned}\tag{21}$$

where

$$\begin{aligned}\nabla^2 &= g^{11} \frac{\partial^2}{\partial \xi^2} + g^{22} \frac{\partial^2}{\partial \eta^2} + g^{33} \frac{\partial^2}{\partial \zeta^2} + 2g^{12} \frac{\partial^2}{\partial \xi \partial \eta} + 2g^{13} \frac{\partial^2}{\partial \xi \partial \zeta} \\ &+ 2g^{23} \frac{\partial^2}{\partial \eta \partial \zeta} + f^1 \frac{\partial}{\partial \xi} + f^2 \frac{\partial}{\partial \eta} + f^3 \frac{\partial}{\partial \zeta}\end{aligned}\tag{21a}$$

h_i are the metric coefficients in the chosen orthogonal coordinates x^i , and g^{ij} is the conjugate metric tensor in the transformed coordinates $\xi^i (= \xi, \eta, \zeta)$. Note that, for cylindrical polar coordinates (x, r, θ) , h_i are $(1, 1, r)$, respectively.

Equations (21) can be solved numerically in the transformed domain (ξ, η, ζ) when proper boundary conditions are specified on all boundary surfaces (i.e., constant ξ , η and ζ). If $f^1 = f^2 = f^3 = 0$, the transformation is said to be homeomorphic. In general, however, non-zero values are assigned

to these functions to exercise control over the grid distribution. Solutions of equations (21) to obtain numerical grids for particular shapes are presented in Section III.2(a).

(b) Reynolds Equations in Transformed Coordinates

Although, as noted earlier, it is possible to transform both the independent (x^1, x^2, x^3, t) and the dependent (U, V, W, k, ϵ) variables to the (ξ, η, ζ) coordinates, we will consider only the transformation of the independent variables, leaving the velocity components U, V, W in the original (x^1, x^2, x^3) coordinates in the physical plane. Also, as mentioned earlier, the cylindrical polar coordinates (x, r, θ) appear to be most convenient for the description of the flow field around practical ship forms. Thus, in this study, equations (1) and (16) [i.e., (11) through (15)] will be used as the basic equations in the physical plane to derive the equations in the transformed domain (ξ, η, ζ) . Transformed equations resulting from other orthogonal coordinates, which may be useful in other applications, are given in Appendix I of Chen and Patel (1985a). Using these general transformation relations, equation (16) for an unsteady three-dimensional flow can be written in the following form:

$$\begin{aligned}
 & g^{11} \phi_{\xi\xi} + g^{22} \phi_{\eta\eta} + g^{33} \phi_{\zeta\zeta} + 2g^{12} \phi_{\xi\eta} + 2g^{13} \phi_{\xi\zeta} + 2g^{23} \phi_{\eta\zeta} \\
 & + f^1 \phi_{\xi} + f^2 \phi_{\eta} + f^3 \phi_{\zeta} = \frac{R_\phi}{J} [\alpha_\phi^1 (b_1^1 \phi_{\xi} + b_1^2 \phi_{\eta} + b_1^3 \phi_{\zeta}) \\
 & + \alpha_\phi^2 (b_2^1 \phi_{\xi} + b_2^2 \phi_{\eta} + b_2^3 \phi_{\zeta}) + \alpha_\phi^3 (b_3^1 \phi_{\xi} + b_3^2 \phi_{\eta} + b_3^3 \phi_{\zeta})] \\
 & + R_\phi \phi_t + s_\phi
 \end{aligned} \tag{22}$$

where

$$\begin{aligned}
 \alpha_\phi^1 &= U - \frac{b_\phi}{J} (b_1^1 v_{t,\xi} + b_1^2 v_{t,\eta} + b_1^3 v_{t,\zeta}) \\
 \alpha_\phi^2 &= V - \frac{c_\phi}{J} (b_2^1 v_{t,\xi} + b_2^2 v_{t,\eta} + b_2^3 v_{t,\zeta}) \\
 \alpha_\phi^3 &= W - \frac{d_\phi}{J} (b_3^1 v_{t,\xi} + b_3^2 v_{t,\eta} + b_3^3 v_{t,\zeta})
 \end{aligned} \tag{23}$$

and b_ϕ , c_ϕ and d_ϕ are as defined in equation (17). Hereafter, the subscripts (ξ, η, ζ) on ϕ ($= U, V, W, k, \epsilon$) and v_t denote derivatives.

Equation (22) is identical with equation (A-84) in Appendix I of Chen and Patel (1985a). It can be rearranged into a general convective-transport equation of the form

$$g^{11}\phi_{\xi\xi} + g^{22}\phi_{\eta\eta} + g^{33}\phi_{\zeta\zeta} = 2A_\phi\phi_\zeta + 2B_\phi\phi_\eta + 2C_\phi\phi_\xi + R_\phi\phi_t + S_\phi \quad (24)$$

where

$$2A_\phi = \frac{R_\phi}{J} (b_1^{3\alpha 1} + b_2^{3\alpha 2} + b_3^{3\alpha 3}) - f^3 \quad (25a)$$

$$2B_\phi = \frac{R_\phi}{J} (b_1^{2\alpha 1} + b_2^{2\alpha 2} + b_3^{2\alpha 3}) - f^2 \quad (25b)$$

$$2C_\phi = \frac{R_\phi}{J} (b_1^{1\alpha 1} + b_2^{1\alpha 2} + b_3^{1\alpha 3}) - f^1 \quad (25c)$$

$$S_\phi = s_\phi - 2(g^{12}\phi_{\xi\eta} + g^{13}\phi_{\xi\zeta} + g^{23}\phi_{\eta\zeta}) \quad (25d)$$

and the source functions s_ϕ are given by

$$\begin{aligned} s_U = R_U & \left[\frac{1}{J} (b_1^1 p_\xi + b_2^2 p_\eta + b_3^3 p_\zeta) + \frac{2}{3J} (b_1^1 k_\xi + b_2^2 k_\eta + b_3^3 k_\zeta) \right. \\ & - \frac{1}{J^2} (b_2^1 v_{t,\xi} + b_2^2 v_{t,\eta} + b_2^3 v_{t,\zeta}) (b_1^1 v_\xi + b_1^2 v_\eta + b_1^3 v_\zeta) \\ & \left. - \frac{1}{J^2} (b_3^1 v_{t,\xi} + b_3^2 v_{t,\eta} + b_3^3 v_{t,\zeta}) (b_1^1 w_\xi + b_1^2 w_\eta + b_1^3 w_\zeta) \right] \end{aligned} \quad (26a)$$

$$\begin{aligned} s_V = R_V & \left\{ -\frac{W^2}{r} + \frac{1}{J} (b_2^1 p_\xi + b_2^2 p_\eta + b_2^3 p_\zeta) + \frac{2}{3J} (b_2^1 k_\xi + b_2^2 k_\eta + b_2^3 k_\zeta) \right. \\ & - \frac{1}{J^2} (b_1^1 v_{t,\xi} + b_1^2 v_{t,\eta} + b_1^3 v_{t,\zeta}) (b_2^1 u_\xi + b_2^2 u_\eta + b_2^3 u_\zeta) \end{aligned}$$

$$\begin{aligned}
& - \frac{1}{J} (b_3^1 v_{t,\xi} + b_3^2 v_{t,\eta} + b_3^3 v_{t,\zeta}) [\frac{1}{J} (b_2^1 w_\xi + b_2^2 w_\eta \\
& + b_2^3 w_\zeta) - \frac{w}{r}] \} + \frac{2}{rJ} (b_3^1 w_\xi + b_3^2 w_\eta + b_3^3 w_\zeta) + \frac{v}{r^2} \quad (26b)
\end{aligned}$$

$$\begin{aligned}
s_W = R_W \{ & \frac{wv}{r} + \frac{1}{J} (b_3^1 p_\xi + b_3^2 p_\eta + b_3^3 p_\zeta) + \frac{2}{3J} (b_2^1 k_\xi + b_2^2 k_\eta + b_2^3 k_\zeta) \\
& - \frac{1}{J^2} (b_1^1 v_{t,\xi} + b_1^2 v_{t,\eta} + b_1^3 v_{t,\zeta}) (b_3^1 u_\xi + b_3^2 u_\eta + b_3^3 u_\zeta) \\
& - \frac{1}{J} (b_2^1 v_{t,\xi} + b_2^2 v_{t,\eta} + b_2^3 v_{t,\zeta}) [\frac{1}{J} (b_3^1 v_\xi + b_3^2 v_\eta + b_3^3 v_\zeta) - \frac{w}{r}] \\
& - \frac{2v}{rJ} (b_3^1 v_{t,\xi} + b_3^2 v_{t,\eta} + b_3^3 v_{t,\zeta}) \} - \frac{2}{rJ} (b_3^1 v_\xi + b_3^2 v_\eta + b_3^3 v_\zeta) + \frac{w}{r^2} \quad (26c)
\end{aligned}$$

$$s_k = - R_k (G - \varepsilon) \quad (26d)$$

$$s_\varepsilon = - R_\varepsilon (C_{\varepsilon 1} \frac{\varepsilon}{k} G - C_{\varepsilon 2} \frac{\varepsilon^2}{k}) \quad (26e)$$

with

$$\begin{aligned}
G = v_t \{ & \frac{2}{J^2} (b_1^1 u_\xi + b_1^2 u_\eta + b_1^3 u_\zeta)^2 + \frac{2}{J^2} (b_2^1 v_\xi + b_2^2 v_\eta + b_2^3 v_\zeta)^2 \\
& + 2 [\frac{1}{J} (b_3^1 w_\xi + b_3^2 w_\eta + b_3^3 w_\zeta) + \frac{v}{r}]^2 \\
& + \frac{1}{J^2} (b_1^1 v_\xi + b_1^2 v_\eta + b_1^3 v_\zeta + b_2^1 u_\xi + b_2^2 u_\eta + b_2^3 u_\zeta)^2 \\
& + \frac{1}{J^2} (b_1^1 w_\xi + b_1^2 w_\eta + b_1^3 w_\zeta + b_3^1 u_\xi + b_3^2 u_\eta + b_3^3 u_\zeta)^2 \\
& + [\frac{1}{J} (b_2^1 w_\xi + b_2^2 w_\eta + b_2^3 w_\zeta + b_3^1 v_\xi + b_3^2 v_\eta + b_3^3 v_\zeta) - \frac{w}{r}]^2 \} \quad (26f)
\end{aligned}$$

The radius r , the geometric coefficients b_i^j and g^{ij} , and the Jacobian J which appear in the above equations are functions of the coordinates only. When either analytic or numerical transformations are employed to generate the grid distribution, $r = r(\xi, \eta, \zeta)$ is known in the transformed plane. The geometric coefficients b_i^j and g^{ij} for the present transformation are

$$(b_i^j) = \begin{bmatrix} b_1^1 & b_2^1 & b_3^1 \\ b_1^2 & b_2^2 & b_3^2 \\ b_1^3 & b_2^3 & b_3^3 \end{bmatrix} = \begin{bmatrix} r(r_\eta \theta_\zeta - r_\zeta \theta_\eta) & r(x_\zeta \theta_\eta - x_\eta \theta_\zeta) & x_\eta r_\zeta - x_\zeta r_\eta \\ r(r_\zeta \theta_\xi - r_\xi \theta_\zeta) & r(x_\xi \theta_\zeta - x_\zeta \theta_\xi) & x_\zeta r_\xi - x_\xi r_\zeta \\ r(r_\xi \theta_\eta - r_\eta \theta_\xi) & r(x_\eta \theta_\xi - x_\xi \theta_\eta) & x_\xi r_\eta - x_\eta r_\xi \end{bmatrix} \quad (27)$$

and

$$\begin{aligned} gg^{11} &= g_{22} g_{33} - g_{23}^2 \\ gg^{22} &= g_{11} g_{33} - g_{13}^2 \\ gg^{33} &= g_{11} g_{22} - g_{12}^2 \\ gg^{12} &= gg^{21} = g_{13} g_{23} - g_{12} g_{33} \\ gg^{13} &= gg^{31} = g_{12} g_{23} - g_{13} g_{22} \\ gg^{23} &= gg^{32} = g_{12} g_{13} - g_{23} g_{11} \end{aligned} \quad (28)$$

where

$$\begin{aligned} g_{11} &= x_\xi^2 + r_\xi^2 + r^2 \theta_\xi^2 \\ g_{22} &= x_\eta^2 + r_\eta^2 + r^2 \theta_\eta^2 \\ g_{33} &= x_\zeta^2 + r_\zeta^2 + r^2 \theta_\zeta^2 \\ g_{12} &= g_{21} = x_\xi x_\eta + r_\xi r_\eta + r^2 \theta_\xi \theta_\eta \\ g_{13} &= g_{31} = x_\xi x_\zeta + r_\xi r_\zeta + r^2 \theta_\xi \theta_\zeta \\ g_{23} &= g_{32} = x_\eta x_\zeta + r_\eta r_\zeta + r^2 \theta_\eta \theta_\zeta \end{aligned} \quad (29)$$

and

$$g = g_{11} g_{22} g_{33} + 2g_{12} g_{13} g_{23} - (g_{23})^2 g_{11} - (g_{13})^2 g_{22}$$

$$- (g_{12})^2 g_{33} \quad (30)$$

is the determinant of the metric tensor g_{ij} . Also, the Jacobian can be expressed as

$$J = \sqrt{g} = \begin{vmatrix} x_\xi & x_n & x_\zeta \\ r_\xi & r_n & r_\zeta \\ r\theta_\xi & r\theta_n & r\theta_\zeta \end{vmatrix} \quad (31)$$

It should be recalled here that (U, V, W) represent the velocity components in the physical cylindrical polar coordinates (x, r, θ) . Equations (24) through (26), together with the equation of continuity (1), which transforms to:

$$(b_1^1 U + b_2^1 V + b_3^1 W)_\xi + (b_1^2 U + b_2^2 V + b_3^2 W)_n + (b_1^3 U + b_2^3 V + b_3^3 W)_\zeta = 0 \quad (32)$$

are the Reynolds-averaged Navier-Stokes equations for unsteady, three-dimensional flows.

III.2. NUMERICAL SOLUTION PROCEDURES

In this section we describe the numerical techniques used for the solution of the grid-generation equations (21), the fully-elliptic convective-diffusion equations (24), and the equation of continuity (32). Details of the numerical method used in grid generation, together with some examples, are presented in Section (a). The finite-analytic numerical method of Chen and Chen (1982, 1984) and Chen and Patel (1985a) is then revised and extended to solve the five transport equations for $\phi = U, V, W, k$ and ϵ with a guessed pressure field. This is described in Section (b). The continuity equation is used to obtain equations which enable the determination of the pressure and pressure-correction fields from the velocity field. This procedure is described in Section (c). The treatment of the boundary conditions is described in Section (d), and the overall numerical solution algorithm is summarized in Section (e).

(a) Grid Generation

The numerical curvilinear coordinate system is constructed by solving equations (21). Because the orthogonal coordinates x^i in the physical plane can be selected arbitrarily and the control functions f^i are independent of these coordinate, it is possible to generate the numerical coordinates in terms of the simplest Cartesian coordinates (x, y, z) , and then transform them into other orthogonal coordinates which are chosen to specify the velocity components in the equations of motion. As noted earlier, it is desirable to use cylindrical polar coordinates as the basic coordinate system for the present applications to three-dimensional ship forms. It is also desirable to choose the transverse sections of the hull as the constant- ξ stations, i.e., $\xi = \xi(x)$, so that the computing effort required for grid generation and flow calculations can be significantly reduced. With this choice, equations (21) reduce to

$$\begin{aligned}
 g^{11}x_{\xi\xi} + f^1x_\xi &= 0 \\
 g^{11}r_{\xi\xi} + g^{22}r_{nn} + g^{33}r_{\zeta\zeta} + 2g^{12}r_{\xi n} + 2g^{13}r_{\xi\zeta} + 2g^{23}r_{n\zeta} \\
 + f^1r_\xi + f^2r_n + f^3r_\zeta &= \frac{1}{r} \\
 g^{11}\theta_{\xi\xi} + g^{22}\theta_{nn} + g^{33}\theta_{\zeta\zeta} + 2g^{12}\theta_{\xi n} + 2g^{13}\theta_{\xi\zeta} + 2g^{23}\theta_{n\zeta} \\
 + f^1\theta_\xi + f^2\theta_n + f^3\theta_\zeta &= 0
 \end{aligned} \tag{33}$$

relating the numerical coordinates (ξ, n, ζ) to the cylindrical coordinates (x, r, θ) in the physical plane. Equivalently, these equations can also be written in Cartesian coordinates (x, y, z) as

$$\begin{aligned}
 g^{11}x_{\xi\xi} + f^1x_\xi &= 0 \\
 g^{11}y_{\xi\xi} + g^{22}y_{nn} + g^{33}y_{\zeta\zeta} + 2g^{12}y_{\xi n} + 2g^{13}y_{\xi\zeta} + 2g^{23}y_{n\zeta} \\
 + f^1y_\xi + f^2y_n + f^3y_\zeta &= 0
 \end{aligned} \tag{34}$$

$$g^{11}z_{\xi\xi} + g^{22}z_{\eta\eta} + g^{33}z_{\zeta\zeta} + 2g^{12}z_{\xi\eta} + 2g^{13}z_{\xi\zeta} + 2g^{23}z_{\eta\zeta} + f^1z_{\xi} + f^2z_{\eta} + f^3z_{\zeta} = 0$$

where $y = r \sin\theta$, $z = r \cos\theta$, and θ is the circumferential or girthwise angle measured from the keel to the waterline. The control functions f^i are the same in both coordinate systems, and, in principle, equations (33) and (34) yield the same numerical coordinates if the same control functions are employed. Numerically, however, the x^i -coordinates used to specify the hull geometry influence the accuracy of the calculated numerical coordinates due to truncation errors. Since, for ship hulls the variation of the surface coordinates (y, z) is much smoother than that of (r, θ) it is preferable to use equations (34) instead of (33). The numerical coordinates thus obtained are then transformed to (x, r, θ) which are used to specify the velocity components in the equations of motion.

For the numerical solutions, it is convenient to rewrite equations (34) in the form

$$g^{11}(x_{\xi\xi} - 2ax_{\xi}) = 0 \quad (35a)$$

$$g^{11}(y_{\xi\xi} - 2ay_{\xi}) + g^{22}(y_{\eta\eta} - 2by_{\eta}) + g^{33}(y_{\zeta\zeta} - 2cy_{\zeta}) + 2g^{12}y_{\xi\eta} + 2g^{13}y_{\xi\zeta} + 2g^{23}y_{\eta\zeta} = 0 \quad (35b)$$

$$g^{11}(z_{\xi\xi} - 2az_{\xi}) + g^{22}(z_{\eta\eta} - 2bz_{\eta}) + g^{33}(z_{\zeta\zeta} - 2cz_{\zeta}) + 2g^{12}z_{\xi\eta} + 2g^{13}z_{\xi\zeta} + 2g^{23}z_{\eta\zeta} = 0 \quad (35c)$$

where a , b and c are modified control functions defined by

$$2a = -\frac{f^1}{2g^{11}}$$

$$2b = -\frac{f^2}{2g^{22}}$$

$$2c = -\frac{f^3}{2g^{33}}$$
(36)

In order to solve equations (35), it is necessary to prescribe the boundary conditions and the control functions. The boundary conditions are determined by the preselected size of the solution domain and the desired number of grid points in the axial (ξ), radial (n) and circumferential (ζ) directions.

In all the calculations considered here, the first station $\xi = 1$, is located at $x = 0.3$ where the boundary layer is thin, and the last station $\xi = LL$ is placed in the far wake where upstream viscous diffusion is negligible. In the radial direction, there are MM points with $n = 1$ corresponding to the hull surface or wake centerplane, and $n = MM$ being the exterior boundary. The latter is placed typically at a distance of the order of one ship length from the hull for calculations corresponding to an unrestricted stream. Alternatively, it may be chosen to coincide with the walls of a wind tunnel or towing tank. In the girthwise direction, NN stations are used, with $\zeta = 2$ and $NN - 1$ corresponding to the keel ($\theta = 0^\circ$) and the waterplane ($\theta = 90^\circ$), respectively; and $\zeta = 1$ and NN are used to enforce the plane-of-symmetry conditions. In order to avoid a sudden change of numerical grid near the stern region where the hull ends abruptly, an imaginary wake centerplane is specified to ensure a smooth variation of geometric coefficients in this region. The vertical extent of the wake centerplane is reduced linearly up to a station $\xi = LE$ in the wake. The depth of the centerplane is kept constant beyond that station.

In general, the grid control functions f^i are three-dimensional and can be arbitrarily specified to yield the desired grid distribution. There are, however, no general rules for the determination of the most appropriate grid-control functions. For the present study, the grid-control functions used in Chen and Patel (1985b) were modified and generalized to provide control of the numerical coordinates in the radial as well as the girthwise directions. In particular, the function f^2 which controls the grid concentration in the n -direction is continuously adjusted to achieve a direct control of the grid spacing between the constant- n lines. The grid-generation technique is outlined below.

The choice of $x = x(\xi)$ simplifies the control function a because it is uniquely determined from equation (35a), i.e.,

$$2a = \frac{x_{EE}}{x_\xi} = f_n(\xi \text{ only}) \quad (37)$$

In other words, the function a is related to the distribution of the axial stations, which is chosen to concentrate grid points near the stern and in the near wake.

In a similar manner, the function c is related to the grid distribution in the circumferential or girthwise direction, $\theta = \tan^{-1}(y/z)$. In general, c can be a function of ξ, n and ζ to yield desired grid spacings between the constant- ζ lines in the ζ -direction. For the present applications, however, it is sufficient to employ a one-dimensional control function $c(\zeta)$ which is fixed in the axial as well as the radial directions, i.e.,

$$2c = \frac{\theta_{\zeta\zeta}}{\theta_\zeta} = f_n(\zeta \text{ only}) \quad (38)$$

with $\theta = \theta(\zeta)$ prescribed on the outer boundary at the upstream station.

The specification of the function b , which controls the grid distribution in the n -direction, requires greater care since it must satisfy several conflicting requirements at the same time. First, in the present treatment of the wall boundary conditions using wall functions, it is necessary to require at least two near-wall grid points to lie in the logarithmic law-of-the-wall region (say $50 < y^+ < 500$). Second, it is desirable (although not necessary) to have an orthogonal grid in the wall region to facilitate the application of the boundary conditions. Third, the grid concentration must be such that there is a sufficient number of points across the boundary layer whose thickness varies greatly in the axial as well as in the girthwise directions. Fourth, and perhaps the most difficult, is the problem of obtaining a sufficiently accurate solution in the neighborhood of geometric singularities. It is obvious that a three-dimensional control function is needed to make the local adjustments to meet all these requirements.

As noted above, the grid-control functions used in Chen and Patel (1985b) were modified by adding a three-dimensional local correction function to

provide greater control of the grid distribution near the hull surface and the wake centerplane. We choose

$$b = b_0 + b_c \quad (39)$$

where b_0 is the two-dimensional grid control function given in Chen and Patel (1985b), i.e.,

$$\begin{aligned} 2b_0 &= \frac{1}{r_n} (r_{nn} + \frac{g^{33}}{g^{22}} r_{\zeta\zeta} - \frac{1}{rg^{22}}) \Big|_{\zeta=2} \\ &= \frac{1}{z_n} (z_{nn} + \frac{g^{33}}{g^{22}} z_{\zeta\zeta}) \Big|_{\zeta=2} \\ &= f_n(\xi, n) \end{aligned} \quad (40)$$

Since this control function is obtained from the prescribed grid distribution $z = z(\xi, n)$ and the associated transverse curvature $z_{\zeta\zeta}$ on the keel plane $\zeta = 2$, there is very little control for the grid distribution away from the keel. This was evident from the results presented in Chen and Patel (1985b) which showed a lack of near-wall grid concentration around the waterplane, especially in the stern and the near-wake regions. In order to improve the resolution in the wall layer and the near wake, a three-dimensional correction function is applied to control the normal distance distribution in the girthwise direction by

$$b_c = c A(\xi, \zeta) e^{-d(n-2)} \quad (41)$$

$$\text{where } A(\xi, \zeta) = \frac{n(\xi, 2, \zeta)}{n(\xi, 2, 2)} - 1$$

and $n(\xi, 2, \zeta)$ is the normal distance between $n = 2$ and the body surface which is $n = 1$. The control parameters c and d are chosen to yield the desired grid distributions. Note that $A(\xi, \zeta) = 0$ if $n(\xi, 2, \zeta) = n(\xi, 2, 2)$ for all girthwise stations. In other words, if the control function b is updated continuously, the final correction function will be zero when the solution converges, and

the normal distance thus obtained will be constant in the girthwise direction. It is, however, not necessary to satisfy this relation exactly although it is desirable to be able to control the near-wall grid spacing directly. For the present calculations, a compromise solution was arrived at by updating b only a few times during the iterative process and then fixing it when a satisfactory grid distribution was reached. The correction function b_C was updated every 20 iterations between iteration numbers 40 and 200, and then kept unchanged for subsequent iterations. The grid control function thus obtained was enforced only up to a station $\xi = MIB$ near the stern. Beyond that, the f^2 function is reduced linearly to zero, and remained zero in the far wake. For consistency, the grid distribution $z(\xi, n, 2)$ on the keel plane was allowed to move freely based on the prescribed function b in this region. It should be noted here also that the correction function diminishes exponentially away from the hull surface and wake centerplane. This leads to a nearly-orthogonal numerical grid for much of the solution domain while providing the control of the grid spacing in the wall layer.

Equations (35), with the control functions specified by equations (37) through (41), were solved by an exponential-linear scheme described in Chen and Patel (1985a). With this scheme, the discretized equations (35) can be written

$$\begin{aligned}
 & (2g^{11}a \coth a + 2g^{22}b \coth b + 2g^{33}c \coth c)_{\xi, n, \zeta} \phi_{\xi, n, \zeta} \\
 & = (g^{11}a \operatorname{csch} a)_{\xi, n, \zeta} (e^{-a} \phi_{\xi+1, n, \zeta} + e^a \phi_{\xi-1, n, \zeta}) \\
 & + (g^{22}b \operatorname{csch} b)_{\xi, n, \zeta} (e^{-b} \phi_{\xi, n+1, \zeta} + e^b \phi_{\xi, n-1, \zeta}) \\
 & + (g^{33}c \operatorname{csch} c)_{\xi, n, \zeta} (e^{-c} \phi_{\xi, n, \zeta+1} + e^c \phi_{\xi, n, \zeta-1}) \\
 & + 0.5g^{12}_{\xi, n, \zeta} (\phi_{\xi+1, n+1, \zeta} + \phi_{\xi-1, n-1, \zeta} - \phi_{\xi+1, n-1, \zeta} - \phi_{\xi-1, n+1, \zeta}) \\
 & + 0.5g^{13}_{\xi, n, \zeta} (\phi_{\xi+1, n, \zeta+1} + \phi_{\xi-1, n, \zeta-1} - \phi_{\xi+1, n, \zeta-1} - \phi_{\xi-1, n, \zeta+1}) \\
 & + 0.5g^{23}_{\xi, n, \zeta} (\phi_{\xi, n+1, \zeta+1} + \phi_{\xi, n-1, \zeta-1} - \phi_{\xi, n+1, \zeta-1} - \phi_{\xi, n-1, \zeta+1}) \quad (42)
 \end{aligned}$$

where ϕ represents either y or z . With the Neumann boundary conditions specified on all boundaries of the constant- ξ^1 stations, equations (42) are solved by a tridiagonal-matrix algorithm using line-by-line iterations.

(b) Finite-Analytic Discretization for the Transport Equations

In order to correctly handle the elliptic nature of the flow past arbitrary three-dimensional shapes, the finite-analytic method of Chen and Chen (1982, 1984) is revised and extended to solve the five transport equations for mean velocities (U, V, W) and turbulence quantities (k, ϵ). The most general version of this method would involve an analytic solution of the linearized transport equations in a three-dimensional element and would result in a 28-point discretization formula. While such a scheme may be required for the solution of highly three-dimensional flows, for applications to many aerodynamic and hydrodynamic problems it suffices to use a simplified method to reduce computer time and storage. Here, we adopt a hybrid method which combines a two-dimensional local analytic solution in the $\eta\xi$ -plane with a one-dimensional local analytic solution in the ξ -direction. Details of this numerical scheme are described in the following.

In the finite-analytic approach, equations (24) are locally linearized in each rectangular numerical element, $\Delta\xi = \Delta\eta = \Delta\xi = 1$, by evaluating the coefficients of the convective terms at the interior node P of each local element (Figure 4), i.e.,

$$g_P^{11}\phi_{\xi\xi} + g_P^{22}\phi_{\eta\eta} + g_P^{33}\phi_{\xi\xi} = 2(C_\phi)_P\phi_\xi + 2(B_\phi)_P\phi_\eta + 2(A_\phi)_P\phi_\xi + (R_\phi)_P\phi_t + (S_\phi)_P \quad (43)$$

Introduction of the coordinate-stretching functions

$$\xi^* = \frac{\xi}{\sqrt{g_P^{11}}} \quad , \quad \eta^* = \frac{\eta}{\sqrt{g_P^{22}}} \quad , \quad \xi^* = \frac{\xi}{\sqrt{g_P^{33}}} \quad (44)$$

in equation (43) reduces it to the standard three-dimensional convective-transport equation described in Chen and Chen (1982, 1984), i.e.,

$$\phi_{\xi^*\xi^*} + \phi_{\eta^*\eta^*} + \phi_{\xi^*\xi^*} = 2C\phi_{\xi^*} + 2B\phi_{\eta^*} + 2A\phi_{\xi^*} + R\phi_t + (S_\phi)_P \quad (45)$$

$$\text{where } A = \frac{(A_\phi)_P}{\sqrt{g_P^{33}}} , \quad B = \frac{(B_\phi)_P}{\sqrt{g_P^{22}}} , \quad C = \frac{(C_\phi)_P}{\sqrt{g_P^{11}}} , \quad R = (R_\phi)_P$$

for a numerical element with dimensions

$$\begin{aligned} \Delta \xi^* &= \ell = \frac{1}{\sqrt{g_P^{11}}} \\ \Delta \eta^* &= k = \frac{1}{\sqrt{g_P^{22}}} \\ \Delta \zeta^* &= h = \frac{1}{\sqrt{g_P^{33}}} \end{aligned} \quad (46)$$

For the type of applications considered here, it is convenient to decompose equation (45) into a one-dimensional and a two-dimensional partial differential equation in the following way:

$$2C\phi_{\xi\xi}^* - \phi_{\xi\xi}^{**} + R_\phi \phi_t + S_\phi = G(\xi^*, \eta^*, \zeta^*, t) \quad (47)$$

$$\phi_{\eta\eta}^{**} + \phi_{\zeta\zeta}^{**} - 2B\phi_{\eta\eta}^* - 2A\phi_{\zeta\zeta}^* = G(\xi^*, \eta^*, \zeta^*, t) \quad (48)$$

If we further require the source functions G and S_ϕ to be constant in each local element and the time derivatives to be approximated by a backward-difference formula, equations (47) and (48) reduce to the standard one- and two-dimensional convective-transport equations described in Chen and Chen (1982), respectively. The analytic solution of the one-dimensional equation (47) can be readily obtained as:

$$\phi = a(e^{2C\xi^*} - 1) + b\xi^* + c \quad (49)$$

By substituting the exponential-linear solution (49) into equation (47), the source function $G(0,0,0,0) = g$ becomes

$$\begin{aligned}
g &= (2C\phi_{\xi^*} - \phi_{\xi^*}^* \phi_{\xi^*}^* + R_{\phi} \phi_t + S_{\phi})_P \\
&= (C_U + C_D)\phi_P - C_U \phi_U - C_D \phi_D + \frac{R}{\tau} (\phi_P - \phi_P^{n-1}) + (S_{\phi})_P
\end{aligned} \tag{50}$$

with

$$C_U = \frac{C e^{C\ell}}{\ell \sinh C\ell}, \quad C_D = \frac{C e^{-C\ell}}{\ell \sinh C\ell}$$

where the subscripts U and D denotes the upstream and downstream nodal values (Figure 4), respectively, superscript (n-1) denotes the value at the previous time step, and τ is the time step.

By specifying a combination of exponential and linear boundary functions, which are derived from the natural solutions of the governing equations, on all four boundaries, $n^* = \pm k$ and $\xi^* = \pm h$, of the transverse section of each local element (ξ -plane), i.e.,

$$\begin{aligned}
\phi(k, \xi^*) &= a_n (e^{2A\xi^*} - 1) + b_n \xi^* + c_n \\
\phi(-k, \xi^*) &= a_s (e^{2A\xi^*} - 1) + b_s \xi^* + c_s \\
\phi(n^*, h) &= a_e (e^{2Bn^*} - 1) + b_e n^* + c_e \\
\phi(n^*, -h) &= a_w (e^{2Bn^*} - 1) + b_w n^* + c_w
\end{aligned} \tag{51}$$

where a, b and c are constants, the two-dimensional equation (48) can be solved analytically by the method of separation of variables or any other analytic technique. Details of the solution procedure are described in Chen & Chen (1982, 1984). When the local analytic solution thus derived is evaluated at the central node P of the element, the following nine-point finite-analytic algebraic equation is obtained:

$$\begin{aligned}
\phi_P &= C_{NE}\phi_{NE} + C_{NW}\phi_{NW} + C_{SE}\phi_{SE} + C_{SW}\phi_{SW} + C_{EC}\phi_{EC} + C_{WC}\phi_{WC} \\
&\quad + C_{NC}\phi_{NC} + C_{SC}\phi_{SC} - C_P g
\end{aligned} \tag{52}$$

where

$$c_{SC} = \left(\frac{e^{Bk}}{2 \cosh Bk} \right) P_A$$

$$c_{NC} = e^{-2Bk} c_{SC}$$

$$c_{WC} = \left(\frac{e^{Ah}}{2 \cosh Ah} \right) P_B$$

$$c_{EC} = e^{-2Ah} c_{WC}$$

$$c_{SW} = \left(\frac{e^{Ah+Bk}}{4 \cosh Ah \cosh Bk} \right) (1 - P_A - P_B)$$

$$c_{SE} = e^{-2Ah} c_{SW}$$

$$c_{NW} = e^{-2Bk} c_{SW}$$

$$c_{NE} = e^{-2Ah-2Bk} c_{SW}$$

$$c_p = \frac{h \tanh Ah}{2A} (1 - P_A) = \frac{k \tanh Bk}{2B} (1 - P_B)$$

$$P_A = 4E_2 Ah \cosh Ah \cosh Bk \coth Ah$$

$$P_B = 1 + \frac{Bh \coth Bk}{Ak \coth Ah} (P_A - 1)$$

and

$$E_2 = \sum_{m=1}^{\infty} \frac{-(-1)^m (\lambda_m h)}{[(Ah)^2 + (\lambda_m h)^2]^2 \cosh \sqrt{A^2 + B^2 + \lambda_m^2} k}$$

$$\lambda_m h = (m - \frac{1}{2}) \pi$$

The above coefficients are simple rearrangements of those given in Chen & Che, but are more convenient for efficient numerical calculations. Note that some of them are interrelated as follows:

$$C_{NC} + C_{SC} = P_A$$

$$C_{EC} + C_{WC} = P_B \quad (53)$$

$$C_{NE} + C_{NW} + C_{SE} + C_{SW} = 1 - P_A - P_B$$

Since both P_A and P_B are positive and $(P_A + P_B) < 1$, the finite-analytic coefficients are always positive. Also, the exponents in these coefficients provide a gradual upwind bias as the cell Reynolds numbers $|2Ah|$ and/or $|2Bk|$ increase. Thus, the behavior of the convective-diffusion equation is properly captured and numerical diffusion is minimized due to the inclusion of all corner points. For large cell Reynolds numbers, the series summation in E_2 can be avoided by considering the asymptotic expressions of P_A and P_B based on the theory of characteristics, i.e.,

$$\begin{aligned} Ak \coth Ah > Bh \coth Bk : P_A &= 0, P_B = 1 - Bh \coth Bk/Ak \coth Ah \\ Ak \coth Ah < Bh \coth Bk : P_B &= 0, P_A = 1 - Ak \coth Ah/Bh \coth Bk \end{aligned} \quad (54)$$

Since the "downstream" influence is negligible at large cell Reynolds numbers, the above approximations do not introduce a significant error in the solution, but the computing time is greatly reduced.

By substituting the nonhomogeneous term g from equation (50) into equation (52), a twelve-point finite-analytic formula for unsteady, three-dimensional, elliptic equations can be obtained in the form

$$\begin{aligned} \phi_P &= \frac{1}{1 + C_P [C_U + C_D + \frac{R}{\tau}]} \{ C_{NE} \phi_{NE} + C_{NW} \phi_{NW} + C_{SE} \phi_{SE} + C_{SW} \phi_{SW} + C_{EC} \phi_{EC} + C_{WC} \phi_{WC} \\ &\quad + C_{NC} \phi_{NC} + C_{SC} \phi_{SC} + C_P (C_U \phi_U + C_D \phi_D + \frac{R}{\tau} \phi_P^{n-1}) - C_P (S_\phi)_P \} \end{aligned} \quad (55)$$

or

$$\phi_P = \frac{1}{1 + C_P [C_U + C_D + \frac{R}{\tau}]} \{ \sum_1^8 C_{nb} \phi_{nb} + C_P (C_U \phi_U + C_D \phi_D + \frac{R}{\tau} \phi_P^{n-1}) - C_P (S_\phi)_P \} \quad (55a)$$

where the subscript nb denotes neighboring nodes (NE:northeast, NW:northwest, etc.). It is seen that ϕ_p depends upon all the eight neighboring nodal values in the transverse plane as well as the values at the upstream and downstream nodes ϕ_U and ϕ_D , and the values at the previous time step ϕ_p^{n-1} . When the cell Reynolds number $2C$ becomes large, $C_U + 2C/\ell = (C_\phi)_p$ and $C_D + 0$, and equation (55) reduces to the partially-parabolic formulation of Chen and Patel (1985a) which used $C_U = (C_\phi)_p$ and $C_D = 0$. Thus, the extension of the earlier partially-parabolic method to the present fully-elliptic form is straightforward, and if ϕ_D is obtained from the previous time step, the same algorithm can be employed for both formulations.

Since equations (55) are implicit, both in space and time, at the current station of calculation, their assembly for all elements results in a set of simultaneous algebraic equations. These equations are solved by the tridiagonal-matrix algorithm. Because it is not necessary to obtain a fully-converged intermediate solution for steady flows, only ten line-by-line internal iterations are used during each global sweep. Furthermore, the finite-analytic coefficients appearing in equations (55) are not updated during these internal iterations for economy of computation time.

(c) Solution of the Continuity Equation: Velocity-Pressure Coupling

If the pressure is known, equations (55) can be employed to solve the five convective-diffusion equations (24) for U, V, W, k and ϵ . However, the pressure is not known a priori and must be determined by requiring the velocity field to satisfy the equation of continuity (32). Since a direct method for the simultaneous solution of all six equations is not feasible with present computer capacity, it is necessary to convert the equation of continuity into an algorithm for the calculation of the pressure field. The SIMPLER algorithm of Patankar (1980) has been modified and extended for this purpose. A staggered-grid system is adopted. Figure 5 shows the locations of the nodes for U, V, W , and p in this grid. The turbulence quantities k and ϵ are evaluated at the pressure nodes. The dashed lines represent the control volume faces, and the pressure is calculated at the center of the control volume. For convenience, U_d, V_n, W_e and p_p in Figure 5 are assigned the same index, i.e., they are denoted by $U_{\xi\eta\zeta}, V_{\xi\eta\zeta}, W_{\xi\eta\zeta}$ and $p_{\xi\eta\zeta}$, respectively. Recall

that the velocity components U, V , and W are in the longitudinal, radial and circumferential directions. In other words, they are, in general, neither perpendicular to the control surfaces nor in the direction of the coordinate lines. However, due to the choice of the cylindrical polar coordinates in the physical plane, these components do not become parallel to the control surfaces.

In the staggered grid, the twelve-point finite-analytic formulae (equation 55) for the momentum equations yield the velocity components:

$$\begin{aligned}
 U_d &= \frac{1}{1+C_d(C_U + C_D + \frac{R_U}{\tau})_d} \left\{ \sum_{n=1}^8 C_{nb} U_{nb} + C_d [(C_U)_d U_u + (C_D)_d U_d + \frac{(R_U)_d}{\tau} U_d^{n-1} - (S_U)_d] \right\} \\
 V_n &= \frac{1}{1+C_n(C_U + C_D + \frac{R_V}{\tau})_n} \left\{ \sum_{n=1}^8 C_{nb} V_{nb} + C_n [(C_U)_n V_u + (C_D)_n V_d + \frac{(R_V)_n}{\tau} V_n^{n-1} - (S_V)_n] \right\} \\
 W_e &= \frac{1}{1+C_e(C_U + C_D + \frac{R_W}{\tau})_e} \left\{ \sum_{n=1}^8 C_{nb} W_{nb} + C_e [(C_U)_e W_u + (C_D)_e W_d + \frac{(R_W)_e}{\tau} W_e^{n-1} - (S_W)_e] \right\}
 \end{aligned} \tag{56}$$

where C_d , C_n and C_e are the finite-analytic coefficients C_p evaluated at the staggered velocity nodes d , n and e in Figure 5. Note that the above equations contain the pressure-gradient terms inside the source functions. An equation for this unknown pressure field is obtained as follows.

If we decompose the actual velocity field (U, V, W) in the momentum equations (56) into a pseudovelocity field $(\tilde{U}, \tilde{V}, \tilde{W})$ plus the pressure-gradient terms contained in the source functions, i.e.,

$$\begin{aligned}
 U_d &= \tilde{U}_d - \frac{C_d}{1+C_d(C_U + C_D + \frac{R_U}{\tau})_d} \left\{ \frac{R_U}{J} (b_1^1 p_\xi + b_1^2 p_n + b_1^3 p_\zeta) \right\}_d \\
 V_n &= \tilde{V}_n - \frac{C_n}{1+C_n(C_U + C_D + \frac{R_V}{\tau})_n} \left\{ \frac{R_V}{J} (b_2^1 p_\xi + b_2^2 p_n + b_2^3 p_\zeta) \right\}_n
 \end{aligned} \tag{57}$$

$$W_e = \tilde{W}_e - \frac{C_e}{1 + C_e (C_U + C_D + \frac{R_W}{\tau})_e} \left\{ \frac{R_W}{J} (b_3^1 p_\xi + b_3^2 p_\eta + b_3^3 p_\zeta) \right\}_e$$

so that the pseudovelocities contain no pressure terms, then an equation for pressure can be derived by requiring the velocity field to satisfy the discretized equation of continuity (32), i.e.,

$$(b_1^1 U + b_2^1 V + b_3^1 W)_d - (b_1^1 U + b_2^1 V + b_3^1 W)_u + (b_1^2 U + b_2^2 V + b_3^2 W)_n - (b_1^2 U + b_2^2 V + b_3^2 W)_s + (b_1^3 U + b_2^3 V + b_3^3 W)_e - (b_1^3 U + b_2^3 V + b_3^3 W)_w = 0 \quad (58)$$

The resulting pressure equation will contain many pressure nodes (see Muraoka (1980, 1982) for example) if nonorthogonal coordinates are employed. It is therefore desirable to simplify the algorithm by introducing modified pseudovelocities ($\hat{U}, \hat{V}, \hat{W}$) by decomposing the velocity components as follows:

$$\begin{aligned} \hat{U}_d &= \hat{U}_d - d_d (p_D - p_P) \\ \hat{V}_n &= \hat{V}_n - d_n (p_N - p_P) \\ \hat{W}_e &= \hat{W}_e - d_e (p_E - p_P) \end{aligned} \quad (59)$$

where

$$\begin{aligned} d_d &= \frac{(R_U b_1^1)_d C_d}{J_d [1 + C_d (C_U + C_D + \frac{R_U}{\tau})_d]} \\ d_n &= \frac{(R_V b_2^2)_n C_n}{J_n [1 + C_n (C_U + C_D + \frac{R_V}{\tau})_n]} \end{aligned} \quad (59a)$$

$$d_e = \frac{(R_w b_3^3)_e c_e}{J_e [1 + c_e (c_u + c_d + \frac{R_w}{\tau})_e]}$$

The modified pseudovelocities ($\hat{U}, \hat{V}, \hat{W}$) defined above still contain part of the pressure-gradient terms if the coordinate system is nonorthogonal (i.e., $b_i^j \neq 0$ for $i \neq j$, see equation 57). These pressure-gradient terms can be evaluated from the pressure field known at the previous time step or iteration without losing any accuracy or generality. If we require the velocity field to satisfy the equation of continuity (58), a simpler pressure equation can be derived in terms of the modified pseudovelocities ($\hat{U}, \hat{V}, \hat{W}$). Note that eighteen velocity components are involved in equation (58) for each control volume. However, due to the staggered grid system employed here, only six of these, namely, U_d , U_u , V_n , V_s , W_e , and W_w , can be obtained directly from the governing equations (56). It is, therefore, necessary to approximate the remaining twelve by interpolations. A simple linear interpolation is used here to evaluate these from the velocity field known at the previous time step or iteration, so that the continuity equation becomes

$$(b_1^1 U)_d - (b_1^1 U)_u + (b_2^2 V)_n - (b_2^2 V)_s + (b_3^3 W)_e - (b_3^3 W)_w + D_1 = 0 \quad (60)$$

where

$$D_1 = (b_2^1 V + b_3^1 W)_d - (b_2^1 V + b_3^1 W)_u + (b_1^2 U + b_3^2 W)_n - (b_1^2 U + b_3^2 W)_s + (b_1^3 U + b_2^3 V)_e - (b_1^3 U + b_2^3 V)_w \quad (60a)$$

is the mass source obtained from the velocity field at the previous time step or sweep. An equation for pressure is then derived by substituting equations (59) into (60), i.e.,

$$a_p p_p = a_d p_D + a_u p_U + a_n p_{NC} + a_s p_{SC} + a_e p_{EC} + a_w p_{WC} - \hat{D} \quad (61)$$

where

$$a_d = (b_1^1)_d d_d$$

$$\begin{aligned}
 a_u &= (b_1^1)_u d_u \\
 a_n &= (b_2^2)_n d_n \\
 a_s &= (b_2^2)_s d_s \\
 a_e &= (b_3^3)_e d_e \\
 a_w &= (b_3^3)_w d_w \\
 a_p &= a_d + a_u + a_e + a_w + a_n + a_s
 \end{aligned} \tag{61a}$$

and

$$\hat{D} = (b_1^1 \hat{U})_d - (b_1^1 \hat{U})_u + (b_2^2 \hat{V})_n - (b_2^2 \hat{V})_s + (b_3^3 \hat{W})_e - (b_3^3 \hat{W})_w - D_1 \tag{61b}$$

The modified pseudovelocities (\hat{U} , \hat{V} , \hat{W}) contain the neighboring nodal values of velocity, source functions, and part of the pressure-gradient terms. All of them can be evaluated from the information known at the previous time step or iteration. Therefore, apart from the interpolations for D_1 , the pressure equation (61) is still an exact algebraic representation of the equation of continuity (32). In this fashion, the pressure field can be obtained directly from an estimated velocity field.

Although the guessed pressure field can be updated directly by equation (61), in practice the new pressure field may produce a velocity field which does not satisfy the equation of continuity. An iterative procedure is therefore required to correct this erroneous velocity field to achieve more rapid convergence. Here, a velocity-correction formula, similar to that used in the SIMPLE algorithm, is derived in terms of the pressure-corrections.

If we denote the imperfect velocity field resulting from an imperfect pressure field p^* by (U^*, V^*, W^*) , then the discretized momentum equations (59) can be written as

$$U_d^* = \hat{U}_d^* - d_e (p_D^* - p_p^*)$$

$$V_n^* = \hat{V}_n^* - d_n(p_{NC}^* - p_p^*) \quad (62)$$

$$W_e^* = \hat{W}_e^* - d_e(p_{EC}^* - p_p^*)$$

In order to improve the guessed pressure field, such that (U^*, V^*, W^*) will eventually satisfy the equation of continuity, one needs to know how the velocity components respond to a change in the pressure field. Such a relation can be obtained by subtracting equation (62) from equation (59), i.e.,

$$\begin{aligned} U_d - U_d^* &= (\hat{U}_d - \hat{U}_d^*) - d_d(p_d' - p_p') \\ V_n - V_n^* &= (\hat{V}_n - \hat{V}_n^*) - d_n(p_{NC}' - p_p') \\ W_e - W_e^* &= (\hat{W}_e - \hat{W}_e^*) - d_e(p_{EC}' - p_p') \end{aligned} \quad (63)$$

where $p' = p - p^*$ is the pressure correction, and $(U - U^*)$, $(V - V^*)$ and $(W - W^*)$ are the corresponding velocity corrections. If we require the velocity field to satisfy the equation of continuity (60), an equation for the pressure correction p' can be derived. However, due to the implicit nature of the velocity corrections arising from the pseudovelocities, the resulting pressure correction equation would involve the pressure corrections at all grid points. It is not necessary to retain such a complicated formulation because both the pressure- and velocity-corrections are zero in the final converged solution. Since both the pressure- and velocity-corrections become trivial when the solution converges, it is possible to omit that part of the velocity-corrections, $(\hat{U} - \hat{U}^*)$, $(\hat{V} - \hat{V}^*)$ and $(\hat{W} - \hat{W}^*)$, which represents the indirect influence of velocity corrections. With this approximation, the velocity-corrections are expressed explicitly in terms of the pressure-corrections as

$$\begin{aligned} U_d &= U_d^* - d_d(p_d' - p_p') \\ V_n &= V_n^* - d_n(p_{NC}' - p_p') \\ W_e &= W_e^* - d_e(p_{EC}' - p_p') \end{aligned} \quad (64)$$

By requiring the velocity field to satisfy the equation of continuity (58), a pressure-correction equation is then obtained in the form

$$a_p p_p = a_d p_D + a_u p_U + a_n p_{NC} + a_s p_{SC} + a_e p_{EC} + a_w p_{WC} - D^* \quad (65)$$

with

$$D^* = (b_1^1 U^*)_d - (b_1^1 U^*)_u + (b_2^2 V^*)_n - (b_2^2 V^*)_s + (b_3^3 W^*)_e - (b_3^3 W^*)_w - D_1 \quad (65a)$$

where the coefficients a_p , a_d , etc., are as defined in equations (61a). Note that the pressure-correction equation (65) is similar to the pressure equation (61). Although, unlike the pressure equation, the pressure-correction equation is not exact, the approximations made influence only the rate of convergence but not the final converged solution.

The systems of algebraic equations formed by the assembly of the pressure and pressure-correction equations, (61) and (65), respectively, are solved by the tridiagonal-matrix algorithm with several line-by-line internal iterations. The finite-analytic coefficients a_p , a_d , etc., are updated in each upstream to downstream global sweep, but remain the same during the internal iterations.

(d) Boundary Conditions

For the calculation of ship stern and wake flows considered in this report, it is assumed that the ship is symmetric about a vertical centerplane and the waterplane is regarded as a plane of symmetry. The appropriate boundary conditions are then as follows (see Figure 2).

(1) Initial or Upstream Section ($\xi = 1$)

The distribution of the velocity components (U, V, W) and the turbulence parameters (k, ϵ) are assumed known at an upstream transverse section either from detailed boundary-layer calculations or from simple correlations. Boundary conditions for pressure and pressure-correction are not required in the present staggered-grid arrangement since the pressure is implicitly determined

by the specification of the velocity components. Also, since the velocity components are known, there are no corrections to be made, i.e. $(\hat{U}, \hat{V}, \hat{W})_u = (\hat{U}^*, \hat{V}^*, \hat{W}^*)_u = (\hat{U}, \hat{V}, \hat{W})_u$.

(2) Exit or Downstream Plane

The exit plane is usually located in the wake far downstream from the stern, and the zero pressure gradient ($p_\xi = 0$) condition is specified there. Since axial diffusion in the far wake is negligible, the exit conditions for the transport quantities $\phi = U, V, W, k, \epsilon$ in the momentum and turbulence-model equations are simply $\phi_{\xi\xi} = 0$.

(3) Body Surface (n=1)

For laminar flows, the numerical solution is usually carried out upto the solid surface using no-slip conditions, i.e., $U=V=W=0$ (see, for example, Chen and Patel, 1987a). Strictly speaking, the same conditions should also be used in turbulent flow calculations. This, however, will require a large number of grid points to resolve the large gradients in the near-wall region and, more importantly, an appropriate near-wall turbulence model to account for the wall-proximity effects. In view of the complexity involved in resolving the near-wall flow, it is preferable to employ a simpler wall-function approach which avoids the solution of the equations of motion and turbulence model in the wall region. In the present study, the two-point wall-function approach of Chen and Patel (1985a,b, 1988) is employed with necessary modifications to determine the boundary conditions on a fictitious boundary ($n=2$) located in the fully-turbulent logarithmic layer.

The present wall-function approach differs from the usual practice in two respects. First, the effects of pressure gradients on the flow in the wall region are taken into account by the use of a generalized law of the wall given by Patel (1973), i.e.,

$$\frac{q}{U_\tau} = \frac{1}{\kappa} \left\{ \ln \left[\frac{4}{\Delta_\tau} \frac{(1 + \Delta_\tau y^+)^{1/2} - 1}{(1 + \Delta_\tau y^+)^{1/2} + 1} \right] + 2[(1 + \Delta_\tau y^+)^{1/2} - 1] \right\} + B + 3.7 \Delta_p \quad (6)$$

in which U_τ is the friction velocity defined by $U_\tau = \sqrt{\tau_w / \rho U_0^2}$, $y^+ = \text{Re } U_\tau y$ is the dimensionless distance measured in the direction normal to the surface, $\Delta_p = \nabla p / \text{Re } U_\tau^3$ is the dimensionless pressure gradient, Δ_τ is the dimensionless shear-stress gradient which is approximated by $1/2 \Delta_p$, q is the magnitude of the velocity, $\kappa = 0.42$ is the von Karman constant, and $B = 5.45$. Second, we ensure that at least two points ($n = 2$ and 3 in Figure 6) are located in the logarithmic region and explicitly satisfy equation (66) at both. This avoids the need for a separate analysis for the flow between the wall and the first near-wall mesh point which is used in almost all previous applications of wall functions. For the present calculations, as in the earlier study of Chen and Patel (1985a,b, 1988), equation (66) is employed to improve the prediction of the wall shear stress and the associated boundary conditions in adverse pressure gradients, while the usual logarithmic law of the wall (i.e., $\Delta_\tau = \frac{1}{2} \Delta_p = 0$) is used in favorable pressure gradients.

In the present procedure, a value for U_τ is assumed and the boundary conditions at $n = 2$ are determined from equation (66) and the assumptions of local equilibrium for k and ϵ , i.e.,

$$\frac{q_2}{U_\tau} = \frac{1}{\kappa} \left\{ \ln \left[\frac{4}{\Delta_\tau} \frac{(1 + \Delta_\tau y_2^+)^{1/2} - 1}{(1 + \Delta_\tau y_2^+)^{1/2} + 1} \right] + 2[(1 + \Delta_\tau y_2^+)^{1/2} - 1] \right\} + B + 3.7 \Delta_p \quad (67a)$$

$$k_2 = \frac{U_\tau^2}{\sqrt{C_\mu}} \quad (67b)$$

$$\epsilon_2 = \frac{U_\tau^3}{\kappa y_2} \quad (67c)$$

The numerical solution then provides the velocity at $n = 3$ and U_τ is updated by requiring this velocity also to satisfy equation (66), i.e., by solving

$$\frac{q_3}{U_\tau} = \frac{1}{\kappa} \left\{ \ln \left[\frac{4}{\Delta_\tau} \frac{(1 + \Delta_\tau y_3^+)^{1/2} - 1}{(1 + \Delta_\tau y_3^+)^{1/2} + 1} \right] + 2[(1 + \Delta_\tau y_3^+)^{1/2} - 1] \right\} + B + 3.7 \Delta_p \quad (68)$$

by a root-finding technique. Thus, an iterative procedure is used to satisfy the wall boundary conditions in the case of turbulent flow, and to determine U_τ . Typically, five iterations are required to obtain satisfactory convergence.

By anchoring the solution at two near-wall mesh points on the law of the wall, the present wall-function approach removes much of the sensitivity of the numerical solution to the location of the first mesh point which has been observed in previous treatments. The procedure is quite straightforward for two-dimensional and axisymmetric flows. For three-dimensional flows, however, an additional assumption concerning the direction of the velocity vector is required to determine the individual components (U, V, W) because the law of the wall gives only the velocity magnitude. In Chen and Patel (1985a), it was assumed that q_2 is parallel to the wall and there is no rotation of the velocity vector between $n=2$ and $n=3$ in planes parallel to the surface. Although the latter approximation resulted in some simplification in the application of the wall-function boundary conditions, it led to the underprediction of the secondary velocities in the stern and wake regions. The approach of Chen and Patel (1985a) was, therefore, modified to account for the rotation of the velocity vector in the wall layer.

To use the law-of-the-wall formula (66), it is convenient to relate the velocity components (U, V, W) in the governing equations to the physical components (q^ξ, q^η, q^ζ) along the body-fitted coordinates as follows:

$$q = (U, V, W) = q^\xi \tilde{\tau}_\xi + q^\eta \tilde{\tau}_\eta + q^\zeta \tilde{\tau}_\zeta \quad (69)$$

where $\tilde{\tau}_\xi, \tilde{\tau}_\eta$ and $\tilde{\tau}_\zeta$ are unit tangents in the body-fitted coordinates given by

$$\begin{aligned} \tilde{\tau}_\xi &= \frac{1}{\sqrt{g_{11}}} (x_\xi, r_\xi, r\theta_\xi) \\ \tilde{\tau}_\eta &= \frac{1}{\sqrt{g_{22}}} (x_\eta, r_\eta, r\theta_\eta) \end{aligned} \quad (70)$$

$$\xi_\zeta = \frac{1}{\sqrt{g_{33}}} (x_\zeta, r_\zeta, r\theta_\zeta)$$

Thus,

$$\begin{aligned} U &= \frac{x_\xi}{\sqrt{g_{11}}} q^\xi + \frac{x_\eta}{\sqrt{g_{22}}} q^\eta + \frac{x_\zeta}{\sqrt{g_{33}}} q^\zeta \\ V &= \frac{r_\xi}{\sqrt{g_{11}}} q^\xi + \frac{r_\eta}{\sqrt{g_{22}}} q^\eta + \frac{r_\zeta}{\sqrt{g_{33}}} q^\zeta \\ W &= \frac{r\theta_\xi}{\sqrt{g_{11}}} q^\xi + \frac{r\theta_\eta}{\sqrt{g_{22}}} q^\eta + \frac{r\theta_\zeta}{\sqrt{g_{33}}} q^\zeta \end{aligned} \quad (71)$$

and the inverse relations are

$$\begin{aligned} q^\xi &= \frac{\sqrt{g_{11}}}{J} (b_1^1 U + b_2^1 V + b_3^1 W) \\ q^\eta &= \frac{\sqrt{g_{22}}}{J} (b_1^2 U + b_2^2 V + b_3^2 W) \\ q^\zeta &= \frac{\sqrt{g_{33}}}{J} (b_1^3 U + b_2^3 V + b_3^3 W) \end{aligned} \quad (72)$$

The geometric coefficients appearing in the above relations are evaluated at the wall, $\eta=1$, so that the rotation of the velocity vector can be determined relative to the surface coordinates. The projection of the velocity vector on the surface, \tilde{q}^* (i.e., without q^η component) and the angle β between this and the ξ -direction of the surface coordinates are given by

$$\tilde{q}^* = \tilde{q}^\xi \xi_\xi + \tilde{q}^\zeta \zeta_\zeta \quad (73)$$

$$\tan \beta = \frac{\tilde{q}^\zeta \sin \gamma}{\tilde{q}^\xi + \tilde{q}^\zeta \cos \gamma}$$

where γ is the angle between $\tilde{\tau}_\xi$ and $\tilde{\tau}_\zeta$. Alternatively, one can also evaluate the components q_ξ^* and q_ζ^* when the magnitude and direction of the vector \tilde{q}^* are specified, i.e.,

$$q_\xi^* = \frac{\tilde{q}^* \sin \beta}{\sin \gamma} \quad (74)$$

$$q_\zeta^* = \tilde{q}^* \cos \beta - q_\xi^* \cos \gamma$$

In the present procedure, we first impose the constraint that q_2 is parallel to the wall and therefore require $q_2^n = 0$. However, instead of the no rotation (i.e., $\beta_2 = \beta_3$) assumption imposed in Chen and Patel (1985a), the effect of the velocity vector rotation in the near wall region is taken into account by determining the direction of q_2 using a quadratic extrapolation of the angles β_3 , β_4 and β_5 of the velocity vectors at $n = 3, 4$ and 5 . The angle β_2 thus obtained is then used in equation (74) to calculate the velocity components at $n = 2$ from:

$$\begin{aligned} q_2^\xi &= q_2 \cos \beta_2 - q_2^\zeta \cos \gamma \\ q_2^\zeta &= \frac{q_2 \sin \beta_2}{\sin \gamma} \\ q_2^n &= 0 \end{aligned} \quad (75)$$

Note that $q_2 = q_2^*$ since it is assumed that q_2 is parallel to the wall, i.e. $q_2^n = 0$.

The iterative, two-point, wall-function approach for a three-dimensional flow can be summarized as follows. With an assumed U_τ , and therefore q_2 from equation (67), equations (75) give the components q_2^ξ , q_2^n , q_2^ζ , and equations (71) give the components (U_2, V_2, W_2) which are required as the boundary conditions for the numerical solution. In turn, this solution gives (U_3, V_3, W_3) and hence q_3 . A new value of U_τ is obtained from equation (68), and equations (72) and (76) are used to find q^* and β at $n = 3, 4$ and 5 for the quadratic extrapolation to determine β_2 . Finally, q_2 is obtained from equation (67)

using the new U_τ , q_2^ξ , q_2^ζ , q_2^n found from equations (75). These provide the updated boundary conditions for the numerical solution and the procedure is iterated to convergence.

It should also be noted that in evaluating the distance y normal to the wall, required in the law of the wall, it is necessary to determine the direction cosine between ξ_n and η^n . This is given by

$$\cos \alpha = \xi_n \cdot \eta^n = \frac{b_1^2 x_n + b_2^2 r_n + b_3^2 r\theta_n}{\sqrt{g g_{22} g^{22}}} \quad (76)$$

in which all the geometric coefficients are again evaluated at the wall, i.e., at $n = 1$.

(4) Outer Boundary

In order to simulate the flow past a body in an unrestricted uniform stream, the outer boundary of the solution domain is placed at a large distance from the body. The boundary conditions then become

$$U = 1, \quad W = 0, \quad \frac{\partial k}{\partial \eta} = \frac{\partial \epsilon}{\partial \eta} = 0, \quad p = 0 \quad (77)$$

The radial component of velocity (V) at the outer boundary is not specified but is determined by the solution. The outer boundary can also be made to coincide with the walls of a wind tunnel or towing tank, in which case the boundary conditions are identical with those described in the previous section.

While the calculations presented in this report are of the type described above, we also recognize that the outer boundary can be made to coincide with a surface in the inviscid flow provided appropriate match conditions are provided. This viscous-inviscid matching approach is not pursued further.

(5) Symmetry Planes

On the centerplane, i.e., the ship keel and the wake centerplane,

and on the undisturbed free surface, i.e., the waterplane, symmetry conditions

$$W = 0, \quad \frac{\partial U}{\partial \xi} = \frac{\partial V}{\partial \xi} = \frac{\partial k}{\partial \xi} = \frac{\partial \epsilon}{\partial \xi} = 0 \quad (78)$$

are enforced for the transport quantities.

(6) Initial Conditions ($t = 0$)

For the steady-flow calculations considered here, the initial conditions for the transport quantities $\phi \equiv (U, V, W, k, \epsilon)$ are taken directly from the values known at the immediately upstream station during the first sweep and the pressure is assumed to be zero throughout the flow field. Although it is possible to assume more realistic initial conditions and thus accelerate the convergence of the solution, these rather crude initial conditions have been used not only to simplify the use of the method but also to demonstrate its versatility.

(e) The Overall Solution Algorithm

With the grid distributions employed for the large Reynolds numbers considered here, the cell Reynolds number in the ξ - direction is quite large. Consequently, in equations (55), the influence coefficient C_D is much smaller than C_{ij} . In other words, the streamwise diffusion is small compared to streamwise convection and transverse diffusion. This enables us to adopt a partially-parabolic solution algorithm with minor modifications, rather than a fully iterative scheme, to solve the elliptic equations. As noted earlier, the present twelve-point finite-analytic formula contains only one additional influence coefficient C_D which is not present in a partially-parabolic formulation. If ϕ_D is evaluated using the value known from previous sweep or time step, then the partially-parabolic solution algorithm of Chen and Patel (1985a) can be employed also to solve the elliptic equations. Thus, the influence of streamwise diffusion in the fully-elliptic equations is conveniently taken into account without significantly increasing computer storage or computation time.

For transient problems, where the initial and boundary conditions are properly specified, the overall numerical solution procedure may be summarized as follows:

1. Construct the body-fitted coordinate system for the given body shape and solution domain, and calculate the geometric coefficients b_j^j , g_{ij} , J , etc. from equations (27) to (31).
2. Specify the initial conditions for the velocity and turbulence fields. Set $p = 0$ everywhere initially.
3. Specify the velocity and turbulence profiles at the first station $\xi = 1$ (these may be time dependent).
4. Calculate the finite-analytic coefficients for momentum, pressure, and pressure-correction equations at the downstream station from equations (52) and (61), respectively. Store only the finite-analytic coefficients a_d , a_r , and a_e for the pressure equation.
5. Solve the momentum equations based on the updated-pressure field to obtain the starred velocity field (U^* , V^* , W^*). This system of algebraic equations is solved by a tridiagonal matrix algorithm.
6. Calculate the mass source D^* , and solve the pressure correction equation (65) by tridiagonal matrix algorithm.
7. Correct the velocity field using the velocity-correction formulae (64), but do not correct the pressure field.
8. Update wall-function boundary conditions using the newly-obtained velocity field and repeat steps (5) to (7) for several internal iterations.
9. Calculate the pseudovelocities $(\hat{U}, \hat{V}, \hat{W})$ in terms of the velocity field from equation (59). Store only D for later use.
10. Solve equations (55) for turbulence quantities ($\phi = k, \epsilon$) by tridiagonal-matrix algorithm.
11. March to the next downstream station and repeat steps (3) to (9).
12. After reaching the last downstream station, solve the pressure equation (61) by tridiagonal matrix algorithm. Several iterations from downstream to upstream are employed to update the three-dimensional elliptic pressure field.
13. Repeat steps (3) to (11) for several sweeps until both the pressure and velocity fields have converged within a specified tolerance.
14. Return to step (2) for the next time step.

15. Stop if the steady-state solution is achieved, or if time exceeds the maximum time period assigned. For steady-flow calculations, one may relax the convergence criterion in step (12) and use a larger time increment for the intermediate solutions.

In the present study, only one sweep was used in step (12) for each time step. Also, as noted earlier, instead of specifying the initial conditions for velocity and turbulence profiles everywhere at $t = 0$, only the profiles at the first station $\xi = 1$ are specified, and the downstream profiles are taken from the immediately upstream station (i.e., $\phi_p = \phi_U$ at $t = 0$) during the first global sweep.

IV. SOME NUMERICAL ASPECTS OF THE METHOD

It was noted in Section II that many components of the present calculation method have been tested by applying it to study the flow past geometrically simpler bodies. In this report, therefore, we will be specifically concerned with the flow around ship hulls.

Before discussing the selection of specific hull forms as test cases and presenting the corresponding results, it is useful to evaluate and document certain numerical aspects of the method. These are discussed in relation to the calculations performed for one of the test cases, namely the SSPA Liner, the physical aspects of which will be considered in the next section. For the purposes of the present section it is simply a representative hull form which is used to examine the convergence properties of the algorithms, dependence of the solutions on the grid and size of the numerical solution domain, and the computer times required to obtain acceptably accurate solutions.

IV.1 CONVERGENCE

Two important measures of the performance of an iterative numerical method are the number of iterations required to obtain a converged solution and the influence of the grid. Here, we shall examine first the convergence history of several representative quantities for a typical calculation with a $(50 \times 30 \times 15)$ grid in the (x, r, θ) directions. In this particular application, as well as in all others, the calculations were performed for 160 time steps (or sweeps) to assure full convergence of the solutions although much fewer sweeps are actually required to obtain an acceptable solution.

Figure 7 shows the convergence of the distributions of pressure, C_p ($= 2p$), and friction velocity U_t , along the keel and waterline coordinates and their extensions into the wake, and wake centerline velocity U_c . It is seen that all these quantities converge monotonically in less than 60 time steps or global sweeps. Recall that the solutions were started with a constant ambient pressure ($p=0$) throughout the solution domain. The calculated pressure and velocity fields clearly capture all the important features of the final converged solutions in less than 20 sweeps. This is particularly encouraging because it eliminates the need for generating an initial pressure field from a potential-flow calculation.

Other tests of convergence of the solutions made on the mass source terms appearing in the pressure and pressure-correction equations also showed monotonic convergence similar to that depicted for the flow parameters shown in the above figures.

IV.2 GRID DEPENDENCE

Calculations were performed with four different (x, r, θ) grids in the solution domain: $\{0.3 < x < 4.5, r_s < r < 1.0, 0 < \theta < \pi/2\}$, to examine the sensitivity of the numerical solutions to grid refinement. Some information on these calculations is given in Table 1, and typical views of the four grids are shown in Figure 8. In the stern and near wake regions, the finest grid, $(74 \times 30 \times 21)$, has nearly twice as many nodes in each direction compared with the coarsest one, $(41 \times 15 \times 12)$. The coarsest grid calculation converged in only 15 iterations and required only about 40 cpu seconds on the CRAY XMP/48. On the other hand, the finest grid required about 30 cpu minutes to achieve the same level of convergence. This is due to the significant increase of the number of grid nodes as well as the number of global sweeps (110) needed for convergence.

Table 1. Summary of Grid Dependence Tests

CASE ==>	I	II	III	IV
Grid points				
in x-direction	41	74	50	74
in r-direction	15	15	30	30
in θ -direction	12	12	15	21
Total nodes	7,380	13,320	22,500	46,620
Time Step, τ	1.0	0.5	0.3	0.5
Memory, 10^6	0.32	0.51	0.84	1.63
cpu, sec/iteration	2.6	5.3	6.0	16.6
Iterations for convergence	15	60	55	110
Total cpu (secs)	40	320	330	1830

Figure 9 shows the results obtained with the four grid arrangements with regard to the flow parameters considered before. It is quite evident that the three finer grids yield nearly identical results. On the other hand, the solution with the coarsest grid shows some departure from the other three. This is presumably due to an inadequate numerical resolution and less accurate specifications of boundary conditions at the hull surface and along the wake centerline. Nevertheless, it is quite encouraging to note that even the coarsest grid calculation is able to capture many of the important features of the flow which are evident from the data discussed later. Consequently, the coarse grid solutions may be used to guide the selection of principal param-

eters in a design process. Refined calculations can then be made in regions where significant variations in body geometry or flow features occur.

IV.3 SOLUTION DOMAIN

In some earlier studies of well known two-dimensional, axisymmetric, and simple three-dimensional bodies, it was found that, with the simple uniform stream boundary conditions employed here the numerical solutions were quite sensitive to the size of the solution domain. The most critical quantity to be examined in this regard is the pressure distribution since its influence penetrates much farther into the inviscid-flow region compared to the velocity field. In order to properly capture the entire zone of viscous-inviscid interaction, the outer boundary should be placed at a distance sufficiently far away from the body such that the uniform flow and zero pressure conditions are indeed appropriate. Similarly, the downstream boundary must be located in the far wake where upstream propagation of pressure becomes negligible.

For the present applications to ship stern and wake flows, we have varied the location of the outer and downstream boundaries over a wide range to examine the influence of domain size on the solutions. Calculations were performed for four different combinations of downstream and outer boundaries, namely

$0.3 < x < 23.1, r_s < r < 2.00$ with a $(57 \times 35 \times 15)$ grid,
 $0.3 < x < 4.53, r_s < r < 0.95$ with a $(50 \times 31 \times 15)$ grid,
 $0.3 < x < 1.95, r_s < r < 0.47$ with a $(45 \times 27 \times 15)$ grid,
 $0.3 < x < 1.34, r_s < r < 0.22$ with a $(41 \times 22 \times 15)$ grid.

The grids for the three smaller domains were obtained by simply deleting an appropriate number of outer and downstream grid lines from the grid generated for the largest solution domain. Therefore, the four solutions correspond to essentially the same grid distributions. It is seen from Figure 10 that the solutions with the two larger domains are essentially the same. It is also clear that the smallest domain is too small to correctly predict the pressure distribution over the hull. These calculations suggest that domain dependency can be eliminated by choosing an outer boundary which is farther than about a half ship length from the axis, and the downstream boundary at a similar

distance from the stern. For all remaining calculations we have chosen the domain $0.3 < x < 4.5$, $r_s < r < 1.0$, which is more than adequate to capture the viscous-inviscid interaction.

IV.4 COMPUTING TIMES

The initial development of the present computer code and some preliminary calculations were performed on a Prime 9950 minicomputer of the University of Iowa. Quite encouraging results were obtained even though the finest grid that could be tested was just $(30 \times 19 \times 14)$. However, it also became clear that a computer with greater speed and larger memory was needed in order to realize the full potential of the method. Therefore, subsequent studies in grid refinement, domain dependence, and convergence were performed on the CRAY XMP/24 supercomputer of the Naval Research Laboratory (NRL) and the CRAY XMP/48 machine of the National Center for Supercomputing Applications (NCSA) at the University of Illinois.

In order to fully utilize the vectorization capabilities of the CRAY supercomputers, several major revisions had to be made in the original code. These included vectorization of the tridiagonal algorithm and the subroutines for the calculation of the finite-analytic coefficients. These code optimizations resulted in a 70-percent saving in cpu time compared to the corresponding scalar calculations. The optimized code on the CRAY supercomputer runs about 150 times faster than the original one on a Prime 9950. A typical ship stern and wake flow calculation with a $(50 \times 30 \times 15)$ grid now takes about 5-10 minutes of cpu time to obtain fully converged solutions. It is estimated that the same calculations would require almost 15 hours of cpu time on the Prime 9950.

V. TEST CASES AND COMPARISONS WITH EXPERIMENTS

One of the major problems of assessing the performance of a complex computational method which is composed of many numerical and physical models and approximations is to find sufficiently detailed and varied test cases for which reliable information is available from other, independent sources. For turbulent flows, this has invariably involved recourse to experimental information. Ideally, it is desirable to have available experimental data sets which are (a) reliable with respect to accuracy, (b) complete enough to pro-

vide the necessary initial and boundary conditions required to carry out a meaningful calculation, and (c) contain sufficient additional information which could be used to evaluate the performance of the calculation method and its components. These requirements were brought sharply into focus at the 1980-81 Stanford Conferences on Complex Turbulent Shear Flows at which attempts were made to identify such data sets for the evaluation of turbulence models. In fact, it became quite evident at that time that few such data sets existed. This was particularly the case for three-dimensional flows.

The situation with regard to the present topic of ship stern and wake flow is not very different. In spite of the numerous experimental studies which were mentioned in Section II.2, there is not a single data set which satisfies all of the requirements noted above. However, this does not mean that the available information cannot be used to provide guidance in the development and evaluation of calculation methods. If the limitations are recognized, the data can still be used to evaluate certain aspects of the overall computation procedure. This also implies that it is desirable to make comparisons with many sets of data, obtained on different hulls, by different techniques, and in different facilities. In view of this, we have selected five cases for which reasonably extensive data are available. In what follows, we shall briefly present the rational for selecting each of them.

The Wigley parabolic hull was selected as the first test case because it has been used in many previous studies of wave and viscous resistance in ship hydrodynamics and because it has a rather simple stern shape. The latter feature is attractive in the evaluation of calculation methods with respect to the prediction of the very near wake and the subsequent evolution of the three-dimensional wake.

As noted earlier, the Wigley hull was one of four shapes selected for the ITTC Cooperative Experimental Program which sought to establish a comprehensive data base, and one of two on which extensive measurements were reported. However, as noted in ITTC (1987), many of these experiments were restricted only to force components. Among the experiments concerned with the details of the viscous flow over the stern and in the wake, the most complete are those of Sarda (1986) on a double model in a wind tunnel. In fact, these experiments were carried out specifically to study the stern and wake flow, and document the evolution of the wake from the thin boundary layer on the

hull. The measurements included surface pressure distribution, mean velocity field, and all components of the Reynolds-stress tensor. The comparisons between these experiments and the present computations are greatly facilitated by the fact that the data were collected in a Cartesian coordinate system and are available on tape.

The second test case is the SSPA 720 Cargo Liner. The boundary layer on a double model of this hull form was measured in a wind tunnel by Larsson (1974). These are among the most well documented mean-flow measurements in three-dimensional boundary layers, and were carefully examined and recompiled in a convenient form in preparation for the SSPA-ITTC Workshop on Ship Boundary Layers (Larsson, 1981). These data were supplemented by corresponding turbulence measurements by Lofdahl (1982) and Lofdahl and Larsson (1984). Because these experiments were conducted to study the hull boundary layer, rather than the stern and wake flow, the measurements were made in a coordinate system suitable for three-dimensional boundary layers. As discussed by Chen and Patel (1985b), this makes it difficult to compare the data with calculations which use generalized coordinates because the errors involved in the interpolations are not insignificant. Nevertheless, the data of Larsson and Lofdahl are most useful in scrutinizing some critical aspects of the calculation method, and also in gaging the advances that have been made over the methods which led to the results shown in Figure 1(a).

The HSVA Tanker is the third test case. Mean flow measurements in the boundary layer on a double model of this hull were first made in a wind tunnel by Hoffman (1976) and other measurements on the same model have been reported since then. For example, quite detailed mean-velocity field data were obtained by Wieghardt and Kux (1980) and Wieghardt (1982, 1983), and some turbulence measurements were reported by Knaack (1984), and Knaack, Kux and Wieghardt (1985). Recent communications with these authors indicate that other experiments on this hull are still continuing.

For the comparisons made in this report, we have used the tabulated stern and wake flow data supplied on tape by Dr. Kux. Comparison of the present calculations with these data was greatly facilitated by the fact that the calculated results could be readily interpolated into the Cartesian coordinates in which the measurements were made. The earlier boundary-layer measurements of Hoffman were used only as a guide to determine appropriate initial

conditions. Recall that these measurements had led to the selection of this hull as the second test case at the SSPA-ITTC Workshop. Comparison of the present results with those presented at the Workshop (Figure 1b) would again indicate the progress that has been made in the prediction of stern and wake flows. Furthermore, the HSVA Tanker is of fuller form than the SSPA hull and therefore provides a more severe test of the calculation method.

The next test case is somewhat similar to the previous one insofar as it also involves a full form hull and mean-flow measurements on a double model in a wind tunnel. This is the SR107 Ore Carrier which has been the subject of many collaborative experiments in Japan (see, for example, Nagamatsu, 1981; Okajima, Toda, and Suzuki, 1985). Although these data are restricted to the stern and wake region, and therefore there is some uncertainty concerning the proper initial conditions, they were selected because they enable the evaluation of the calculation method against somewhat similar data sets obtained in quite different facilities. Here again, the use of Cartesian coordinates in the experiments made it convenient to carry out detailed comparisons.

The fifth and final case considered is the well known Series 60, $C_b = 0.60$ hull. This is the second hull for which the ITTC Cooperative Experimental Program led to the collection of extensive towing-tank data. As in the case of the Wigley hull, however, most of these experiments were concerned with force components and none documented the stern and wake flow in as much detail as that on the other hulls mentioned above. Fortunately, quite extensive data for this hull have recently become available from an independent study.

Here, we shall use the data obtained in the course of a joint research program on propeller-hull interaction between Osaka University and the University of Iowa. These experiments included measurements with and without an operating propeller and will be described in a forthcoming report by Toda, et al., (1988). For the present purposes, we will consider only the measurements without the propeller. These experiments on the Series 60 are particularly suitable for the present study for two reasons. First, they were designed specifically with the goal of obtaining data for the validation of modern computational methods, and therefore the measurement coordinates and locations were selected to facilitate direct comparisons with predictions. Secondly, the measurements were made in a towing tank on a large model at a

relatively low Froude number, and therefore comparisons with double-body calculations give some information on the influence of the free surface in the absence of a strong wave system.

Taken together, the five hull forms selected here provide a rather comprehensive set of test cases for the validation of the computational method. Included are simple and complex geometries with different bow and stern shapes, and different fullness, data obtained on double models in different wind tunnels and those obtained with a conventional model in a towing tank, and finally, measurements with instrumentation of varying degrees of sophistication. In the following sections, we shall point out further features of each of the data sets which have a bearing on the evaluation of the performance of calculation procedures, in general, and the present method, in particular. In the calculations presented below, all attempts have been made to carefully match the conditions prevailing in the experiment but lack of some critical information on the experiment, on the one hand, and limitations of the calculation method, on the other, need to be borne in mind in drawing general conclusions from the comparisons.

Before presenting the results for the individual cases, it is useful to first describe some features that are common to all of them. Among these are the notation used, and the procedure for the generation of initial and boundary conditions.

All coordinates and geometrical parameters have been rendered dimensionless using the ship length L as the characteristic scale, the coordinate x being measured from the bow, rather than from midships. The velocity components are nondimensionalized by a constant reference velocity, U_0 , which is either the velocity of the model or the velocity in the tunnel working section. Finally, pressures and stresses are made dimensionless using the same reference velocity, and ambient density and viscosity. All other quantities will be defined when they are first introduced. It should also be noted that the dimensionless coordinates (x, y, z) are used interchangeably with upper case notations (X, Y, Z) in the figures.

The initial and boundary conditions required by the present method were discussed in general terms in Section III.2 (d). To obtain solutions for a particular shape, it is necessary to prescribe the conditions at the upstream and outer surfaces of the solution domain. Here, we have employed uniform-

stream conditions at the outer boundary (i.e., $U = 1$, $W = 0$, and $p = 0$) and, therefore, the solutions correspond to the flow around double bodies in an unrestricted stream. In other words, wind-tunnel or towing-tank blockage effects are not taken into account.

At the upstream section, $x = 0.3$, it is necessary to prescribe the distributions of (U, V, W, k, ϵ) at all grid points, within the thin boundary layer as well as in the inviscid flow outside. As explained earlier, it is not necessary to prescribe the pressure because it is determined implicitly from the equation of continuity. The specification of the five quantities, for which there are corresponding transport equations, requires some care because they must properly reflect the upstream history of the flow. In all cases we prescribe a girthwise distribution of the boundary-layer thickness δ , the friction coefficient $C_f = 2 U_\tau^2$, and the velocity at the edge of the boundary layer U_δ . These are estimated from either previous boundary-layer and inviscid-flow calculations, or guessed and then adjusted to obtain agreement with data at the first measurement station downstream from the initial section. These quantities are used, together with the law of the wall and the law of the wake, to generate the profiles of the longitudinal velocity U inside the boundary layer, and the reduction from U_δ to unity in the inviscid flow is assumed to take place as r^{-2} . In the first instance, V and W components are set to zero, and k and ϵ are obtained from correlations for a flat-plate boundary layer. As the solution progresses, however, the values of V , W , k and ϵ are updated by scaling those calculated at the first downstream section. This process is continued only for the first 20 global sweeps, and then the initial profiles are fixed. This rather intricate procedure for the generation of the initial conditions does not affect the principal quantity, i.e., the axial velocity profile. However, it ensures that the subsequent solution is carried out with initial profiles of transverse velocity components and turbulence parameters which are compatible with the governing equations. The procedure is quite automatic and results in solutions which are not sensitive to initial conditions.

V.1 WIGLEY PARABOLIC HULL

(a) Available Experimental Information

The experiments of Sarda (1986) were carried out on a 10 ft (3.048 m) long double model suspended by cables in a 5 ft (1.52 m) octagonal-section, return-circuit, closed wind tunnel in which the freestream turbulence level was less than 0.5 percent. The measurements were made at a Reynolds number $Re = U_0 L / v = 4.5 \times 10^6$. Although measurements could be made only upto a distance of 8 ft (2.44 m, or 0.8 L) downstream of the stern, these experiments document the wake considerably farther than the other experiments discussed subsequently. The boundary layer on the hull was tripped by means of studs of standard design at $x = 0.05$.

The available data include the pressure distribution on the hull measured by surface pressure taps, mean-velocity components measured by a five-hole pitot probe, and components of the mean velocity, the Reynolds-stress tensor, and triple products of fluctuating velocity components measured by means of a three-sensor hotwire probe. The velocity and turbulence measurements were made at several longitudinal sections in the range $0.5 < x < 1.8$, i.e., from midships to 0.8 ship lengths downstream of the stern.

(b) Body Shape and Numerical Grid

The coordinates of the Wigley hull are given by

$$2\bar{Y}/B = [1 - (2\bar{X}/L - 1)^2] [1 - 2\bar{Z}/D]^2 \quad (79)$$

where $(\bar{X}, \bar{Y}, \bar{Z})$ are Cartesian coordinates with the origin at the bow, and the ship length (L): beam (B): draft (D) ratio is 10:1:0.625.

The solution domain extends from a section 0.3 ship lengths from the bow to 3.524 ship lengths downstream of the stern, and from the hull to a cylindrical surface located one ship length from the ship longitudinal axis. In terms of the coordinate variables, the solution domain is defined by $0.3 < x < 4.524$, $r_s < r < 1.0$. This domain is covered by $50 \times 30 \times 15$ grid points in the axial, radial, and circumferential directions, respectively, giving a total of 22,500 grid nodes.

Some views of the numerically-generated grid are shown in Figure 11. The grid-control functions f^i used to obtain this grid were given in equation (41). The parameters appearing therein are as follows:

$$c = \begin{cases} 0.6 & \text{if } A < 0 \\ 0.2 & \text{if } A > 0 \end{cases}$$

$$d = 0.2$$

The following are some of the noteworthy features of this grid. First, the coordinate surface $n = 2$, just off the hull in the radial direction, is arranged in such a way that at all locations it lies in the range $90 < y^+ < 250$, y^+ being the normal distance from the hull. Recall that such a constraint is necessary for the wall-functions approach to be applicable. Other investigators who also employ wall functions have placed the first near-wall grid surface much closer to the hull than the one used here. While such solutions can be also obtained with the present method, we believe that they cannot be trusted because the underlying assumptions of the law of the wall and energy equilibrium are no longer valid. In other words, grids finer than the ones used here can be justified only if the wall-function approach is abandoned in favor of direct solutions of the governing equations all the way upto the wall. Secondly, we note that the grid is concentrated near the stern and in the near-wake to resolve the large gradients which occur at the trailing edge. Third, the grid spacing is increased very rapidly in the radial and longitudinal directions. In fact, the final step size in the radial and axial directions is of the order of 0.2 and 0.8, respectively. The use of such large steps while maintaining solution accuracy is made possible by the finite-analytic discretization of the transport equations.

(c) Description of Results and Comparisons with Experiments

Here, as in all subsequent cases, we shall first examine the distributions of pressure and wall shear stress on the hull surface, and then the details of the flow field. Figure 12 shows the distribution of pressure coefficient C_p ($= 2p$) and friction velocity U_τ along the keel and the waterline planes of symmetry. Girthwise distributions of C_p and the magnitude of the friction coefficient C_f ($= 2U_\tau^2$) at a few transverse sections are shown in Figure 13. The data of Sarda (1986) and some unpublished results from Watmuff

and Joubert (1985) are also shown in Figures 12 and 13. In the case of Watmuff and Joubert the pressure datum was adjusted to match the potential flow value at midships. The direction of the wall shear stress can be seen from the limiting or wall streamlines plotted in Figure 14. This last figure was obtained from the calculated wall shear stress vectors over the hull, starting from the initial section at $x = 0.3$.

In Figure 12 the experimental data are restricted to the waterline because there are no pressure taps along the sharp keel. The potential-flow pressure distributions were obtained at the David Taylor Research Center using the XYZ computer program. It is seen that the present calculations are in good agreement with the data of Watmuff and Joubert, but both are considerably higher than the measurements of Sarda near the stern, $x > 0.94$. The discrepancy between the two sets of measurements is somewhat surprising because both experiments were performed under similar conditions. Although the reason for the observed differences is not entirely clear, Sarda noted that the geometry of his model was not precisely the same as that of the mathematical form, his model being thicker in the bow and stern regions. Potential-flow calculations for the actual experimental shape is obviously needed to determine if the differences in geometry are indeed responsible for the differences in the data. Despite these uncertainties, however, we note that the present results are in good agreement with the potential-flow solutions over much of the hull where the boundary layer is thin. The level of disagreement between the data of Sarda and the calculations over the midbody is also consistent with the expected tunnel-blockage effect in the experiments. In the stern region, the calculated pressure gradients are smaller than those in potential flow as is to be expected from the displacement effect of the viscous flow.

The calculated friction velocities along the waterline follow the trends shown by the data, which were obtained from Clauser plots of measured velocity profiles, although the measurements are somewhat lower than the predicted values. It is seen that the friction velocity decreases along the waterline due to the continuous thickening of the boundary layer. On the other hand, the calculated friction velocity increases along the keel in spite of the adverse pressure gradient that is present. This is due to a reduction in the boundary layer thickness produced by flow divergence out of the keel plane.

From Figure 13 it is seen that the calculated girthwise distributions of pressure are in agreement with the two sets of measurements upto $x = 0.95$. The marked disagreement between the calculations and the data of Watmuff and Joubert at the next section, $x = 0.962$, is most likely due to interference from the model support in the experiment. Further downstream, the calculations agree with the data of Watmuff and Joubert but, as noted already, lie above the measurements of Sarda.

The calculations and experiments indicate that in the region $0.5 < x < 0.9$ the pressure decreases in the girthwise direction from the keel towards the waterline. This is in agreement with potential-flow theory, as would be expected in regions where the boundary layer is thin. Although the girthwise gradient is small, it is responsible for the secondary motion from the keel towards the waterline. Around $x = 0.8$, the pressure shows an increase towards the waterline in a region whose girthwise extent increases downstream. Eventually, for $x > 0.9$, there is an increase in pressure all the way from the keel to the waterline. This reversal of trend from the predictions of inviscid theory is associated with the changes in the girthwise distribution of boundary layer thickness over the stern.

The calculated and measured wall shear-stress coefficients shown in Figure 13 indicate similar general trends but there exist systematic differences, particularly at the most upstream station, where the calculated values are higher than the measurements. Although somewhat better agreement could be secured in this respect by adjustments in the initial conditions at $x = 0.3$, this was not pursued further partly because the agreement between the calculations and the data improves downstream ($x > 0.92$). The decrease in wall shear stress magnitude from the keel towards the waterline is consistent with the thinning of the boundary layer along the keel and a thickening along the waterline brought about by the crossflow. The general direction of the crossflow and the changes in the direction of the wall shear stress are best seen from the wall streamlines of Figure 14.

An overview of the flow pattern is provided by Figure 15 which shows the velocity vectors projected onto the horizontal waterplane and the vertical centerplane. These plots were constructed by interpolation of the numerical results. Contours of the axial velocity (U) and velocity vectors projected into transverse sections (V and W components) are shown in Figures 16(a) and

(b) for some representative sections at midships, over the stern, in the near wake, and farther downstream. Here, the transverse velocity plots also indicate the grid distribution. We recall that all of these figures show information close to the hull although the total solution domain is much larger. The measurements of Sarda are shown in Figures 17 (a) and (b) for comparison.

Among the major features evident from Figures 15 and 16 are the following. In the longitudinal direction, the boundary layer grows rapidly along the waterline but remains thin along the keel. This is due to the secondary motion which is directed from the keel towards the waterline, in the viscous flow as well as in the outer inviscid flow. The transport of the boundary layer fluid towards the waterline is also indicated by the convergence of the wall streamlines in Figure 14. The direction of the transverse motion is also consistent with that expected from considerations of the pressure gradients associated with an inviscid flow. From potential-flow pressure distribution on the front half of the hull we would expect the secondary flow in the boundary layer up to midships and perhaps for some distance downstream to be directed towards the keel, resulting in a thicker boundary layer at the keel. These features were observed in the measurements of Sarda at $x = 0.5$ (see Figure 17) and also in his boundary-layer calculations. The present calculations at $x = 0.5$ indicate that although a thicker boundary layer is observed at the keel at this section, the secondary motion is directed towards the keel only in a small layer close to the keel. This difference, although small, is most likely due to the use of simple flat-plate profiles for initial conditions (at $x = 0.3$) in the present calculation. While the use of a boundary-layer calculation to obtain the initial conditions would reduce this difference, additional difficulties arise in handling the sharp keel within the framework of boundary-layer theory.

Examination of the velocity field over the stern and in the near wake shows no dramatic changes in the flow structure. In particular, there is no evidence of a stern vortex, although there is obviously longitudinal vorticity associated with the transverse velocity components. The transverse components decay rather rapidly in the wake. The calculations predict a quite rapid recovery of the wake to what appears to be an almost axisymmetric state by $x = 1.5$, a half ship length from the stern. This is at variance with the measurements shown in Figure 17 which indicate a rather slow development of the wake.

The calculated distributions of the velocity components (U, V, W), pressure (p), and turbulent kinetic energy (k) are compared with the measurements of Sarda (1986) in Figure 18 at several sections in the range $0.5 < x < 1.5$. The calculated results were interpolated to determine the variation of the various quantities in the horizontal (y) direction at different depths ($z = \text{constant}$), $z = 0$ being the waterplane. Note that the horizontal axis in these figures is y^* , the distance from the hull surface. For profiles below the keel ($z < -0.0625$) and in the wake ($x > 1$), of course, $y^* = y$. The data obtained with a five-hole pitot and a triple-sensor hotwire are included to show the experimental uncertainty, particularly with respect to the components V and W . In the case of pressure, the original data which were obtained with the pitot probe were referenced to a pressure in the wind tunnel some distance upstream of the model. The pressure measured in the wake at $x = 1.5$ was nearly uniform but higher than the reference pressure. The calculations, on the other hand, predicted almost zero pressure relative to the pressure in the uniform stream. In view of this, a constant ($= -0.06$) reference-pressure correction has been added to the data to obtain the so-called corrected pressures shown in Figure 18. In other words, the calculated and measured pressures have been matched in the wake at $x = 1.5$. Such a constant correction obviously does not alter the pressure gradients and therefore enables us to compare the calculated and measured gradients. On the other hand, it is not a correction for tunnel blockage although blockage may be responsible for a part of the observed pressure difference. A more likely possibility is an error in probe calibration. Figure 18 contains a great deal of information regarding the details of the flow and on the performance of the calculation method. To aid the understanding of the many issues involved, we shall discuss the results starting with those at midships and progressing downstream into the wake.

The results at midships (Figure 18a) indicate that the boundary layer is thin and the girthwise variation of its thickness is captured adequately by the simple initial conditions prescribed at $x = 0.3$. There are differences in the shapes of the axial velocity profiles at some depths, and in the shapes and magnitudes of the transverse components particularly close to the wall. In spite of the differences between the pitot and hotwire data, it is clear that the generally negative values of V and W measured in the experiments are not captured by the calculations. We have already commented on this difference. It appears that further refinements in the initial conditions could

have been made to secure better agreement at this first measurement section. In spite of the differences in the mean velocity field, we see that the calculated pressure is in reasonable agreement with the corrected data. The small departures between the two close to the wall are believed to be due to probe interference. Finally, the profiles of turbulent kinetic energy are also matched rather well except at the keel ($z = -0.0625$).

The flow over the stern is described by the results at four sections, $x = 0.90, 0.95, 0.967$ and 0.983 . Here, the profiles of the axial velocity indicate that the girthwise distribution of the thickness of the viscous region is predicted rather well, including the near-disappearance of the boundary layer at the keel. There is, however, a tendency for the calculated velocities to be larger close to the wall. This is most likely associated with the use of the wall functions. The correction for pressure gradients in the law of the wall are presumably not sufficient to completely describe the wall layer. With respect to the transverse components of velocity, the calculations predict the general trends and magnitudes rather well. Unfortunately the scatter in the data and the differences between the pitot and hotwire results preclude more definitive conclusions. The predicted distributions of pressure are in good agreement with the corrected data with the possible exception of a short fetch close to the stern. The profiles of turbulent kinetic energy are also predicted quite well except very close to the wall where the measured values are generally larger. This feature is presumably related to the differences in the axial velocity profiles noted above and may again be due to the inadequacy of the wall functions.

The results at the next three stations, namely, $x = 1.002, 1.017$ and 1.050 , illustrate the rapid changes that take place in the neighborhood of the centerplane ($y^* = y = 0$) of the extreme near wake. First, we note that the calculated results do not extend to the centerplane because of the way in which the plane-of-symmetry boundary conditions are enforced. However, this is not the principal reason for the quite major differences between the calculations and measurements. Previous calculations for a flat plate (Patel and Chen, 1987) and for bodies of revolution (Chen and Patel, 1987b, 1988) indicate similar tendencies, i.e., an overestimation of the velocity and an underestimation of the turbulent kinetic energy along the wake centerline. This is attributed to the fact that the flow in the sublayer and the blending zone of

the upstream boundary layer has not been considered as a result of the application of wall functions in the turbulence model. The lower measured velocities and higher measured turbulence are therefore associated with the physics of the flow in the near-wall region. The secondary velocity components also indicate systematic differences, presumably due to the same reason. In spite of the discrepancy in the inner portion of the very near wake, it is encouraging to note that the flow in the outer part continues to be predicted satisfactorily in all respects.

The subsequent evolution of the wake is depicted by the results at the next four sections, $x = 1.1, 1.2, 1.3$ and 1.5 . It is clear that the differences which arose in the inner part of the wake at the stern persist for quite large distances, particularly with regard to the profiles of axial velocity and turbulent kinetic energy. The scatter in the data is such that definitive conclusions concerning the secondary motion cannot be reached but there is some evidence to suggest that the calculations predict a more rapid decay of the secondary flow than is observed in the data. This was also seen from comparisons of Figures 16 and 17. Finally, we observe that the pressure at these distances is nearly uniform, and the comparison between the data and the calculations for $x = 1.5$ show that a constant correction on the measured pressures is justified.

(d) Summary

Insofar as the flow over the hull and the stern is concerned, it is clear that the present calculations predict all essential features of the mean flow with reasonable accuracy. No attempt has been made here to compare the present results with those obtained earlier by solutions of the boundary-layer equations (e.g. by Sarda, 1986), but it is expected that the differences may be significant only in the stern region because there is only a weak viscous-inviscid interaction on this rather slender hull. With regard to the turbulence, we have chosen to examine only the turbulent kinetic energy, a quantity which can be measured with a greater degree of precision than the individual Reynolds-stress components, and which directly enters the turbulence model used in the method. The results could of course be analyzed further to examine other aspects of turbulence modelling. This has not been pursued in view of the following.

Perhaps the most interesting aspect of the calculations for the Wigley hull is the very large and marked influence of using the wall functions in the turbulence model on the prediction of the wake. The experiments indicate that the three dimensionality and turbulence generated in the near-wall region of the stern flow persist for quite large distances in the wake. This is presumably because the pressure gradients in the stern region of this hull are too weak to significantly affect the development of the near wake. It is clear that further improvements in the prediction of the wake would require replacement of the wall functions with a turbulence model that would enable accurate resolution of the near-wall layers.

V.2 SSPA CARGO LINER

(a) Hull Geometry and Available Experimental Information

The experiments of Larsson (1974) were conducted on a double model of a cargo liner in a 1.25 m x 1.80 m wind tunnel, with a freestream turbulence level of about 0.2 percent. The model was supported from the tunnel floor by two struts. The tests were conducted at a Reynolds number of 5×10^6 , based on model length $L = 2$ m. The hull offsets are shown in Figure 19. The beam and draft of the model are 0.283 m and 0.118 m, respectively, and the block coefficient is 0.675. Larsson made extensive potential-flow calculations, with and without tunnel walls, to study the effect of wind-tunnel blockage on the hull pressure distribution. These calculations have been used here to correct the measured pressures for blockage.

As this was an investigation of the hull boundary layer, measurements of velocity profiles were made in streamline coordinates, i.e., the two velocity components in planes parallel to the hull surface, along and normal to the inviscid-flow streamlines on the hull, were measured along local normals to the hull. The inviscid streamlines calculated by Larsson, and along which his measurements were made, are shown in Figure 19(c). The mean-velocity measurements were made by hotwires and covered the range $0.20 < x < 0.95$. In a later investigation, Lofdahl (1982) (see also Lofdahl and Larsson, 1984) measured all six components of the Reynolds-stress tensor by hotwires along the same streamlines. However, his measurements were restricted to the region $0.75 < x < 0.95$, where the boundary layer was thick enough for probe size and interference effects to be small.

(b) Numerical Grid

As in the previous case, the solution domain is defined by $0.3 < x < 4.524$, $r_s < r < 1.0$, and covered by $50 \times 30 \times 15$ grid points in the axial, radial, and circumferential directions, respectively. From Section IV.2, we recall that this is not the finest grid that was employed to study the grid dependence of the present method. Some views of the numerically-generated grid are shown in Figure 20. The grid-control functions f^i used to obtain this grid were given in equation (41). The parameters appearing therein are as follows:

$$c = \begin{cases} 0.10 & \text{if } A < 0 \\ 0.01 & \text{if } A > 0 \end{cases}$$

$$d = 0.2$$

With this choice, the first grid node just off the hull lies in the range $40 < y^+ < 250$.

(c) Description of Results and Comparisons with Experiments

We have already mentioned the difficulties of interpolating data obtained in boundary-layer coordinates to make comparisons with solutions obtained in numerical coordinates of the type used here. We shall therefore restrict the comparisons only to those quantities which are either unaffected by the choice of coordinates or are insensitive to differences in the coordinates. Among the former are the distributions of pressure and wall shear stress on the hull. Figure 21 shows the distribution of pressure and friction velocity U_τ along the keel and the waterline planes of symmetry. Girthwise distributions of pressure and the magnitude of the friction coefficient at a few transverse sections are shown in Figure 22. The direction of the wall shear stress can be seen from the limiting streamlines plotted in Figure 23. The last figure was obtained by integration of the wall shear stress vectors starting from the initial section at $x = 0.3$. The data of Larsson (1974), with and without blockage correction in the case of pressure, are also shown in Figures 21 and 22.

Figures 21 and 22 indicate that the effect of wind tunnel blockage is quite significant in the pressure distributions and that the calculations are in quite good agreement with the data corrected for blockage. It is seen that at midships the pressure is essentially uniform around the girth, but girthwise gradients develop as the geometry changes. These gradients become large near the keel as the transverse surface curvature increases, and a region of low pressure develops some distance from the keel. The associated girthwise pressure gradient is such that there is a divergence of flow out of the keel and a thinning of the boundary layer along the keel. There is also a secondary motion towards the low pressure region from above. This convergence of flow from both sides into a region around midgirth leads, as we shall see, to a thickening of the viscous layer there. The relationship between the pressure distribution and the wall shear stress is not immediately obvious from Figures 21 through 23, but, as will become clear later, the low values of the wall shear stress occur where the viscous layer becomes thick. Figure 23 shows the divergence of wall streamlines out of the keel over much of the hull, but a rather complex pattern develops over the stern. The strong convergence of streamlines in an area just above the keel at the stern is frequently interpreted as evidence of a longitudinal vortex and even separation. However, as will become clear as we examine the details of the flow for other hulls, this pattern by itself is not an indication for either a vortex or flow separation.

The flow pattern on the waterplane and in the vertical centerplane, constructed by interpolation of the numerical results, is shown in Figure 24. The thickening of the boundary layer over the stern in the waterplane, and the thinning of the boundary layer along the keel are clearly seen from these views as is the evolution of the three-dimensional wake. Contours of the axial velocity (U) and velocity vectors projected into transverse sections (V and W components) are shown in Figure 25 for some representative sections in the range $0.5 < x < 1.1$. The transverse velocity plots also give an indication of the grid distribution. At midships, the secondary flow is directed away from the keel as well as from the waterplane. This leads to the thickening of the layer around midgirth which is already evident by $x = 0.7$. This process continues as the secondary motion becomes stronger, particularly near the keel where the hull geometry changes more rapidly. We now see that the regions of low wall shear stress in Figure 22 coincide with the regions of

thickening of the viscous layer. By $x = 0.95$, the thickness of the viscous layer is almost as large as the draft of the model. At and downstream of the stern, the secondary motion gives the impression of a longitudinal vortex, but the strength of this motion diminishes quite rapidly.

The contours of the axial component of velocity shown in Figure 25 may be compared with those of the magnitude of mean velocity, reconstructed by Broberg and Larsson (1984) from the measurements of Larsson (1974) and Lofdahl (1982), which are shown in Figure 26. We note again not only the difference in the quantities but also the fact that the experimental contours are not based on measurements in transverse sections. The error involved is small, however, and there is good agreement between the calculations and measurements with regard to the major features of the stern flow.

More detailed comparisons between experiments and calculations are attempted in Figure 27. The calculated results were interpolated to determine the variation, with distance N normal to the transverse section of the hull, of the resultant velocity parallel to the hull (Q), its component (C) normal to the direction of the calculated streamline at the location of the measured boundary-layer edge, and the turbulent kinetic energy (k), at each of the points on the hull for which experimental data are available. All of these quantities are relatively insensitive to the remaining differences between the computational and experimental locations. Also, we note that C is the so-called crossflow velocity in the terminology of boundary-layer theory.

Figure 27a shows the profiles of Q and C . Figure 27b shows semilogarithmic plots of Q versus $N^* = U_0 N / v$, the format of the Clauser plots which were used for the experimental determination of the wall shear stress from the measured velocity profiles. Figure 27c shows the distributions of the turbulent kinetic energy. Comparisons are presented for five transverse sections, namely, $x = 0.50, 0.75, 0.85, 0.90$, and 0.95 , the last four of which coincide with those where the turbulence measurements of Lofdahl were made. For convenience, the girthwise locations of the measurement stations, the normals to the transverse section at those stations, and the hull section just downstream of the measurement section (from Figure 19) are shown in each figure. The line numbers correspond to the potential-flow streamlines calculated by Larsson, lines 1 and 10 being the keel and waterline, respectively. The data are shown by symbols at all stations where measurements were made.

Considering the midship section first, we see that the thickness of the boundary layer and the longitudinal velocity profiles are predicted quite well. The crossflow, which is small, is captured only qualitatively. The Clauser plots indicate that the calculations reproduce the logarithmic layer indicating that the placement of the near-wall nodes in the numerical grid is satisfactory for the wall functions approach to be applicable. It is also seen that further grid refinement can be made by pulling the near-wall nodes closer to the wall, but as we have already shown in Section IV.2, adding points in the grid does not by itself provide greater accuracy. More importantly, the agreement between the calculations and data in the inner region is indicative of the accuracy with which the large gradients in the wall layer are resolved in the numerical solutions. The agreement in the Clauser plots is, of course, reflected in the agreement shown earlier with respect to the wall shear stress. Finally, there is nothing remarkable about the turbulent kinetic energy profiles at midships; they resemble those in a flat-plate boundary layer.

The section $x = 0.75$ may be the most downstream section at which the flow could still be regarded as of the boundary-layer type. Here, the velocity magnitude and the crossflow component are predicted with reasonable accuracy everywhere except at line 6, where it is the data which appear to be spurious. The profiles of turbulent kinetic energy at this section begin to show a trend which becomes very pronounced further downstream. We observe that the calculated values are generally larger than the measurements and, at line 5, which is roughly where the thickness of the viscous layer is the greatest, the k distribution develops a plateau.

The final three sections considered in Figure 27 ($x = 0.85, 0.90, 0.95$) lie in the stern-flow region where the viscous layer can no longer be regarded as a boundary layer. From the results at these sections we make the following observations. First, the variation of the thickness of the viscous layer, around the girth and in the axial direction, are predicted with considerable accuracy. Secondly, the mean velocity profiles are described quite well by the calculations although, as evidenced by the logarithmic plots, there is a tendency for the calculated velocities to be somewhat larger in the near wall region. Thirdly, the general shapes of the crossflow profiles are predicted but there exist differences in magnitude. The differences may, however, be of

the same order as the uncertainties of interpolation. Fourthly, the predicted turbulent kinetic energy is considerably larger than that measured. Finally, we note a very characteristic two-layer feature developing around midgirth (see line 5 at $x = 0.85$; and lines 3,5,7 at $x = 0.90$ and 0.95) which suggests the existence of a thin layer of fluid close to the wall in which k diminishes rapidly, and a much larger layer farther out where there is a plateau in k and a gradual decrease to zero outside the viscous region. Although there is a hint of such a two-layer structure in the calculated profiles, it is obvious that the present turbulence model fails to capture the changes that are taking place in the turbulence in the flow over the stern.

(d) Summary

The calculations for the SSPA liner confirm the capability of the present numerical method to predict the essential features of the pressure and mean-velocity fields in considerable detail. This is particularly surprising in view of the differences between the calculated and measured turbulent kinetic-energy distributions, and leads to the conclusion that the turbulence in the outer part of the viscous layer is inactive and is simply being convected with the mean flow. The success of the calculations must therefore come from the use of the wall functions which essentially reproduce the observed logarithmic layer close to the surface. This also suggests that further improvements are most likely to result from refinement of the treatment of the flow in the near-wall region. Since the experiments on this hull did not extend into the wake, it is not possible to comment on the quality of the wake calculations.

Finally, we note that these calculations have also pointed out the importance of wind-tunnel blockage, particularly with regard to the hull pressure distribution. The effects of blockage on the velocity distributions are too small to be seen on the various plots. Because the present method can also take into account wind-tunnel walls by appropriate relocation of the external boundary of the solution domain, it would be of interest to carry out such a calculation to study the blockage effect in greater detail.

V.3 HSVA TANKER

(a) Hull Geometry and Available Experimental Information

The offsets of the HSVA Tanker are shown in Figure 28. The boundary layer measurements by Hoffman (1976), and the detailed stern-flow measurements of Wieghardt and Kux (1980) and Wieghardt (1982, 1983), were made on a double model of this hull in a 1.2 m square, slotted-wall wind tunnel, in which the turbulence level was of the order of 1 percent. The slotted walls are usually meant to reduce or eliminate blockage effects. The model was supported in the tunnel by means of wires and a sting at the stern. The nominal length of the model was 2.74 m but for reference length we have used the length between perpendicuars, $L = 2.634$ m. The model beam and draft are 0.43 m and 0.15 m, respectively, and the block coefficient is 0.85.

The locations of the measurement sections in the experiments of Wieghardt and Kux are shown in Figure 29. The data were obtained at nine axial sections in the range -157 mm $< \bar{X} < 200$ mm, in the notation of Figure 29. This corresponds to $0.9103 < x < 1.044$ in the present notation. The measurements were made by means of a five-hole pitot probe, and included the three components of mean velocity (U, V, W) in Cartesian coordinates and pressure. The closely spaced measurements enabled the determination of the mean vorticity field. The calculations were performed for a Reynolds number of 5×10^6 which corresponds to the experimental value.

(b) Numerical Grid

As in the two previous cases, the chosen solution domain is defined by $0.3 < x < 4.524$, $r_s < r < 1.0$ and was covered by $50 \times 30 \times 15$ grid points in the axial, radial, and circumferential directions, respectively. Some views of the numerically-generated grid are shown in Figure 30. The grid-control functions f^i used to obtain this grid were given in equation (41). The parameters appearing therein are as follows:

$$c = \begin{cases} 0.20 & \text{if } A < 0 \\ 0.02 & \text{if } A > 0 \end{cases}$$

$$d = 0.25$$

With this choice, the first grid node just off the hull lies in the range $50 < y^+ < 250$.

(c) Description of Results and Comparisons with Experiments

Figure 31 shows the distribution of pressure and friction velocity along the keel and the waterline planes of symmetry, and the girthwise distributions of pressure and the magnitude of the friction coefficient are shown in Figure 32 at a few transverse sections. In these figures we have included the data from the boundary-layer experiments of Hoffman (1976) at a Reynolds number of 4.8×10^6 . The section $x = 0.9418$ corresponds to the most downstream measurement section in his experiments and to the $X = -73$ mm section in the later experiments of Wieghardt and Kux. From Figure 31 we see that the pressure distribution is in good agreement with the data except along the keel at the stern. The lower predicted values of friction velocity along the keel are consistent with the differences in the pressure distributions. These differences are again evident from the girthwise variations at $x = 0.9417$ shown in Figure 32. These suggest that the stern flow in the neighborhood of the keel is not being described with sufficient accuracy. This may be due, at least in part, to differences between the actual hull geometry and that implied in the calculations by the chosen numerical grid.

The direction of the wall shear stress can be seen from the limiting streamlines plotted in Figure 33. This shows a region around midgirth at the stern into which the wall streamlines converge. This is the area of maximum thickness of the viscous layer. These features, like those of the results presented in the previous two figures, are qualitatively similar to those discussed earlier for the SSPA liner.

The rather complex stern geometry of the tanker and some general features of the resulting flow pattern are seen from Figure 34. Comparison with the corresponding figure (Figure 24) for the more slender SSPA hull shows that the flow pattern is qualitatively similar. However, these views of the flow tend to mask the very significant differences that exist.

Figure 35 presents comparisons between the experimental data and calculations with respect to the mean-velocity field. The contours of axial velocity and projections of the velocity vectors in transverse sections are shown at six sections. Particularly noteworthy here is the very fine grid used for the

measurements. Here, the measurements and calculations correspond to transverse sections and therefore the comparisons do not involve the uncertainties which were present in the case of the SSPA liner.

At the most upstream section, $x = 0.6433$, we see that the boundary layer is thin except around the turn of the bilge. Although the local crossflow is quite weak, the thicker boundary layer is the result of flow convergence towards the turn over some distance upstream. By the next section, $x = 0.9103$, the boundary layer has thickened considerably near midgirth. The following section, $x = 0.9418$, corresponds to the last measurement section in the experiments of Hoffman and the data shown in Figure 1b. Comparison of the calculations with the recent and more detailed data indicates that the general features of the U contours and the transverse velocity components are predicted at all sections but there are differences particularly close to the hull around $z = -0.04$. The gaps in the data at these depths at $x = 0.9549$ and 0.9692 are regions of low velocity which could not be resolved by the pitot probe. At the three downstream sections, some of the velocity contours are missing partly because the predicted velocities are larger and partly due to the use of the wall functions. The wall functions could of course be used to reconstruct the contours close the hull and wake centerplane but this has not been done here. Comparisons of specific contours, for example $U = 0.5$ and 0.9 at the last three sections reveal that the predictions are in remarkably good agreement with the measurements. The solutions also capture the major features of the secondary motion, including the magnitudes, but this is not immediately obvious from Figure 35.

In order to make a detailed assessment of the predictions, the results of the calculations were interpolated to obtain the distributions of the three velocity components (U, V, W) and pressure (p) in the Cartesian coordinates which were employed for the measurements. This makes it possible to plot the profiles of these parameters in, say, the horizontal direction (y) at different depths ($z = \text{constant}$). The results are shown in Figure 36. Although there is a great deal of similarity in the results because of the closely spaced stations, we have included all ten transverse sections here to facilitate future reference and comparisons by others using different methods. In general, we see that the calculations are in rather remarkable agreement with the data in all respects except in small regions close to the hull or in the

neighborhood of the wake centerplane just downstream of the ship. Before discussing these features it is useful to point out that y in these profiles is measured from the ship centerplane and therefore one gets a rough idea of the hull shape at each section. Also, $z = 0$ is the waterplane and the keel is at $z = -0.051$.

Reference to Figure 29 shows that the first five sections are located in the region where the keel is still horizontal ($x = 0.9621$ corresponding to section $\bar{X} = -19$ mm), the next section is just where the stern is almost perpendicular ($x = 0.9692$ corresponds to $\bar{X} = 0$), and the remaining four sections are located downstream of the propeller plane. It is important to keep in mind the local geometry, and particularly the changes in it, in order to understand the results shown in Figure 36. It is convenient to discuss these in three stages, roughly corresponding to the three regions identified above.

In the first region, upto $x = 0.9621$ (Figure 36a-e), we see that the U and V components are in good agreement with the data but the vertical component W shows a characteristic difference that persists downstream. The magnitude of the W component changes rather rapidly with distance from the hull surface in the region where the surface is nearly vertical, i.e., where W is nearly parallel to the surface. At the two downstream sections, we also observe increasing differences in the horizontal V component. The prediction of the pressure field is quite satisfactory, except in small layers close to the hull which roughly coincide with the regions in which we see differences in the W velocity component. There are two possible explanations for the differences between the calculations and measurements. One is that the wall-functions approach employed here does not completely capture the details of the secondary motion. The second and more likely possibility is that the numerical grid does not resolve the local geometry in sufficiently fine detail to predict the secondary motions and the associated pressure field.

The plots for $x = 0.9692$ (Figure 36f) reveal that the differences between the calculations and measurements now extend to the U and V components, and the characteristic features of the W component noted above continue. A careful examination of these differences indicates that they stem principally from the truncation of the local geometry implied by the numerical grid employed, and from the way in which the hull and wake boundary conditions are enforced in the local numerical cells at this section within the framework of the

staggered grid used in the present velocity-pressure coupling method. However, previous experience with problems involving discontinuities of boundary conditions, from no slip on the hull to zero stress on the wake centerplane, suggests that improved results can be obtained by more refined grids and a more direct treatment of the flow in the near-wall layer than made in the wall-functions approach.

The results at the final four sections ($x > 0.9786$, Figure 36g-j) indicate the development of the near wake. Here, the differences which were generated upstream continue. Also, we see that the calculations predict a rather rapid increase in axial velocity in the wake centerplane, a feature which was also observed in the case of the Wigley hull (see Figure 18f-1). This is most likely due to the use of the wall-functions which do not resolve the flow in the near-wall layer on the hull upstream. It is interesting to note the decay of the calculated as well as the measured secondary motion with downstream distance. At the last section the calculated U and V components are again in reasonably good agreement with data while the differences in W and p persist.

As we have already noted, the measurements of Wieghardt and Kux were made in such detail that it was possible to carry out the differentiations required to determine the mean vorticity field. In spite of the uncertainties involved in processing both the measured and computed data, a comparison between the computed and measured vorticity is a particularly acid test of a computational method because it is an examination of differences in velocity gradients rather than just velocity components. Such a comparison is presented in Figures 37 and 38. Figure 37 shows the contours of the longitudinal component of vorticity, $[\partial W / \partial y - \partial V / \partial z]$, while Figure 38 shows the contours of the magnitude of the vorticity vector, $(\omega_x^2 + \omega_y^2 + \omega_z^2)^{1/2}$. These plots show that the calculations reproduce not only the general features of the contours but also the magnitudes. The differences close to the hull and around the wake centerplane are to be expected from the differences in the velocity distributions discussed above. An additional and new feature that becomes apparent from the vorticity comparisons, however, is that the calculations indicate a somewhat larger diffusivity compared with the measurements. This is presumably due to an overestimation of the eddy viscosity by the standard $k-\epsilon$ turbulence model. We have already commented on this feature in

connection with the prediction of the turbulent kinetic energy in the previous cases.

(d) Discussion

The HSVA tanker represents a more severe test of the calculation method than the previous two hulls because of its high block coefficient and rather abrupt changes in stern geometry. In addition to the observations that have been made on the basis of the previous calculations, the comparisons between the numerical results and the very extensive experimental data for the present case suggest the need for (a) more refined treatment of the stern geometry, (b) better resolution of the flow in the near-wall layer, and (c) some correction for the higher rates of diffusion of mean vorticity predicted by the calculations.

V.4 SR107 ORE CARRIER

(a) Hull Geometry and Experimental Information

The offsets of this hull are shown in Figure 39. Experiments on a double model of this form were conducted in the 1.8 m x 1.8 m wind tunnel of Osaka University (Okajima et al., 1985 and Nishio et al., 1988). The 2 m long model was supported in the tunnel by means of wires along the keel. The model beam and draft are 0.2927 m and 0.1126 m, respectively, and the block coefficient is 0.826. The data were obtained at five axial sections in the range $0.8 < x < 1.0$ in the present notation. The measurements were by means of a five-hole pitot probe, and included the three components of mean velocity (U, V, W) in Cartesian coordinates and pressure. The closely spaced measurements enabled the determination of the mean vorticity field. The calculations were performed for a Reynolds number of 2.4×10^6 which corresponds to the experimental value.

(b) Numerical Grid

The numerical solution domain chosen for this case is the same as in the previous cases and is defined by $0.3 < x < 4.524$, $r_s < r < 1.0$. This was again covered by $50 \times 30 \times 15$ grid points in the axial, radial, and circumferential directions, respectively. Some views of the numerically-generated grid

are shown in Figure 40. The grid-control functions f^i used to obtain this grid were given in equation (41). The parameters appearing therein are as follows:

$$c = \begin{cases} 0.10 & \text{if } A < 0 \\ 0.01 & \text{if } A > 0 \end{cases}$$

$$d = 0.2$$

With this choice, the first grid node just off the hull lies in the range $60 < y^+ < 250$.

(c) Description of Results and Comparisons with Experiments

Comparison of Figure 39 with Figure 28 shows the difference in the bow and stern shapes of the SR107 and the HSVA hulls although both are relatively full forms. The measurements in the two experiments were made in a very similar manner and therefore it is convenient to present the results for the present case in essentially the same format. Thus, Figures 41 and 42 show the hull pressure and friction distributions, Figure 43 shows the calculated wall streamlines, Figure 44 shows the flow pattern in the waterplane and in the vertical centerplane, and Figures 45 through 48 give details of the velocity and vorticity fields. In general, these results are qualitatively similar to the corresponding results for the HSVA hull. However, the level of agreement between the measured and computed pressure distributions shown in Figures 41 and 42 is particularly noteworthy.

An overview of the velocity field is given by Figure 45 which shows the contours of the axial velocity component and projections of the velocity vectors in five transverse sections. These may be compared with Figure 35. The wake of the support wires at the keel is seen from the results at $x = 0.8$, and this is responsible for the somewhat thicker boundary layer measured along the keel further downstream. The reason for the abrupt thickening of the boundary layer around the turn of the bilge shown by the data at $x = 0.8$ is not clear but its effect is observed at almost all stations downstream. The difference between the calculations and experiments in this regard is most likely due to the inadequacy of the simple initial conditions used in the calculations at $x = 0.3$. Presumably, the bulbous bow of this model induces a

level of three dimensionality that is not captured by the initial conditions. The initial conditions could of course have been adjusted to obtain a better fit to the measurements at the first measurement section but this has not been attempted here.

The results of Figure 45 show yet another feature that was absent in the previous cases. The SR107 model included a propeller boss and a rudder post, which are visible in the plots for $x = 0.975$. These details, however, were not considered in the present calculations and the stern sections were simply faired as shown. It is clear from the comparisons between the calculations and measurements, particularly at sections $x = 0.95$, 0.975 , and 1.00 , that there is a considerable local effect of these features on the velocity field. The differences are of course more pronounced in the transverse components.

The aforementioned differences should be kept in mind in assessing the detailed comparisons of the velocity components and pressure presented in Figure 46. The format is the same as that used in the case of the HSVA tanker (see Figure 36). It is quite remarkable that the predicted values of all three velocity components are in good agreement with the data everywhere at the first section, $x = 0.8$, except around $z = -0.045$, a region that corresponds to the thick boundary layer mentioned earlier. The pressures measured at this section show a rather curious behavior although the calculations and data are in good agreement very close to the hull. In fact, the measured trends are rather difficult to understand. The persistence of this feature at other stations downstream would suggest a consistent error in the data.

The distributions of the velocity components at $x = 0.9$ are very similar to those at $x = 0.8$. Some differences begin to appear at $x = 0.95$. These are consistent with the effects of the propeller boss and rudder post mentioned above. A particularly noteworthy feature of the results at $x = 0.95$ and 1.00 , however, is their marked resemblance with those obtained around the stern of the HSVA tanker. Comparison of the SR107 results at $x = 1.00$ with those for the HSVA tanker at $x = 0.988$ (Figure 36), for example, reveals very similar distributions of all velocity components. This leads us to reiterate the previous observations concerning the need for a better resolution of the local geometry and flow.

Contours of the longitudinal component of vorticity, $\omega_x = (\partial W / \partial y - \partial V / \partial z)$, are shown in Figure 47, and Figure 48 shows contours of $\{(\partial U / \partial z)^2 + (\partial U / \partial y)^2\}^{1/2}$, which is approximately $(\omega_y^2 + \omega_z^2)^{1/2}$, the resultant of the y-and z-components of vorticity. It is clear that the calculations are in remarkable general agreement with the experimental results. Some of the details are not completely captured by the solutions for reasons which we have already discussed. It is, however, interesting to note that the overall vorticity field is not markedly affected by the presence of the propeller boss and the rudder post. This is evidently due to the fact that while they produce significant distortion of the velocity and pressure fields, they do not generate large amounts of vorticity that can be seen outside their immediate wakes.

(d) Discussion

The solutions for the SR107 hull and comparisons with the corresponding experiments have brought forth three issues which were not evident from the previous test cases. First, we observe that a hull with a bulbous bow may require a more careful treatment of the initial conditions than has been employed in the present calculations. However, the differences observed in this respect may have been exaggerated in the present case by the rather low Reynolds number of the experiments and perhaps an ineffective transition device. Secondly, the local distortions of the velocity and pressure field introduced by such practical geometrical features as a propeller boss and a rudder post need to be taken into account in comparisons between experiments and calculations. Incorporation of such geometrical features would require further development of certain aspects of the computational method. Thirdly, the very marked similarity of the results for the SR107 and HSVA hulls points to the need for refinement of the treatment of the near-wall region in stern flows.

V.5 SERIES 60, $C_b = 0.60$

(a) Hull Geometry and Experimental Information

The geometry of this hull is well known and is shown in Figure 49. The model used in the experiments was fitted with a propeller boss (stern tube) as

shown in Figure 50 but, as in the previous case, the calculations correspond to the bare hull shown in Figure 49. Also, as noted earlier, these experiments differ from the others in that they were conducted in a towing tank. A detailed description of the experiments is given by Toda et al., (1988). For the purposes of the present work, it suffices to note the following. The measurements were made on 4 m long models at a Froude number $Fn = 0.16$ and a Reynolds number $Re = 3.2 \times 10^6$. Two different models were employed, one for the hull pressure distributions and the other for the flow-field measurements. The calculations have been made with a flat free surface ($Fn = 0$) and plane-of-symmetry boundary conditions on it. The available data include the hull pressure distribution measured by surface pressure taps, and profiles of the velocity components (U, V, W) and pressure p measured by a five-hole pitot probe. The latter data were obtained at numerous transverse sections in the range $0.50 < x < 1.10$. The use of Cartesian coordinates, as in the experiments on the HSVA and the SR107 hulls, greatly facilitates detailed comparisons between calculations and experiments.

(b) Numerical Grid

The numerical solution domain chosen for this case is the same as in the previous cases and is defined by $0.3 < x < 4.524$, $r_s < r < 1.0$. This was again covered by $50 \times 30 \times 15$ grid points in the axial, radial, and circumferential directions, respectively. Some views of the numerically-generated grid are shown in Figure 51. The grid-control functions f^i used to obtain this grid were given in equation (41). The parameters appearing therein are as follows:

$$c = \begin{cases} 0.10 & \text{if } A < 0 \\ 0.01 & \text{if } A > 0 \end{cases}$$

$$d = 0.2$$

With this choice, the first grid node just off the hull lies in the range $50 < y^+ < 250$.

(c) Description of Results and Comparisons with Experiments

The variation of pressure and friction velocity along the keel and the waterline are shown in Figure 52. No data is shown for the friction velocity because the velocity profiles have not yet been analyzed through Clauser plots. On the other hand, two sets of data are shown for the pressure. These were obtained during the pitot measurements on the port and starboard sides. The data on the waterline are those measured just below the free surface. The close agreement of the calculations with the measured pressure distribution along the waterline indicates that the effect of the free surface at the low Froude number of these tests is negligible.

The girthwise distributions of pressure, measured by means of surface pressure taps, at four typical transverse sections are shown in Figure 53. Also shown there, for future reference, are the distributions of the friction coefficient C_f . The major features of the hull pressure distribution are predicted quite well except that there appears to be a nearly constant difference between the calculations and data at the first three sections, and a disagreement in a region above the keel at $x = 0.975$. The former could be due to a difference between the reference pressure used in the experiments and the true freestream pressure. The latter, on the other hand, is associated with the presence of the propeller boss in the experiments.

Comparison of the results for the Series 60 with those obtained for the SSPA liner indicates that the general features of the pressure and friction distributions on these hulls are quite similar. This is also the case for the wall streamlines shown in Figure 54, and the flow patterns in the waterplane and the vertical centerplane shown in Figure 55.

The contours of constant axial velocity and the transverse components of velocity are shown in Figure 56. It is clear from the plots of the data that the measurements could not be made very close to the free surface which was relatively flat over the stern region and coincided with the load waterline, $z = 0$. Excellent agreement is observed between the calculated and measured axial velocity contours up to about $x = 0.95$. A close examination of the transverse velocity field indicates that some differences begin to appear above and below $z = -0.032$ which is where the centerline of the propeller boss is located. This is undoubtedly an upstream influence of the boss. The results for $x = 0.975$ and downstream of there clearly show the boss and its effect. It is

seen that this influence is rather localized, as was the case for the SR107 model, and the agreement between the predictions and experiments continues to be quite good elsewhere.

Finally, detailed distributions of the velocity components (U, V, W) and pressure p , are shown in Figure 57 in a format that should be quite familiar by now. In view of the discussion that has already been made of the results for the HSVA tanker (Figure 36) and the SR107 Ore Carrier (Figure 46), we shall point out only the two major distinguishing features of these results. First of all, we see a high level of agreement between the calculations and experimental data in almost all respects up to $x = 0.9$. There are occasional differences which appear to be due to scatter in the data rather than to some flow feature that is not being resolved by the calculations. Secondly, the regions of disagreements at the downstream stations clearly define the influence of the local change in the stern geometry made by the propeller boss. The fact that this influence is localized in the transverse sections is seen from the continued agreement between the experimental data and the bare-hull calculations.

(d) Discussion

These calculations have revealed the similarities in the stern flow of the Series 60 and the SSPA liner. They have also indicated that in the absence of a wave system the effect of the free surface on the viscous flow appears to be quite weak. The detailed comparisons in the velocity profiles clearly delineate the effects of local hull modifications such as that of a propeller boss. These comparisons are presented here in detail because they will be useful in the assessment of future calculations that include such complexities.

VI. SUMMARY AND CONCLUSIONS

A fully-elliptic numerical method for the solution of the complete Reynold-averaged Navier Stokes equations for general three-dimensional flows has been presented. The method uses numerically-generated nonorthogonal coordinates while retaining the velocity components in a convenient orthogonal system. For turbulent flows, closure of the equations is effected by the well

known $k-\epsilon$ turbulence model with the generally accepted values of the constants in the model and a two-point wall-function approach. The various numerical features of the method have been described and evaluated in detail.

The numerical method described here is built into a computer code RANSTERN which consists of three programs. The first of these maps the physical hull surface into the rectangular plane $n = 1$ in the transformed domain (see Figures 2 and 3). Spline functions are used for interpolation of the numerical grid on the hull surface. The surface grid thus obtained is used to provide the boundary conditions for the second program which generates the body-fitted coordinate system for the whole computational domain as described in Section III.2.(a). The flow equations are solved in the third program using the methods described in Section III.2.(b). For the calculations presented in this report, the output from the second program is used directly as input to the third. However, the third program can also accept grids generated by other methods provided the grid-control functions are evaluated in a compatible way.

Calculations have been performed for the flow over the stern and in the wake of five ship hulls for which experimental data are available. Extensive comparisons have been made with the data to understand the important features of such flows and to gage the success with which these can be predicted by the calculation method. The results are presented in detail so that they can be used in the future to assess other methods and further improvements.

The following general conclusions can be drawn from this study.

(1) The present numerical method has many attractive features. Among these are rapid and monotonic convergence to steady-state solutions starting from very simple initial guesses, ability to perform accurate calculations over large solution domains with a relatively modest grid, and the potential capability to calculate unsteady flows.

(2) The method provides an excellent description of the overall features of the flow, including the pressure and friction distributions on the hull, and the mean velocity field in and outside the viscous layer at the stern. Therefore, it can be used in practical applications to calculate viscous resistance, determine the flow ahead of propellers and appendages, and study the problem of scaling the results of model tests to full-scale Reynolds numbers.

(3) Calculations for a typical hull take about 5 to 10 minutes on a supercomputer. It is also possible to make similar calculations on a modern minicomputer in a matter of hours.

(4) The basic features of the numerical method are such that, with minor modifications, it can be utilized for the solution of many other types of problems. With regard to the numerical content of the method, improvements can be made in several areas, the principal one being grid generation and control.

(5) Improvements in the description of the flow in the very near wake would require a more detailed resolution of the local surface geometry and a better description of the flow in the near-wall layers. The second topic involves further developments in turbulence models for near-wall flows.

REFERENCES

Aris, R. (1962), "Vectors, Tensors, and the Basic Equations of Fluid Mechanics", Prentice-Hall, Englewood Cliffs, N.J.

Broberg, L. and Larsson, L. (1984), "A Calculation Method for Ship Stern Flows using an Analytical Body-fitted Coordinate System", Proc. 15th ONR Sym. Naval Hydrodyn., Hamburg, FRG, pp. 525-538.

Chen, C.J. and Chen, H.C., (1984), "Finite Analytic Numerical Method for Unsteady Two-Dimensional Navier-Stokes Equations", Journal of Computational Physics, Vol. 53, pp. 209-226.

Chen, C.J. and Chen, H.C., (1982), "The Finite Analytic Method", Vol. IV, IIHR Report No. 232-IV, Iowa Institute of Hydraulic Research, August, 415 pages.

Chen, H.C. and Chen, C.J., (1984), "Development of Finite Analytic Method for Unsteady Three-Dimensional Navier-Stokes Equations", Computation of Internal Flows: Methods and Applications, pp. 159-165, ASME FED Vol. 14, Fluid Engineering Symposium, New Orleans, LA, 12-16 February.

Chen, H.C. and Patel, V.C. (1984), "Calculation of Stern Flows by a Time-Marching Solution of the Partially-Parabolic Equations", Proc. 15th ONR Sym. Naval Hydrodynamics, Hamburg, FRG, pp. 505-523.

Chen, H.C. and Patel, V.C. (1985a), "Calculation of Trailing-Edge, Stern and Wake Flows by a Time-Marching Solution of the Partially-Parabolic Equations", Iowa Inst. Hydr. Res., Uni. Iowa, IIHR Report No. 285.

Chen, H.C. and Patel, V.C. (1985b), "Numerical Solutions of the Flow over the Stern and in the Wake of Ship Hulls", Proc. 4th Int. Conf. Numeric. Ship Hydrodyn., Washington DC, pp. 492-511.

Chen, H.C. and Patel, V.C. (1987a), "Laminar Flow at the Trailing Edge of a Flat Plate", AIAA Journal, Vol. 25, pp. 920-928.

Chen, H.C. and Patel, V.C. (1987b), "The Wake of an Axisymmetric Body with or without Tail Separation", Proc. 6th Sym. Turb. Shear Flows, Toulouse, France, pp. 11:3:1-6.

Chen, H.C. and Patel, V.C. (1988), "Near-Wall Turbulence Models for Complex Flows Including Separation", AIAA-87-1300; also, AIAA Journal, to appear.

Fukuda, K. and Fujii, A. (1985), "Experimental Study on Reynolds Stress in Ship Stern Flow", Proc. 2nd Int. Sym. Ship Viscous Res., Goteborg, p. 3:1.

Hinatsu, M. and Takeshi, H. 1985, "A Calculation Method for Resistance Prediction Including Viscous-Inviscid Interaction", Proc. 2nd Int. Sym. Ship Viscous Res., Goteborg, p. 10:1.

Hino, T. (1987), "Numerical Simulation of a Viscous Flow around a Ship Model", Soc. Naval Arch. Japan, Spring Meeting, Paper 1-1.

Hoekstra, M. and Raven, H.C. (1985a), "Ship Boundary Layer and Wake Calculation with a Parabolized Navier-Stokes Solution System", Proc. 4th Int. Conf. Numeric. Ship Hydrodyn., Washington DC, pp. 470-491.

Hoekstra, M. and Raven, H.C. (1985b), "Application of a Parabolized Navier-Stokes Solution System to Ship Stern Flow Computation", Proc. Osaka Int. Colloq. Ship Visc. Flow, Osaka, pp. 125-142.

Hoffman, H.P. (1976), "Untersuchung der 3-dimensionalen, turbulenten Grenzschicht an einem Schiffsmodell in Windkanal", Inst. Schiffbau, Uni. Hamburg, Report 343.

Hotta, T. and Hatano, S. (1985), "Turbulence Measurements in the Ship-Stern Boundary Layer of a Tanker Model", J. Soc. Nav. Arch. Japan, Vol. 157, pp. 63-72.

Huang, T.T., Groves, N.C., and Belt, G.S. (1983), "Stern Boundary-Layer Flow on Two Three-Dimensional Bodies having Elliptic Transverse Cross Sections", Proc. 2nd Sym. Num. Phy. Aspects of Aerodyn. Flows, Long Beach.

Huang, S. and Zhou, L.-D. (1985), "A Streamline Iteration Method for Computing the Three-Dimensional Turbulent Flow around the Stern and in the Wake of Ship; First Report: Wigley Ship Model", Proc. 2nd Int. Sym. Ship Viscous Res., Goteborg, p. 13.1.

Ito, N. and Mori, K.-H. (1985), "Near-Wake Computations by Solving the Vorticity Transport Equation on a Body-Fitted Coordinate System", Proc. 4th Int. Conf. Numeric. Ship Hydrodyn., Washington DC, pp. 512-528. Also, Proc. Osaka Int. Colloq. Ship Visc. Flow, Osaka, pp. 175-191.

ITTC (1987), "Report of the Resistance and Flow Committee", Proc. 18th ITTC (International Towing Tank Conference), Kobe, Japan, Vol. I, pp. 47-95.

Janson, C.-E. and Larsson, L. (1985), "Ship Flow Calculations using the Phoenix Computer Code", Proc. 2nd Int. Sym. Ship Viscous Res., Goteborg, p. 17:1.

Kodama, Y. (1985), "Computation of 3-D Incompressible Navier-Stokes Equations for Flow Around a Ship Hull Using an Implicit Factored Scheme", Proc. Osaka Int. Colloq. Ship Visc. Flow, Osaka, pp. 109-124.

Kodama, Y. (1987), "Computation of High Reynolds Number Flows Past a Ship Hull Using the IAF Scheme", Soc. Naval Arch. Japan, Spring Meeting, Paper 1-3.

Knaack, T. (1984), "Laser-Doppler Velocimetrica Messungen an einem Schiffsmodell im Windkanal", Inst. Schiffbau, Uni. Hamburg, Report 439.

Knaack, T., Kux, J., and Wieghardt, K. (1985), "On the Structure of the Flow Field on Ship Hulls", Proc. Osaka Int. Colloq. Ship Visc. Flow, Osaka, pp. 192-208.

Larsson, L. (1974), "Boundary Layers of Ships. Part III: An Experimental Investigation of the Turbulent Boundary Layer on a Ship Model", SSPA, Goteborg, Sweden, Report No. 46.

Larsson, L. (ed.) (1981), "SSPA-ITTC Workshop on Ship Boundary Layers 1980: Proceedings", SSPA, Goteborg, Sweden, Report No. 90.

Lass, H. (1975), "Vector and Tensor Analysis", McGraw-Hill, New York, NY.

Lee, Y-T. (1985), "Viscous-Inviscid Interaction Computations of Three-Dimensional Stern Turbulent Flows", Proc. 2nd Int. Sym. Ship Viscous Res., Goteborg, p. 8:1.

Lofdahl, L. (1982), "Measurements of the Reynolds Stress Tensor in the Thick Three-Dimensional Boundary Layer near the Stern of a Ship Model", Doctoral Thesis, Chalmers University, Goteborg, Sweden. Also, Swedish Maritime Research Center, Goteborg, Sweden, Report No. 61.

Lofdahl, L. and Larsson, L. (1984), "Turbulence Measurements Near the Stern of a Ship Model", J. Ship Res., Vol. 28, pp. 186-201.

Miyata, H. and Inui, T. (1984), "Nonlinear Ship Waves", Advances in Appl. Mech., Vol. 24, pp. 215-288.

Miyata, H., Matsukawa, C., and Kajitani, H. (1985), "A Separating Flow Near the Free Surface", Proc. Osaka Int. Colloq. Ship Visc. Flow, Osaka, pp. 300-318.

Miyata, H., Nishimura, S., and Masuko, A. (1985), "Finite-Difference Simulation of Nonlinear Waves Generated by Ships of Arbitrary Three-Dimensional Configuration", J. Comput. Phys., Vol. 60, pp. 391-436.

Miyata, H., Kajitani, H., Zhu, M., and Kawano, T. (1986), "Nonlinear Forces Caused by Breaking Waves", Proc. 16th Sym. Naval Hydrodyn., Berkeley, pp. 514-536.

Muraoka, K. (1980), "Calculation of Thick Boundary Layer and Wake of Ships by a Partially Parabolic Method", Proc. 13th ONR Sym. Naval Hydrodynamics, Tokyo, Japan, pp. 601-616.

Muraoka, K. (1982), "Calculation of Viscous Flow around Ships with Parabolic and Partially Parabolic Flow Solution Procedure", Trans. West Japan Soc. Naval Arch., Vol. 63, pp. 13-29.

Nagamatsu, T. (1981), "Measurements of Flow Field near the Stern of a Ship Model with High Block Coefficient", Trans. West Japan Soc. Nav. Arch., Vol. 61, pp. 1-13.

Nagamatsu, T. (1985), "Calculation of Ship Viscous Resistance by Integral Method and its Application", Proc. 2nd Int. Sym. Ship Viscous Res., Goteborg, 1985, p. 9:1. Also, J. Soc. Nav. Arch. Japan, Vol 157.

Nishio, S., Tanaka, I., and Ueda, H. (1988), "Separation Flow Field around a Ship Hull at Yaw Angle", J. Kansai Soc. Nav. Arch., Japan, Vol. 210, to appear.

Ogawa, S. and Ishiguro, T. (1987), "A Method for Computing Flow Fields Around Moving Bodies", *Journal of Computational Physics*, Vol. 69, pp. 49-68.

Okajima, R., Toda, Y., and Suzuki, T. (1985), "On a Stern Flow Field with Bilge Vortices", *J. Kansai Soc. Nav. Arch.*, Japan, Vol. 197, pp. 87-95.

Patankar, S.V. (1980), "Numerical Heat Transfer and Fluid Flow", McGraw-Hill, N.Y.

Patel, V.C. (1973), "A Unified View of the Law of the Wall Using Mixing-Length Theory", *The Aeronautical Quarterly*, Vol. 24, pp. 55-70.

Patel, V.C. (1980), "Ship Wakes", *Data Report, Complex Turbulent Flows, Proc. 1980-81 AFOSR-HTM-Stanford Conf.*, Stanford, Ca, Vol. 1, pp. 552-553.

Patel, V.C. (1982), "Some Aspects of Thick Three-Dimensional Boundary Layers", *Proc. 14th ONR Sym. Naval Hydrodynamics*, Ann Arbor, MI, pp. 999-1040.

Patel, V.C. and Chen, H.C. (1986a), "The Flow over Tail and in Wake of Axisymmetric Bodies: A Review of the State-of-the-Art", *J. Ship Research*, Vol. 30, pp. 201-214.

Patel, V.C. and Chen, H.C. (1986b), "Fully-Elliptic Large-Domain Solutions of Trailing-Edge Flows, Including Separation", *Proc. 11th USAF-FRG Data Exchange Agreement Meeting*, Wright-Patterson AFB, Ohio.

Patel, V.C. and Chen, H.C. (1987), "Turbulent Wake of a Flat Plate", *AIAA Journal*, Vol. 25, pp. 1078-1085.

Raven, H.C. and Hoekstra, M. (1985), "A Parabolized Navier-Stokes Method for Ship Stern Flow Calculations", *Proc. 2nd Int. Sym. Ship Viscous Res.*, Goteborg, p. 14:1.

Richmond, M.C., Chen, H.C., and Patel, V.C., (1986), "Equations of Laminar and Turbulent Flows in General Curvilinear Coordinates", *IIHR Report No. 300*, Iowa Institute of Hydraulic Research, March, 79 pages.

Sarda, O.P. (1986), "Turbulent Flow past Ship Hulls - An Experimental and Computational Study", *Ph.D. Thesis, Mechanical Engineering, Uni. Iowa*.

Soejima, S. (1983), "Calculation of Three-Dimensional Boundary Layers on Ship Hulls", *Proc. 2nd Sym. Num. Phy. Aspects of Aerodyn. Flows*, Long Beach.

Soejima, S. (1985), "An Integral Method for Calculating the Viscous Flow Around Ship Stern", *Proc. Osaka Int. Colloq. Ship Visc. Flow*, Osaka, pp. 71-89.

Stern, F. (1985), "Influence of Waves on the Boundary Layer of a Surface-Piercing Body", *Proc. 4th Int. Conf. Numeric. Ship Hydrodyn.*, Washington DC, pp. 383-406.

Stern, F. (1986), "Effects of Waves on the Boundary Layer of a Surface-Piercing Body", *J. Ship Research*, Vol. 30, pp. 256-274.

Stern, F., Yoo, S.Y., and Patel, V.C. (1986), "Viscous-Inviscid Interaction with Higher-Order Viscous-Flow Equations", Iowa Inst. Hyd. Res., The Uni. Iowa, IIHR Rept. 304; also, AIAA Journal, to appear.

Toda, Y., et al., (1988), "Mean-Flow Measurements in the Boundary Layer and Wake of a Series 60, $C_p = 0.60$ Model Ship With and Without Propeller", Iowa Inst. Hydr. Res., Uni. Iowa, IIHR Report in preparation.

Toda, Y., Tanaka, I., and Otsuka, Y. (1985), "An Integral Method for Calculating Three-Dimensional Boundary Layer with Higher Order Effect", Proc. Osaka Int. Colloq. Ship Visc. Flow, Osaka, pp. 32-51.

Tzabiras, G.D. (1984), "Numerical and Experimental Investigation of the Flow Field at the Stern of Double Ship Hulls", Ph.D. Thesis, Dept. Naval Arch., National Tech. Uni., Athens, Greece, (in Greek).

Tzabiras, G.D. (1985), "On the Calculation of the 3-D Reynolds Stress Tensor by Two Algorithms", Proc. 2nd Int. Sym. Ship Viscous Res., Goteborg, p. 15:1.

Watmuff, J.H. and Joubert, P.N. (1985), Uni. Melbourne, private communication.

Wieghardt, K. (1982), "Kinematics of Ship Wake Flow", Seventh David Taylor (Memorial) Lecture, DTNSRDC Report 81/093.

Wieghardt, K. (1983), "Zur Kinematik einer Nachlaufstroemung", Z. Flugwiss. Weltraumforsch., Vol. 7, pp. 149-158.

Wieghardt, K. and Kux, J. (1980), "Nomineller Nachstrom auf Grund von Windkanalkversuchen", Jahrbuch der Schiffbautechnischen Gesellschaft (STG) 1980, Springer-Yerlag, pp. 303-318.

SSPA-ITTC SHIP BL WORKSHOP

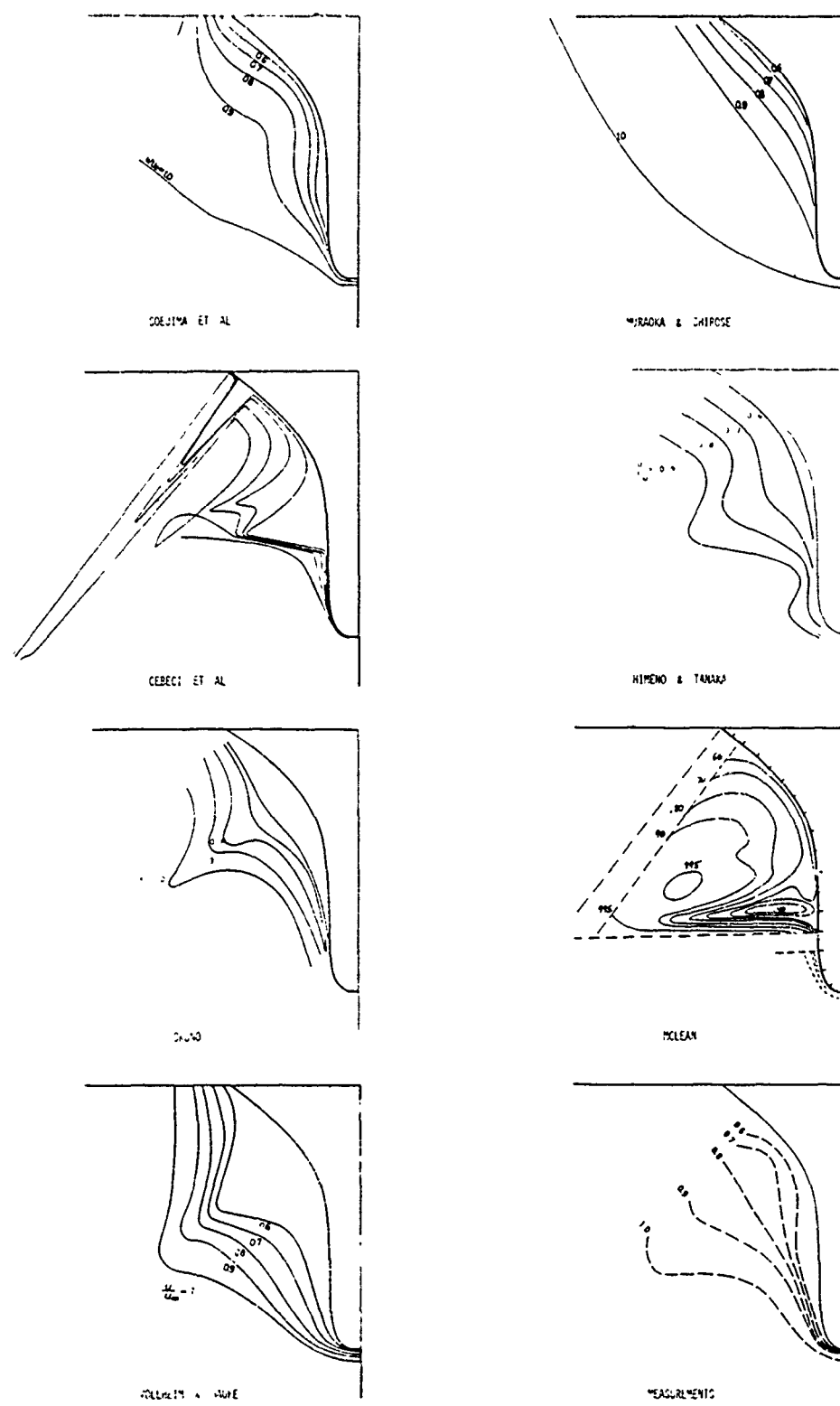
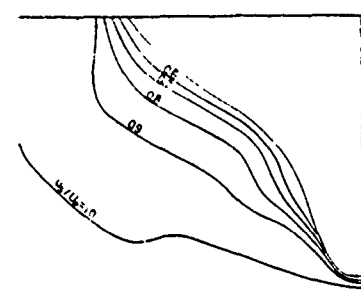
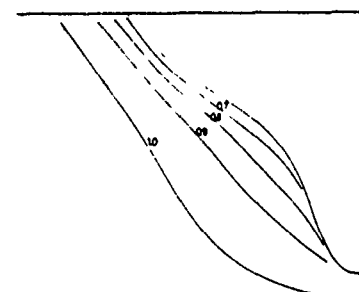


Fig. 1 Contours of the axial component of velocity presented at SSPA-ITTC Workshop
(a) SSPA Cargo Liner, $X=0.95$

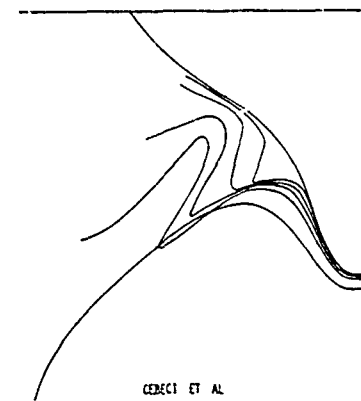
SSPA-ITTC SHIP BL WORKSHOP



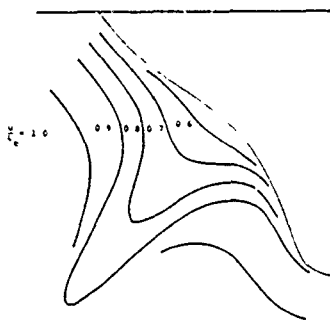
SOEJIMA ET AL



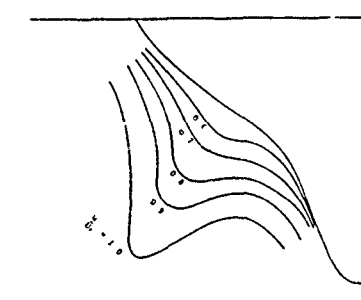
PURAKA & SHIROSE



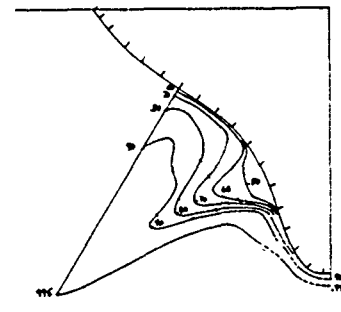
CERECI ET AL



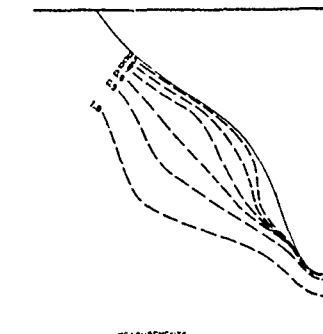
HIRANO & TANAKA



OKUO



MCLEAN



MEASUREMENTS

Fig. 1 Contours of the axial component of velocity presented at SSPA-ITTC Workshop
(b) HSVA Tanker, $X=0.942$

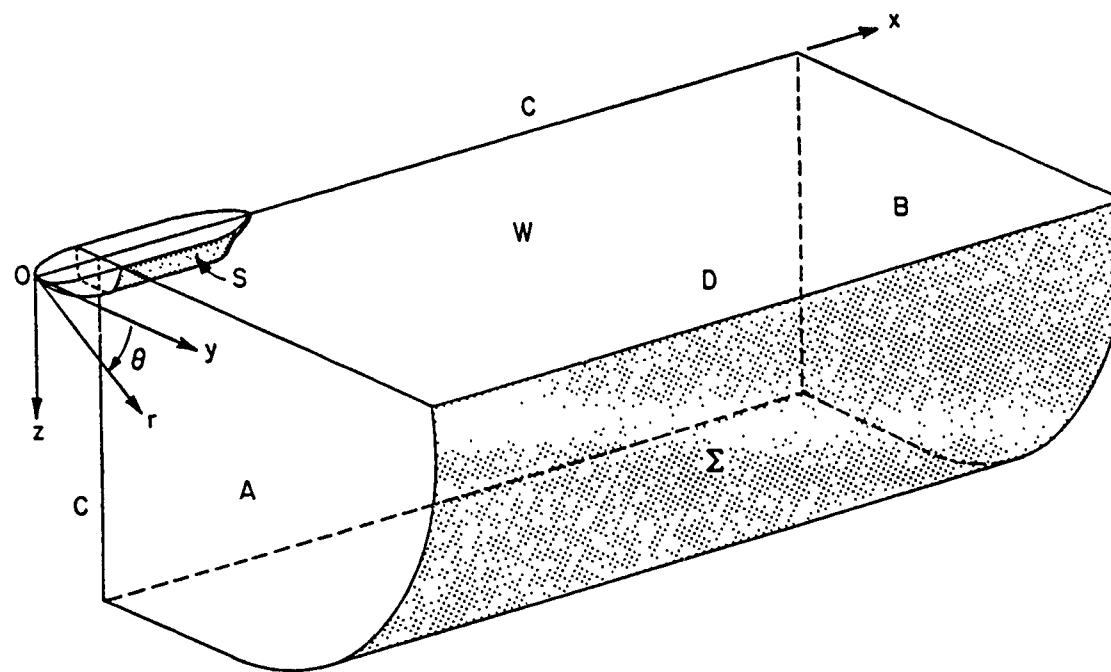


Fig. 2 Physical solution domain

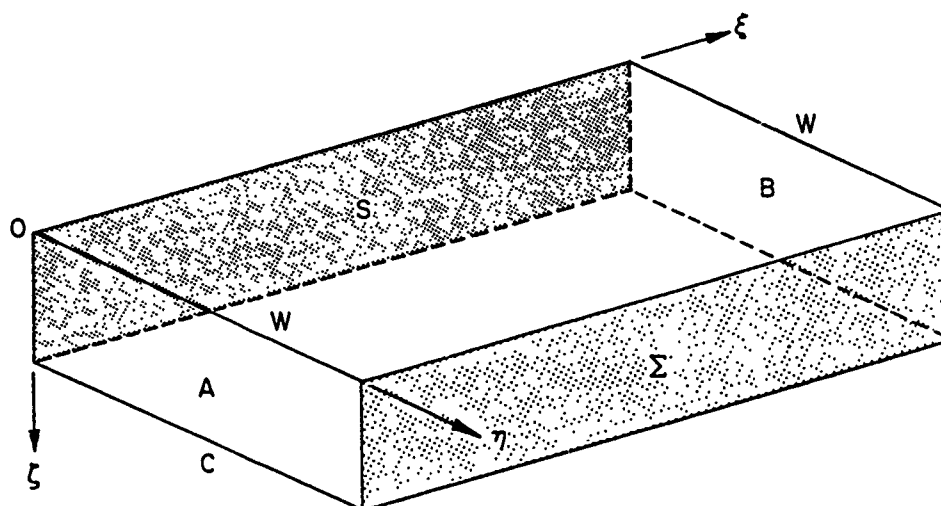


Fig. 3 Transformed domain

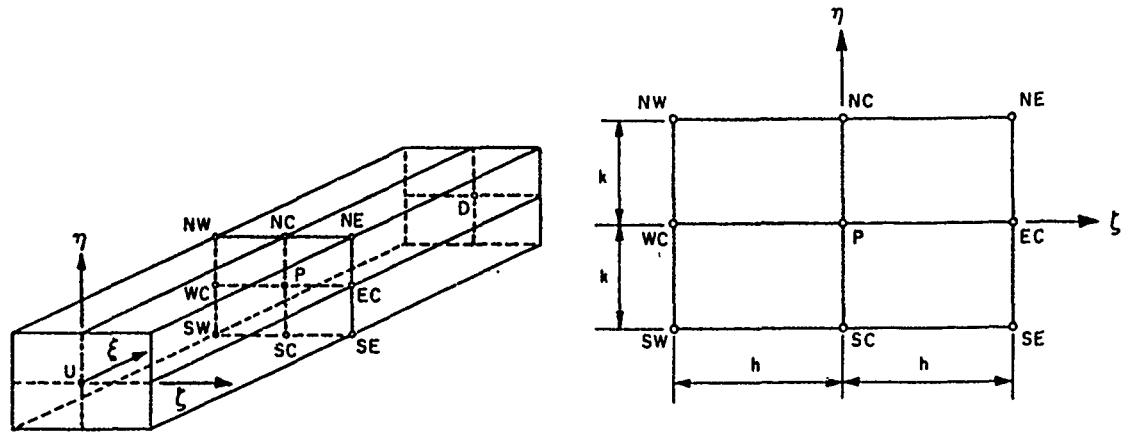


Fig. 4 Local numerical element

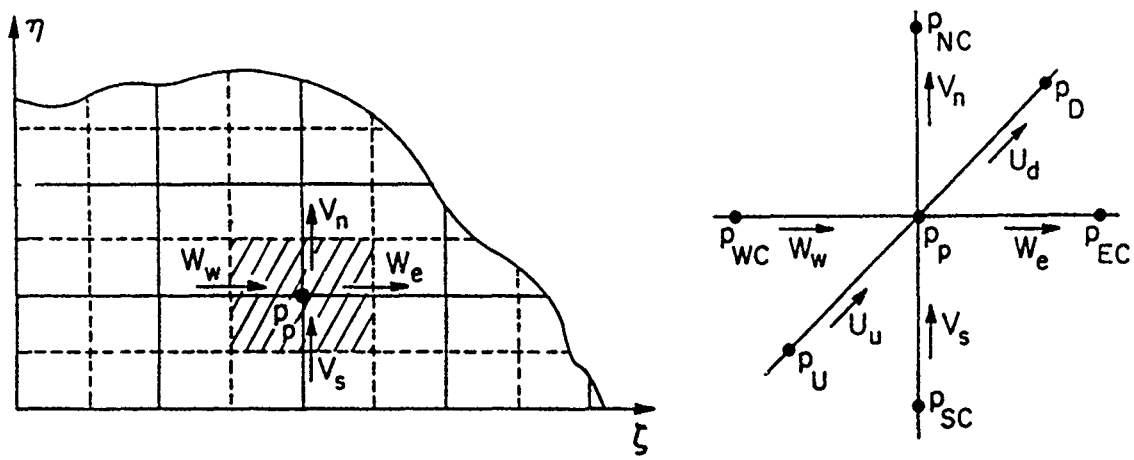
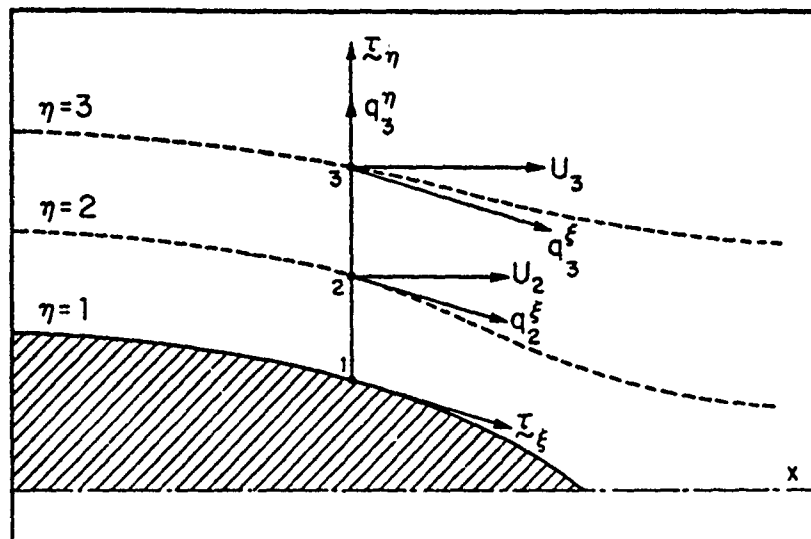
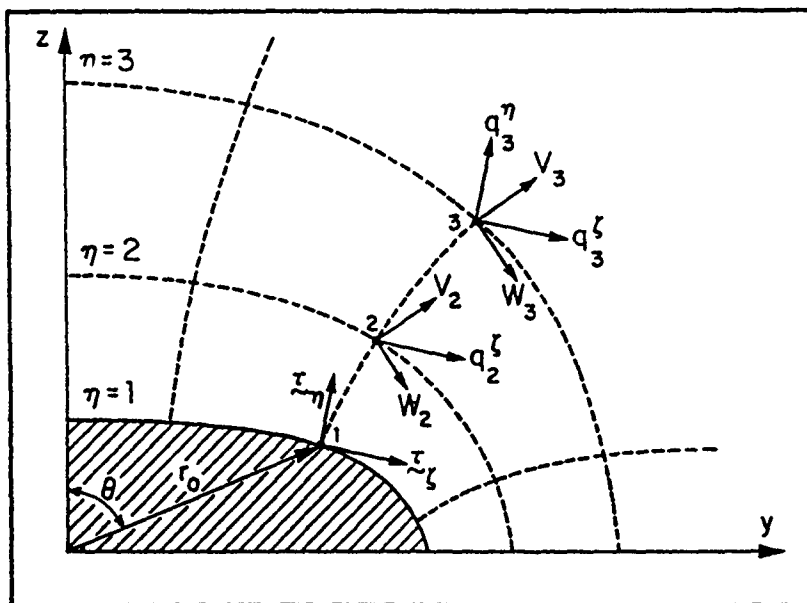


Fig. 5 Locations of the nodes for U , V , W and P in the staggered grid



(a) Longitudinal View



(b) Sectional View

Fig. 6 Notation for wall functions

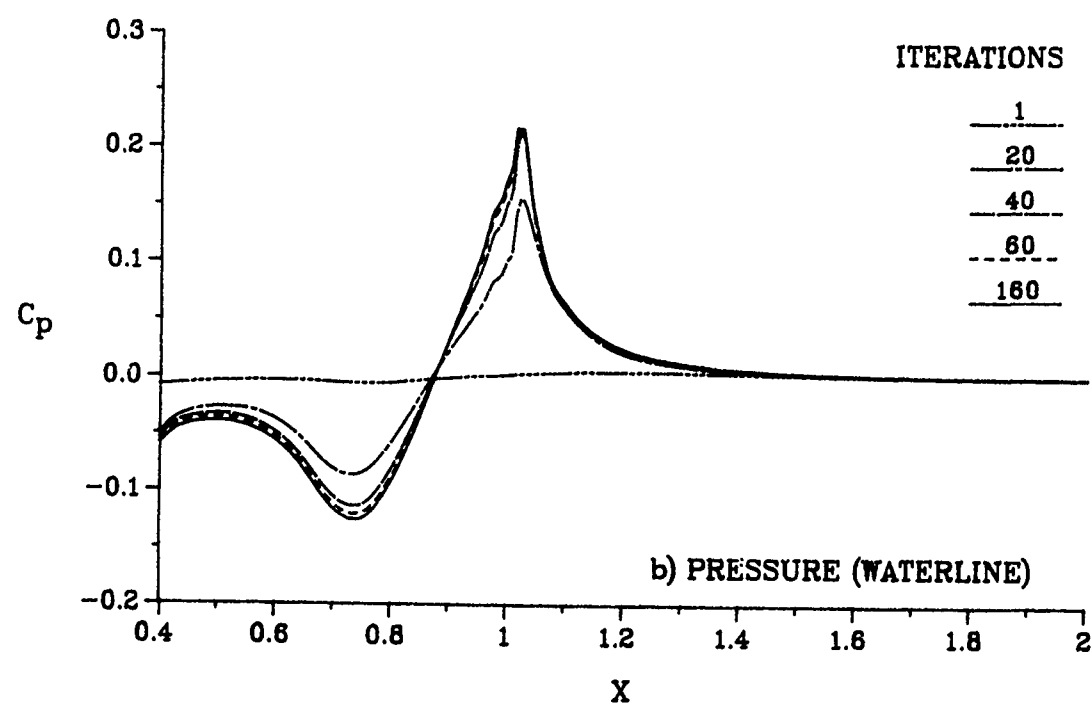
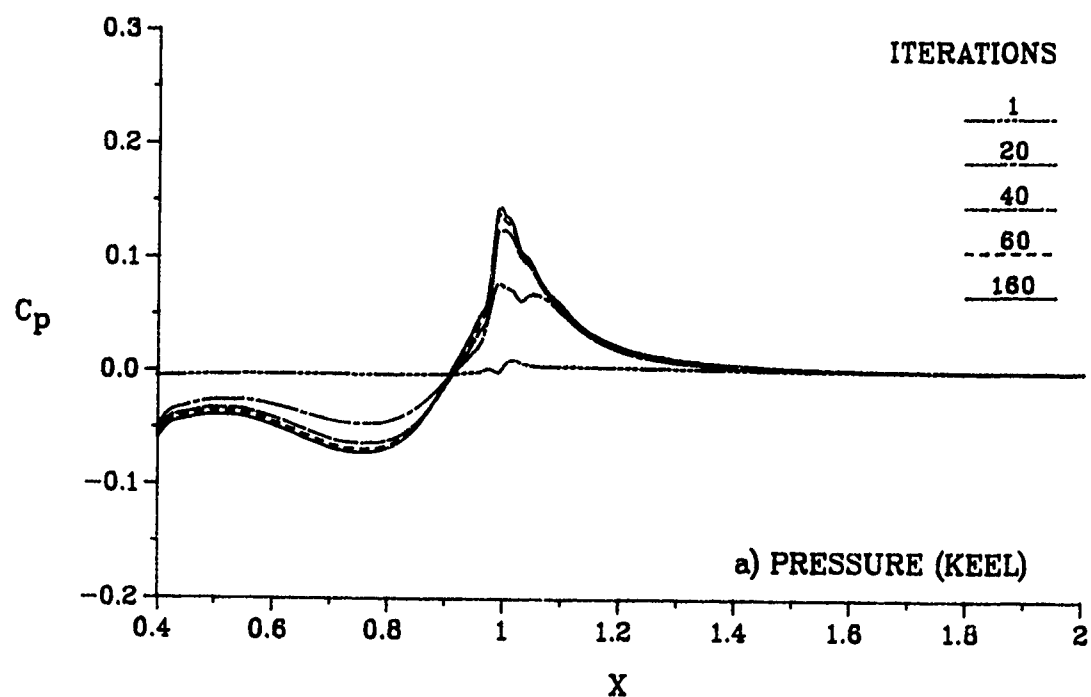


Fig. 7 Convergence history - continued

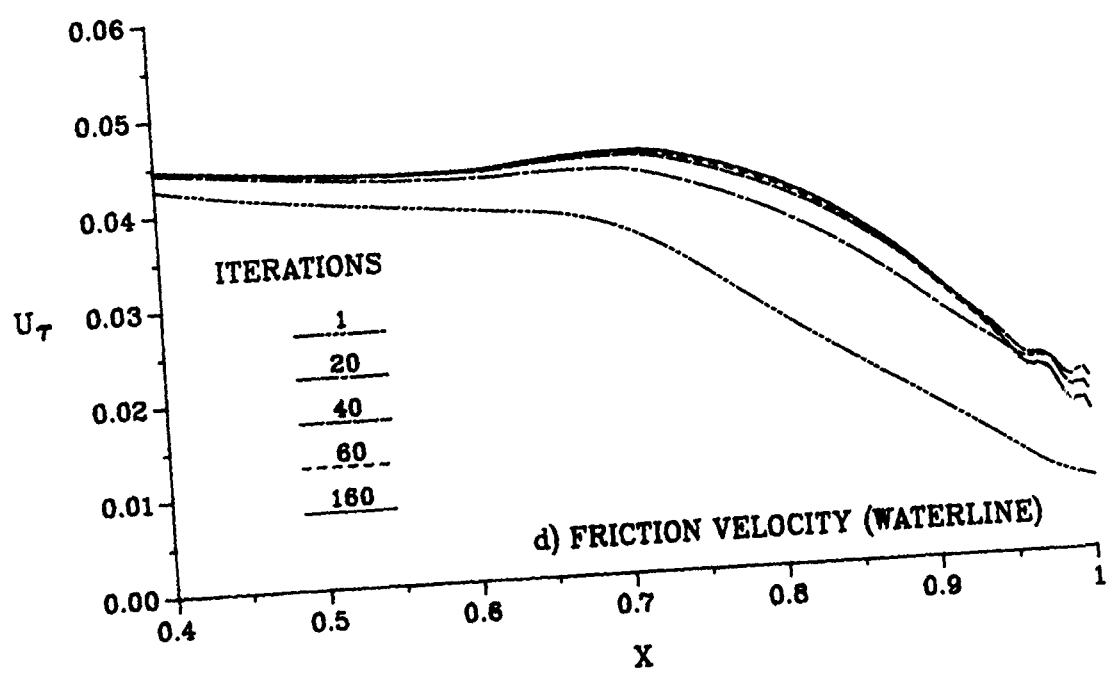
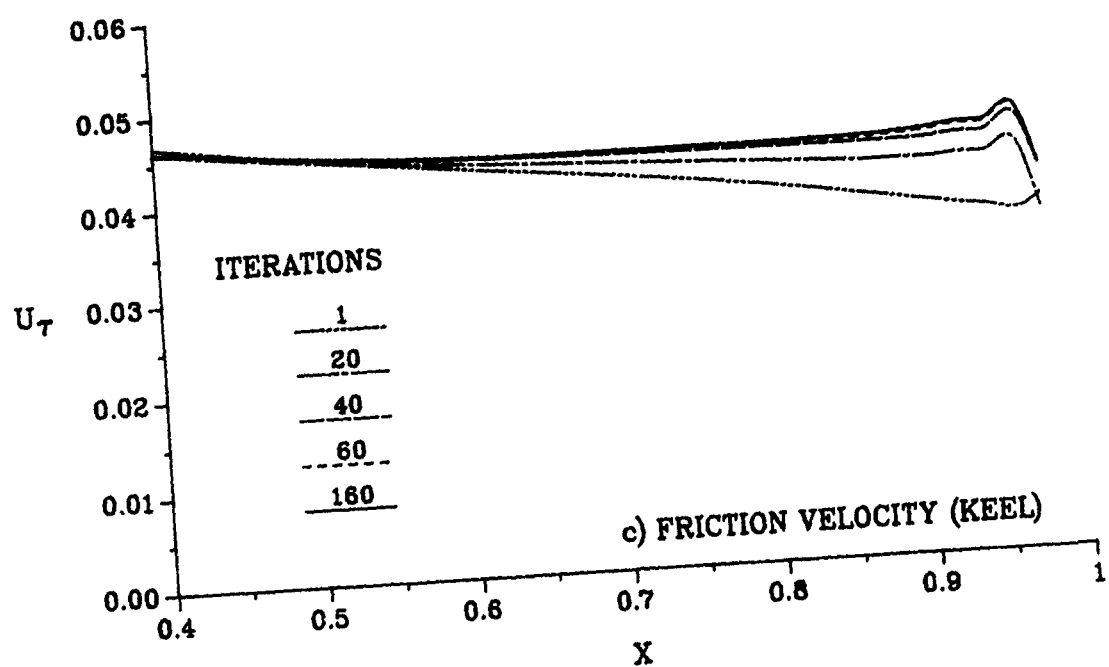


Fig. 7 Convergence history - continued

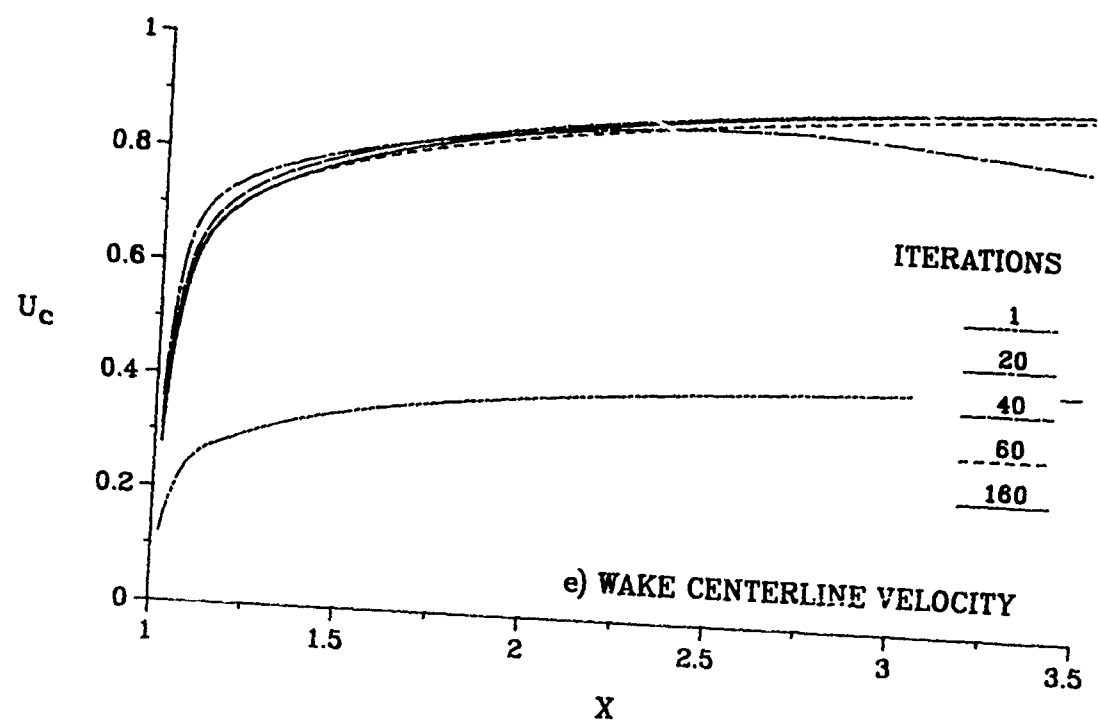


Fig. 7 Convergence history

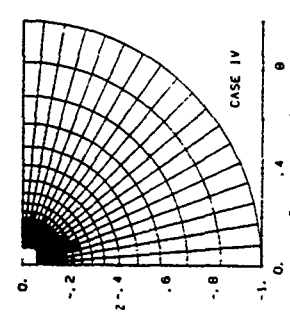
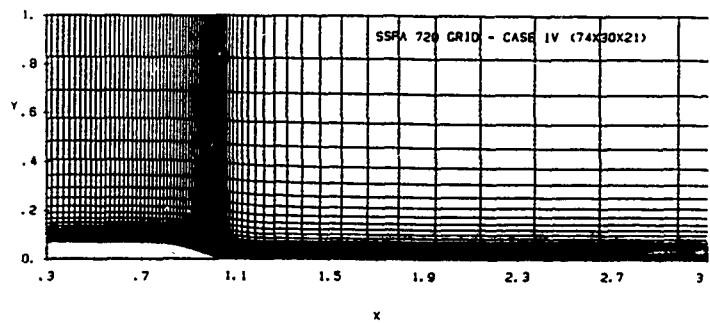
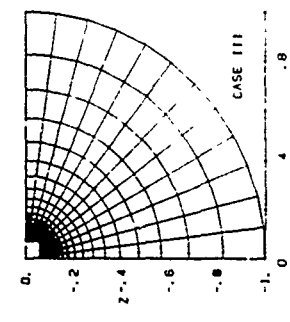
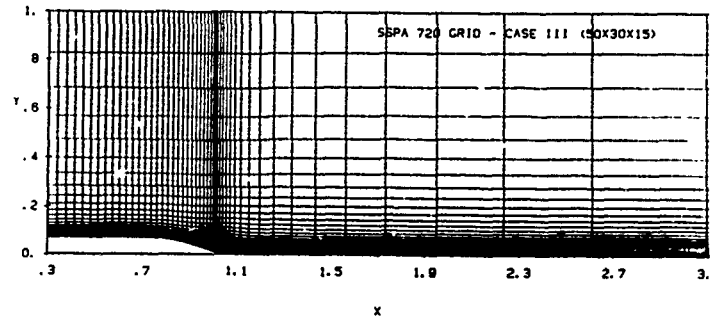
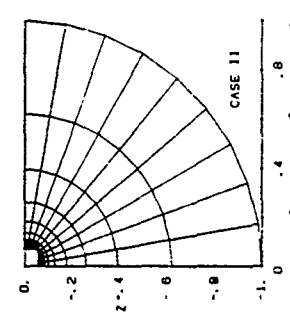
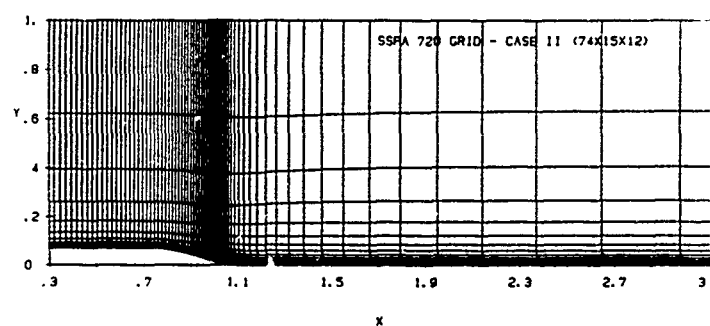
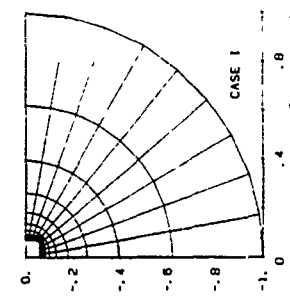
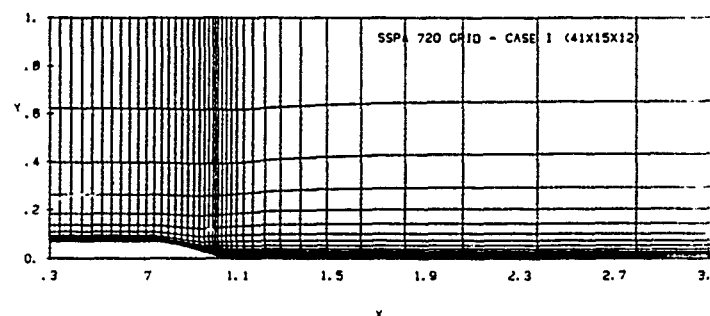


Fig. 8 Views of the four grids used in grid-dependence tests

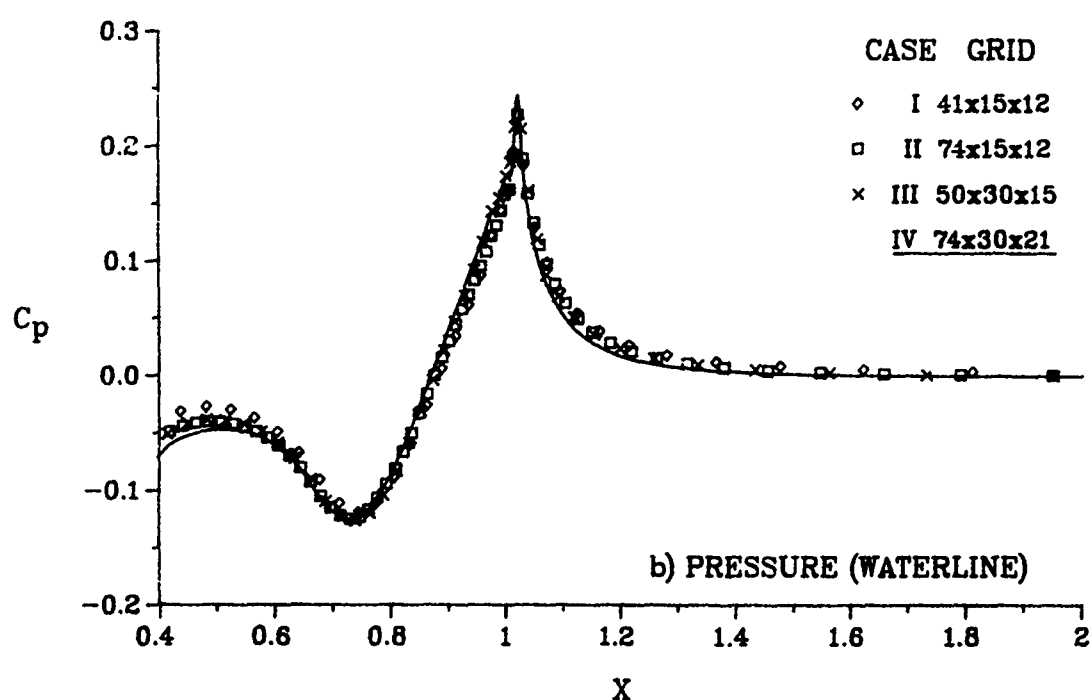
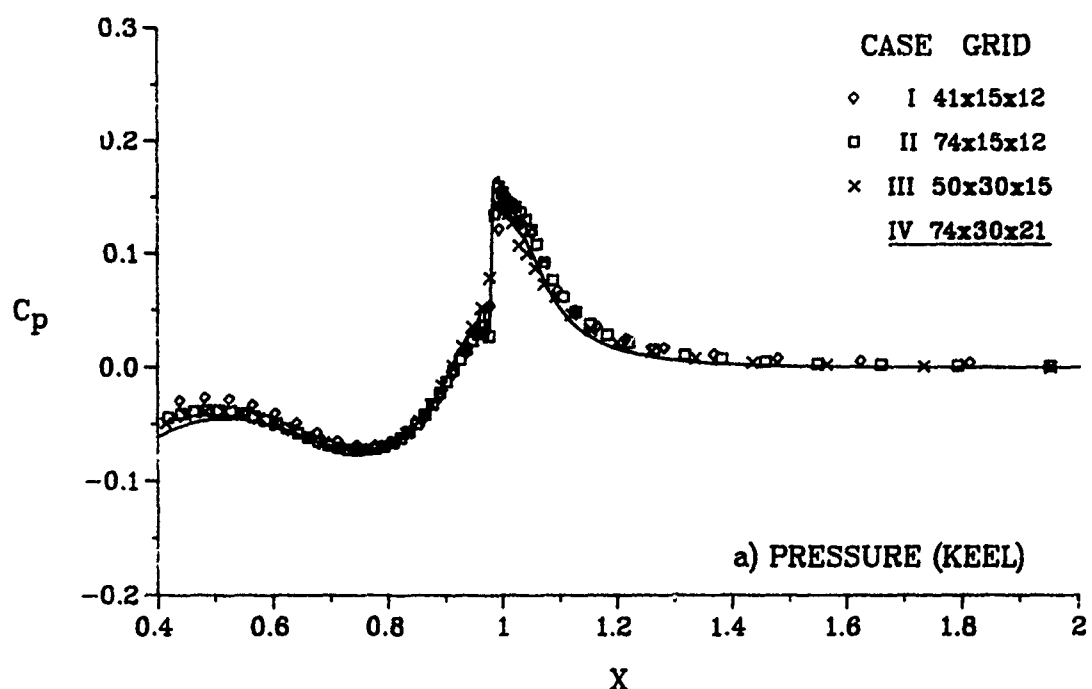


Fig. 9 Grid-dependence tests - continued

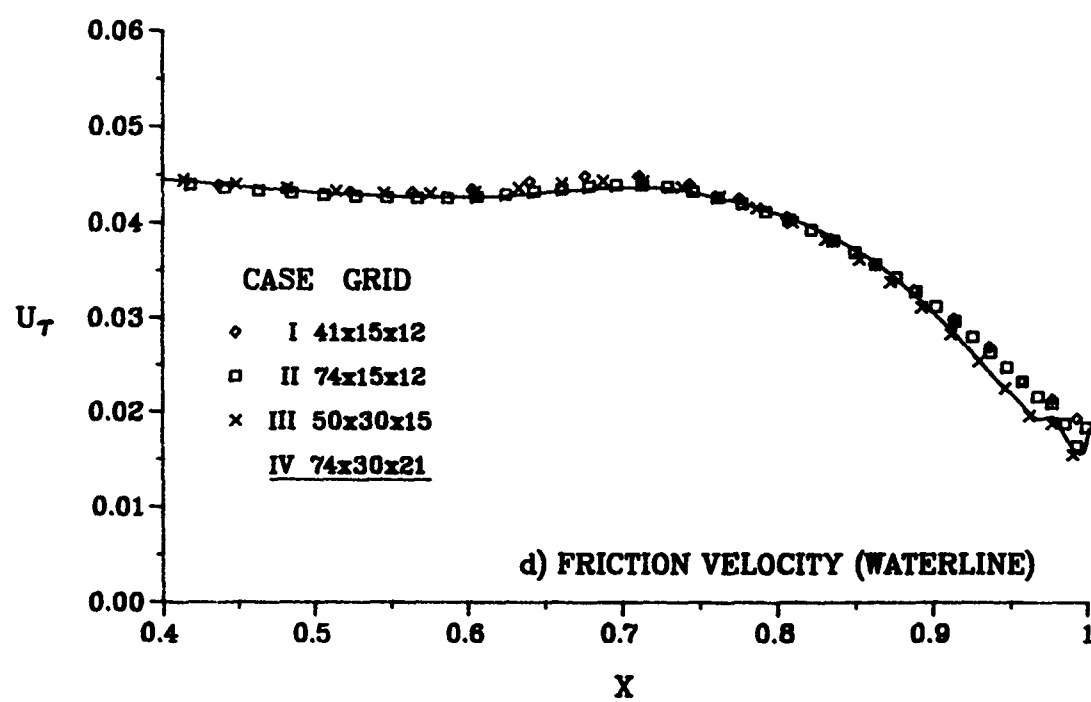
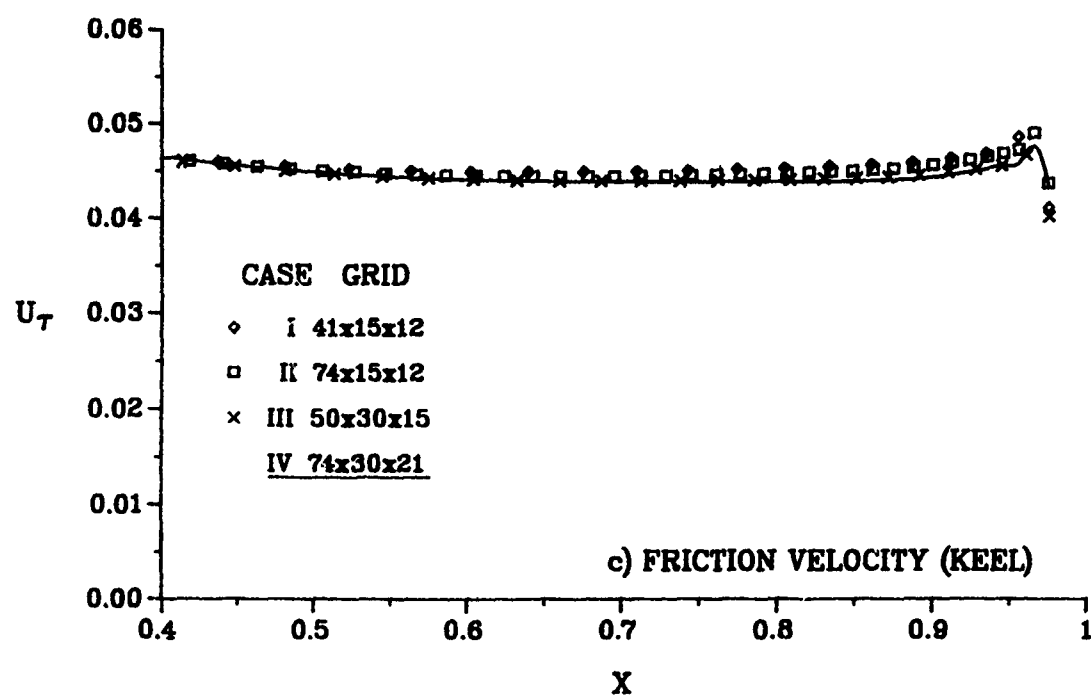


Fig. 9 Grid-dependence tests - continued

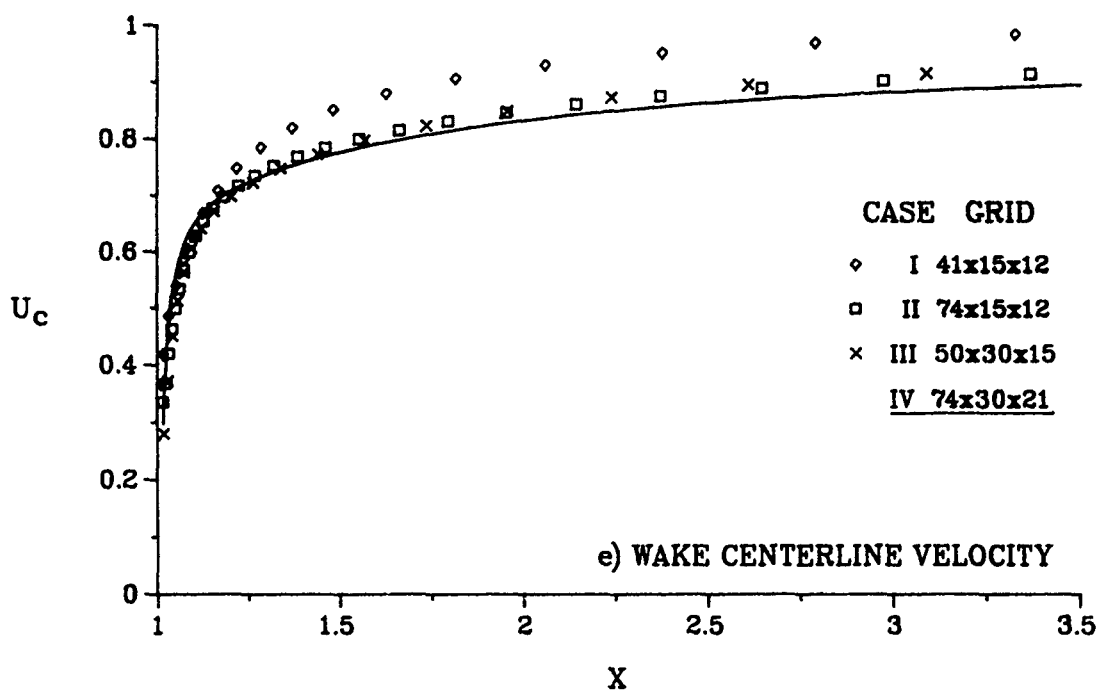


Fig. 9 Grid-dependence tests

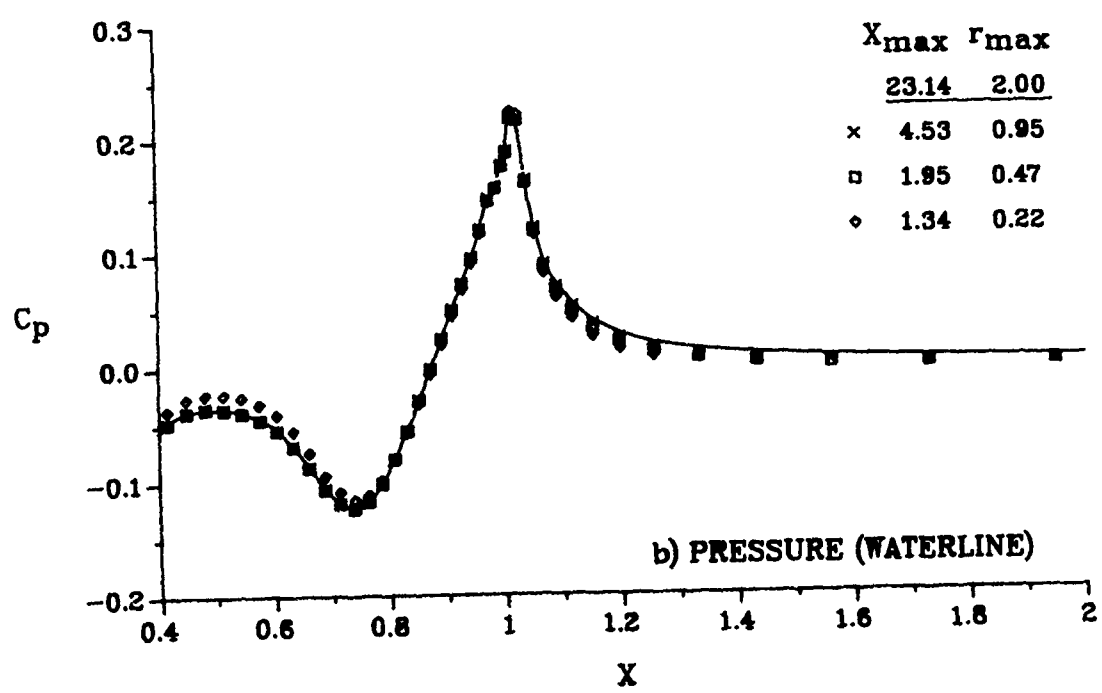
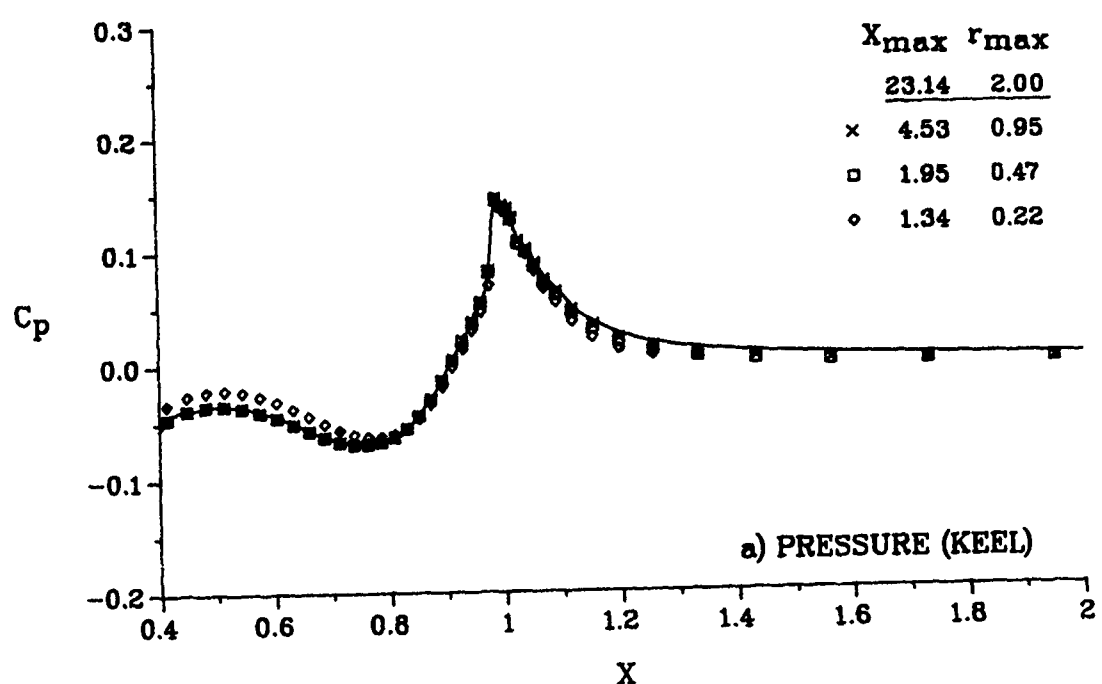


Fig. 10 Influence of solution domain size - continued

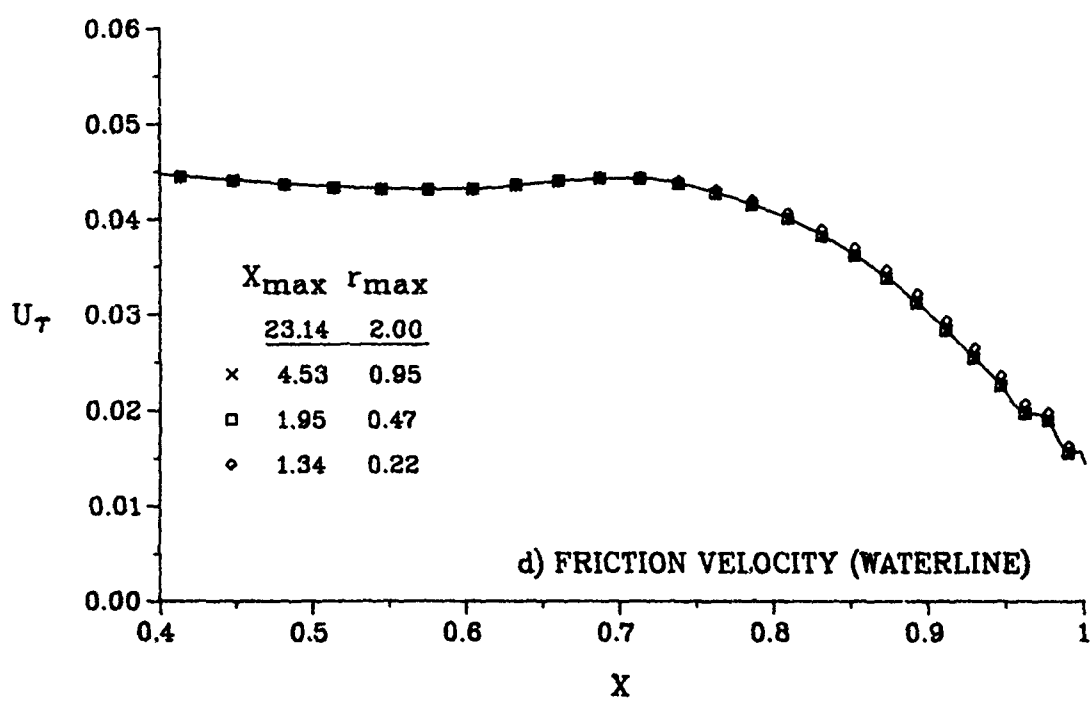
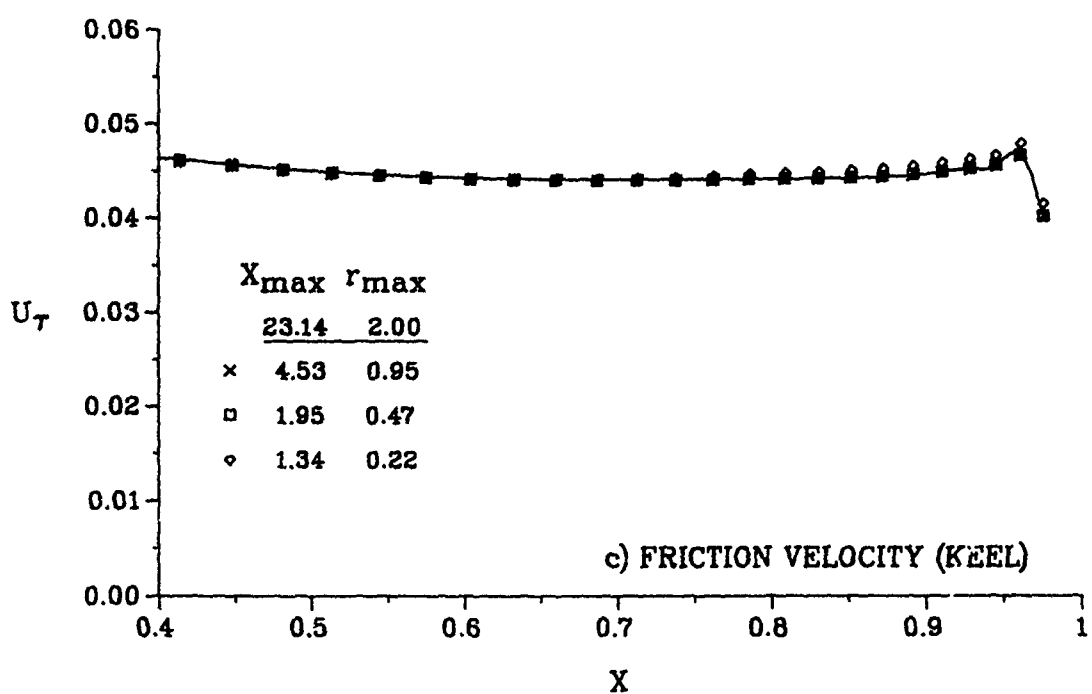


Fig. 10 Influence of solution domain size - continued

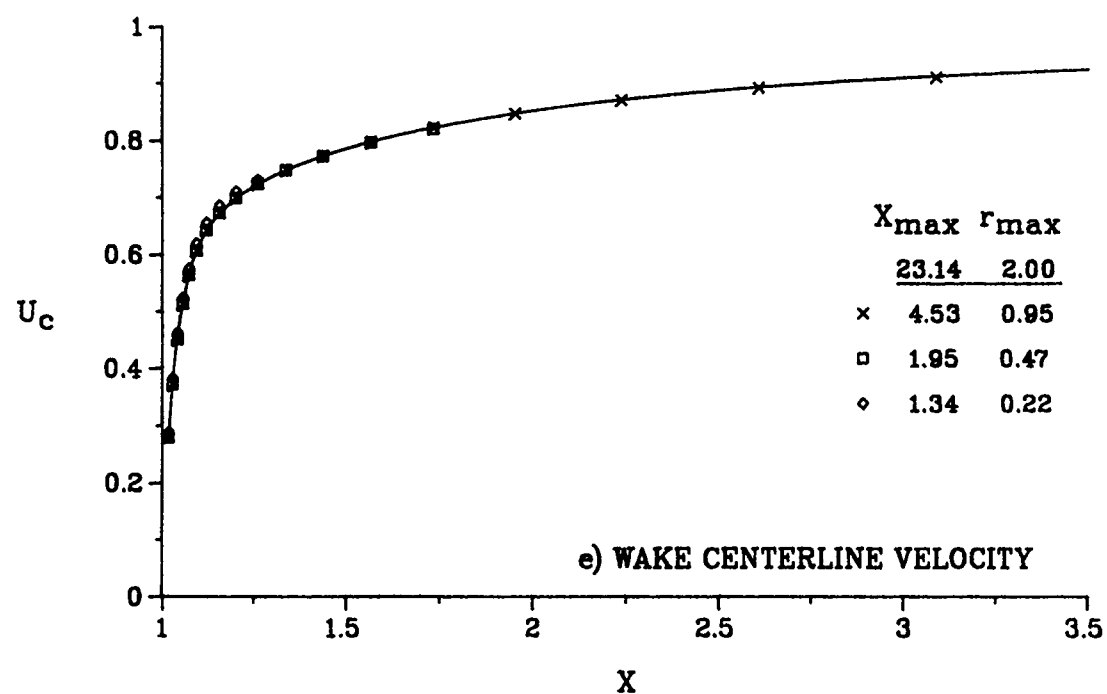


Fig. 10 Influence of solution domain size

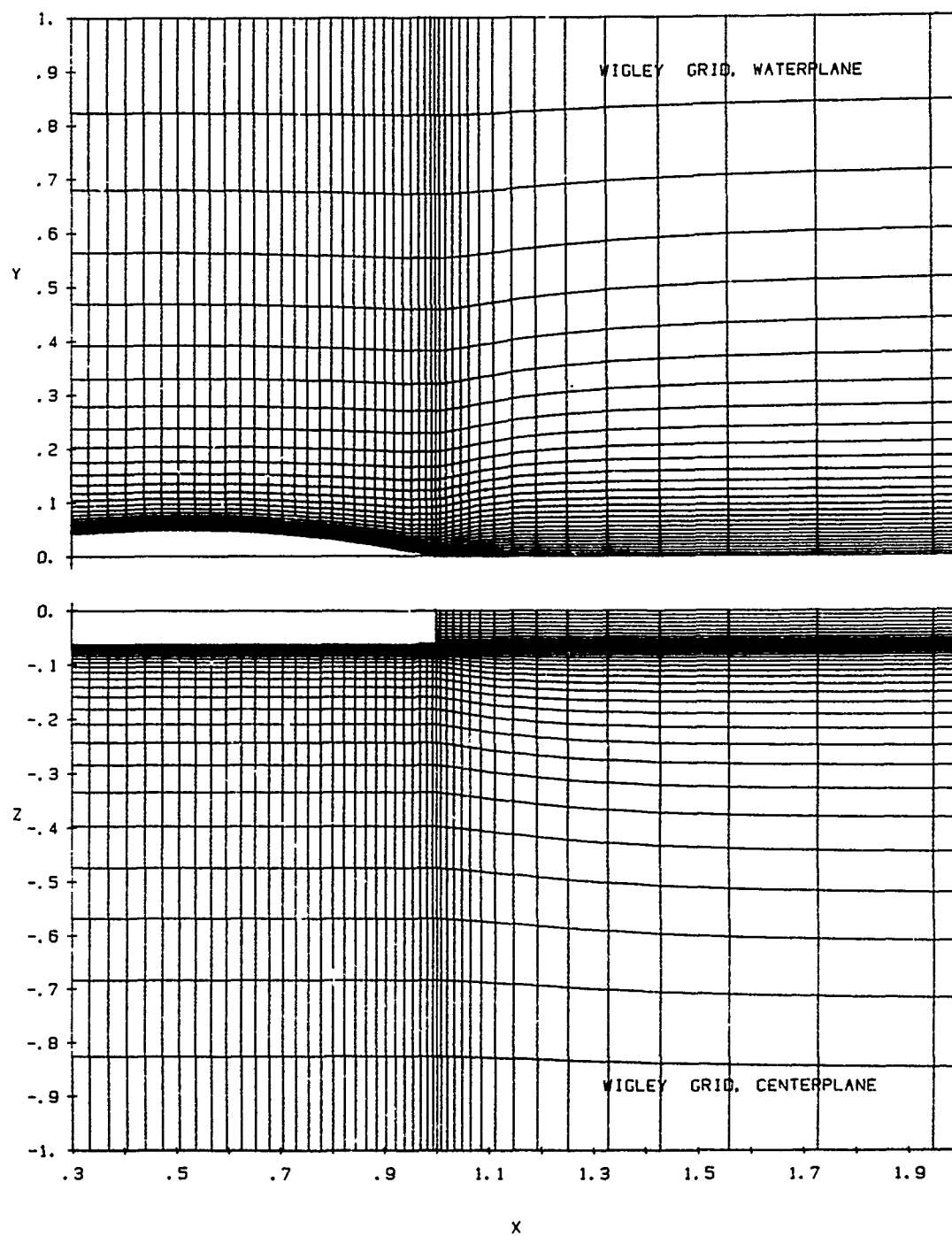


Fig. 11 Typical views of the numerical grid for the Wigley hull
(a) symmetry planes

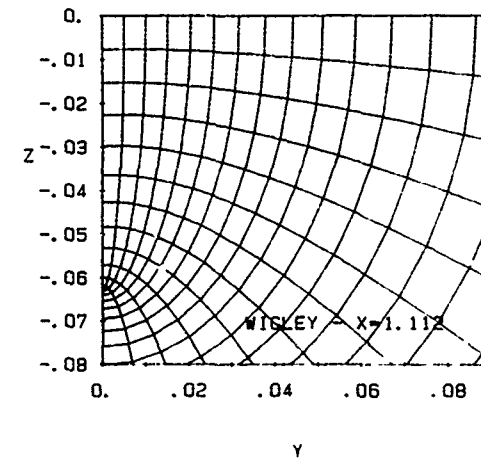
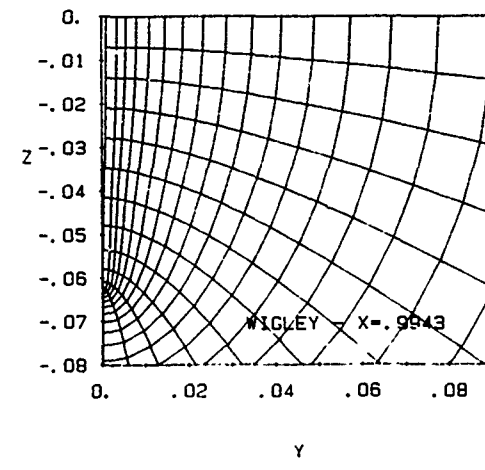
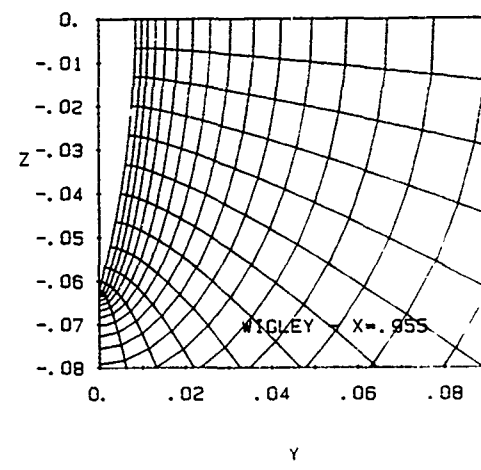
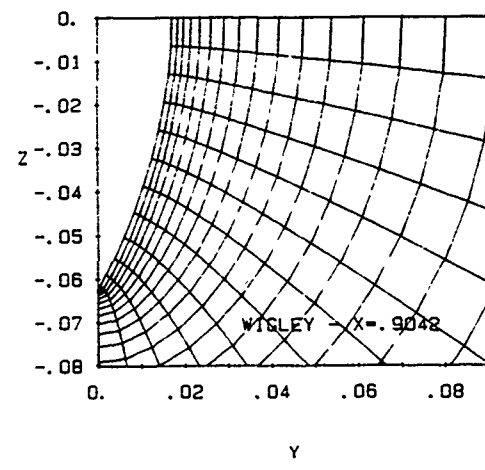
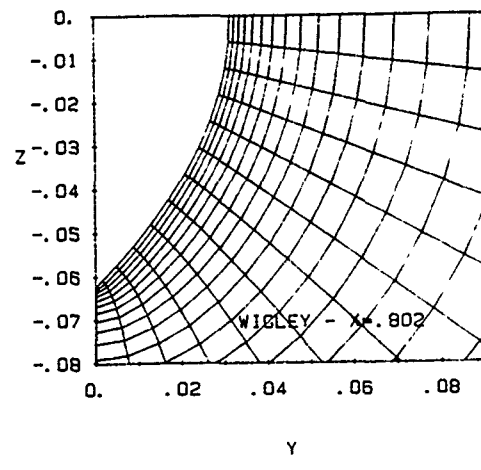
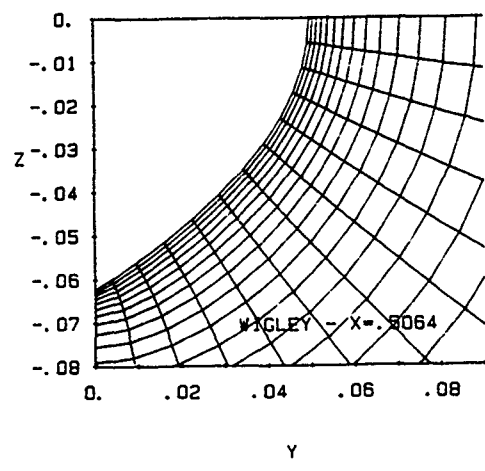


Fig. 11 Typical views of the numerical grid for the Wigley hull
(b) transverse sections

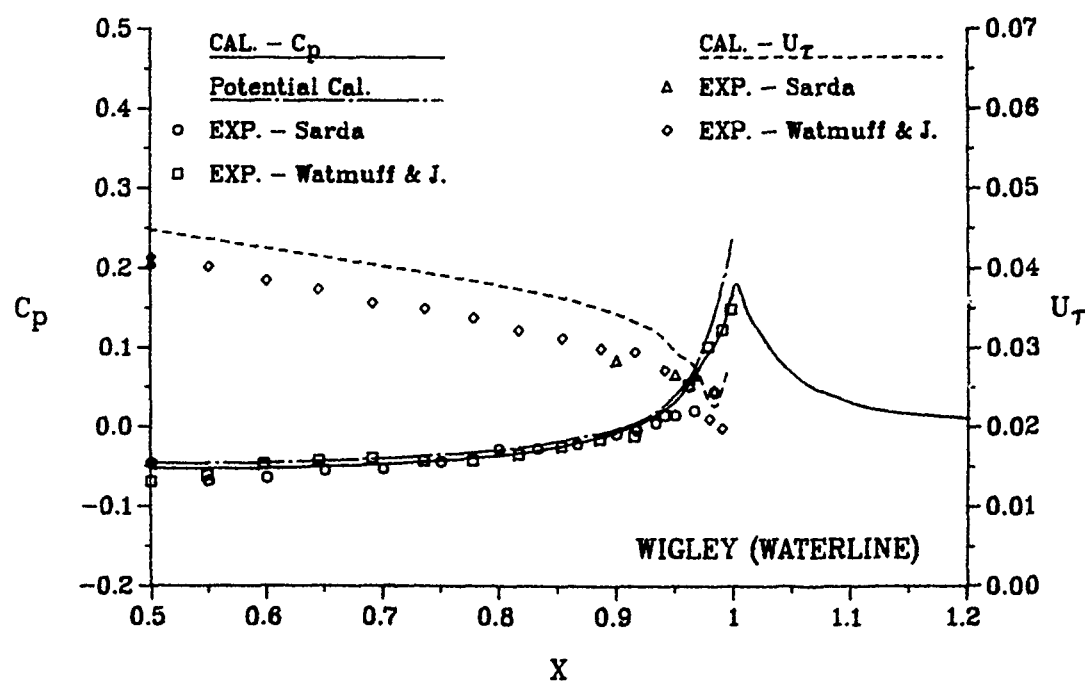
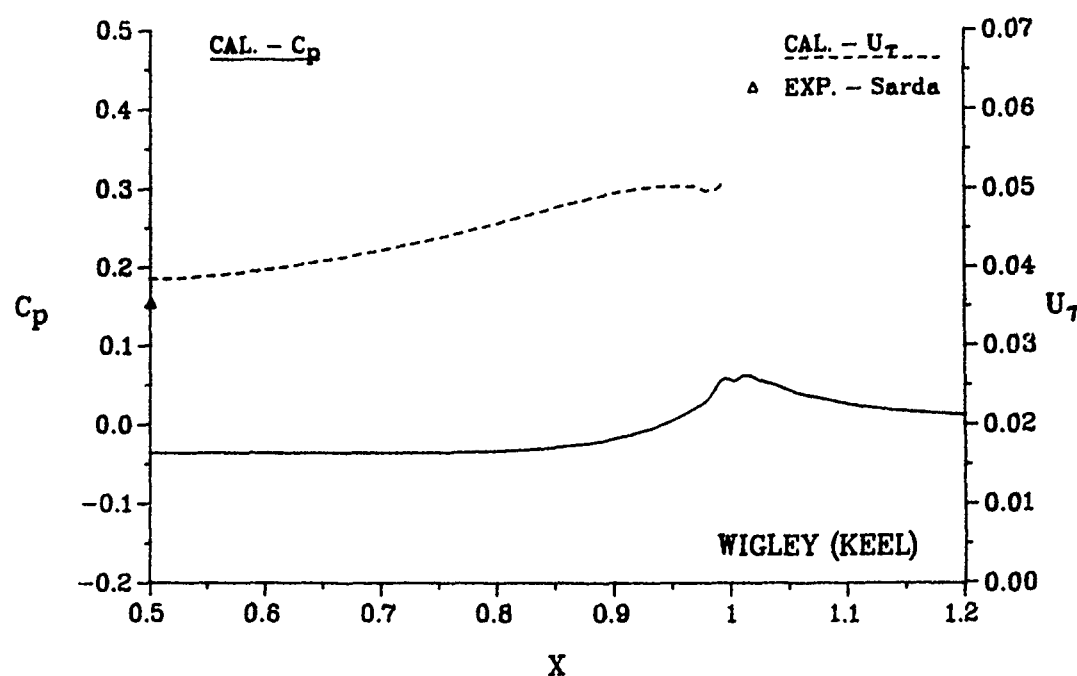


Fig. 12 Pressure and friction velocity along the keel and waterline

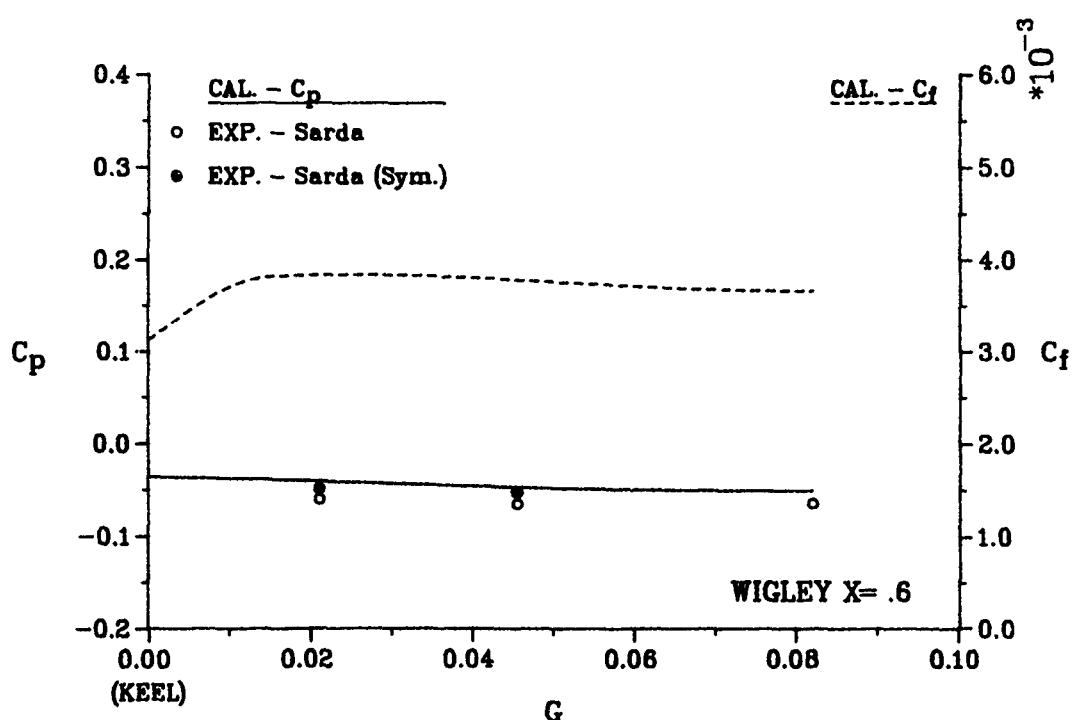
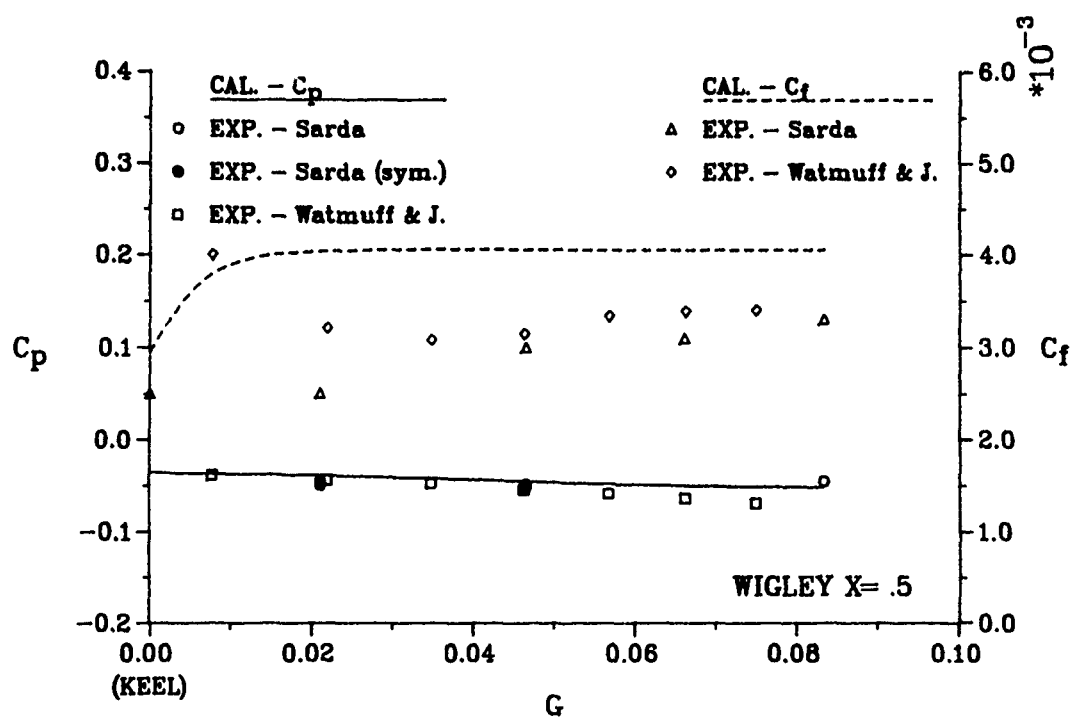


Fig. 13 Girthwise variation of pressure and friction coefficients
 (a) $X = 0.5$; (b) $X = 0.6$

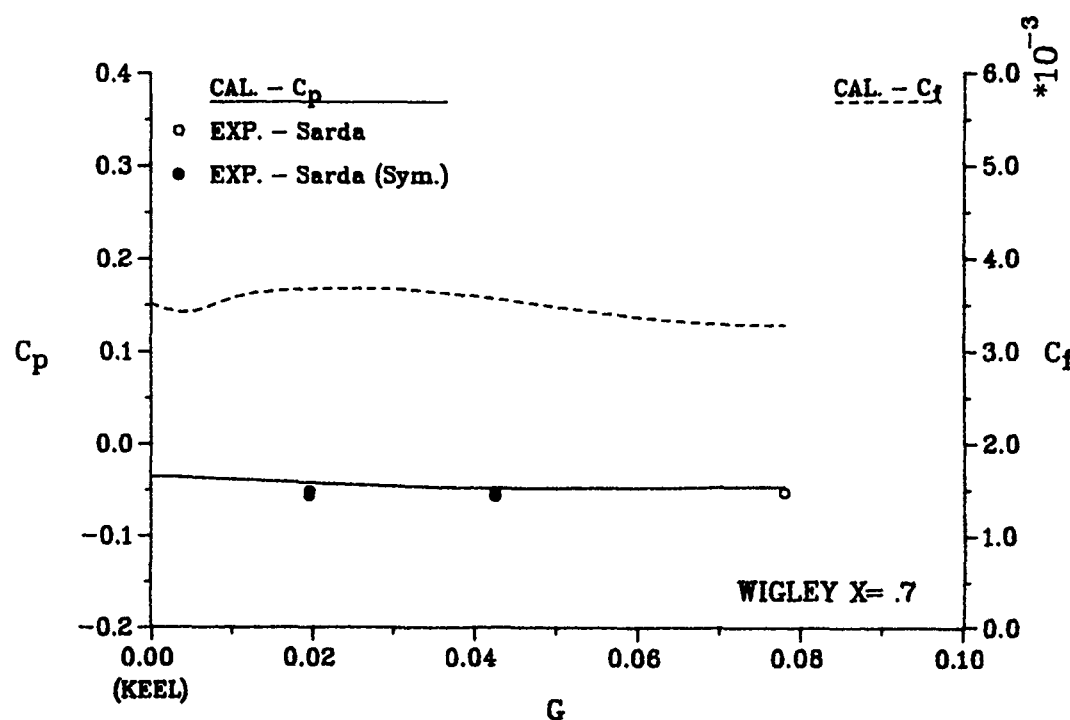
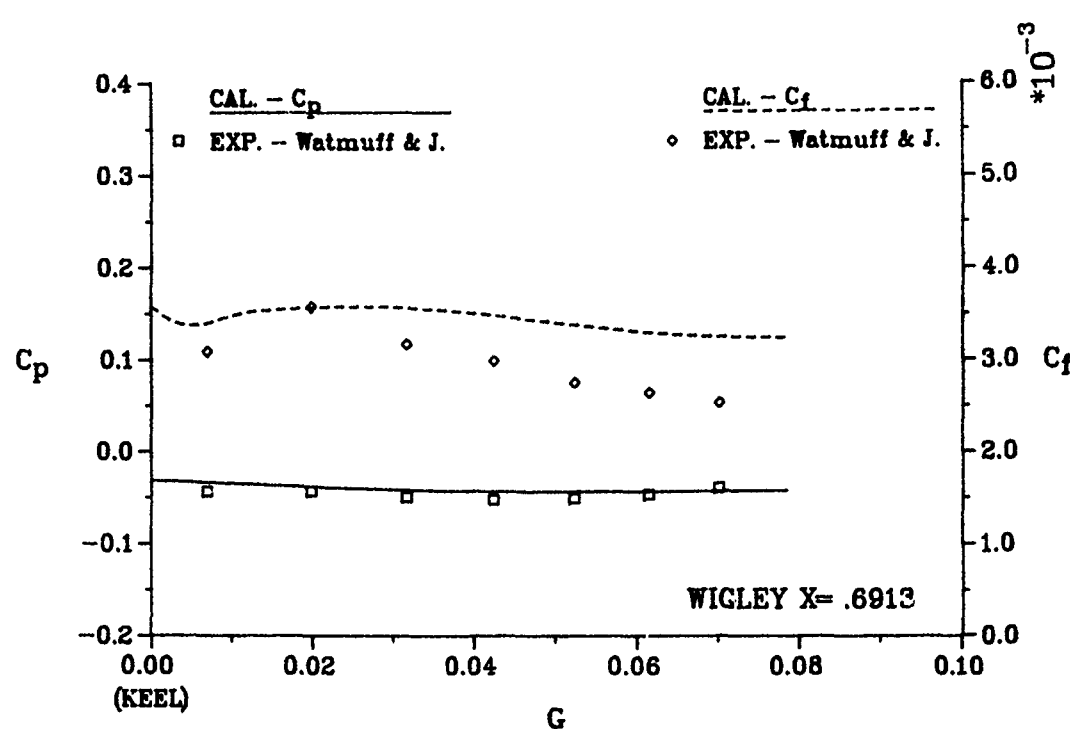


Fig. 13 Girthwise variation of pressure and friction coefficients
(c) $X = 0.6913$; (d) $X = 0.7$

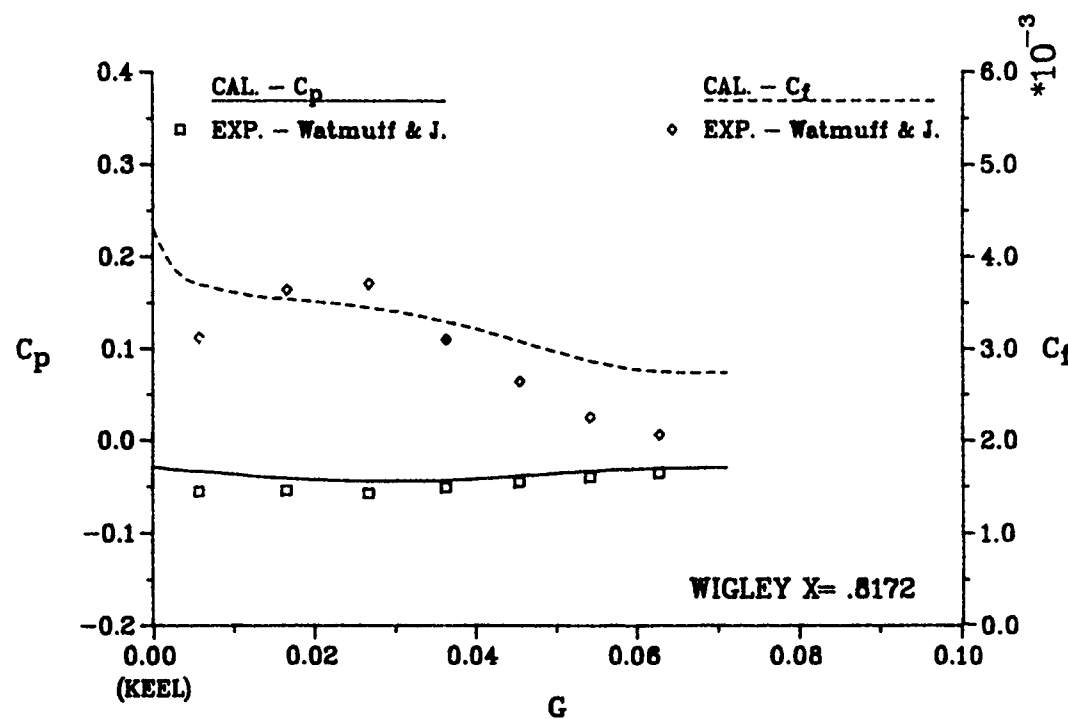
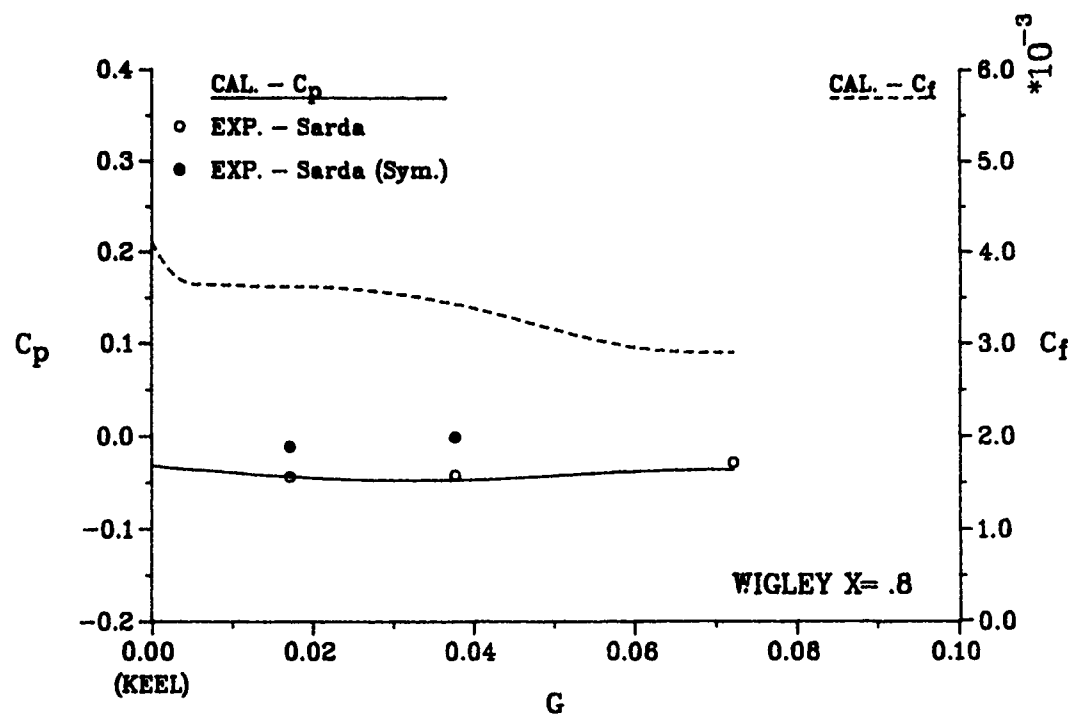


Fig. 13 Girthwise variation of pressure and friction coefficients
(e) X = 0.8; (f) X = 0.8172

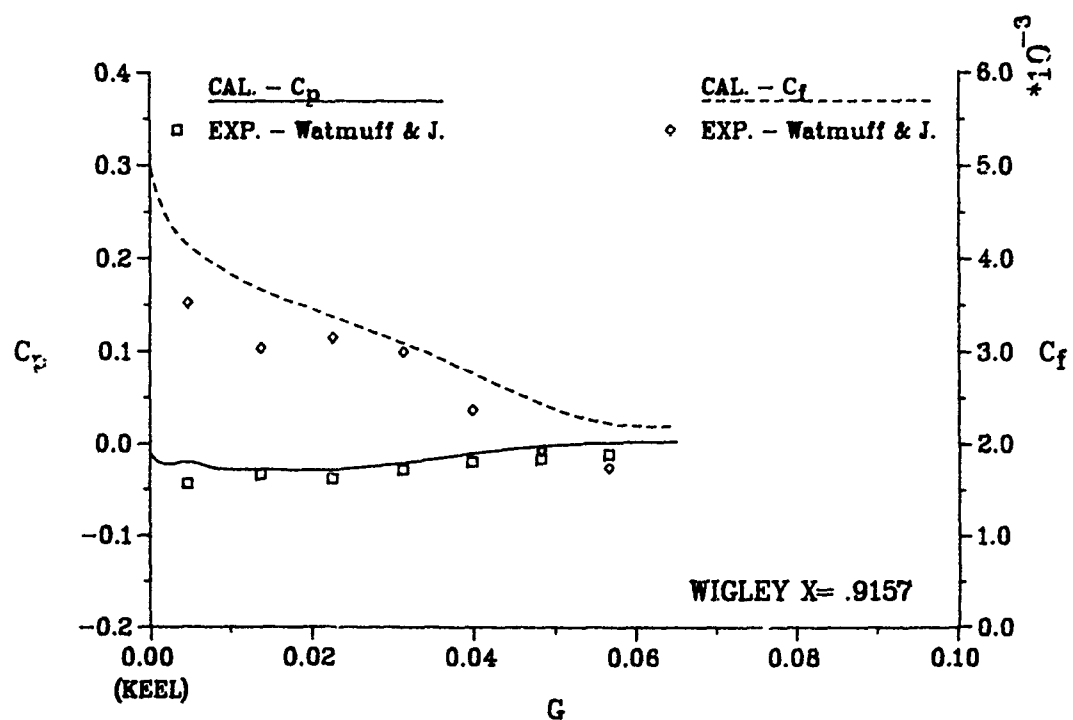
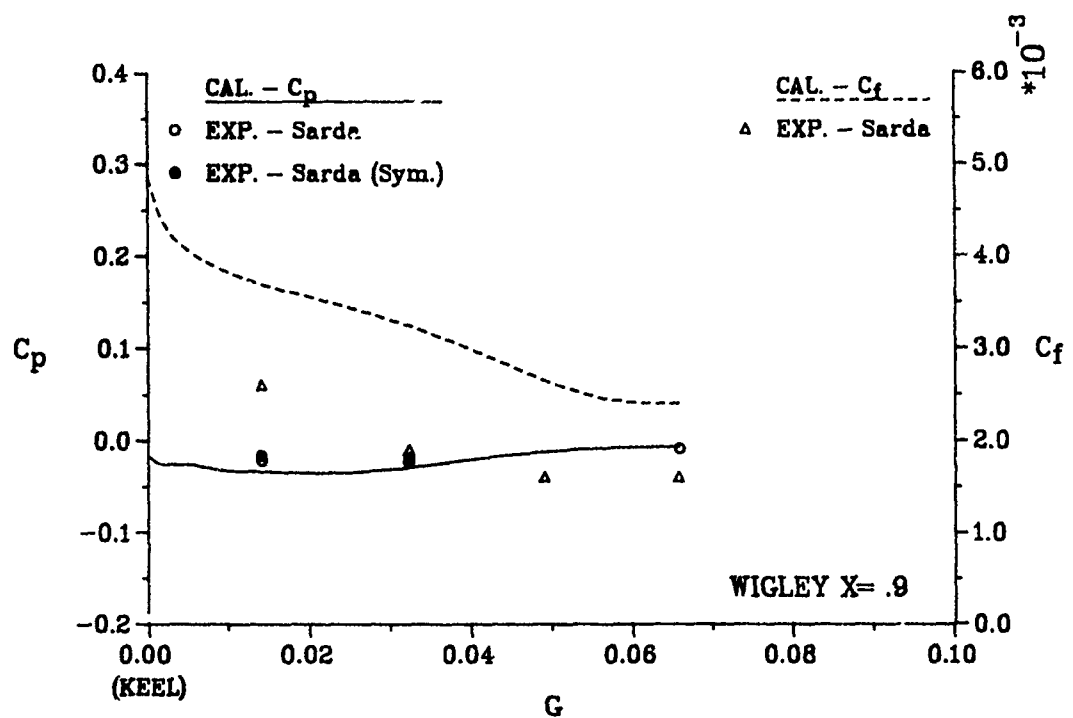


Fig. 13 Girthwise variation of pressure and friction coefficients
(g) $X = 0.9$; (h) $X = 0.9157$

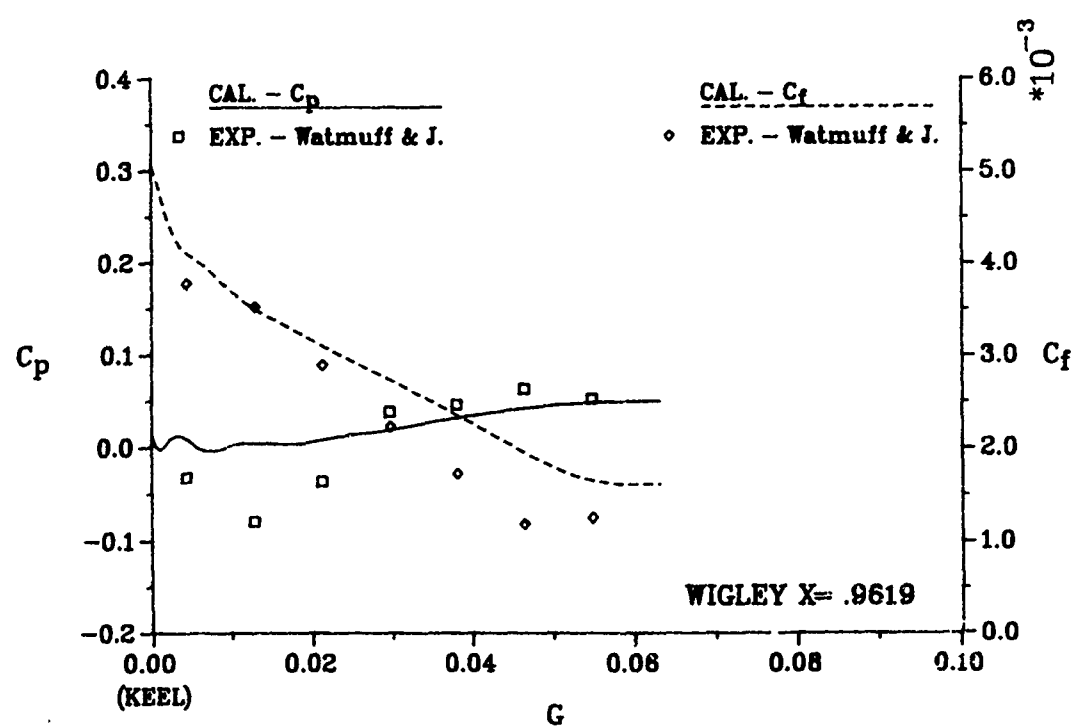
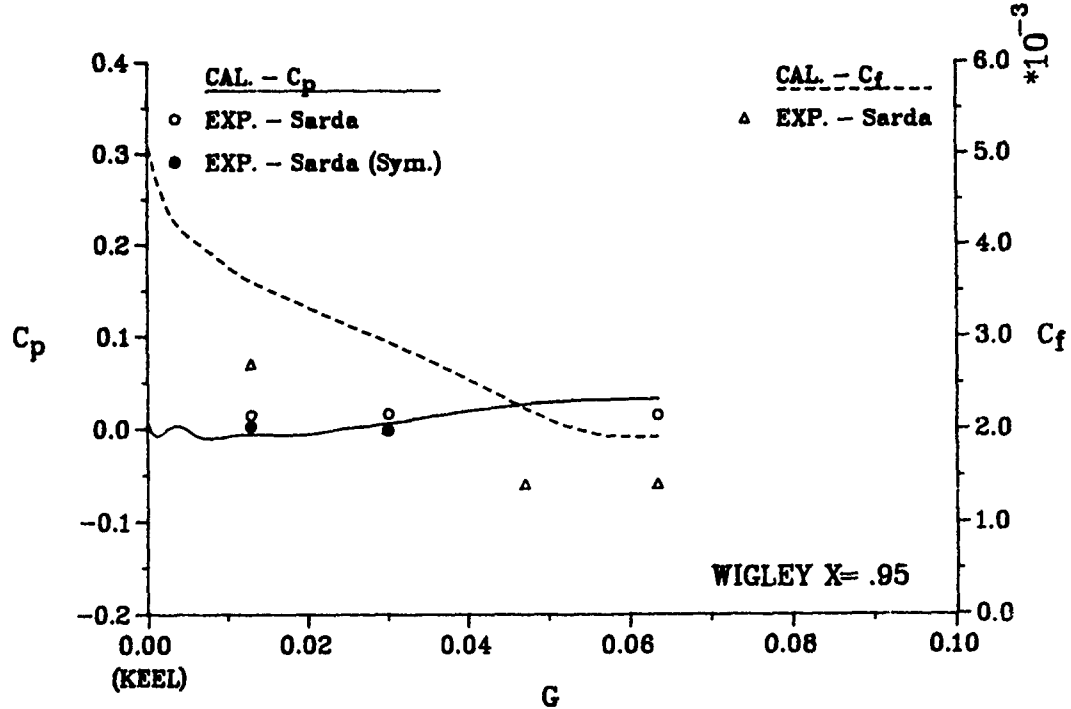


Fig. 13 Girthwise variation of pressure and friction coefficients
(i) $X = 0.95$; (j) $X = 0.9619$

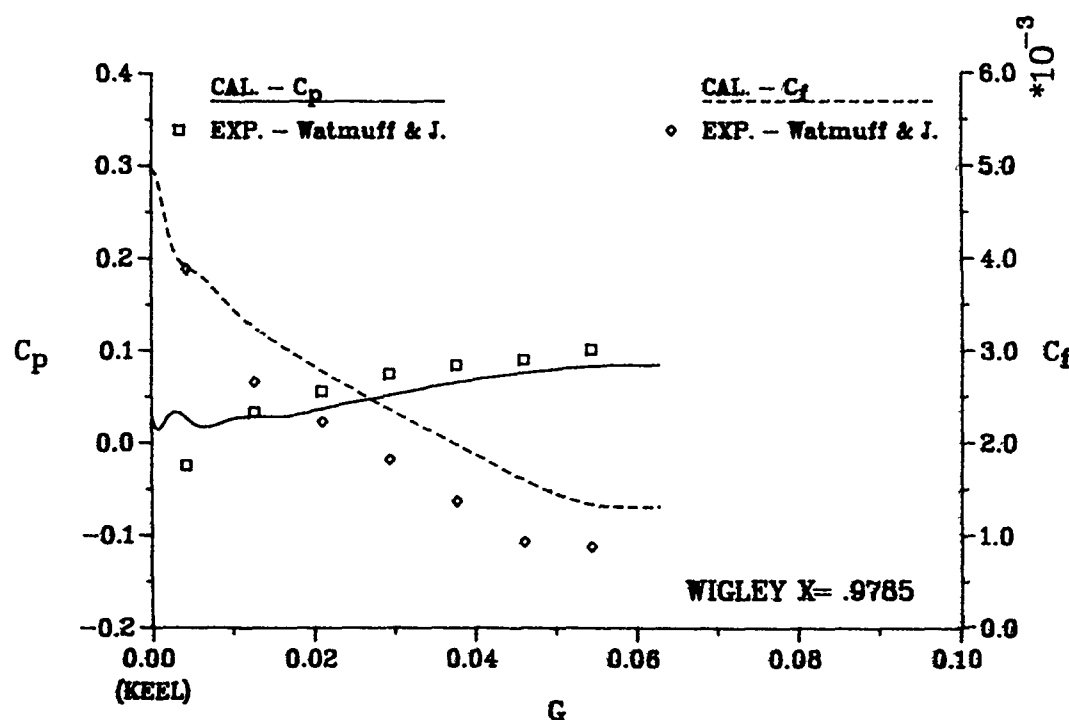
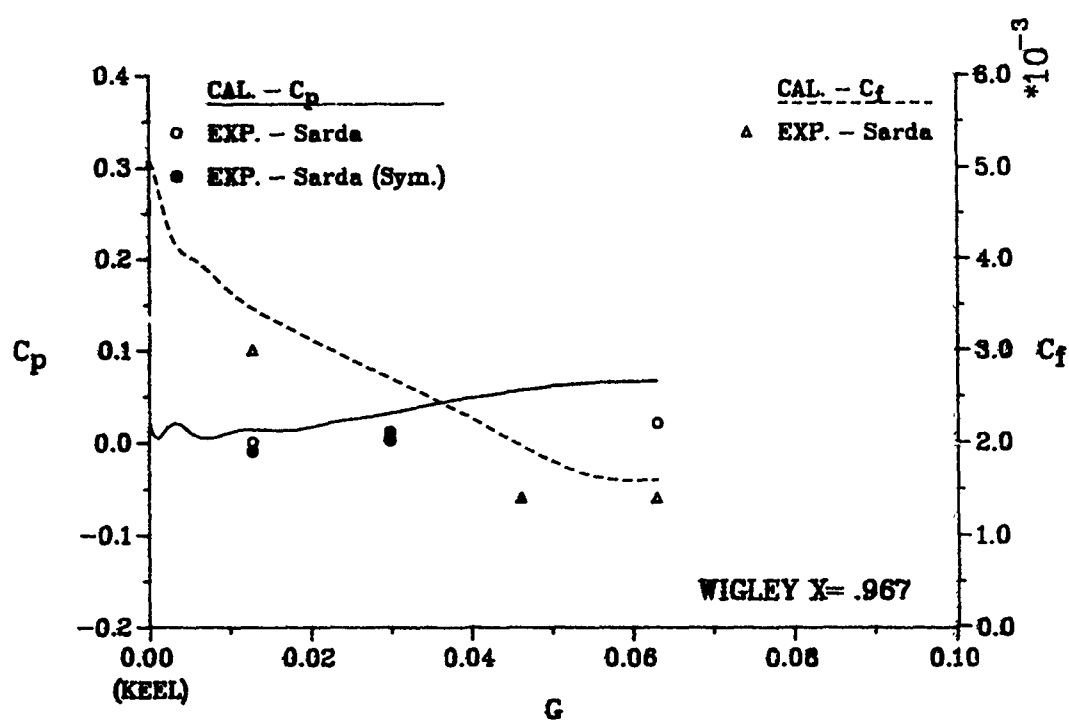


Fig. 13 Girthwise variation of pressure and friction coefficients
(k) $X = 0.967$; (l) $X = 0.9785$

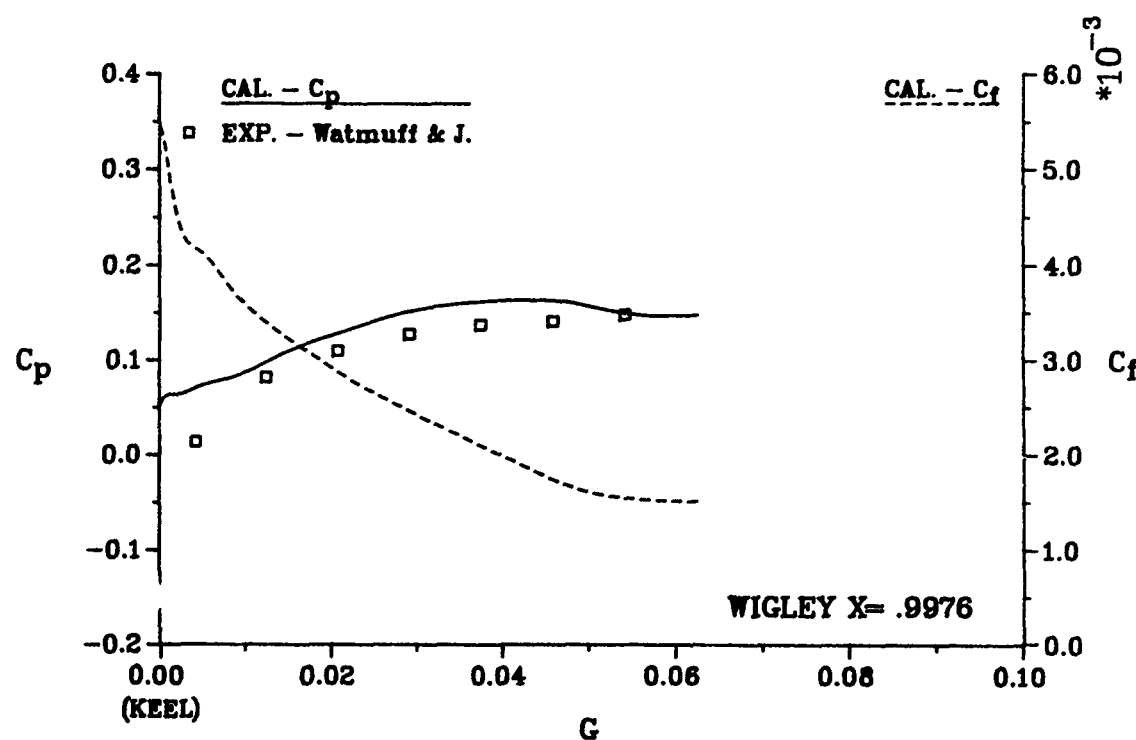
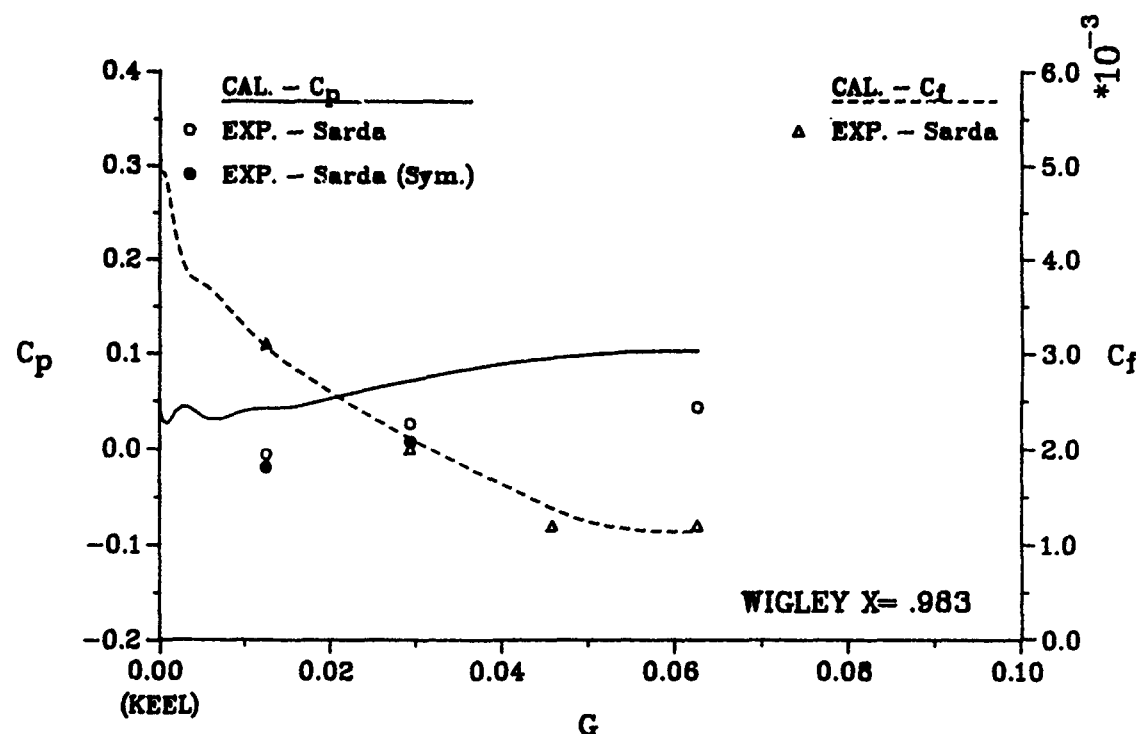


Fig. 13 Girthwise variation of pressure and friction coefficients
(m) $X = 0.983$; (n) $X = 0.9976$

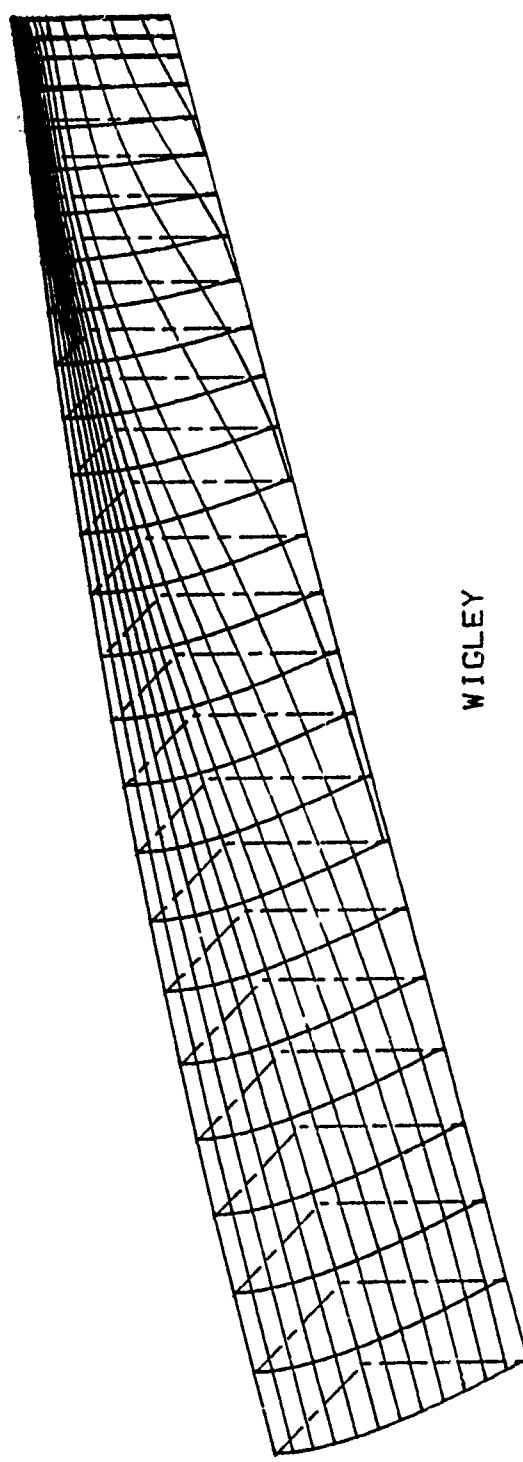


Fig. 14 Calculated wall streamlines

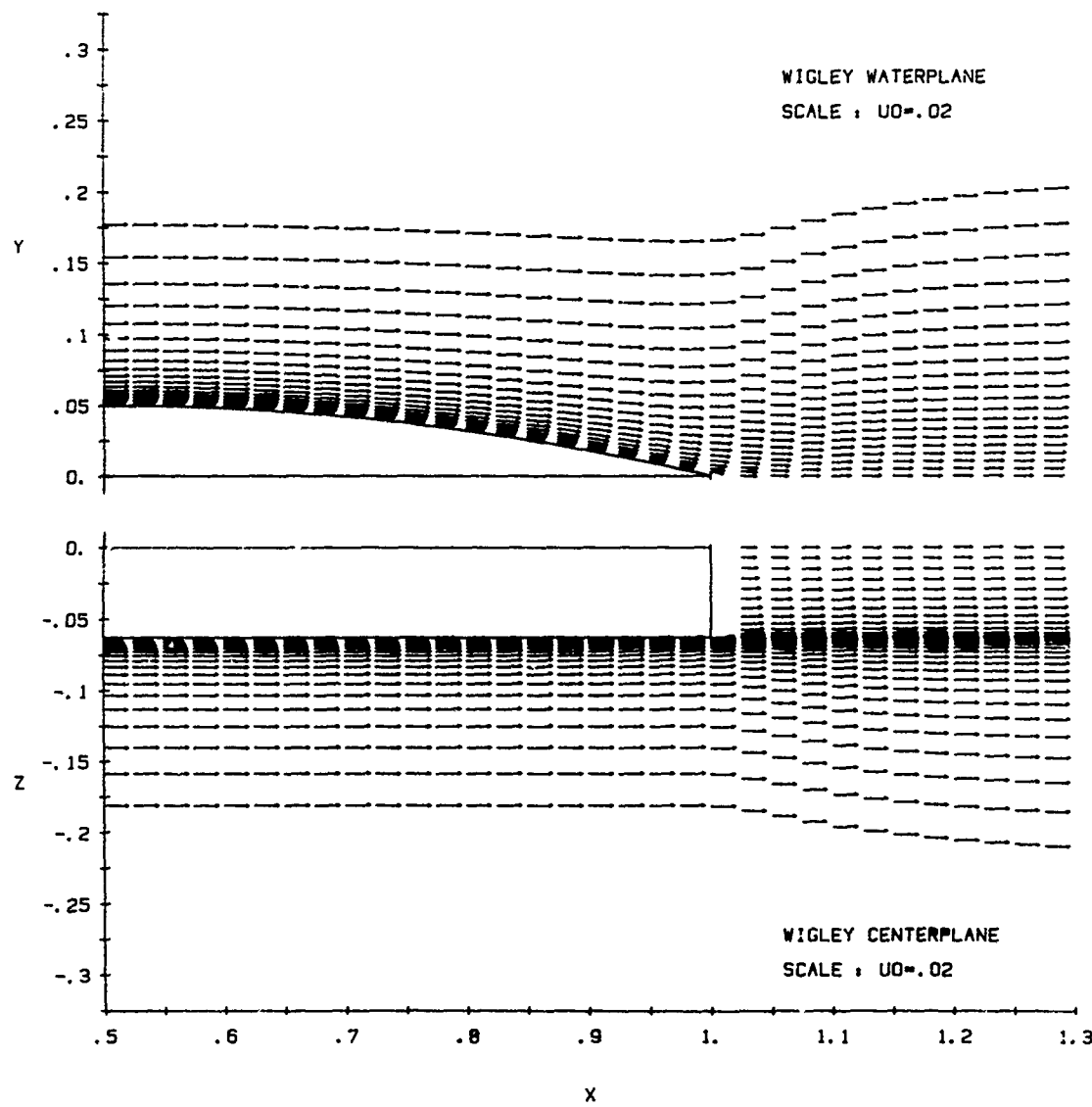


Fig. 15 Velocity vectors in the waterplane (top) and in the vertical centerplane (bottom)

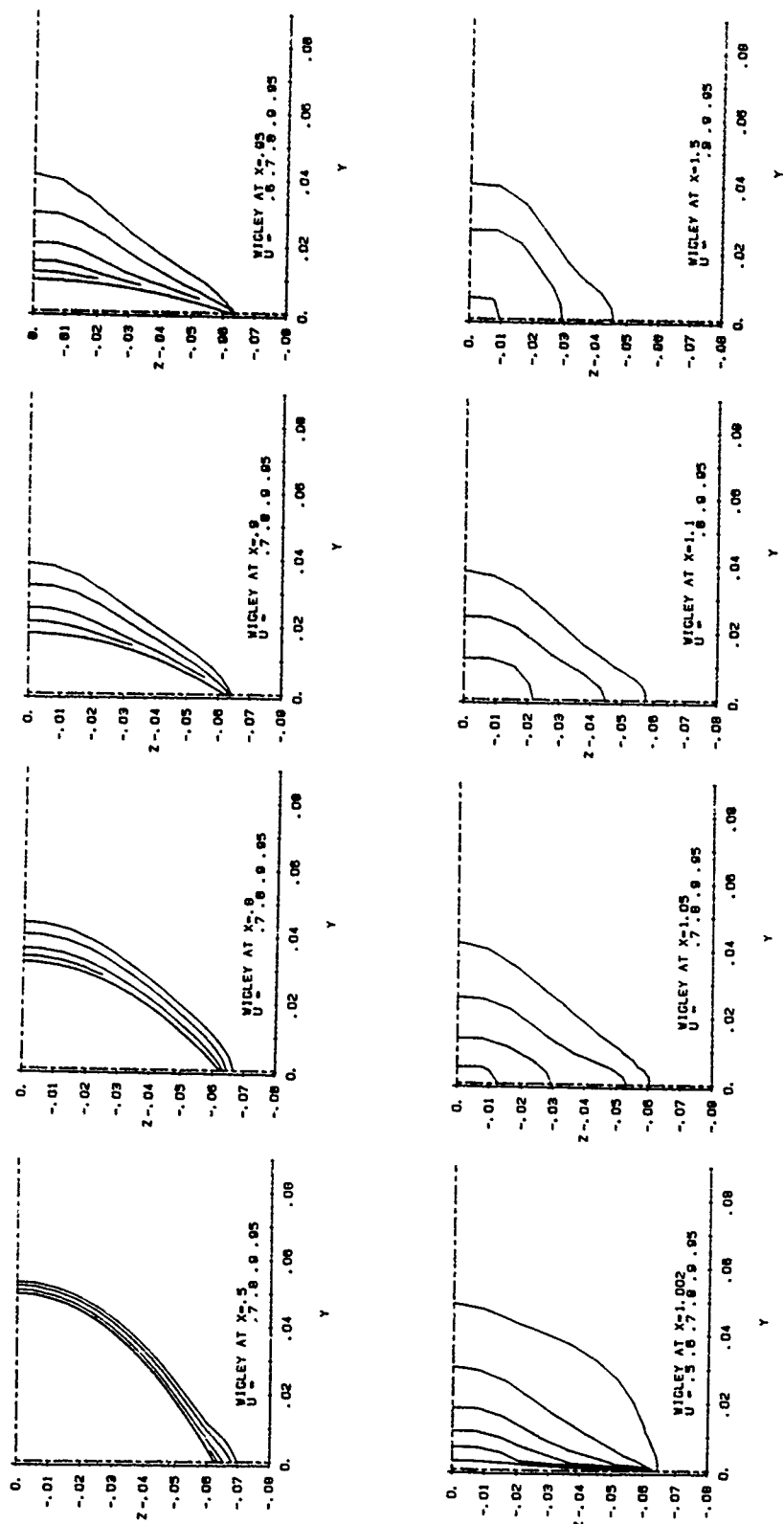


Fig. 16 Velocity field in transverse sections
(a) contours of axial velocity (U)

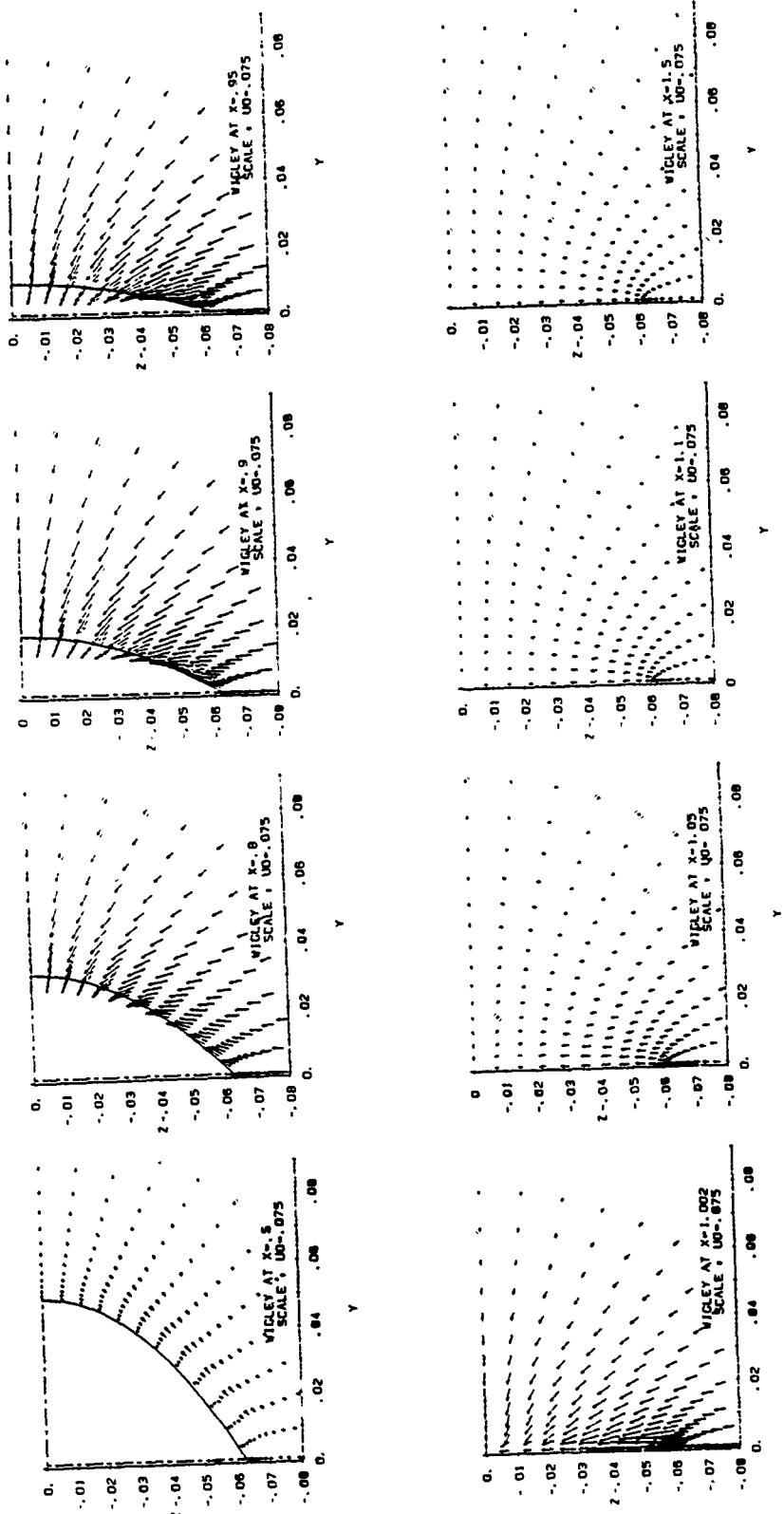


Fig. 16 Velocity field in transverse sections
(b) velocity vectors in transverse sections (V,W)

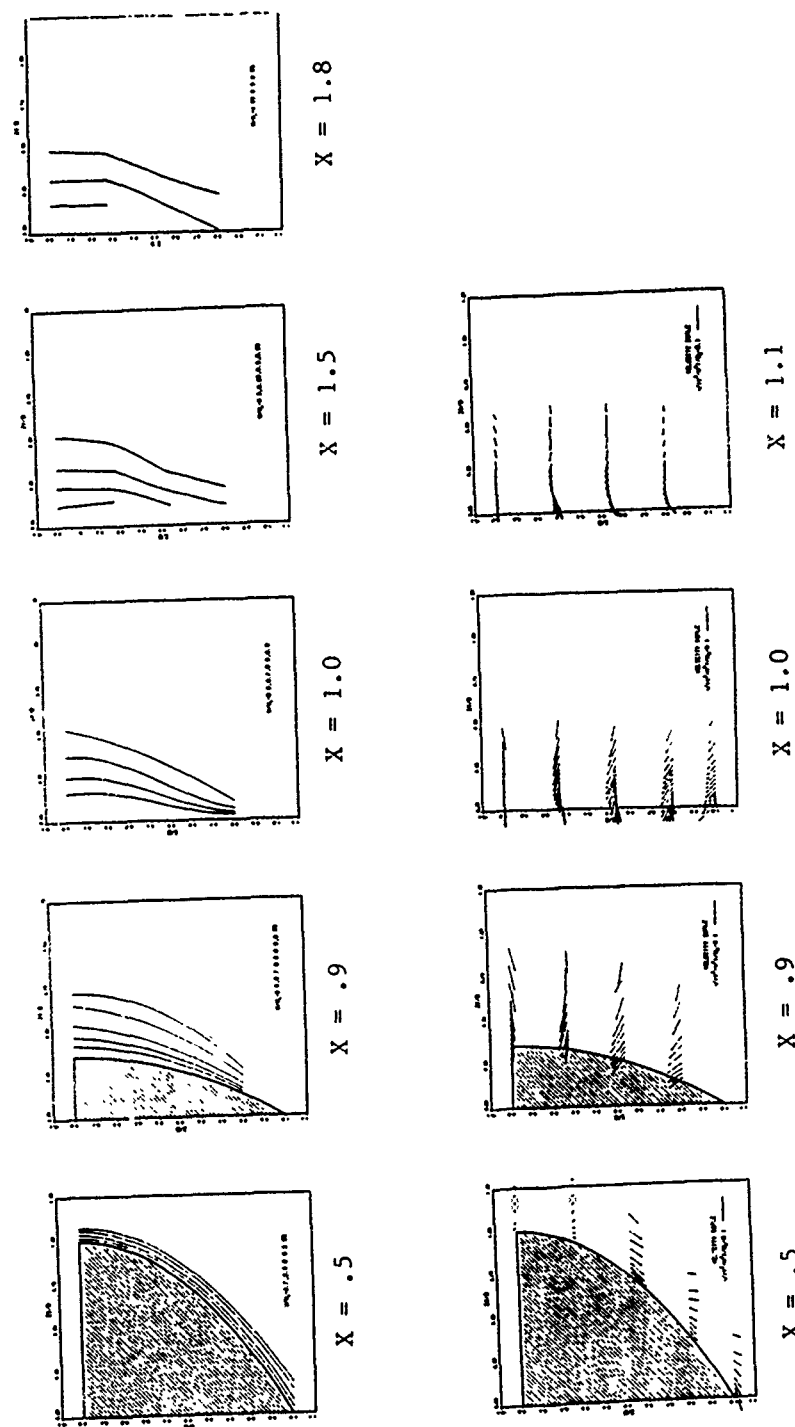


Fig. 17 Velocity field in transverse sections: measurements of Sarda (1986)
Top: contours of axial velocity (U); Bottom: velocity vectors in transverse sections (V,W)

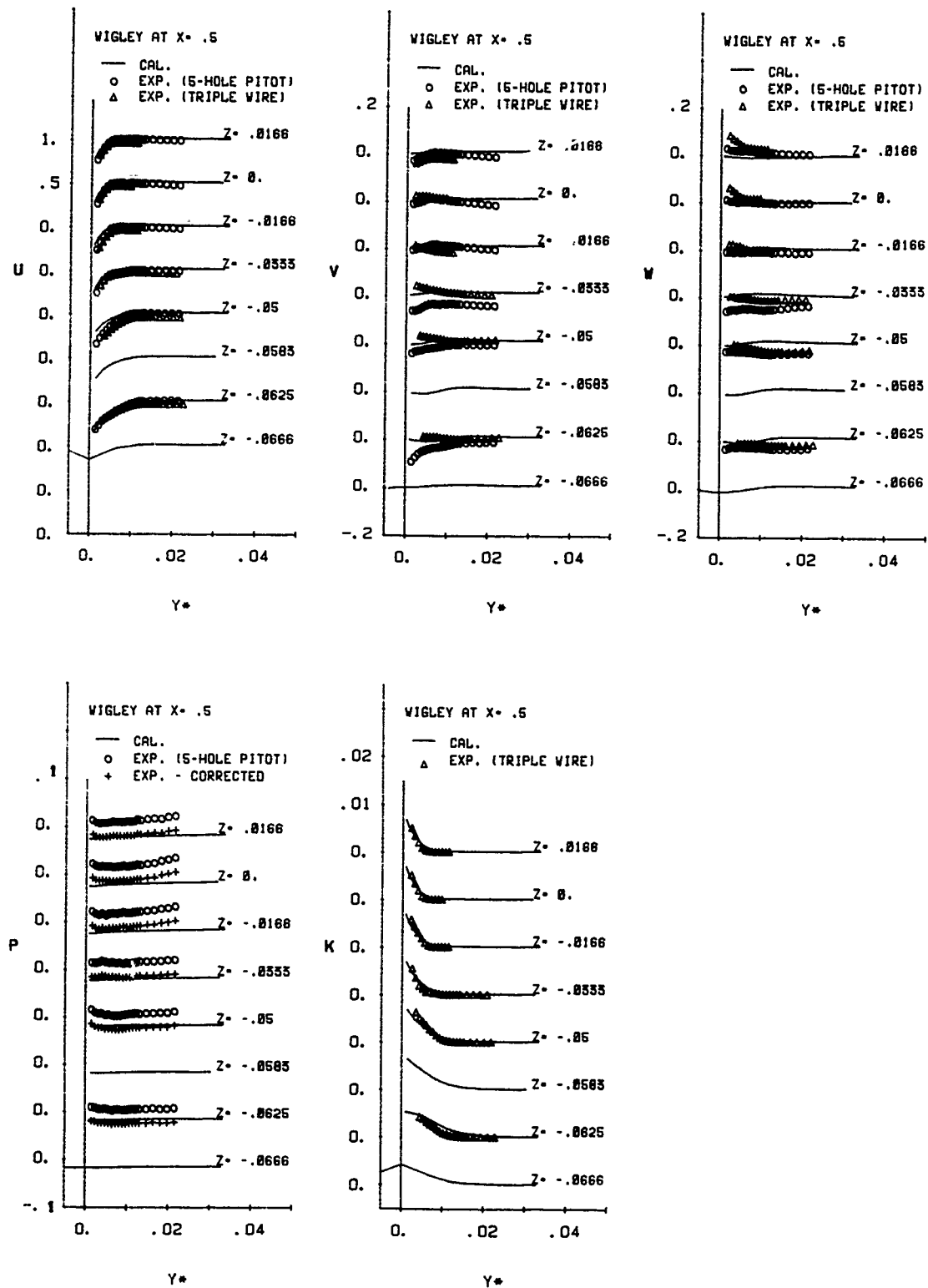


Fig. 18 Profiles of velocity components (U, V, W), pressure (P), and turbulent kinetic energy (k) compared with data of Sarda
(a) $X = 0.5$

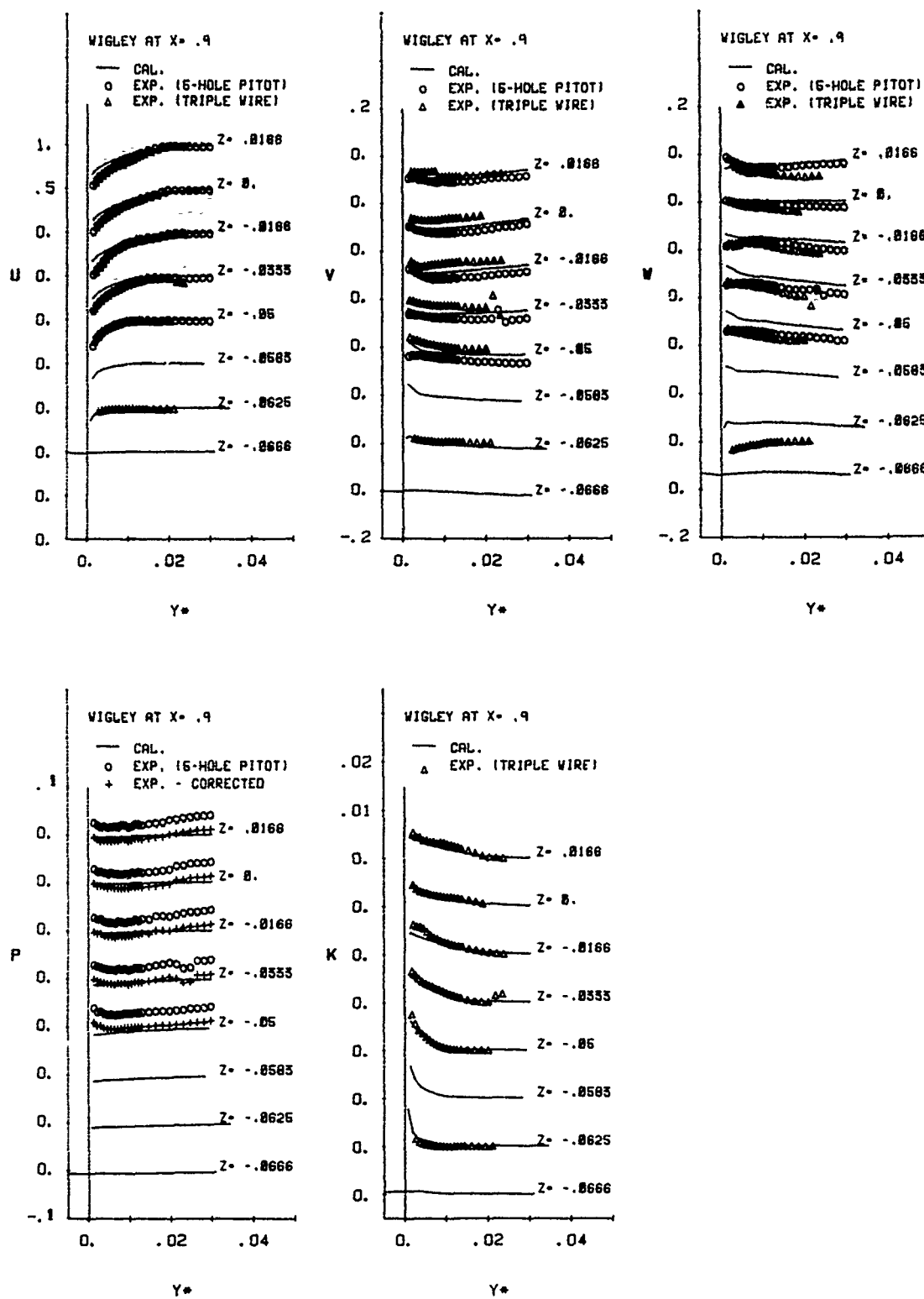


Fig. 18 Profiles of velocity components (U, V, W), pressure (P), and turbulent kinetic energy (K) compared with data of Sarda
(b) $X = 0.9$

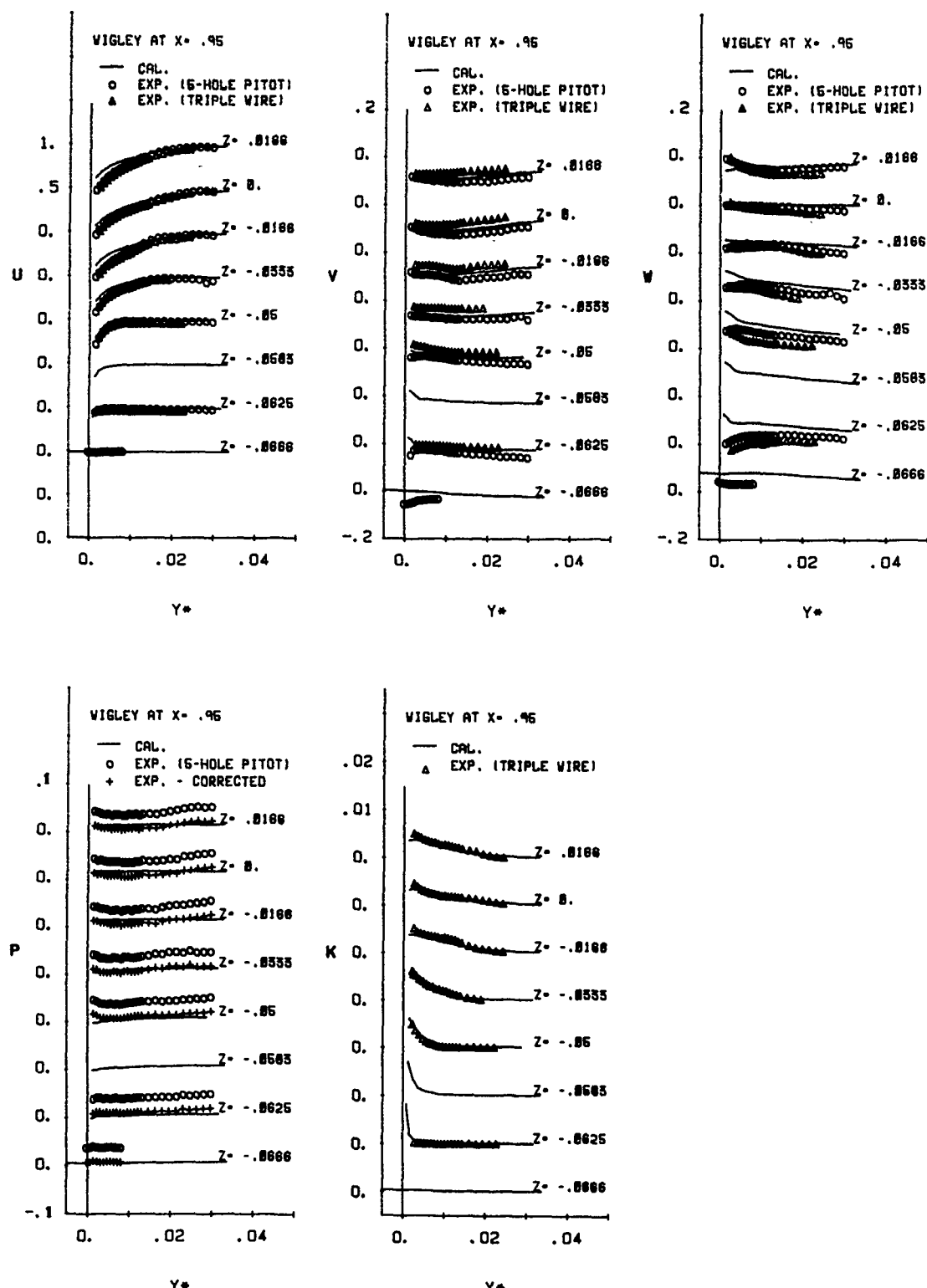


Fig. 18 Profiles of velocity components (U , V , W), pressure (P), and turbulent kinetic energy (K) compared with data of Sarda
(c) $X = 0.95$

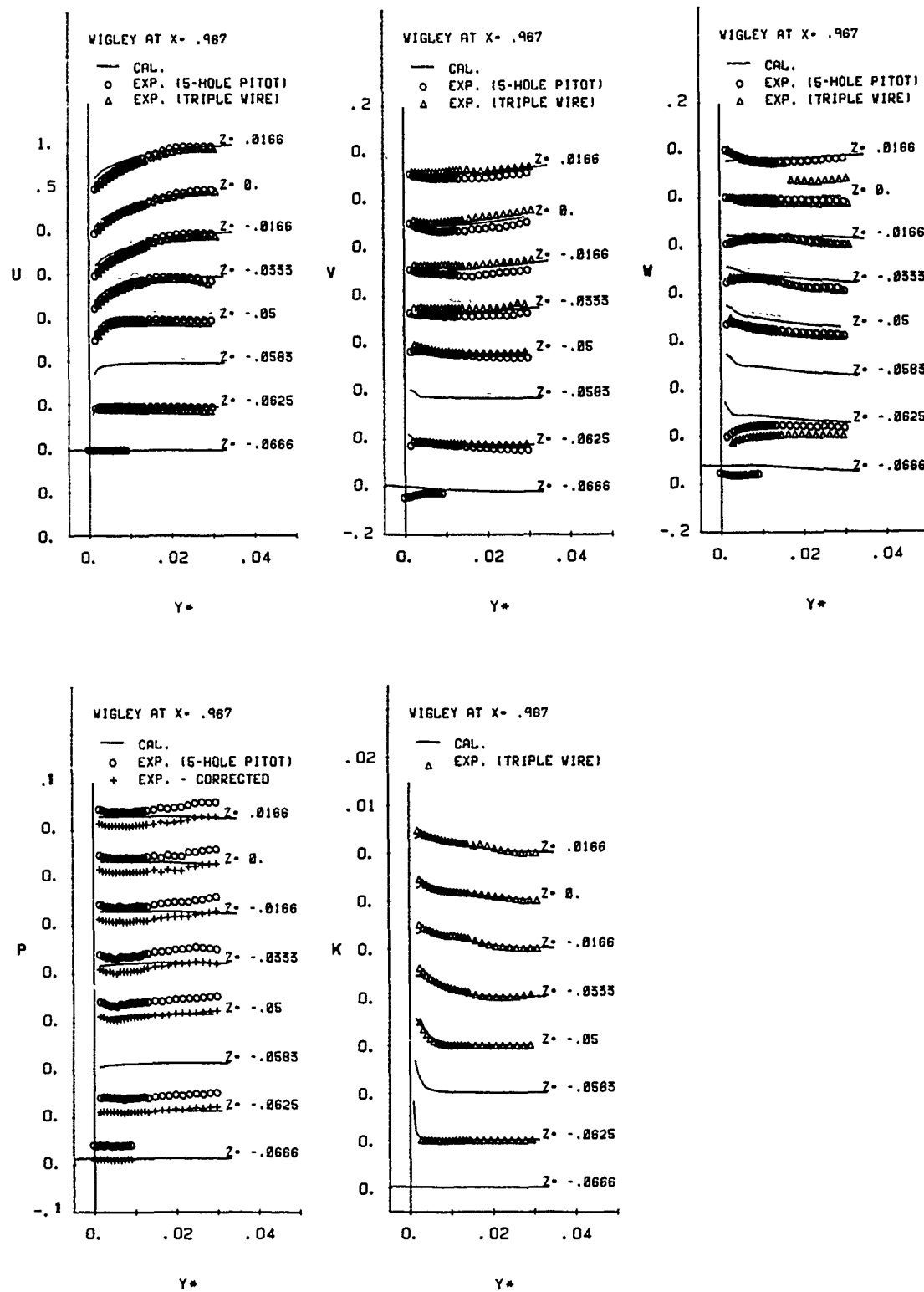


Fig. 18 Profiles of velocity components (U, V, W), pressure (P), and turbulent kinetic energy (K) compared with data of Sarda
(d) $X = 0.967$

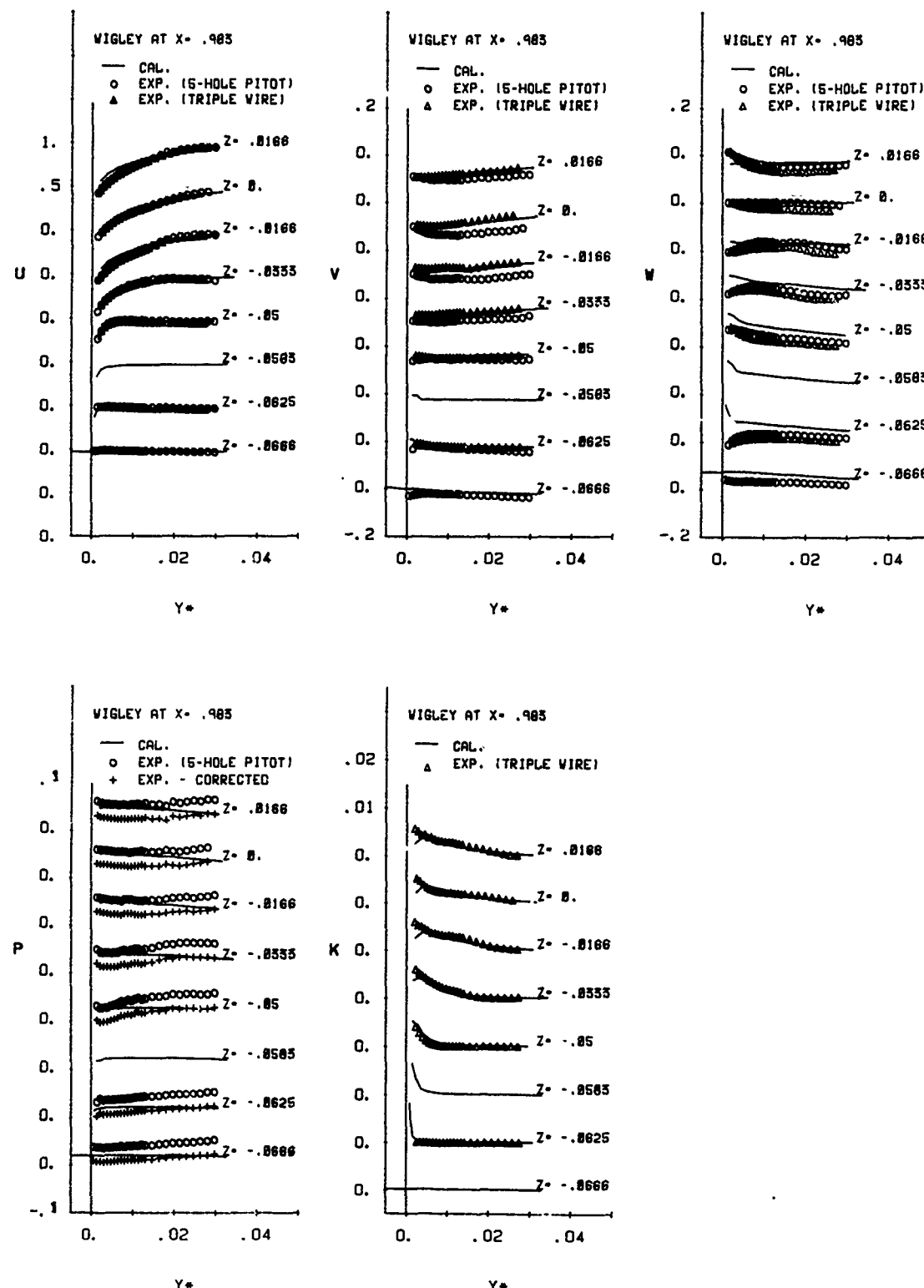


Fig. 18 Profiles of velocity components (U, V, W), pressure (P), and turbulent kinetic energy (k) compared with data of Sarda
(e) $X = 0.983$

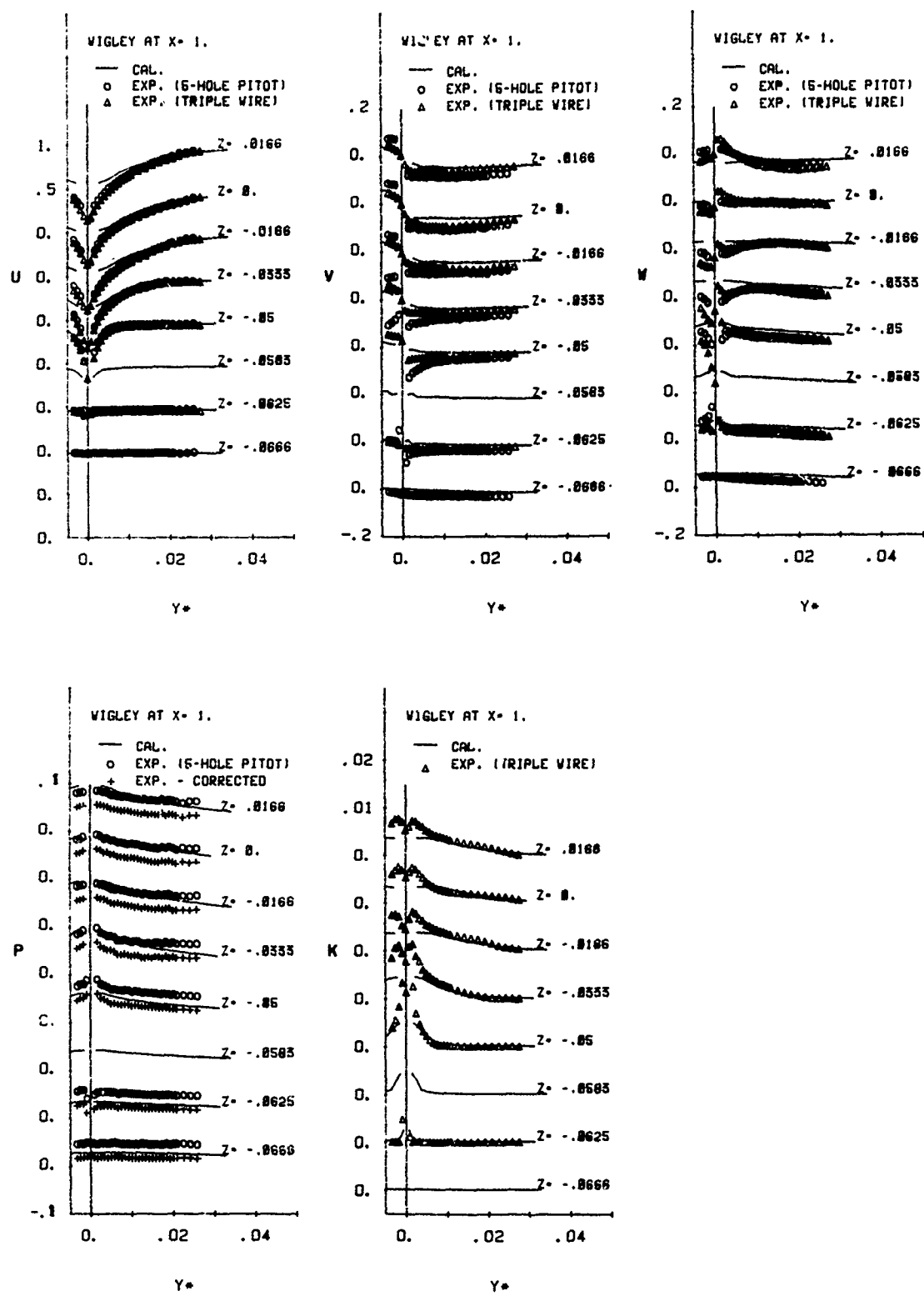


Fig. 18 Profiles of velocity components (U, V, W), pressure (P), and turbulent kinetic energy (k) compared with data of Sarda
(f) $X = 1.002$

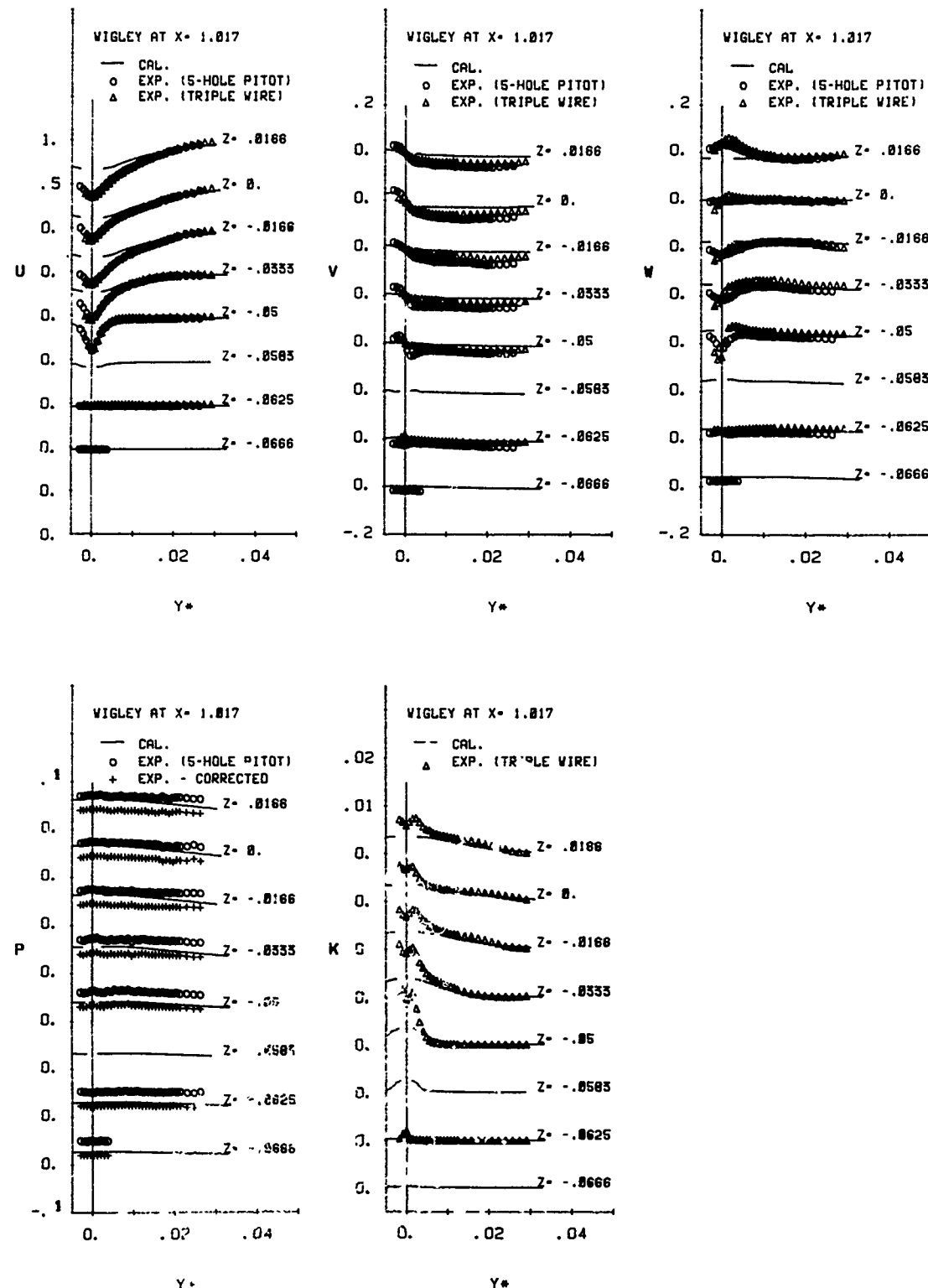


Fig. 18 Profiles of velocity components (U, V, W), pressure (P), and turbulent kinetic energy (k) compared with data of Sarda
(g) $X = 1.017$

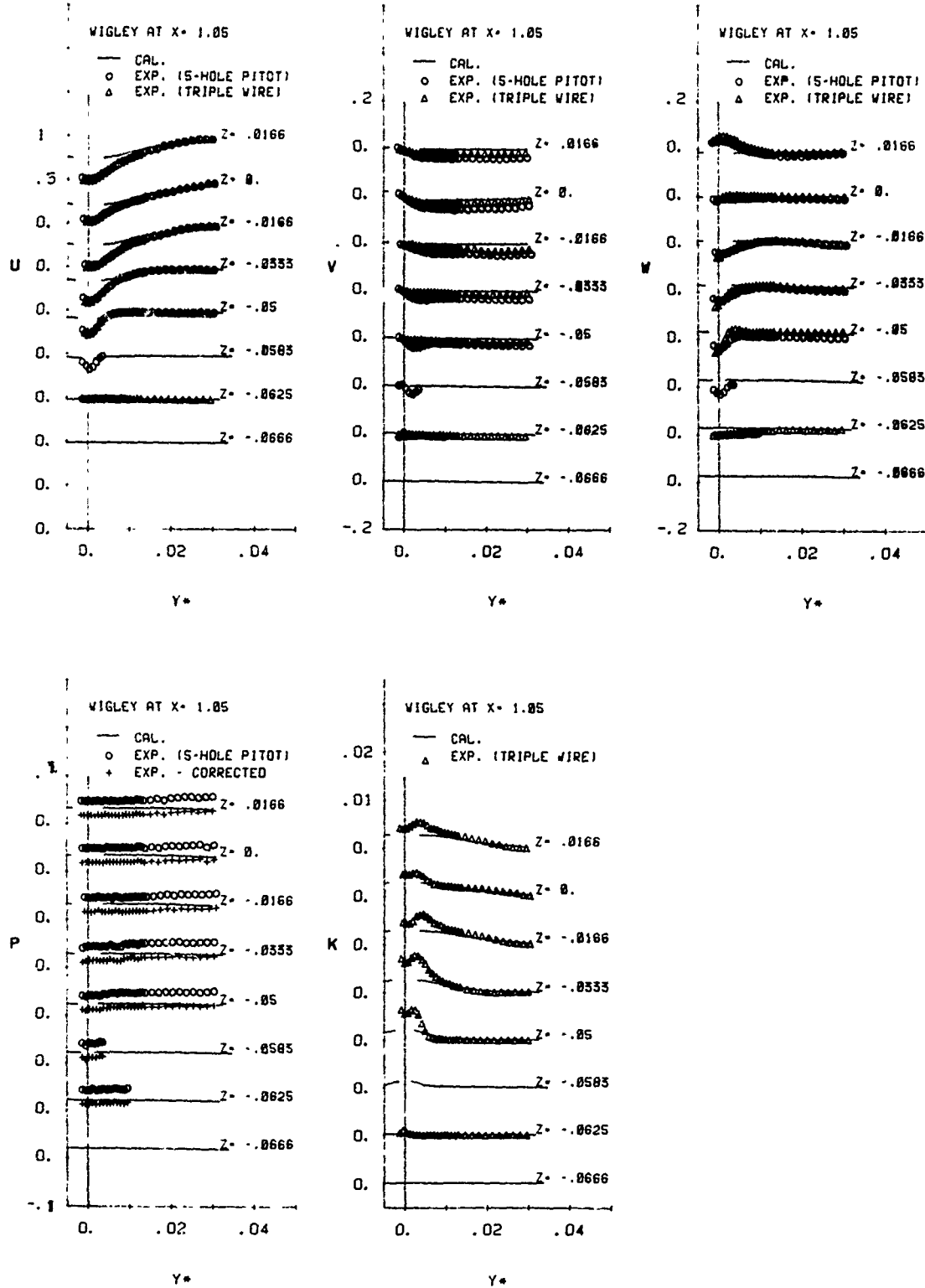


Fig. 18 Profiles of velocity components (U , V , W), pressure (P), and turbulent kinetic energy (k) compared with data of Sarda
(h) $X = 1.05$

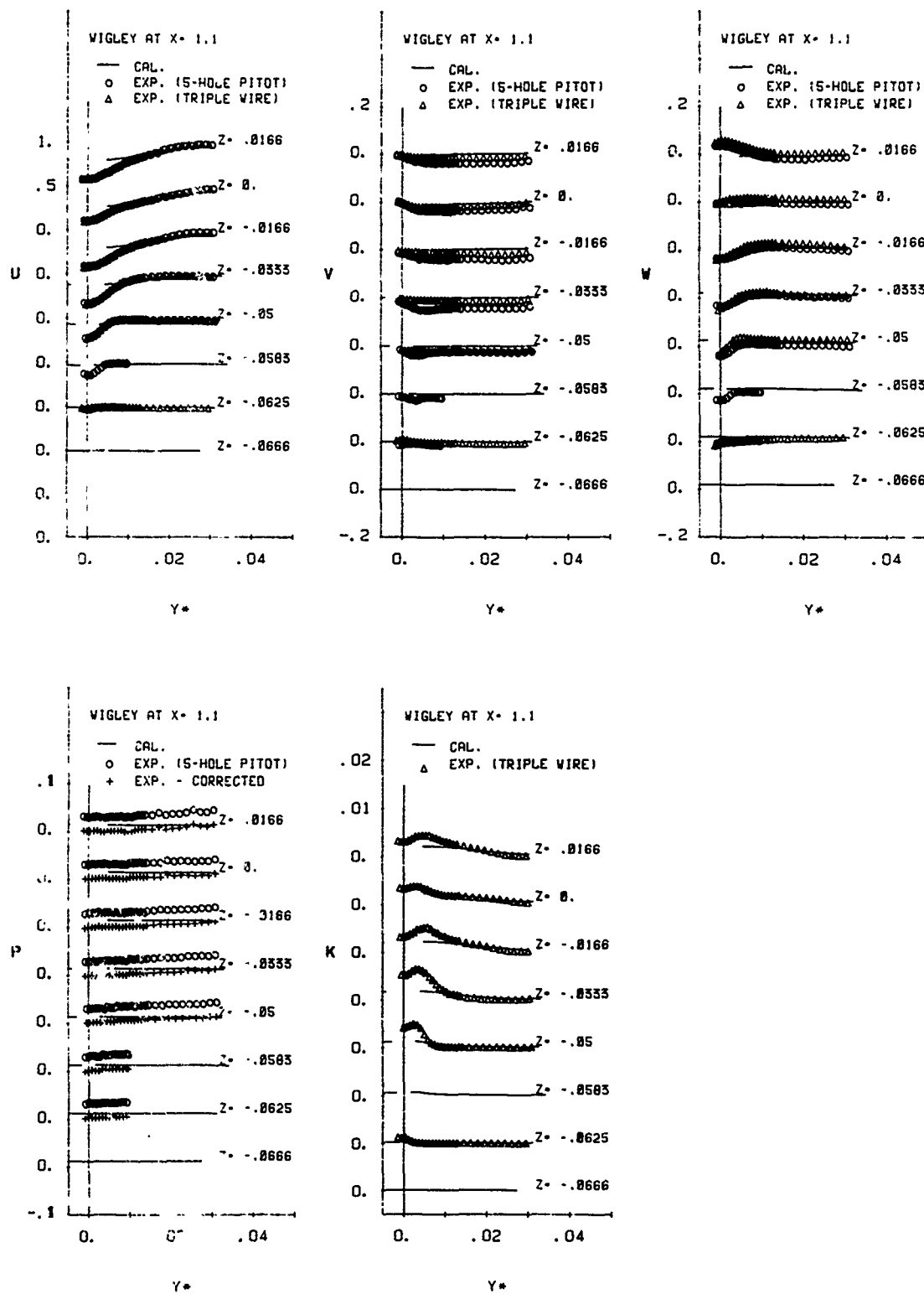
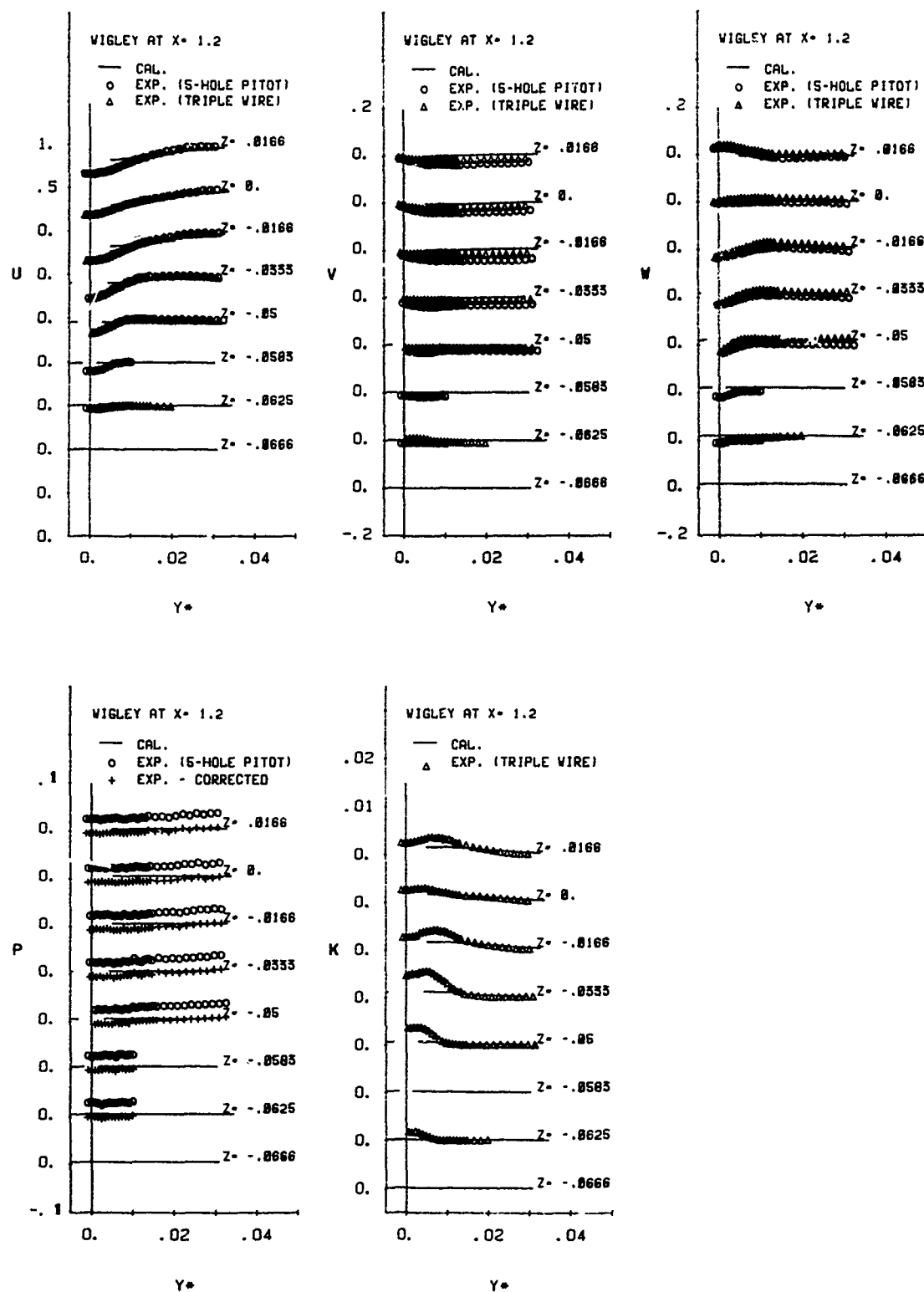


Fig. 18 Profiles of velocity components (U, V, W), pressure (P), and turbulent kinetic energy (k) compared with data of Sarda
(i) $X = 1.1$



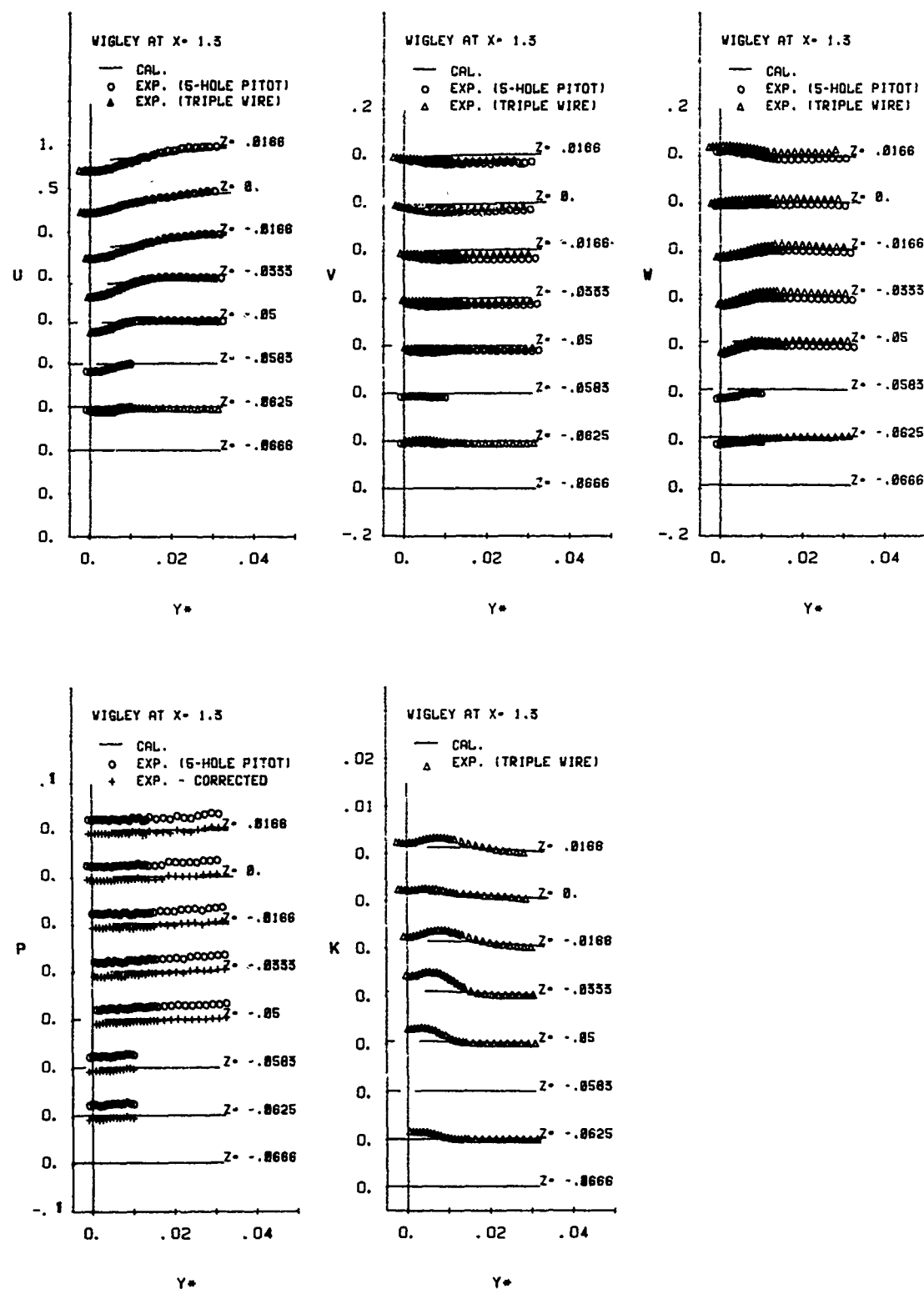


Fig. 18 Profiles of velocity components (U, V, W), pressure (P), and turbulent kinetic energy (k) compared with data of Sarda (k) $X = 1.3$

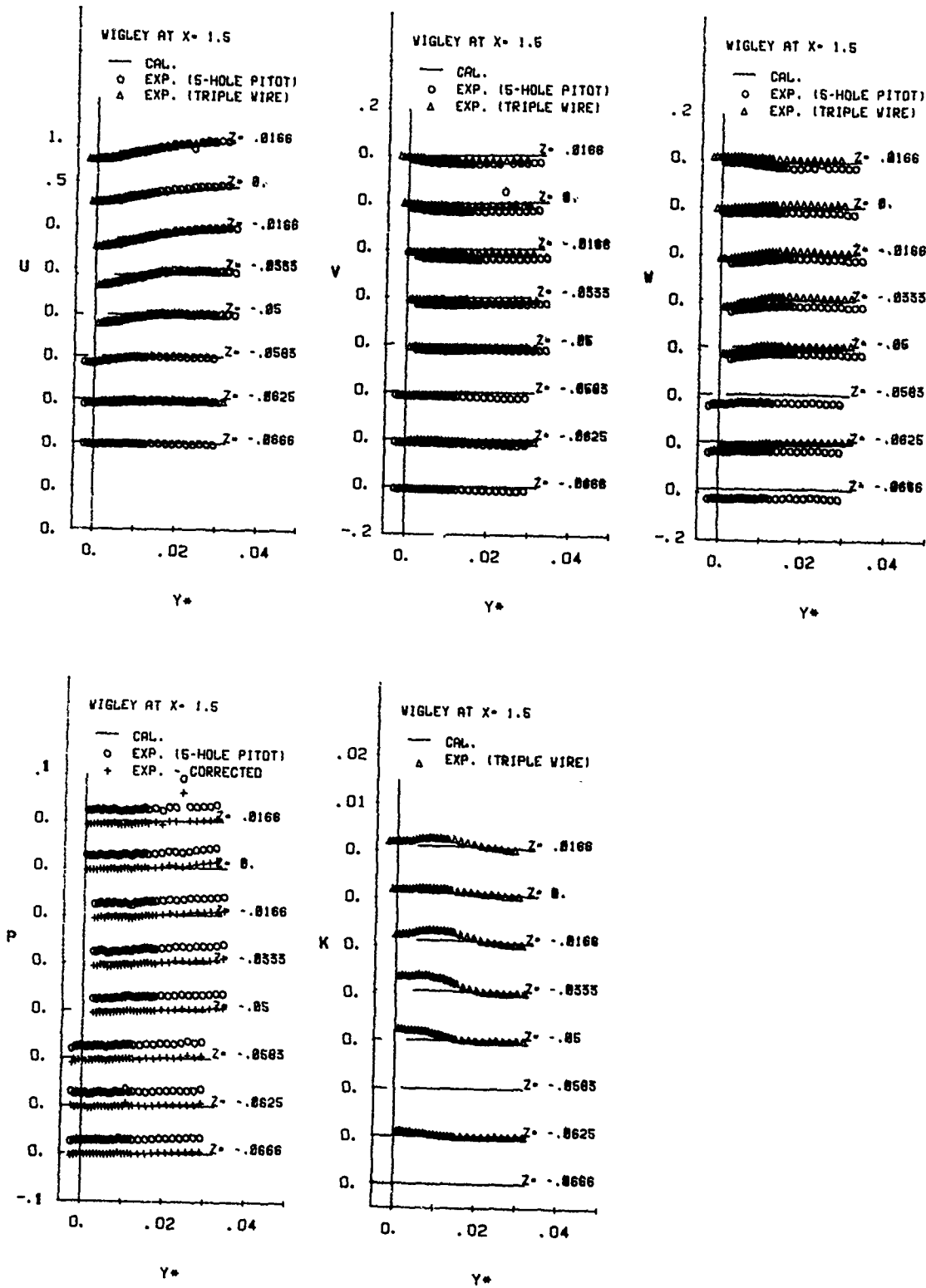


Fig. 18 Profiles of velocity components (U, V, W), pressure (P), and turbulent kinetic energy (k) compared with data of Sarda
(I) $X = 1.5$

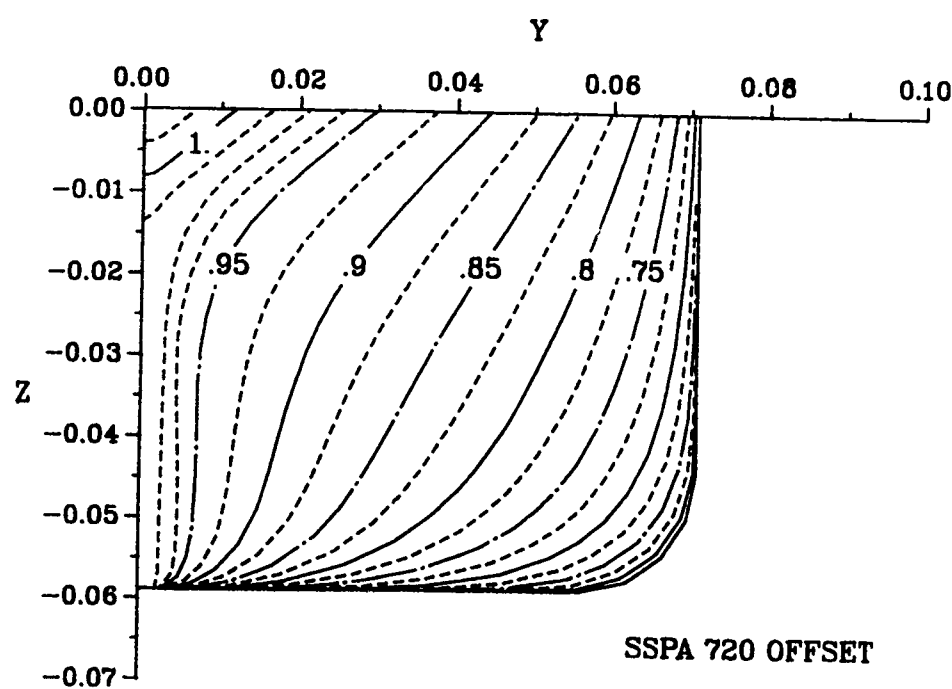
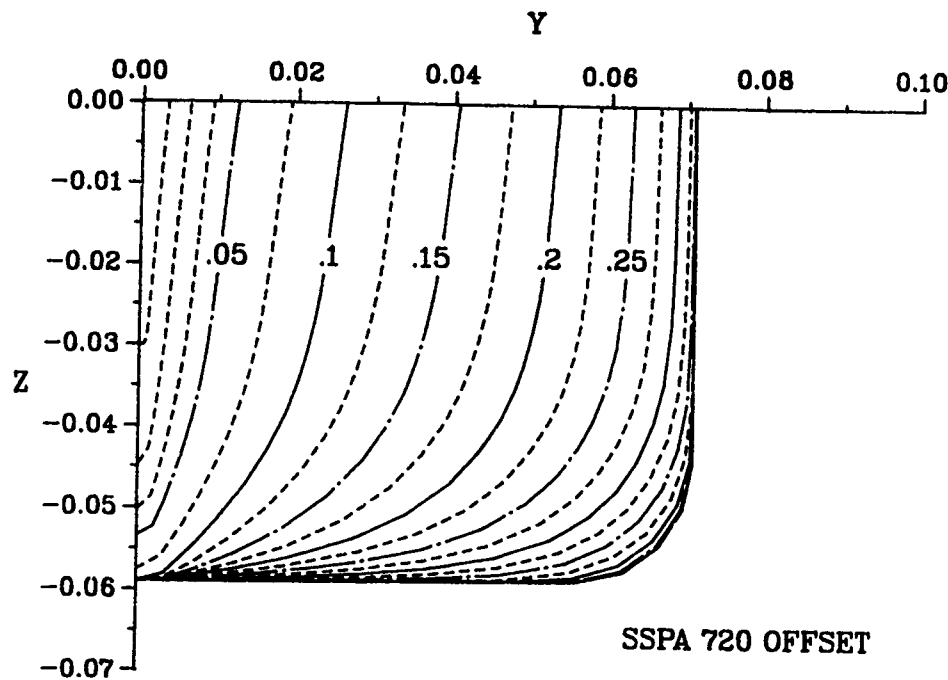


Fig. 19 SSPA 720 Cargo Liner
(a) forebody (b) afterbody

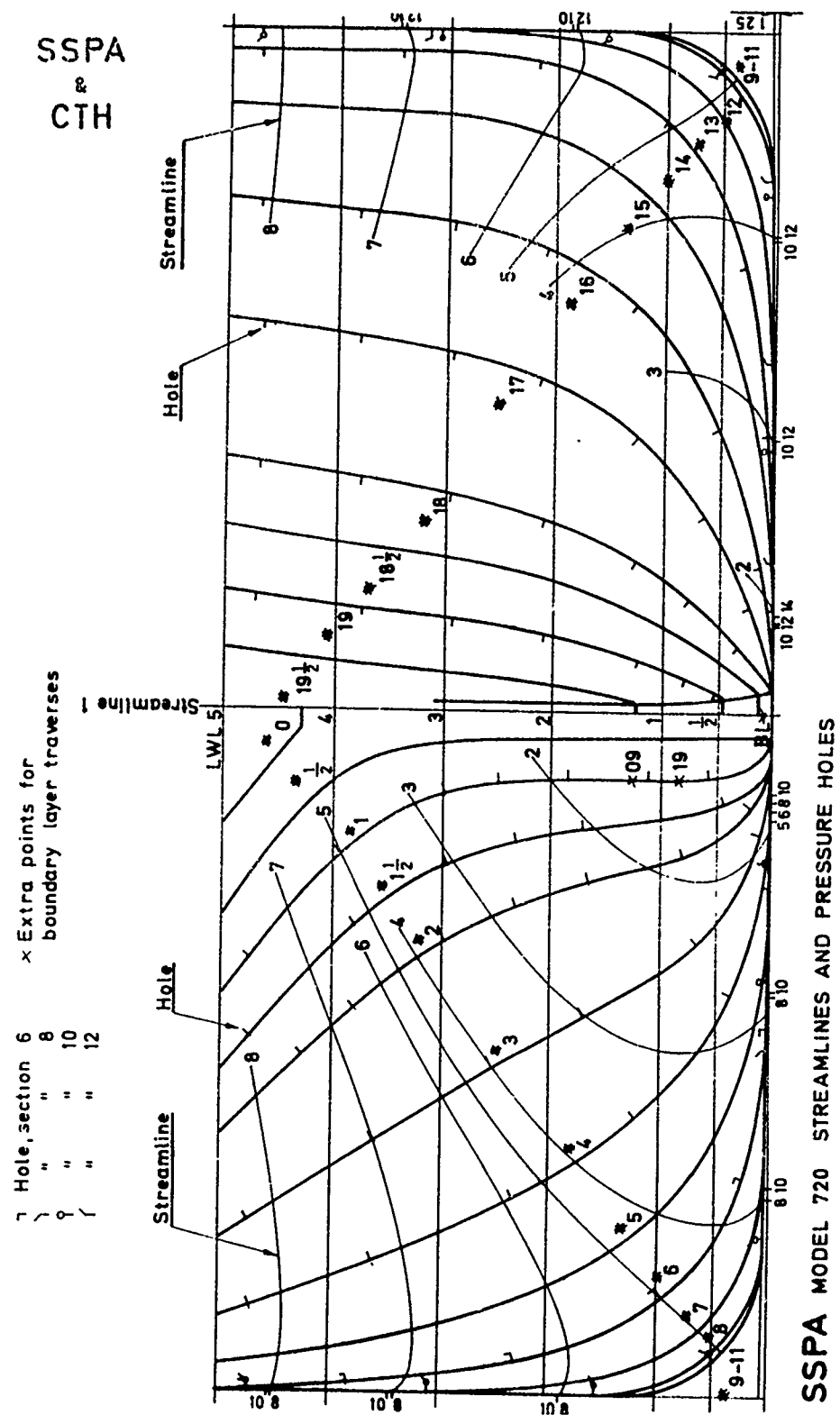


Fig. 19 SSPA 720 Cargo Liner
(c) inviscid streamlines and measurement stations, Larsson (1974)

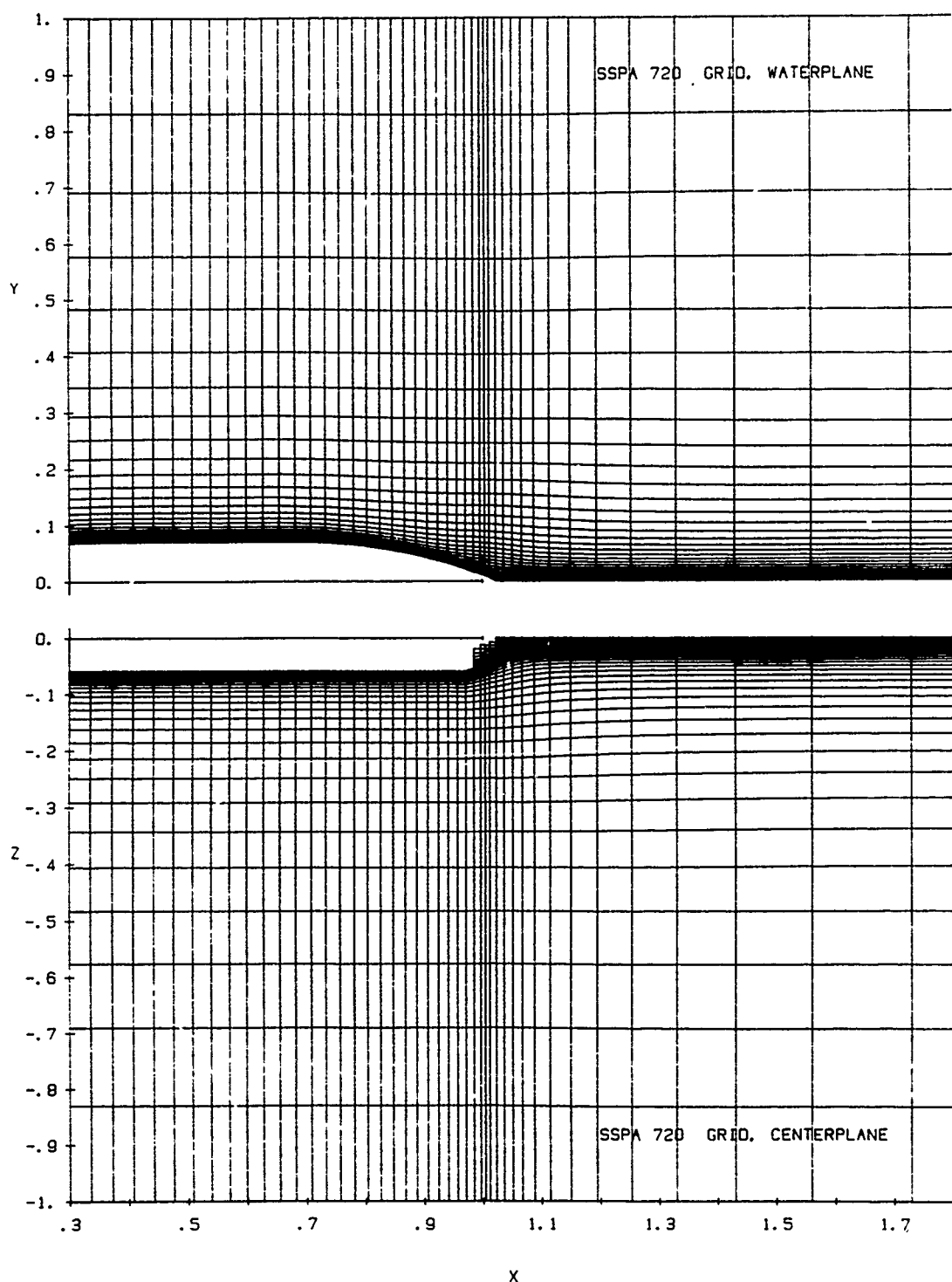


Fig. 20 Typical views of the numerical grid
(a) symmetry planes

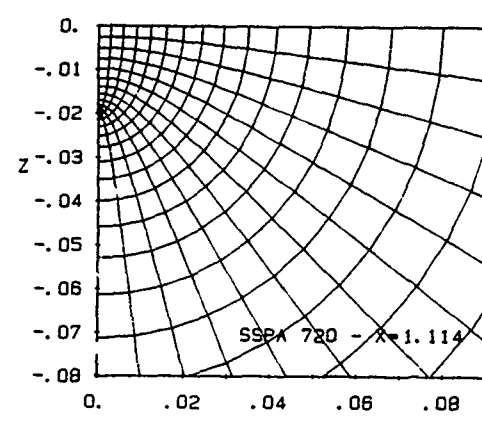
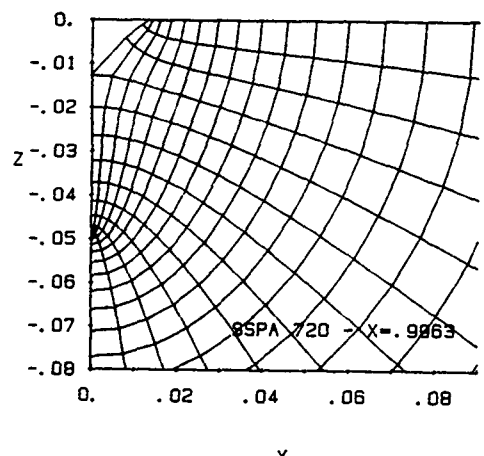
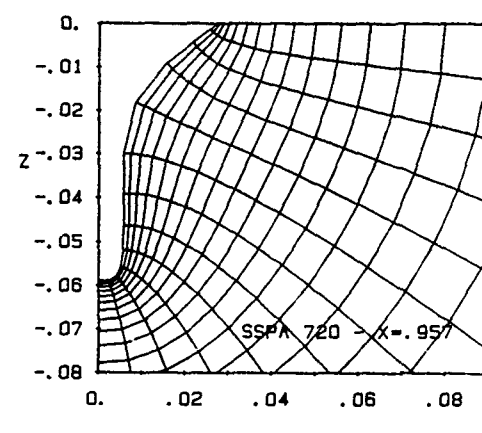
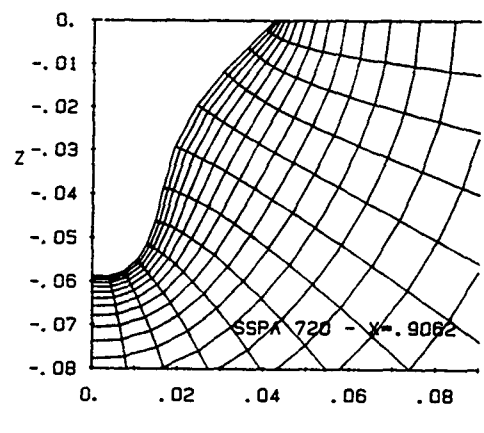
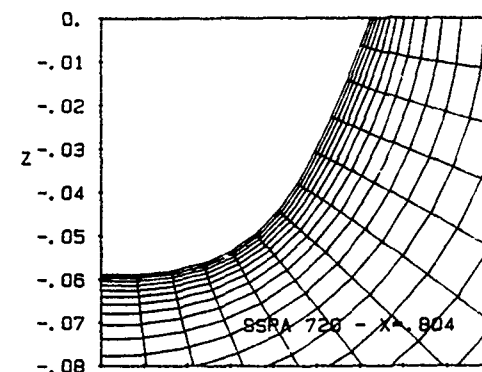
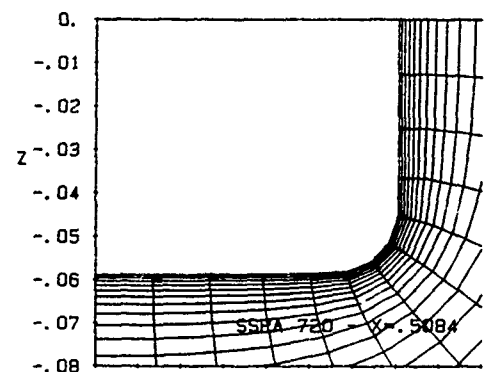


Fig. 20 Typical views of the numerical grid
(b) transverse sections

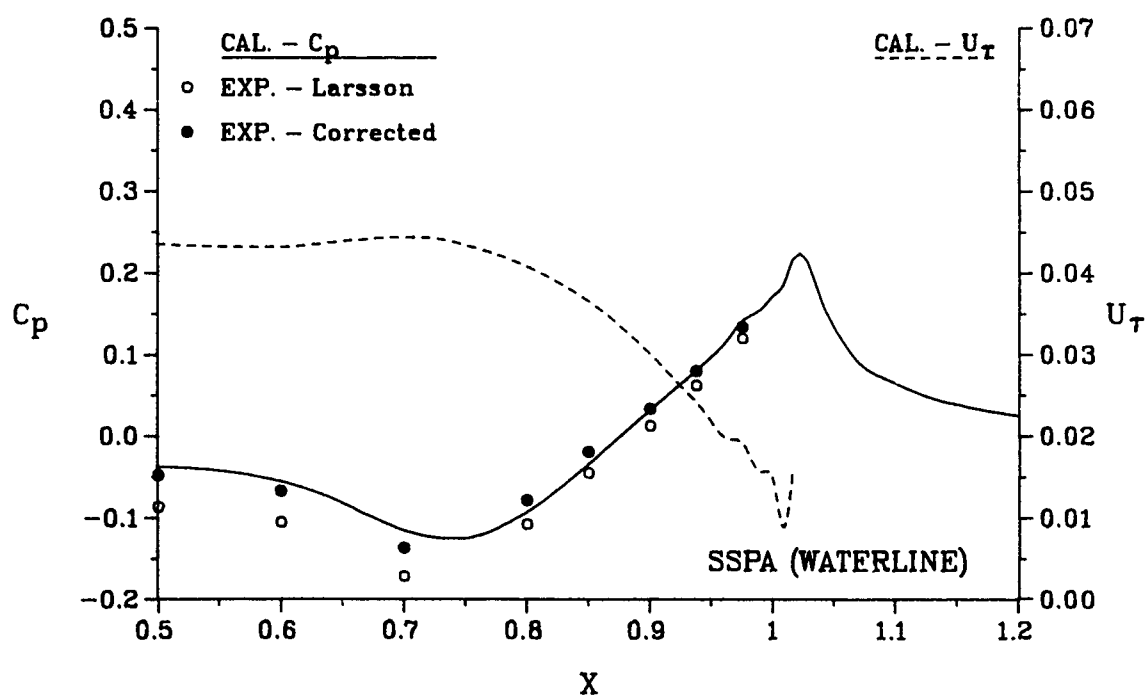
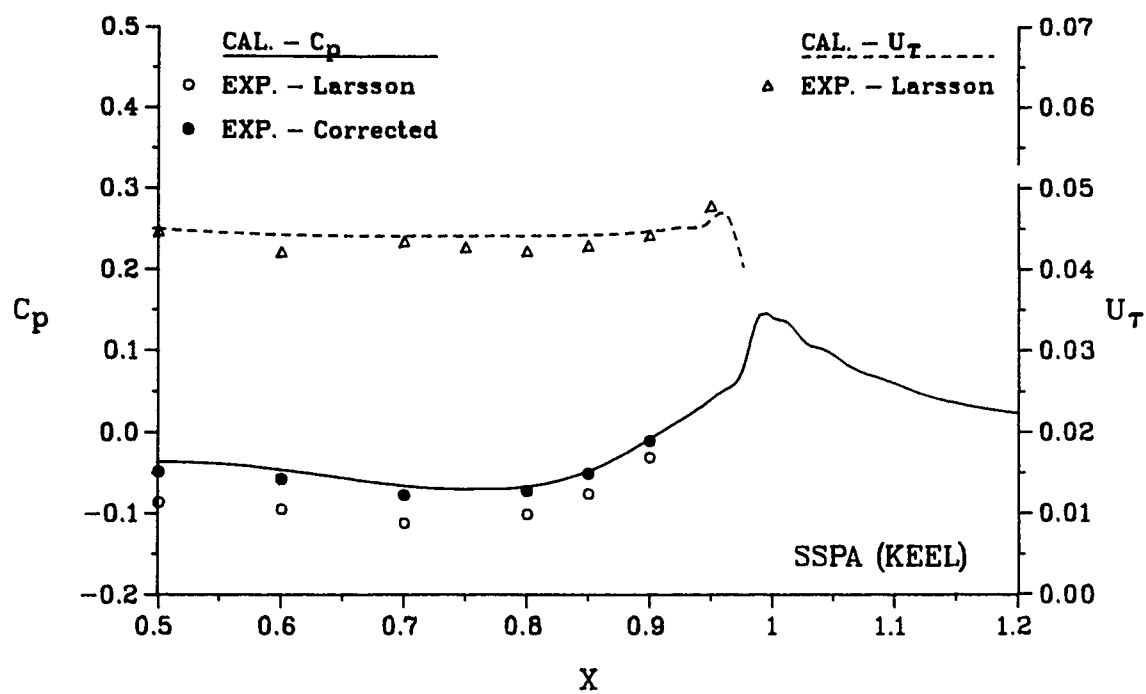


Fig. 21 Pressure and friction velocity along the keel and waterline

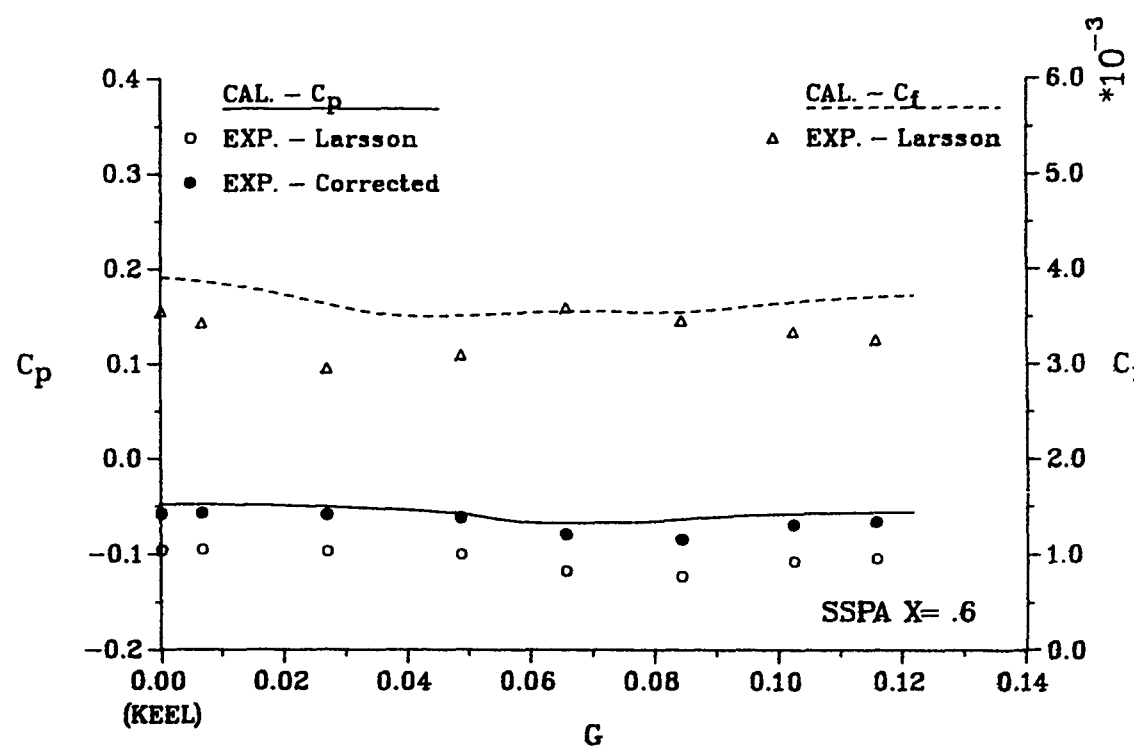
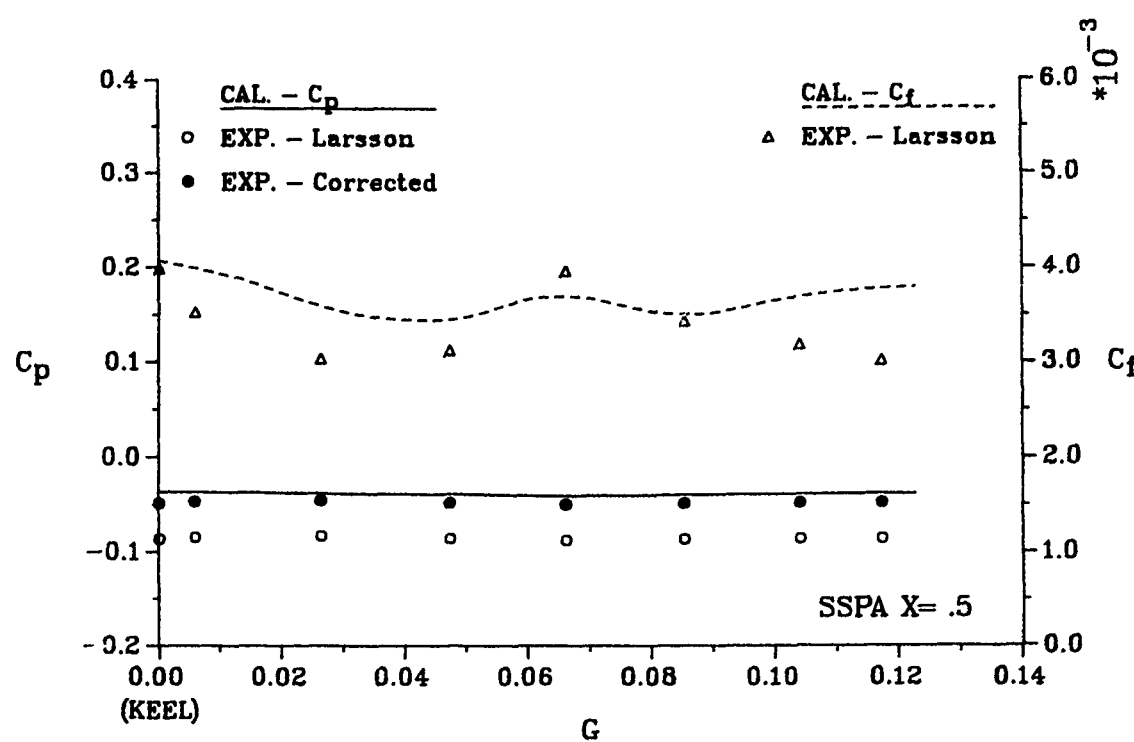


Fig. 22 Girthwise variation of pressure and friction coefficients
(a) $X = 0.5$; (b) $X = 0.6$

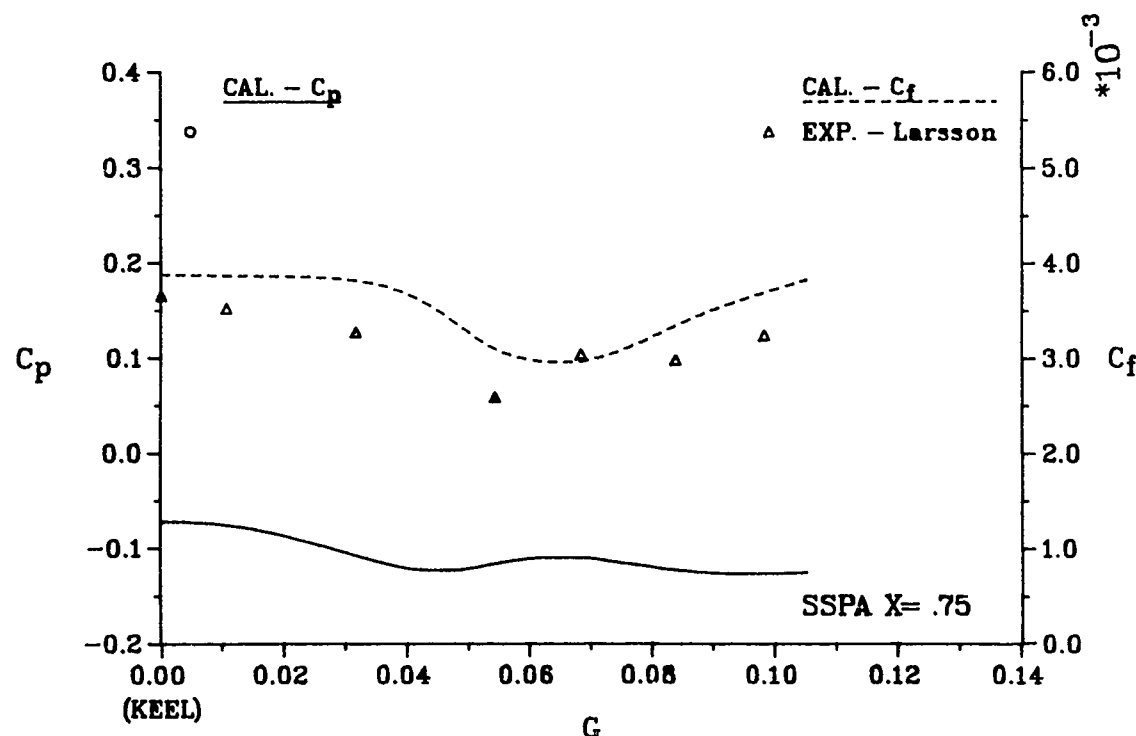
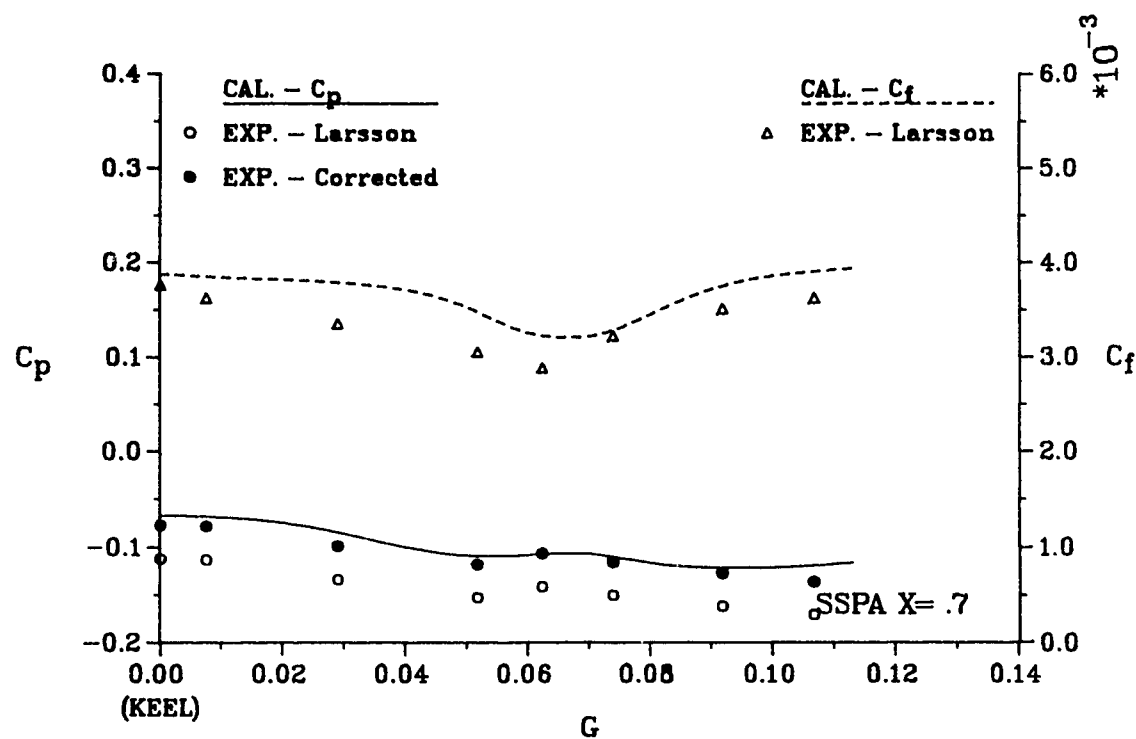


Fig. 22 Girthwise variation of pressure and friction coefficients
(c) $X = 0.7$; (d) $X = 0.75$

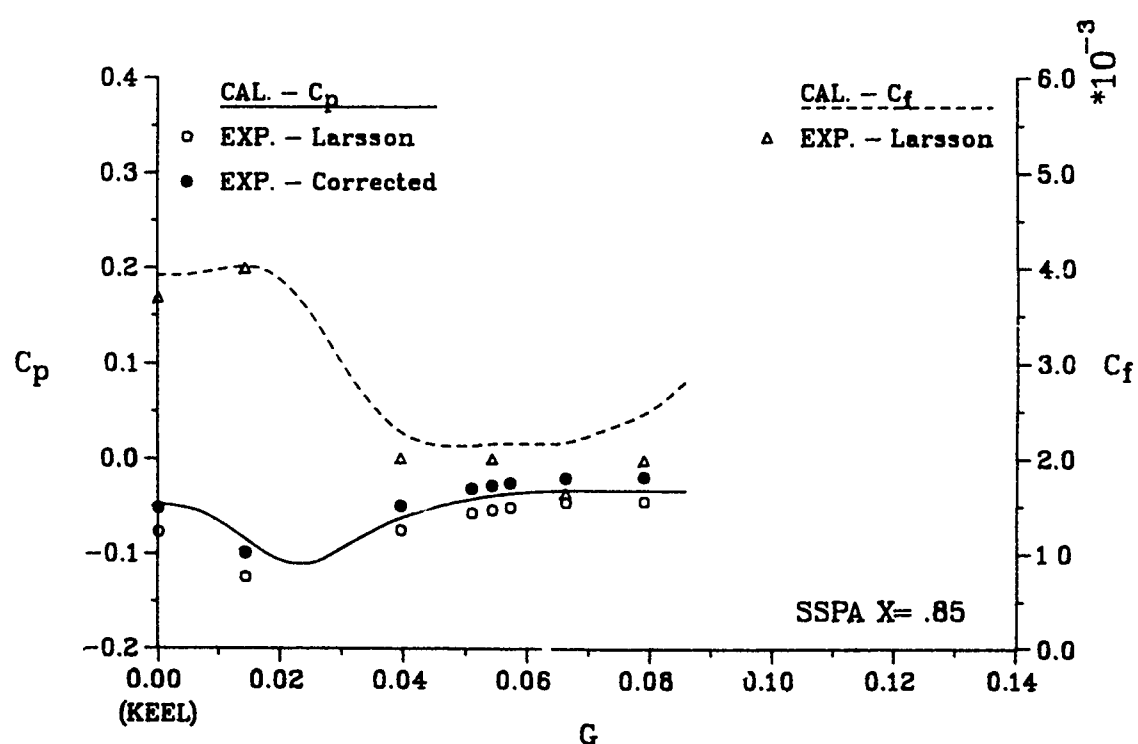
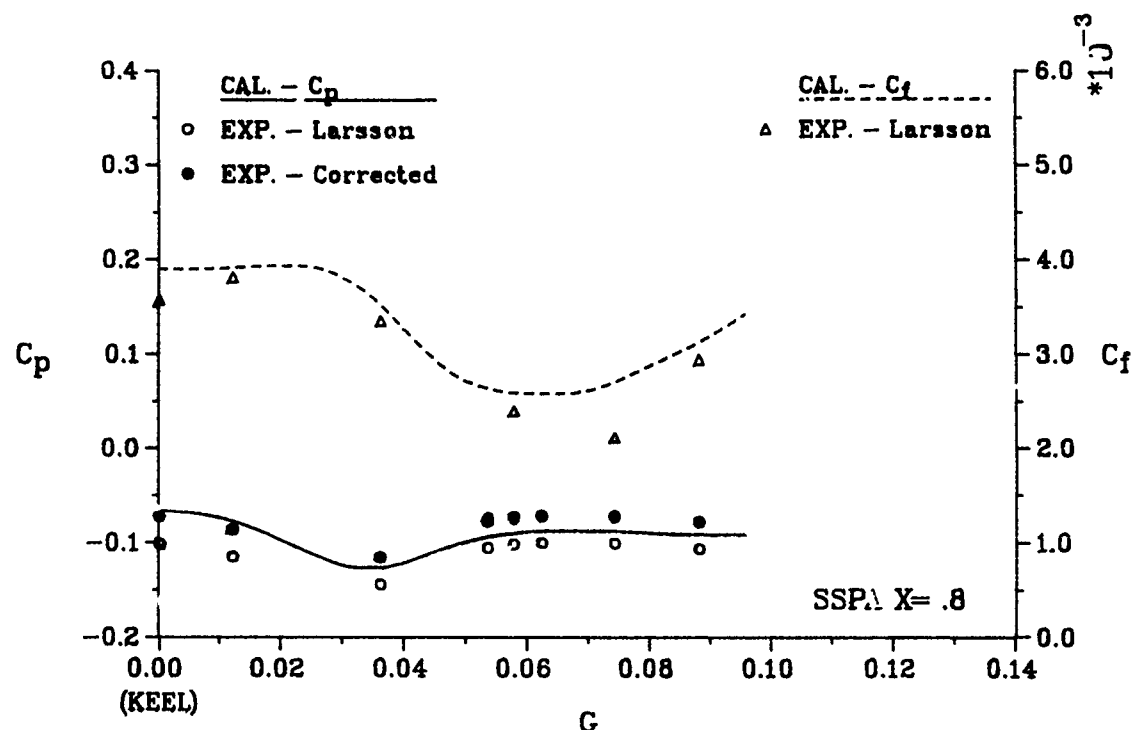


Fig. 22 Girthwise variation of pressure and friction coefficients
(e) $X = 0.8$; (f) $X = 0.85$

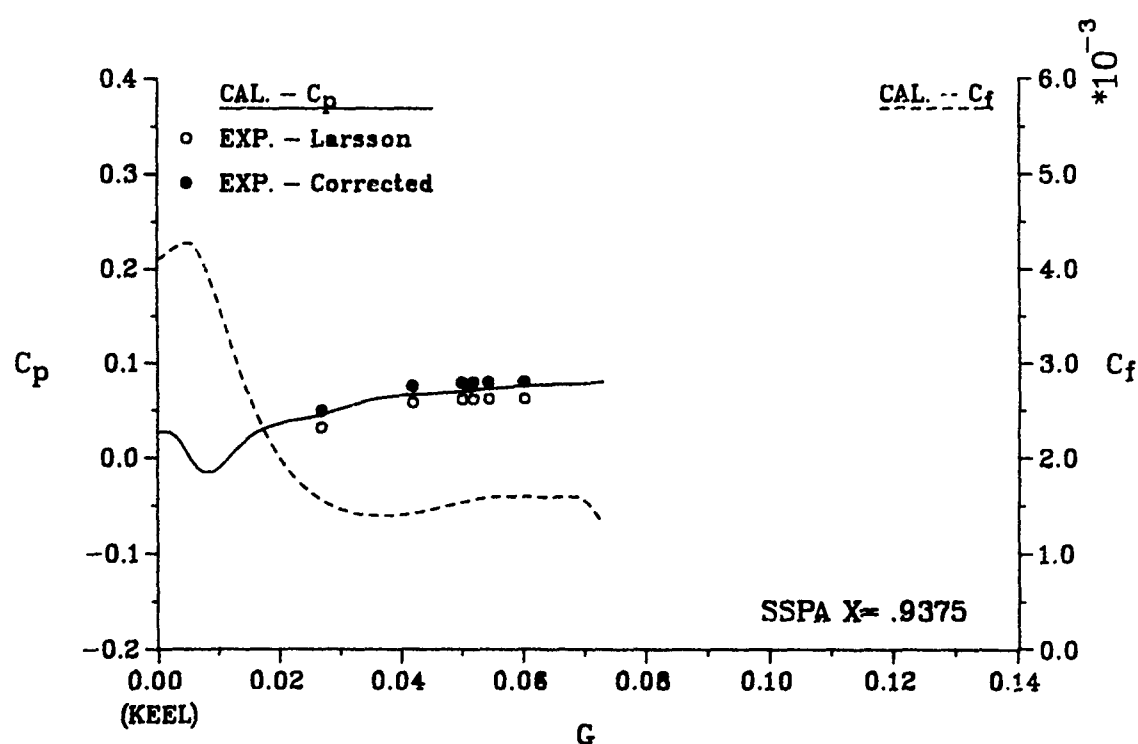
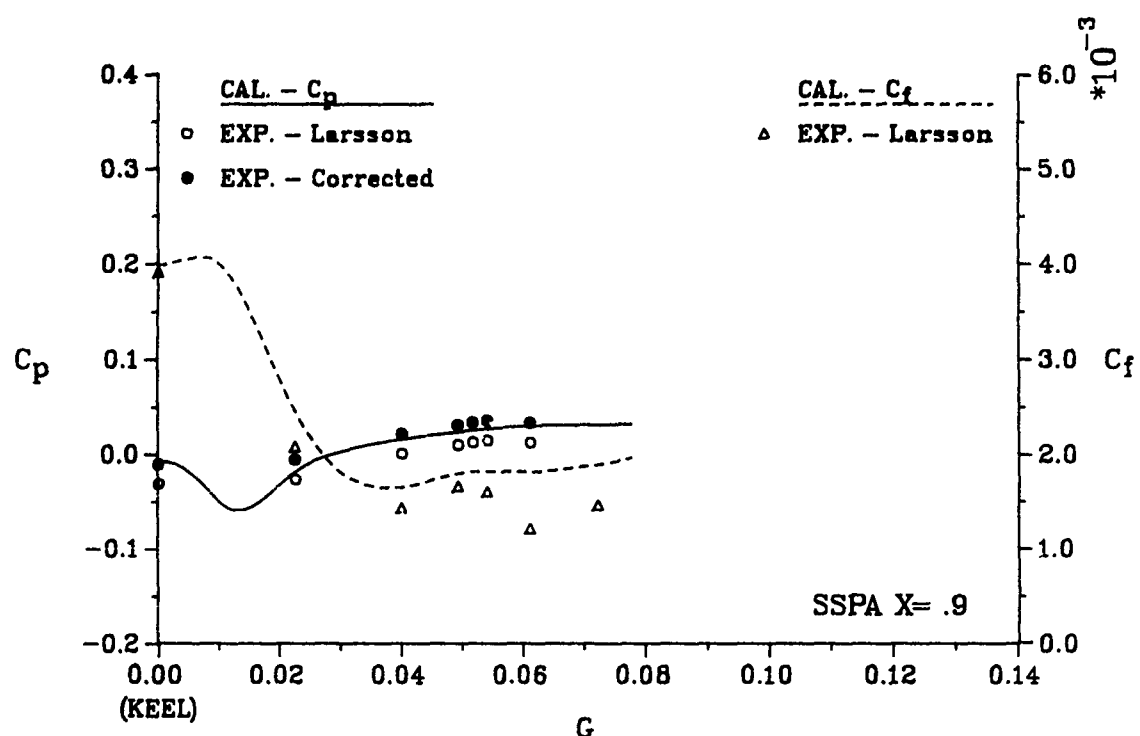


Fig. 22 Girthwise variation of pressure and friction coefficients
(g) $X = 0.9$; (h) $X = 0.9375$

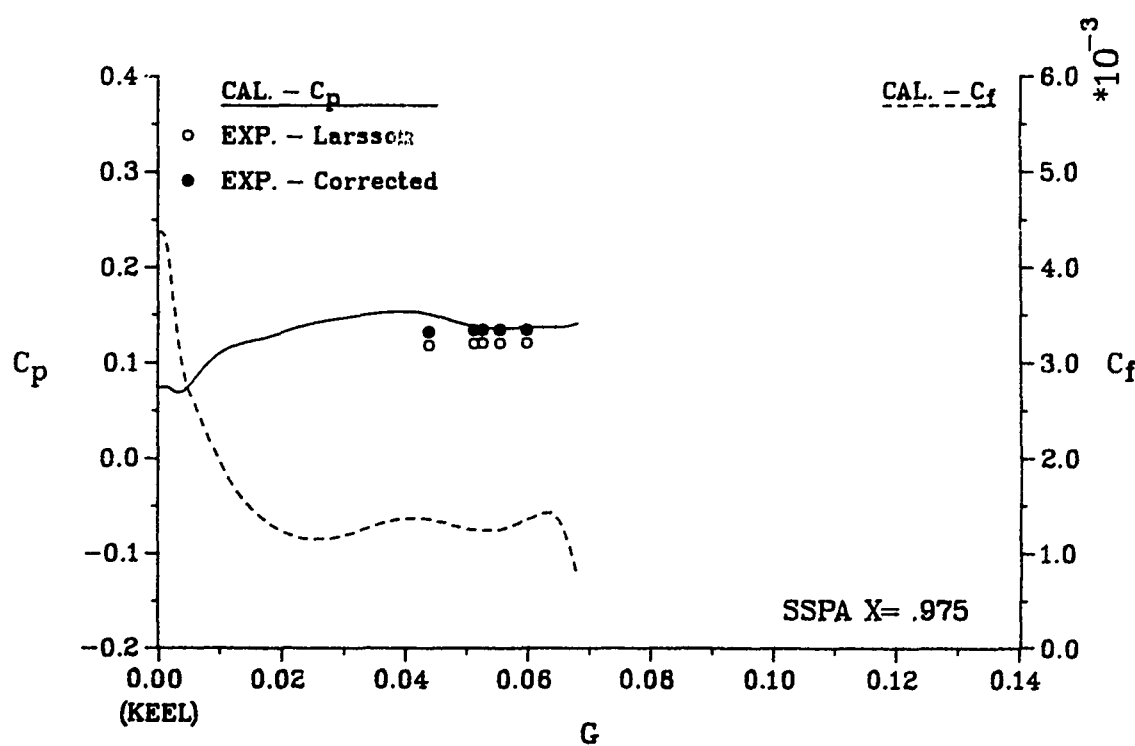
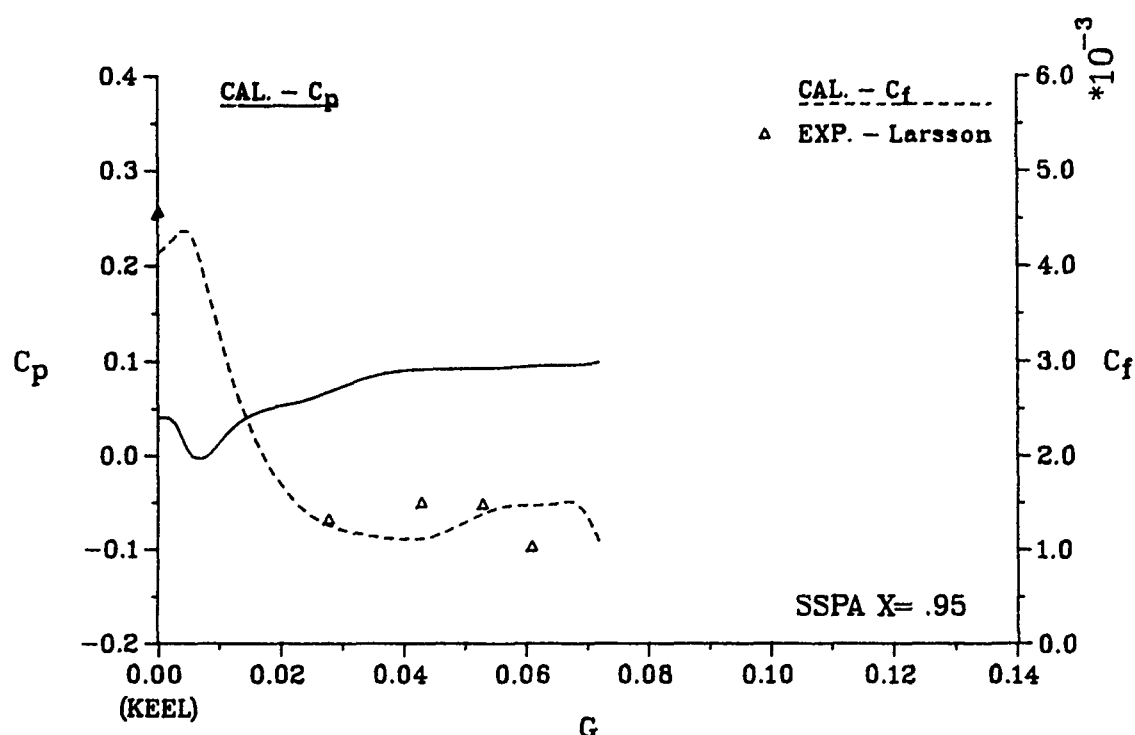


Fig. 22 Girthwise variation of pressure and friction coefficients
(i) $X = 0.95$; (j) $X = 0.975$

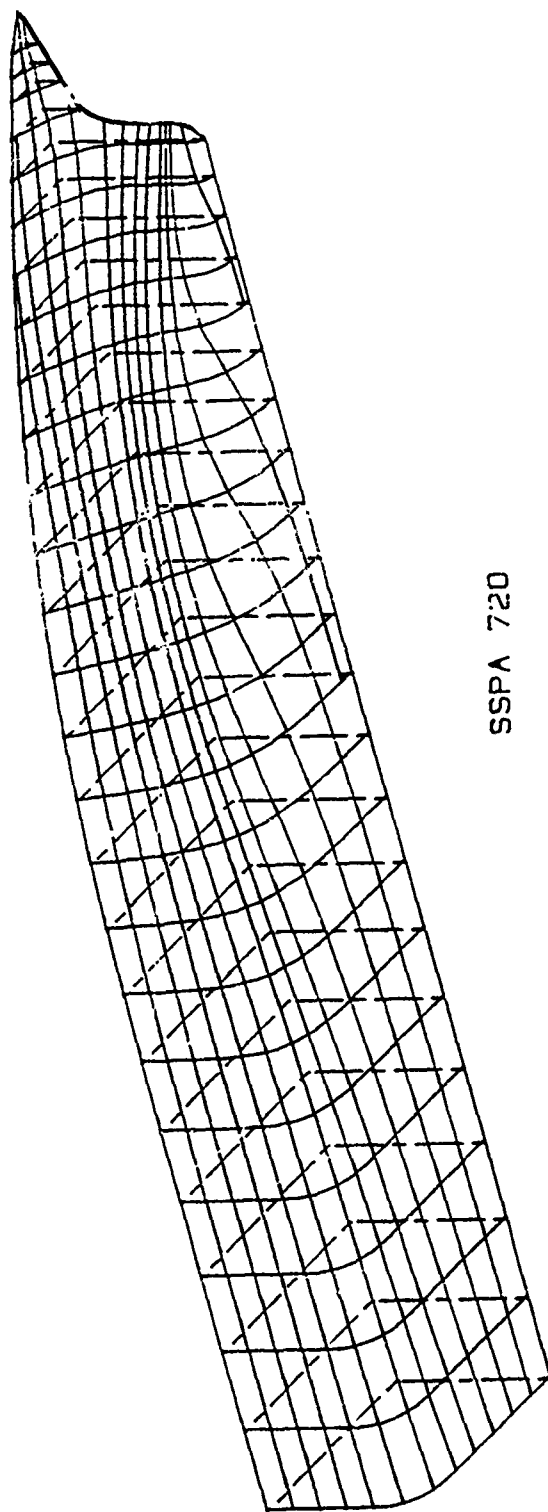


Fig. 23 Calculated wall streamlines

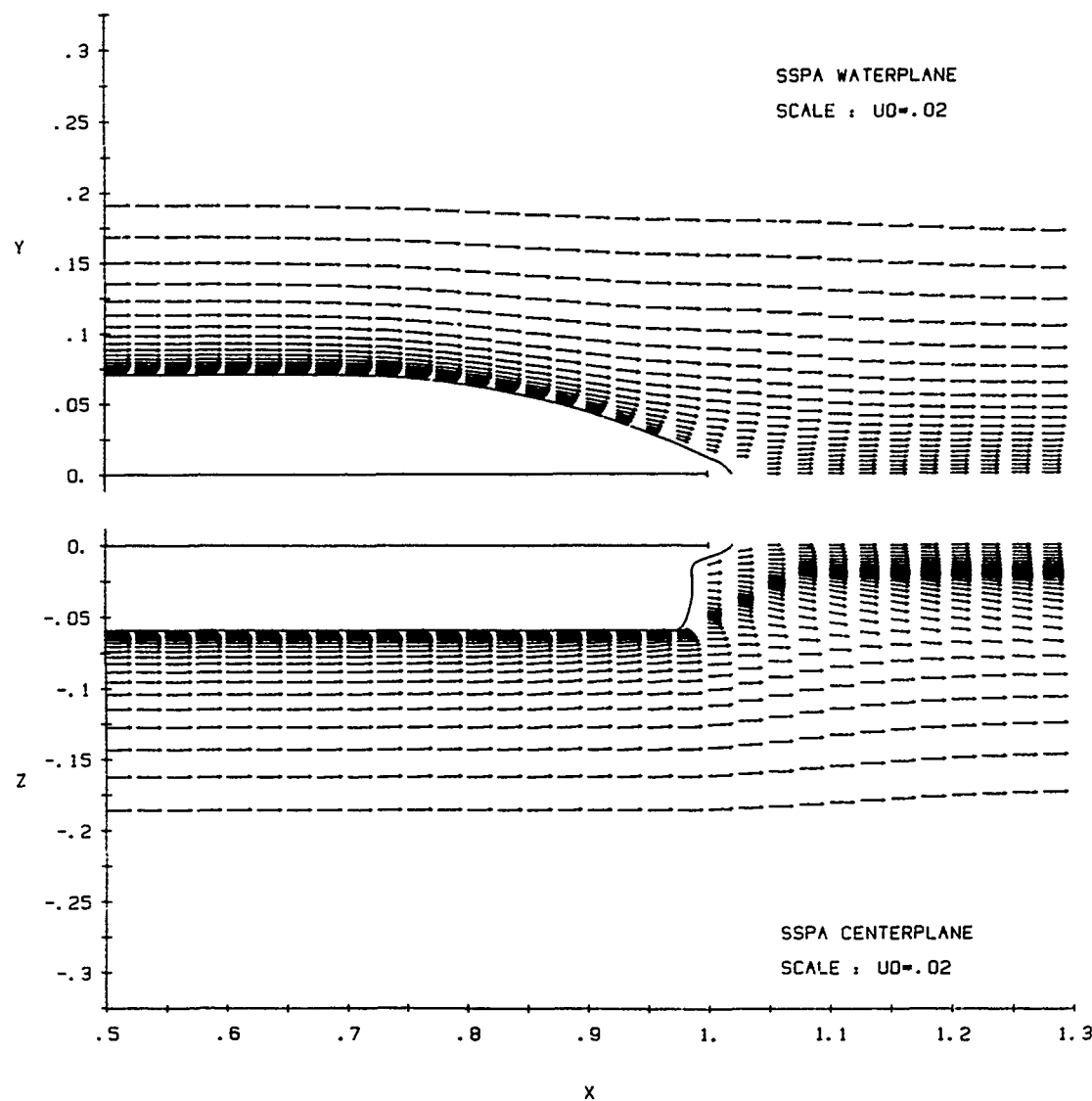


Fig. 24 Velocity vectors in the waterplane (top) and in the vertical centerplane (bottom)

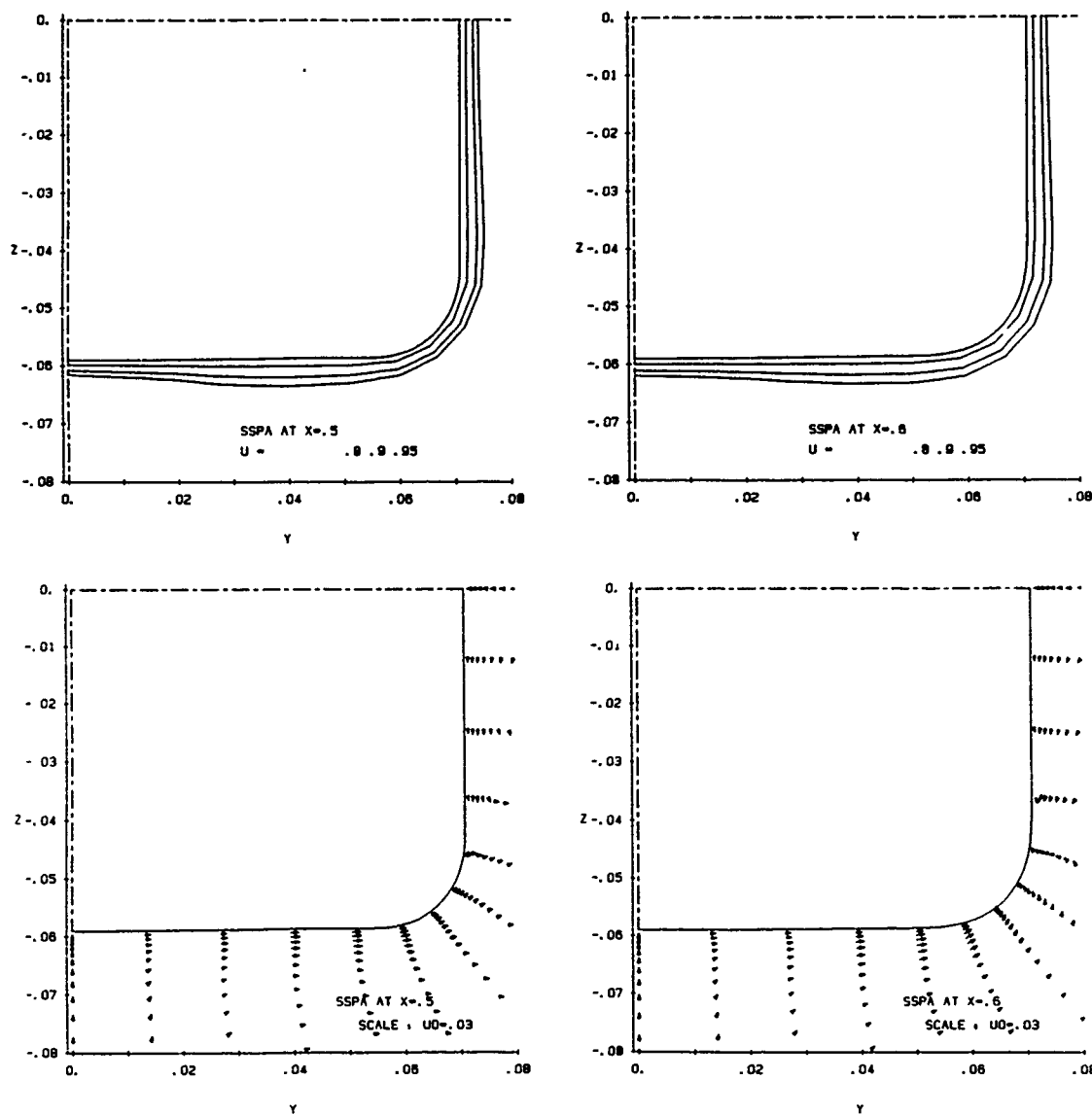


Fig. 25 Velocity field in transverse sections ; (a) $X = 0.5$; (b) $X = 0.6$
 Top: contours of axial velocity (U), Bottom: velocity vectors in transverse sections (V, W)

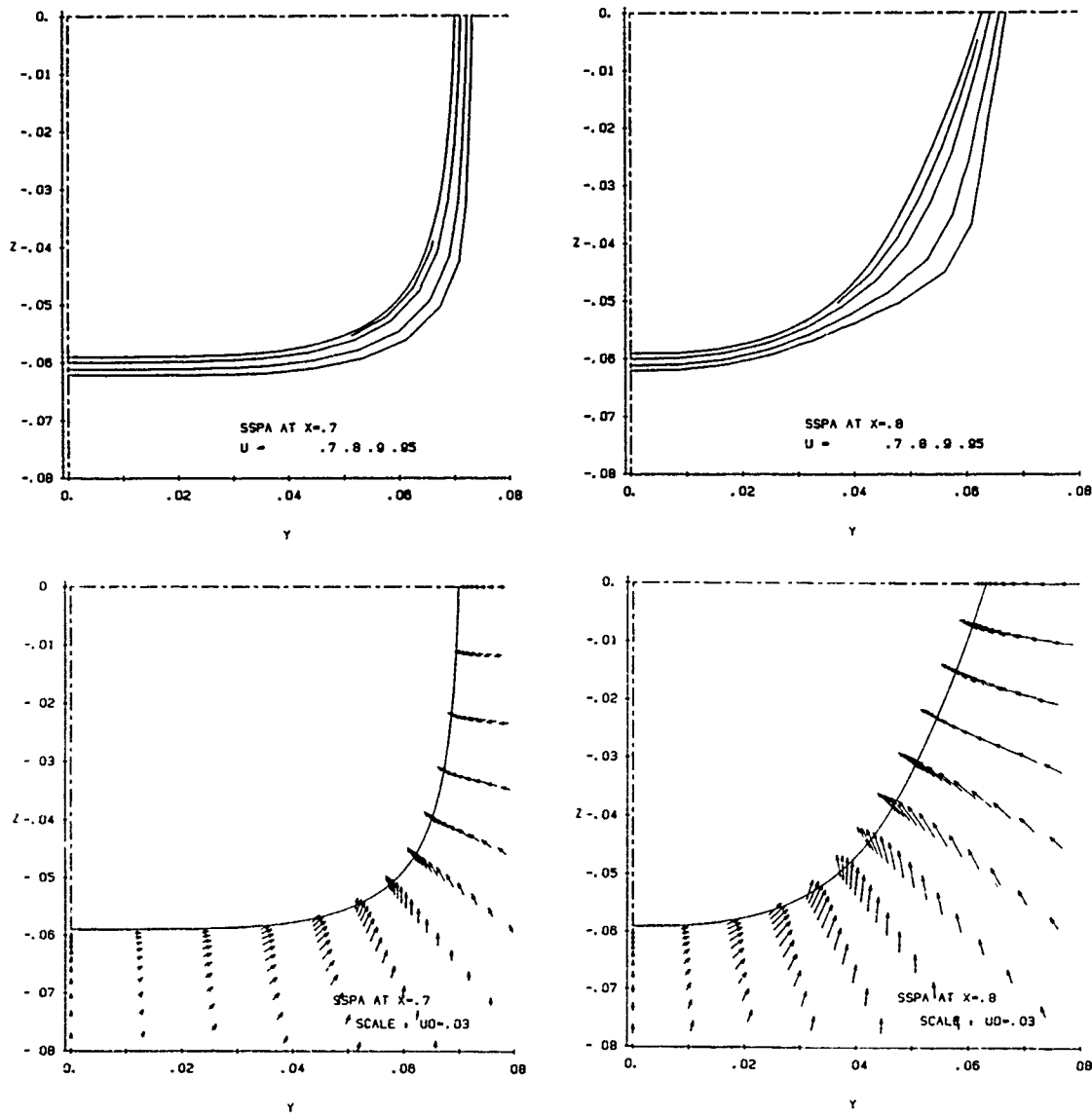


Fig. 25 Velocity field in transverse sections ; (c) $X = 0.7$; (d) $X = 0.8$
 Top: contours of axial velocity (U), Bottom: velocity vectors in transverse sections (V, W)

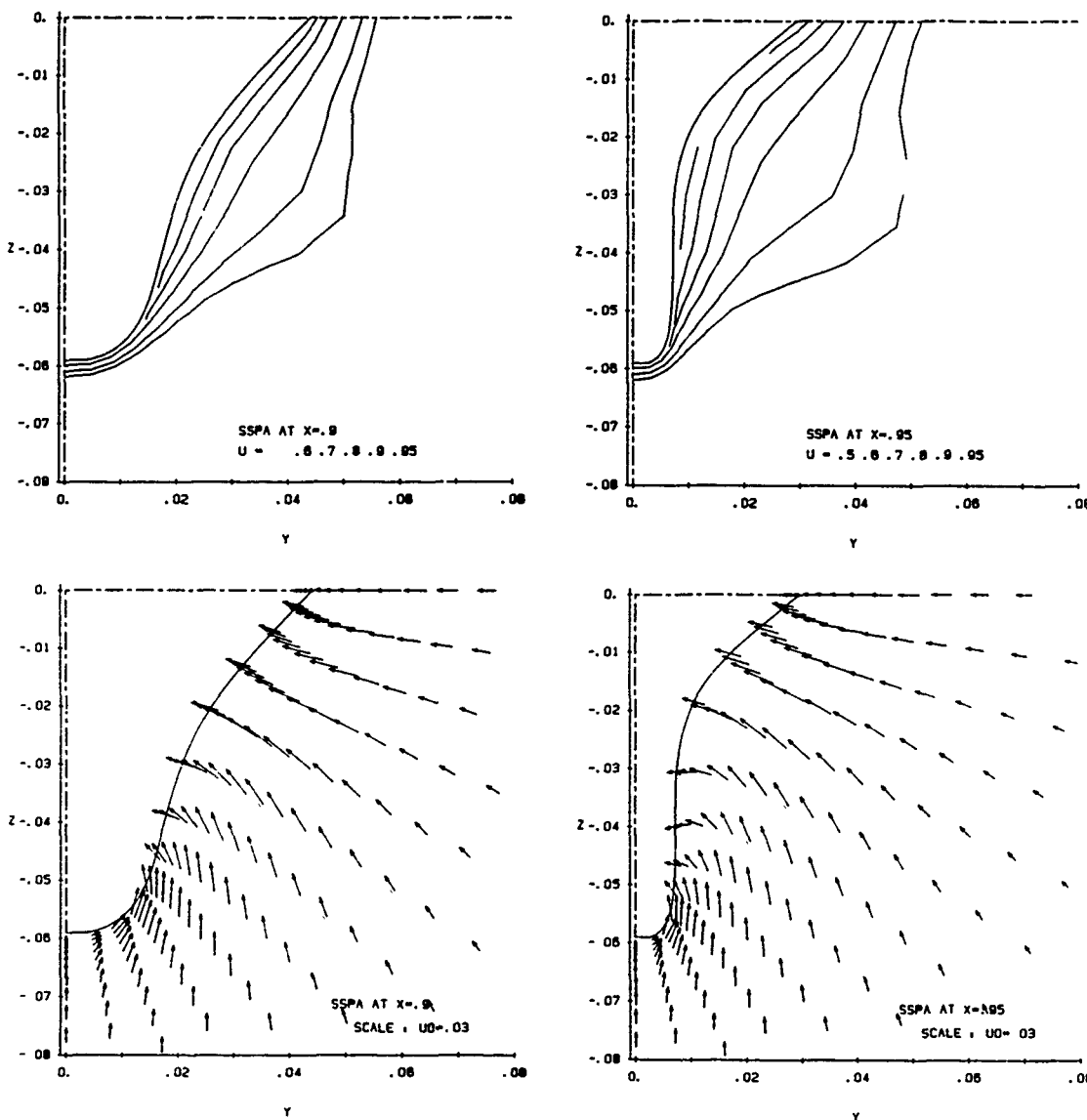


Fig. 25 Velocity field in transverse sections ; (e) $X = 0.9$; (f) $X = 0.95$
 Top: contours of axial velocity (U), Bottom: velocity vectors in transverse sections (V, W)

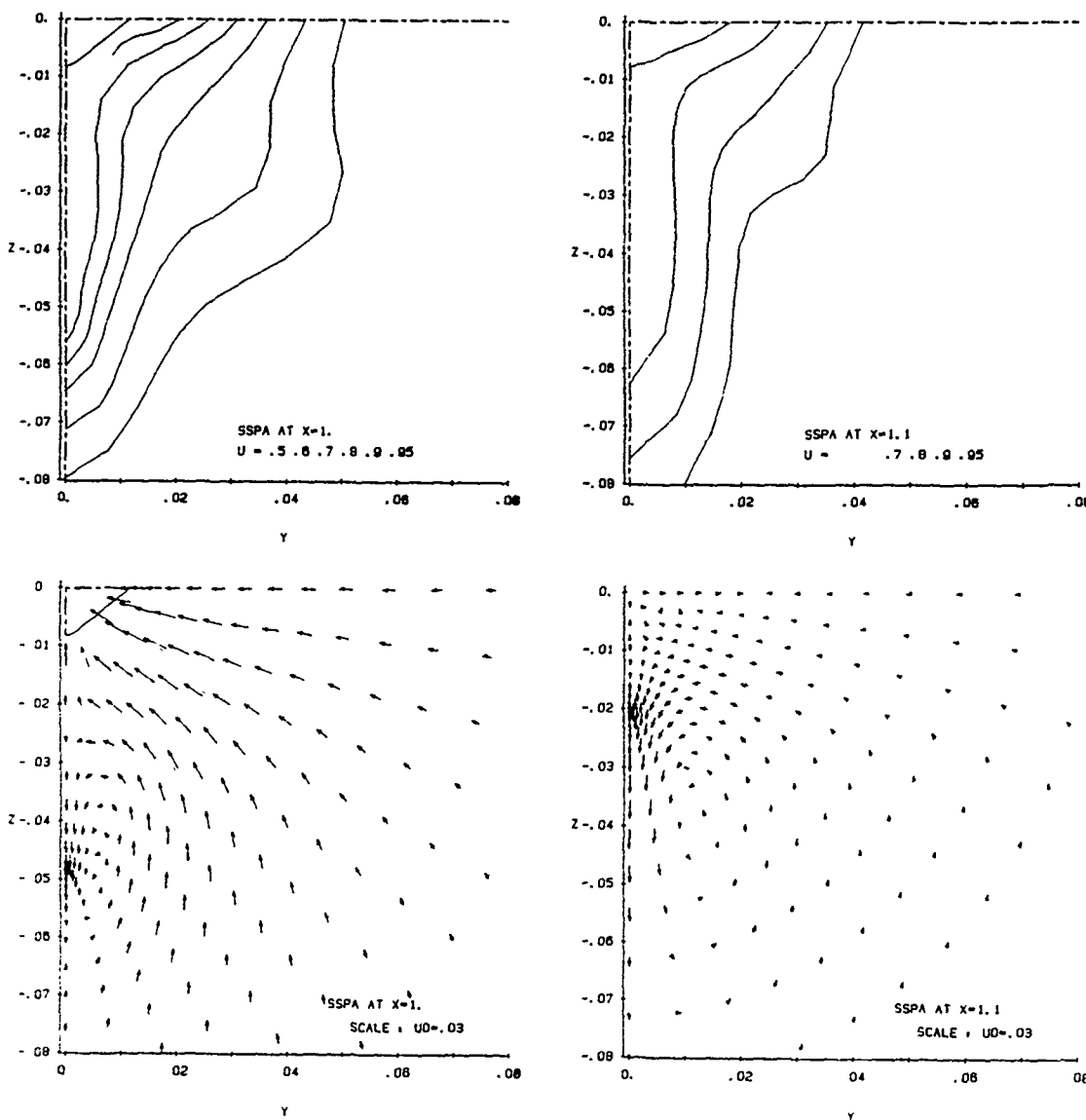
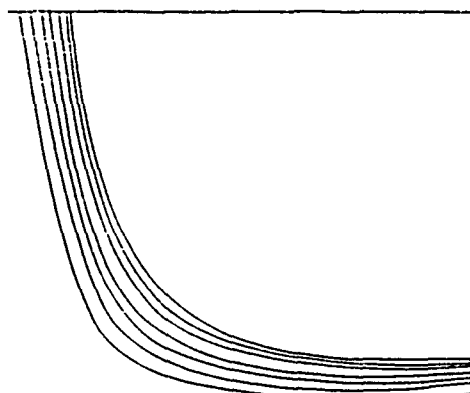
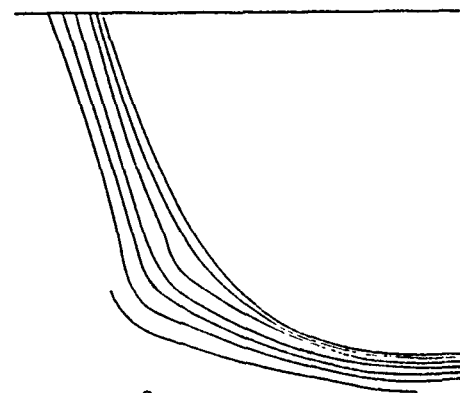


Fig. 25 Velocity field in transverse sections ; (g) $X = 1.0$; (h) $X = 1.1$
 Top: contours of axial velocity (U), Bottom: velocity vectors in transverse sections (V, W)



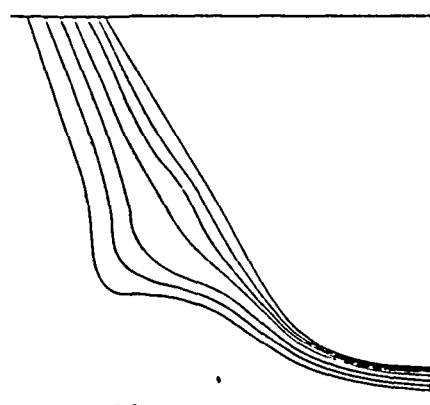
$x = .75$

$(u/U_\infty = 0.7, 0.8, 0.9, 0.95, 1.0, 1.05)$ SSPA model



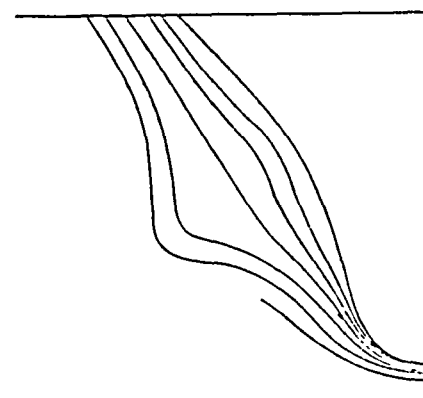
$x = .8$

$(u/U_\infty = 0.7, 0.8, 0.9, 0.95, 1.0, 1.05)$ SSPA model



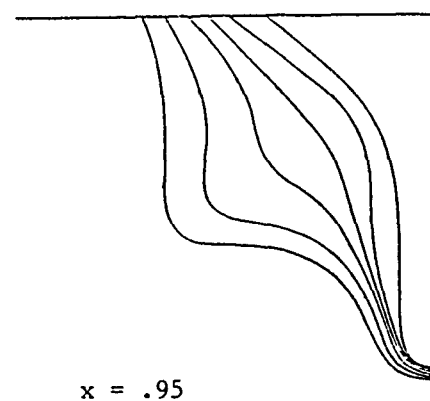
$x = .85$

$(u/U_\infty = 0.6, 0.7, 0.8, 0.9, 0.95, 1.0)$ SSPA model



$x = .9$

$(u/U_\infty = 0.6, 0.7, 0.8, 0.9, 0.95, 1.0)$ SSPA model



$x = .95$

$(u/U_\infty = 0.6, 0.7, 0.8, 0.9, 0.95)$ SSPA model

Fig. 26 Contours of velocity magnitude from experiments, reconstructed by Broberg and Larsson (1984)

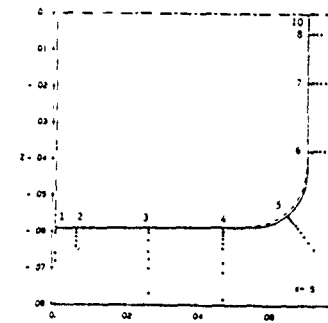
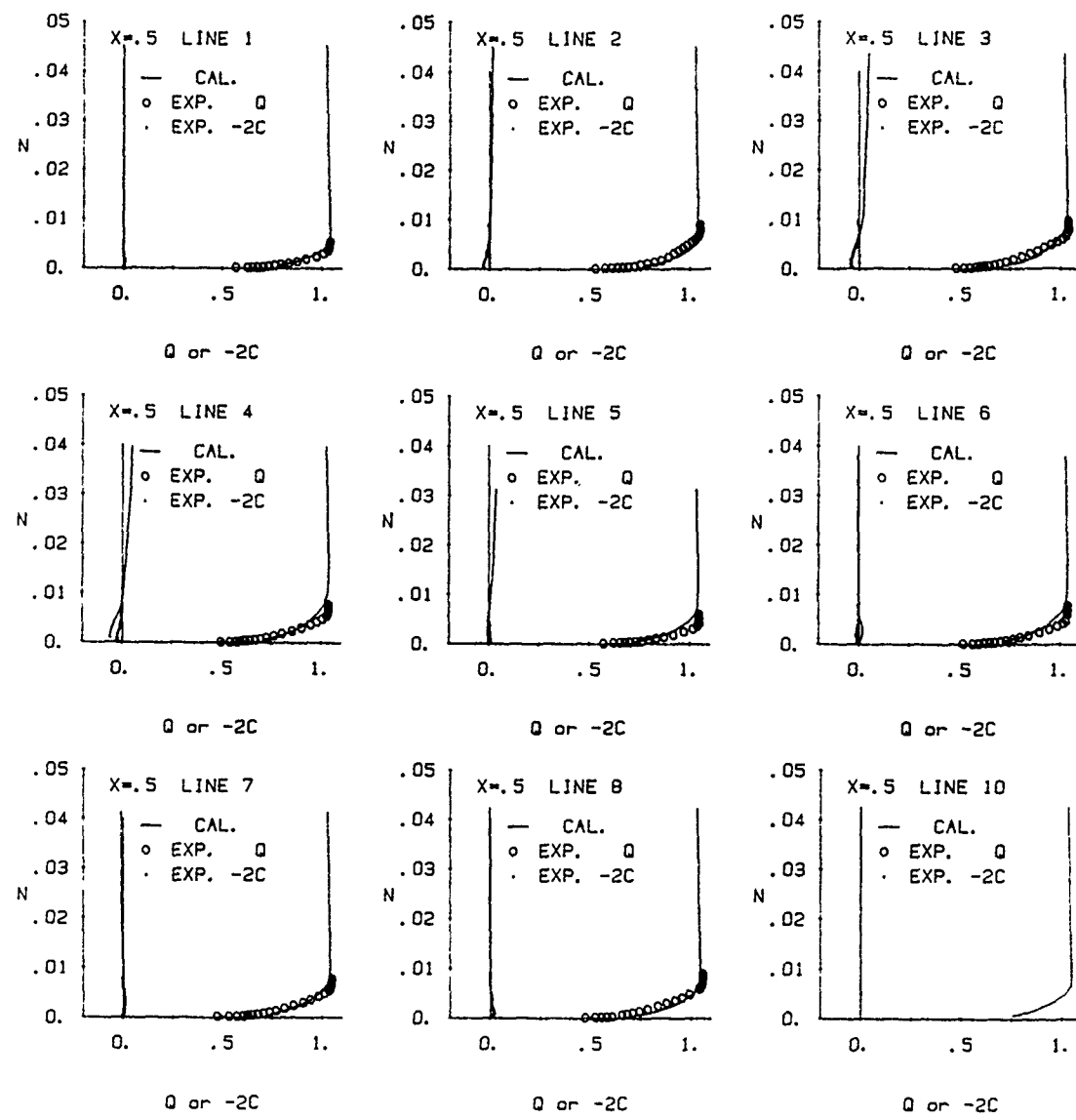


Fig. 27 Comparison between calculations and experiment
 (a) Profiles of resultant velocity (Q) and crossflow velocity (C) : $X = 0.5$

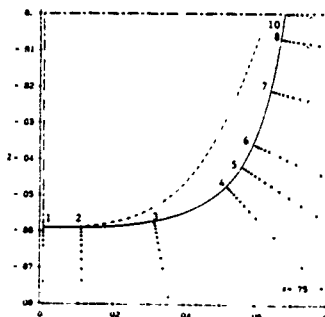
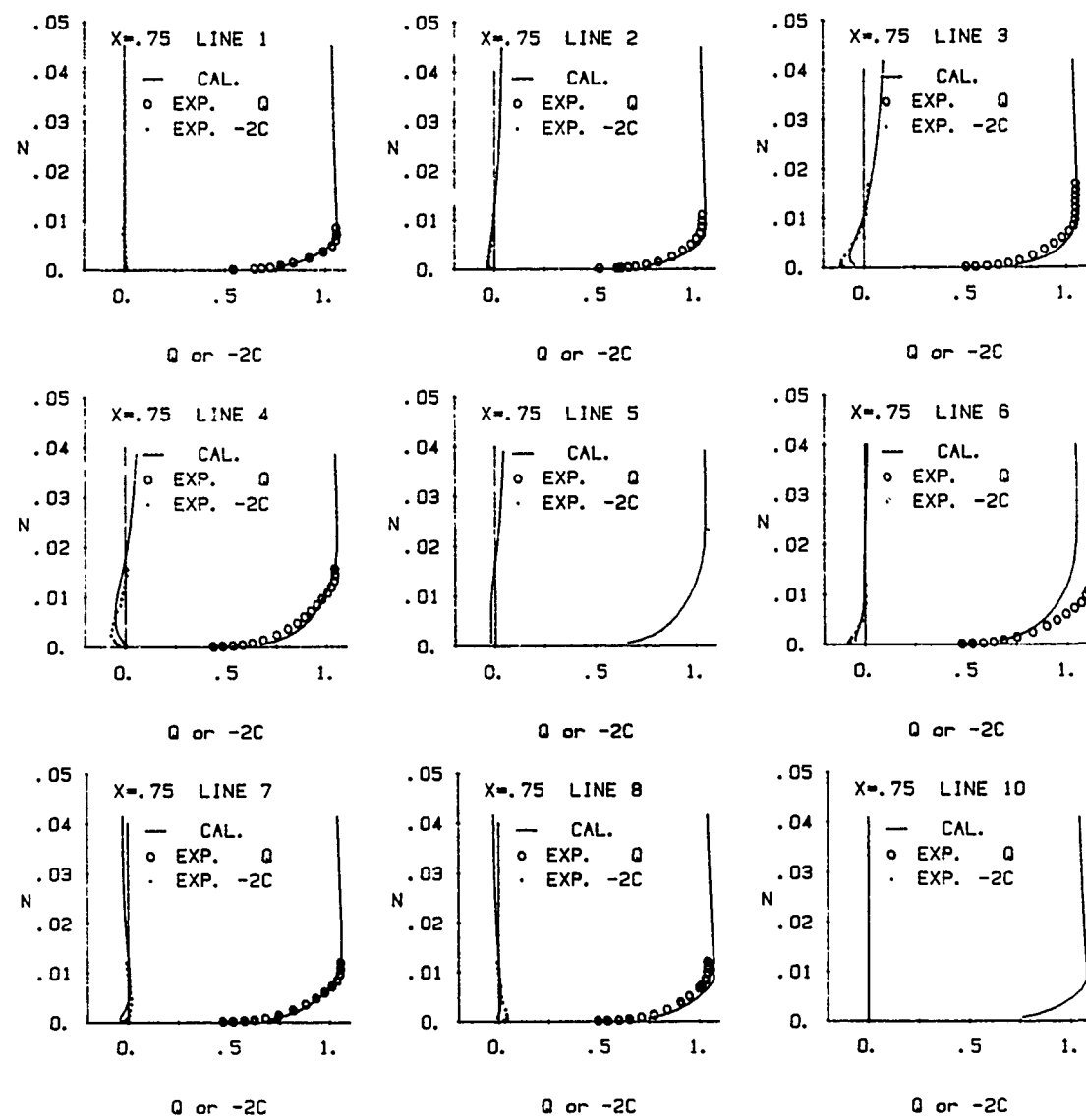


Fig. 27 Comparison between calculations and experiment
 (a) Profiles of resultant velocity (Q) and crossflow velocity (C) : $X = 0.75$

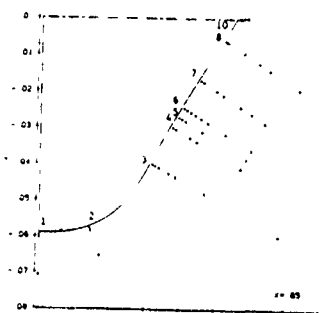
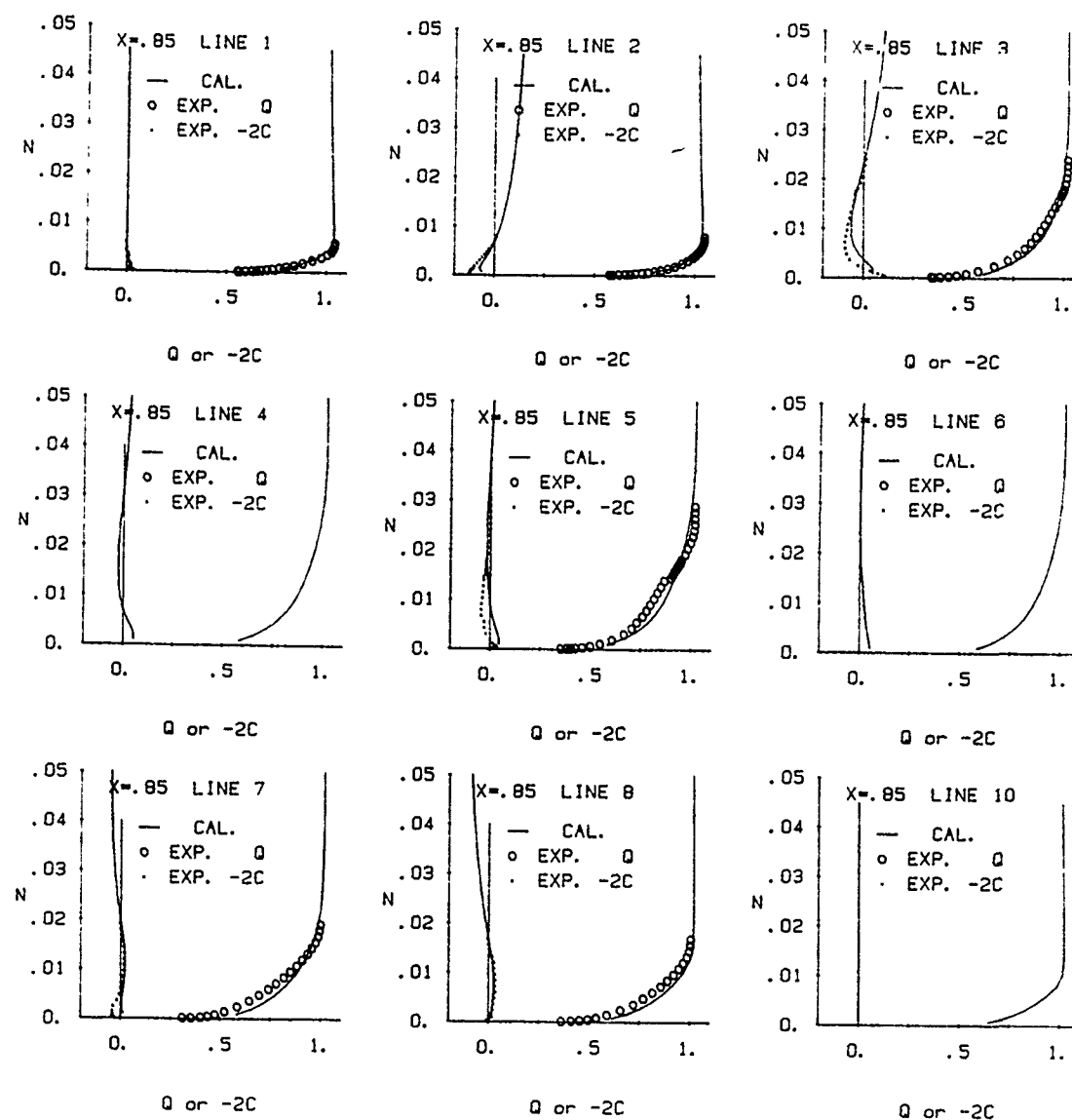


Fig. 27 Comparison between calculations and experiment
 (a) Profiles of resultant velocity (Q) and crossflow velocity (C) : $X = 0.85$

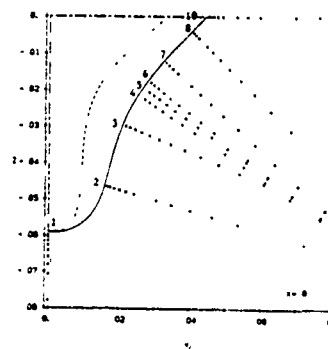
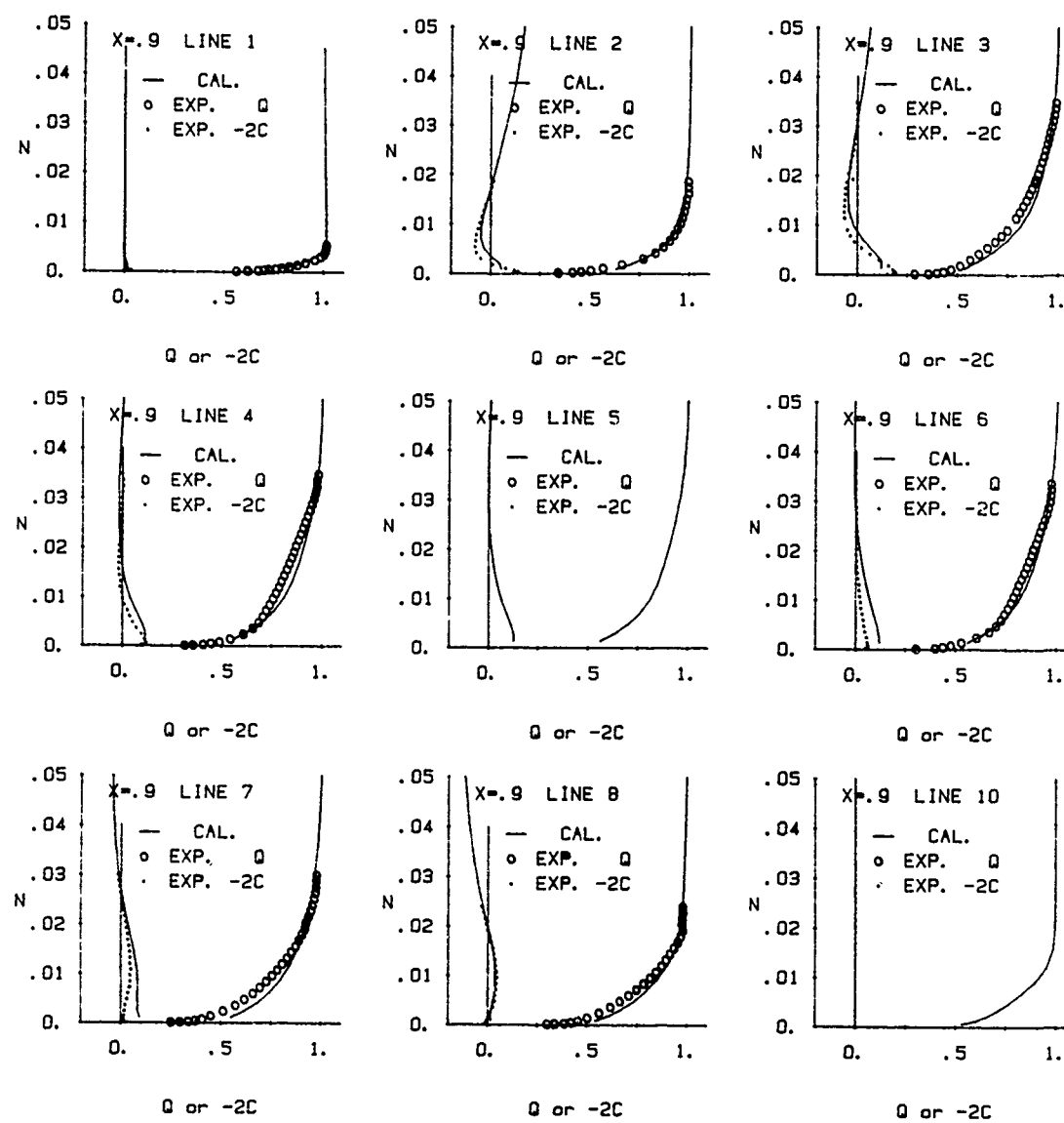


Fig. 27 Comparison between calculations and experiment
 (a) Profiles of resultant velocity (Q) and crossflow velocity (C) : $X = 0.9$

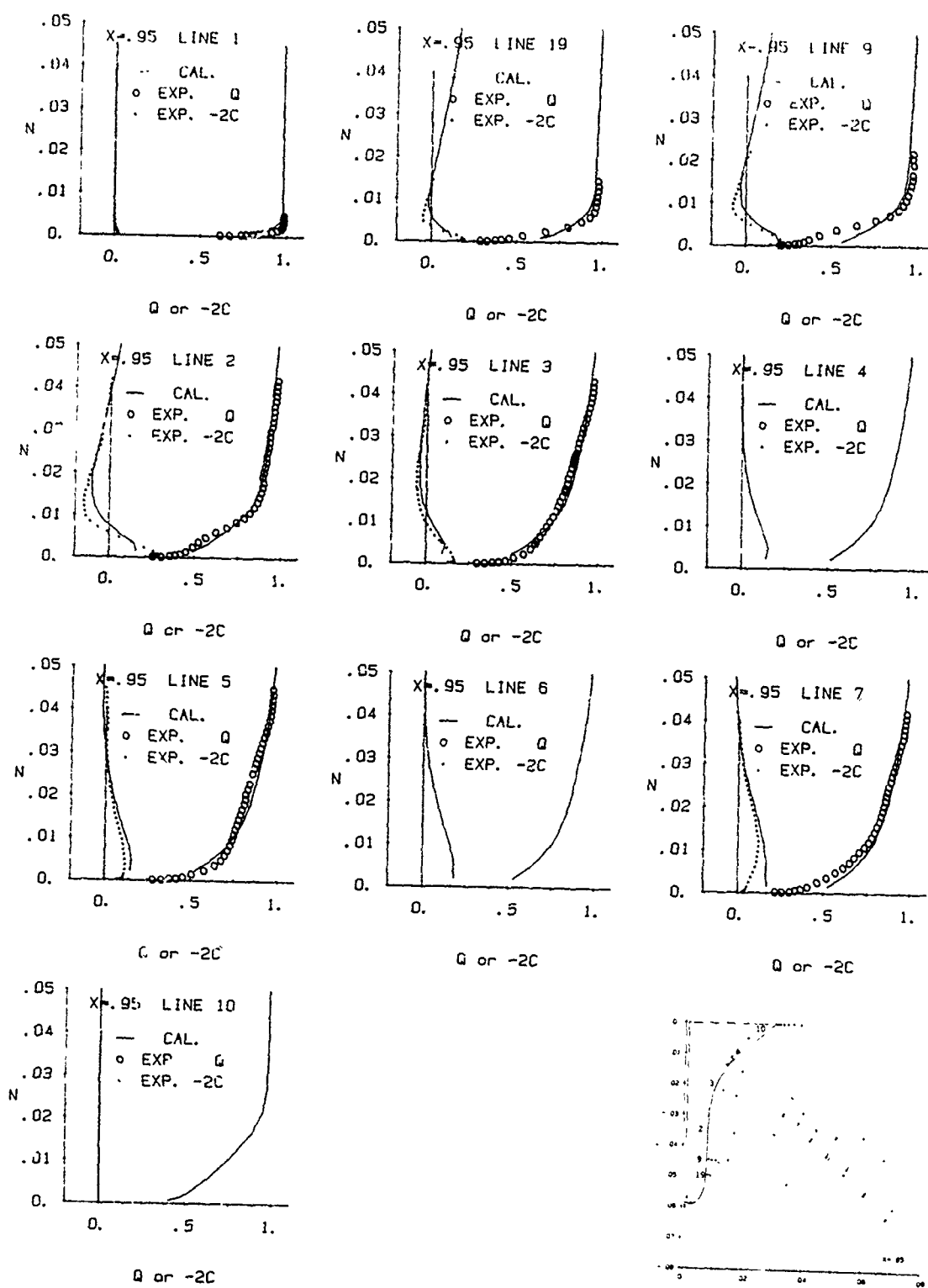


Fig. 27 Comparison between calculations and experiment
 (a) Profiles of resultant velocity (Q) and crossflow velocity (C) : $X = 0.95$

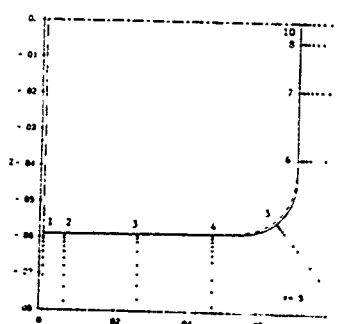
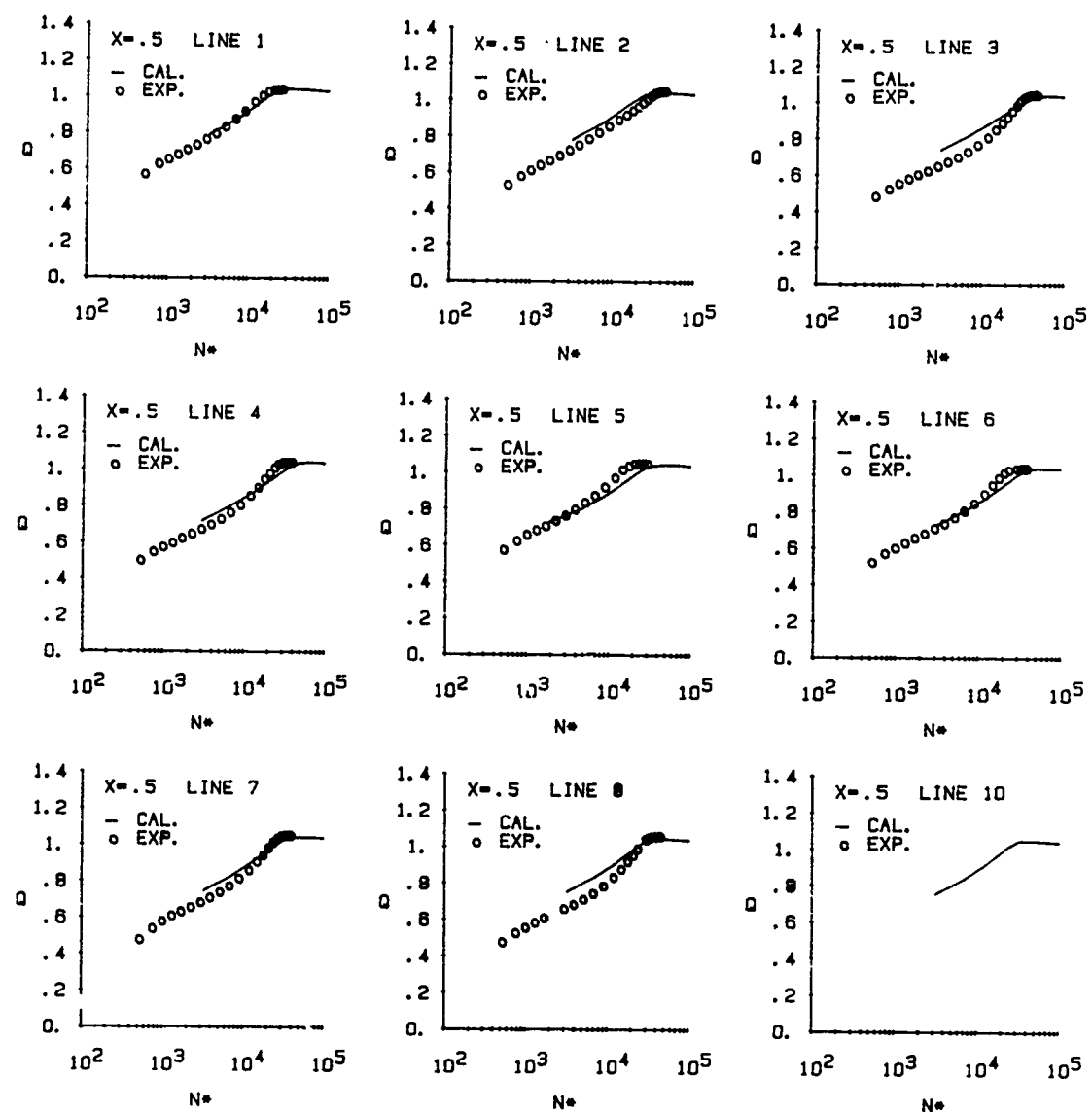


Fig. 27 Comparison between calculations and experiment
 (b) Resultant velocity distribution in logarithmic coordinates : $X = 0.5$

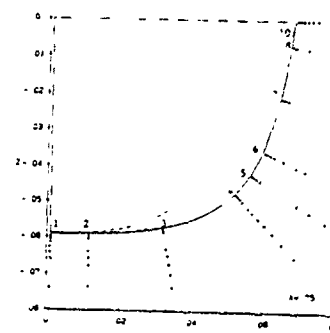
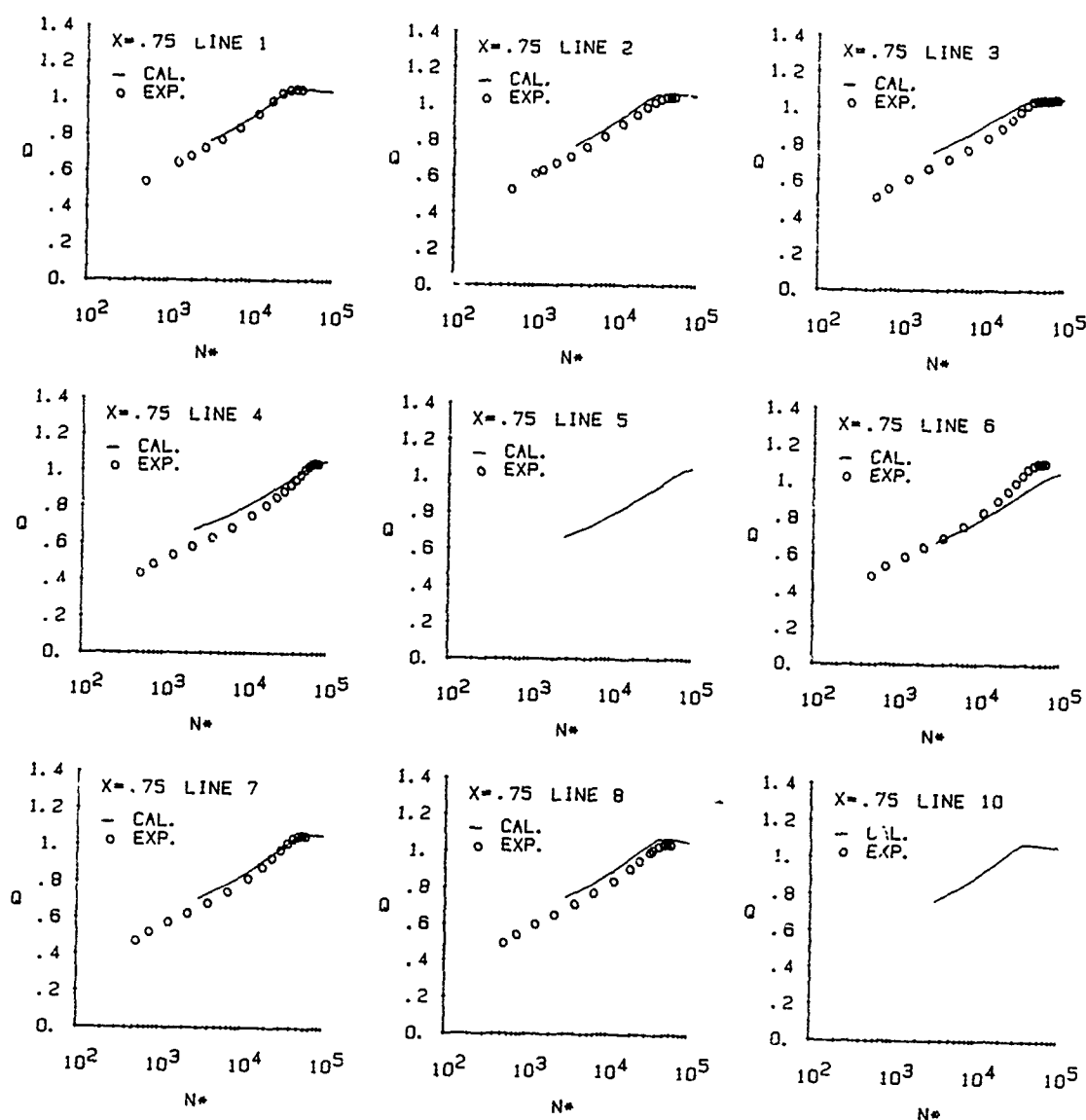


Fig. 27 Comparison between calculations and experiment
(b) Resultant velocity distribution in logarithmic coordinates : $X = 0.75$

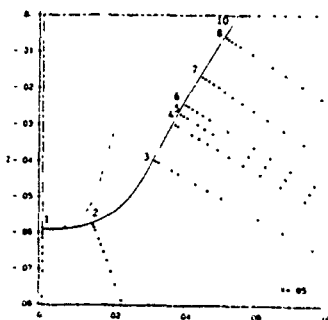
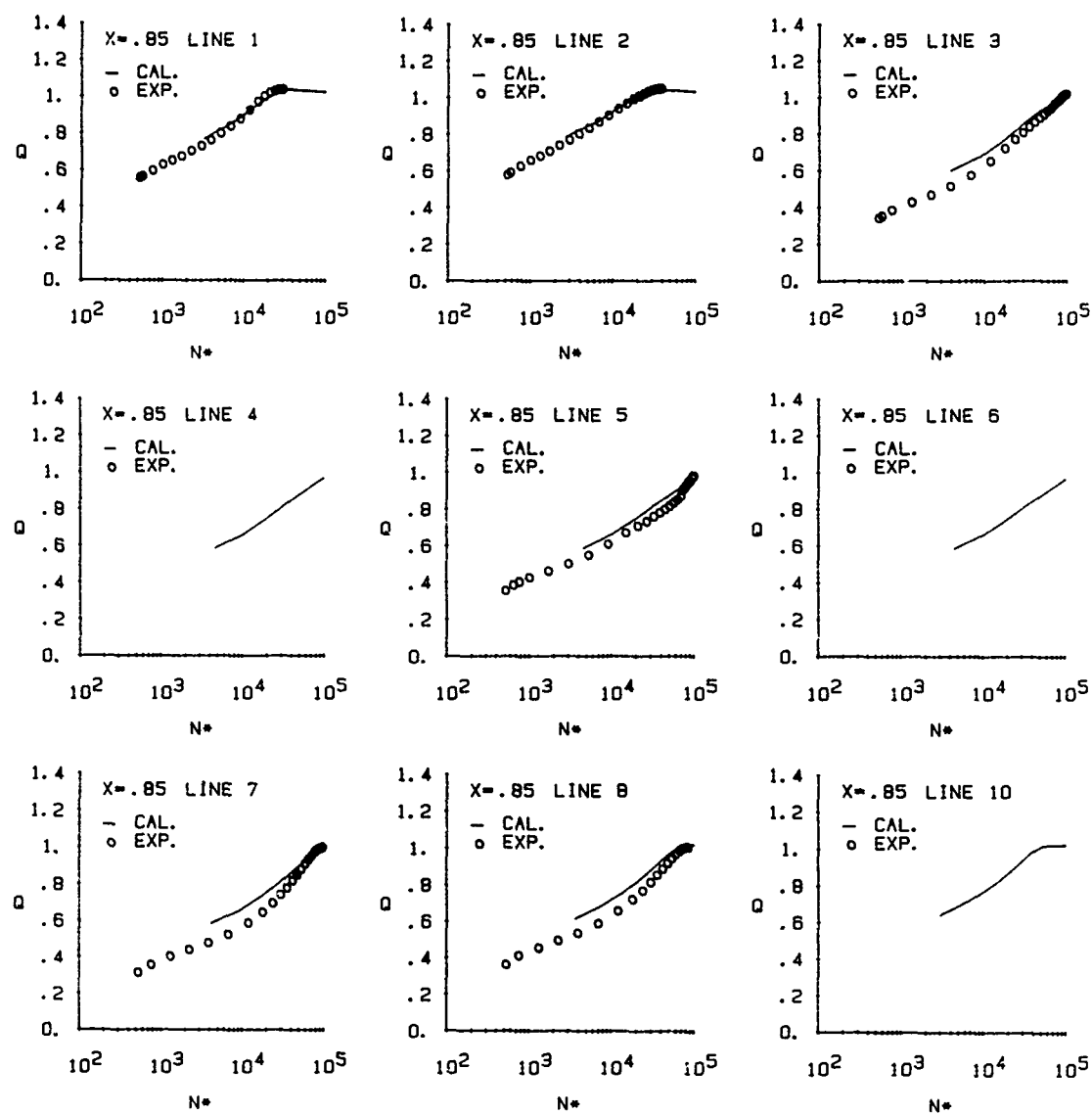


Fig. 27 Comparison between calculations and experiment
 (b) Resultant velocity distribution in logarithmic coordinates : $X = 0.85$

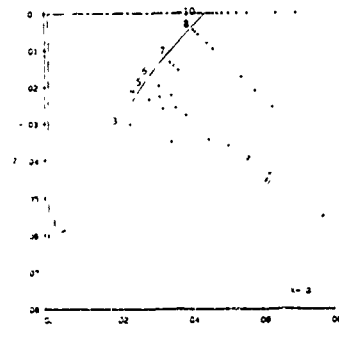
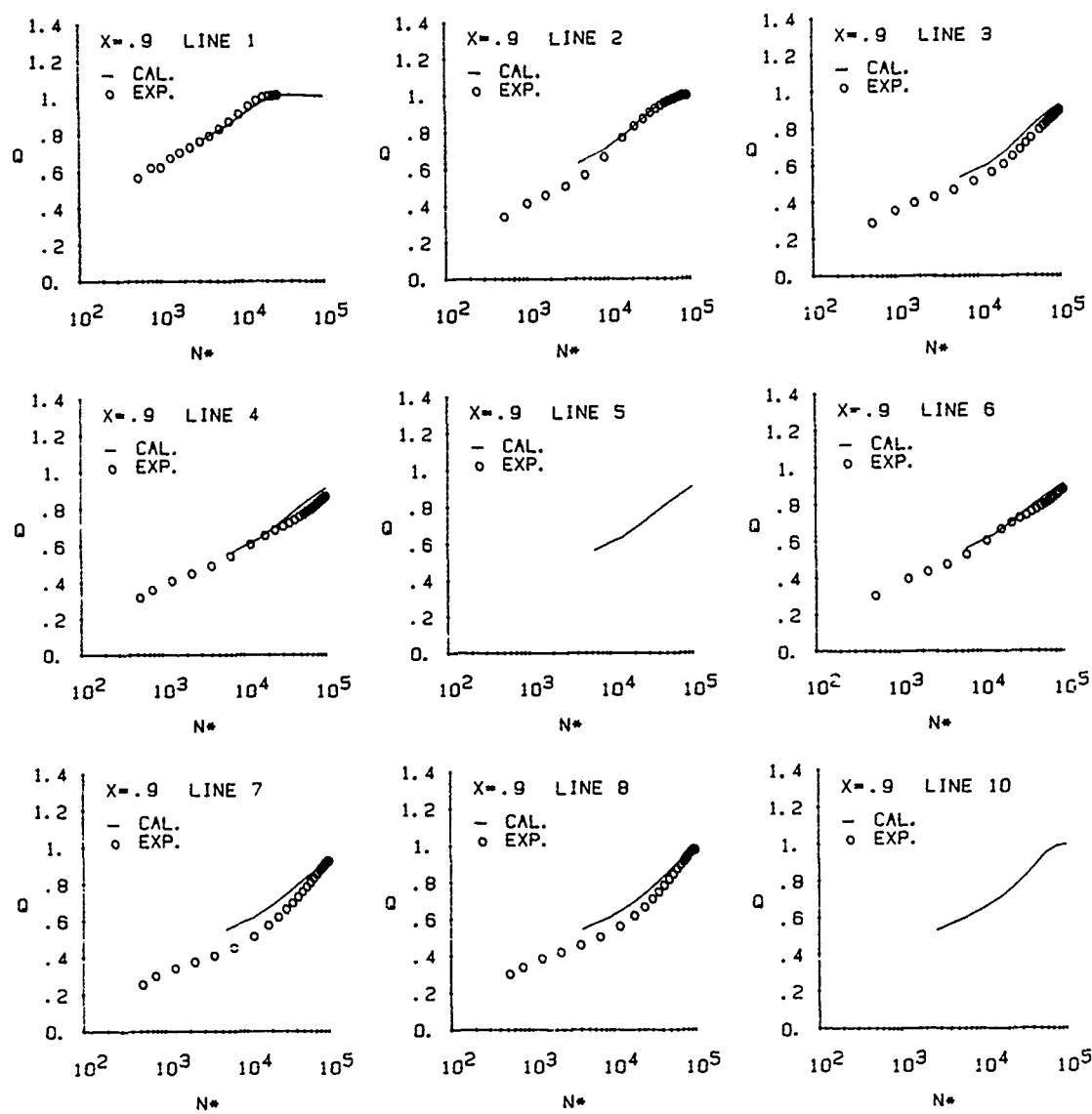


Fig. 27 Comparison between calculations and experiment
(b) Resultant velocity distribution in logarithmic coordinates : $X = 0.9$

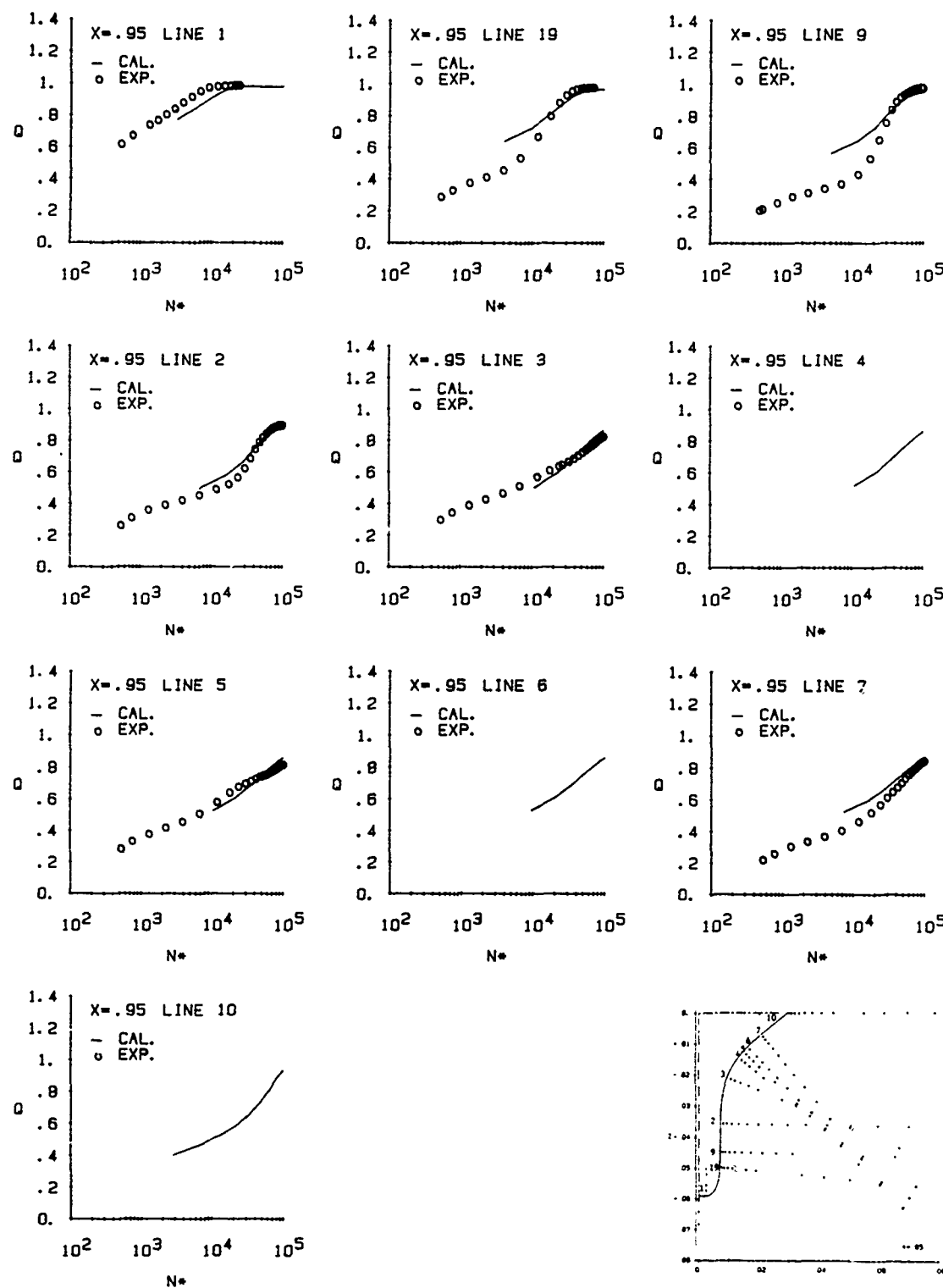


Fig. 27 Comparison between calculations and experiment
(b) Resultant velocity distribution in logarithmic coordinates : $X = 0.95$

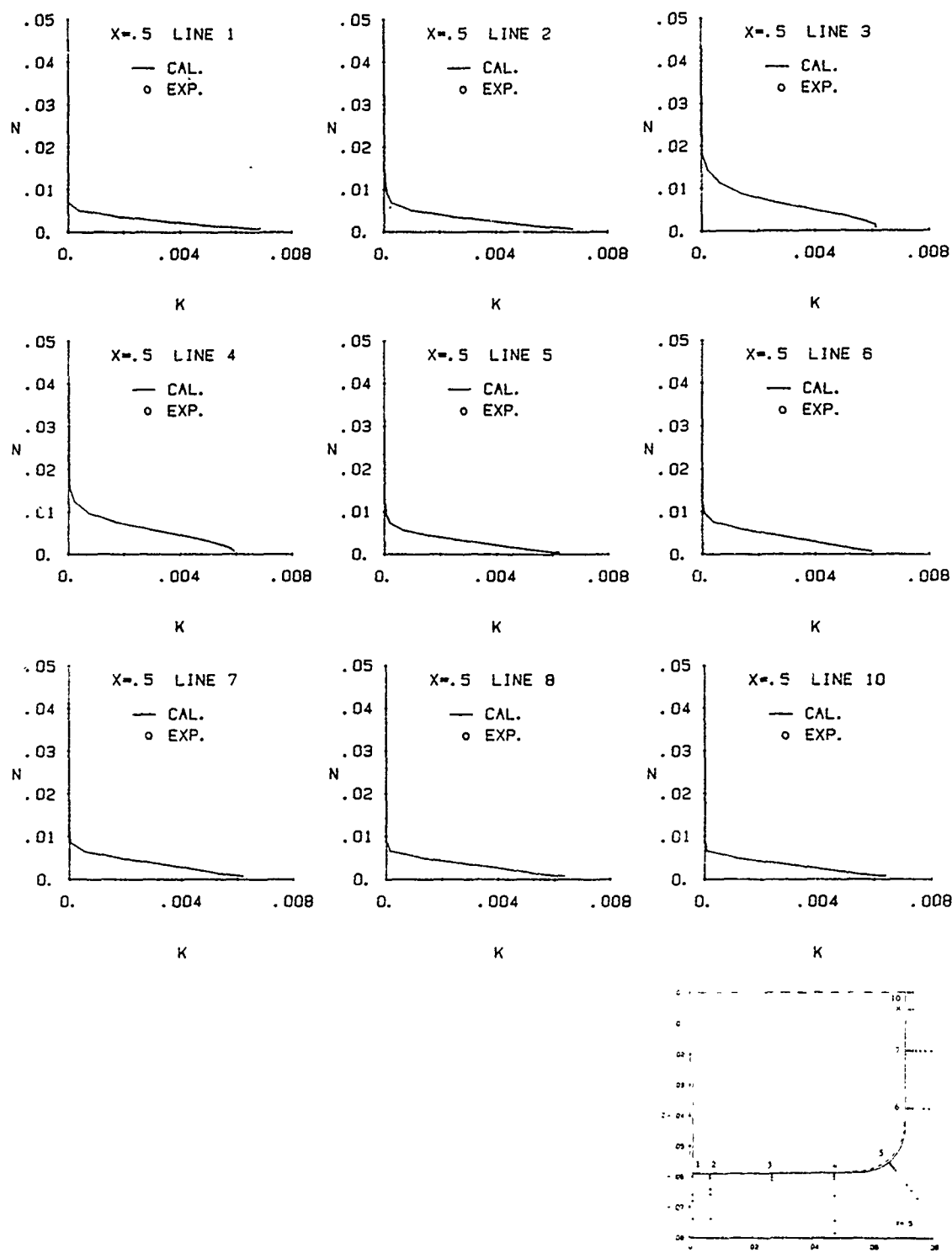


Fig. 27 Comparison between calculations and experiment
(c) Profiles of turbulent kinetic energy (K) : $X = 0.5$

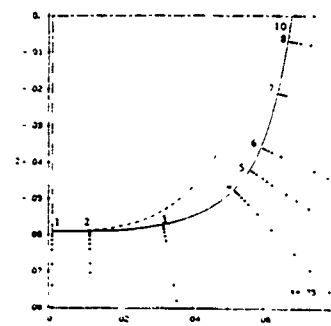
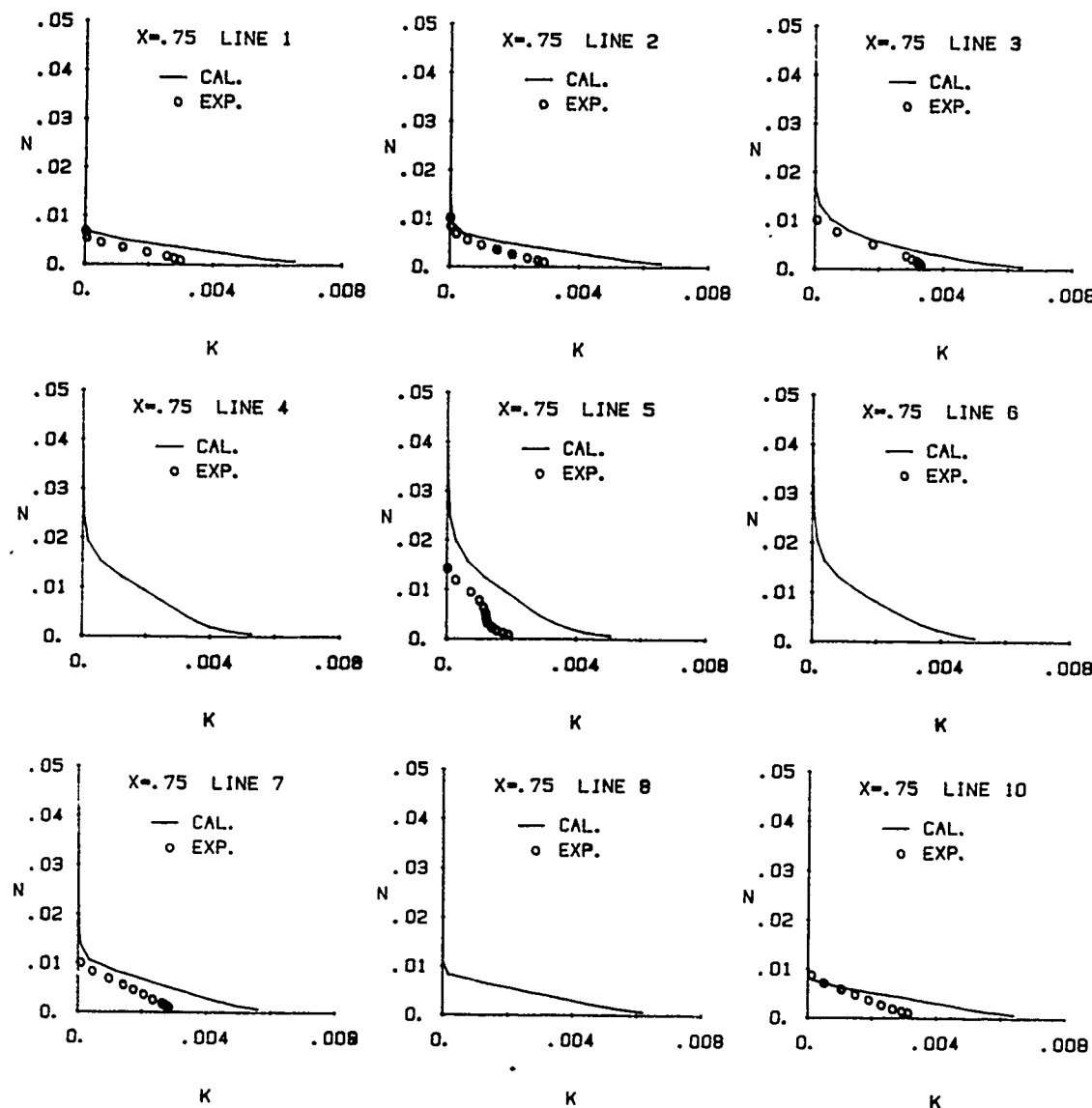


Fig. 27 Comparison between calculations and experiment
(c) Profiles of turbulent kinetic energy (K) : $X = 0.75$

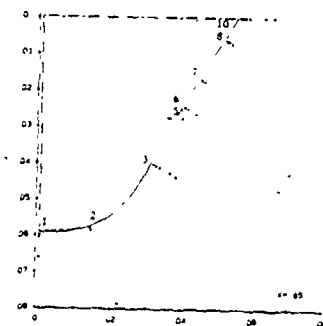
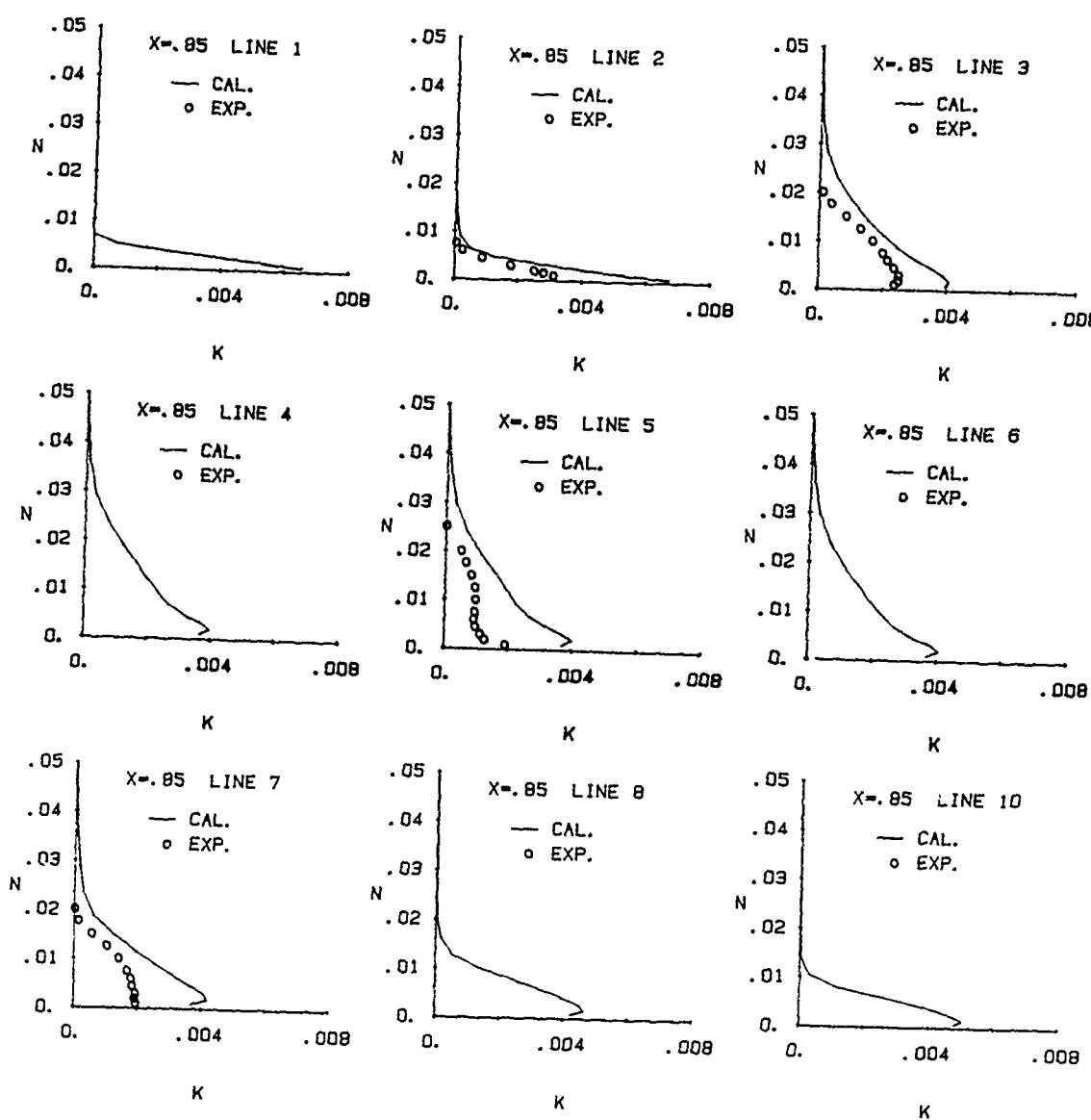


Fig. 27 Comparison between calculations and experiment
(c) Profiles of turbulent kinetic energy (K) : $X = 0.85$

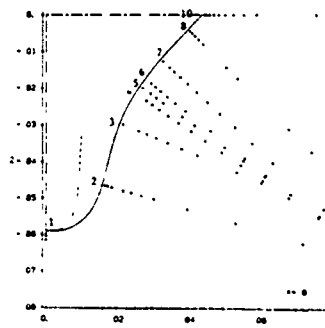
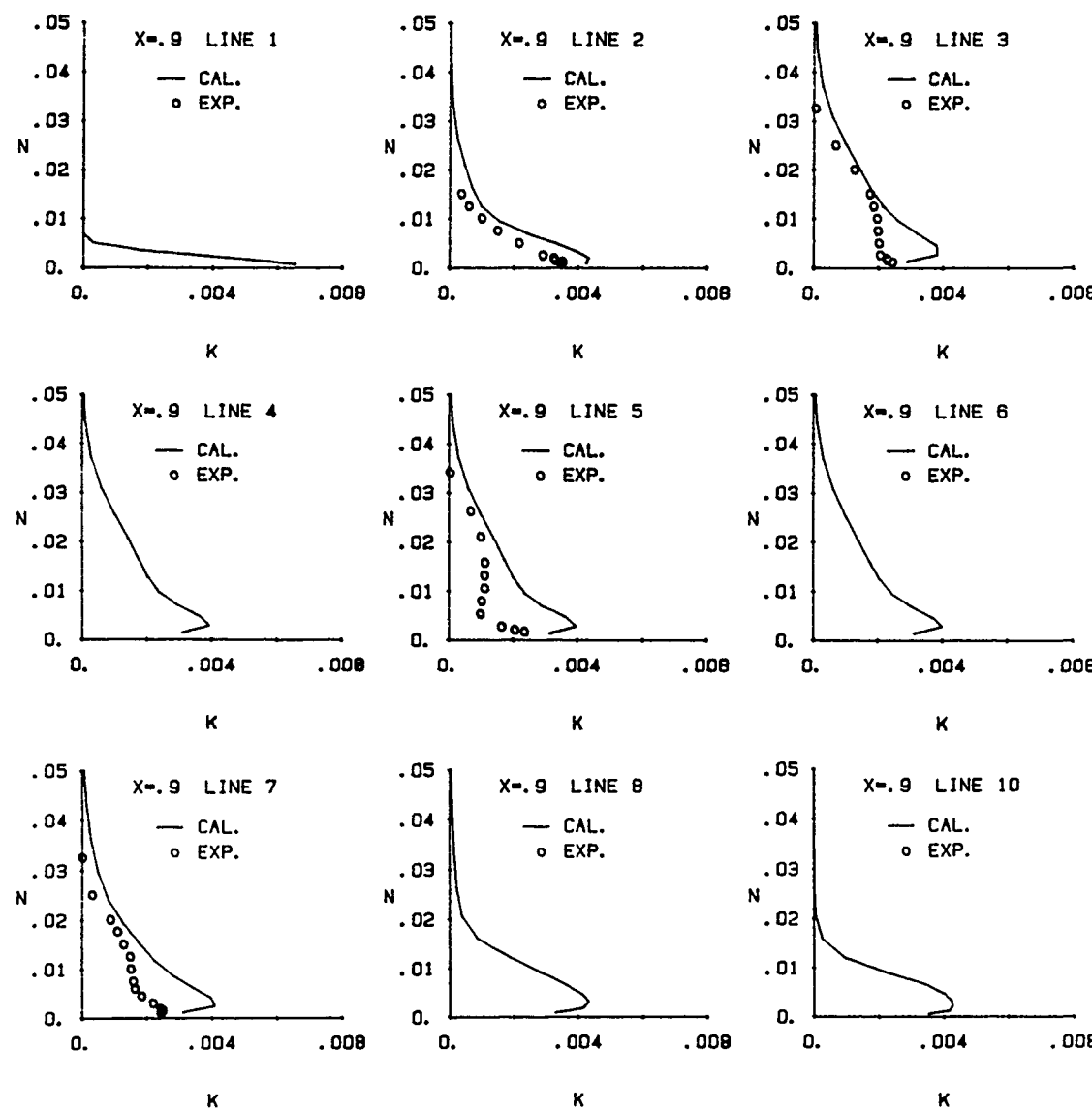


Fig. 27 Comparison between calculations and experiment
(c) Profiles of turbulent kinetic energy (k) : $X = 0.9$

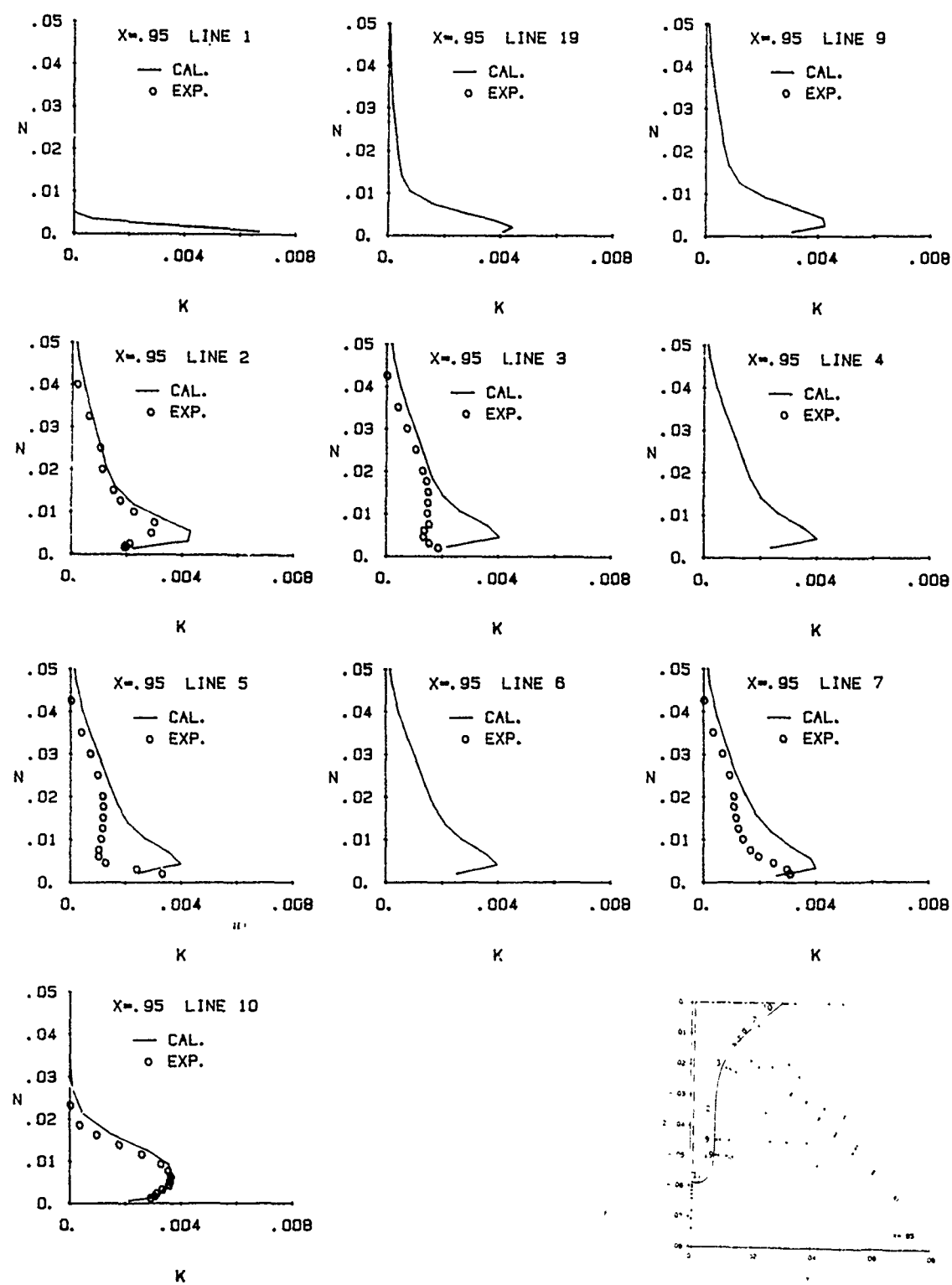


Fig. 27 Comparison between calculations and experiment
(c) Profiles of turbulent kinetic energy (k) : $X = 0.95$

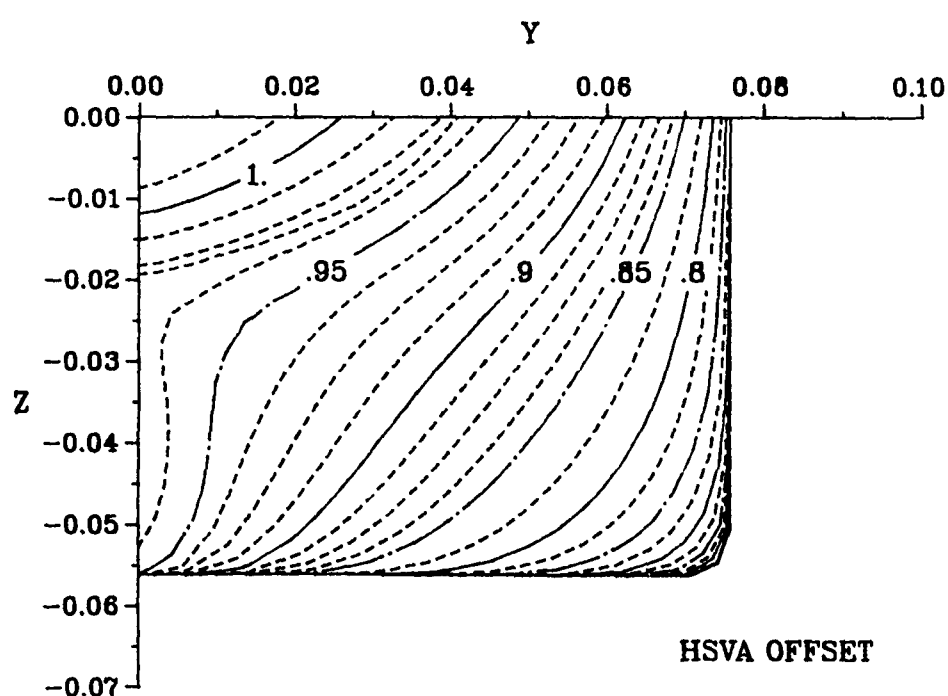
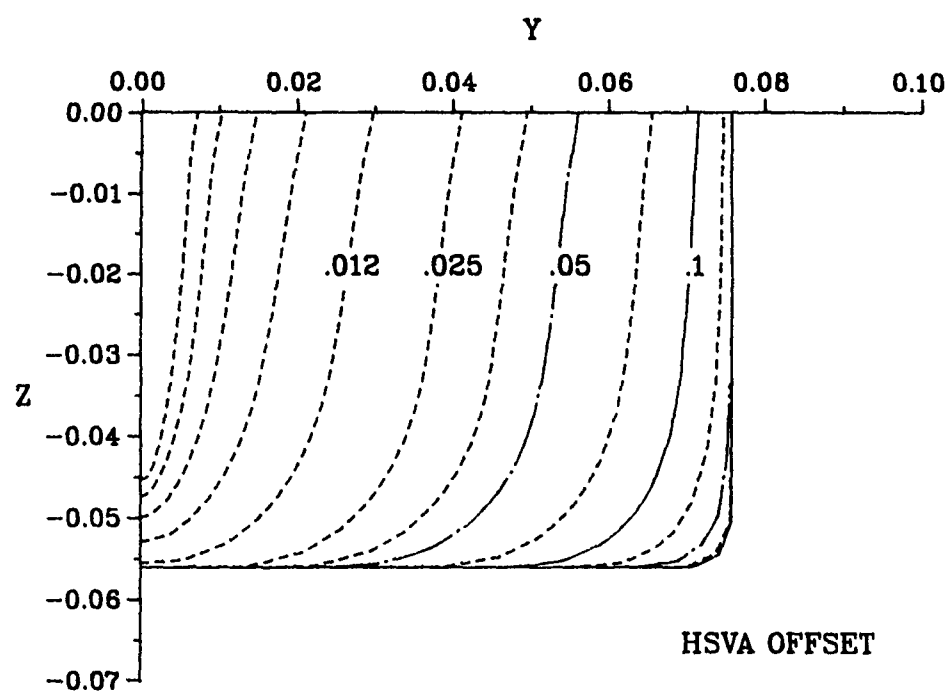


Fig. 28 Offsets of HSVA Tanker
(a) forebody (b) afterbody

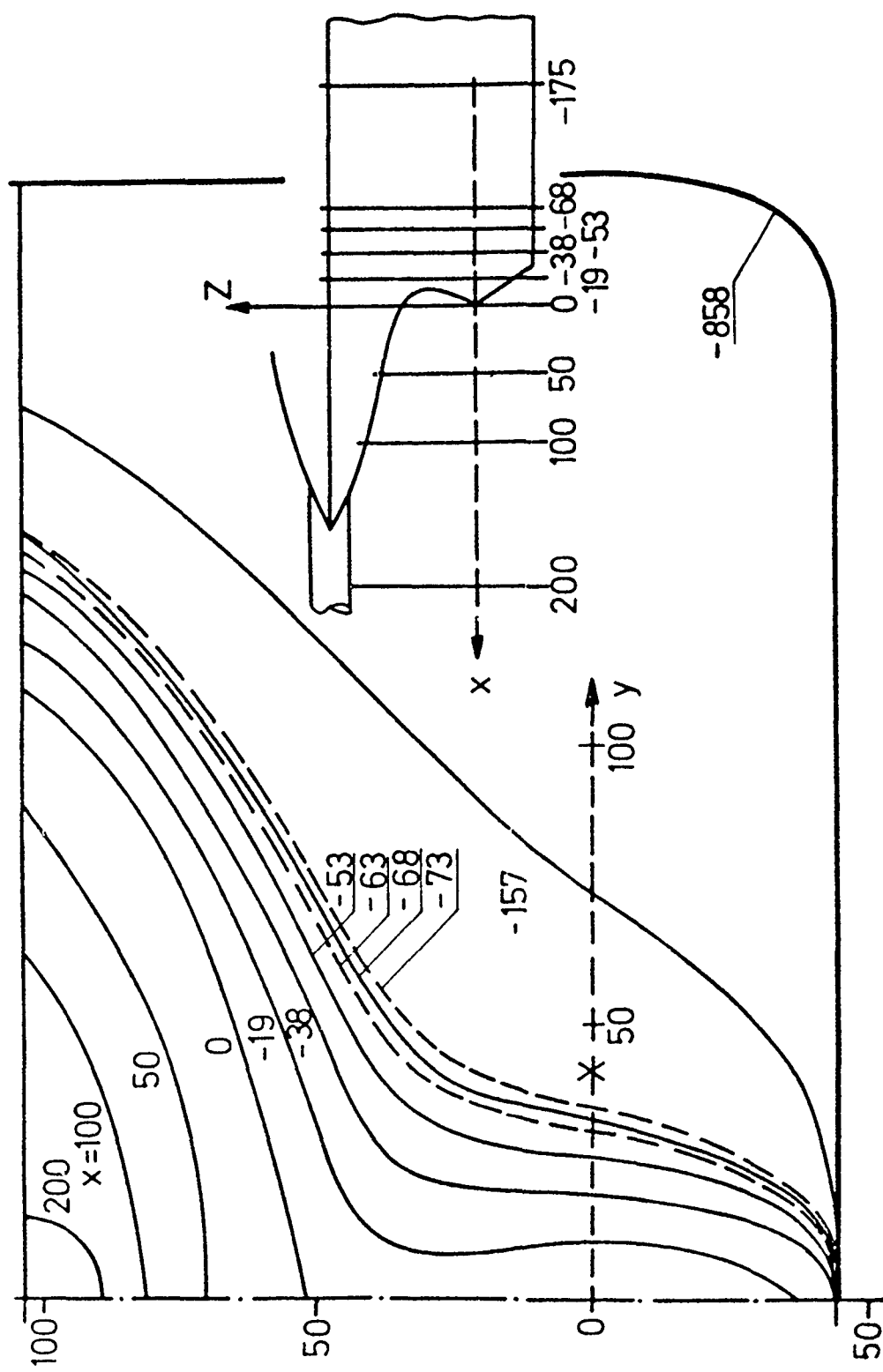


Fig. 29 Measurement stations in the experiments of Wieghardt and Kux (distances in mm)

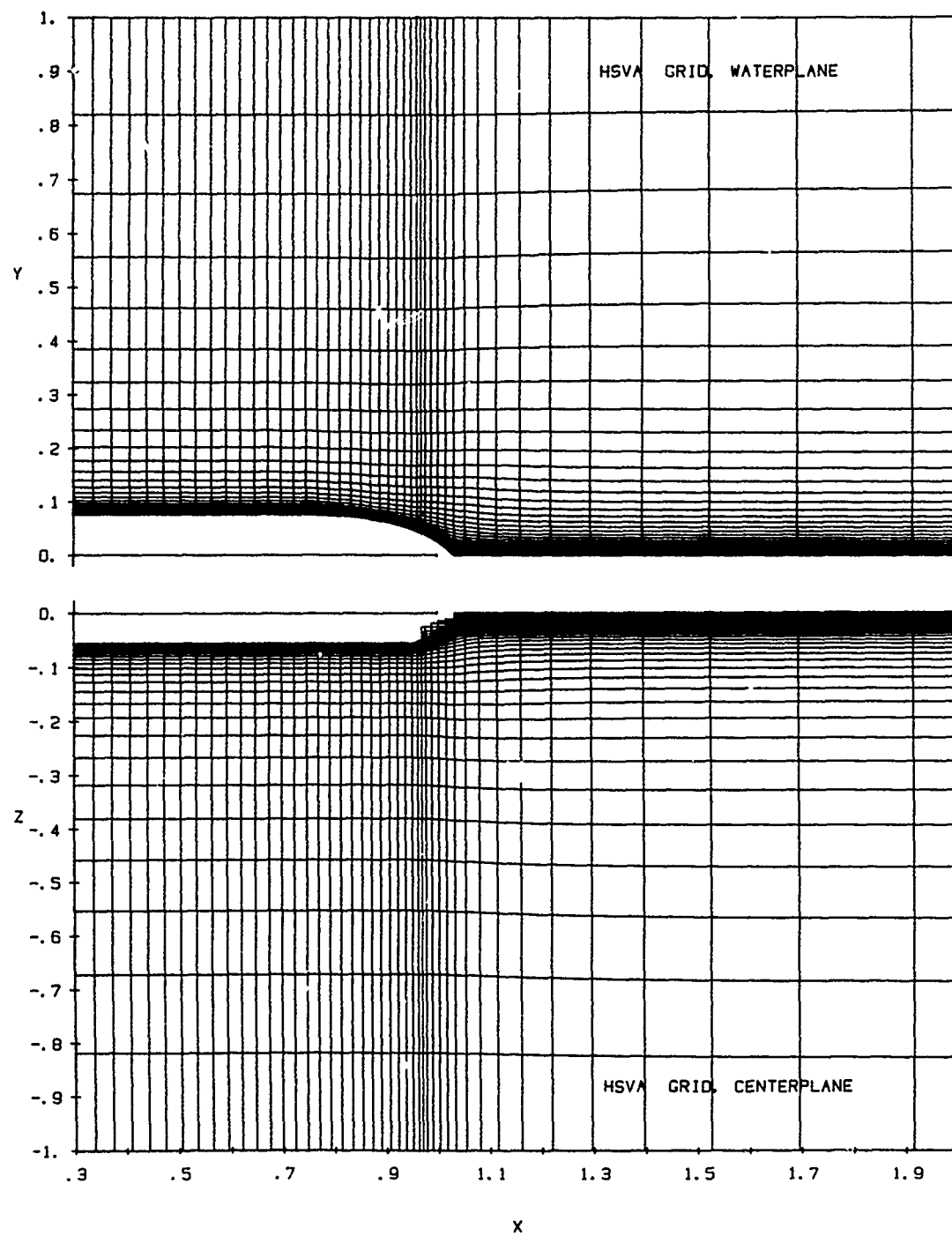


Fig. 30 Typical views of the numerical grid
(a) symmetry planes

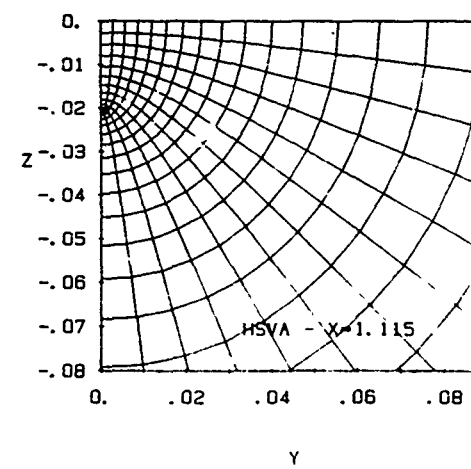
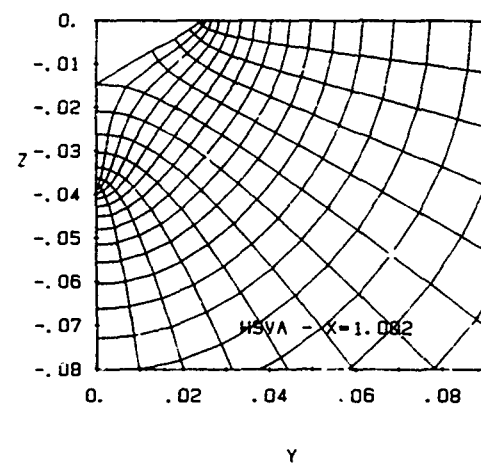
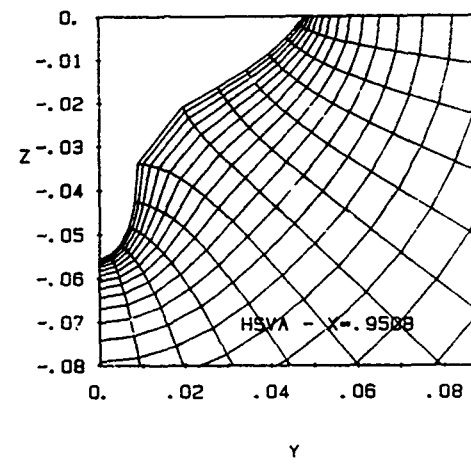
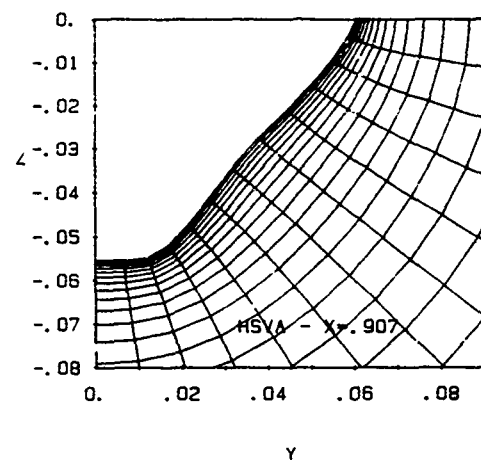
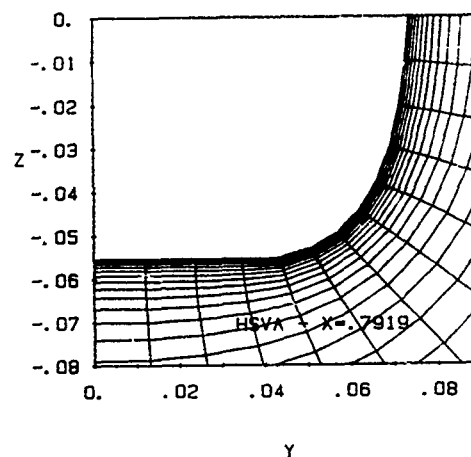
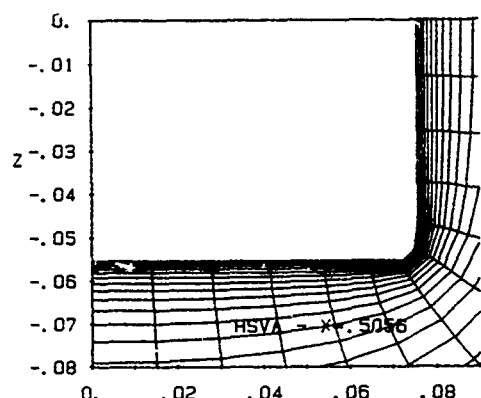


Fig. 30 Typical views of the numerical grid
(b) transverse sections

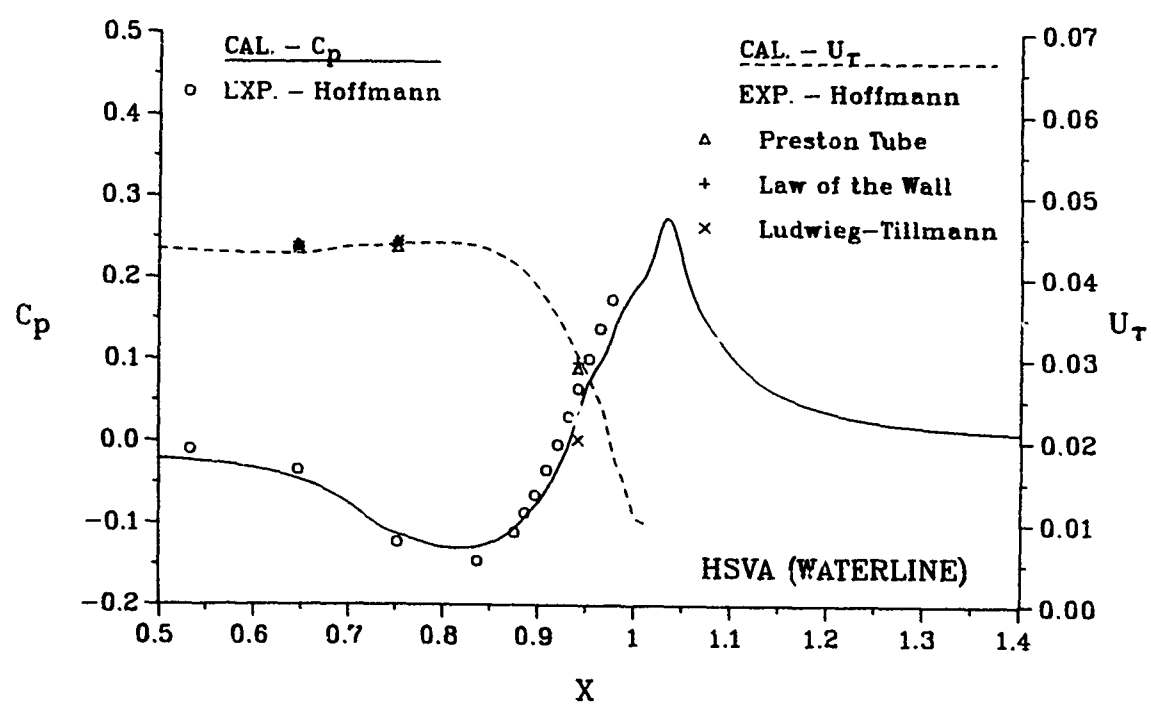
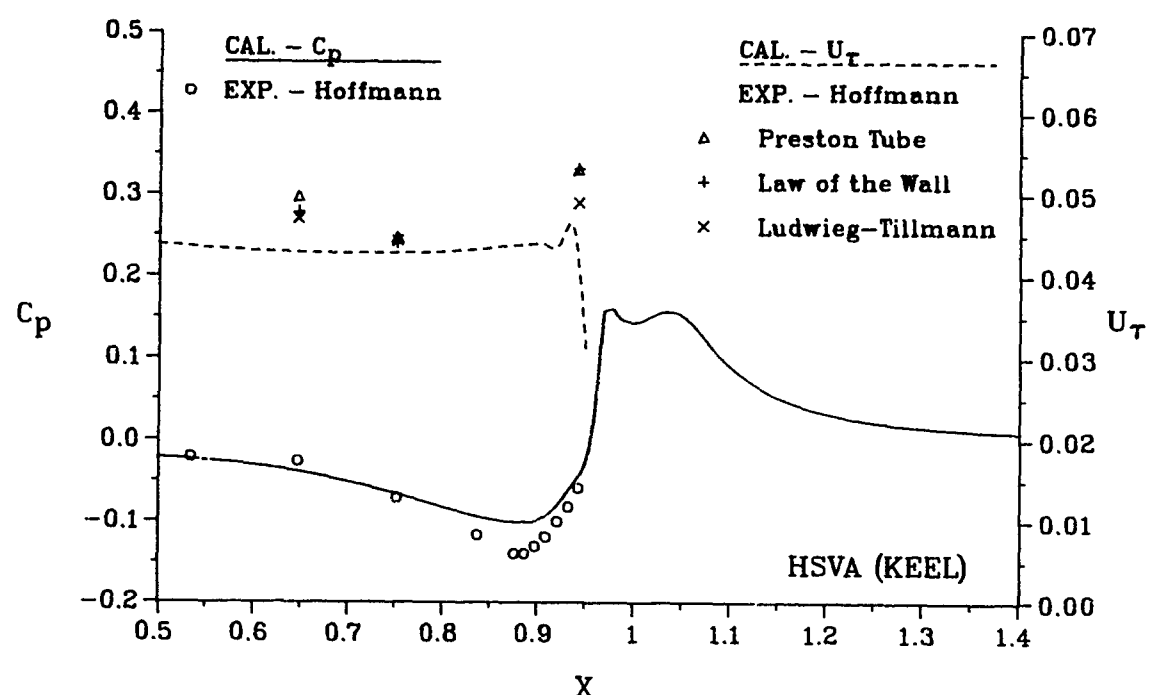


Fig. 31 Pressure and friction velocity along the keel and waterline

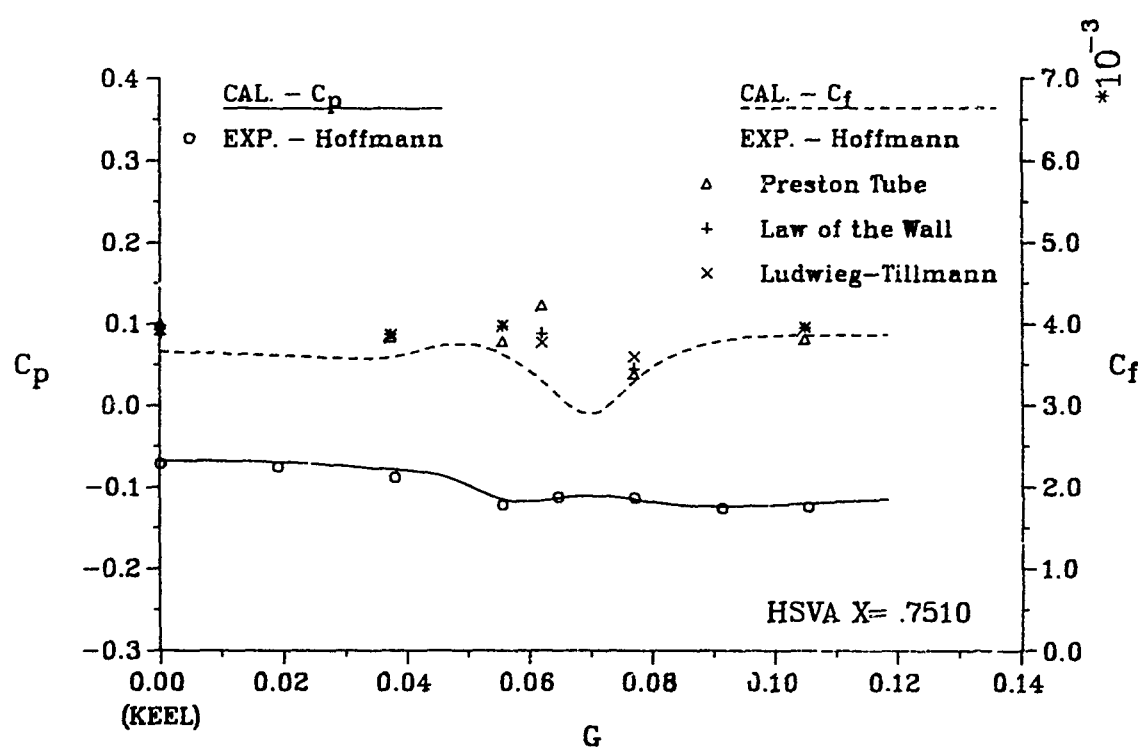
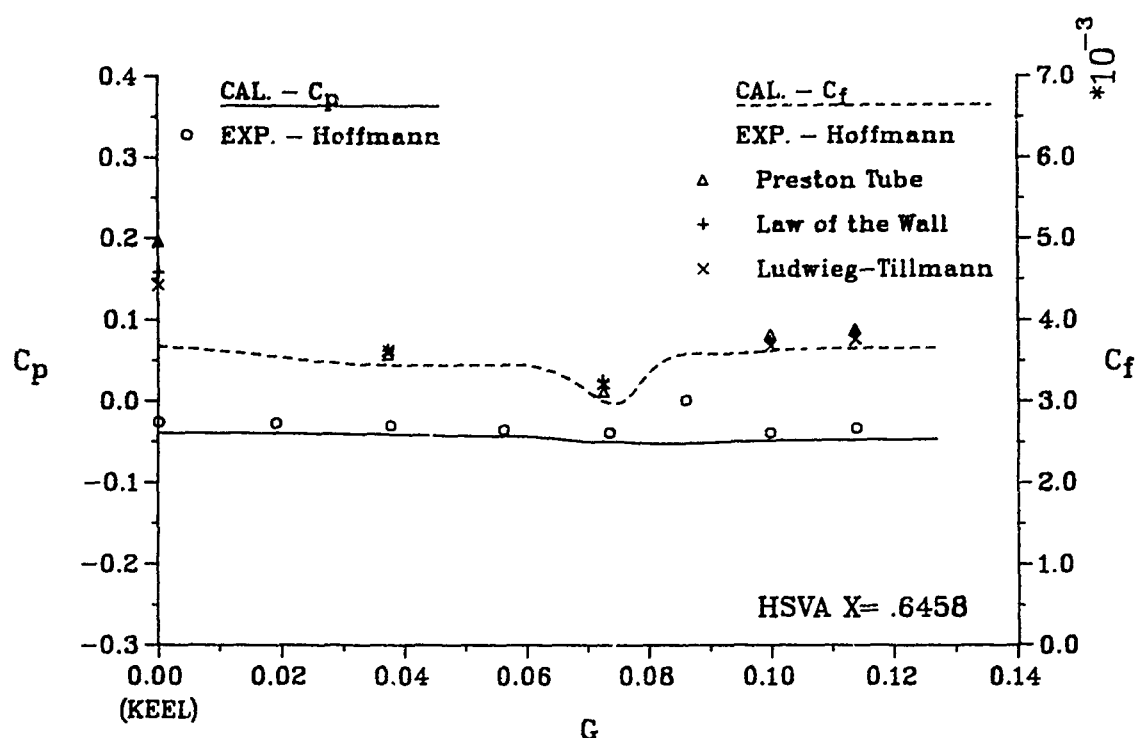


Fig. 32 Girthwise variation of pressure and friction coefficients
 (a) $X = 0.6458$; (b) $X = 0.7510$;

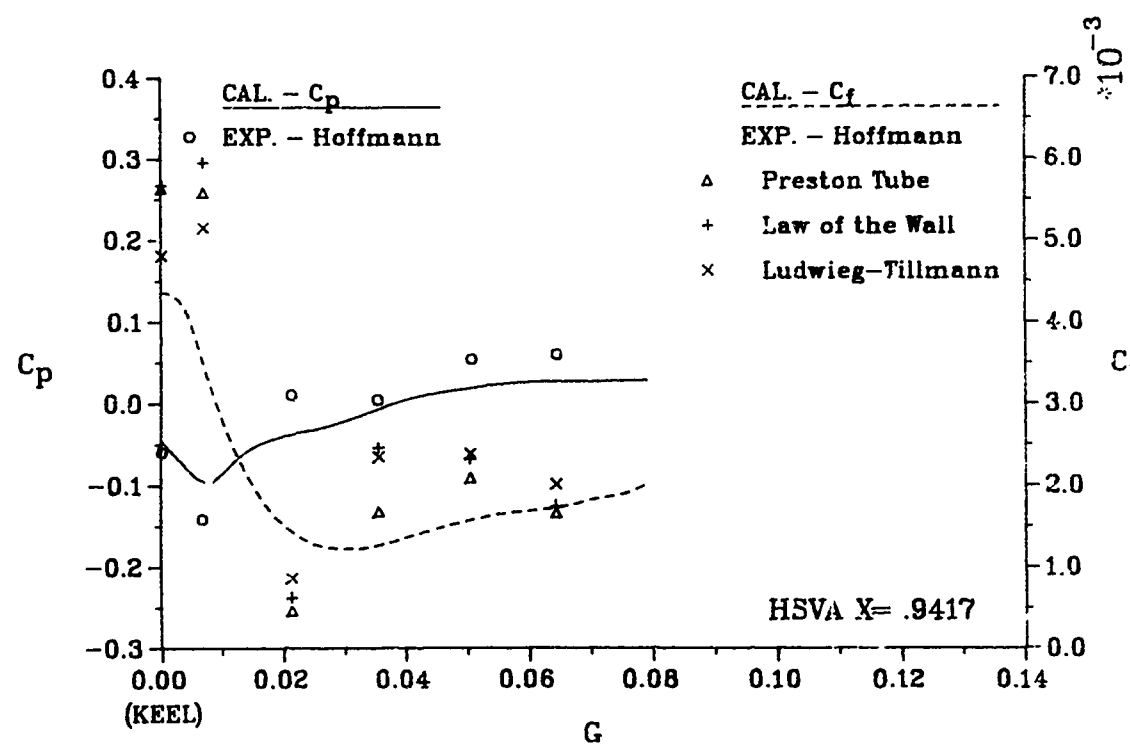
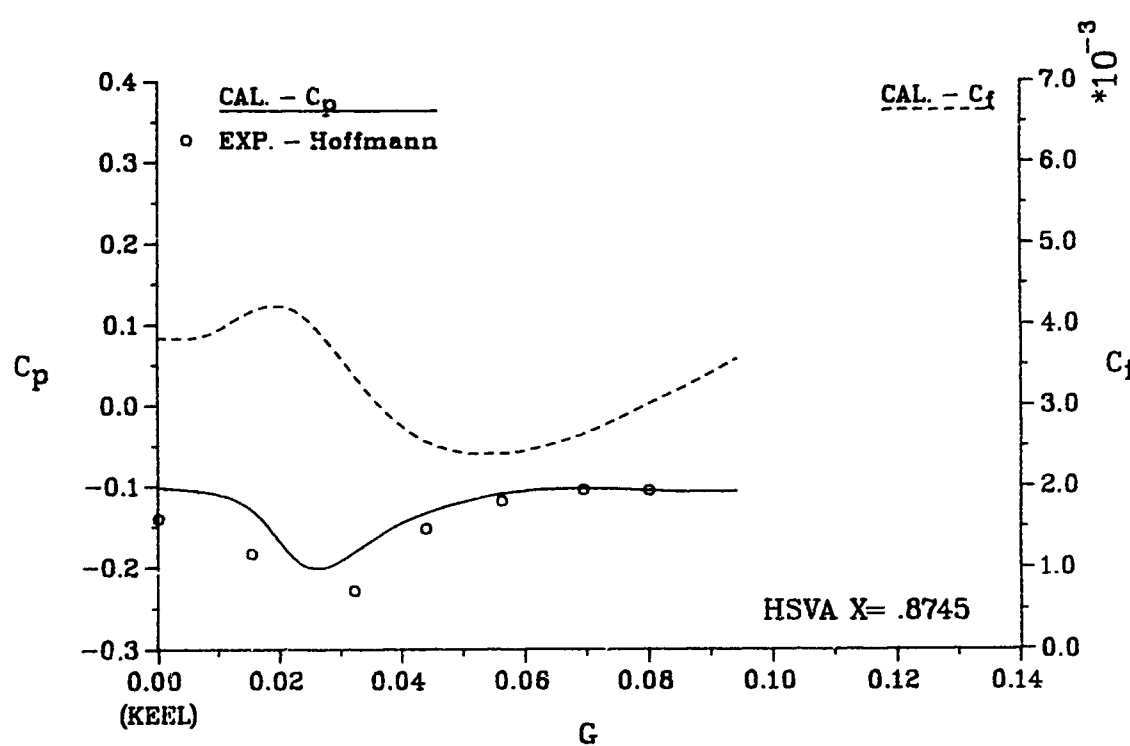


Fig. 32 Girthwise variation of pressure and friction coefficients
(c) $X = 0.8745$; (d) $X = 0.9417$

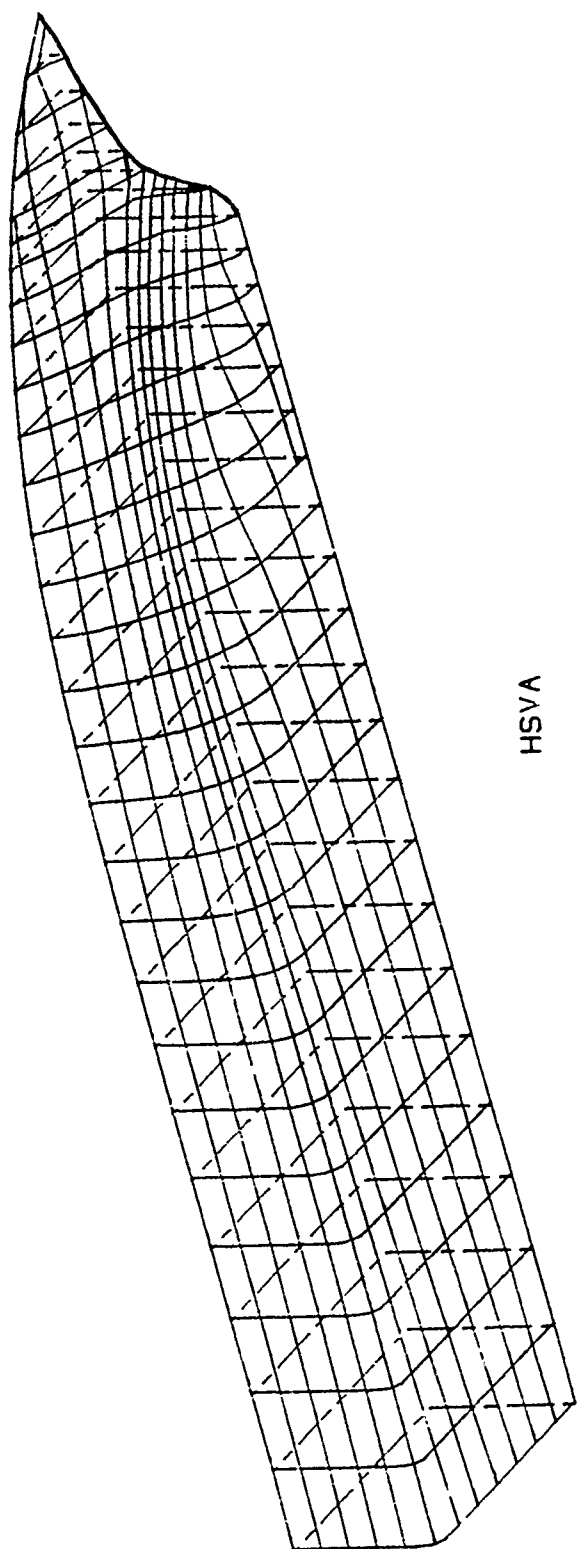


Fig. 33 Calculated wall streamlines

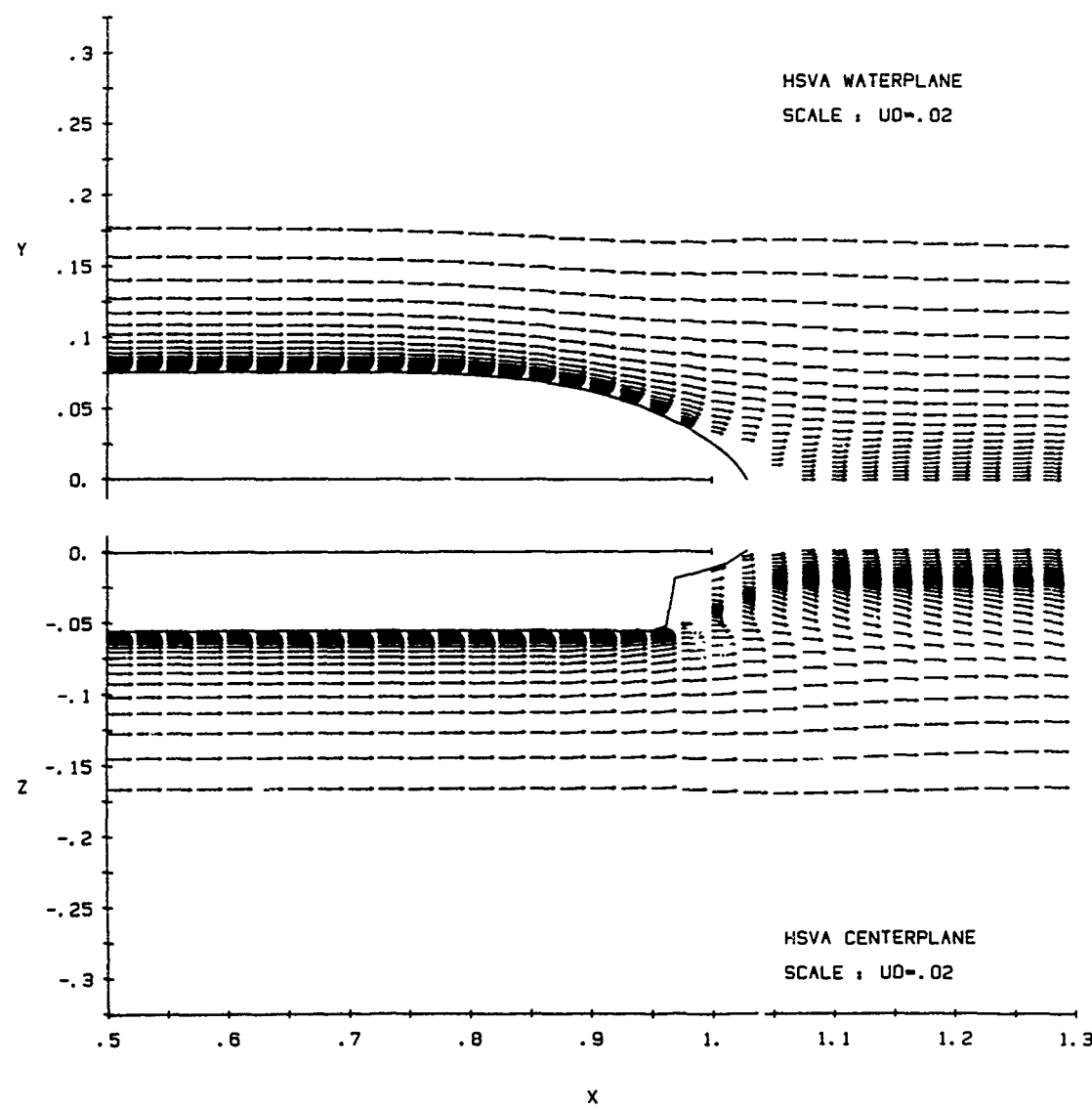


Fig. 34 Velocity vectors in the waterplane (top) and in the vertical centerplane (bottom)

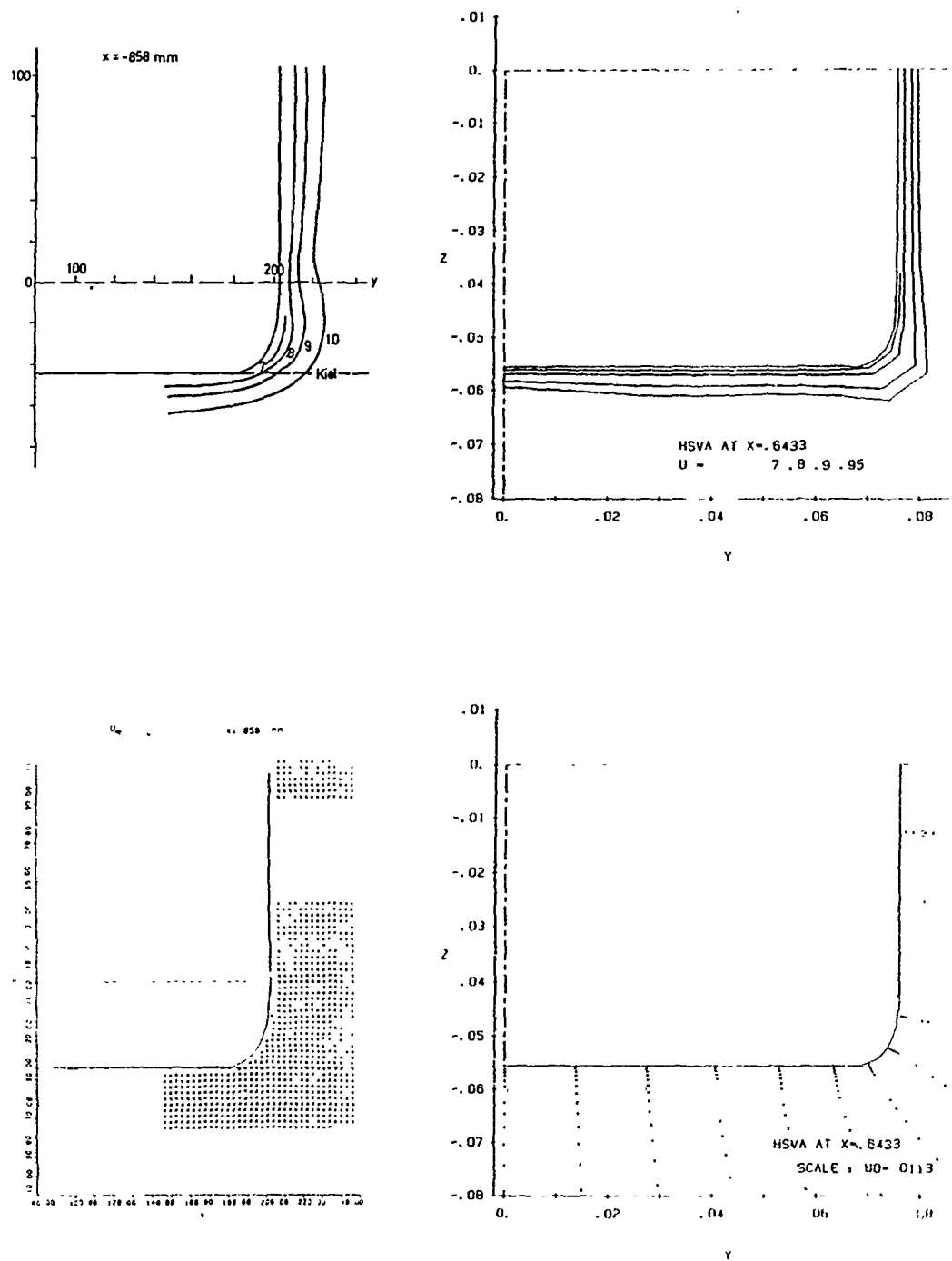


Fig. 35 Velocity field in transverse sections : (a) $X = 0.6433$
 Top: contours of axial velocity (U); Bottom: velocity (V, W) in transverse sections
 Left: experiments of Wieghardt and Kux; Right: present calculations

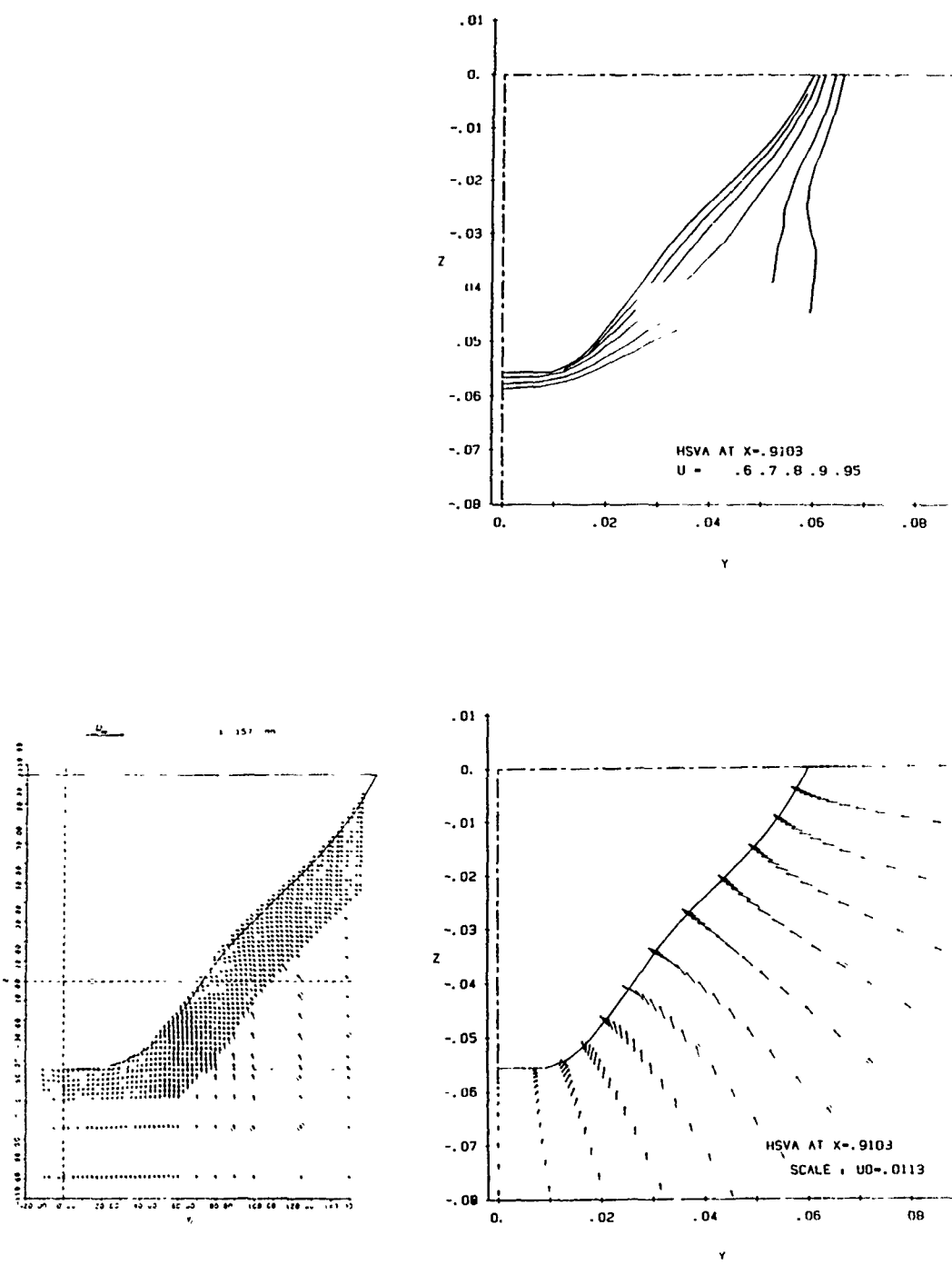


Fig. 35 Velocity field in transverse sections : (b) $X = 0.9103$
 Top: contours of axial velocity (U); Bottom: velocity (V, W) in transverse sections
 Left: experiments of Wieghardt and Kux; Right: present calculations

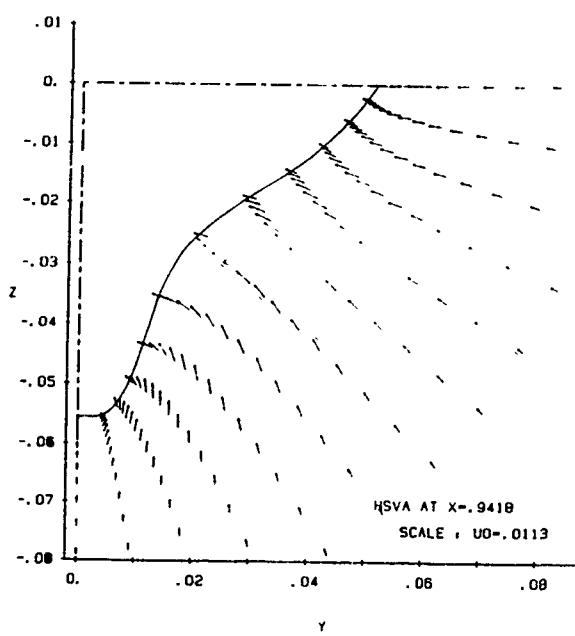
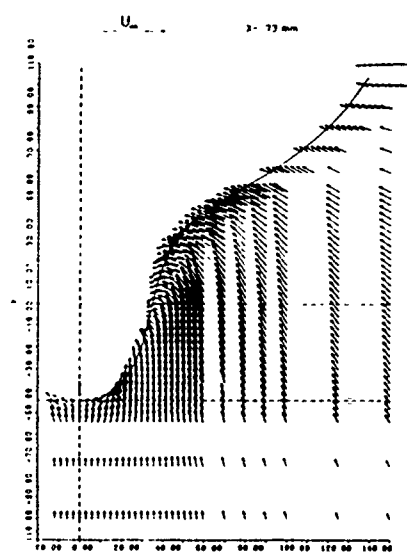
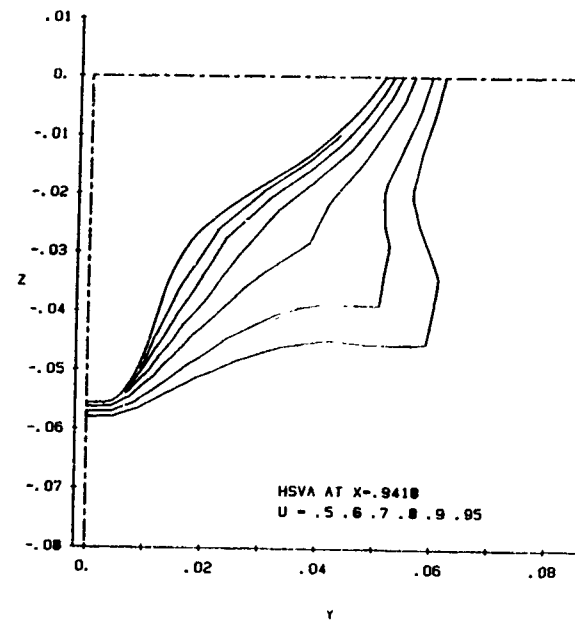
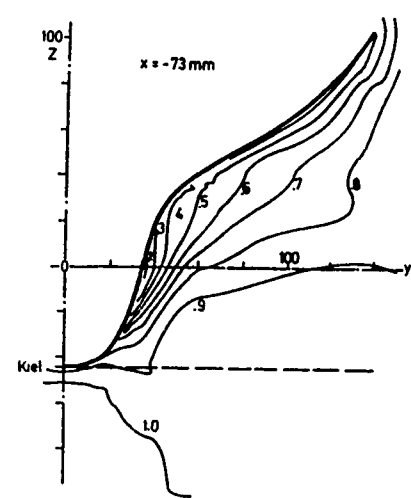


Fig. 35 Velocity field in transverse sections : (c) $X = 0.9418$
 Top: contours of axial velocity (U); Bottom: velocity (V, W) in transverse sections
 Left: experiments of Wieghardt and Kux; Right: present calculations

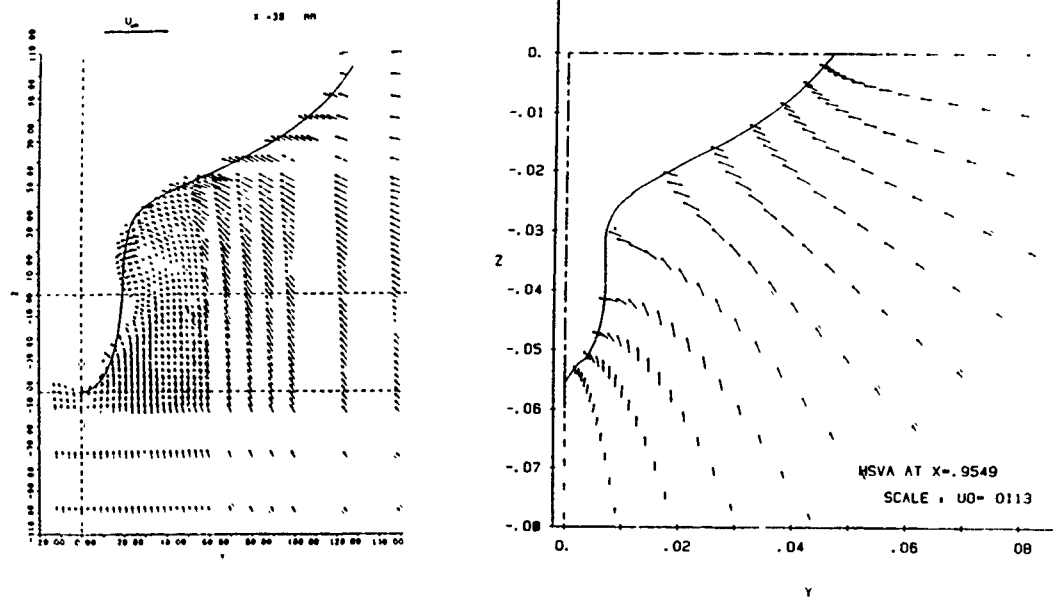
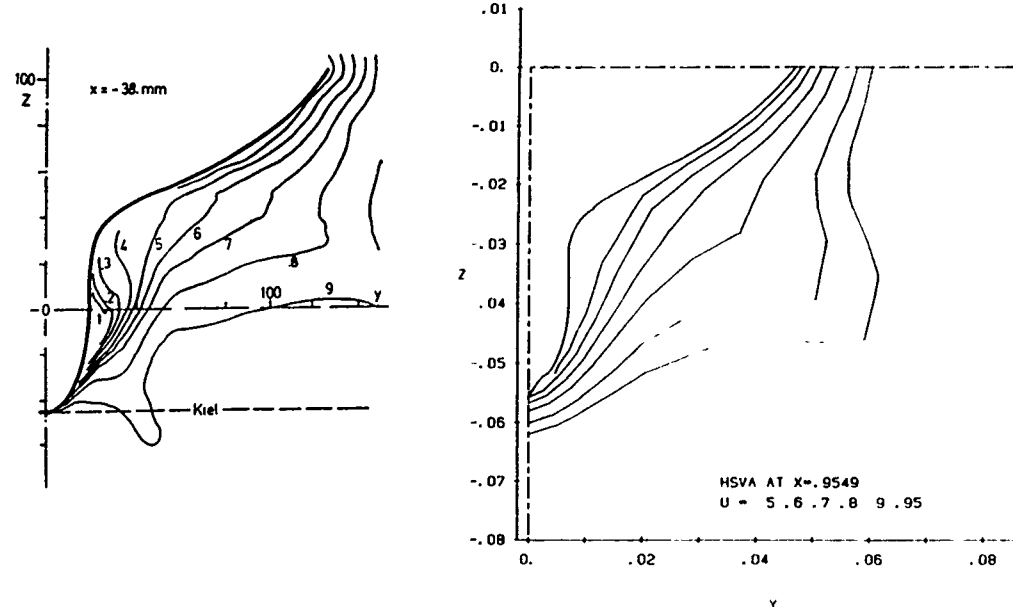


Fig. 35 Velocity field in transverse sections : (d) $X = 0.9549$
 Top: contours of axial velocity (U); Bottom: velocity (V,W) in transverse sections
 Left: experiments of Wieghardt and Kux; Right: present calculations

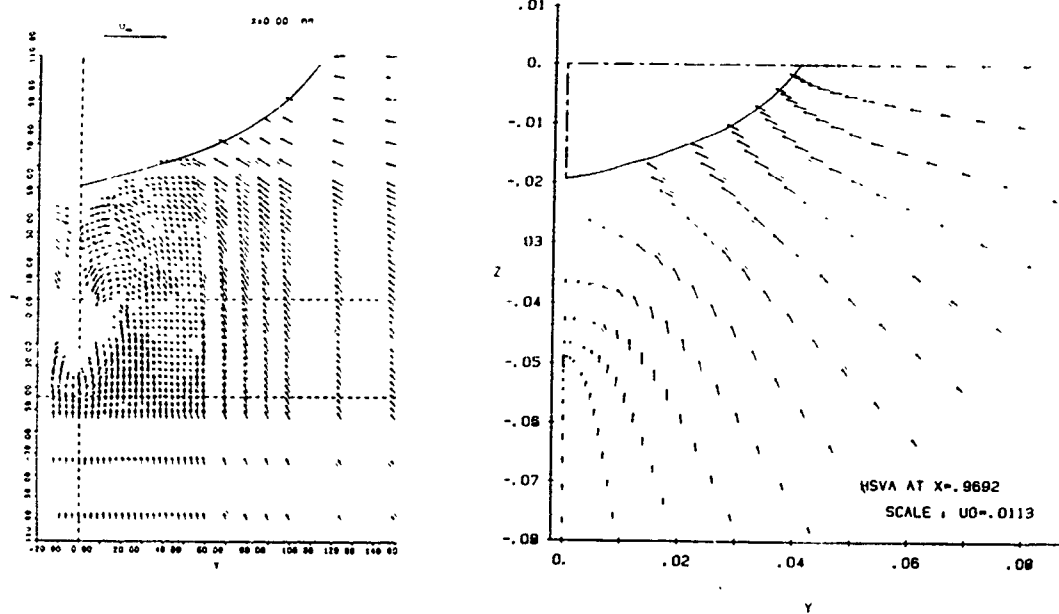
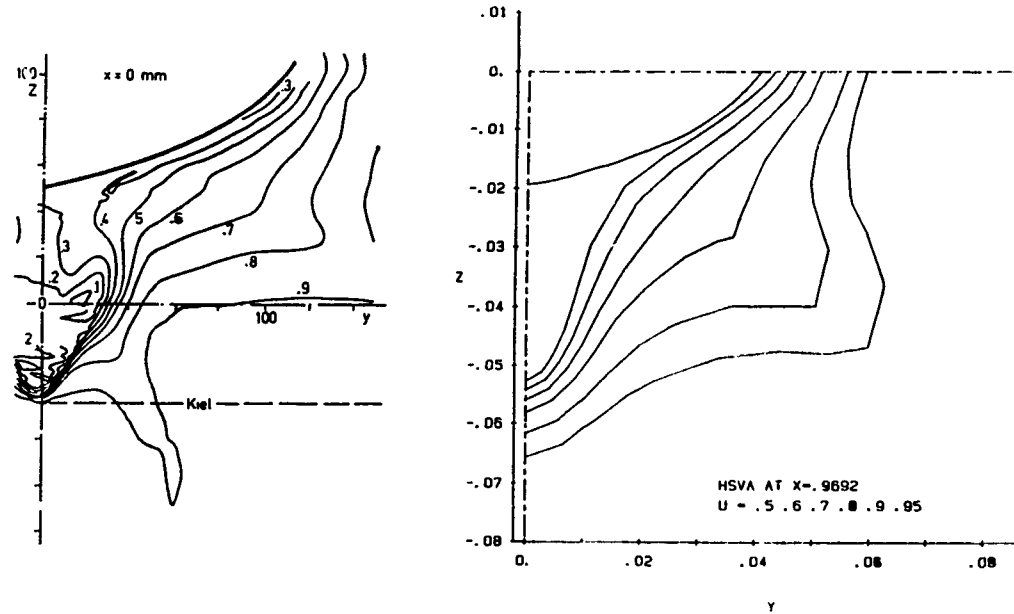


Fig. 35 Velocity field in transverse sections : (e) $X = 0.9692$
 Top: contours of axial velocity (U); Bottom: velocity (V,W) in transverse sections
 Left: experiments of Wieghardt and Kux; Right: present calculations

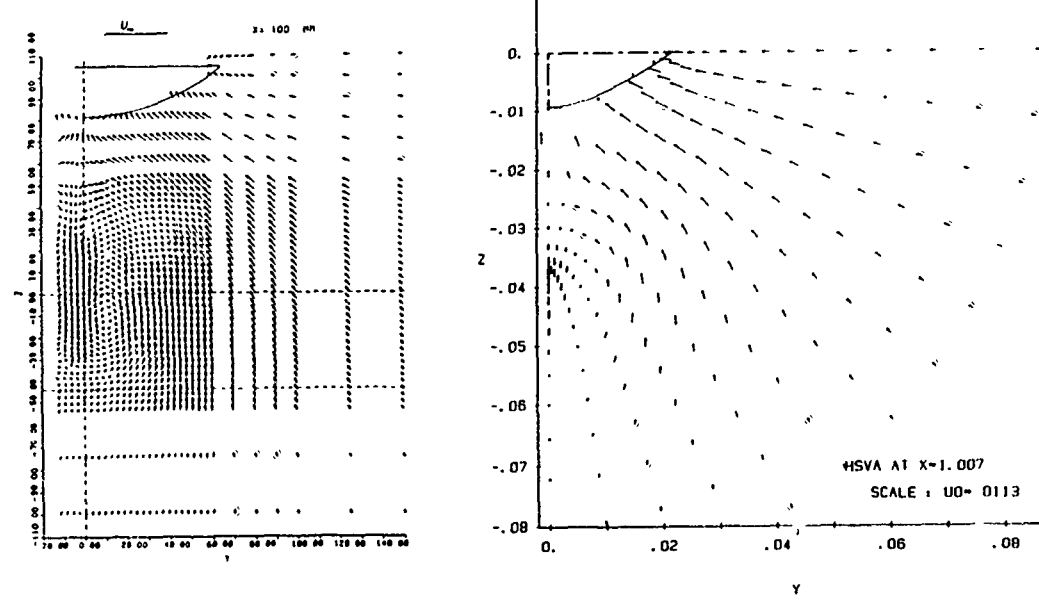
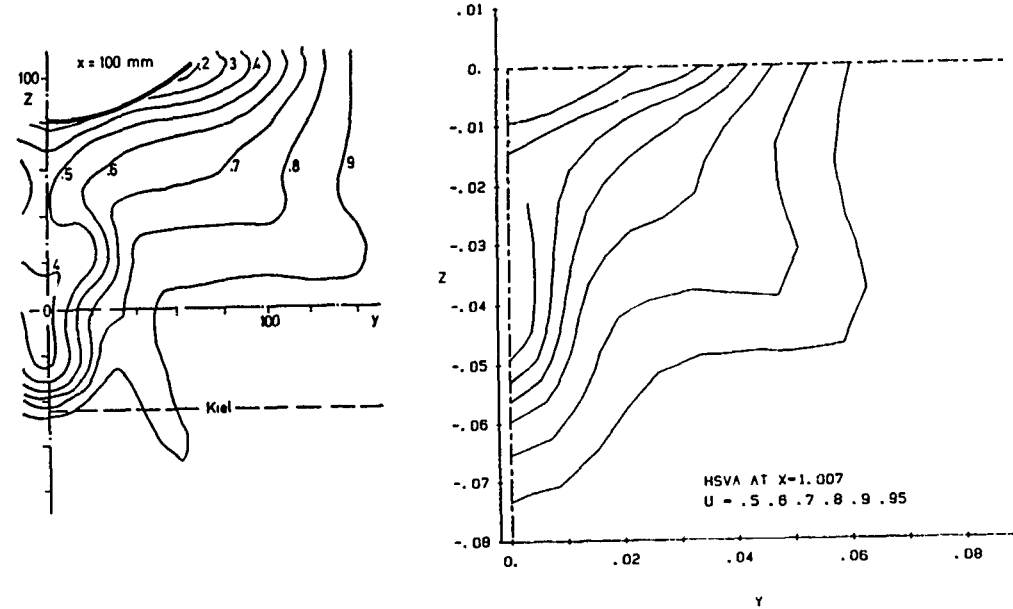


Fig. 35 Velocity field in transverse sections : (f) $X = 1.007$
 Top: contours of axial velocity (U); Bottom: velocity (V, W) in transverse sections
 Left: experiments of Wieghardt and Kux; Right: present calculations

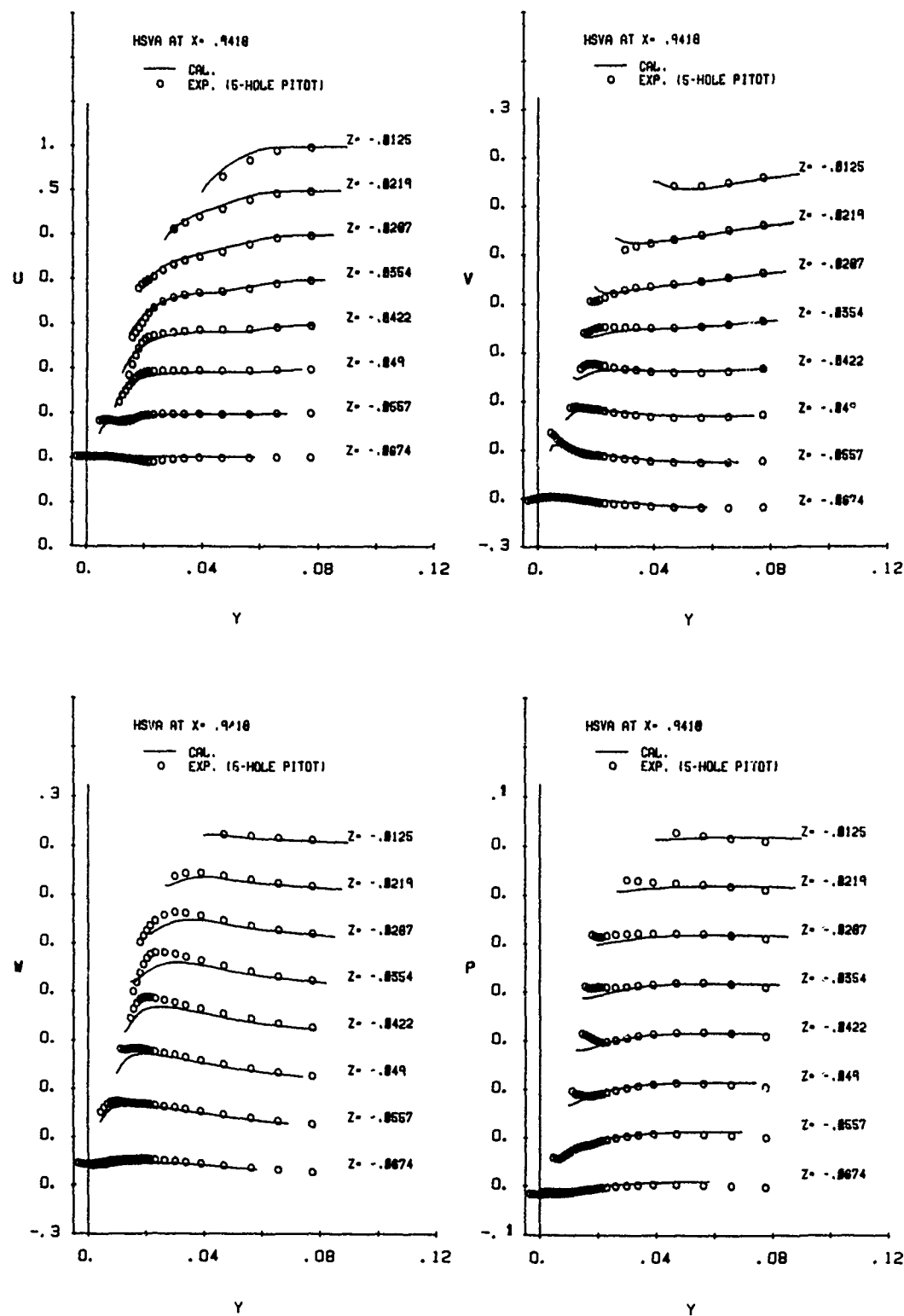


Fig. 36 Detailed comparisons of the velocity and pressure fields: profiles of U, V, W, and P
(a) $X = 0.9418$

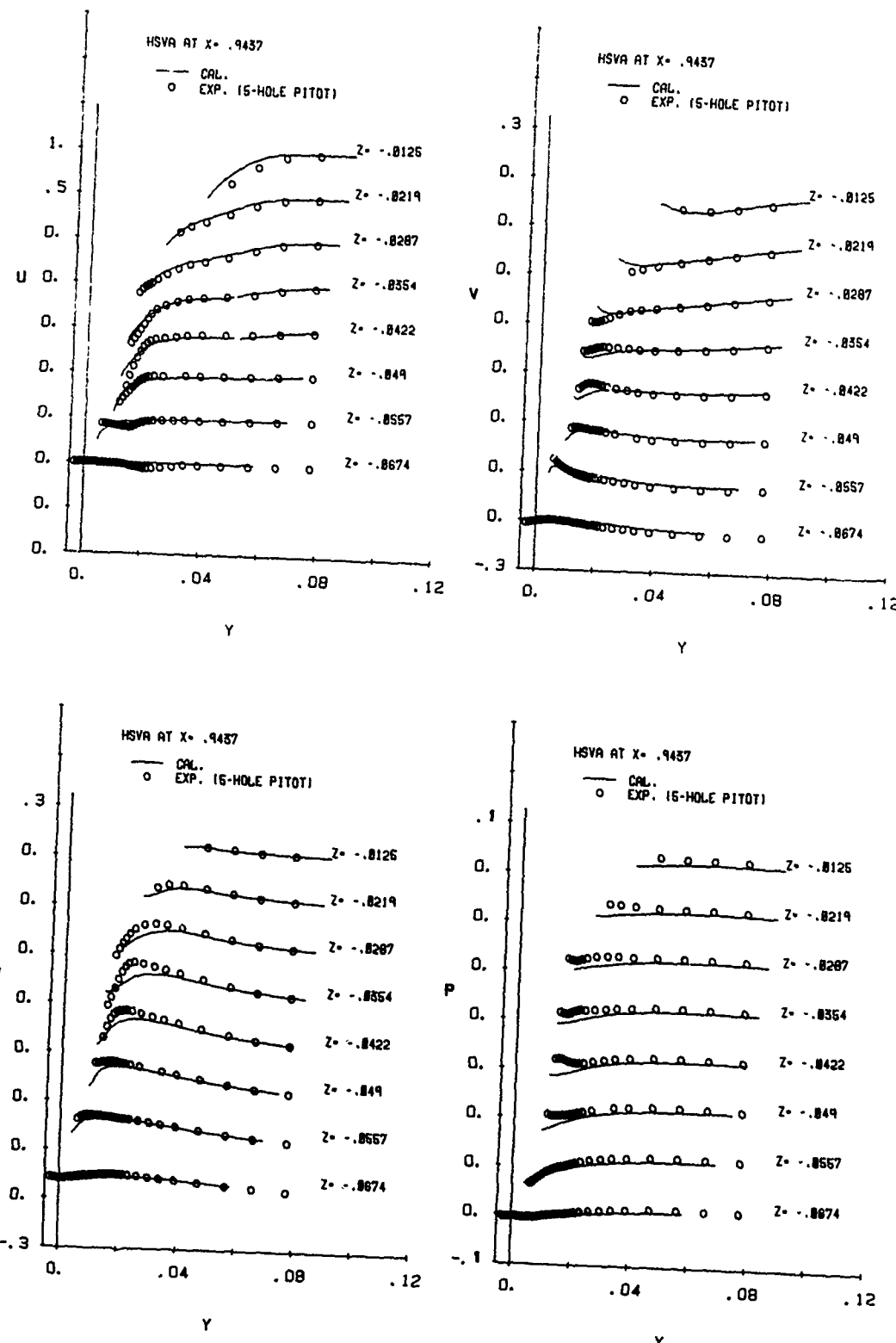


Fig. 36 Detailed comparisons of the velocity and pressure fields: profiles of U, V, W , and P
(b) $X = 0.9437$

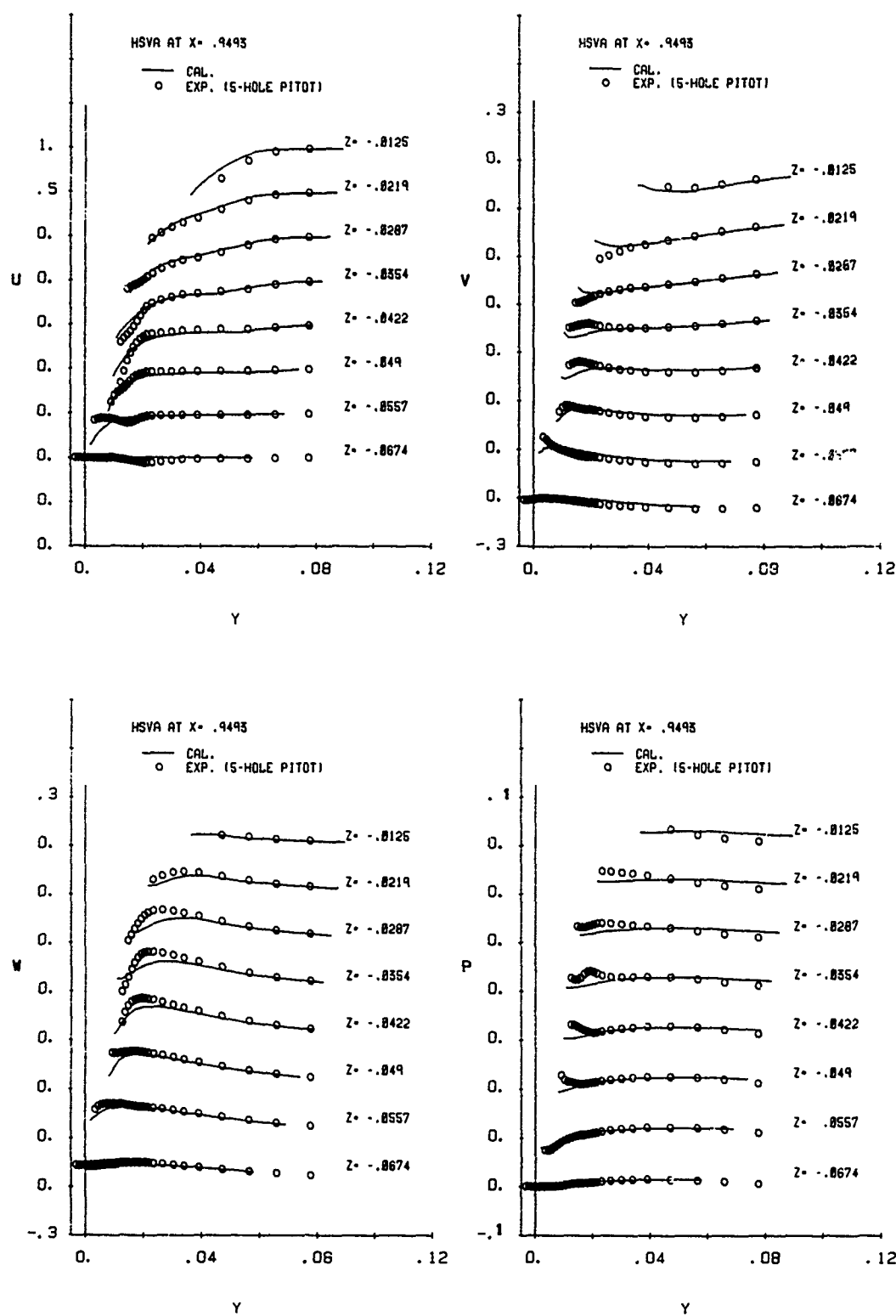


Fig. 36 Detailed comparisons of the velocity and pressure fields: profiles of U, V, W , and P
(c) $X = 0.9493$

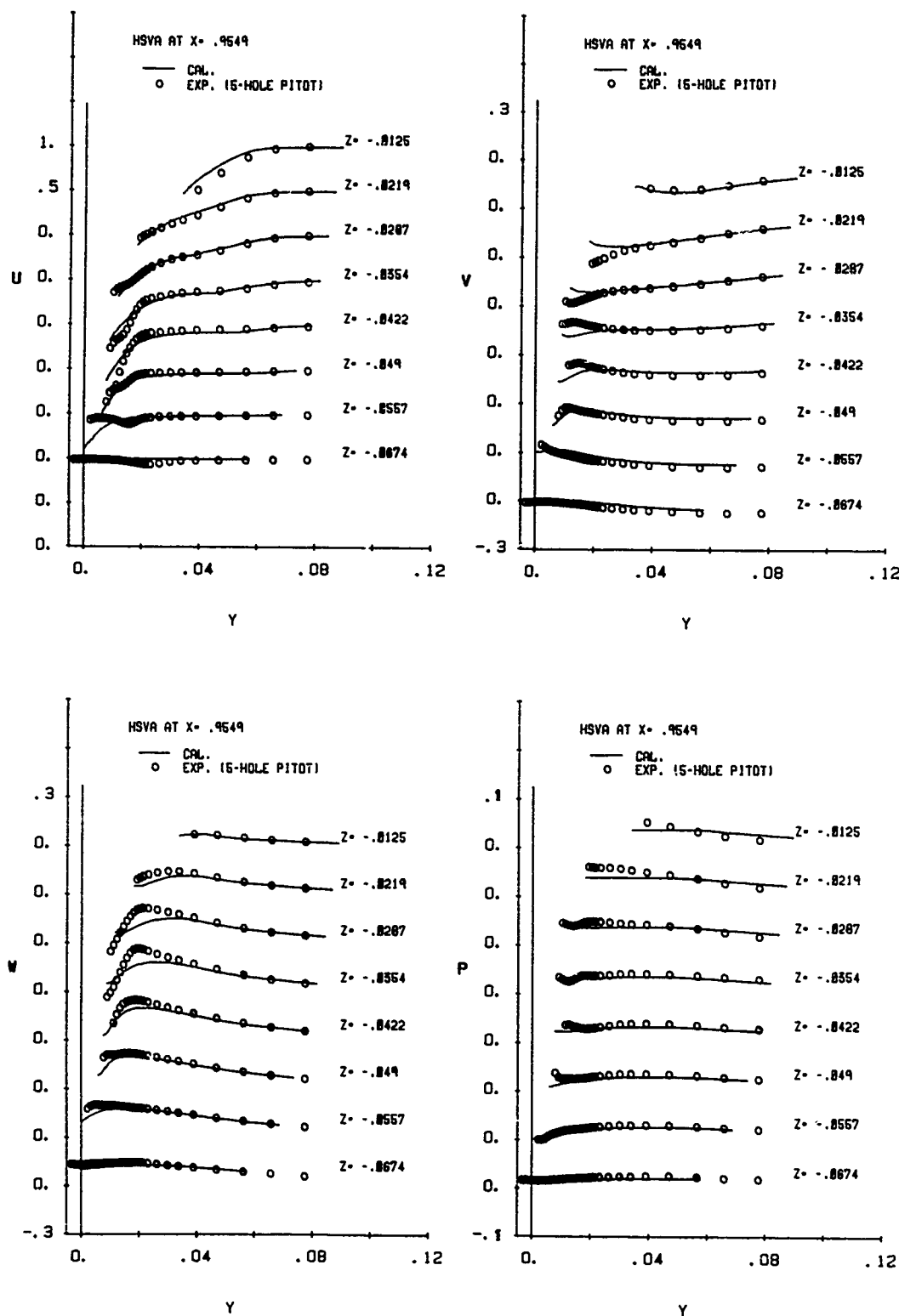


Fig. 36 Detailed comparisons of the velocity and pressure fields: profiles of U, V, W , and P
(d) $X = 0.9549$

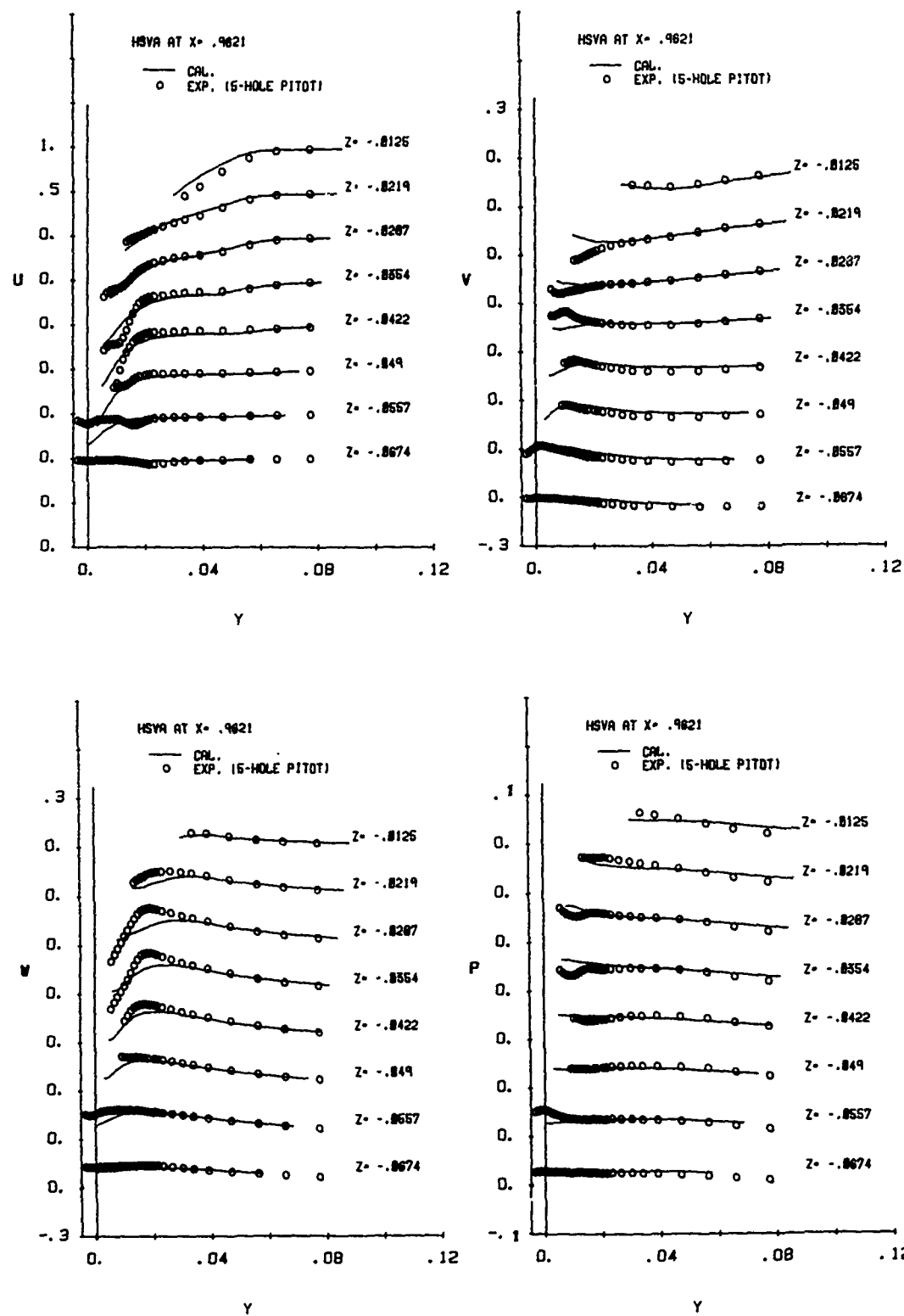


Fig. 36 Detailed comparisons of the velocity and pressure fields: profiles of U,V,W, and P
(e) $X = 0.9621$

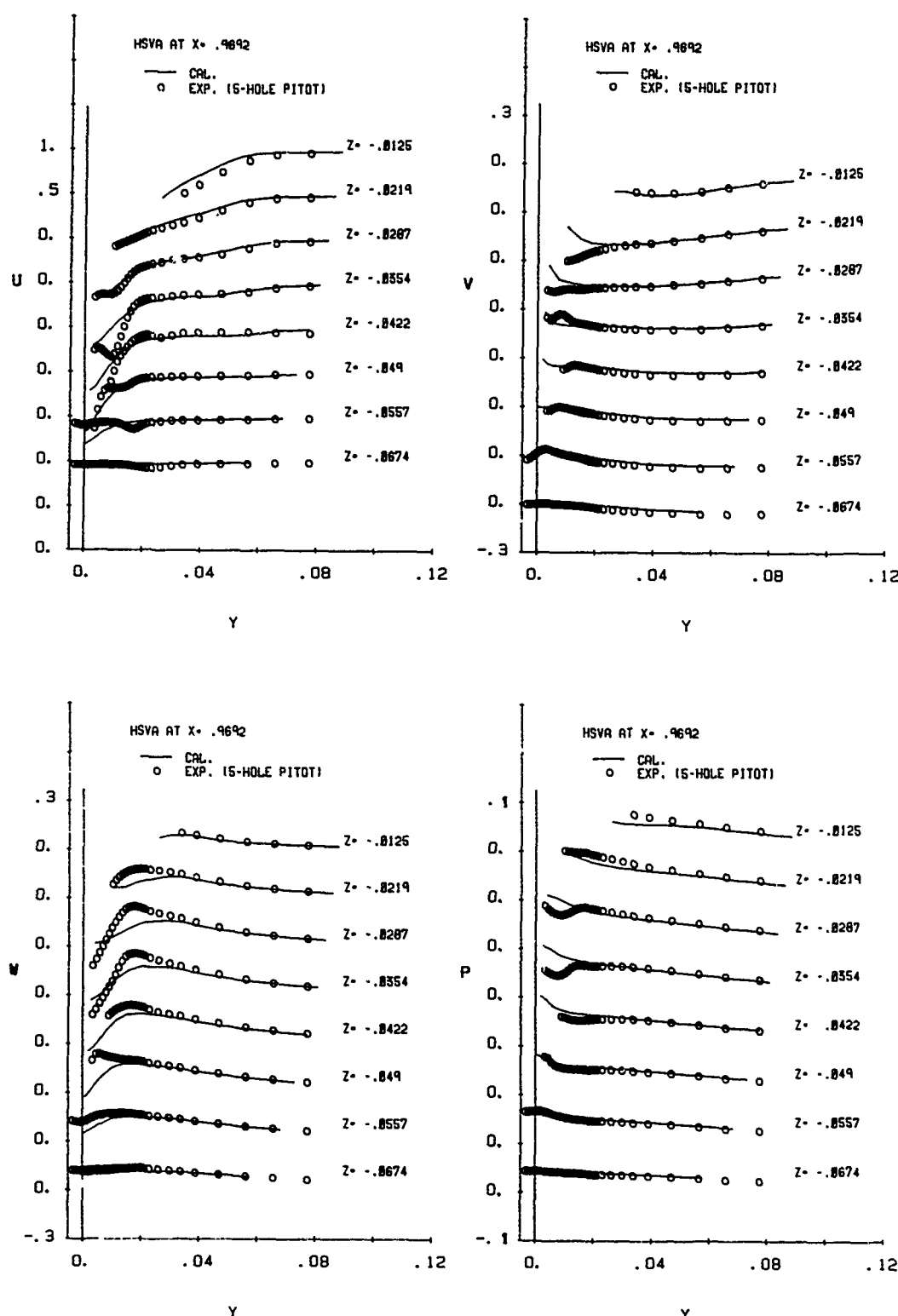


Fig. 36 Detailed comparisons of the velocity and pressure fields: profiles of U,V,W, and P
(i) $X = 0.9692$

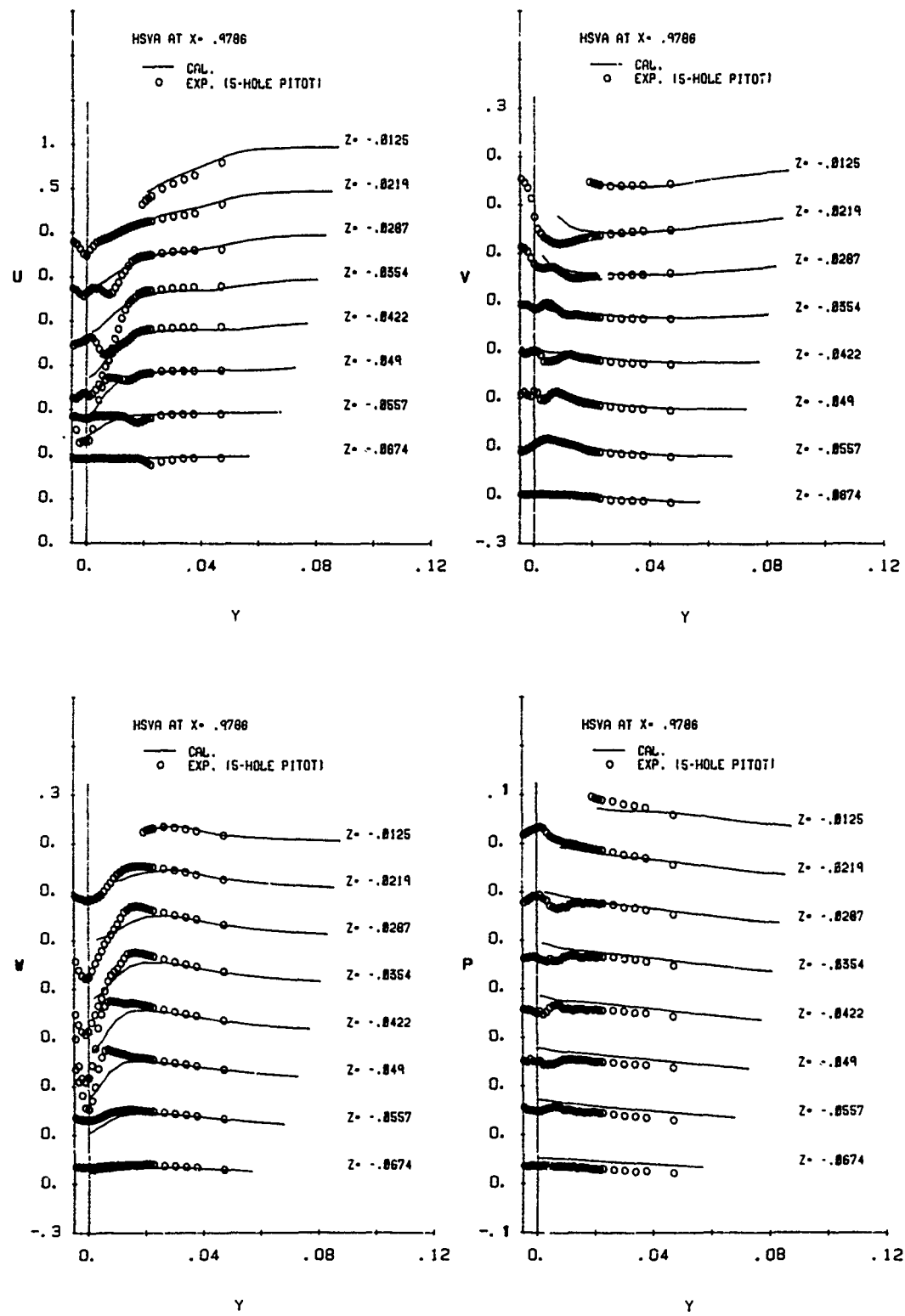


Fig. 36 Detailed comparisons of the velocity and pressure fields: profiles of U, V, W, and P (g) $X = 0.9786$

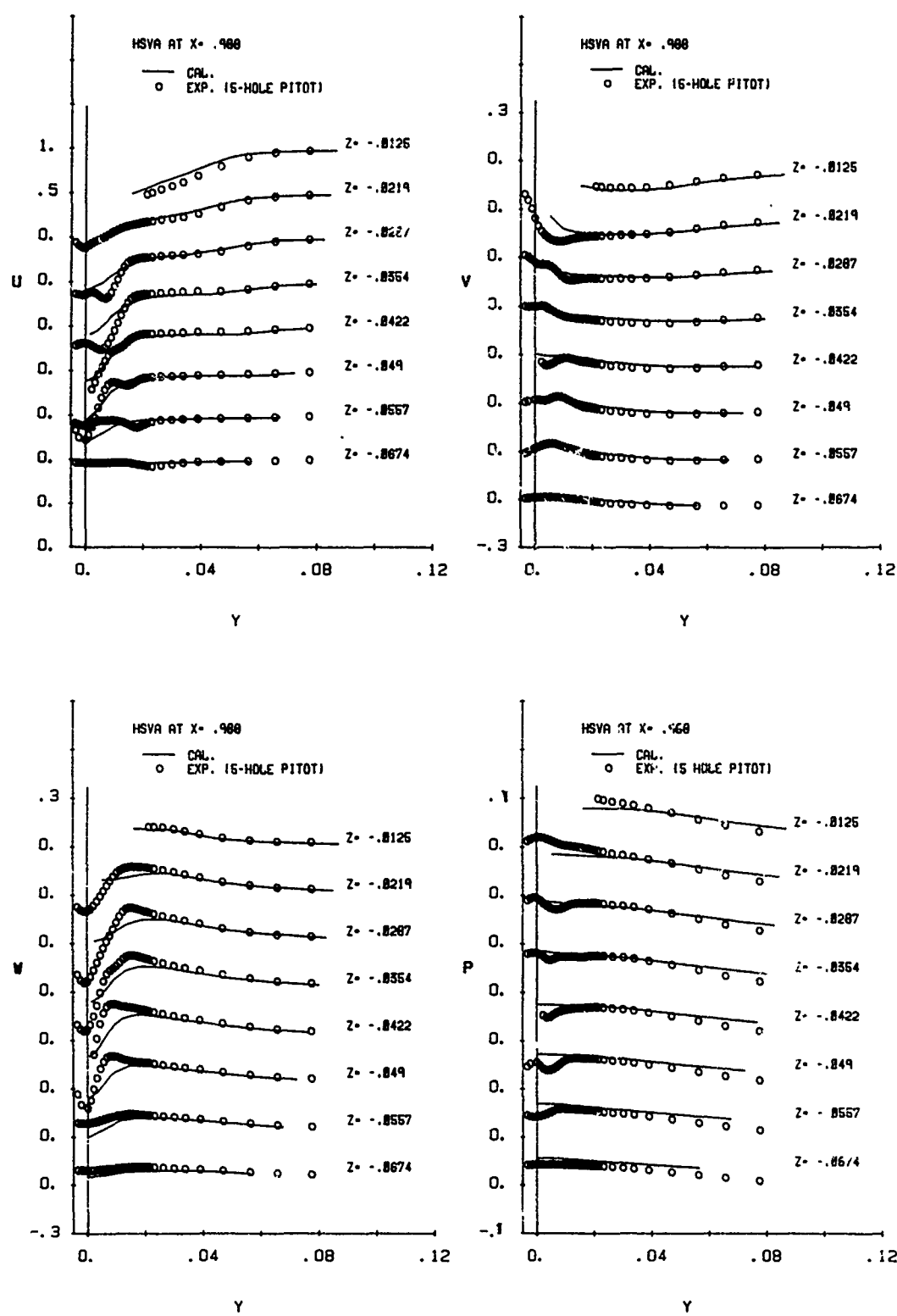


Fig. 36 Detailed comparisons of the velocity and pressure fields: profiles of U, V, W, and P
(h) $X = 0.9880$

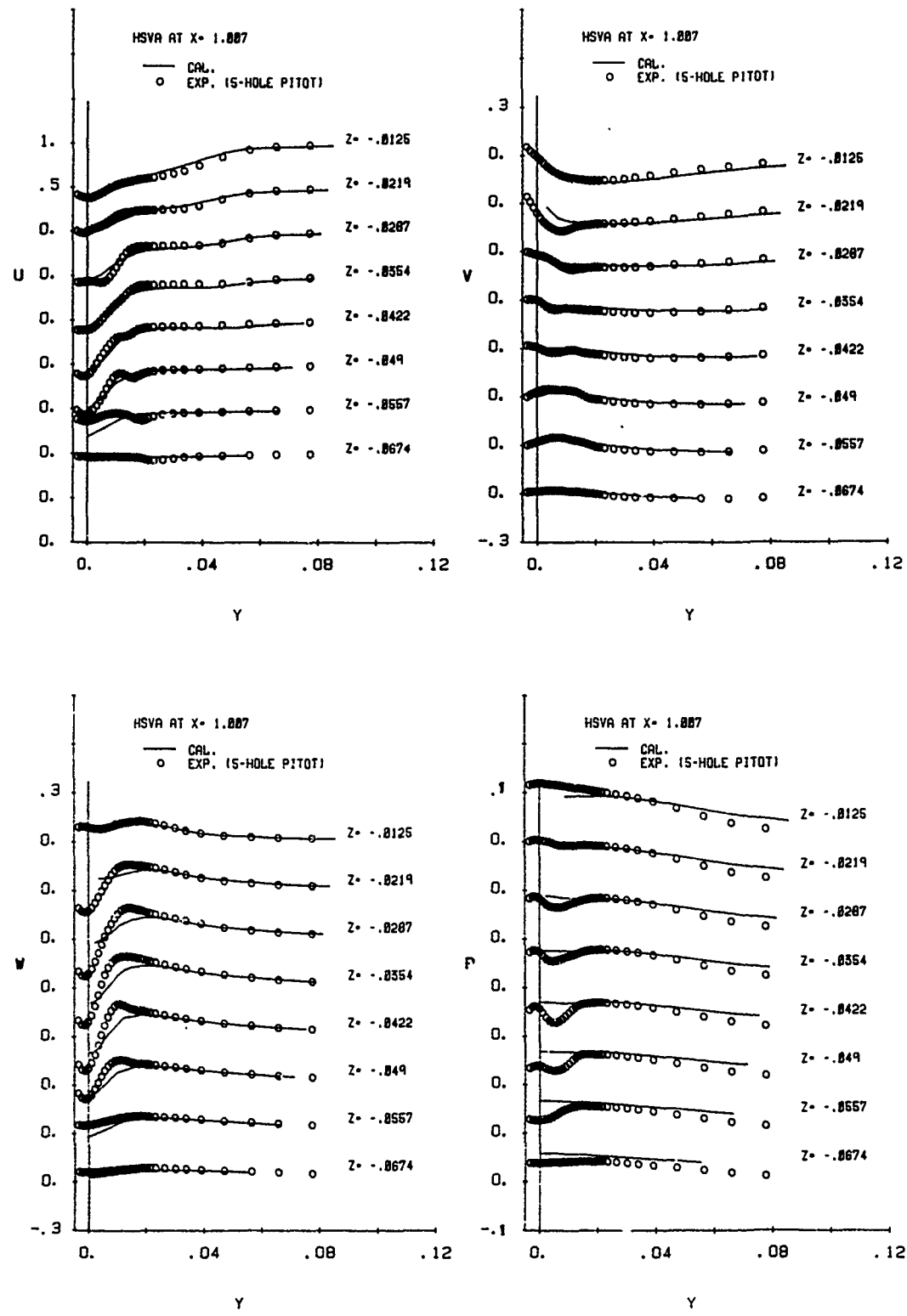


Fig. 36 Detailed comparisons of the velocity and pressure fields: profiles of U,V,W, and P
(I) $X = 1.0070$

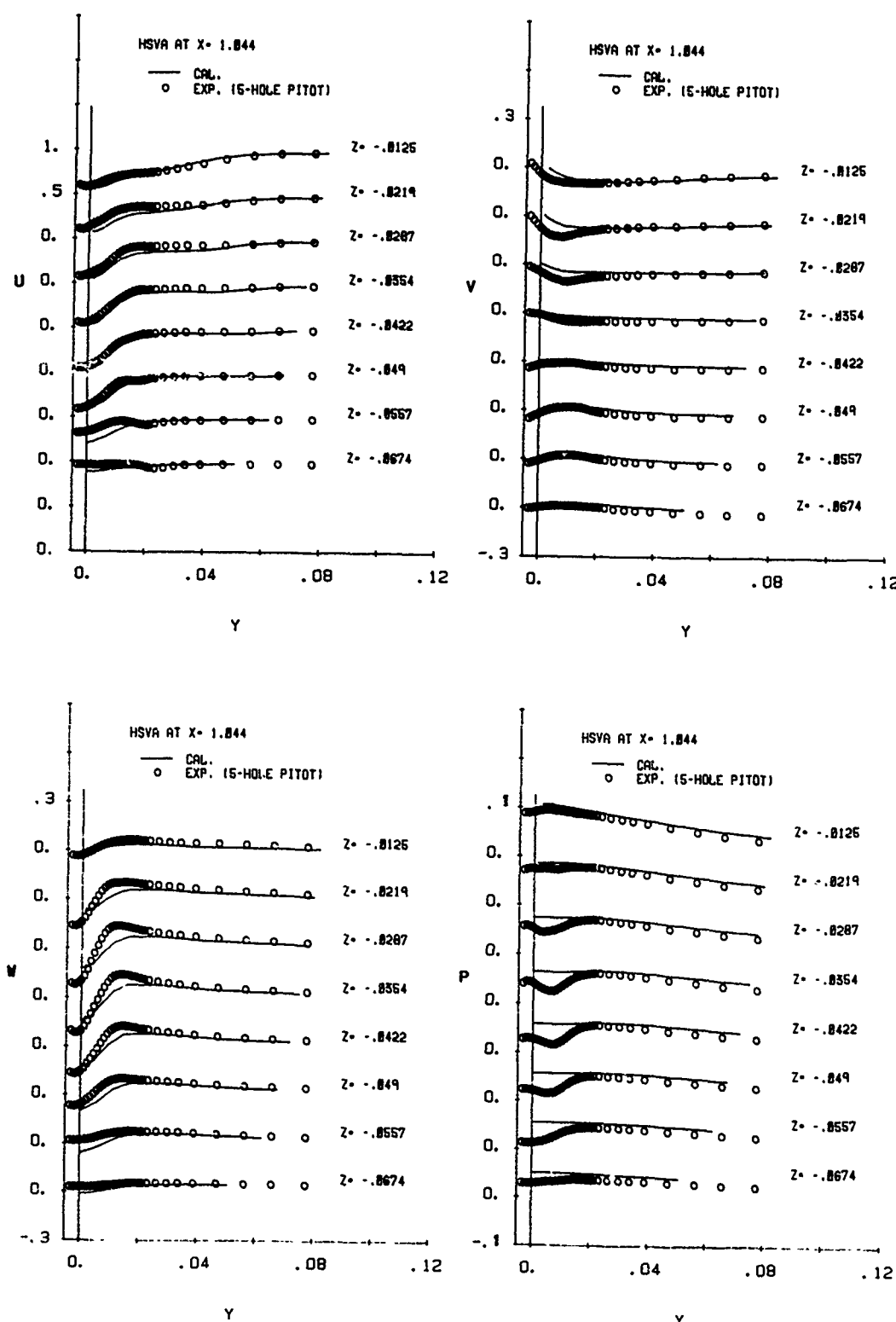


Fig. 36 Detailed comparisons of the velocity and pressure fields: profiles of U,V,W, and P
(j) $X = 1.0440$

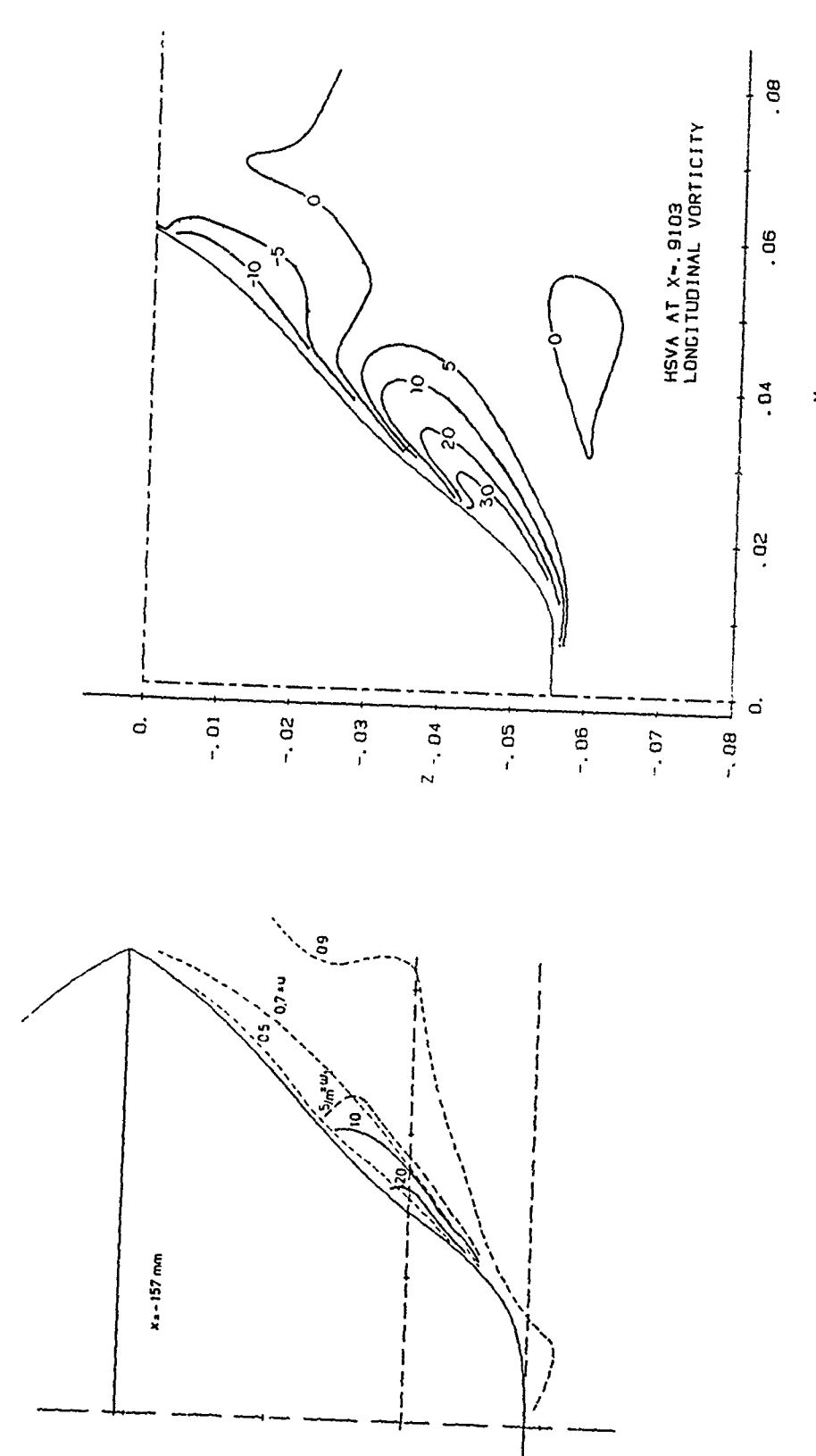


Fig. 37 Contours of longitudinal component of vorticity; experiments (left), calculations (right)
(a) $X = 0.9103$

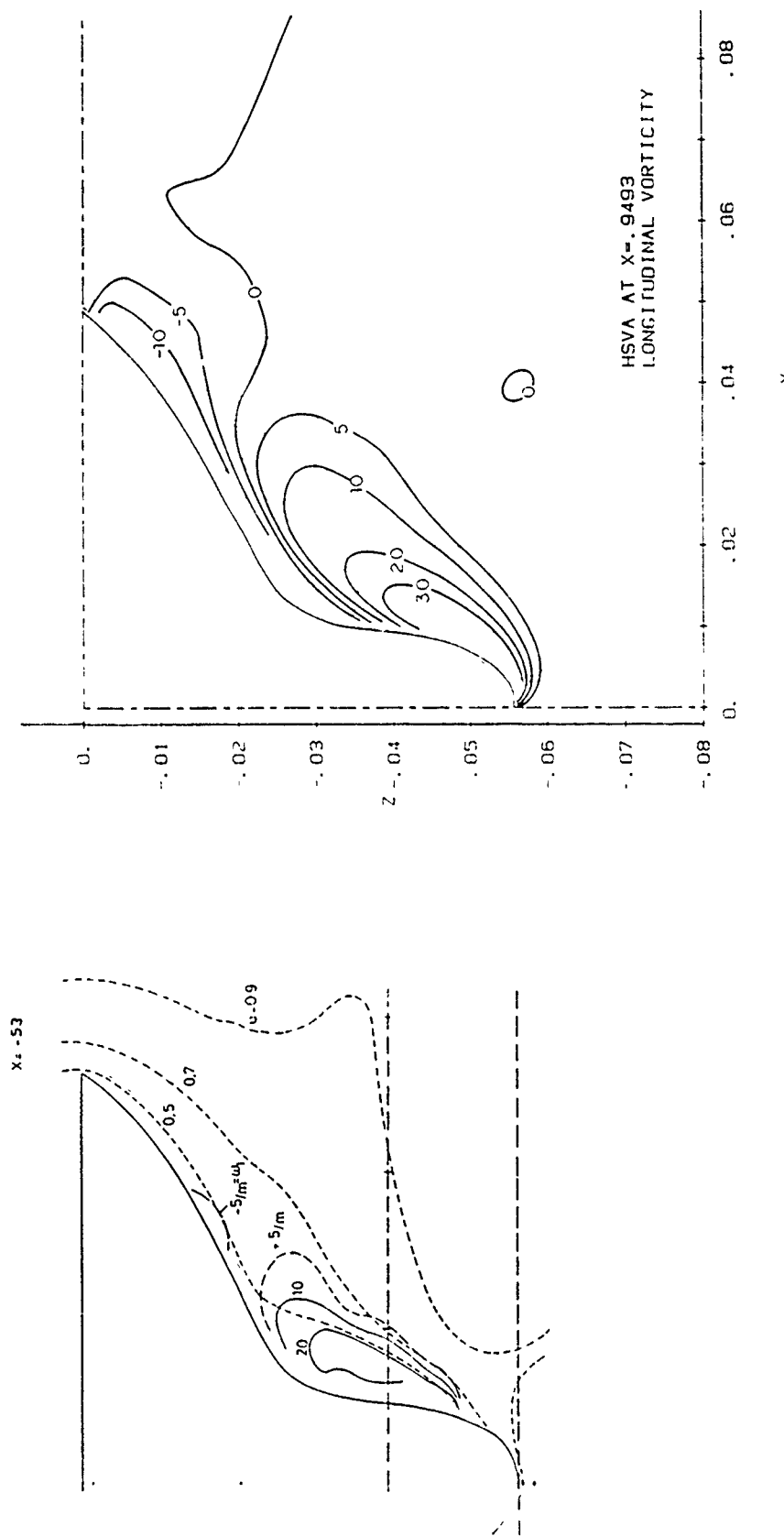


Fig. 37 Contours of longitudinal component of vorticity; experiments (left), calculations (right)
(b) $X = 0.9493$

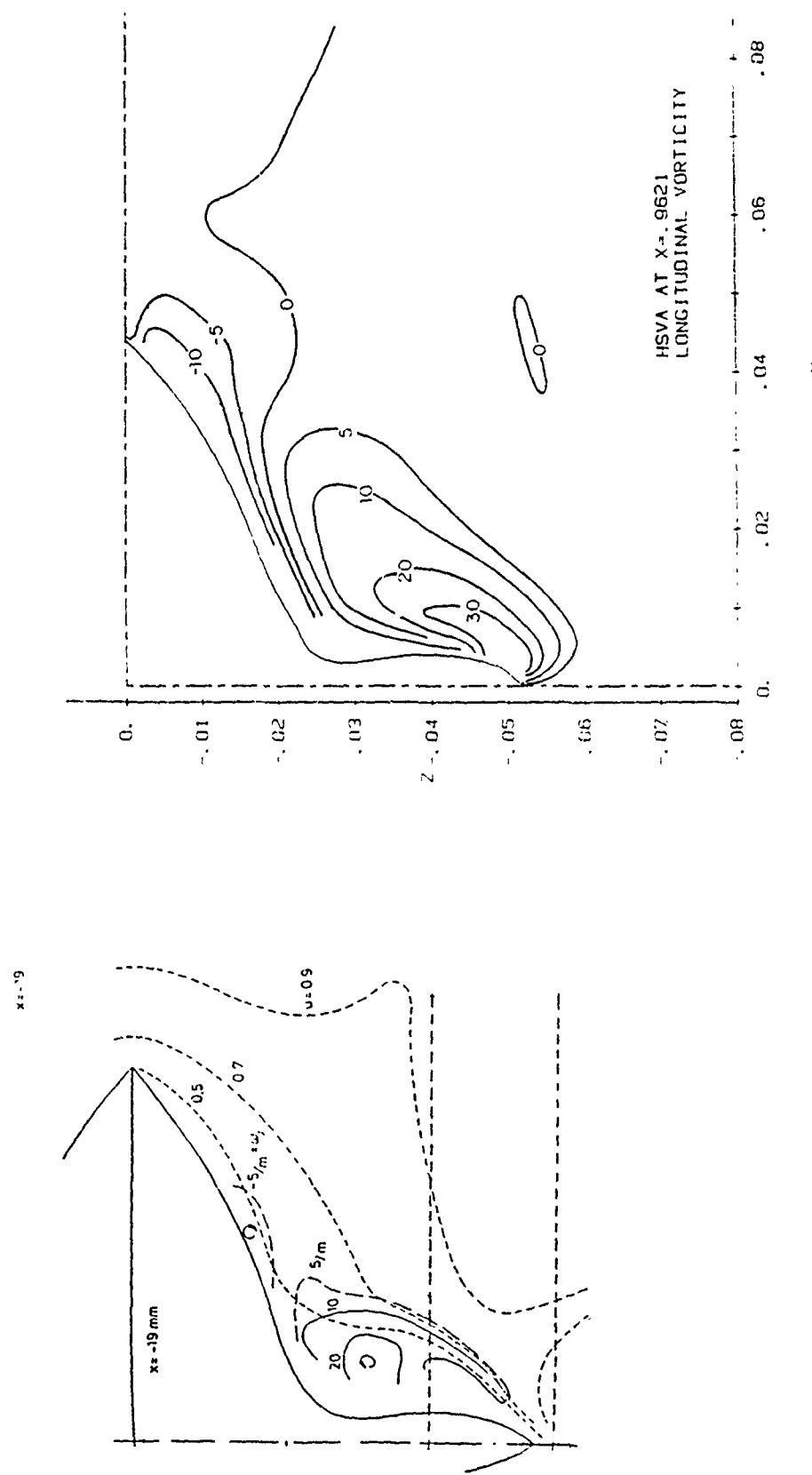


Fig. 37 Contours of longitudinal component of vorticity; experiments (left), calculations (right)
(c) $X = 0.9621$

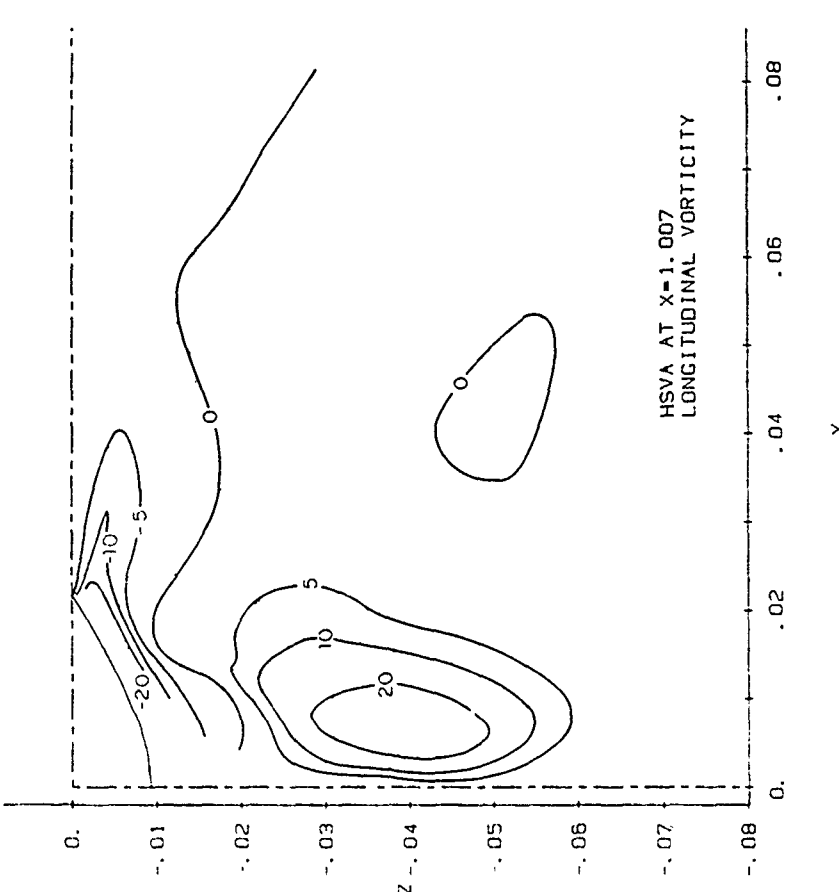
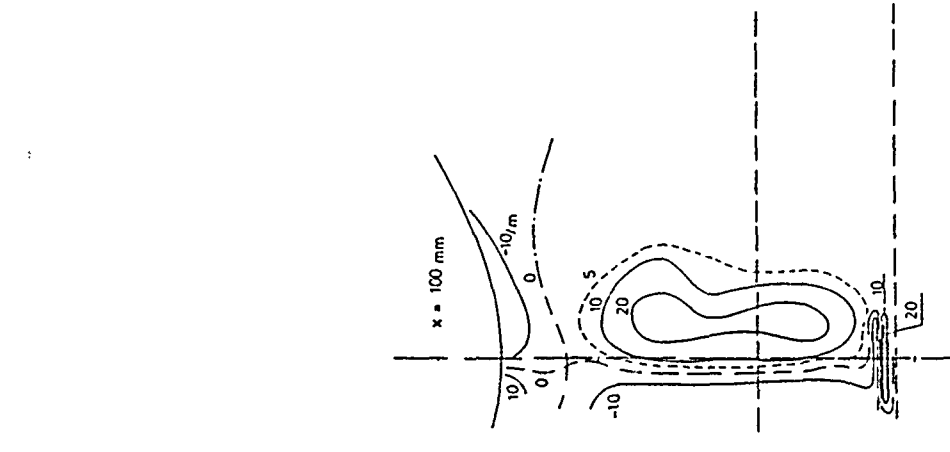


Fig. 37 Contours of longitudinal component of vorticity; experiments (left), calculations (right)
(d) $X = 1.007$

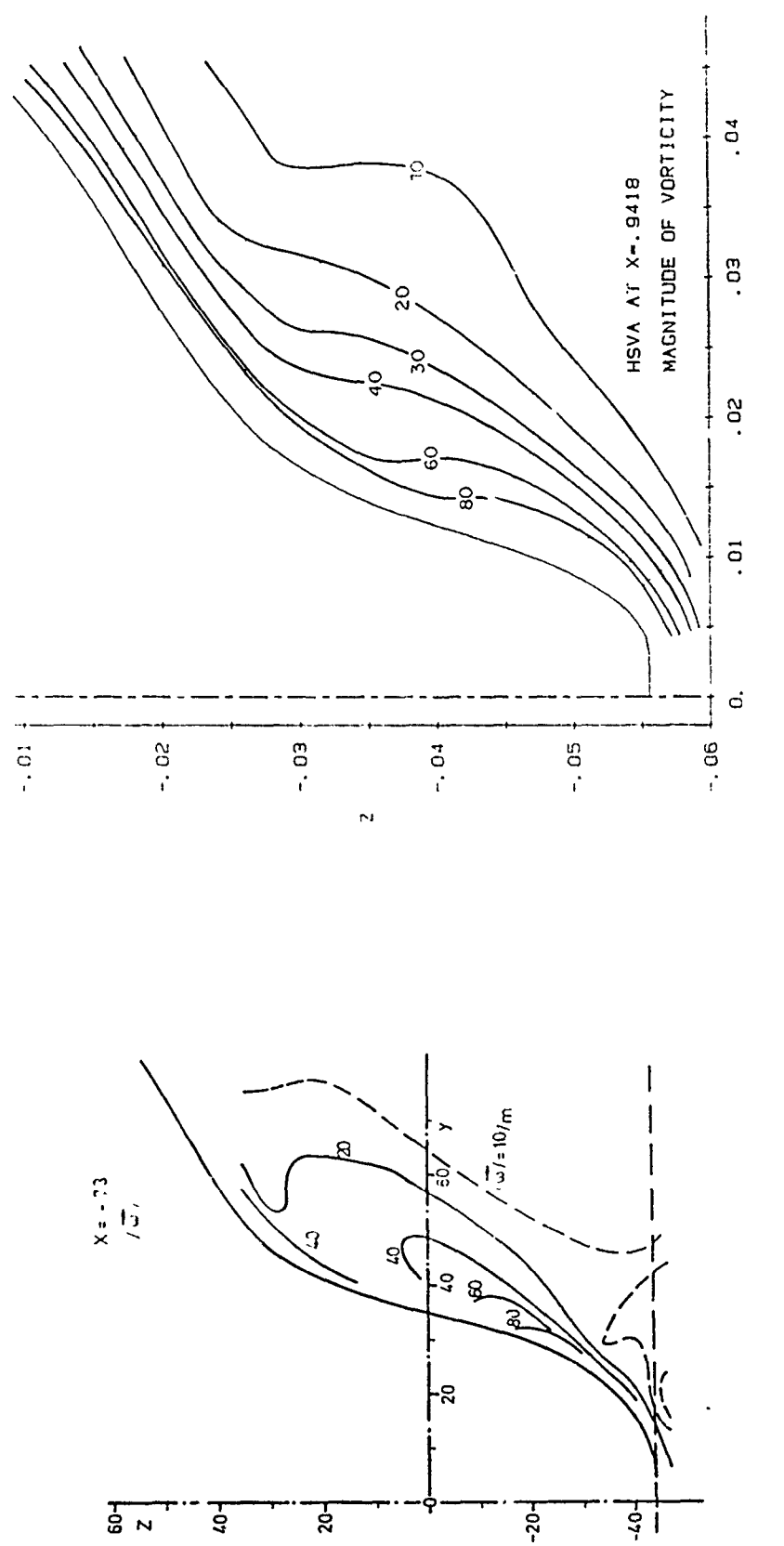


Fig. 38 Contours of magnitude of the vorticity vector; experiments (left), calculations (right)
 (a) $X = 0.9418$

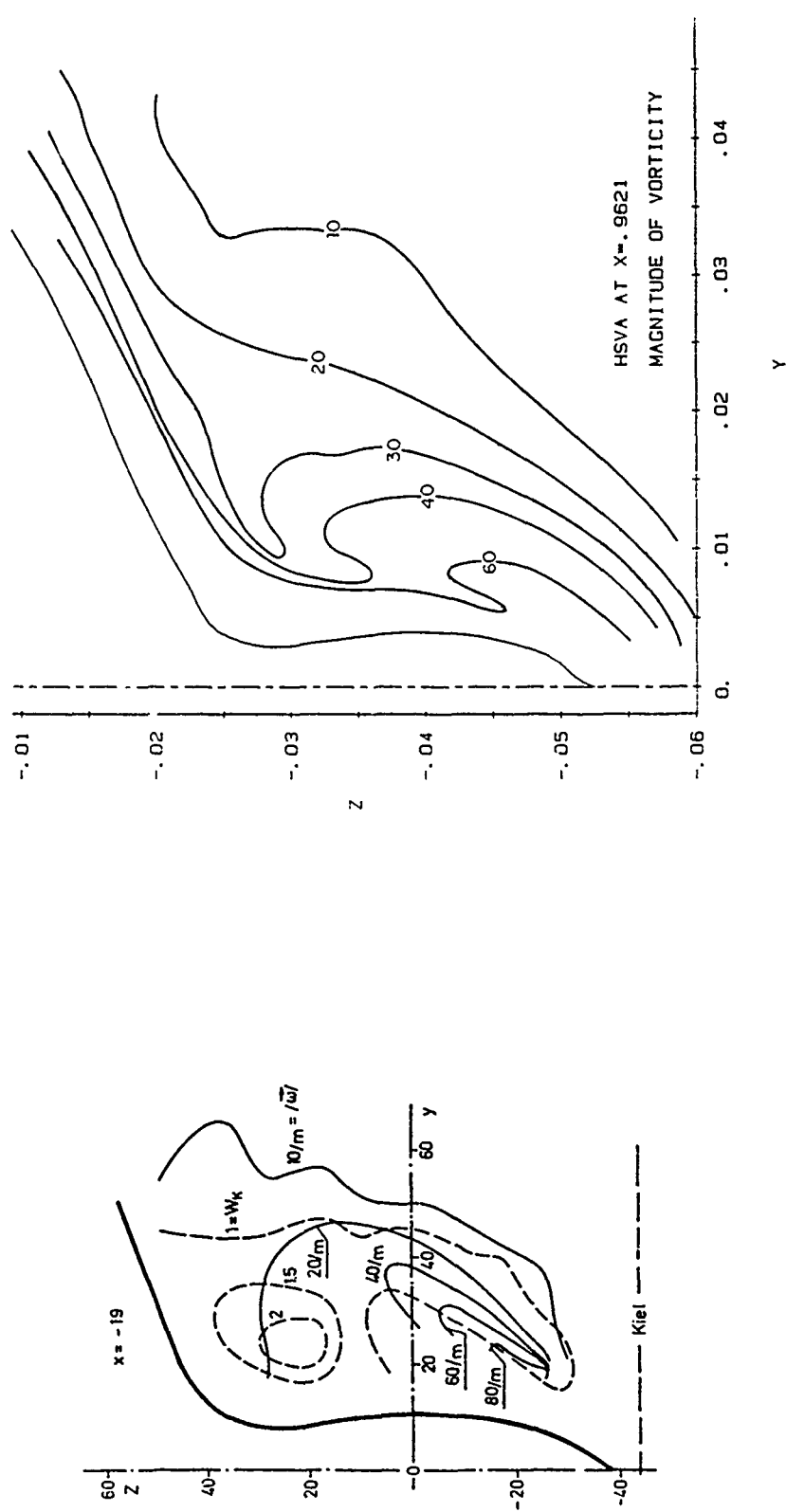


Fig. 38 Contours of magnitude of the vorticity vector; experiments (left), calculations (right)
(b) $X = 0.9621$

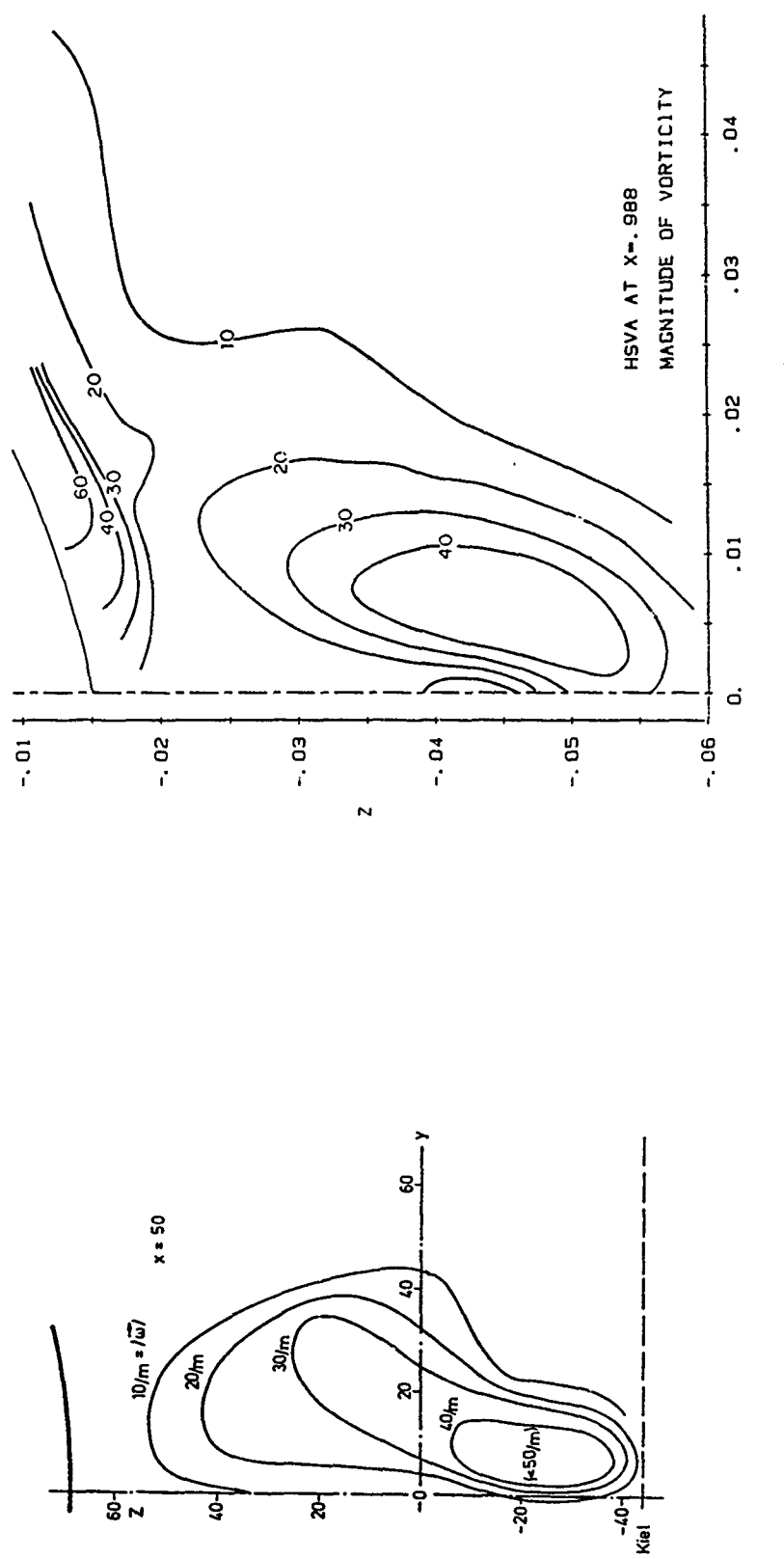


Fig. 38 Contours of magnitude of the vorticity vector; experiments (left), calculations (right)
(c) $X = 0.988$

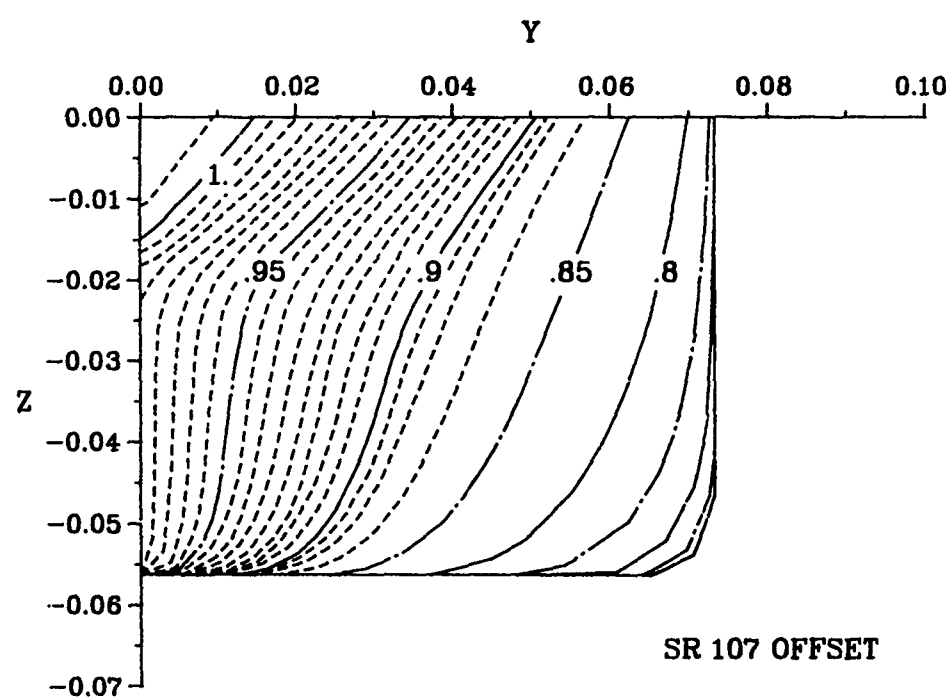
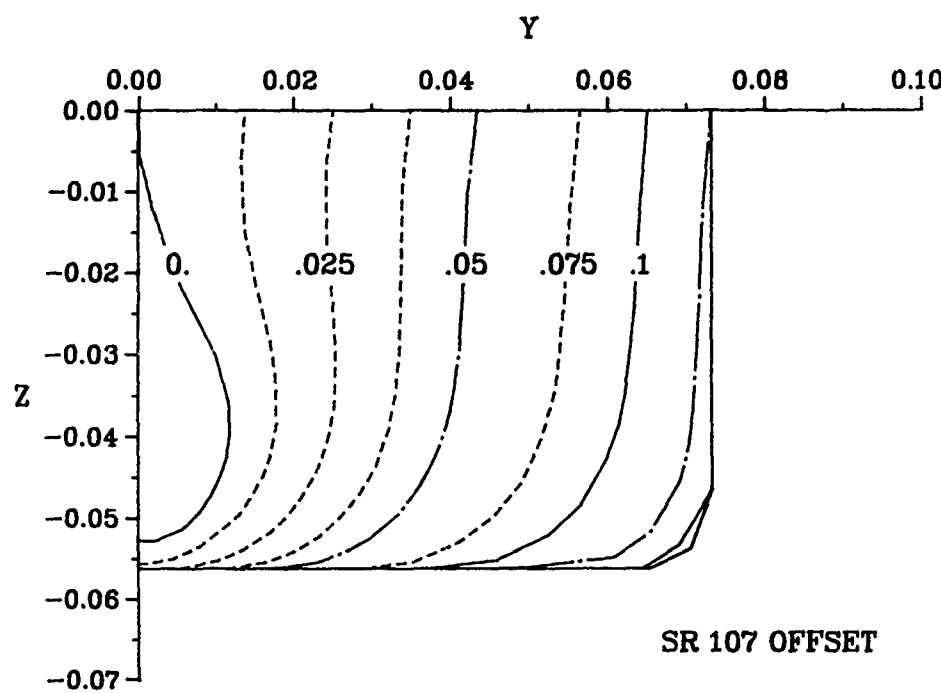


Fig. 39 Offsets of SR107 Ore Carrier
(a) forebody (b) afterbody

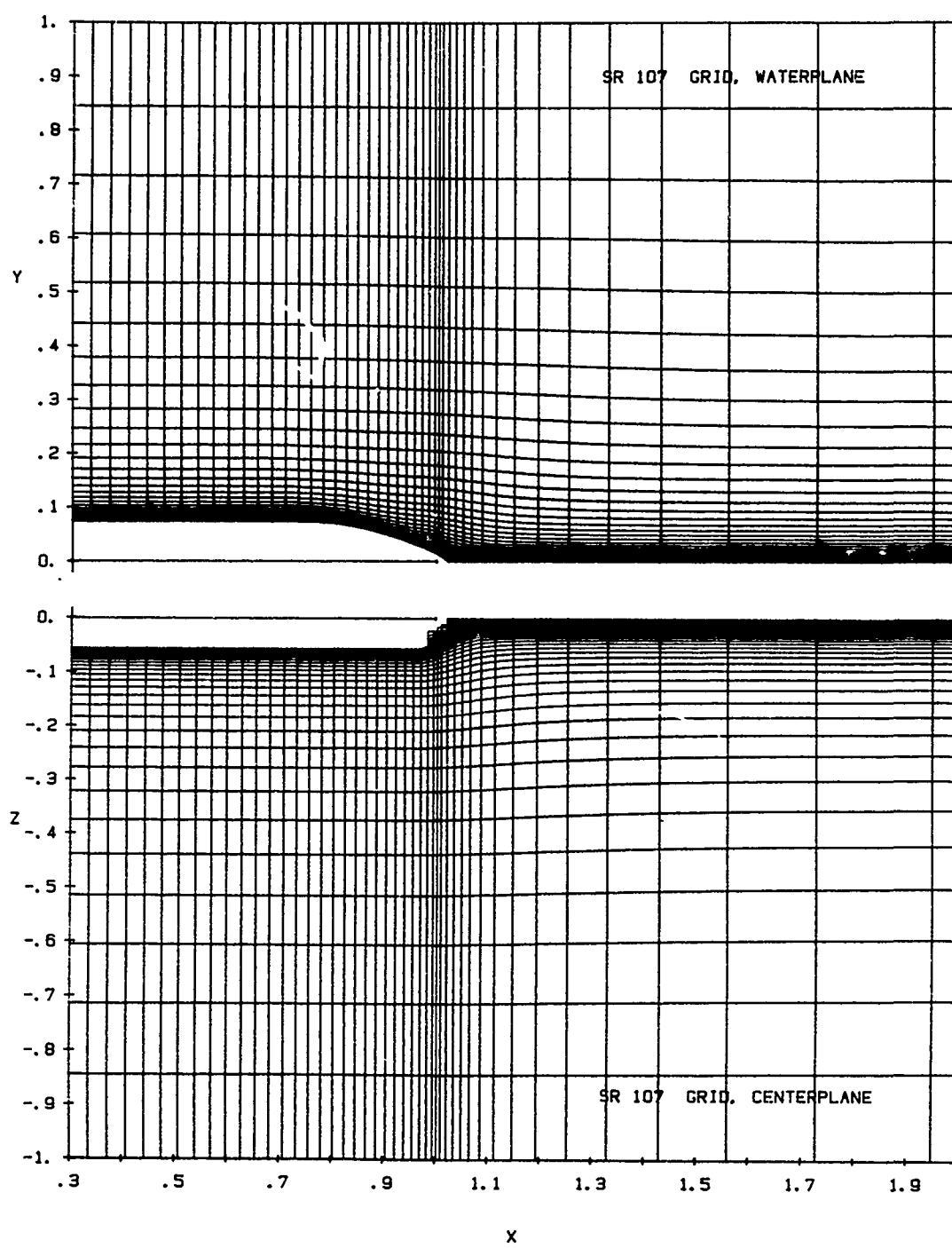


Fig. 40 Typical views of the numerical grid
(a) symmetry planes

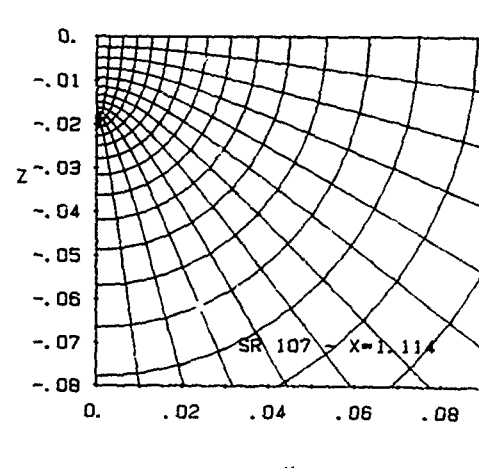
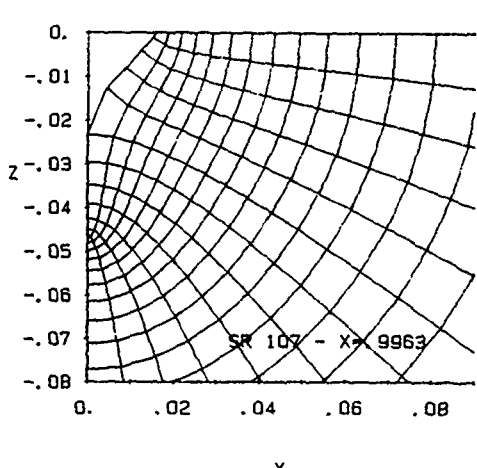
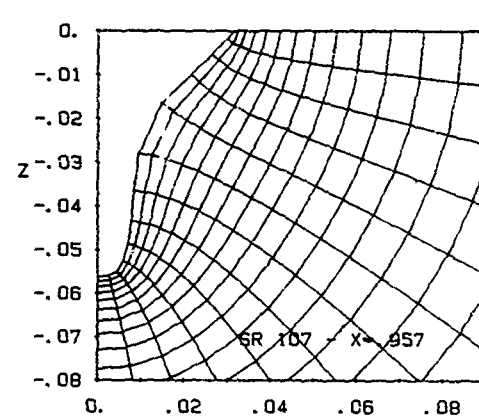
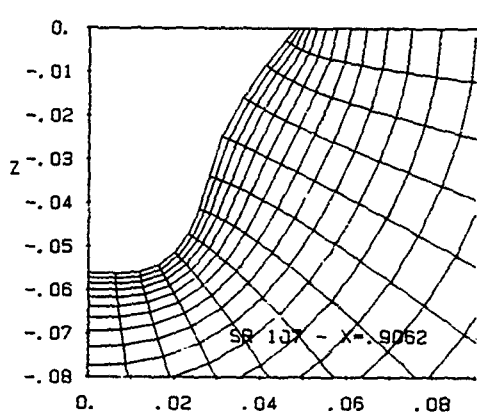
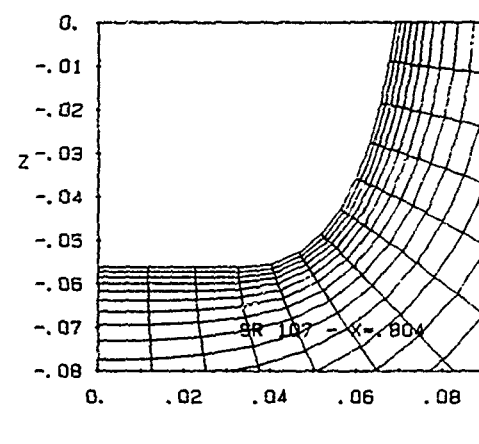
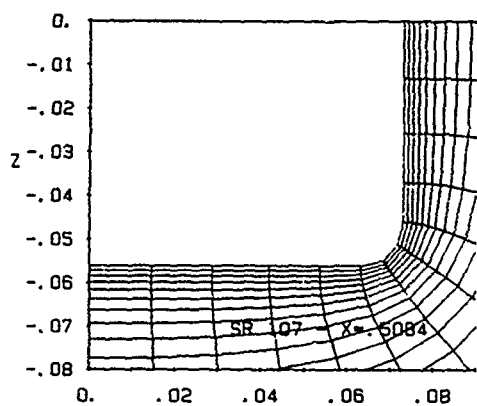


Fig. 40 Typical views of the numerical grid
(b) transverse sections

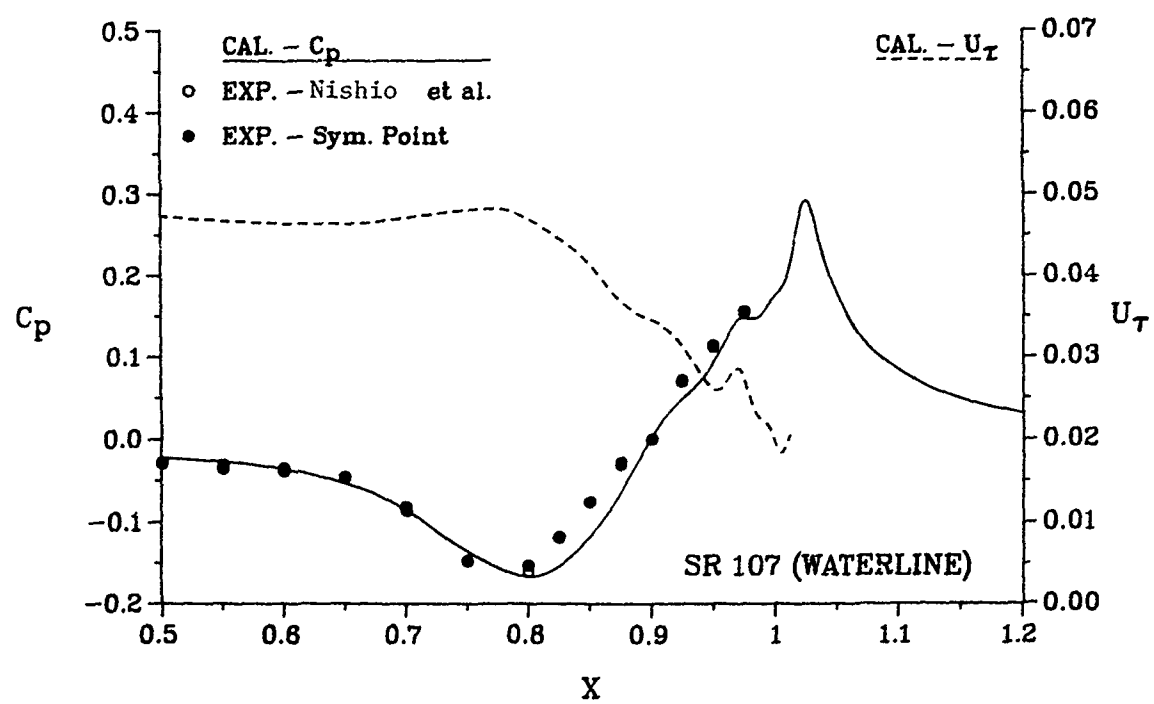
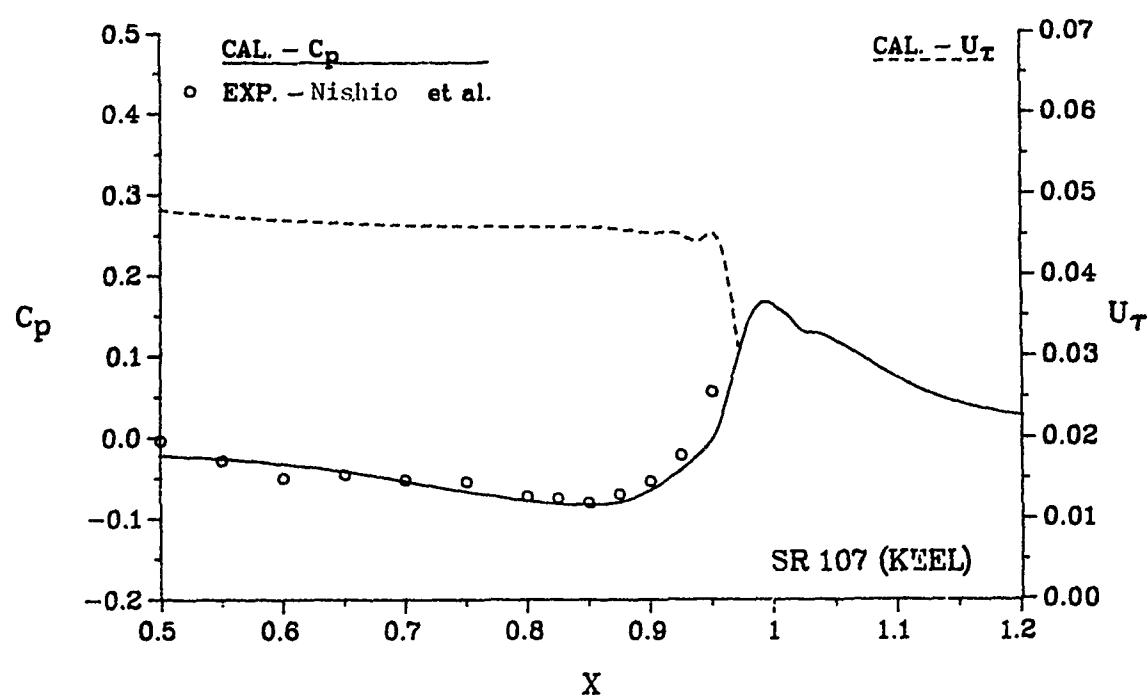


Fig. 41 Pressure and friction velocity along the keel and waterline

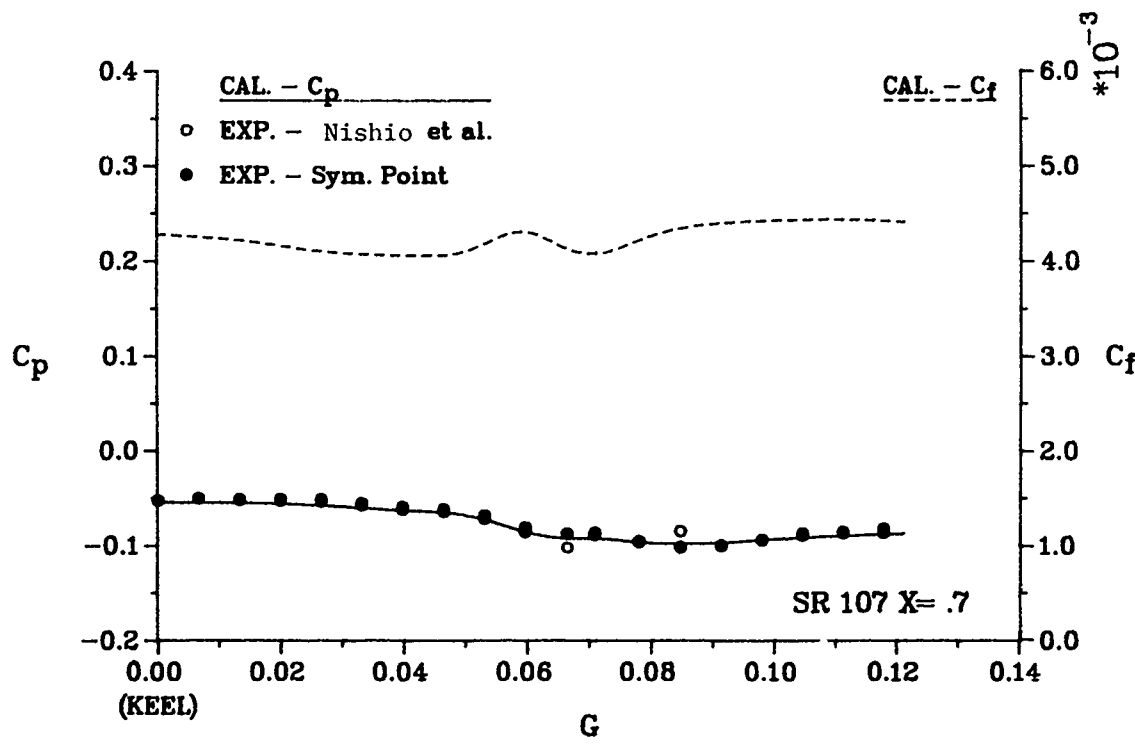
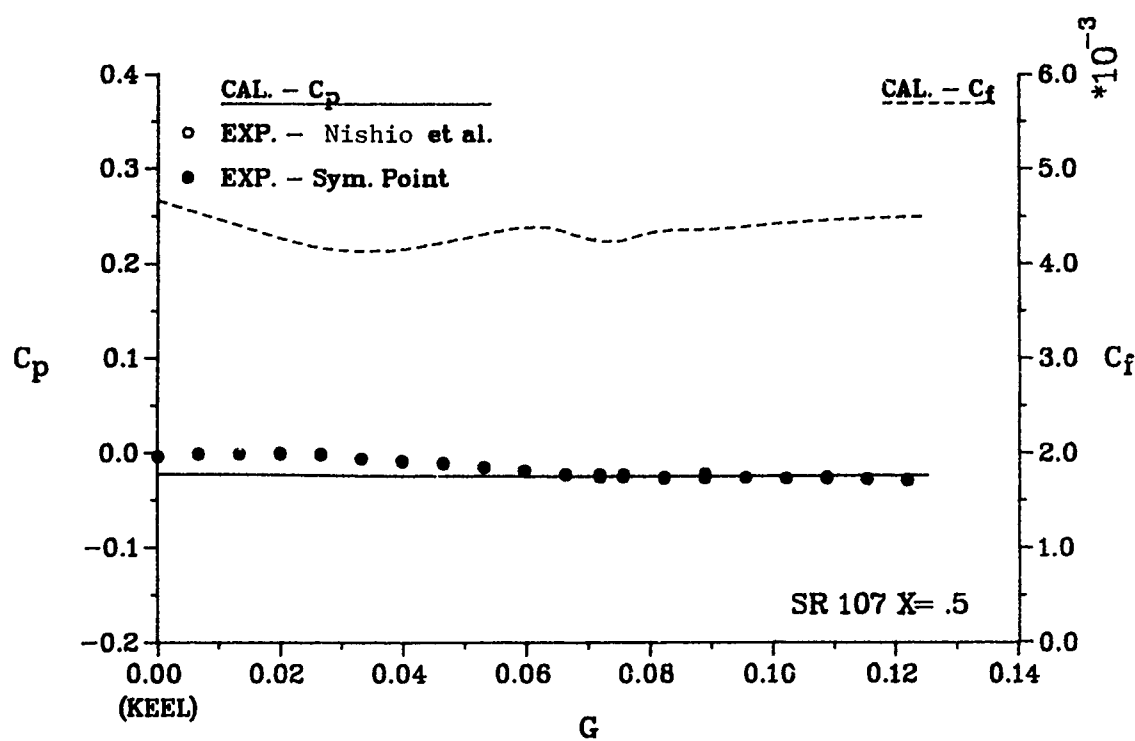


Fig. 42 Girthwise variation of pressure and friction coefficients
 (a) $X = 0.5$; (b) $X = 0.7$

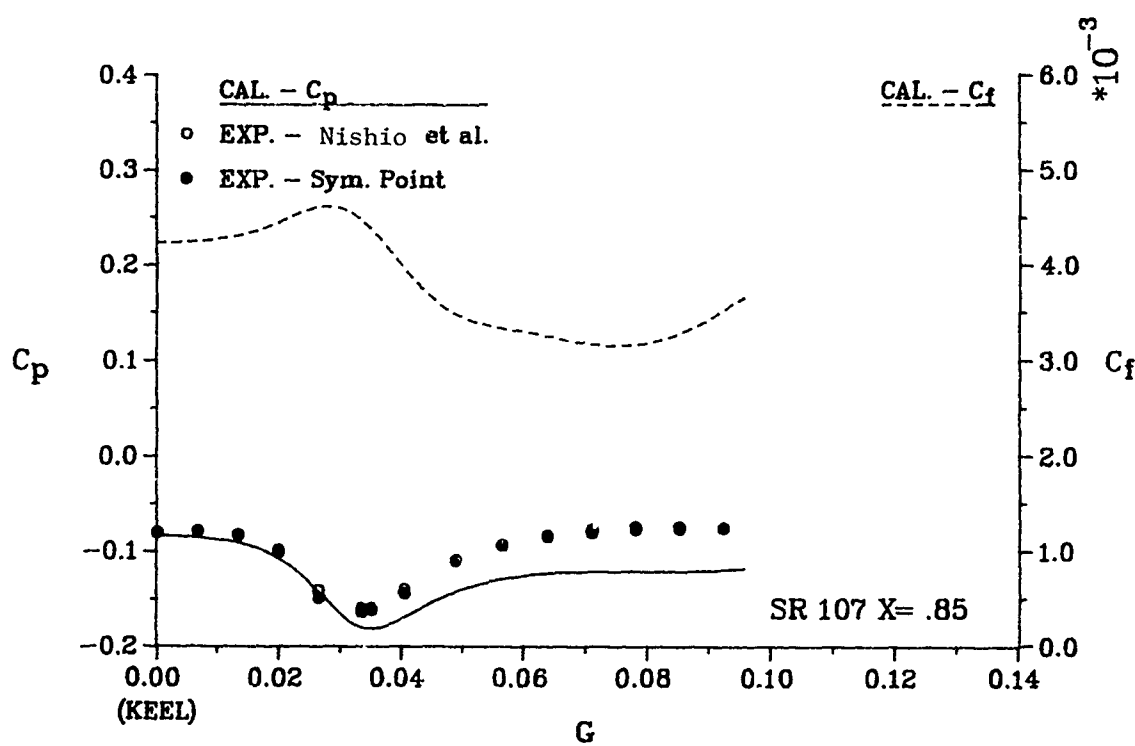
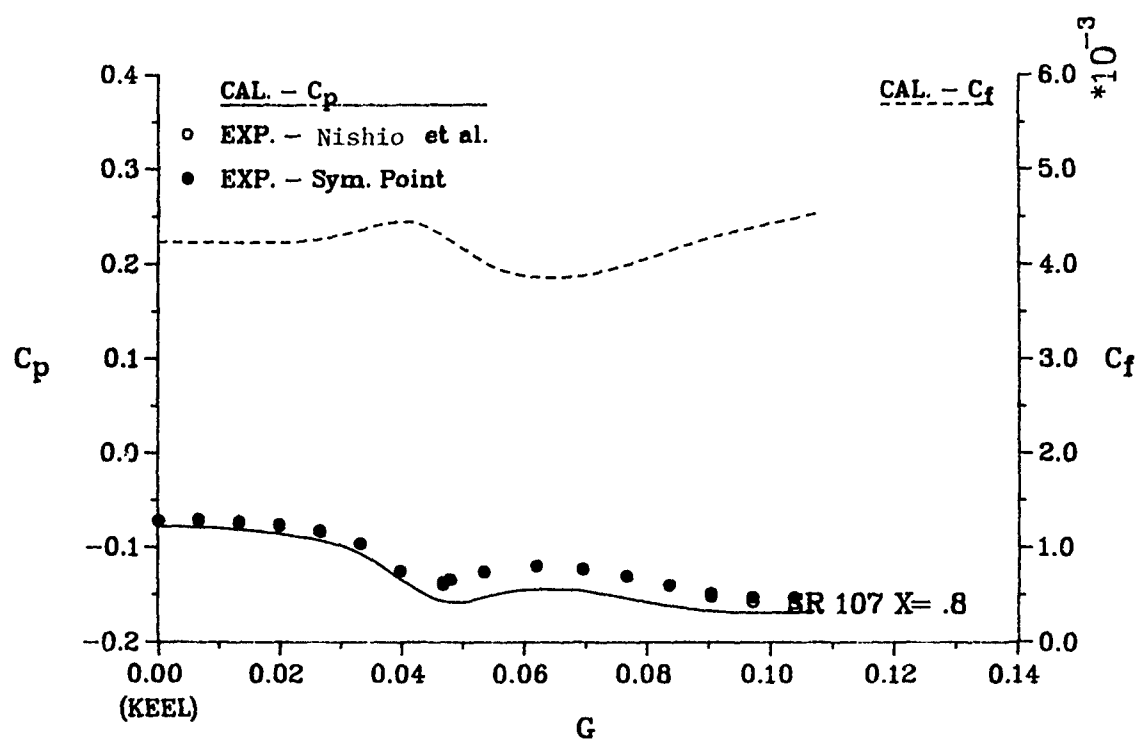


Fig. 42 Girthwise variation of pressure and friction coefficients
(c) $X = 0.8$; (d) $X = 0.85$

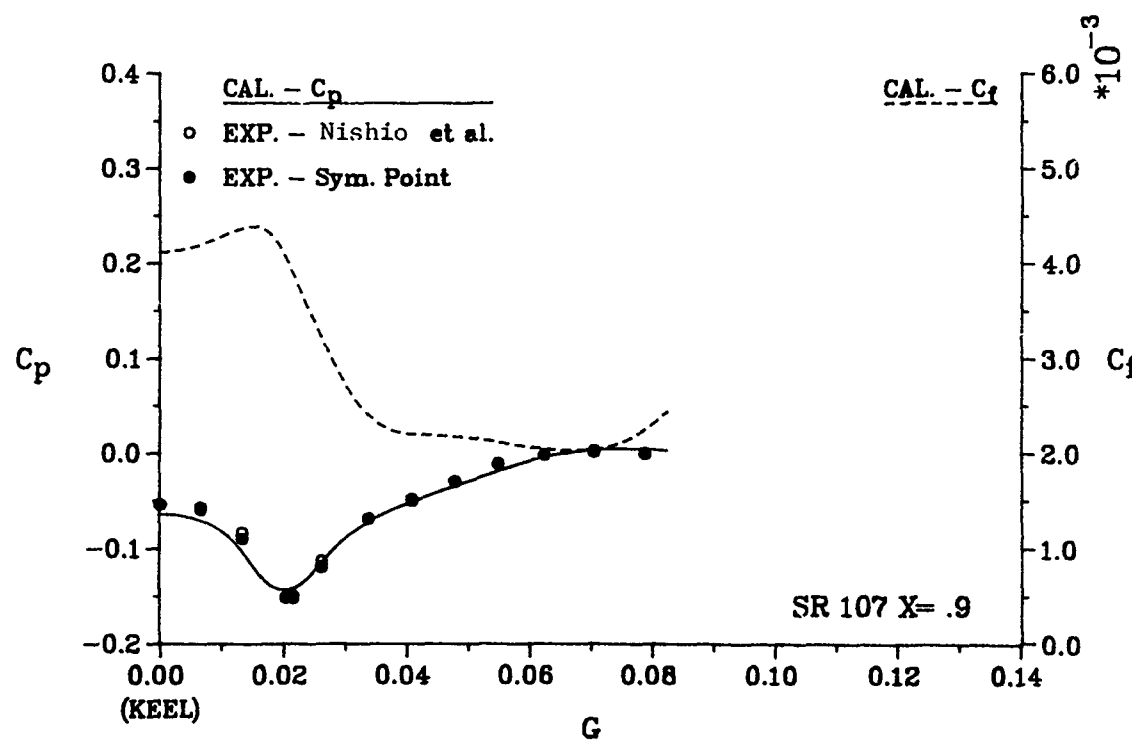
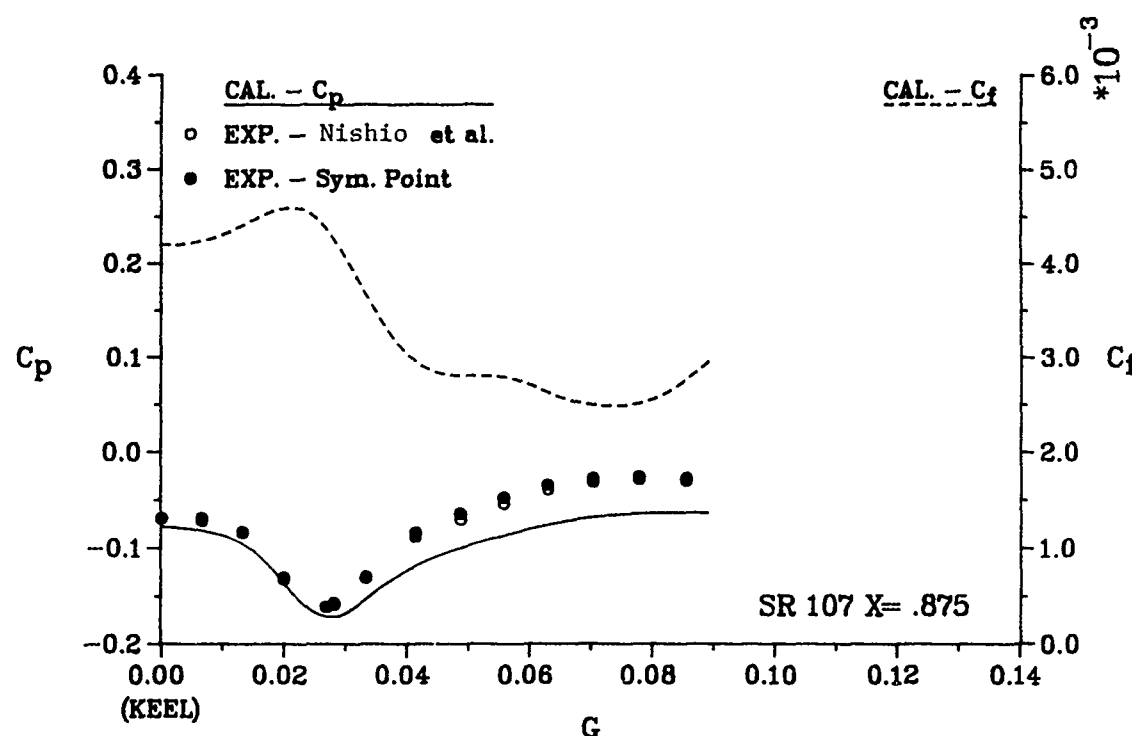


Fig. 42 Girthwise variation of pressure and friction coefficients
(e) $X = 0.875$; (f) $X = 0.9$

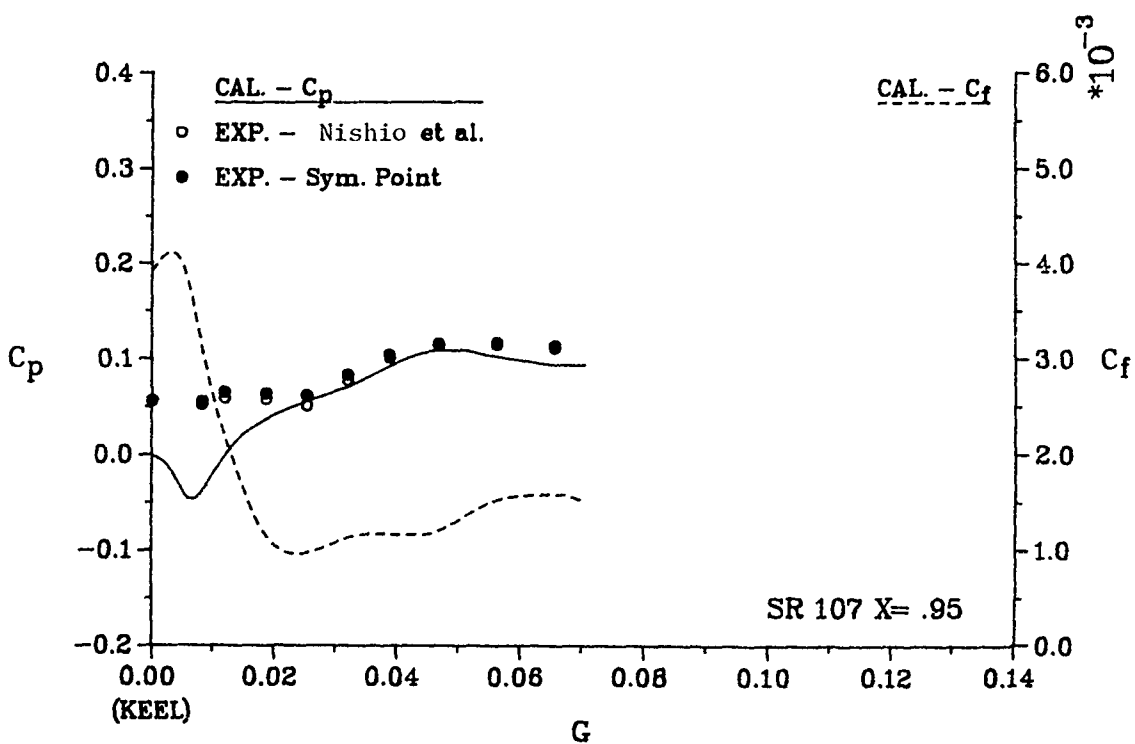
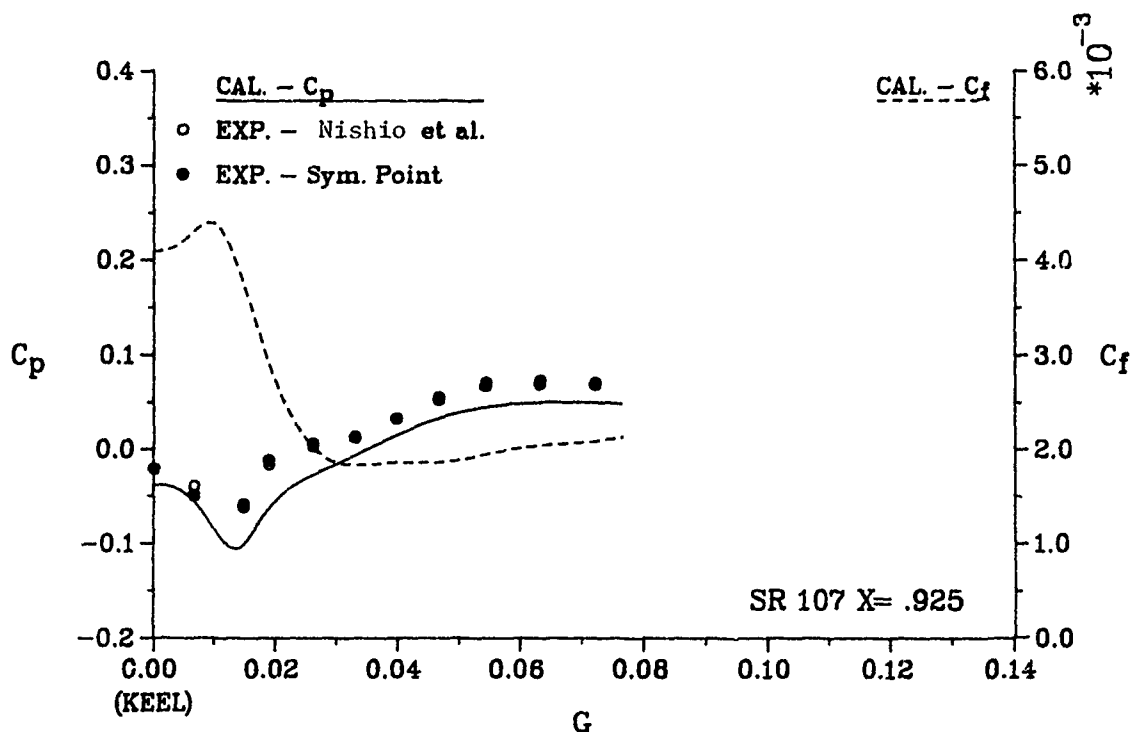


Fig. 42 Girthwise variation of pressure and friction coefficients
(g) $X = 0.925$; (h) $X = 0.95$

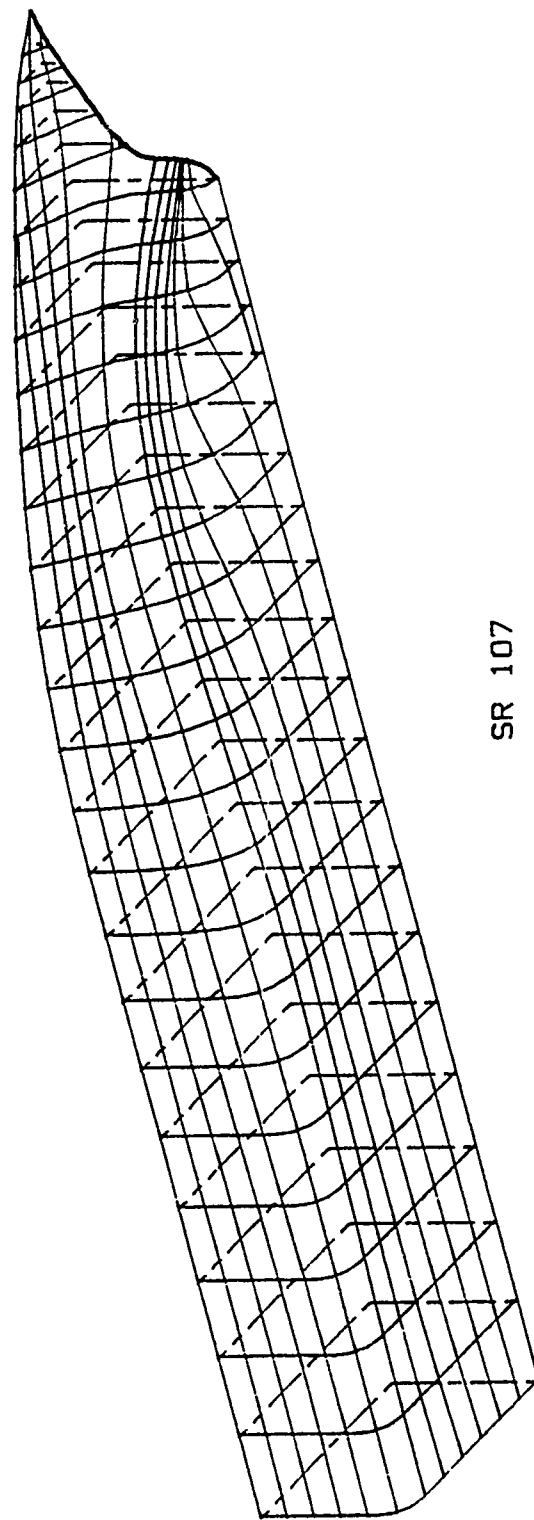


Fig. 43 Calculated wall streamlines

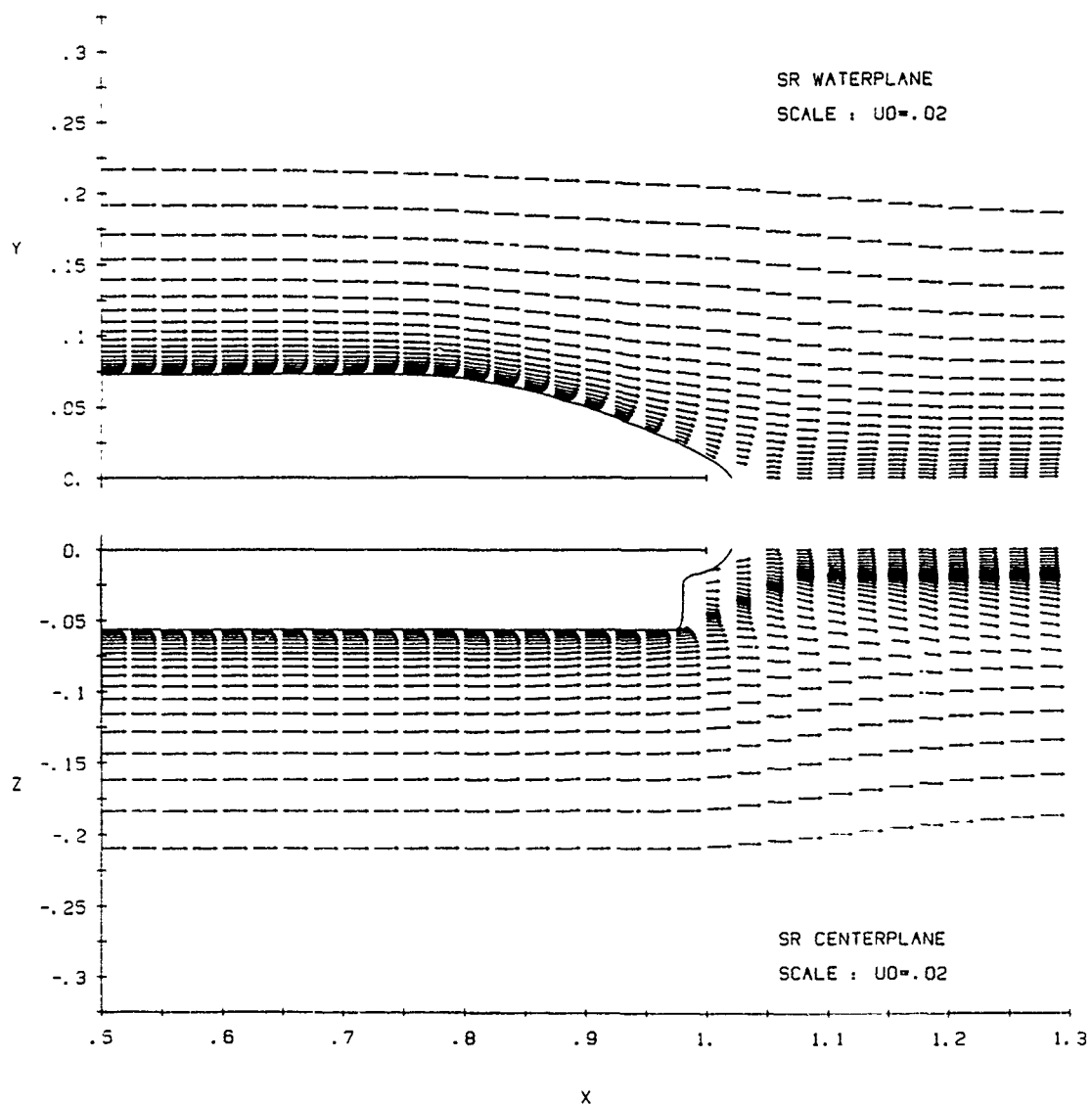


Fig. 44 Velocity vectors in the waterplane (top) and in the vertical centerplane (bottom)

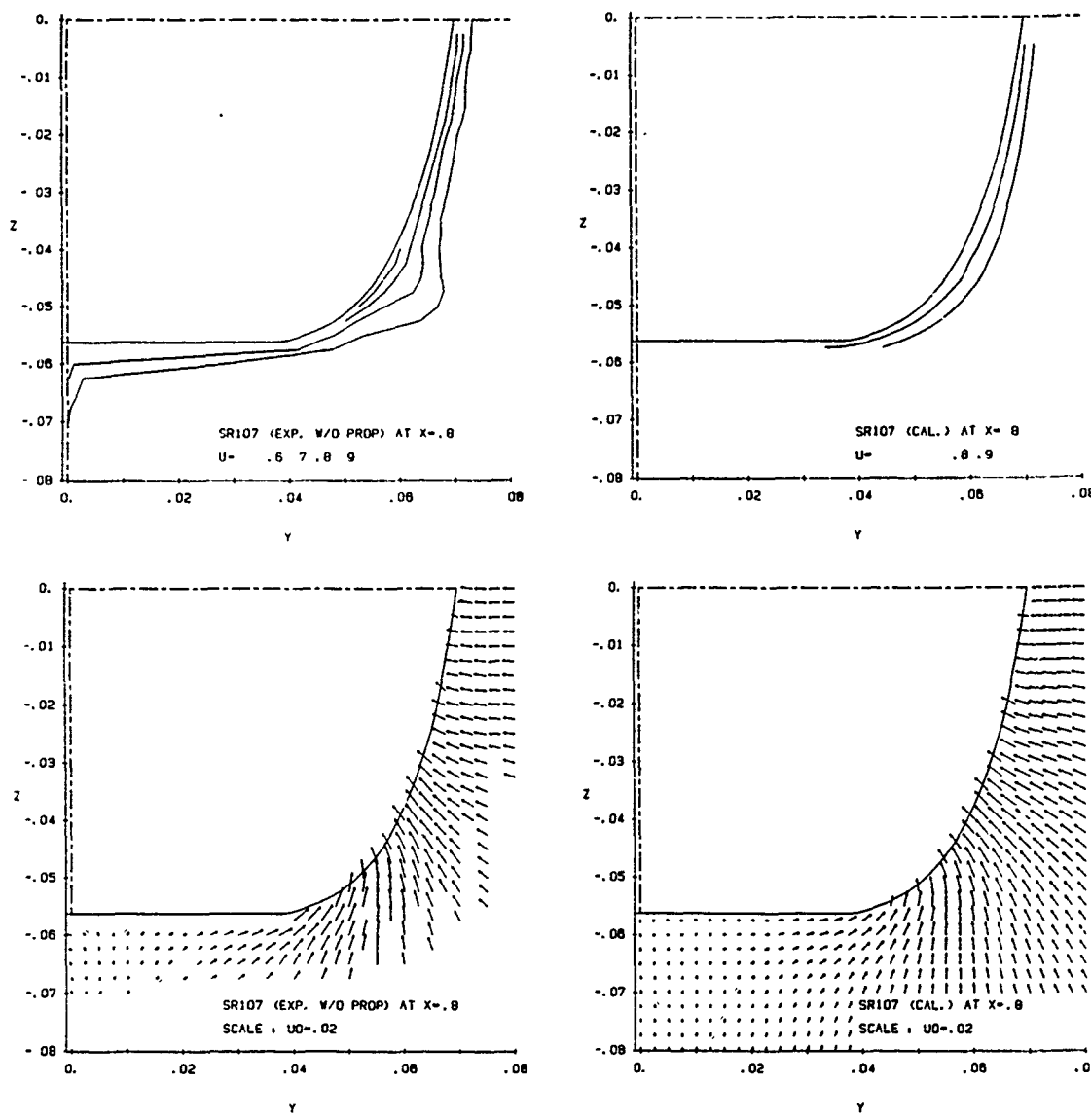


Fig. 45 Velocity field in transverse sections : (a) $X = 0.8$
 Top: contours of axial velocity (U); Bottom: velocity (V, W) in transverse sections
 Left: experiments; Right: calculations

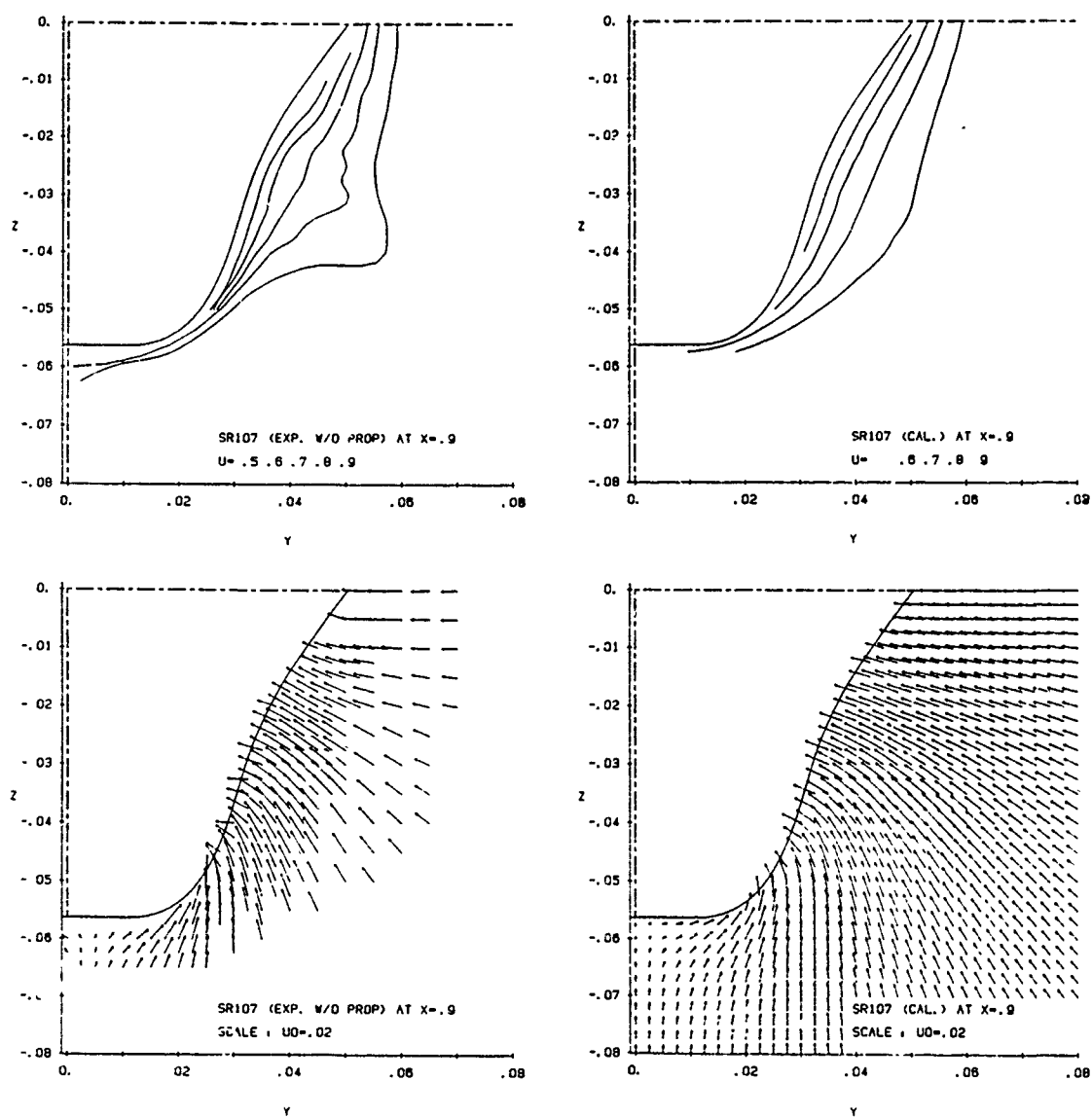


Fig. 45 Velocity field in transverse sections : (b) $X = 0.9$
Top: contours of axial velocity (U); Bottom: velocity (V,W) in transverse sections
Left: experiments; Right: calculations

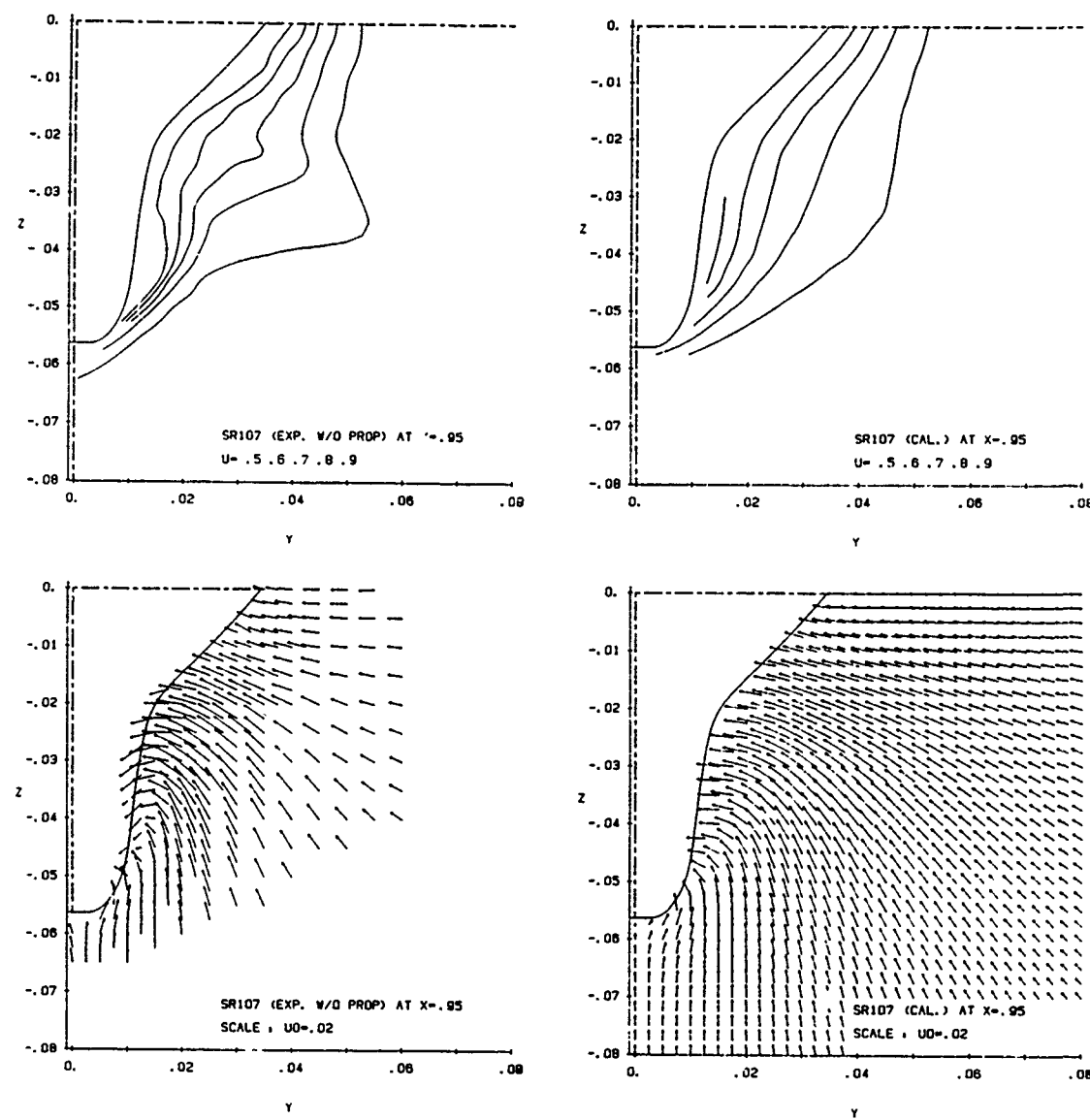


Fig. 45 Velocity field in transverse sections : (c) $X = 0.95$
 Top: contours of axial velocity (U); Bottom: velocity (V, W) in transverse sections
 Left: experiments; Right: calculations

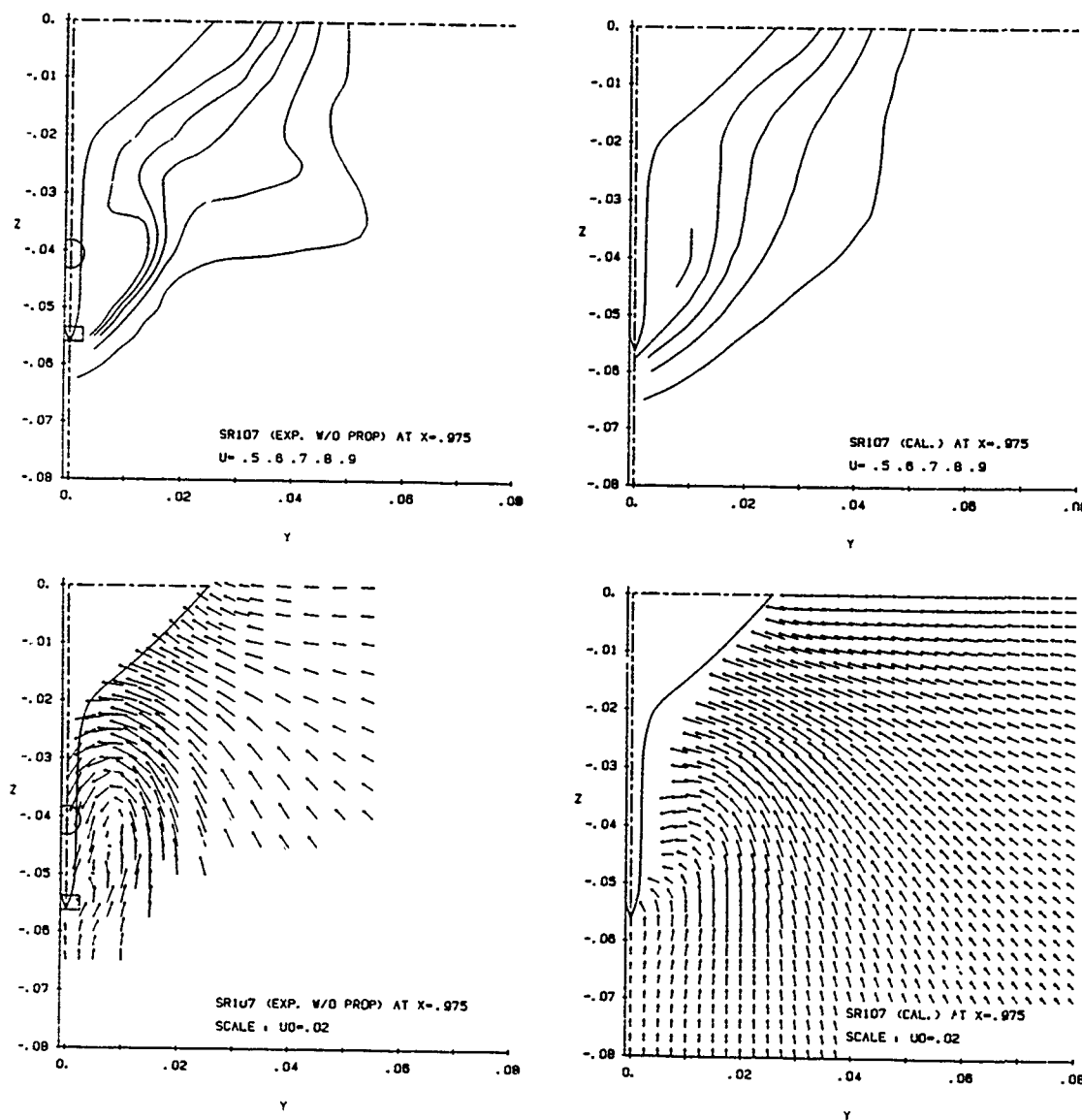


Fig. 45 Velocity field in transverse sections : (d) $X = 0.975$
 Top: contours of axial velocity (U); Bottom: velocity (V, W) in transverse sections
 Left: experiments; Right: calculations

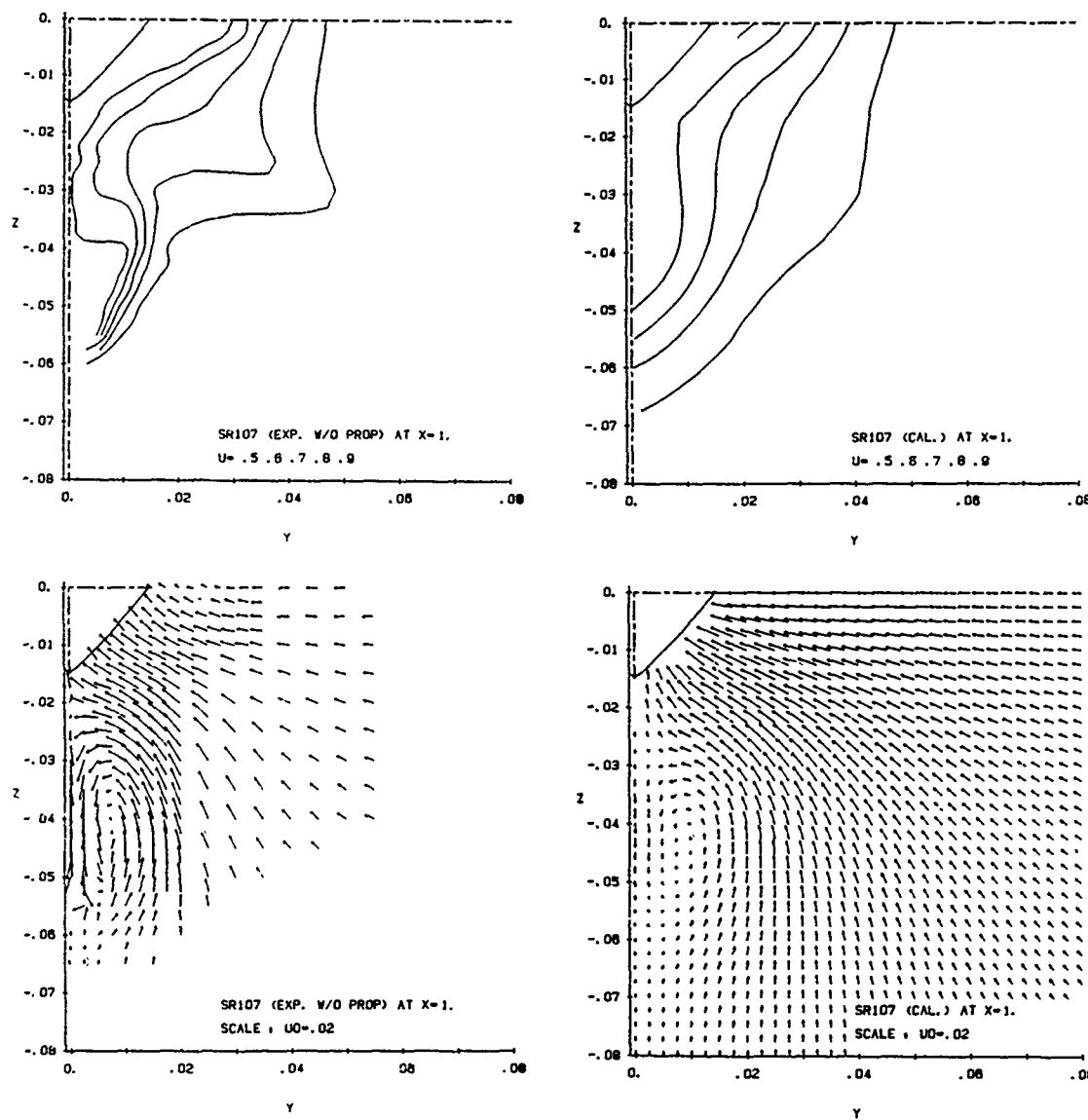


Fig. 45 Velocity field in transverse sections : (e) $X = 1.00$
 Top: contours of axial velocity (U); Bottom: velocity (V, W) in transverse sections
 Left: experiments; Right: calculations

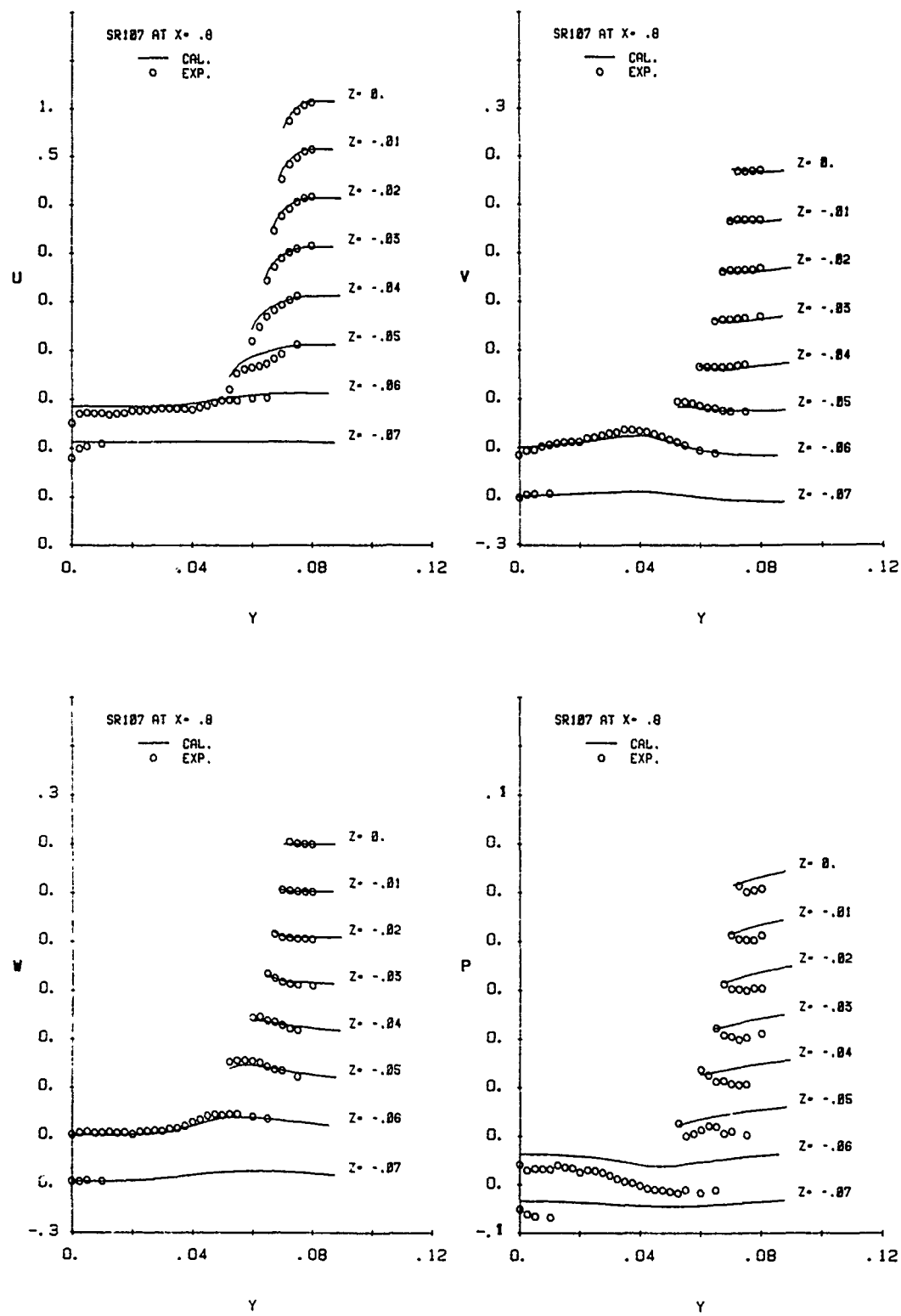


Fig. 46 Detailed comparisons of the velocity and pressure fields: profiles of U, V, W , and P
(a) $X = 0.8$

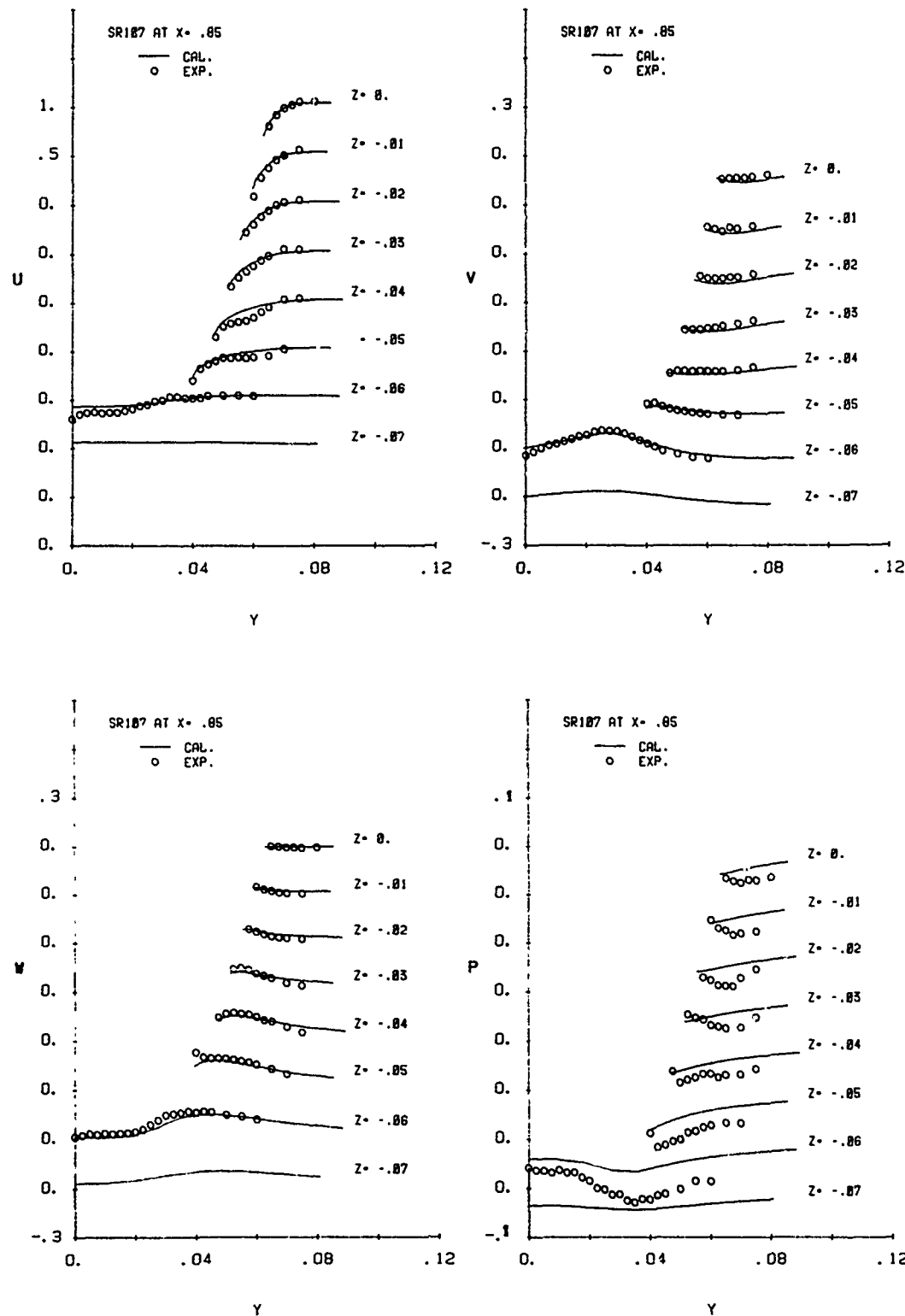


Fig. 46 Detailed comparisons of the velocity and pressure fields: profiles of U,V,W, and P
(b) $X = 0.85$

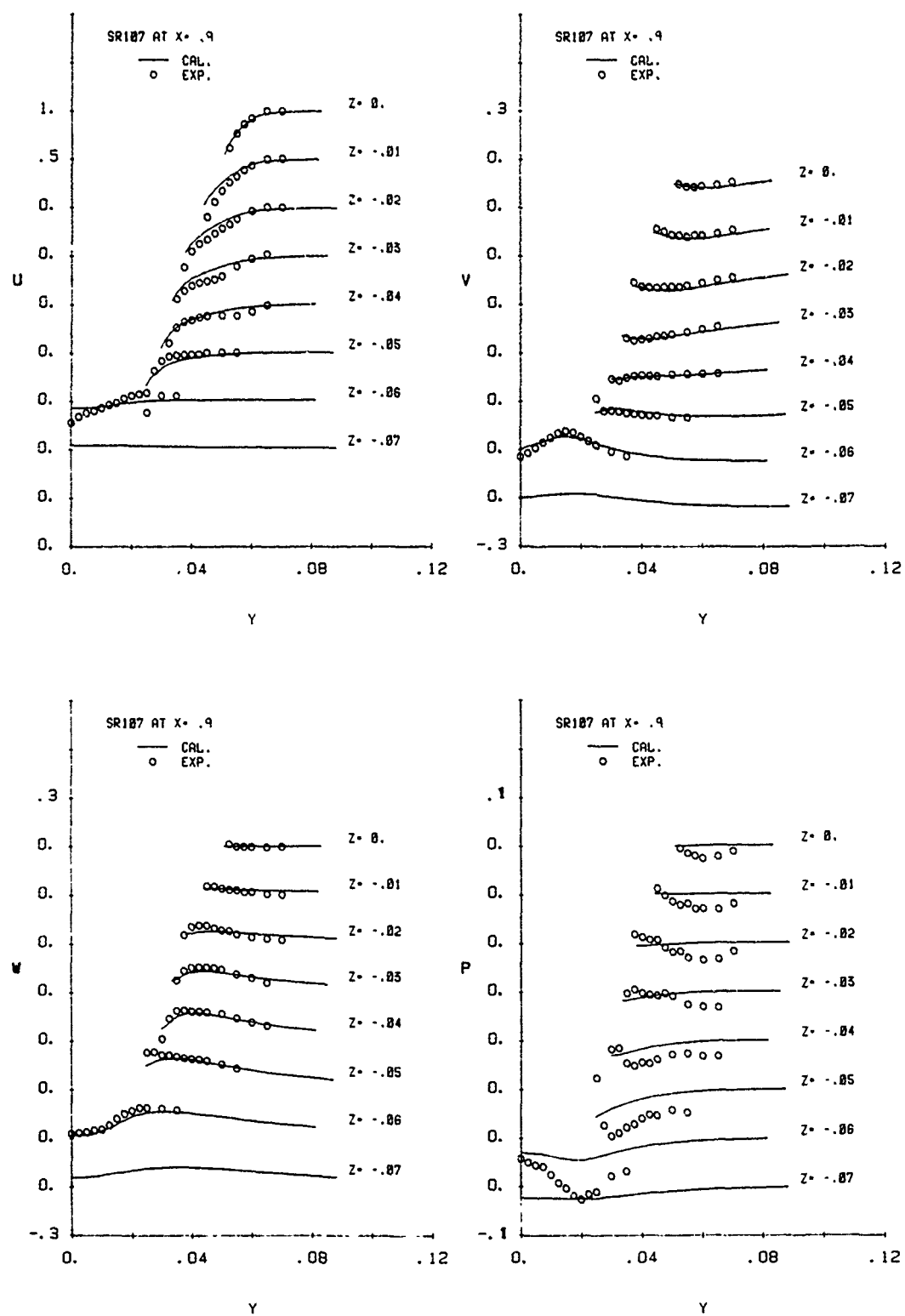


Fig. 46 Detailed comparisons of the velocity and pressure fields: profiles of U, V, W, and P
(c) $X = 0.9$

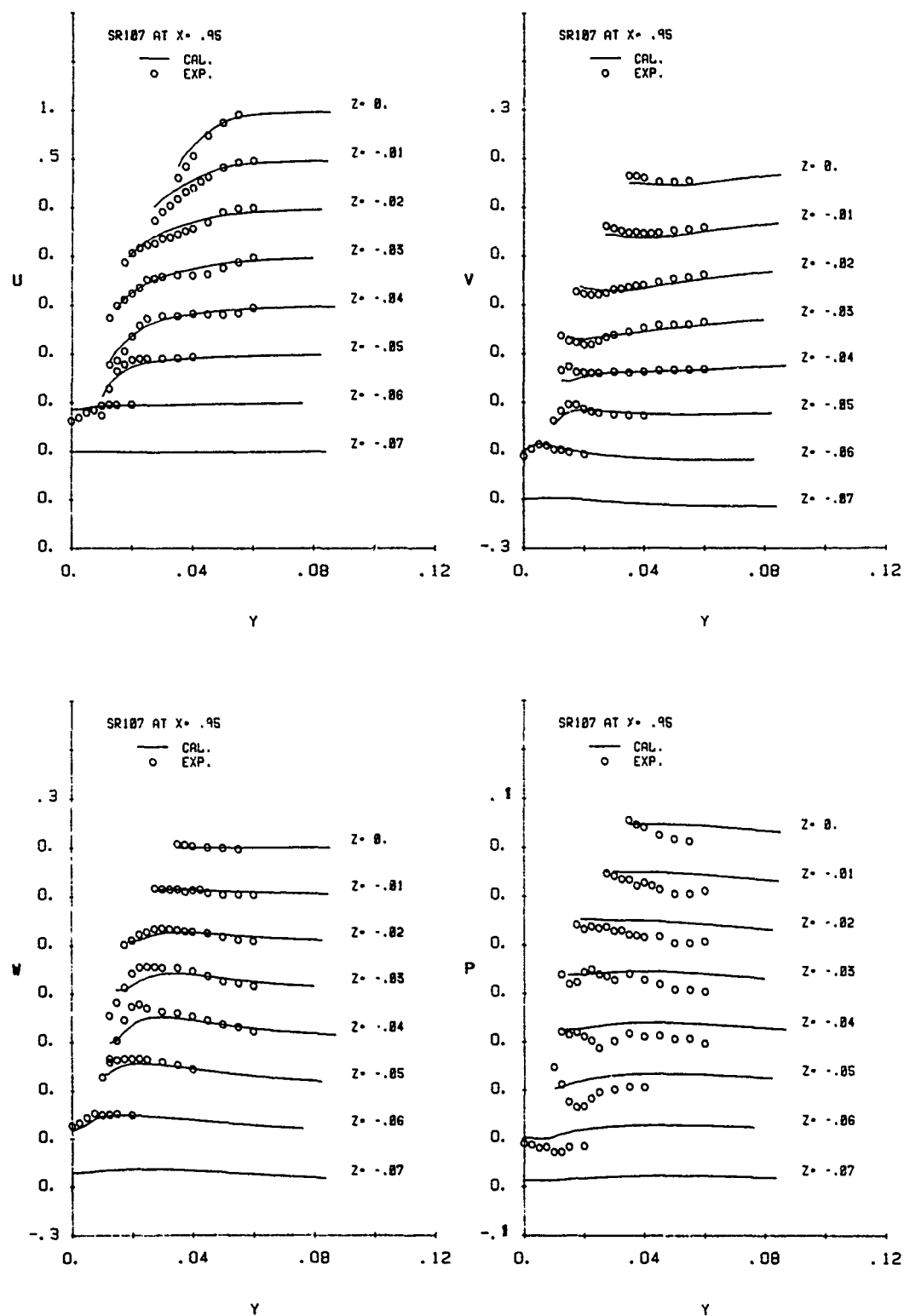


Fig. 46 Detailed comparisons of the velocity and pressure fields: profiles of U, V, W, and P
(d) $X = 0.95$

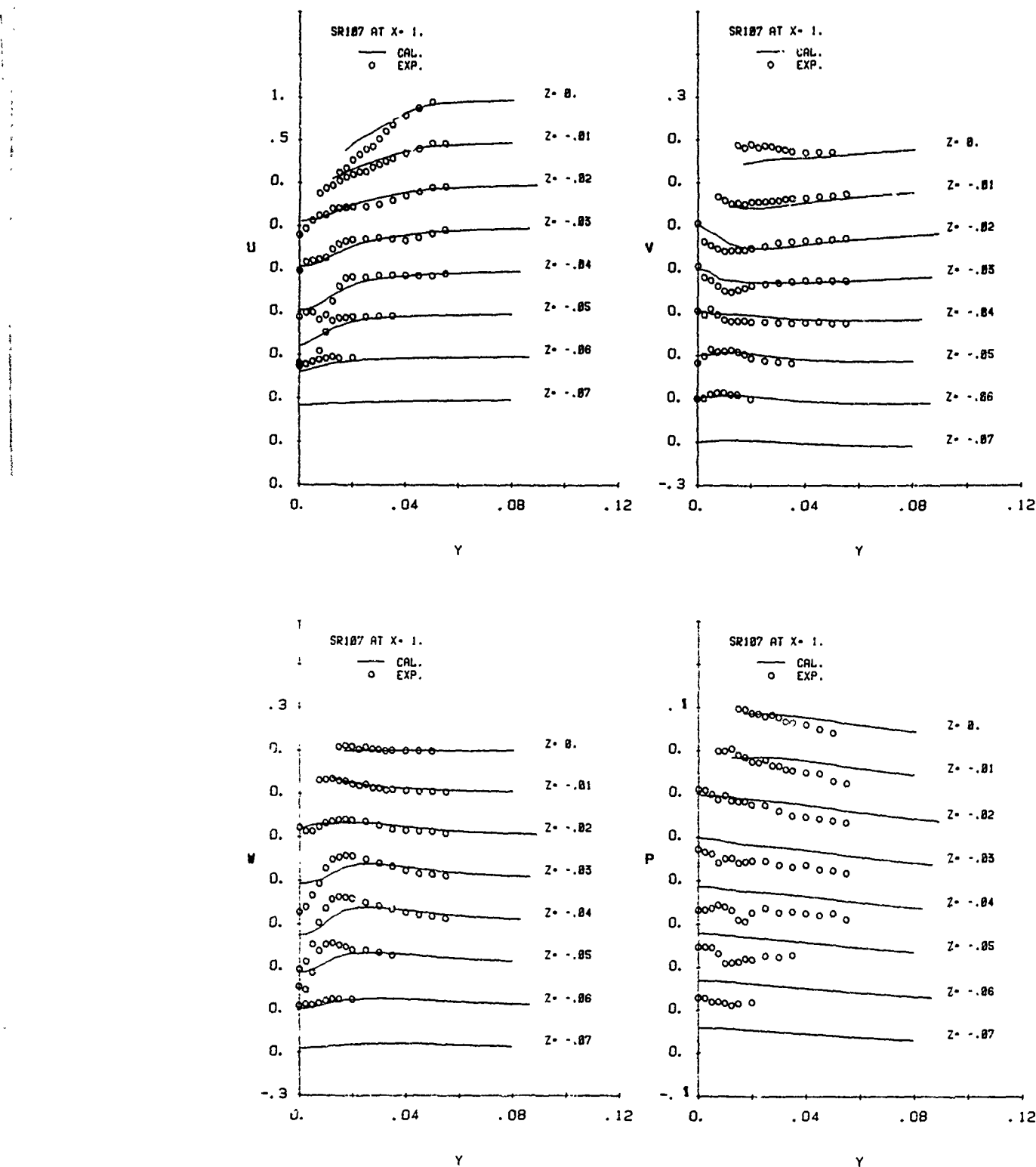


Fig. 46 Detailed comparisons of the velocity and pressure fields: profiles of U,V,W, and P
(e) $X = 1.0$

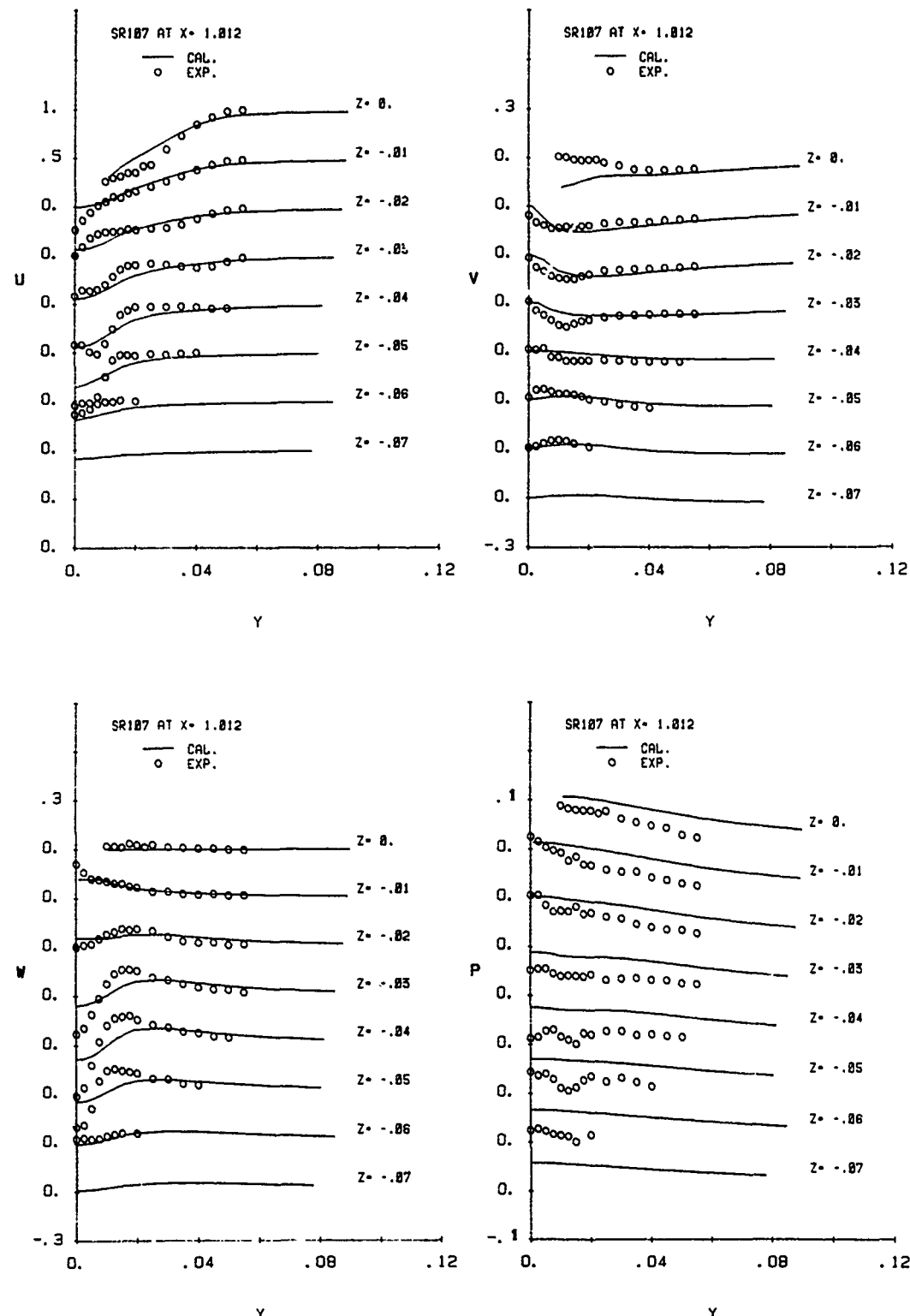


Fig. 46 Detailed comparisons of the velocity and pressure fields: profiles of U, V, W, and P
(f) $X = 1.012$

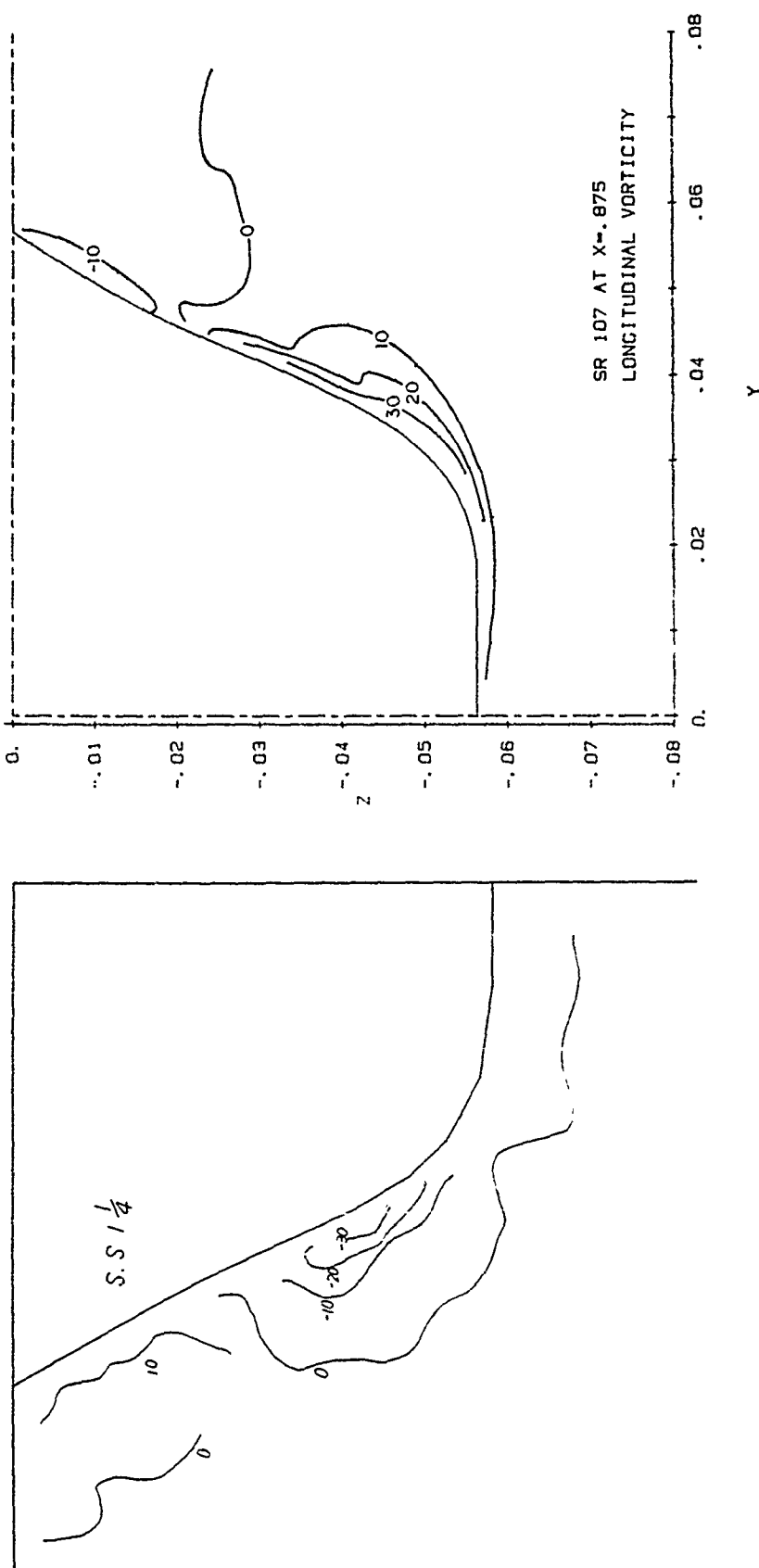


Fig. 47 Contours of longitudinal component of vorticity; experiments (left), calculations (right)
(a) $X = 0.875$

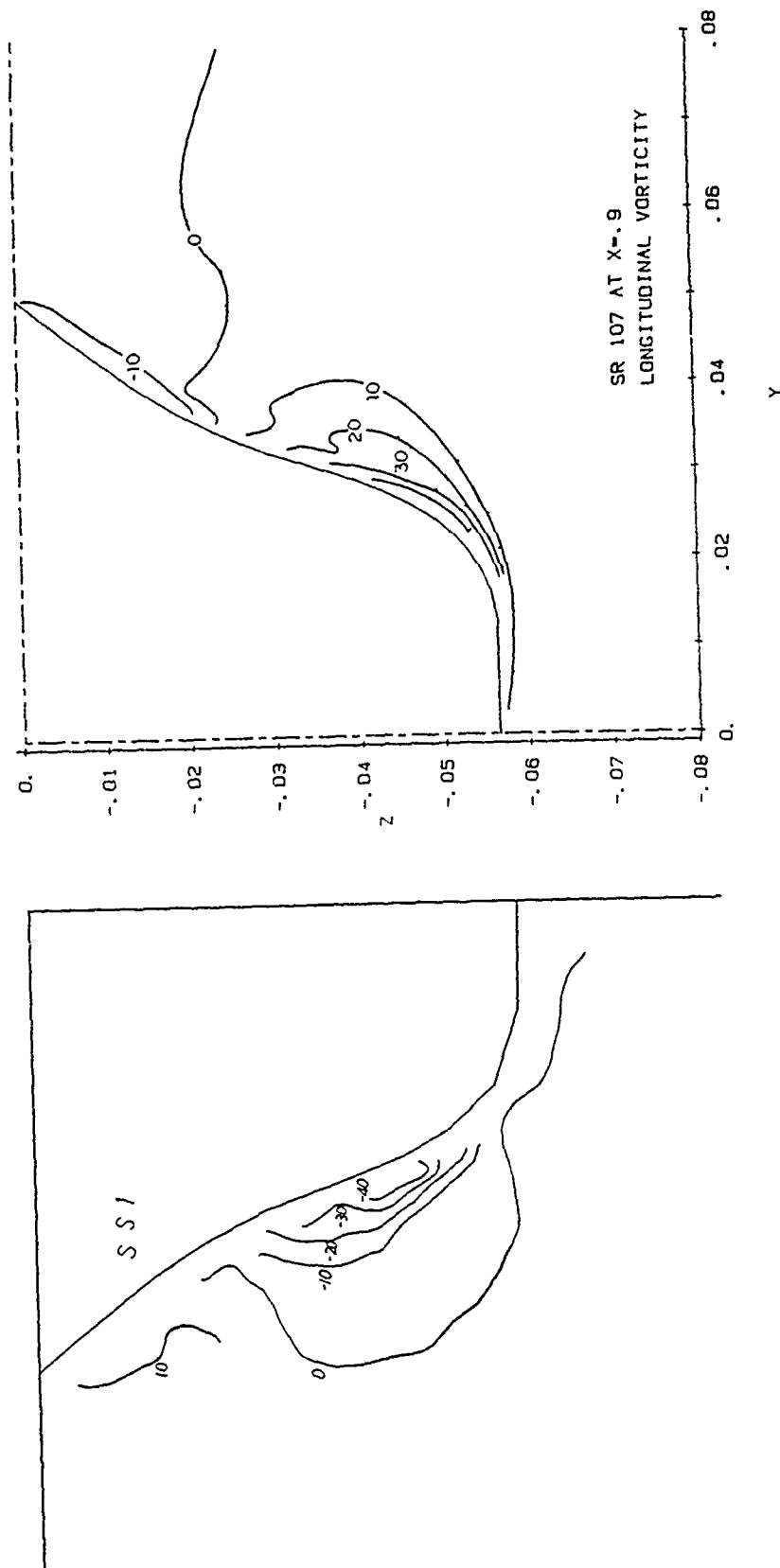


Fig. 47 Contours of longitudinal component of vorticity; experiments (left), calculations (right)
(b) $X = 0.9$

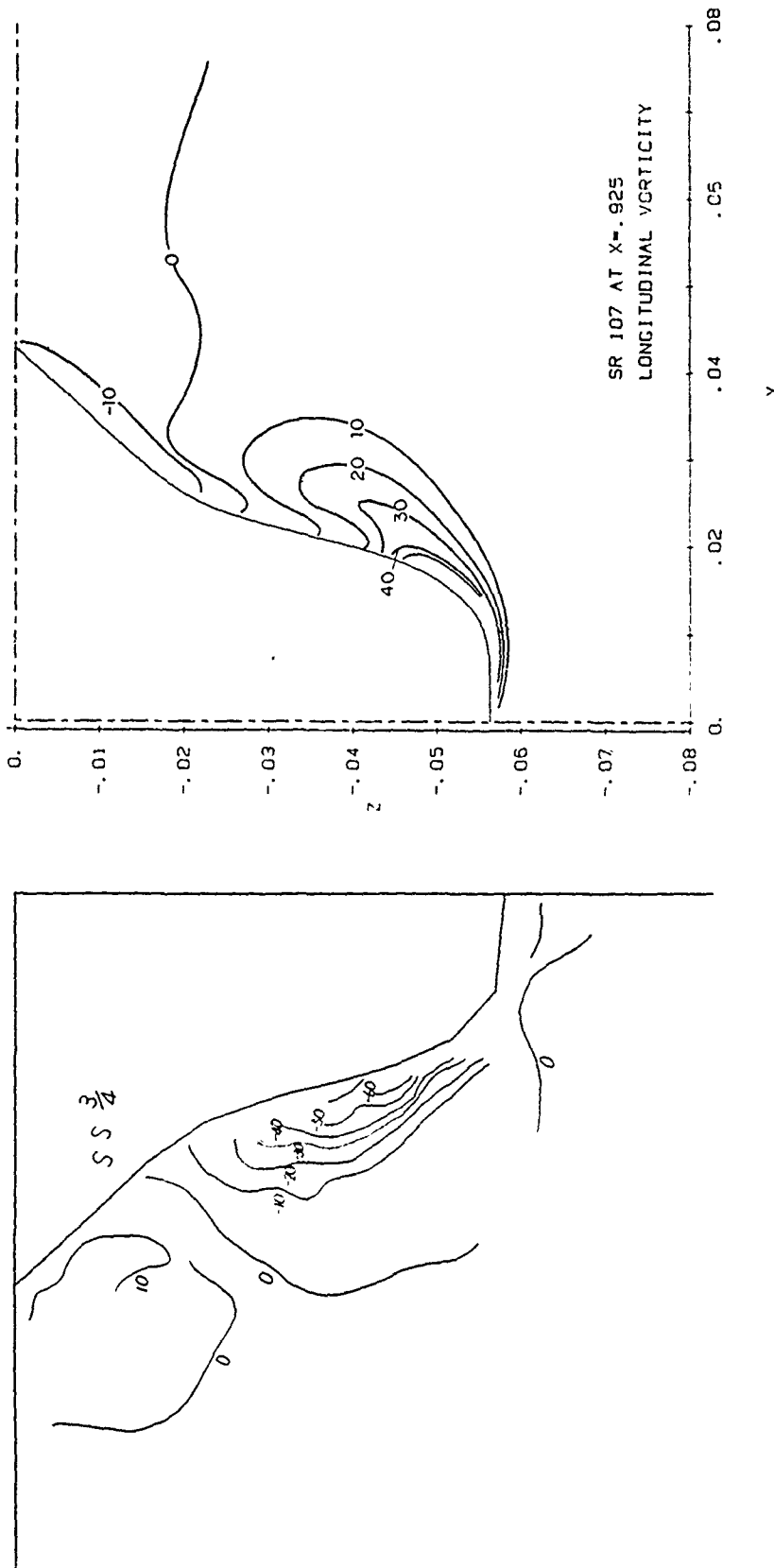


Fig. 47 Contours of longitudinal component of vorticity; experiments (left), calculations (right)
(c) $X = 0.925$

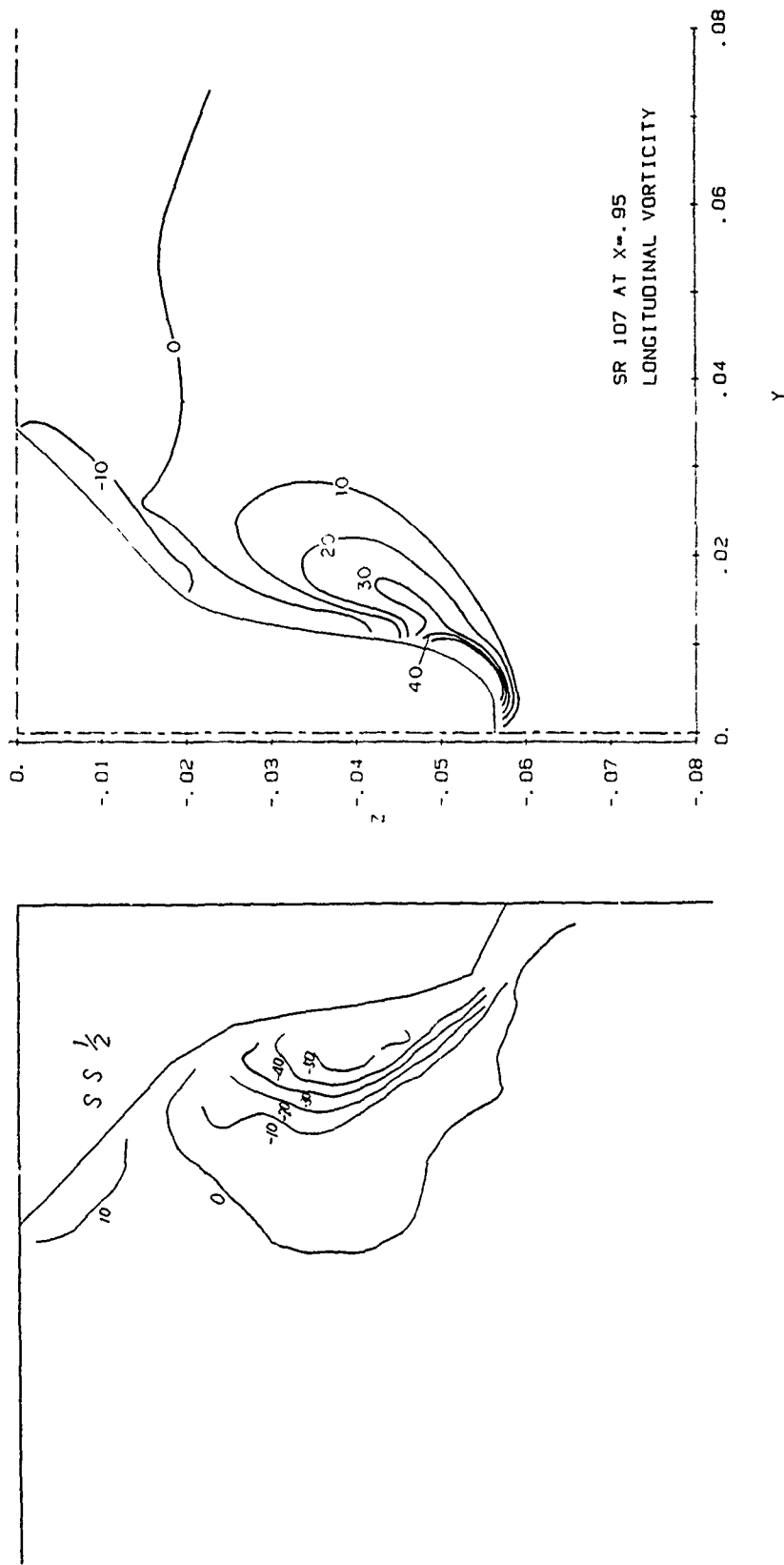


Fig. 47 Contours of longitudinal component of vorticity; experiments (left), calculations (right)
(d) $X = 0.95$

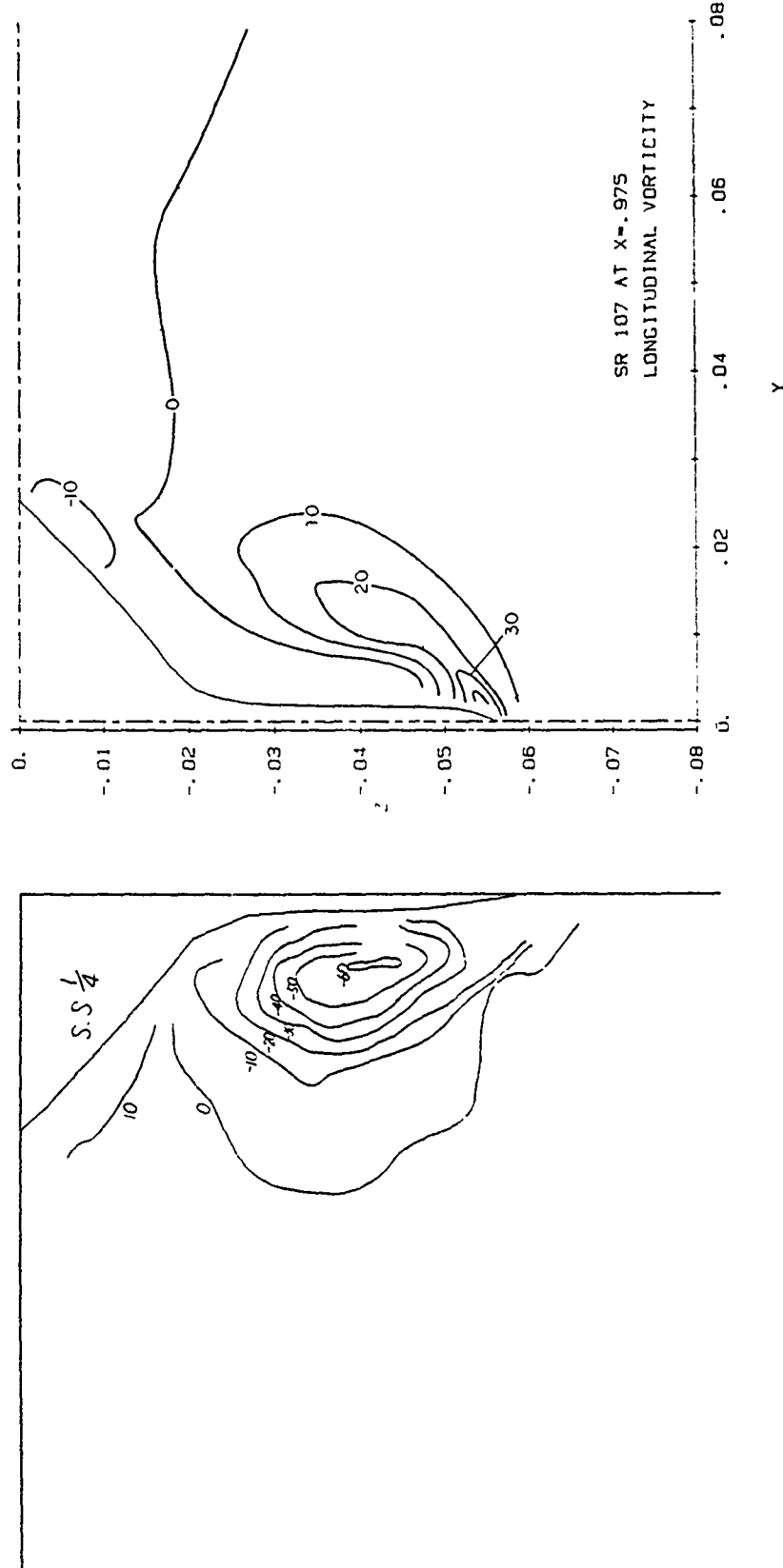


Fig. 47 Contours of longitudinal component of vorticity: experiments (left), calculations (right)
(e) $X = 0.975$

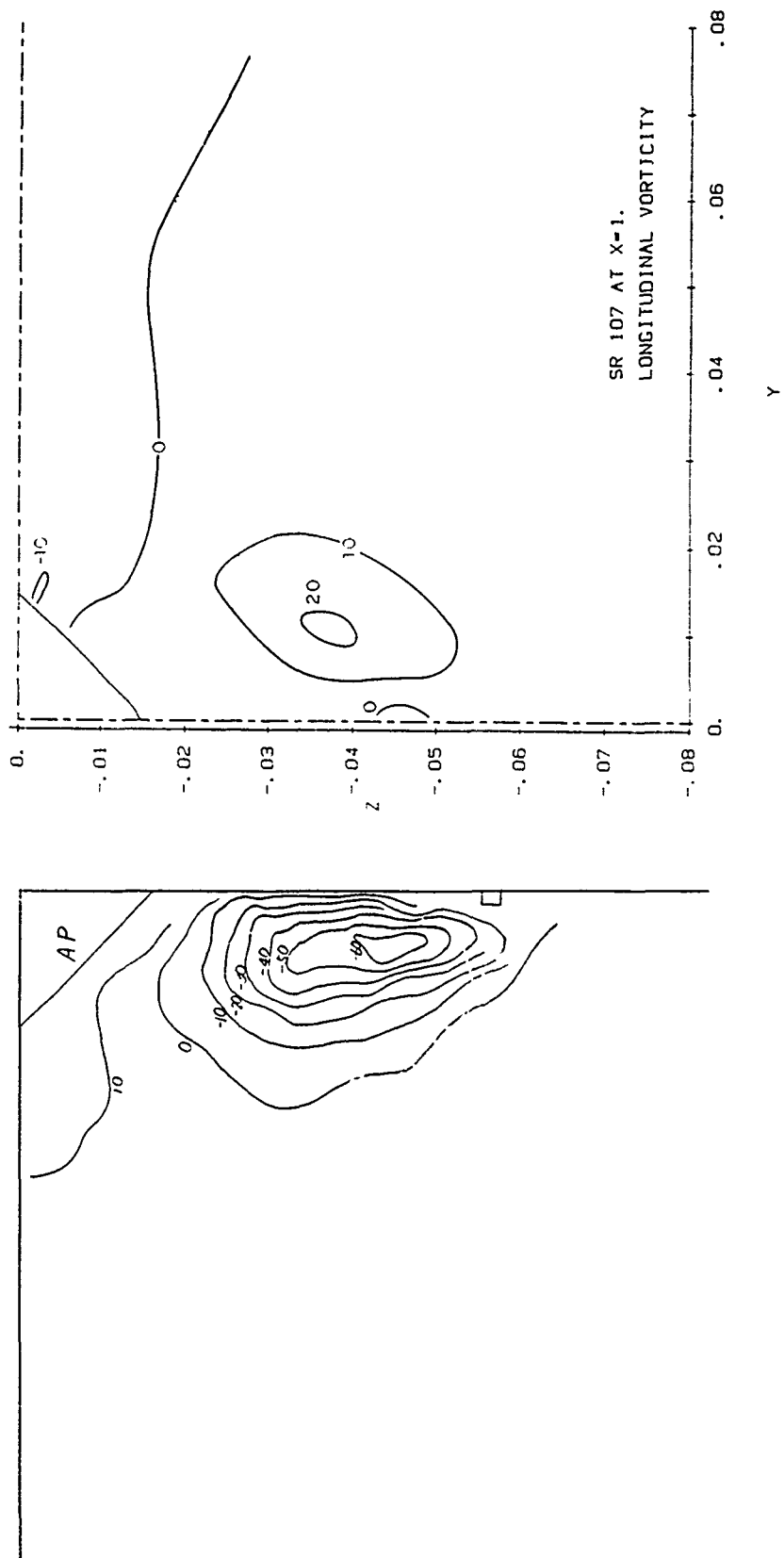


Fig. 47 Contours of longitudinal component of vorticity; experiments (left), calculations (right)
(f) $X = 1.0$

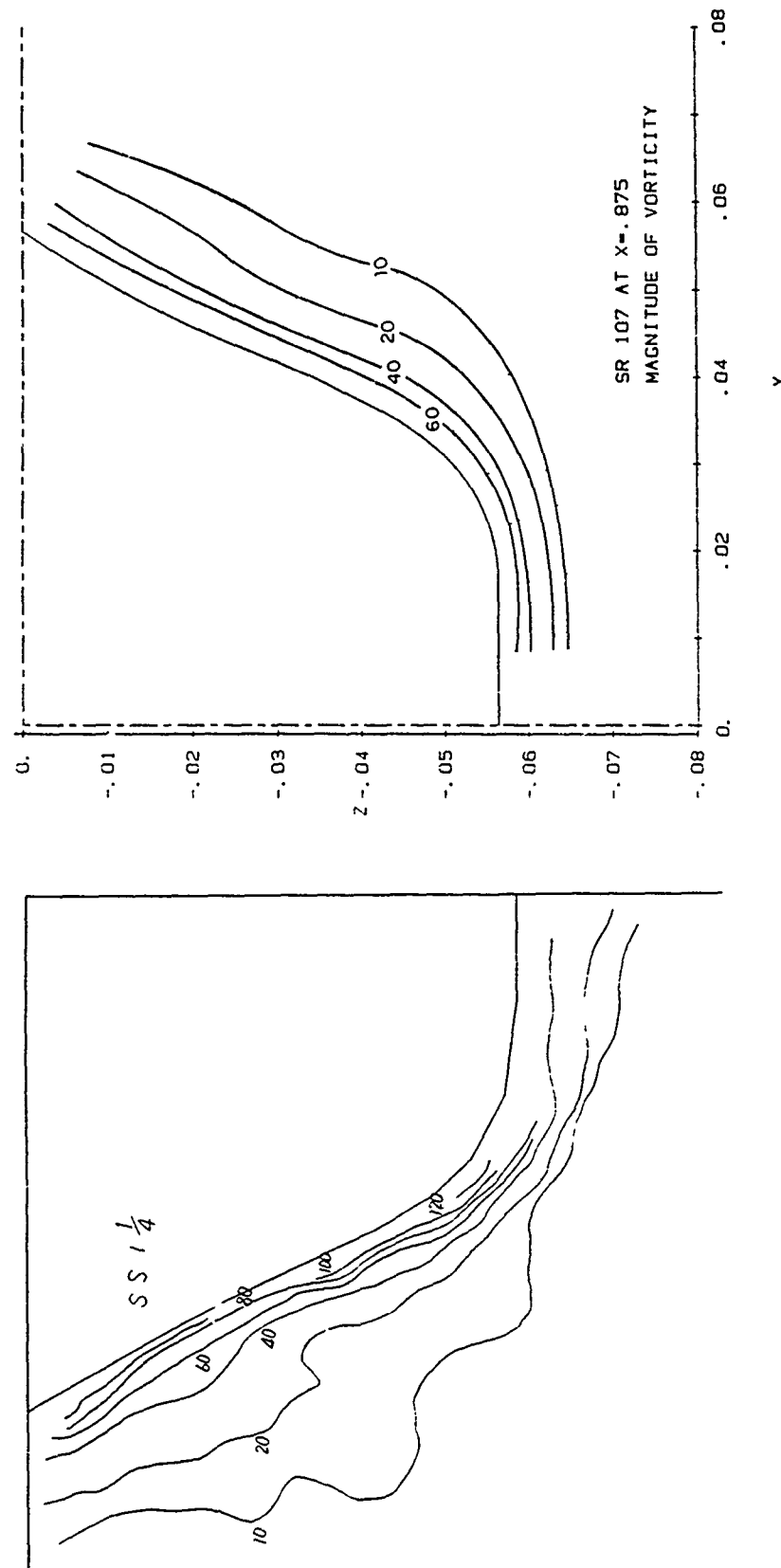


Fig. 48 Contours of magnitude of the vorticity vector; experiments (left), calculations (right)
(a) $X = 0.875$

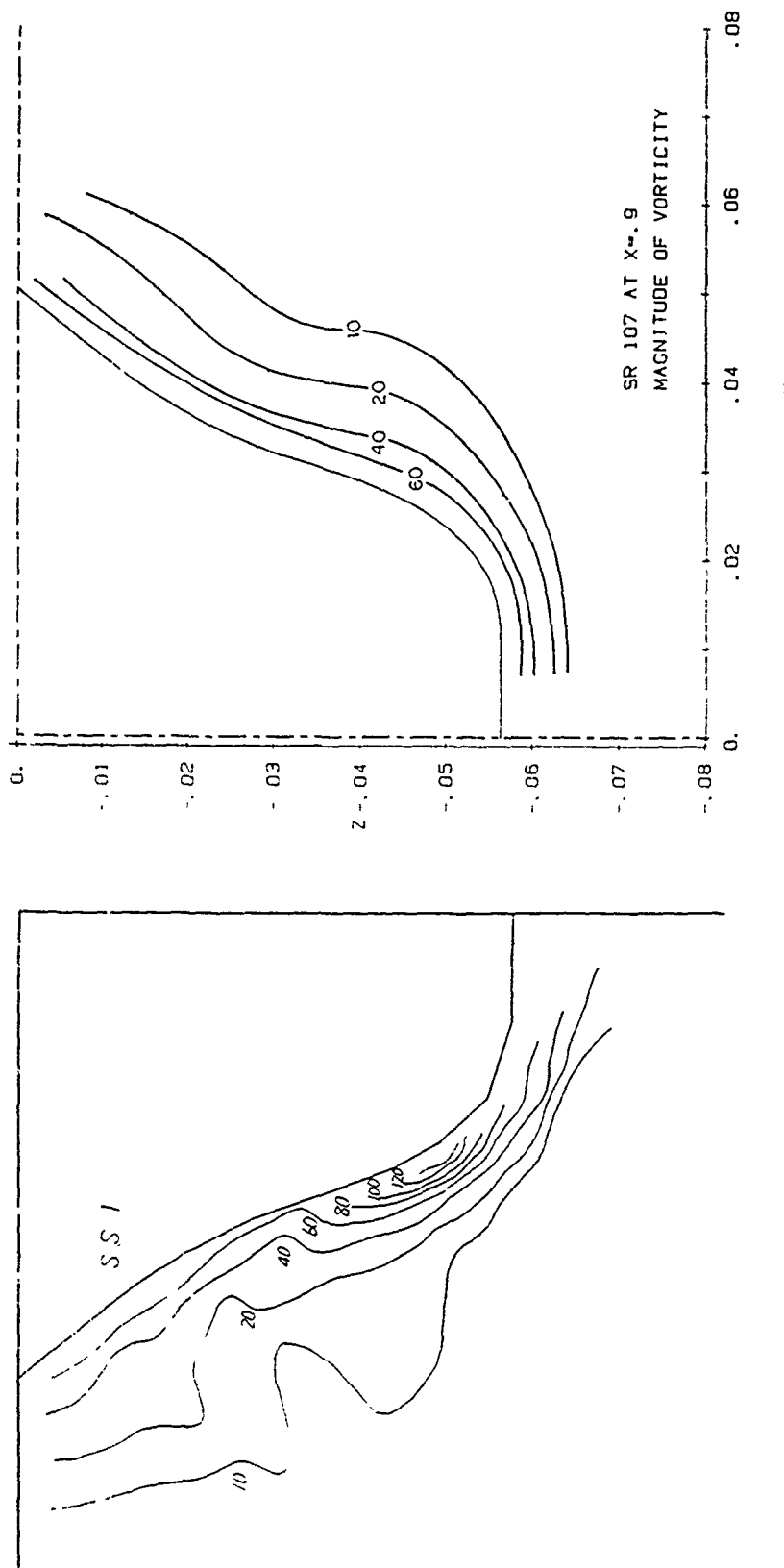


Fig. 48 Contours of magnitude of the vorticity vector; experiments (left), calculations (right)
(b) $X = 0.9$

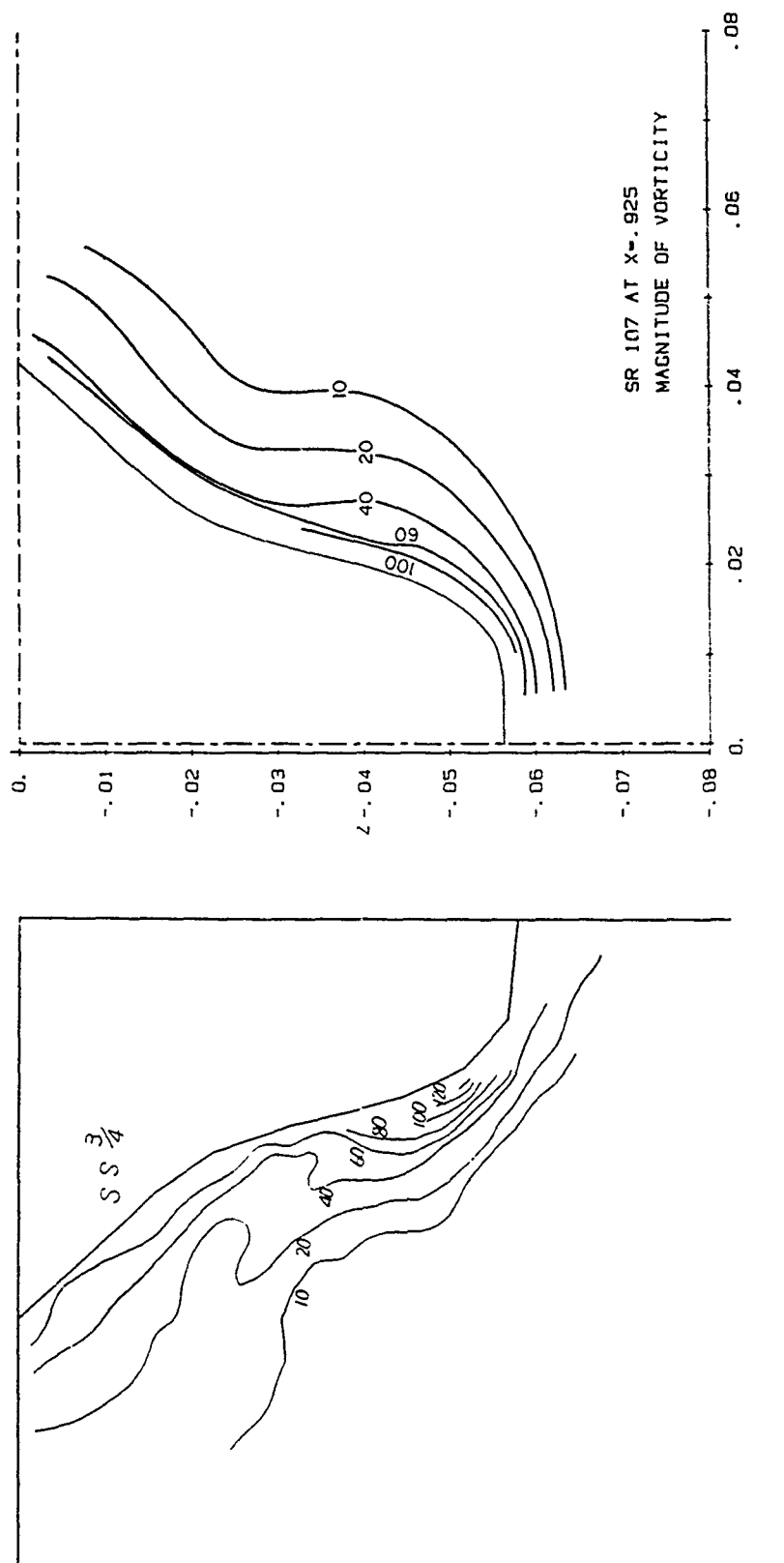


Fig. 48 Contours of magnitude of the vorticity vector; experiments (left), calculations (right)
(c) $X = 0.925$

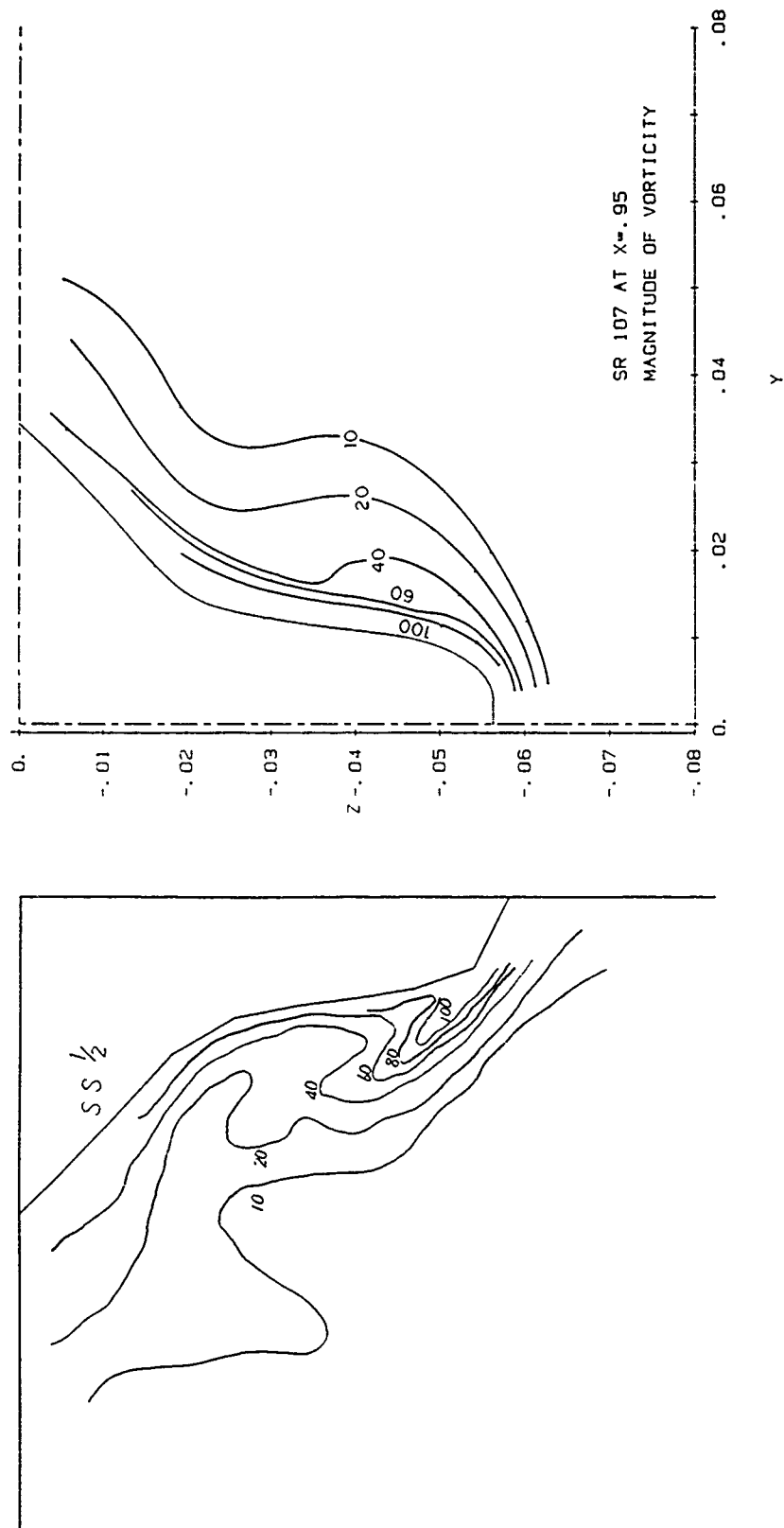


Fig. 48 Contours of magnitude of the vorticity vector; experiments (left), calculations (right)
(d) $X = 0.95$

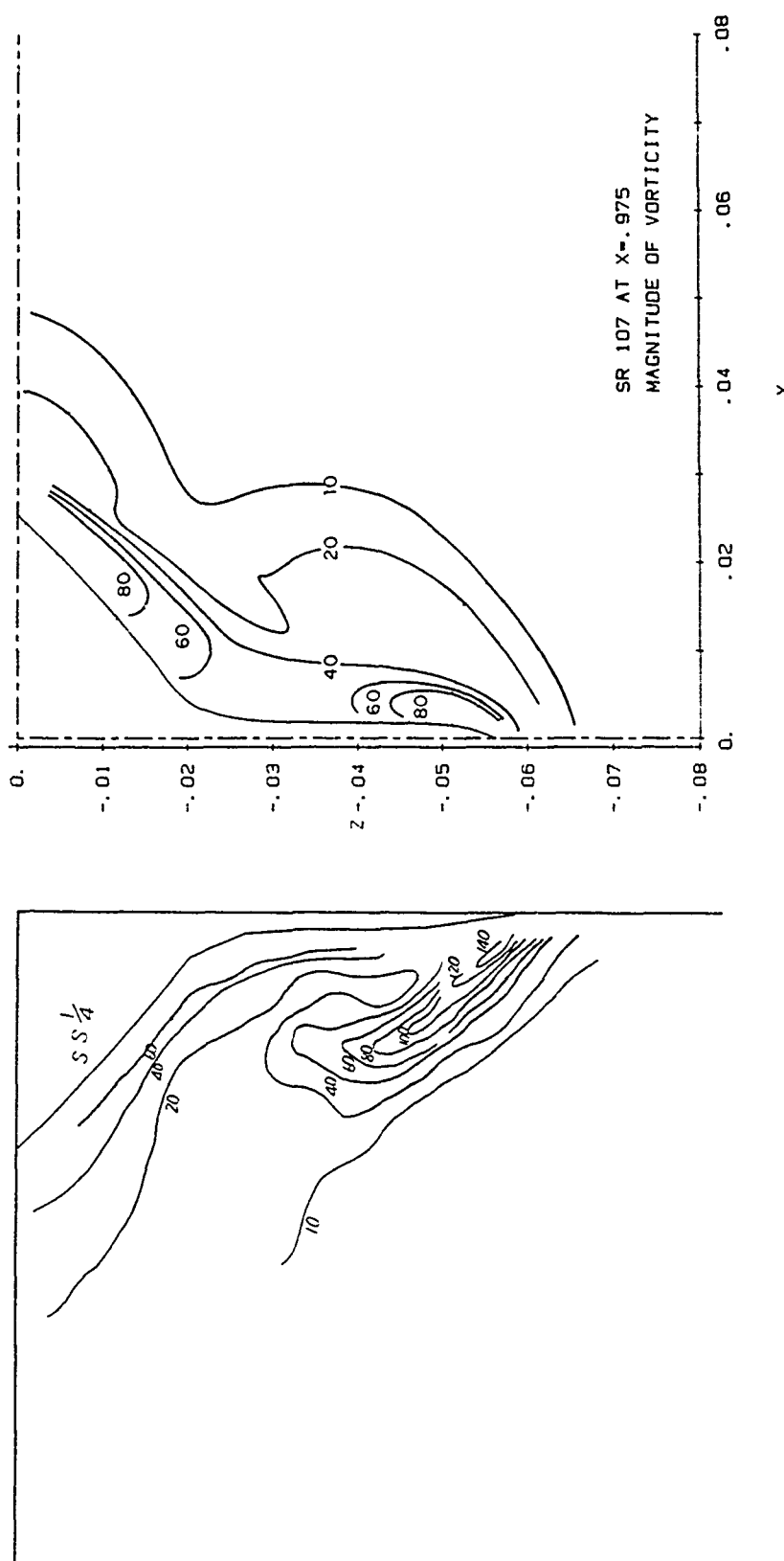


Fig. 48 Contours of magnitude of the vorticity vector; experiments (left), calculations (right)
(e) $X = 0.975$

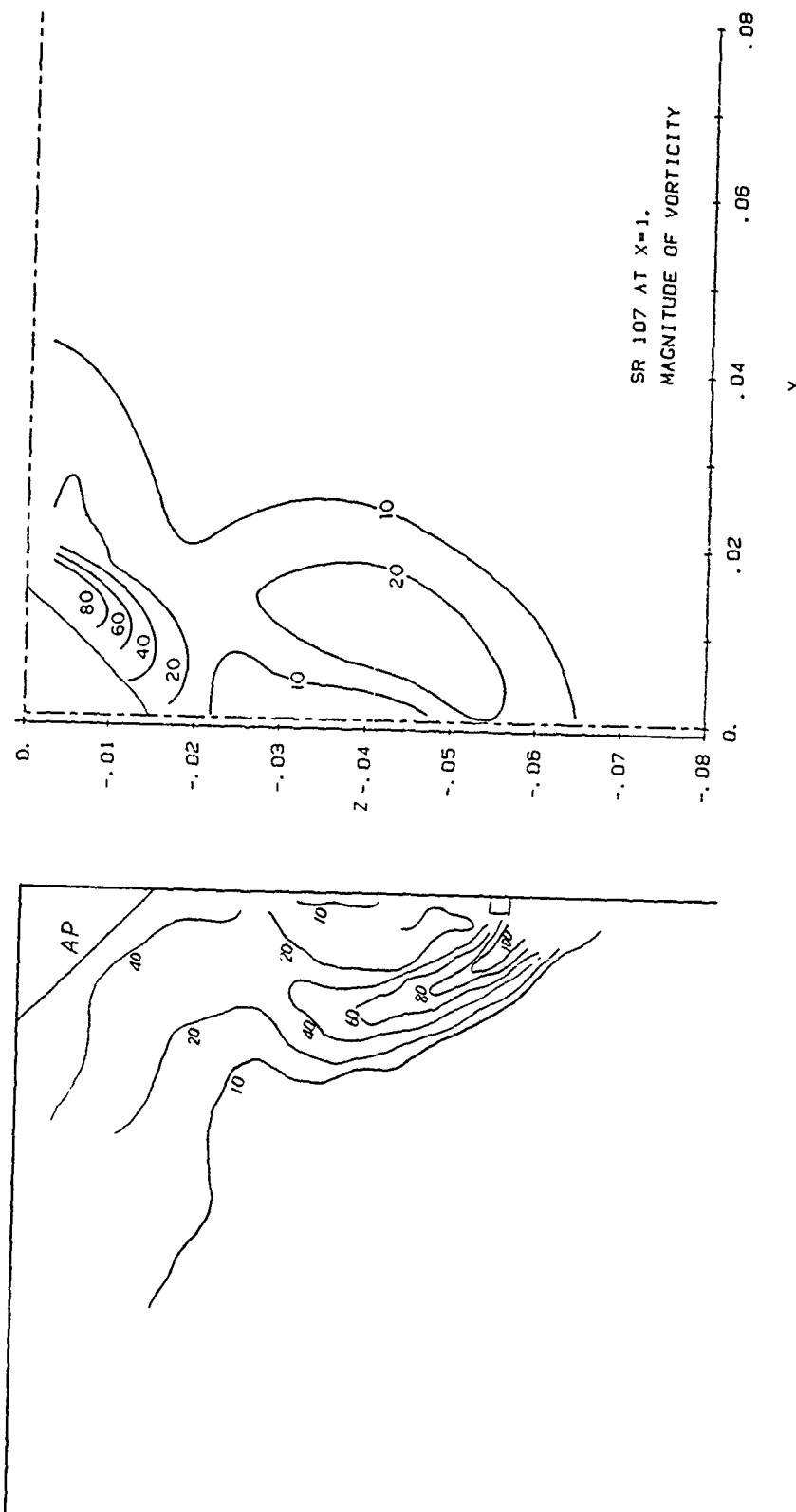


Fig. 48 Contours of magnitude of the vorticity vector; experiments (left), calculations (right)
(f) $X = 1.0$

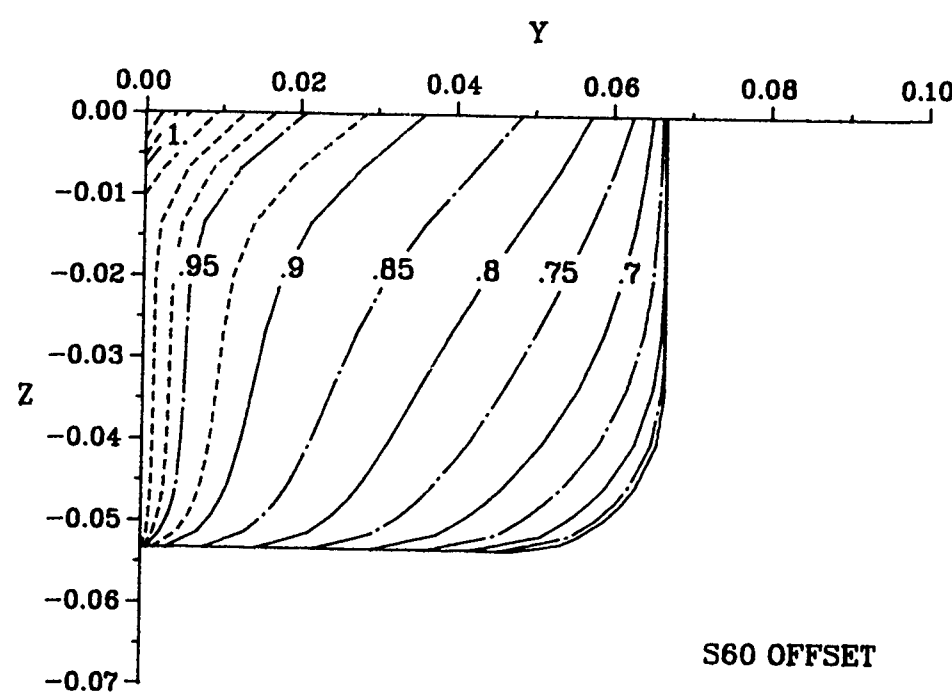
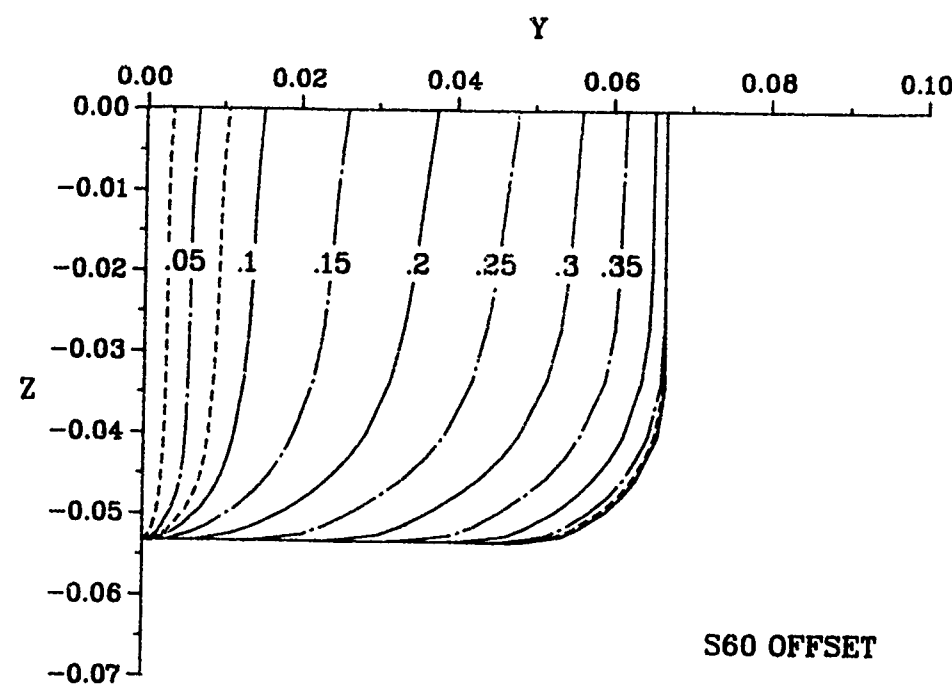


Fig. 49 Offsets of SERIES 60, $C_b = 0.60$ Hull
 (a) forebody (b) afterbody

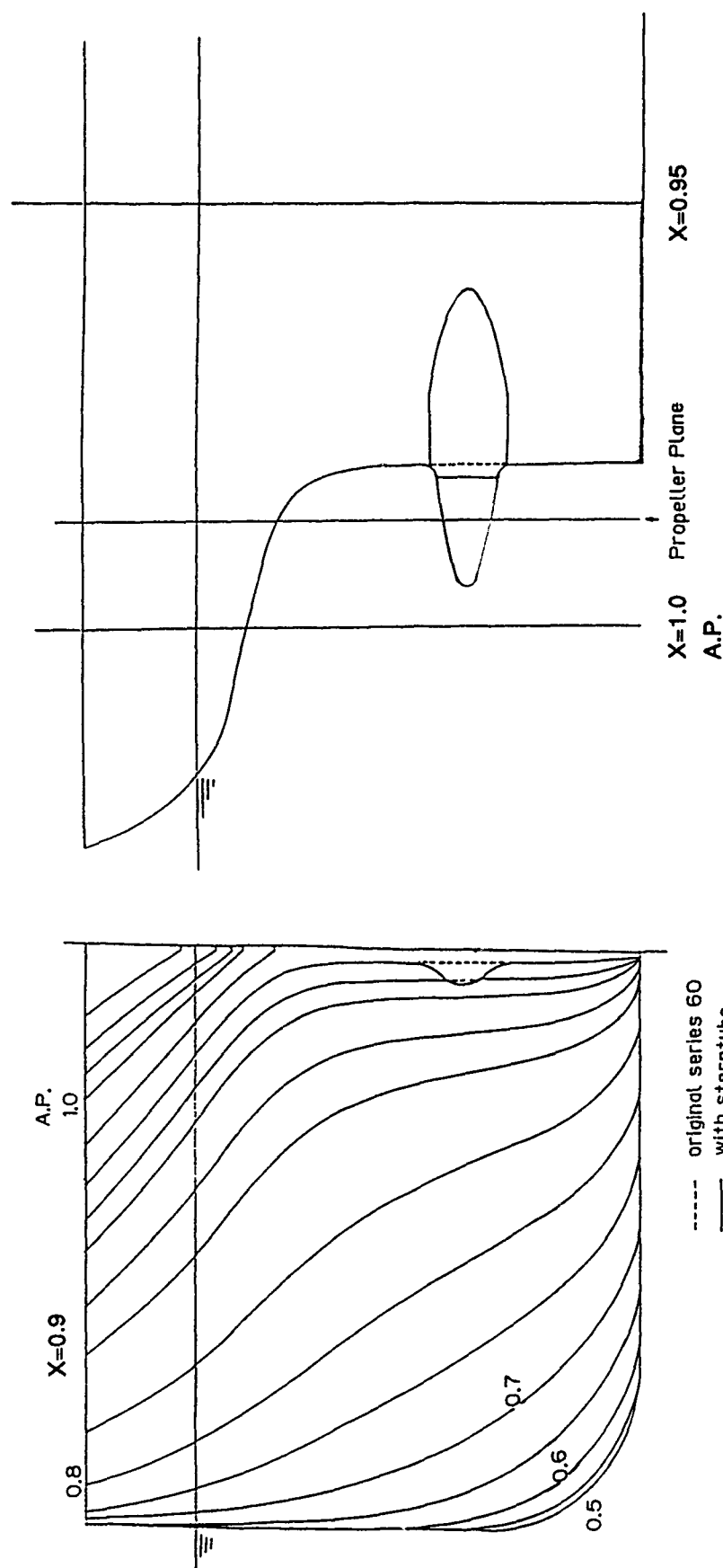


Fig. 50 Geometry and measurement stations in the experiments of Toda et al. (1988)

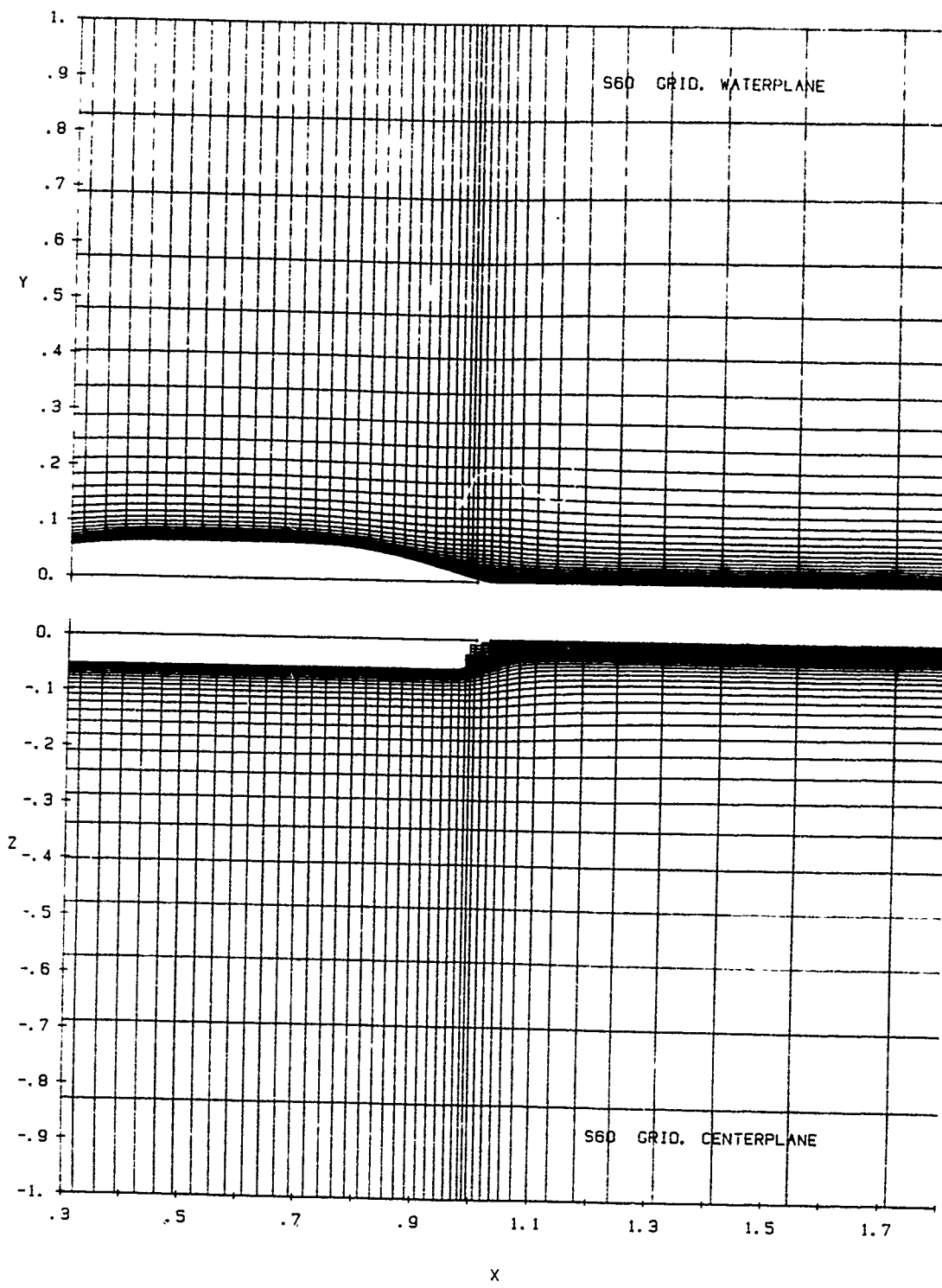


Fig. 51 Typical views of the numerical grid
(a) symmetry planes

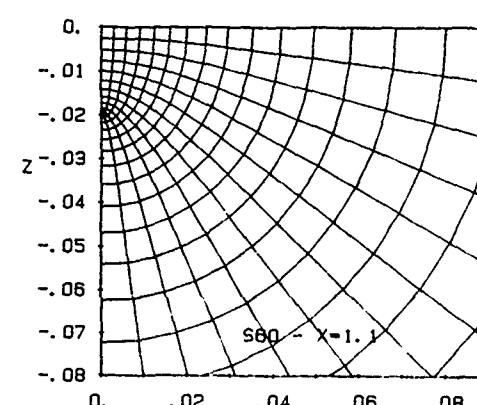
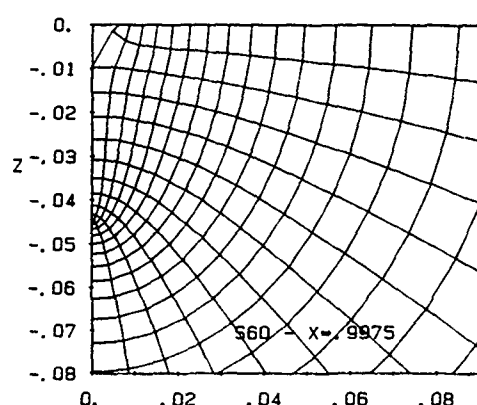
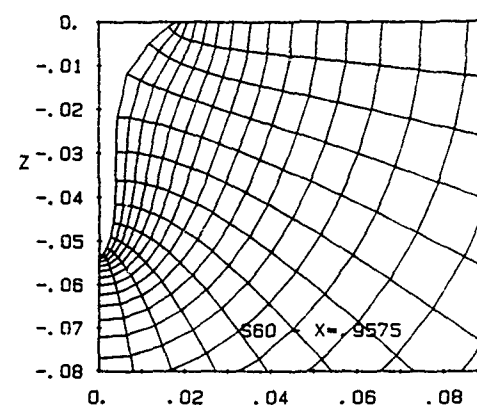
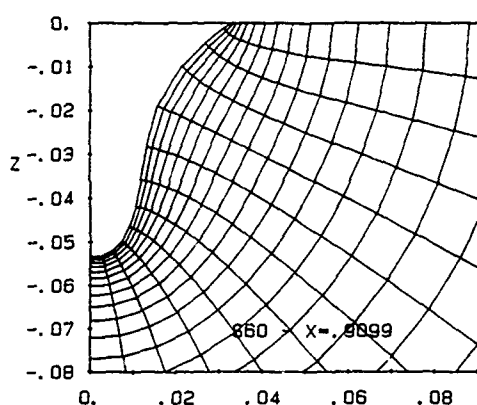
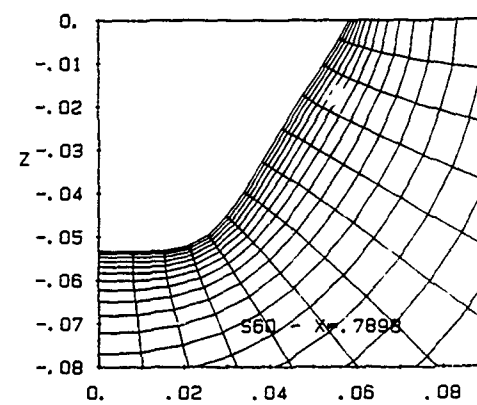
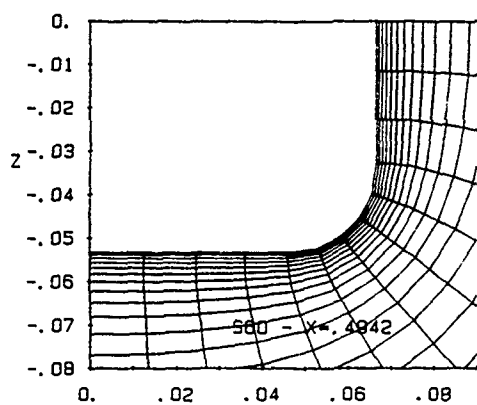


Fig. 51 Typical views of the numerical grid
(b) transverse sections

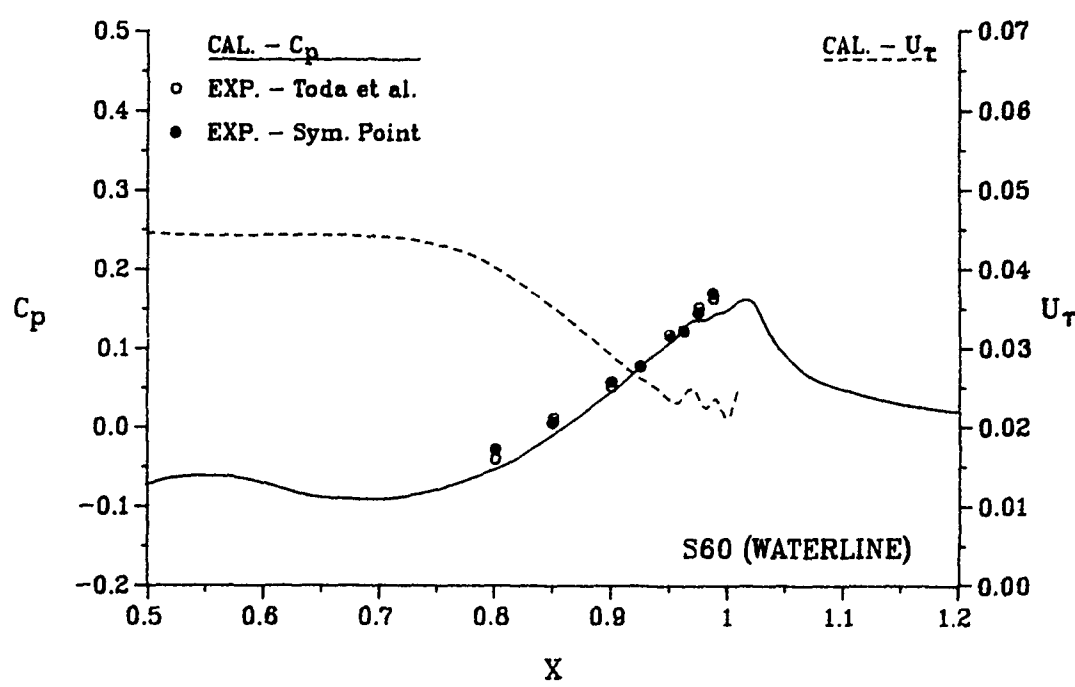
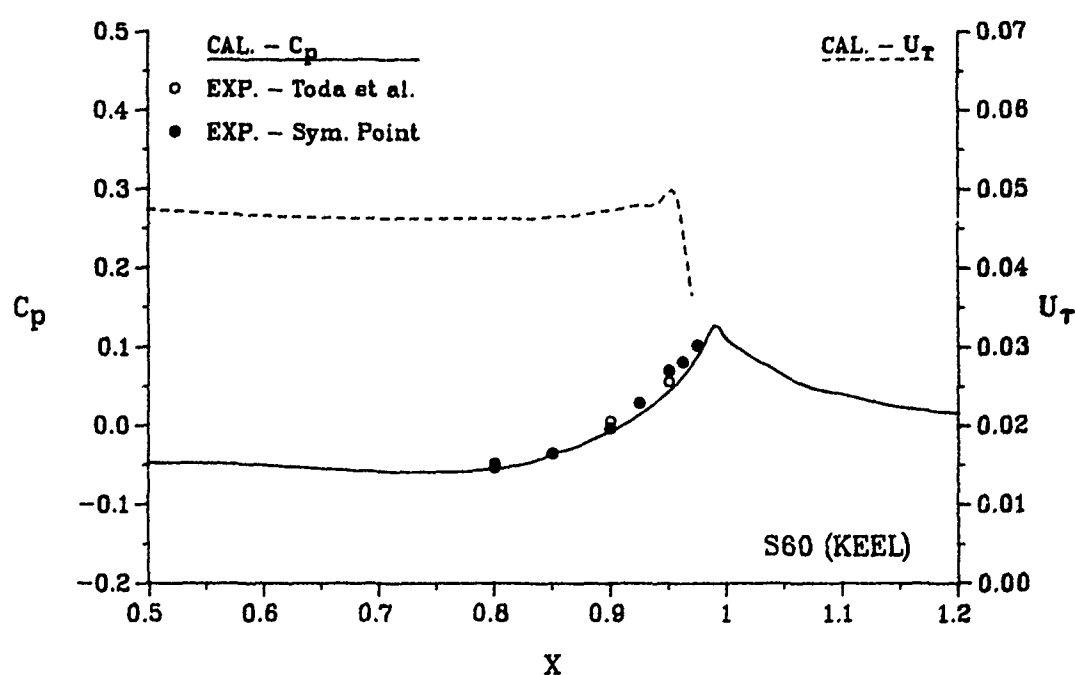


Fig. 52 Pressure and friction velocity along the keel and waterline

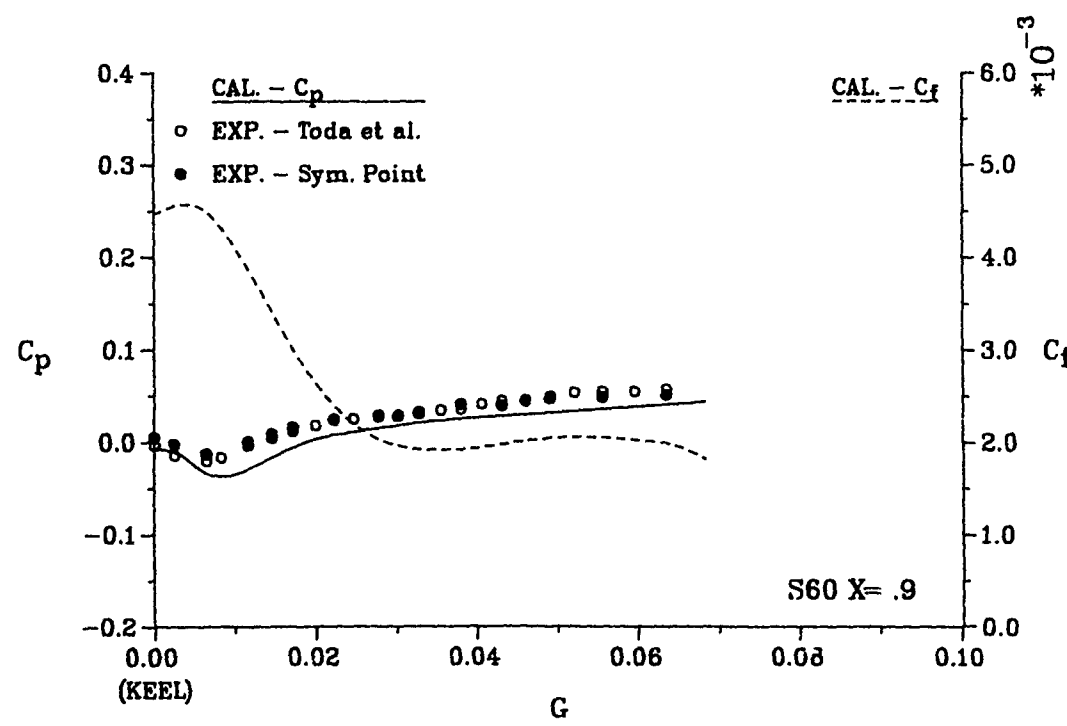
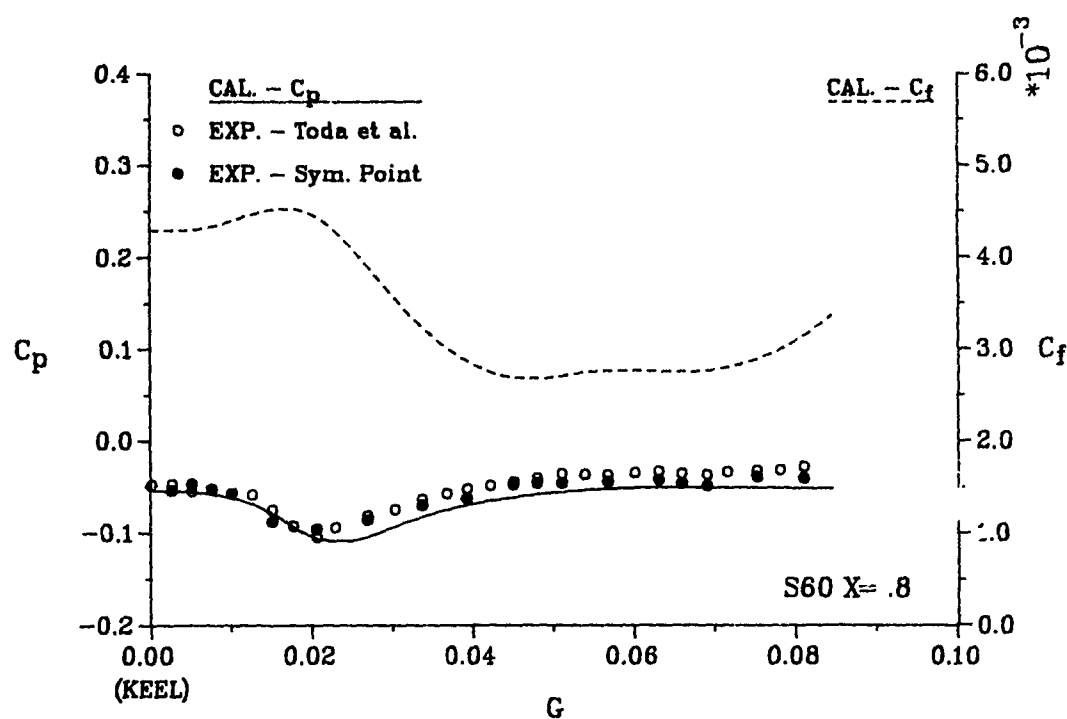


Fig. 53 Girthwise variation of pressure and friction coefficients
(a) $X = 0.8$; (b) $X = 0.9$

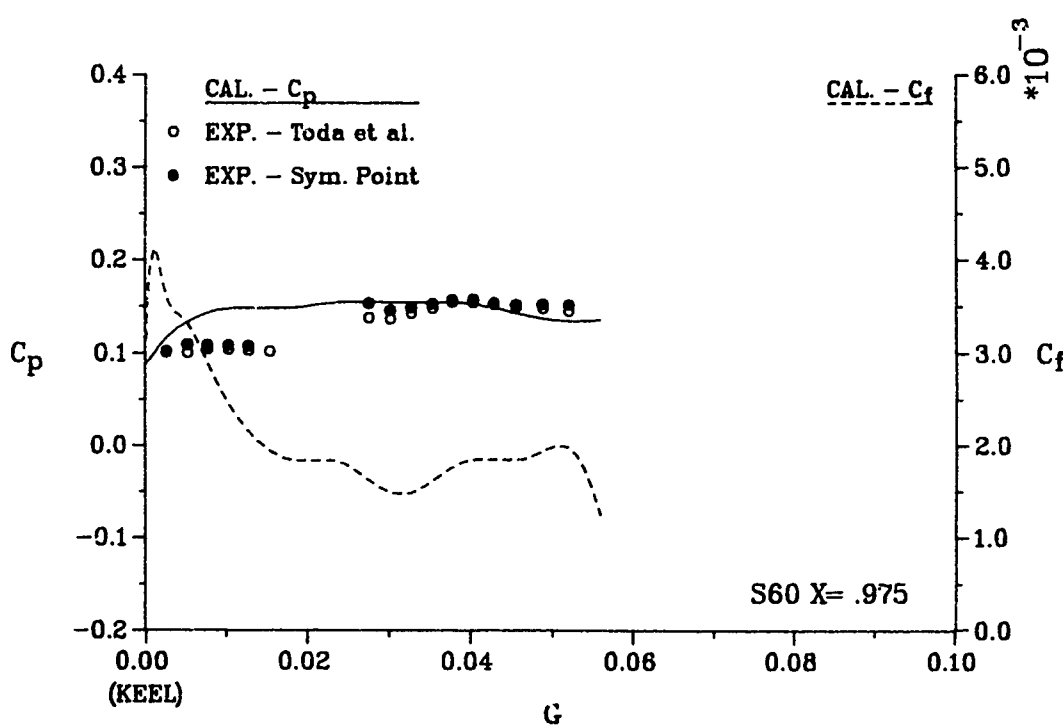
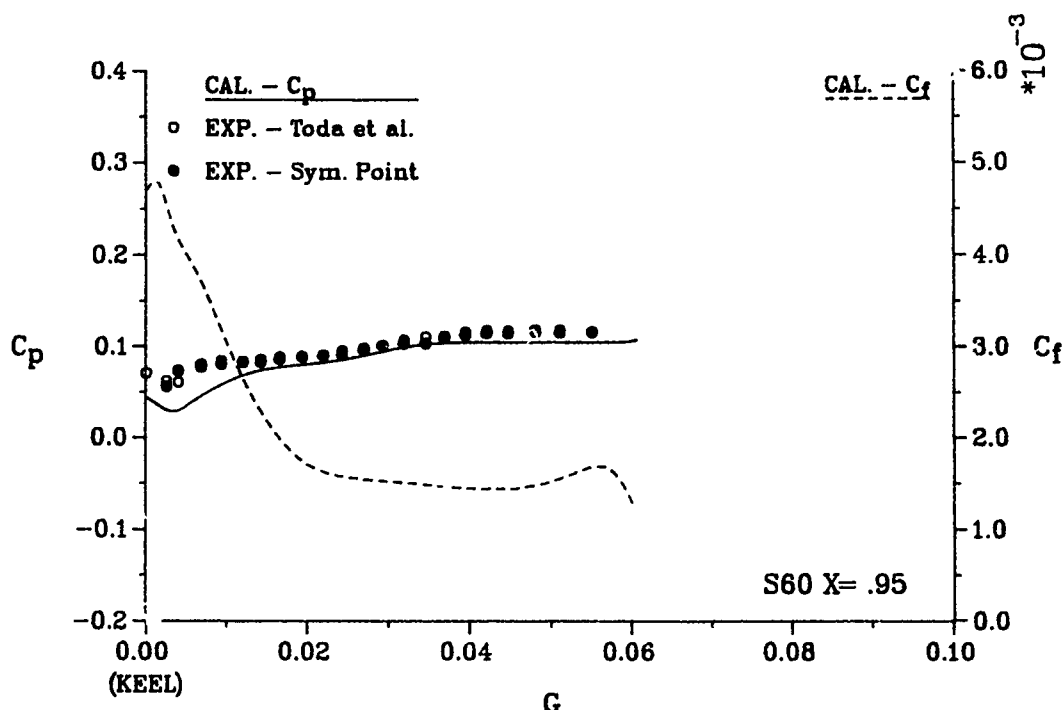


Fig. 53 Girthwise variation of pressure and friction coefficients
(c) $X = 0.95$; (d) $X = 0.975$

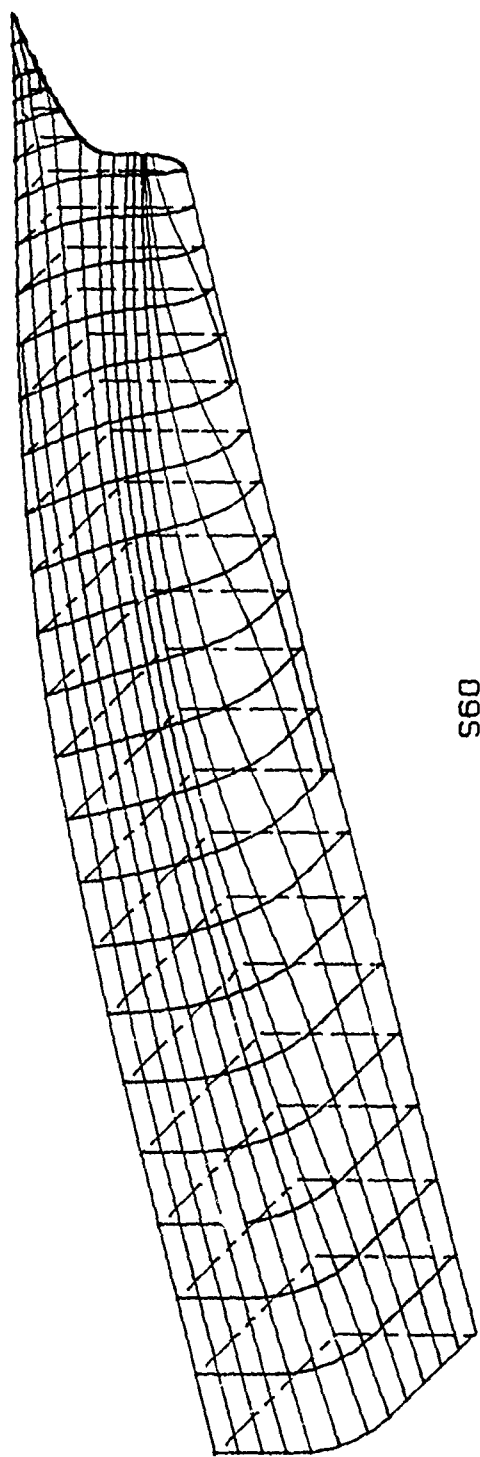


Fig. 54 Calculated wall streamlines

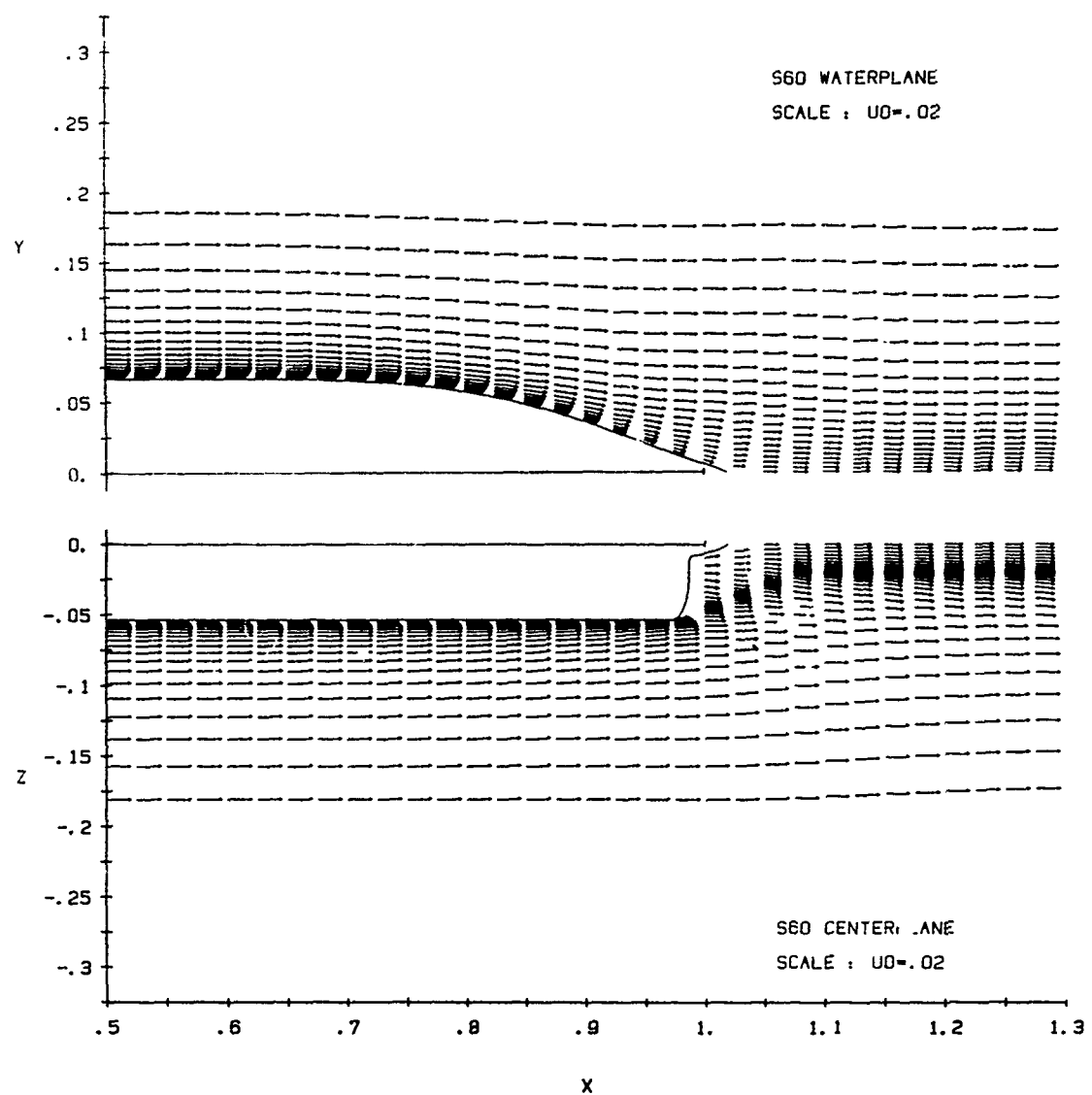


Fig. 55 Velocity vectors in the waterplane (top) and in the vertical centerplane (bottom)

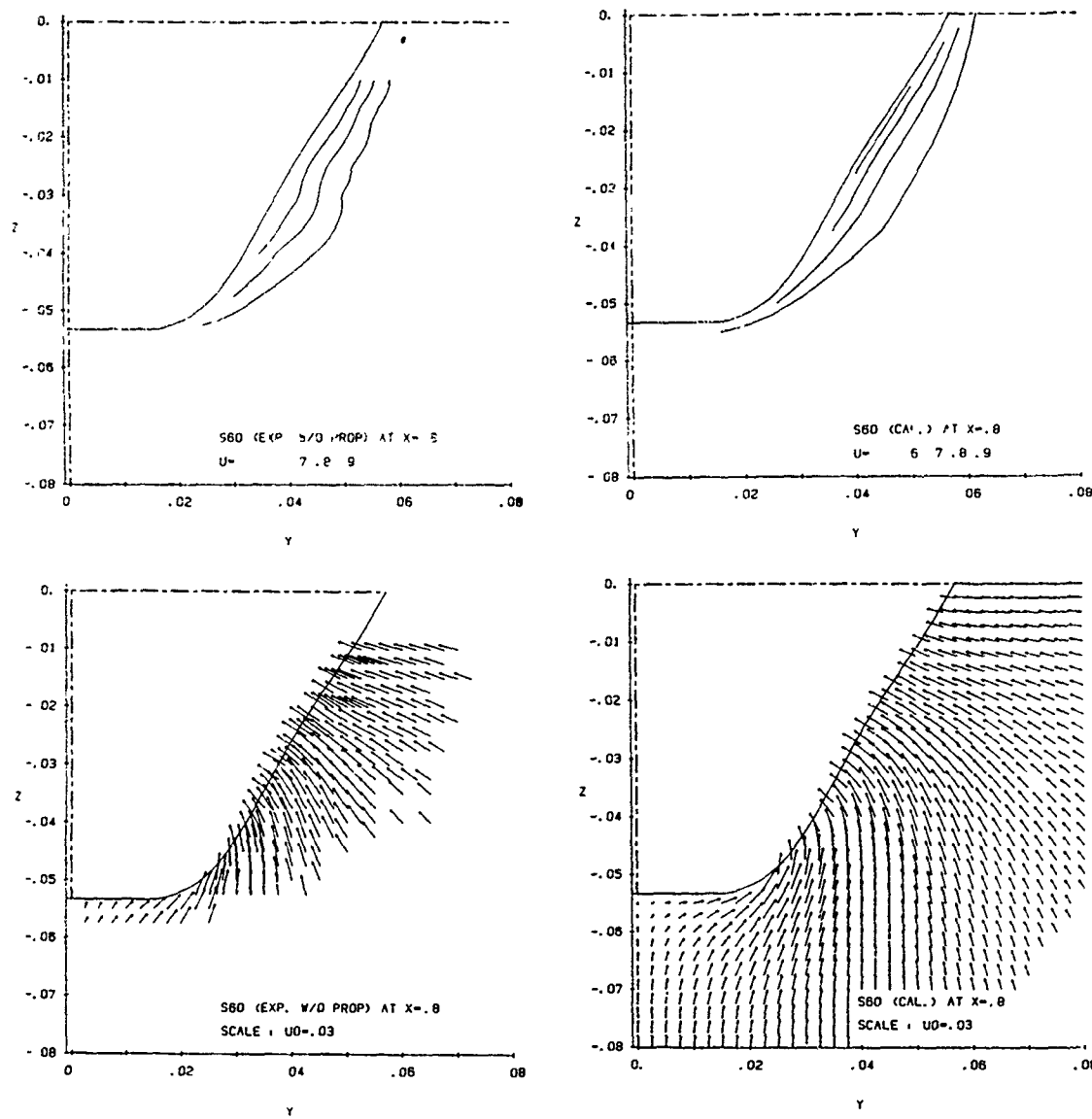


Fig. 56 Velocity field in transverse sections : (a) $X = 0.8$
 Top: contours of axial velocity (U); Bottom: velocity (V, W) in transverse sections
 Left: experiments of Toda et al; Right: present calculations

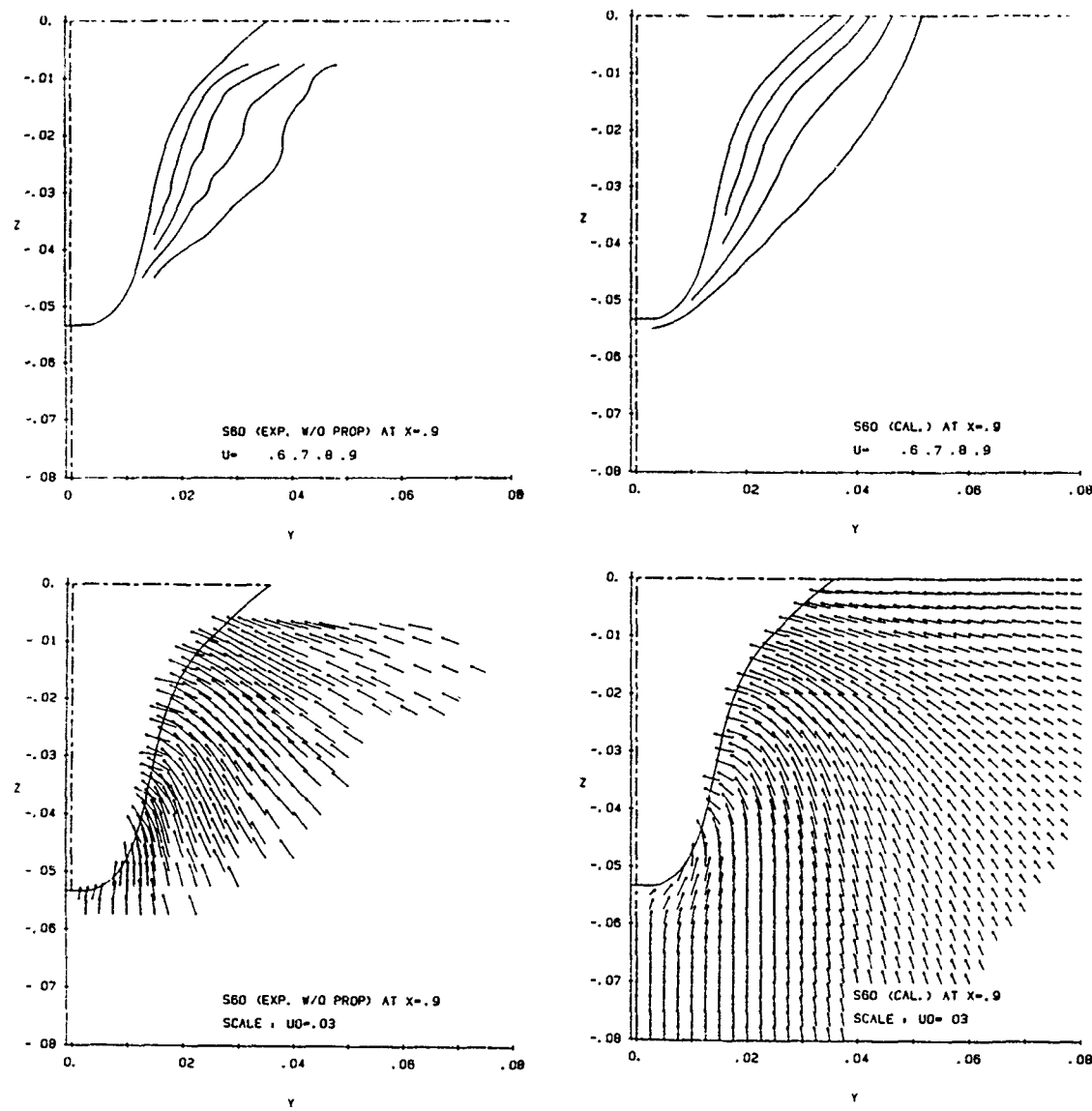


Fig. 56 Velocity field in transverse sections : (b) $X = 0.9$
Top: contours of axial velocity (U); Bottom: velocity (V, W) in transverse sections
Left: experiments of Toda et al; Right: present calculations

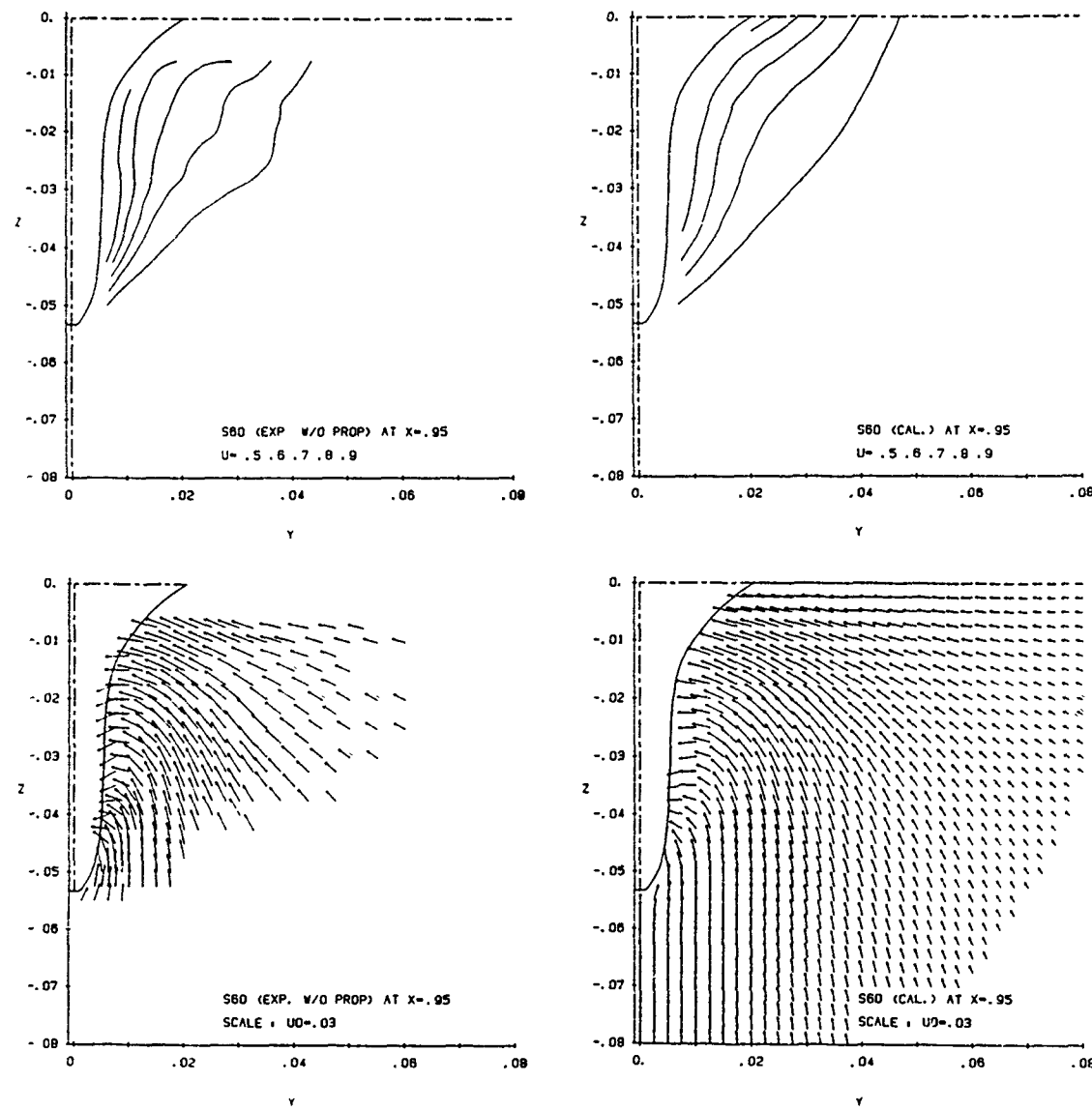


Fig. 56 Velocity field in transverse sections : (c) $X = 0.95$
Top: contours of axial velocity (U); Bottom: velocity (V, W) in transverse sections
Left: experiments of Toda et al; Right: present calculations

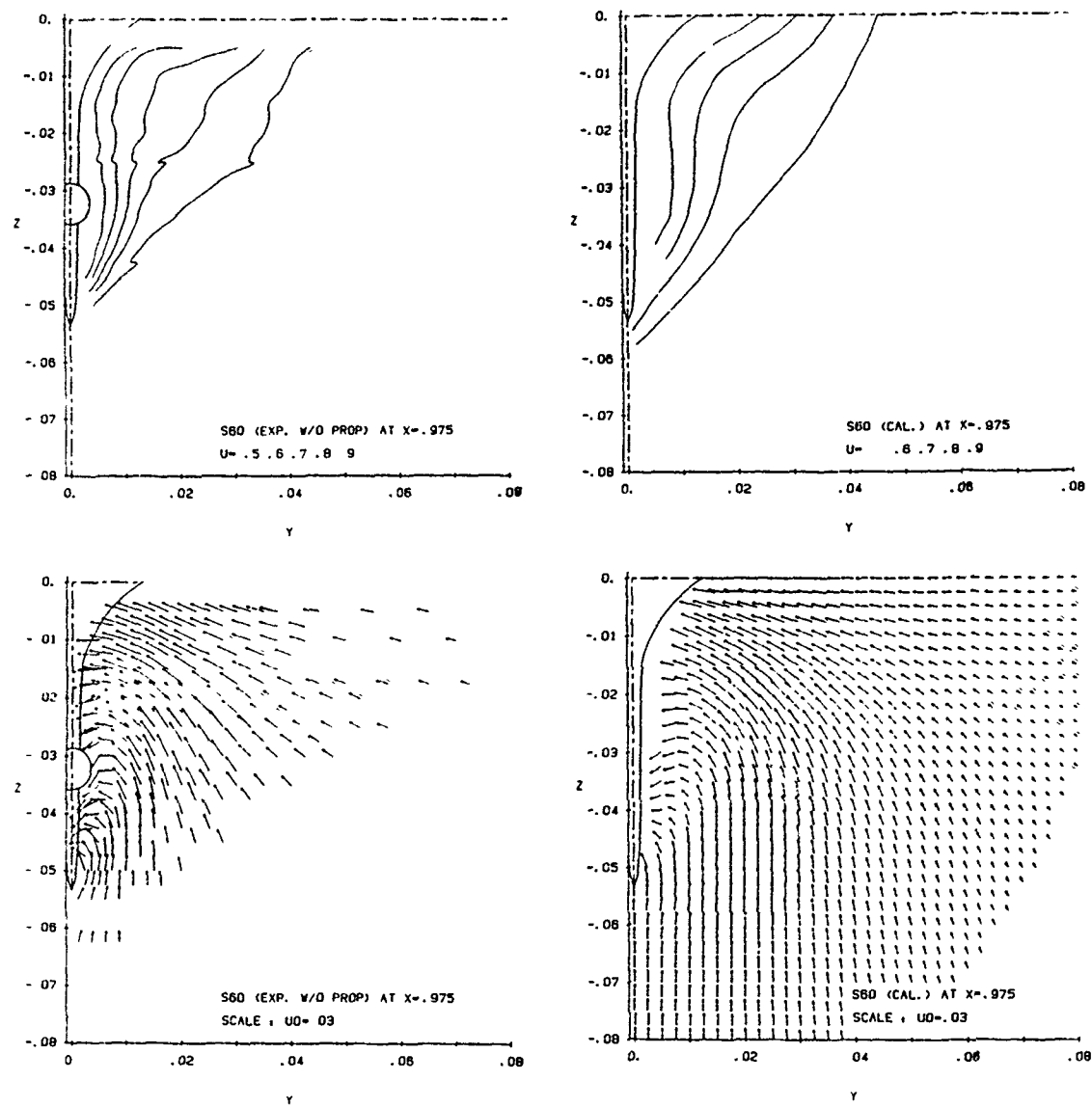


Fig. 56 Velocity field in transverse sections : (d) $X = 0.975$
Top: contours of axial velocity (U); Bottom: velocity (V, W) in transverse sections
Left: experiments of Toda et al; Right: present calculations

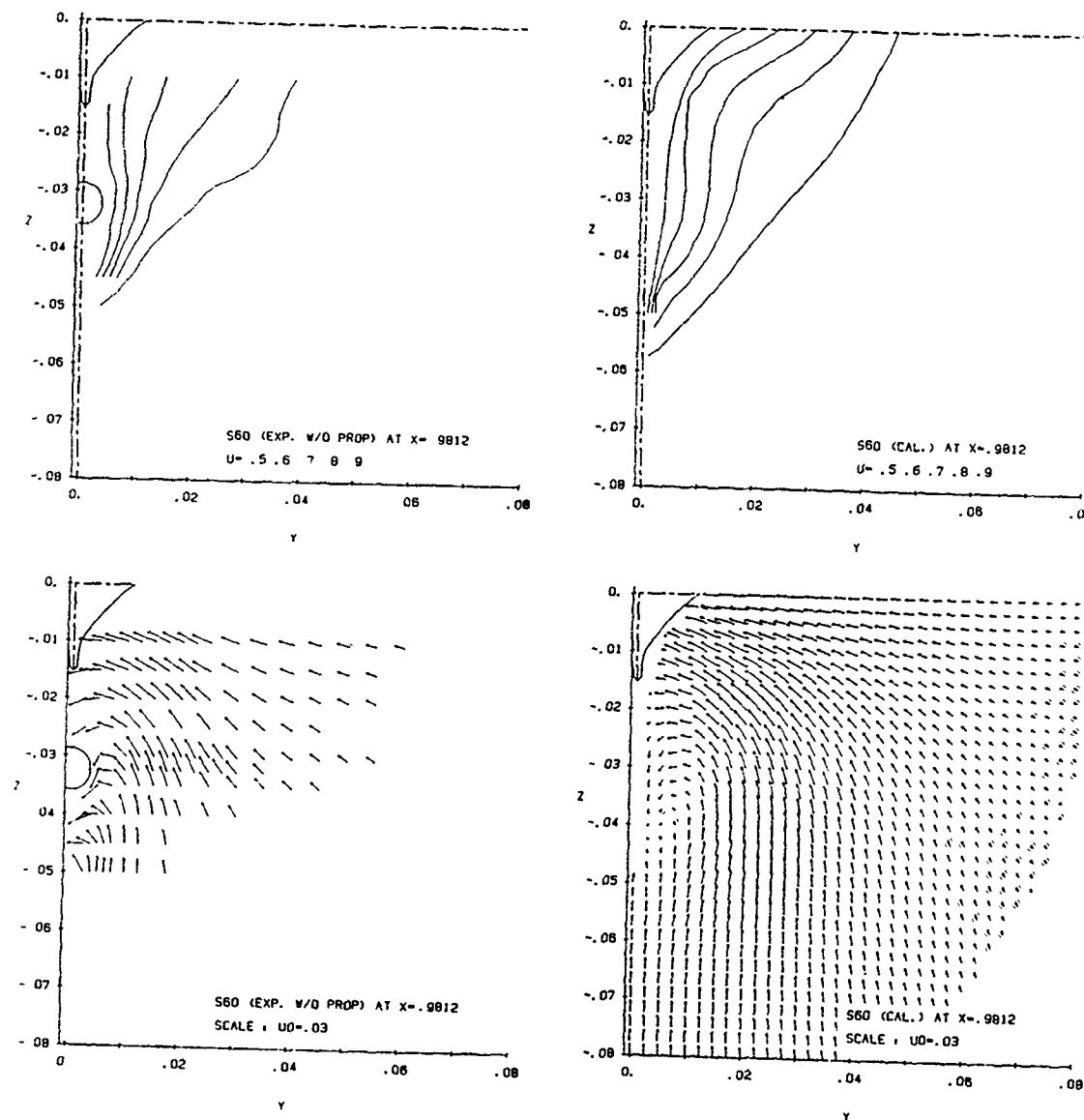


Fig. 56 Velocity field in transverse sections : (e) $X = 0.9812$
 Top: contours of axial velocity (U); Bottom: velocity (V,W) in transverse sections
 Left: experiments of Toda et al; Right: present calculations

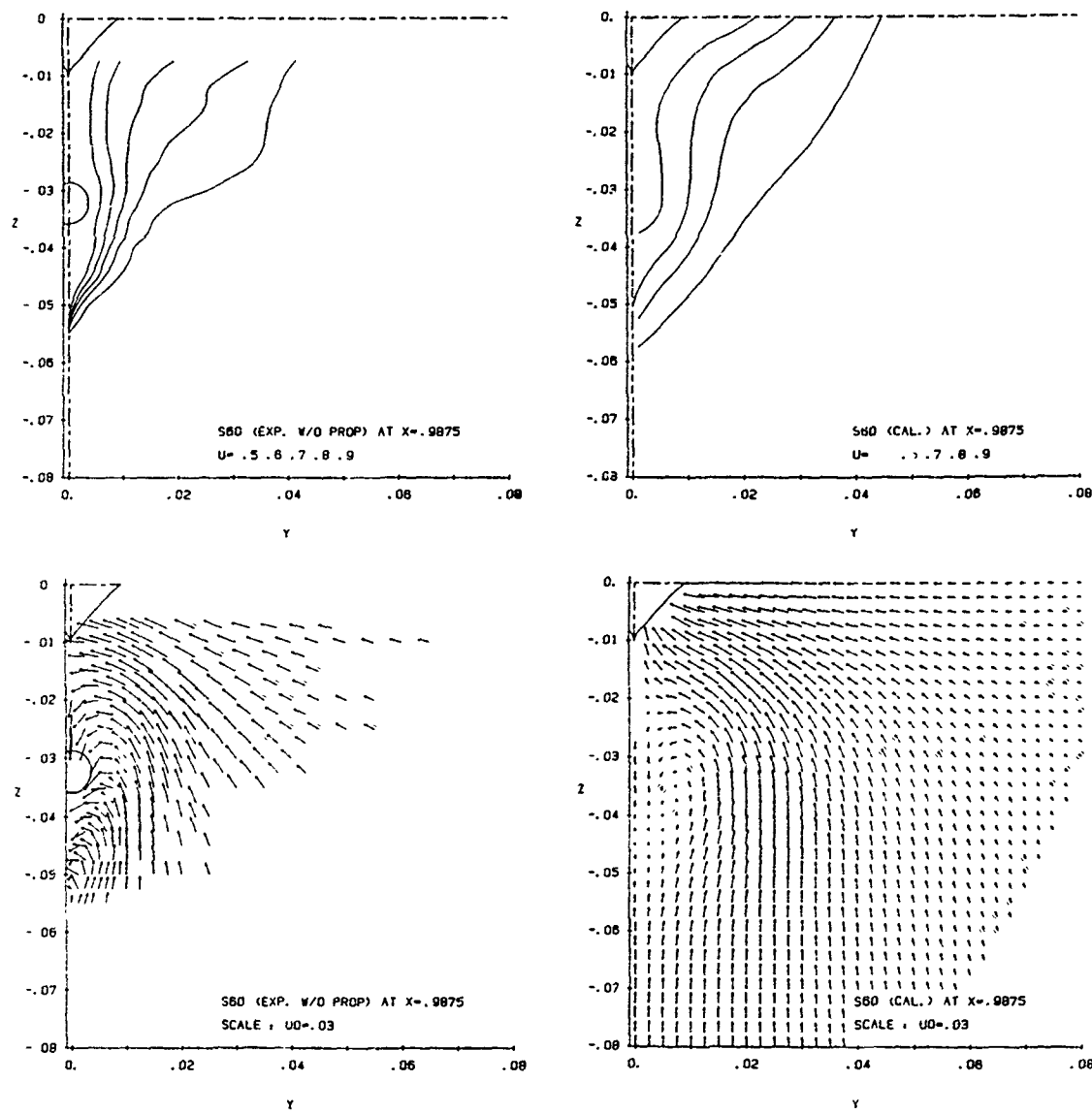


Fig. 56 Velocity field in transverse sections : (f) $X = 0.9875$
 Top: contours of axial velocity (U); Bottom: velocity (V, W) in transverse sections
 Left: experiments of Toda et al; Right: present calculations

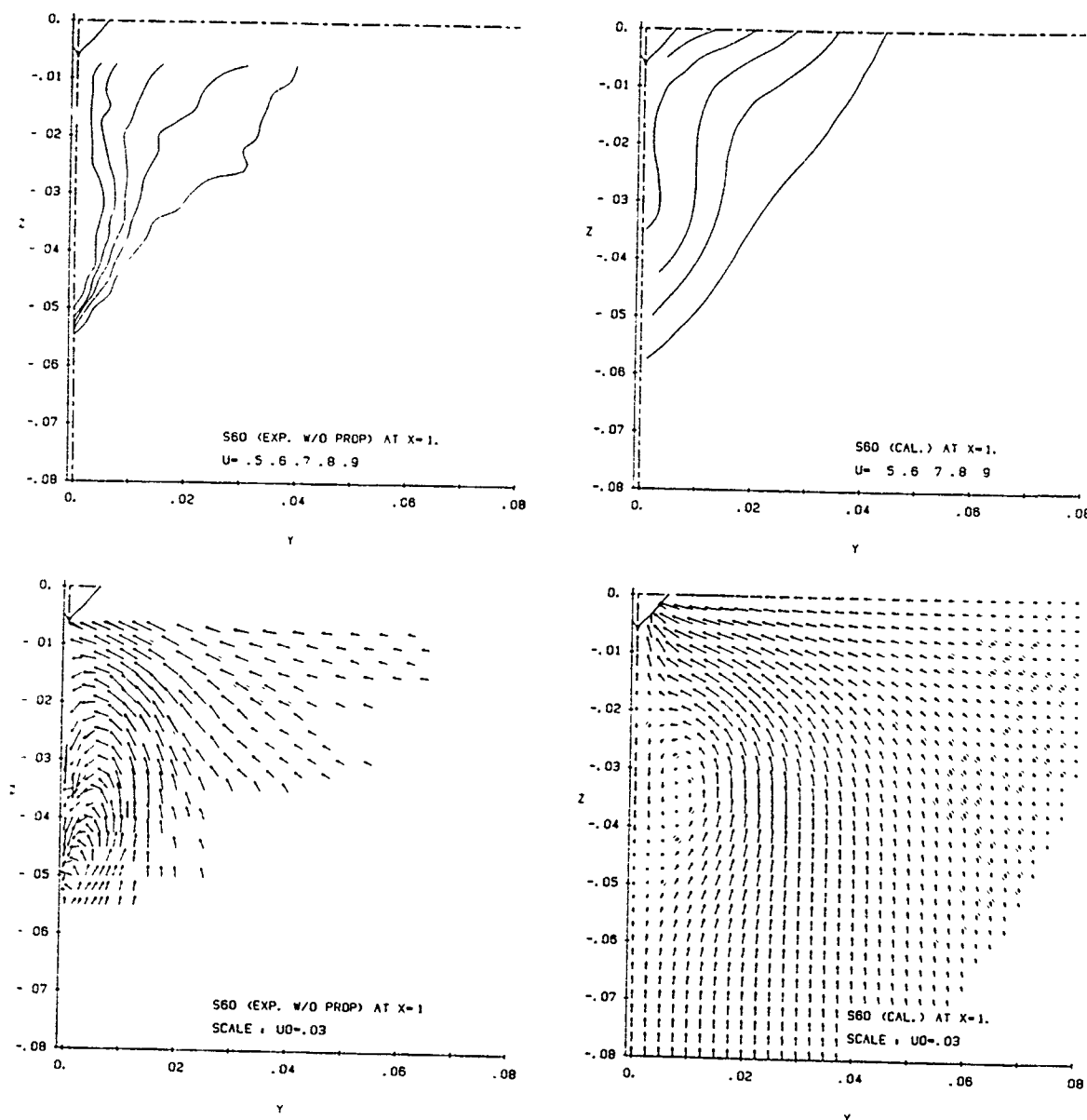


Fig. 56 Velocity field in transverse sections : (g) $X = 1.00$
 Top: contours of axial velocity (U); Bottom: velocity (V, W) in transverse sections
 Left: experiments of Toda et al; Right: present calculations

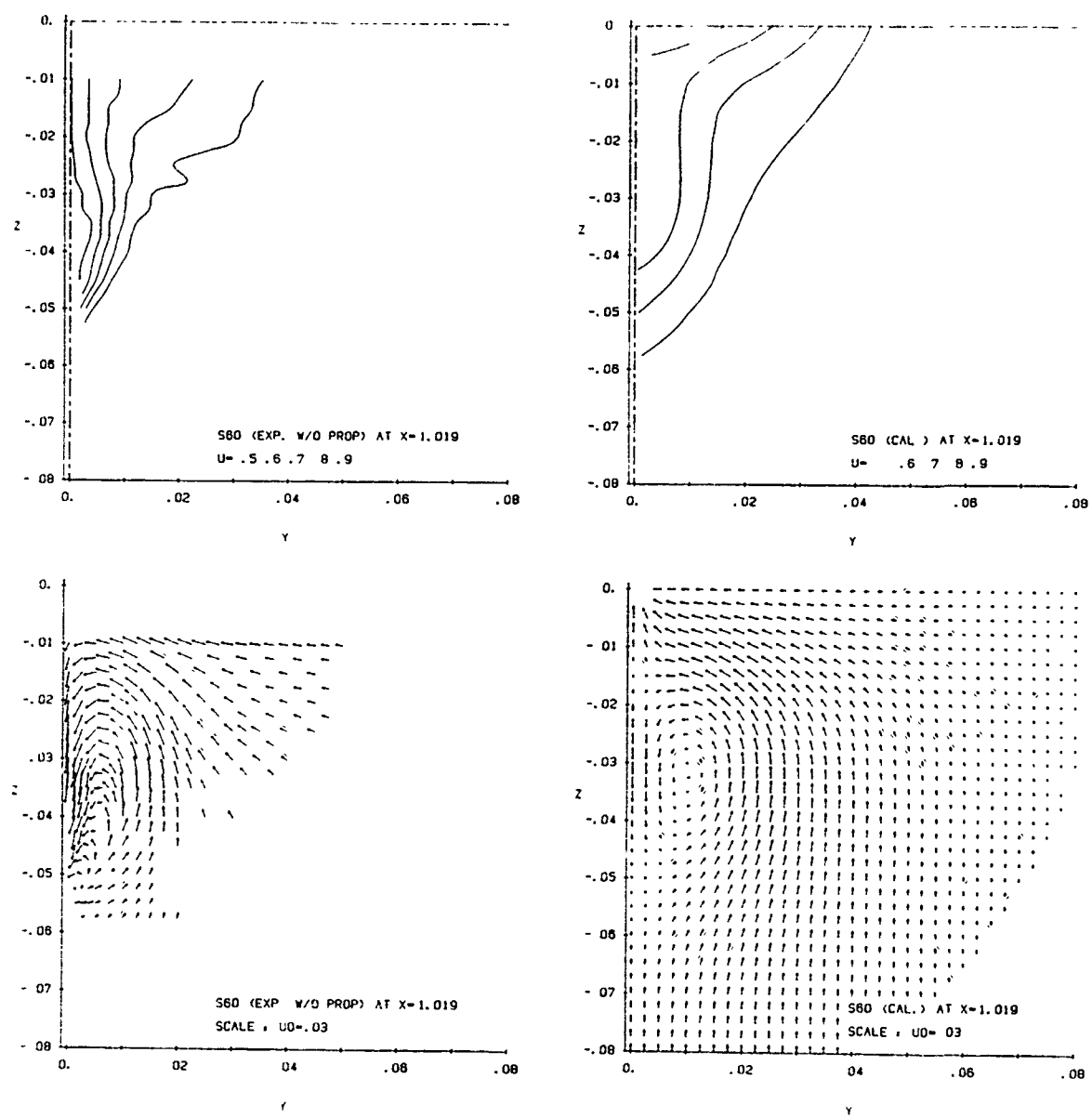


Fig. 56 Velocity field in transverse sections : (h) $X = 1.019$
 Top: contours of axial velocity (U); Bottom: velocity (V,W) in transverse sections
 Left: experiments of Toda et al; Right: present calculations

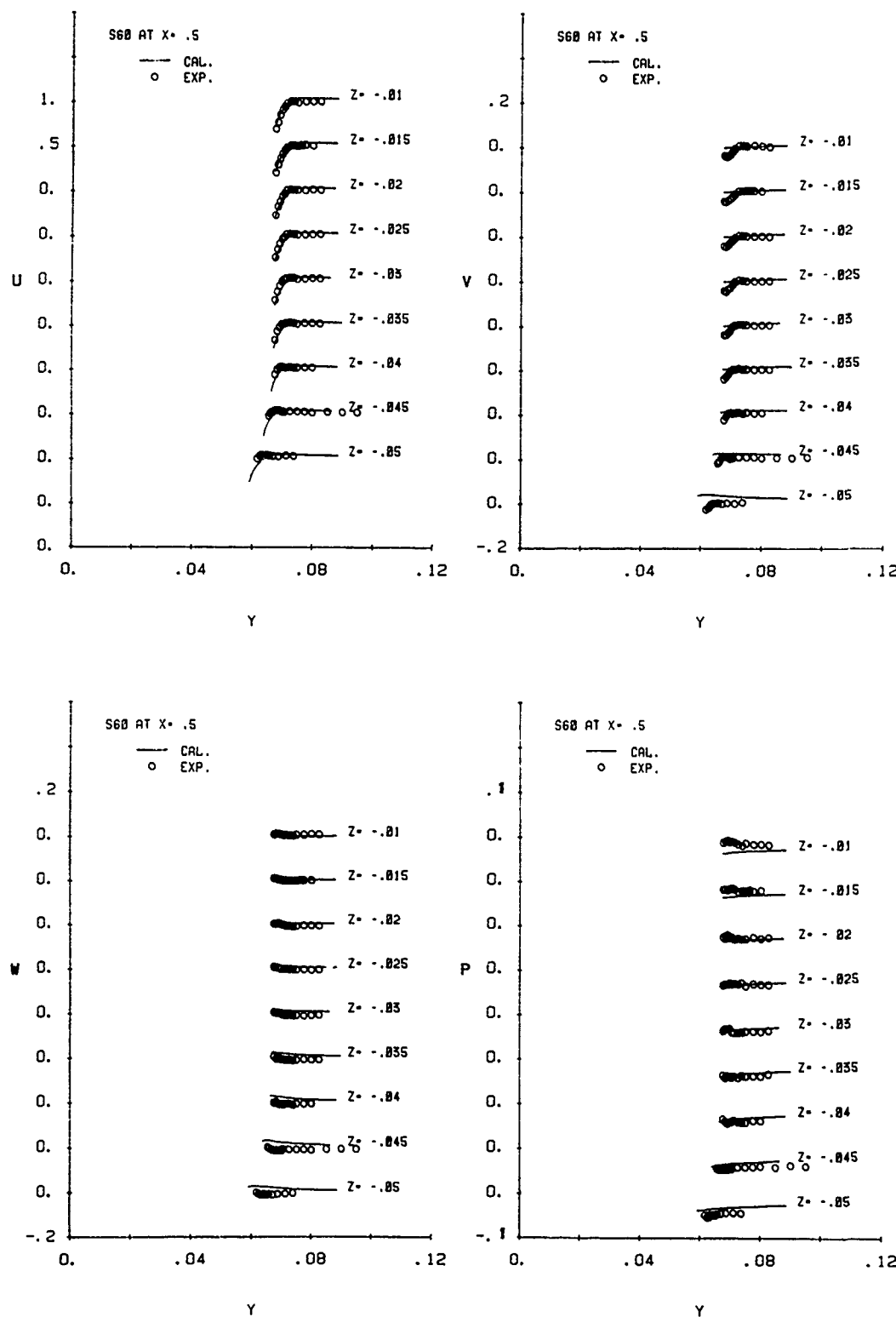


Fig. 57 Detailed comparisons of the velocity and pressure fields: profiles of U, V, W , and P
(a) $X = 0.5$

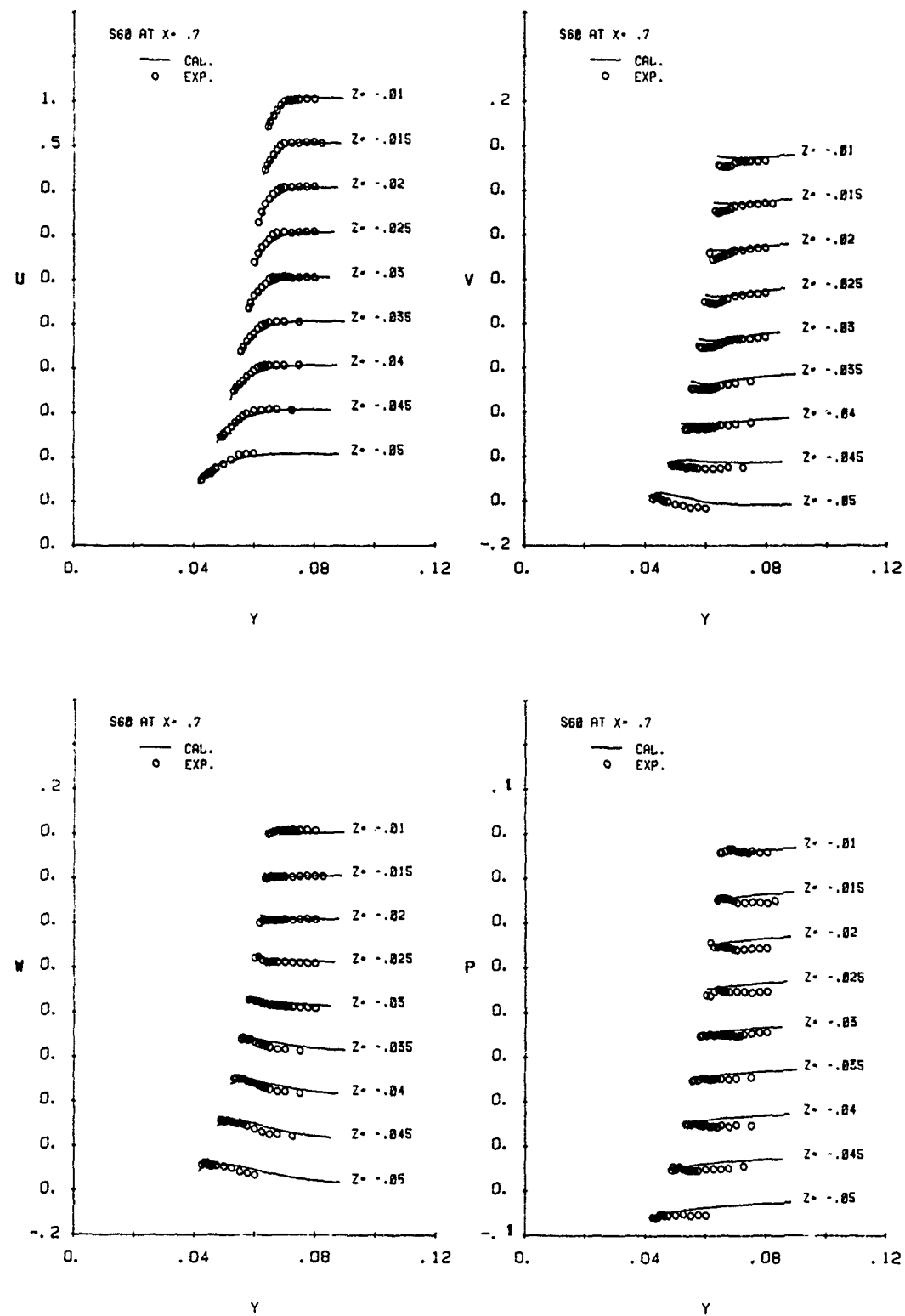


Fig. 57 Detailed comparisons of the velocity and pressure fields: profiles of U, V, W, and P
(b) $X = 0.7$

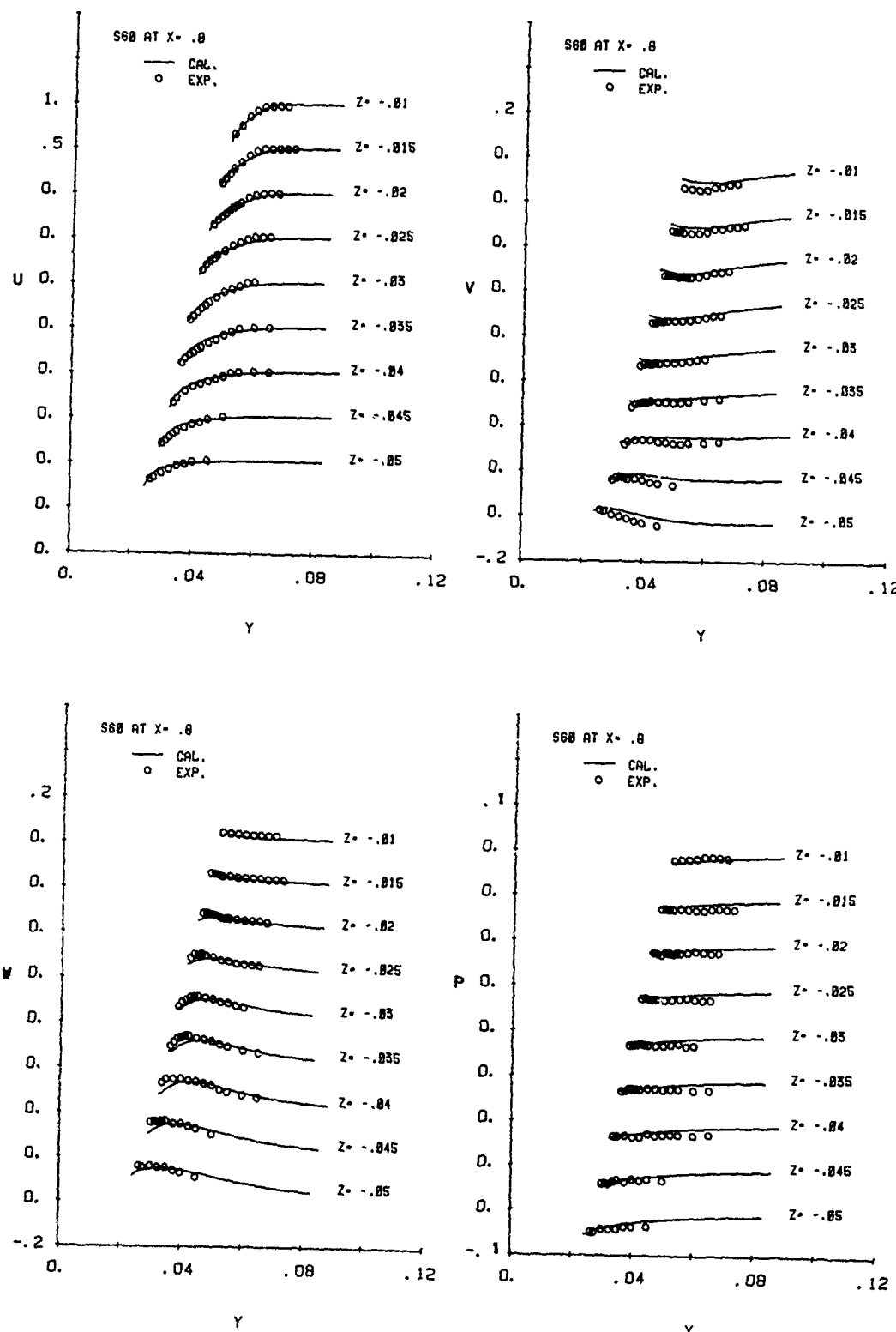


Fig. 57 Detailed comparisons of the velocity and pressure fields: profiles of U, V, W , and P
(c) $X = 0.8$

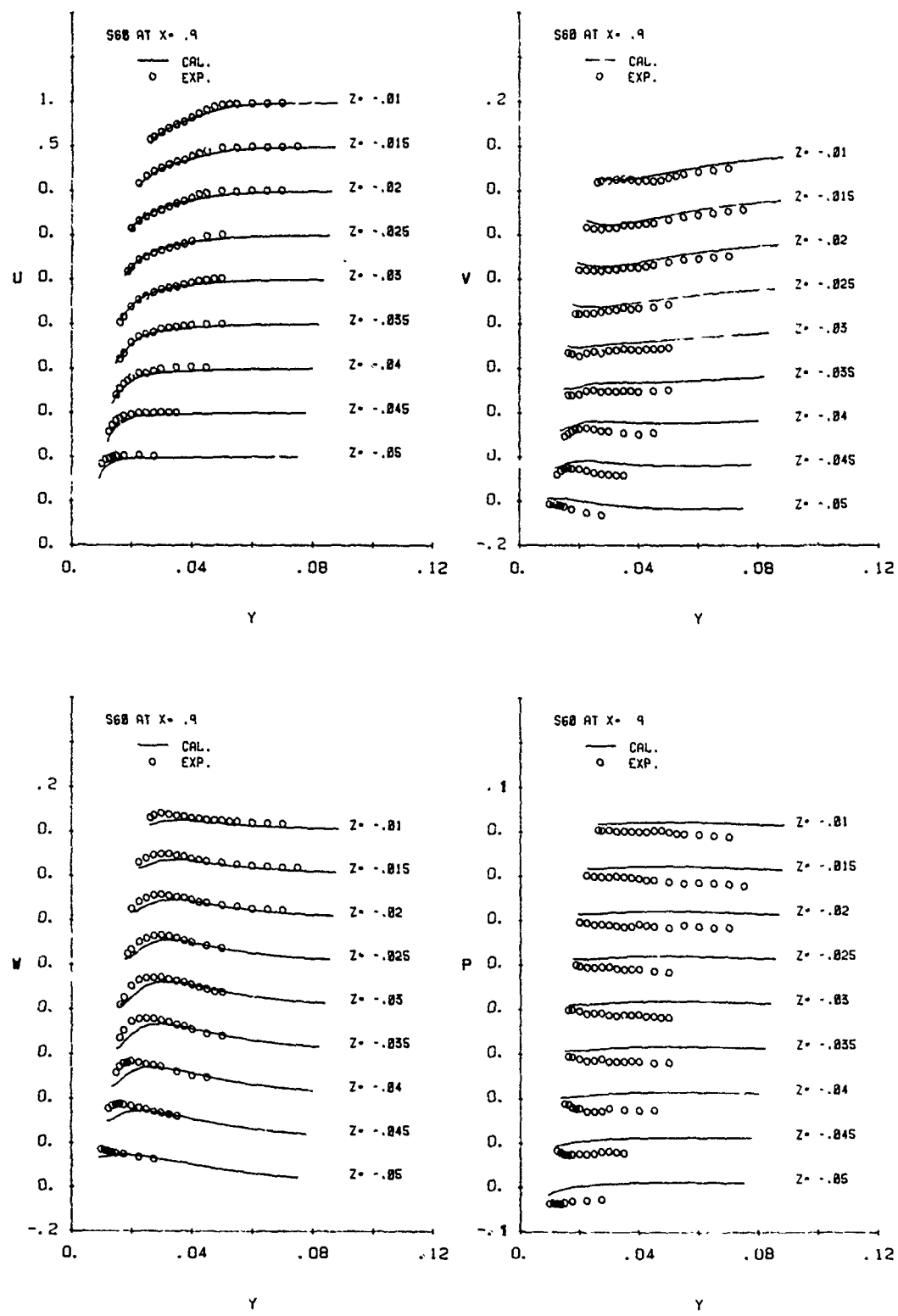


Fig. 57 Detailed comparisons of the velocity and pressure fields: profiles of U, V, W, and P (d) $X = 0.9$

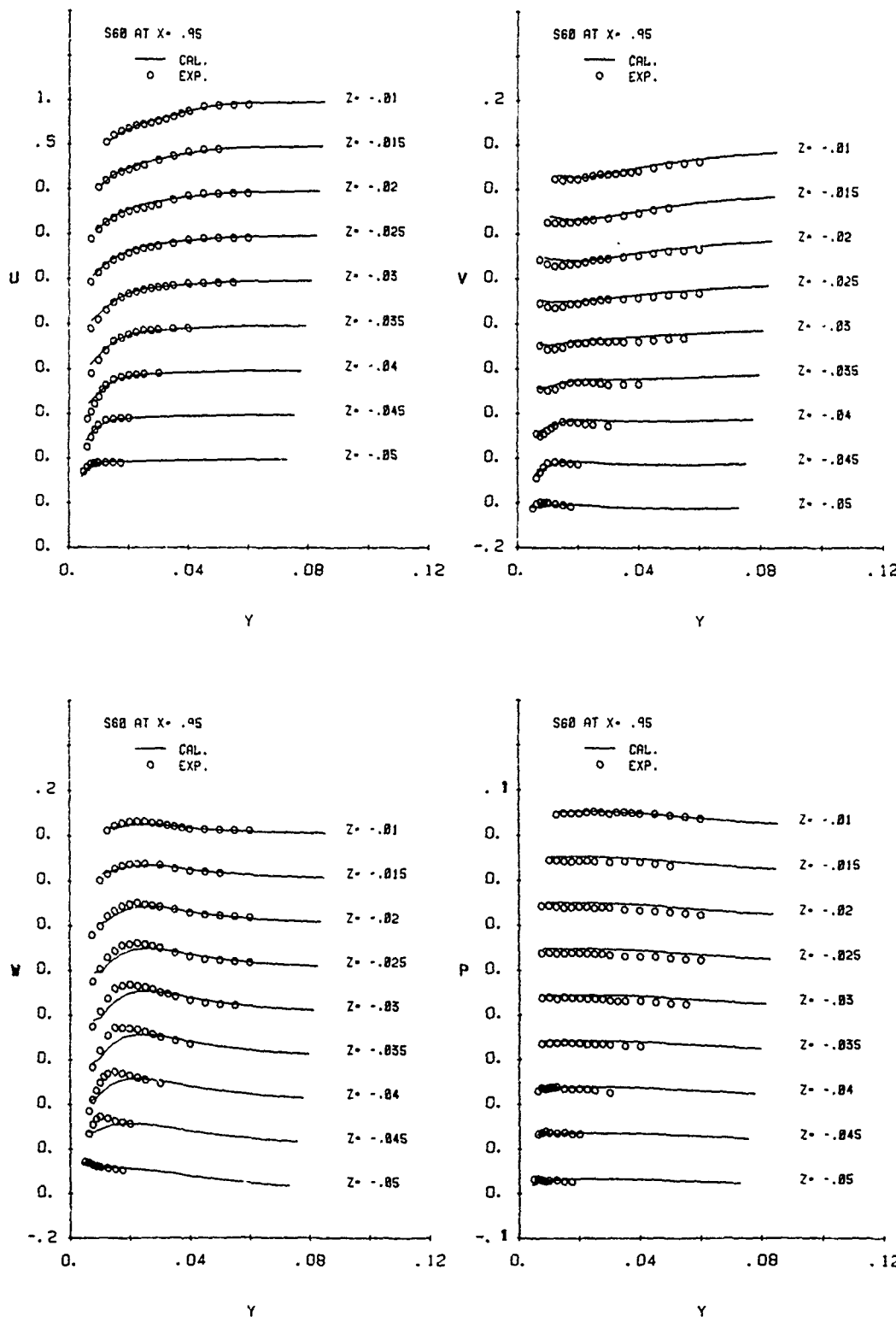


Fig. 57 Detailed comparisons of the velocity and pressure fields: profiles of U, V, W, and P
(e) $X = 0.95$

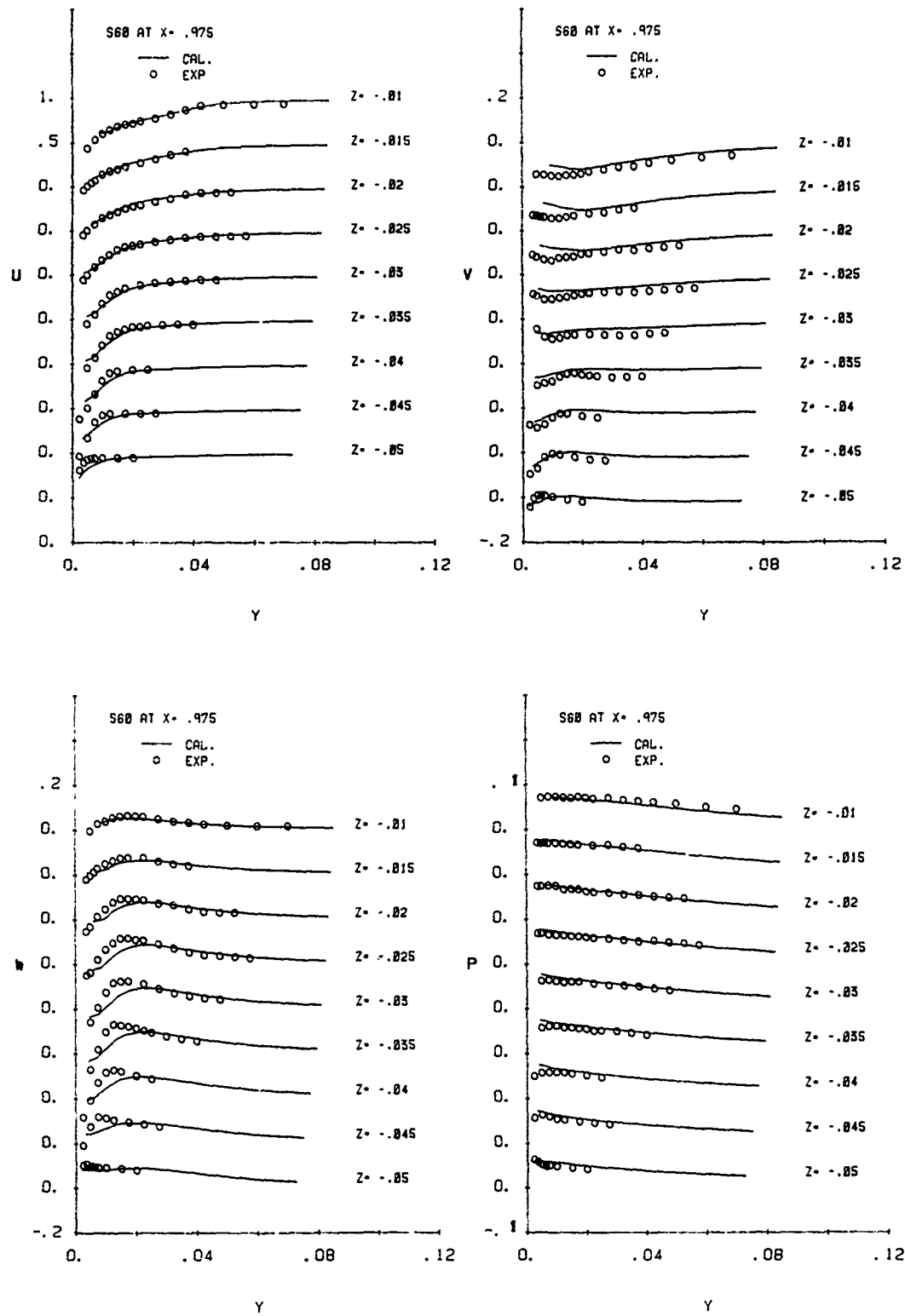


Fig. 57 Detailed comparisons of the velocity and pressure fields: profiles of U,V,W, and P
(f) $X = 0.975$

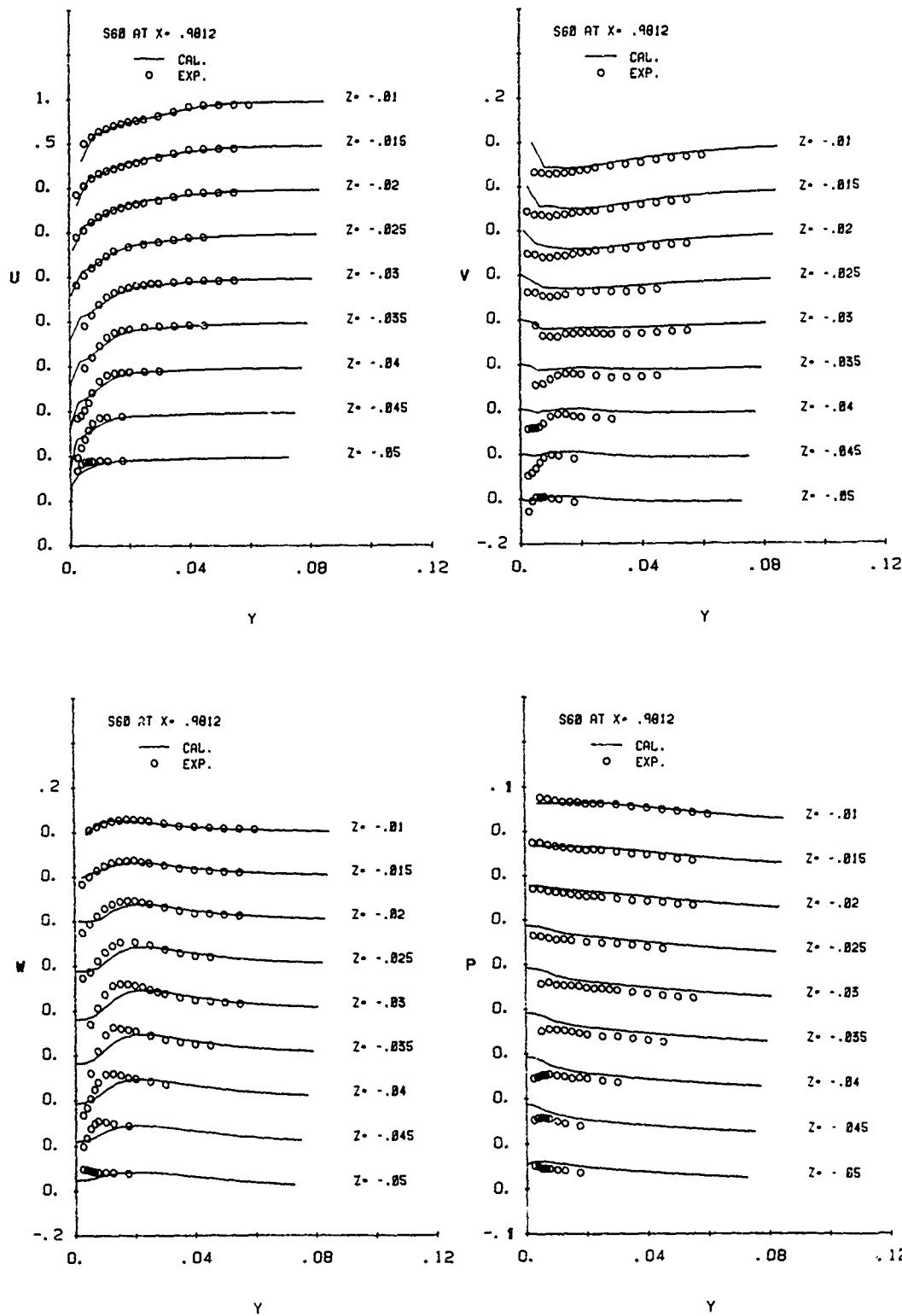


Fig. 57 Detailed comparisons of the velocity and pressure fields: profiles of U, V, W, and P
(g) $X = 0.9812$

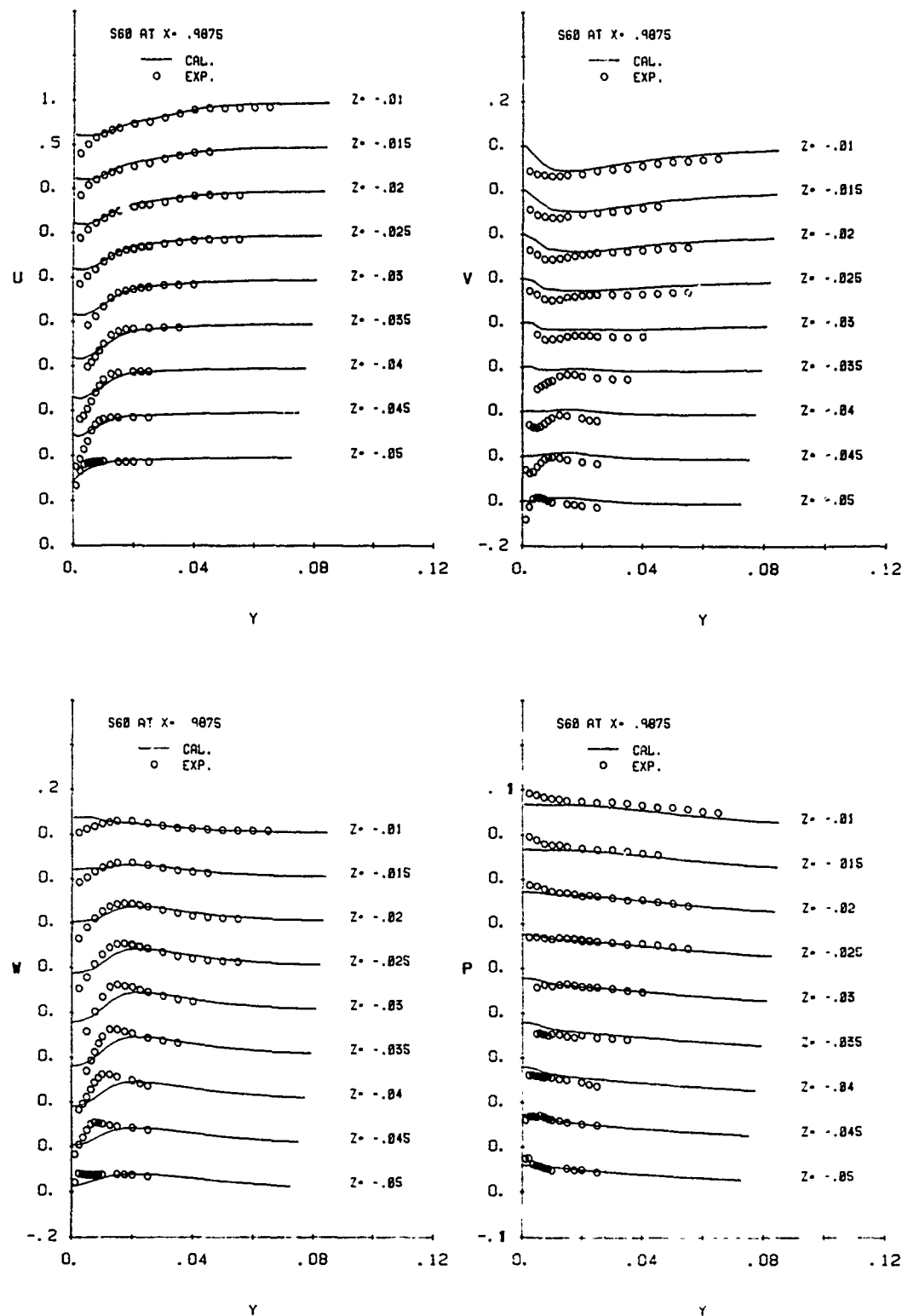


Fig. 57 Detailed comparisons of the velocity and pressure fields: profiles of U, V, W, and P
(h) $X = 0.9875$

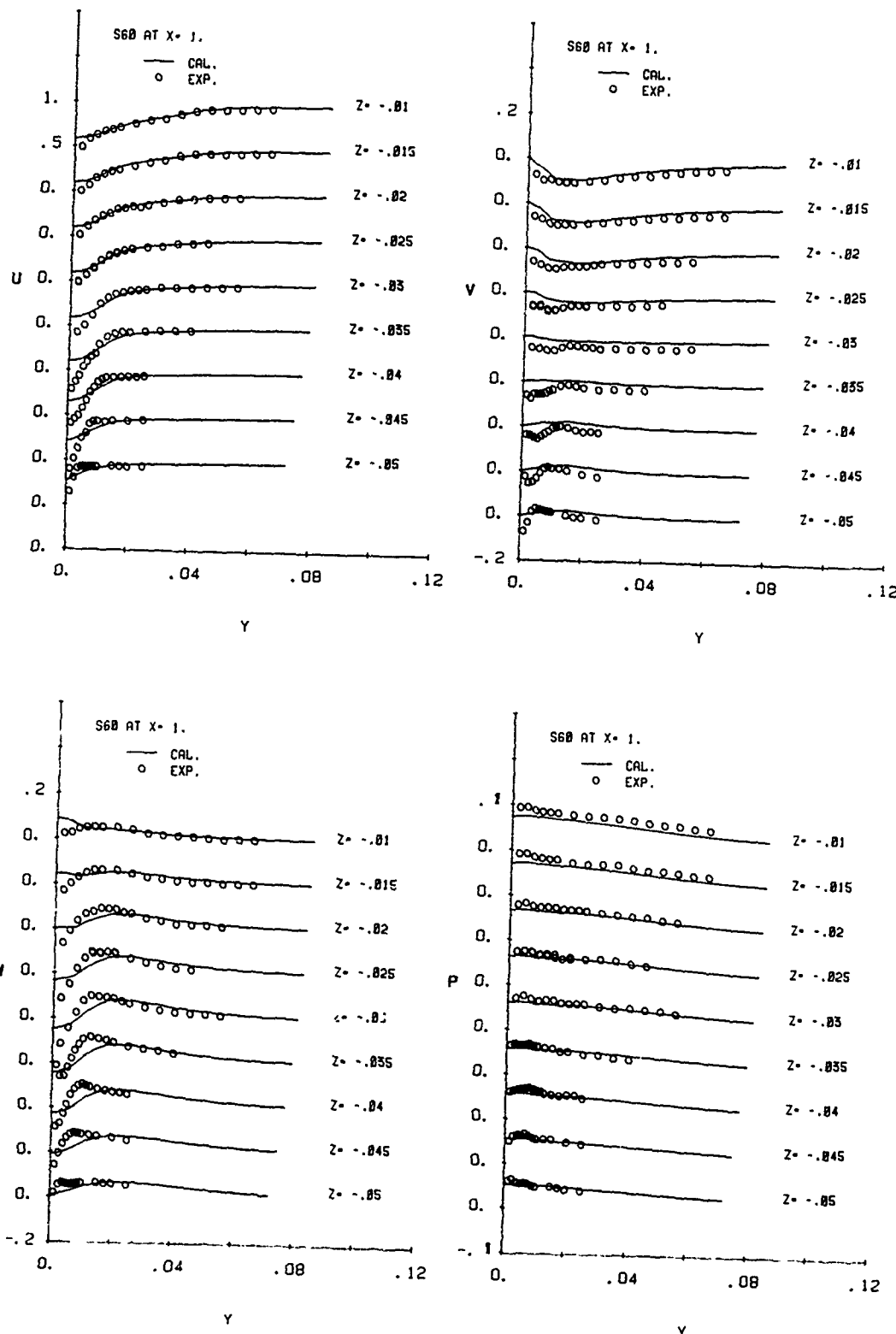


Fig. 57 Detailed comparisons of the velocity and pressure fields: profiles of U, V, W, and P
(i) $X = 1.0$

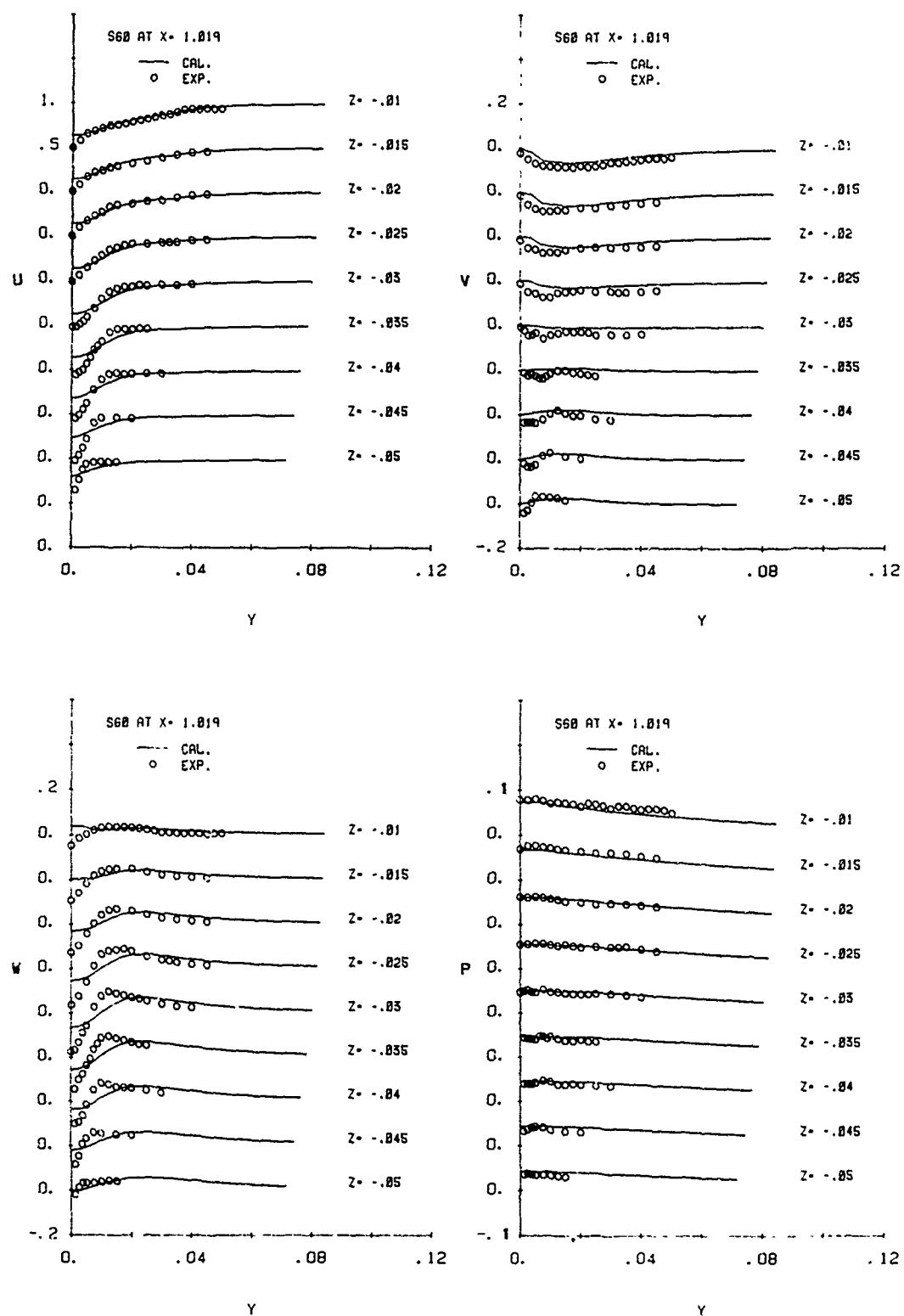


Fig. 57 Detailed comparisons of the velocity and pressure fields: profiles of U, V, W, and P
(j) $X = 1.019$

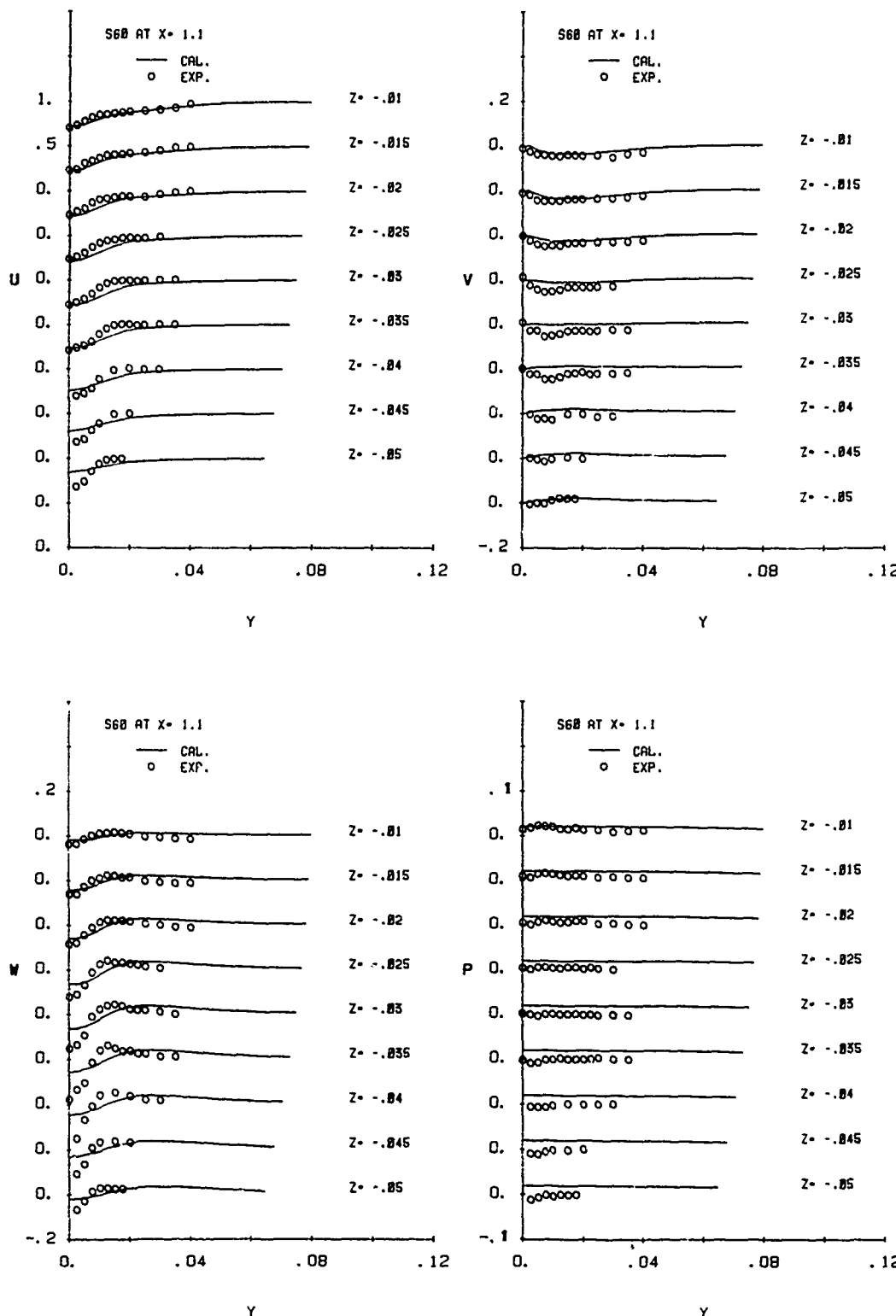


Fig. 57 Detailed comparisons of the velocity and pressure fields: profiles of U,V,W, and P
(k) X = 1.1

**DISTRIBUTION LIST FOR TECHNICAL REPORTS
ONR FLUID DYNAMICS PROGRAM (HYDRODYNAMICS)**

Defense Technical Information
Center
Information Facility
Alexandria, VA 22314
12 copies

NASA Scientific and Technical
Information Facility
P.O. Box 8757
Baltimore/Washington
International Airport
Maryland 21240

Office of Naval Research
Code 432F
800 N. Quincy Street
Arlington, VA 22217
3 copies

Library
David Taylor Naval Ship Research
and Development Center
Code 522.1
Bethesda, MD 20084

Library
U.S. Naval Academy
Annapolis, MD 21402

The Society of Naval Architects and
Marine Engineers
One World Trade Center, Suite 1369
New York, NY 10048

Technical Library
Naval Coastal System Center
Panama City, FL 32401

Technical Library
Naval Ship Engineering Center
Philadelphia Division
Philadelphia, PA 19112

Naval Research Laboratory
Code 2627
Washington, DC 20375

Library
Naval Sea Systems Command
Code 09GS
Washington, DC 20362

Dr. O.M. Griffin
Code 5841
Naval Research Laboratory
Washington, DC 20375

Dr. T.F. Zien
Code R44
Naval Surface Weapons Center
White Oak Lab.
Silver Spring, MD 20910

Dr. W.K. Blake
Code 1905.1
DTNSRDC
Bethesda, MD 20854

Dr. T.T. Huang
Code 1542
DTNSRDC
Bethesda, MD 20084

Prof. T. Sarpkaya
Dept. of Mechanical Engineering
Code 69-SL
Naval Postgraduate School
Monterey, CA 93940

Dr. W.C. Lin
Code 152
DTNSRDC
Bethesda, MD 20084

Mr. J.H. McCarthy
Code 154
DTNSRDC
Bethesda, MD 20084
Mr. D.S. Cieslowski
Code 156
DTNSRDC
Bethesda, MD 20084

Mr. V.J. Monacella
Code 1504
DTNSRDC
Bethesda, MD 20084

Dr. H. Haussling
Code 1843
DTNSRDC
Bethesda, MD 22084

Mr. E.N. Comstock
Code 55W3
Naval Sea Systems Command
Washington, DC 20362

Dr. A.L. Slafkosky
Scientific Advisor
Commandant of the Marine Corps
Code AX
Washington, DC 20380

Maritime Administration
Division of Naval Architecture
14th & E Streets, NW
Washington, DC 20230

Lorenz G. Straub Library
University of Minnesota
St. Anthony Falls Hydraulic
Laboratory
Minneapolis, MN 55414

Technical Library
Naval Ocean Systems Center
San Diego, CA 92152

Librarian
University of California
Department of Naval
Architecture and Offshore
Engineering
Berkeley, CA 94720

Technical Library
Webb Institute of Naval
Architecture
Glen Cove, NY 11542

Library
Stevens Institute of Tech.
Davidson Laboratory
Castle Point Station
Hoboken, NJ 07030

R.E. Gibson Library
The Johns Hopkins University
Applied Physics Laboratory
Johns Hopkins Road
Laurel, MD 20810

Library
Naval Postgraduate School
Monterey, CA 93940

Librarian
Naval Surface Weapons Center
White Oak Laboratory
Silver Spring, MD 20910

Technical Library
Naval Underwater Systems
Center
Newport, RI 02840

Library
Department of Ocean
Engineering
Massachusetts Institute of
Technology
Cambridge, MA 01778
Engineering Societies Library
345 East 47th Street
New York, NY 10017

Library
Dept. of Naval Architecture
and Marine Engineering
University of Michigan
Ann Arbor, MI 48109

Librarian Station 5-2
Coast Guard Headquarters
NASSIF Building
400 Seventh Street, SW
Washington, DC 20591

Library
Applied Research Laboratory
The Pennsylvania State University
P.O. Box 30
State College, PA 16801

Library of Congress
Science and Technology Division
Washington, DC 20540

Library
Marine Physical Laboratory
Scripps Institution of Oceanography
University of California at San Diego
San Diego, CA 92152

Library
Applied Research Laboratories
University of Texas at Austin
Austin, TX 78712

Editor
Applied Mechanics Review
Southwest Research Institute
8500 Culebra Road
San Antonio, TX 78206

Library
Institute of Hydraulic Research
The University of Iowa
Iowa City, IA 52242

Library
Southwest Research Institute
8500 Culebra Road
San Antonio, TX 78228

Mr. Dennis Bushnell
NASA Langley Research Center
Langley Station
Hampton, VA 23365

Dr. A.K.M. Fazle Hussain
University of Houston
Department of Mechanical Engineering
Houston, TX 77004

Professor John L. Lumley
Cornell University
Sibley School of Mechanical and
Aerospace
Engineering
Ithaca, NY 14853

Professor W.W. Willmarth
The University of Michigan
Department of Aerospace Engineering
Ann Arbor, MI 48109

Professor A. Roshko
California Institute of Technology
Graduate Aeronautical Laboratories
Pasadena, CA 91125

Professor Patrick Leehey
Massachusetts Institute of Technology
Department of Ocean Engineering
Cambridge, MA 02139

Professor Eli Reshotko
Case Western Reserve University
Department of Mechanical and
Aerospace Engineering
Cleveland, OH 44106

Dr. Steven A. Orszag
Cambridge Hydrodynamics, Inc.
P.O. Box 1403
Princeton, NJ 08542

Professor Tuncer Cebeci
California State University
Mechanical Engineering Department
Long Beach, CA 90840

Dr. C.W. Hirt
University of California
Los Alamos Scientific Laboratory
P.O. Box 1663
Los Alamos, NM 87544

Prof. Marshall P. Tulin
Department of Mechanical and
Environmental Engineering
University of California at Santa Barbara
Santa Barbara, CA 93106

Prof. S.G. Rubin
Department of Aerospace
Engineering and
Applied Mechanics
University of Cincinnati
Cincinnati, OH 45221

Prof. J.E. Kerwin
Department of Ocean Engineering
Massachusetts Institute of Technology
Cambridge, MA 01778

Dr. Do C. Kwak
Applied Computational
Aerodynamics Branch
NASA Ames Research Center
M/S 202A-14
Moffet Field, CA 94035

Prof. V.C. Patel
Institute of Hydraulic Research
The University of Iowa
Iowa City, IA 52242

Prof. P.G. Saffman
Department of Applied
Mathematics
California Institute of
Technology
Pasadena, CA 91125

Dr. N. Salvesen
Science Applications, Inc.
134 Holiday Court, Suite 318
Annapolis, MD 21401

Prof. O.M. Phillips
Department of Earth and
Planetary Science
Johns Hopkins University
Baltimore, MD 21218

Prof. P.M. Naghdi
Dept. of Mechanical Engineering
University of California
Berkeley, CA 94720

Prof. R.W. Yeung
Dept. of Naval Architecture
and Offshore Engineering
University of California
Berkeley, CA 94720
3 copies

Prof. T. Maxworthy
Dept. of Mechanical Engineering
University of Southern California
University Park
Los Angeles, CA 90089-0192

Prof. J. Schetz
Dept. of Aerospace & Ocean Engineering
Virginia Polytechnic Institute and
State University
Blacksburg, VA 24061
2 copies

Prof. J.B. Keller
Dept. of Mathematics
Stanford University
Stanford, CA 94305

Prof. A.J. Acosta
Dept. of Mechanical Engineering
California Institute of Technology
Pasadena, CA 91125

Prof. J.N. Newman
Dept. of Ocean Engineering
Massachusetts Institute of Technology
Cambridge, MA 01778

Dr. S.J. Shamroth
Scientific Research Associates,
Inc.
P.O. Box 498
Glastonbury, CT 06033

Prof. W.S. Vorus
Dept. of Naval Architecture and
Marine Engineering
University of Michigan
Ann Arbor, MI 48109

Prof. A.H. Nayfeh
Dept. of Engineering Sciences &
Mechanics
Virginia Polytechnic Institute and
State University
Blacksburg, VA 24061

Prof. T.Y. Wu
Dept. of Engineering Science
California Institute of Technology
Pasadena, CA 91125

Dr. J.H. Duncan
Flow Research Company
1320 Fenwick Lane, Suite 401
Silver Spring, MD 20910
Ann Arbor, MI 48109